



minerals

Special Issue Reprint

Novel Methods and Applications for Mineral Exploration, Volume II

Edited by
Paul Alexandre

mdpi.com/journal/minerals



Novel Methods and Applications for Mineral Exploration, Volume II

Novel Methods and Applications for Mineral Exploration, Volume II

Editor

Paul Alexandre



Basel • Beijing • Wuhan • Barcelona • Belgrade • Novi Sad • Cluj • Manchester

Editor

Paul Alexandre
Geology Department
Brandon University
Brandon
Canada

Editorial Office

MDPI
St. Alban-Anlage 66
4052 Basel, Switzerland

This is a reprint of articles from the Special Issue published online in the open access journal *Minerals* (ISSN 2075-163X) (available at: www.mdpi.com/journal/minerals/special_issues/exploration_volume2).

For citation purposes, cite each article independently as indicated on the article page online and as indicated below:

Lastname, A.A.; Lastname, B.B. Article Title. <i>Journal Name</i> Year , <i>Volume Number</i> , Page Range.
--

ISBN 978-3-7258-0524-2 (Hbk)

ISBN 978-3-7258-0523-5 (PDF)

doi.org/10.3390/books978-3-7258-0523-5

Cover image courtesy of sent via Teams LM

© 2024 by the authors. Articles in this book are Open Access and distributed under the Creative Commons Attribution (CC BY) license. The book as a whole is distributed by MDPI under the terms and conditions of the Creative Commons Attribution-NonCommercial-NoDerivs (CC BY-NC-ND) license.

Contents

About the Editor	vii
Preface	ix
Paul Alexandre Editorial for Special Issue “Novel Methods and Applications for Mineral Exploration, Volume II” Reprinted from: <i>Minerals</i> 2023 , <i>13</i> , 1235, doi:10.3390/min13101235	1
Yanxu Liu, Yanling Lai, Wenyong Li, Feng Luo, Lijie Wang and Anqi Cao et al. Estimating Perspectives of Oil and Gas in New Strata in the Southern and Surrounding Dayangshu Basin Reprinted from: <i>Minerals</i> 2023 , <i>13</i> , 706, doi:10.3390/min13050706	6
Nan Wang, Zijian Wang, Qianhui Sun and Jian Hui Coal Mine Goaf Interpretation: Survey, Passive Electromagnetic Methods and Case Study Reprinted from: <i>Minerals</i> 2023 , <i>13</i> , 422, doi:10.3390/min13030422	20
Kui Xiang, Liangjun Yan, Gongxian Tan, Yuanyuan Luo and Gang Yu Complex Resistivity Anisotropy Response Characteristics of Wufeng-Longmaxi Formation Shale in Southern Sichuan Reprinted from: <i>Minerals</i> 2022 , <i>12</i> , 1395, doi:10.3390/min12111395	41
Peixiao Du, Jing Wu, Yang Li, Jian Wang, Chunming Han and Mark Douglas Lindsay et al. Imaging Karatungku Cu-Ni Mine in Xinjiang, Western China with a Passive Seismic Array Reprinted from: <i>Minerals</i> 2020 , <i>10</i> , 601, doi:10.3390/min10070601	56
Sérgio Roberto Bacelar Hühn, Adalene Moreira Silva, Francisco José Fonseca Ferreira and Carla Braitenberg Mapping New IOCG Mineral Systems in Brazil: The Vale do Curaçá and Riacho do Pontal Copper Districts Reprinted from: <i>Minerals</i> 2020 , <i>10</i> , 1074, doi:10.3390/min10121074	72
Wei Wang, Xing Gao and Yanhui Wu A Study on the Imaging Method for the Channel Wave Dispersion Curve Variability Function Reprinted from: <i>Minerals</i> 2022 , <i>13</i> , 50, doi:10.3390/min13010050	101
Stanisław Speczik, Lidia Dziewińska, Waldemar Józwiak and Krzysztof Zieliński Application of Historical Geophysical Materials in Searching for Cu-Ag Ore Deposits—A New Direction of Research Reprinted from: <i>Minerals</i> 2020 , <i>10</i> , 725, doi:10.3390/min10080725	112
Michael A. Wise, Russell S. Harmon, Adam Curry, Morgan Jennings, Zach Grimač and Daria Khashchevskaya Handheld LIBS for Li Exploration: An Example from the Carolina Tin-Spodumene Belt, USA Reprinted from: <i>Minerals</i> 2022 , <i>12</i> , 77, doi:10.3390/min12010077	136
Russell S. Harmon, Michael A. Wise, Adam C. Curry, Joshua S. Mistele, Michael S. Mason and Zach Grimač Rapid Analysis of Muscovites on a Lithium Pegmatite Prospect by Handheld LIBS Reprinted from: <i>Minerals</i> 2023 , <i>13</i> , 697, doi:10.3390/min13050697	164

Joshua Chisambi, Bjorn von der Heyden, Muofhe Tshibalanganda and Stephan Le Roux Gold Exploration in Two and Three Dimensions: Improved and Correlative Insights from Microscopy and X-Ray Computed Tomography Reprinted from: <i>Minerals</i> 2020 , <i>10</i> , 476, doi:10.3390/min10050476	191
Joana Cardoso-Fernandes, Douglas Santos, Cátia Rodrigues de Almeida, Julia Tucker Vasques, Ariane Mendes and Ricardo Ribeiro et al. The INOVMineral Project’s Contribution to Mineral Exploration—A WebGIS Integration and Visualization of Spectral and Geophysical Properties of the Aldeia LCT Pegmatite Spodumene Deposit Reprinted from: <i>Minerals</i> 2023 , <i>13</i> , 961, doi:10.3390/min13070961	211
Danijela Ignjatović Stupar, Vukan Ogrizović, Janez Rošer, Vesna Poslončec-Petrić and Goran Vižintin Conceptual Navigation and Positioning Solution for the Upcoming Lunar Mining and Settlement Missions Based on the Earth’s Mining Experiences: Lunar Regional Navigation Transceiver System Reprinted from: <i>Minerals</i> 2023 , <i>13</i> , 371, doi:10.3390/min13030371	238

About the Editor

Paul Alexandre

Dr. Paul Alexandre is a talented and experienced mineral exploration and metallogeny scientist. He obtained his Ph.D. in France, where he worked on emerald, gold, tungsten, and REE, before moving to Canada, where he studies the deposits of such commodities as lithium, REE, gold, uranium, and base metals. His investigation methods include geochemistry (trace elements and isotopes), mineralogy, geochronology, and geostatistics. He is a dedicated educator who teaches and supervises graduate students at Brandon University in Canada.

Preface

The unmitigated success and indeed significance of the first volume of this Special Issue, published mere three years ago, highlighted the importance of the topic of novel exploration methods, the huge interest of the exploration community, both academia- and industry-based, and, most importantly, the wealth of recent innovation and developments in mineral exploration. Given the interest but also the recent progress, this second volume was quickly envisioned and rapidly produced, corresponding to the desire of the exploration community.

This second volume encapsulates the acceleration in the progress and development of both our theoretical understanding and practical application of mineral exploration. It may be argued that this progress has been primarily driven by recent advances in information and communication technology and computational methods (specifically artificial intelligence and computer learning) and the development of novel analytical methods and the increased portability of existing ones, combined with increased automation of data collection and processing. The exploration innovations are most noticeable in geophysical exploration, with most of them being from the fields of geophysics and analytical development.

In conclusion, the second volume of this Special Issue provides a brief but representative cross-section of the exciting developments in our understanding and practice of mineral exploration and, as such, will no doubt be highly useful, interesting, and thought-provoking for both the academia-based and the practicing exploration geologist.

I would like to take the time to acknowledge those who have contributed, in a big way or small, to the success of this Special Issue. Firstly, I would like to profoundly thank all the authors who shared their research and contributed their papers to this volume. The second most important people are our numerous reviewers, who selflessly and tirelessly contributed their time, efforts, knowledge, and experience to assess and evaluate and then help improve each of the papers in this volume. Of course, this Special Issue owes a lot to the dedicated and highly professional MDPI staff and editors, and specifically those at *Minerals*, and in particular Section Managing Editor Dr. Luke Wu, who has been a driving force behind this project. To all of you, please accept my heartfelt and deepest thank you!

Paul Alexandre
Editor

Editorial

Editorial for Special Issue “Novel Methods and Applications for Mineral Exploration, Volume II”

Paul Alexandre

Department of Geology, Brandon University, John R. Brodie Science Centre, 270–18th Street, Brandon, MB R7A 6A9, Canada; alexandrep@brandonu.ca

1. Introduction

As already exemplified by the highly successful first volume of this Special Issue, both the theoretical understanding of mineral exploration and its practical application in the field are undergoing a profound and significant transformation. This transformation is primarily driven by the numerous societal, economic, and environmental challenges facing the mining industry and our society; some of these challenges have always been present (e.g., economic sustainability, equitable distribution of profits), while others are rather new, such as the dramatically increased demand for the so-called critical minerals as defined by different legislations principally in the Western world. For instance, the European Union, the USA, and Canada, among others, have designed and implemented national programs with the purpose of enhancing the exploration for and the production of a number of commodities deemed crucial not only for economic security, but also and particularly for the implementation of the transition to a low-carbon economy (based on “clean technology”), itself driven by depleting hydrocarbon resources and the urgent need to reduce greenhouse gas emissions in order to address the unfolding climate catastrophe. What is considered as a critical mineral varies somewhat from country to country as a function of national priorities, but typically includes 20 to 30 commodities dominated by lithium, graphite, nickel, cobalt, copper, and the rare earth elements. As we will see later, several papers in this volume deal with critical minerals, specifically lithium and copper.

Another significant factor for the observed transformation of the mineral exploration theory and practice is the unprecedentedly robust technological development the world has experienced: it is—among other things—a major impetus, instrument, and symptom of the changes observed. This is of course logical and has been a constant since the scientific and industrial revolution of the 18th century: better theoretical understanding leads to improved technological advancement, which in turn provides the means necessary for further theoretical growth. Such an interdependency, and indeed a mutually beneficial relationship between science and industry, is what drives the technological progress that strongly affects the theory and practice of mineral exploration today. Specifically, this progress is most visible in two areas: novel computing capabilities (e.g., machine learning and artificial intelligence) and novel analytical methodologies (e.g., laser-induced breakdown spectroscopy, increased portability, and the automation of data collection and interpretation). Combined, these two aspects of technological progress are contributing to a vast paradigmatic change, with orders of magnitude more data (obtained faster and cheaper), treated and indeed interpreted by more powerful computers utilizing artificial intelligence models and machine learning. Not surprisingly, several papers in this volume deal specifically with the application of novel technologies, both analytical and computational, to mineral exploration.

This second installment of this Special Issue entitled “Novel Methods and Applications for Mineral Exploration” represents a brief but representative cross-section of the advancements mentioned above and in particular of the progress made since the first volume was published three years ago. The papers published in this volume are cutting-edge



Citation: Alexandre, P. Editorial for Special Issue “Novel Methods and Applications for Mineral Exploration, Volume II”. *Minerals* **2023**, *13*, 1235. <https://doi.org/10.3390/min13101235>

Received: 11 September 2023
Accepted: 15 September 2023
Published: 22 September 2023



Copyright: © 2023 by the author. Licensee MDPI, Basel, Switzerland. This article is an open access article distributed under the terms and conditions of the Creative Commons Attribution (CC BY) license (<https://creativecommons.org/licenses/by/4.0/>).

and indeed pioneering contributions to our understanding of mineral exploration, both theoretical and in practice and, as such, will be of particular interest to both the academia-based scientist and the practicing exploration geologist, who will undoubtedly find them interesting and useful.

2. Review of the Papers in This Special Issue

The papers published in this Special Issue are diverse, but are strongly dominated by geophysical methods, as in the first volume, with seven papers. Three papers deal with novel analytical technology, one paper deals with WebGIS technology, and one paper deals with lunar navigation. The individual contributions will be briefly presented here.

2.1. Geophysics

Most of the contributions in this volume using geophysical methods combined with novel computational applications are applied papers focusing on commodities such as copper, gold, coal, nickel, and hydrocarbons, and these will be described first.

The first contribution we will consider, by Liu et al. [1], is strictly applied and describes the integration of new high-precision airborne gravity and magnetic data with data from geological exploration and drilling, and the resulting improved understanding of the Jurassic–Cretaceous and the Upper Paleozoic strata of the Dayangshu Basin, China, and their potential to host oil and gas reservoirs. The conclusion of this contribution is that three specific zones, the Liuhe Sag in Dayangshu Basin, the depression in NE Longjiang Basin, and the northern parts of the Taikang swell, have high potential for oil and gas exploration.

Another contribution, by Wang et al. [2], describes the utilization of novel passive electromagnetic methods, the super-low-frequency alternating magnetic component method (SLF) and the audio frequency magnetotelluric method (AMT), to detect and interpret different types of coal mine goaf. Their conclusion, after validation of the method with real-world data from the Henan Province in China, is that these passive electromagnetic interpretation methods have the potential to identify fault structures and water-filled goaf areas with depth of up to 400 m. This paper provides the theoretical background for the application of this novel goaf detection method as a fast and low-cost alternative of traditional methods such as seismics, gravity, logging, radiation and electromagnetic methods.

The next contribution, by Xiang et al. [3], deals with electrical exploration of shale gas reservoir exploration and evaluation. This study measures the resistivity and characterizes the induced polarization parameters of 34 shale samples from southern Sichuan, China; it also analyzes the electrical anisotropy response characteristics under different temperature and pressure conditions, thus defining the specific factors that affect the complex resistivity anisotropy of shales. The major significance of this study is in providing the theoretical basis and describing a set of testing methods that are useful in understanding the electrical anisotropy characteristics of shale gas reservoirs.

Another applied geophysics study, reported by Du et al. [4], also utilizes a passive method, passive seismic in this case. Ambient noise tomography, employing a dense array of 100 temporary detectors, is used to study the shallow crustal structure of Karatung Mine, the second-largest Cu-Ni mine in China, down to almost 1.3 km in depth. Surface wave dispersions at 0.1 to 1.5 s are obtained and inverted for a 3D S-wave structure, which helped identify several zones with distinct velocities. Some of these are identified as intrusive host-rocks and others as highly sulfide mineralized areas. The principle contribution of this study is demonstrating the value of using a very dense array of detectors in the study of ore deposits.

A detailed and extensive geophysical mapping, using gravity and magnetics, is reported for two new IOCG mineral systems in the Archaean São Francisco Craton, Brazil, in the Vale do Curaçá and Riacho do Pontal copper districts (Hühn et al. [5]). Several high-density (3.13 g/cm^3) and high magnetic susceptibility ($SI > 0.005$) areas are identified corresponding to the Caraíba, Surubim, Vermelho, and other minor copper deposits.

The mapping also indicates that the deposits are controlled by NNW and NW-SE structural trends.

The next contribution is more theoretical: Wang et al. [6] report a methodological innovation, specifically the imaging method of dispersion curve variability function. This method follows a precise procedure, based on the breakpoints of the dispersion curve produced by an anomalous body in a seismic study. These breakpoints are classified, counted, and assigned a weighing factor, after which the variability function for the dispersion curve is constructed and then used to visualize the anomalous body. The method is validated by applying it to a real-world and known example, the working face of coal mine 090606 in China, and seems to provide a more accurate image of the known anomaly.

The last geophysics contribution in this Special Issue, by Speczik et al. [7], reports the use of historic seismic and gravimetric data in the exploration for Cu and Ag deposits, with an example from the Nowa Sól deposit in SW Poland. The major significance of the paper is to demonstrate the effectiveness of the new method of effective reflection coefficients (ERC), applied on archival data. Compared to amplitude-based seismic section, the ERC-generated section boasts much higher imaging resolution, allowing the use of the historic data, in particular when combined with drill core information.

2.2. Analytical Innovations

Two contributions in this Special Issue report the use in exploration of a relatively new geochemical exploration tool, hand-held laser-induced breakdown spectroscopy (LIBS), which has the advantage of measuring light elements in situ, lithium in particular. The first of these papers, by Wise et al. [8], describes the application of the method in exploration for Li-Cs-Ta rich pegmatites, with, as an example, the Carolina Lithium Project, situated in the Carolina Tin-Spodumene Belt, which extends from South Carolina into North Carolina, USA. The paper thoroughly describes the method employed—it is indeed mostly a methodological paper—and discusses the strength, weaknesses, limitations and applications of the method in the context of geochemical exploration, including the challenges related to obtaining fully quantitative analyses and the ways to overcome these challenges. The major conclusion of the paper is that hand-held LIBS can indeed be advantageously used in geochemical exploration of pegmatites.

The second contribution using the hand-held LIBS method is by the same team (Harmont et al. [9]) and demonstrates how the tool can be used to analyze muscovite from a lithium-bearing pegmatite. The example is that of the Carolina Lithium Prospect in North Carolina, USA, where more than 130 muscovite samples are analyzed for Li, K, and Rb. It is found that Li contents varies from 0.04 to 0.74 wt% and the K/Rb ratios from 8 and 63. Higher Li is observed in spodumene-bearing pegmatites than in spodumene-free ones. Although the method is described in significant detail, the analytical uncertainty and the detection limits of this method are not apparent.

A very interesting paper by Chisambi et al. [10] describes, in significant detail, the integration of X-ray computed tomography (XCT) with textural, mineralogical and chemical imaging using SEM and optical microscopy, in order to produce a precise 3D image of gold distribution in samples from Manondo-Choma gold prospect in Malawi. This contribution emphasizes the importance of the correlative approach of combining 3D XCT data with 2D mineralogical and chemical data to understand a complex orogenic gold mineralization. The use of XCT in combination with microscopy provides an excellent tool for understanding gold mineralization. Further, this visualization method seems particularly useful in obtaining a better understanding of the complex structures controlling the gold mineralization (and possibly other types of deposits), mostly at the microscopic and mesoscopic scale.

2.3. Other Topics

An interesting contribution by Cardoso-Fernandes et al. [11] presents the results of the INOVMINERAL4.0 project, consisting of a WebGIS-based integration and visualization of

various data from the Aldeia pegmatite deposit in Portugal. The data are obtained by means of unmanned aerial vehicle (LIDAR), on the ground (radiometry), and in the lab (spectral data on 11 samples). The resulting images are compared with those obtained by Landsat 9. The main conclusions are that radiometry can effectively delineate pegmatites from their host rocks; that a spectral data library can be very useful in space-based exploration; and that using a user-friendly webGIS platform facilitates data integration, visualization, and sharing.

Finally, we come to a somewhat futuristic space exploration-related contribution (Ignjatović Stupar et al. [12]). It describes, in considerable depth, a proposed Lunar Regional Navigation Transceiver System (LRNTS), to be used for the accurate—to the centimeter—positioning of facilities and structures that would be placed on the Moon's surface during a potential future settlement mission. The system, using lessons learned from mining, consists of at least nine transceivers, each containing both navigation transmitters and receivers, and placed on the Moon's surface. The case study presented in this paper is a computer simulation of the implementation of this system on the Shackleton Crater. The best of 12 models, using 9 nodes, achieved a horizontal accuracy of 6.7 mm, a vertical accuracy of 11.5 mm, and availability over 95.5% of the study area. These impressive results open up tantalizing prospects for planet exploration and much more.

3. Conclusions

As the reader will without doubt appreciate, exploration theory and practice are advancing at a very high pace. This acceleration is particularly noticeable when we compare this volume with the first volume of this Special Issue, published a mere three years ago, and this reflects the rapid changes in a fast-evolving exploration and mining industry. Some of the drivers in this evolution are recent advances in information and communication technology and computational methods (specifically artificial intelligence and computer learning) and the development of novel analytical methods (e.g., LIBS [8,9]) and the increased portability of existing ones (e.g., PIMA), combined with increased automation of data collection and data processing.

These innovations are most noticeable in geophysical exploration, which, because of its high dependence on computational power, is the major beneficiary [2,3,6]. Clear opportunities for future developments and opportunities can be perceived, as well as for novel applications [11,12]. Interestingly, new understanding and novel methodologies allow us to re-visit and re-process historical geophysical data [7], which is, in itself, interesting and full of potential.

In conclusion, the second volume of this Special Issue provides a brief but representative cross-section of the exciting developments in our understanding and practice regarding mineral exploration and, as such, will no doubt be highly useful, interesting, and thought-provoking for both the academia-based and the practicing exploration geologist.

Conflicts of Interest: The author declares no conflict of interest.

References

1. Liu, Y.; Lai, Y.; Li, W.; Luo, F.; Wang, L.; Cao, A.; Jiang, Z.; Gao, S. Estimating Perspectives of Oil and Gas in New Strata in the Southern and Surrounding Dayangshu Basin. *Minerals* **2023**, *13*, 706. [[CrossRef](#)]
2. Wang, N.; Wang, Z.; Sun, Q.; Hui, J. Coal Mine Goaf Interpretation: Survey, Passive Electromagnetic Methods and Case Study. *Minerals* **2023**, *13*, 422. [[CrossRef](#)]
3. Xiang, K.; Yan, L.; Tan, G.; Luo, Y.; Yu, G. Complex Resistivity Anisotropy Response Characteristics of Wufeng-Longmaxi Formation Shale in Southern Sichuan. *Minerals* **2022**, *12*, 1395. [[CrossRef](#)]
4. Du, P.; Wu, J.; Li, Y.; Wang, J.; Han, C.; Lindsay, M.D.; Yuan, H.; Zhao, L.; Xiao, W. Imaging Karatungk Cu-Ni Mine in Xinjiang, Western China with a Passive Seismic Array. *Minerals* **2020**, *10*, 601. [[CrossRef](#)]
5. Hühn, S.R.B.; Silva, A.M.; Ferreira, F.J.F.; Braitenberg, C. Mapping New IOCG Mineral Systems in Brazil: The Vale do Curaçá and Riacho do Pontal Copper Districts. *Minerals* **2020**, *10*, 1074. [[CrossRef](#)]
6. Wang, W.; Gao, X.; Wu, Y. A Study on the Imaging Method for the Channel Wave Dispersion Curve Variability Function. *Minerals* **2023**, *13*, 50. [[CrossRef](#)]

7. Speczik, S.; Dziewinska, L.; Józwiak, W.; Zielinski, K. Application of Historical Geophysical Materials in Searching for Cu-Ag Ore Deposits—A New Direction of Research. *Minerals* **2020**, *10*, 725. [[CrossRef](#)]
8. Wise, M.A.; Harmon, R.S.; Curry, A.; Jennings, M.; Grimač, Z.; Khashchevskaya, D. Handheld LIBS for Li Exploration: An Example from the Carolina Tin-Spodumene Belt, USA. *Minerals* **2022**, *12*, 77. [[CrossRef](#)]
9. Harmon, R.S.; Wise, M.A.; Curry, A.C.; Mistele, J.S.; Mason, M.S.; Grimač, Z. Rapid Analysis of Muscovites on a Lithium Pegmatite Prospect by Handheld LIBS. *Minerals* **2023**, *13*, 697. [[CrossRef](#)]
10. Chisambi, J.; von der Heyden, B.; Tshibalanganda, M.; Le Roux, S. Gold Exploration in Two and Three Dimensions: Improved and Correlative Insights from Microscopy and X-Ray Computed Tomography. *Minerals* **2020**, *10*, 476. [[CrossRef](#)]
11. Cardoso-Fernandes, J.; Santos, D.; Almeida, C.R.d.; Vasques, J.T.; Mendes, A.; Ribeiro, R.; Azzalini, A.; Duarte, L.; Moura, R.; Lima, A.; et al. The INOVMineral Project's Contribution to Mineral Exploration—A WebGIS Integration and Visualization of Spectral and Geophysical Properties of the Aldeia LCT Pegmatite Spodumene Deposit. *Minerals* **2023**, *13*, 961. [[CrossRef](#)]
12. Ignjatović Stupar, D.; Ogrizović, V.; Rošer, J.; Poslončec-Petrić, V.; Vižintin, G. Conceptual Navigation and Positioning Solution for the Upcoming Lunar Mining and Settlement Missions Based on the Earth's Mining Experiences: Lunar Regional Navigation Transceiver System. *Minerals* **2023**, *13*, 371. [[CrossRef](#)]

Disclaimer/Publisher's Note: The statements, opinions and data contained in all publications are solely those of the individual author(s) and contributor(s) and not of MDPI and/or the editor(s). MDPI and/or the editor(s) disclaim responsibility for any injury to people or property resulting from any ideas, methods, instructions or products referred to in the content.

Article

Estimating Perspectives of Oil and Gas in New Strata in the Southern and Surrounding Dayangshu Basin

Yanxu Liu ¹, Yanling Lai ^{2,*}, Wenyong Li ¹, Feng Luo ¹, Lijie Wang ³, Anqi Cao ¹, Zhexin Jiang ⁴ and Shan Gao ¹

¹ China Aero Geophysical Survey and Remote Sensing Center for Nature Resources, Beijing 100083, China; liwenyong@mail.cgs.gov.cn (W.L.)

² Hebei Institute of Geological Environment Monitoring, Shijiazhuang 050021, China

³ Oil and Gas Engineering Research Institute of Jilin Oilfield Company, Songyuan 138000, China

⁴ College of Geoexploration Science and Technology, Jilin University, Changchun 130026, China

* Correspondence: a340191600@126.com; Tel.: +86-0311-69101682

Abstract: On the basis of elaborating on the regional geological background, this paper analyzes the lithological and sedimentary characteristics and explorative prospects of new strata with oil and gas in the southern and surrounding areas of Dayangshu Basin. Based on the latest high-precision airborne gravity and magnetic comprehensive survey data, combined with the latest data from geological explorations, physical surveys, and drilling, and the use of basin structure layering combination methods, we clarified the characteristics of the bottom of the Jurassic–Cretaceous and the occurrence characteristics of the Upper Paleozoic in the study area and revealed the determinative effect of multi-period structures on the most important sedimentary layers. Then, we summarized the accumulation conditions and prediction methods of hydrocarbons and proposed the oil and gas prospects of these deep new strata. The results show that the Liuhe Sag in Dayangshu Basin, the depression in the northeast of Longjiang Basin, and the northern parts of the Taikang swell have good source–reservoir–cap combination conditions and favorable structural characteristics for oil and gas, where there is a high potential for exploration.

Keywords: oil and gas; occurrence characteristics; airborne gravity and magnetism; new strata; exploration potential; Dayangshu Basin



Citation: Liu, Y.; Lai, Y.; Li, W.; Luo, F.; Wang, L.; Cao, A.; Jiang, Z.; Gao, S. Estimating Perspectives of Oil and Gas in New Strata in the Southern and Surrounding Dayangshu Basin. *Minerals* **2023**, *13*, 706. <https://doi.org/10.3390/min13050706>

Academic Editor: Paul Alexandre

Received: 8 March 2023

Revised: 24 April 2023

Accepted: 26 April 2023

Published: 22 May 2023



Copyright: © 2023 by the authors. Licensee MDPI, Basel, Switzerland. This article is an open access article distributed under the terms and conditions of the Creative Commons Attribution (CC BY) license (<https://creativecommons.org/licenses/by/4.0/>).

1. Introduction

The exploration of Dayangshu Basin began in the late 1950s. In the beginning, the purpose was to find coal and metal ores, and then oil and gas exploration began to be carried out. Due to the low level of exploration, the geological conditions relating to petroleum in the basin are not well understood, and only a preliminary understanding of the relevant geological issues is available. Additionally, the basin lacks airborne gravity data, and the airborne physical survey method is the most effective for sedimentary basin investigation. Previous aeromagnetic surveys suffer from scattered areas and inconsistent accuracy and measurement scales [1–11].

At present, the implementation of integrated aerial gravity and magnetic surveys has greatly enhanced the capabilities and application areas of aerial geophysical surveys [2,6,7,12]. In particular, a series of important results and steps have been made in the deep structural analysis of key oil and gas basins in China's onshore and offshore areas, and the lithological composition of tectonic layers, the controlling role of multi-phase tectonic stress fields in relation to sedimentary layers [13–16], and the distribution patterns of favorable oil- and gas-bearing structures [9,17–26].

Based on the newly collected high-precision airborne gravity and magnetic data, this paper reveals the lithological characteristics of new oil- and gas-bearing systems in the southern part of Dayangshu Basin, the spread pattern of deep new systems, the influence of multi-phase tectonics over sedimentary layers, and the characteristics of oil and gas

reservoirs. The results provide a reference for the exploration of new oil- and gas-bearing formations in Dayangshu Basin and similar areas.

2. Regional Geological Background

2.1. Stratum

According to the ground outcrops and drilling data, the stratigraphy of the region can be seen from old to new in the Palaeoproterozoic, Lower Paleozoic, Upper Paleozoic, Triassic, Jurassic, Cretaceous, and Cenozoic (Figure 1).

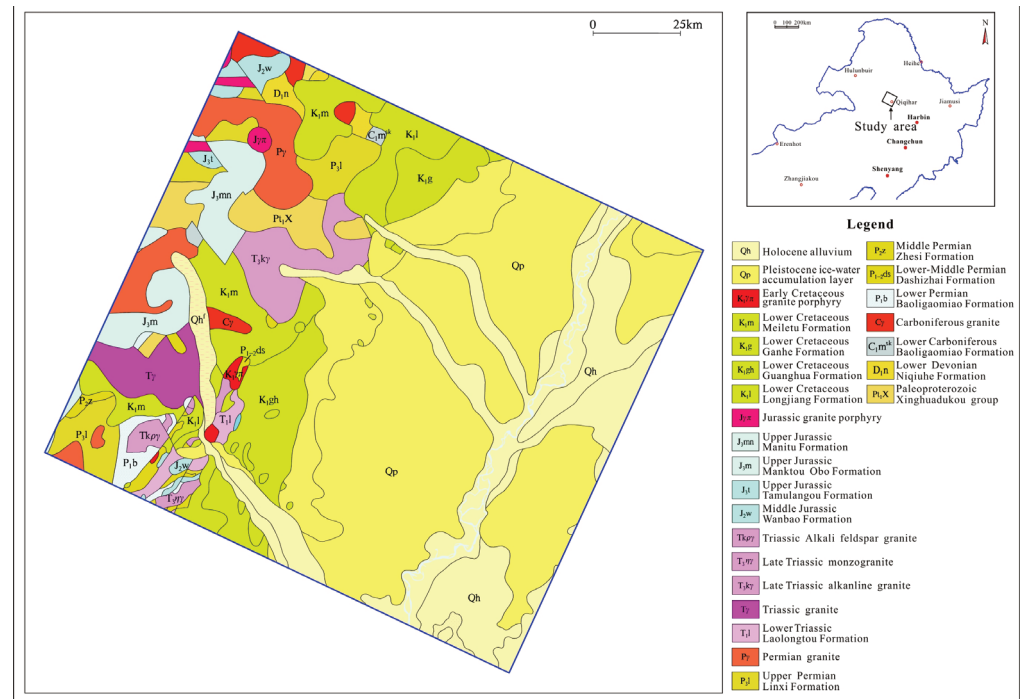


Figure 1. A geological map of the study area.

2.2. Regional Structural

With the exploration of regional geological structures and the revelation of deep structures, tectonic evolution played an important role in the analysis of crustal structures and the development of geological structures [6,10,15,27,28].

The western boundary of Dayangshu Basin is toward the Daxinganling supercrustal fault zone, and the eastern boundary is toward the western boundary of Songliao Basin. There are two nearly east–west crust faults across Dayangshu Basin near the Hailar-Jiayin and Boketu-Namur Rivers and Dayangshu Basin is divided into three sections in the north–south direction. Among them, the Daxinganling fault zone, developed on the west side of Dayangshu Basin, has an important influence on the formation and evolution of Dayangshu Basin.

2.3. Regional Magmatic Rocks

According to the differences in formation environment, heterogeneity of fault activity, and different formation times, the size of magmatic rocks is quite different and the lithofacies and rock types are diverse. It even presents the landscape of a magmatic rock belt with specific spatial distribution rules. Magmatic activities often have important influences on regional tectonic history [29,30].

The magmatic activity in the study area and its periphery is very frequent, and it can be divided into five major cycles from old to new: Pre-Auranian, Garidonian, Hercynian, Yanshanian, and Xishanian, among which, the Hercynian and Yanshanian are the most intense. Both intrusive rocks and volcanic rocks are widely distributed. There are many

kinds of intrusive rocks, including ultramafic, basic, neutral, acidic, and basic rocks; volcanic rocks are mainly acidic, neutral, and basic rocks.

3. Data and Methods

3.1. Aero Gravity and Magnetic Data

We use the comprehensive aeromagnetic measurements collected in 2018 by the China Natural Resources Airborne Physical Exploration and Remote Sensing Center in the southern part of Dayanshu Basin at a scale of 1:100,000, with a survey line direction of 115–295°, a cut line direction of 25–205°, and an average flight height of 175 m above ground. The total accuracy of spatial gravity measurements after data processing in the study area is $0.26 \times 10^{-5} \text{ m/s}^2$, and the total accuracy of aeromagnetic measurement is 0.69 nT.

3.2. Physical Properties and Other Data

According to the distribution of stratigraphy and bedrock outcrop in the study area, the field survey completed 103 physical measurement points, obtained 3127 magnetization rate data, 435 density data, collected 454 specimens (including 8 magnetically oriented specimens); collected 5 seismic profiles, 3 boreholes, 2 geodetic electromagnetic bathymetric profiles, etc.

3.3. Constructing Layering Method

In this paper, based on aeromagnetic and gravity data, combined with the determination and analysis of stratigraphic density and magnetization rate parameters, different geophysical methods [31] are combined with seismic and drilling data as constraints, among which, the anomaly stripping method and Parker's iteration method are used for the depth of the Mesozoic bottom surface; the wavelet decomposition method is used for the regional gravity anomaly caused by the deep (mainly Moho surface) [32–37]; the calculated depth data are corrected with known drilling and seismic data as constraint control in the calculation process, and the thickness of the Upper Paleozoic and the depth of the Jurassic–Cretaceous bottom surface are obtained, respectively.

4. Oil and Gas Reservoir Characteristics of the Study Area

Based on the data of drilling and oil and gas exploration in Dayangshu Basin and nearby Longjiang Basin and Songliao Basin, this paper studies the geological conditions of these areas and surrounding areas as they relate to oil and gas, focusing on the source rock, reservoir, cap, and their combination, as well as the local structure and trap type.

4.1. Oil and Gas Source Rocks

The oil and gas source rocks in the study area, from top to bottom, mainly include the Upper Paleozoic Linxi Formation, the Dashiizhai Formation, the Zhezhi Formation, the Lower Cretaceous Ganhe Formation, the Jiufengshan Formation, and the Longjiang Formation.

4.1.1. Upper Paleozoic Oil and Gas Source Rocks

The Upper Permian and the Middle Permian all developed from dark mudstone. These dark mudstones show high organic matter abundance; the types of organic matter are mostly type II and type III, and the stage of evolution of this matter is high and mostly mature, meaning it has good oil and gas generation potential, and thus constitutes the main oil and gas source rocks in the region.

4.1.2. Lower Cretaceous Oil and Gas Source Rocks

The Ganhe Formation is mainly distributed in the depressional zone of Dayangshu Basin, and in the southern depressional zone, the stratigraphic thickness of the formation

reaches over 2400 m. The maximum thickness of oil and gas source rocks in this formation reaches over 80 m, and it is thicker in the central part, becoming thinner toward the sides.

The Jiufengshan Formation developed in both the depression and uplift areas of the southern part of Dayangshu Basin; its thickness is relatively large in the depression area, reaching over 1000 m. The maximum thickness of oil and gas source rocks in the Jiufengshan Group is over 180 m, and the thicker strata of this group are distributed in the northeast of the Yang D1 well and the southwest of the Yang D2 well, with a trend of gradual thinning toward the sides.

The Longjiang Formation is mainly distributed in the southern depression of Dayangshu Basin, and then less so in the central and northern parts of the basin. The maximum thickness of oil and gas source rocks in the Longjiang Formation exceeds 40 m, and the thickest part of the formation is distributed in Dural and its southern area, south of the Yang D1 well and southeast of Dingjiatun.

The evaluation index of oil-bearing rocks indicates that all three sets of dark mudstone in the basin have oil- and gas-producing abilities, and the main oil and gas source rock is the Jiufeng Mountain Formation.

4.2. Reservoirs

The geological and geophysical data of the study area show that the Lower Cretaceous Longjiang, Jiufengshan, and Ganhe Formations have developed reservoirs. The Upper Paleozoic reservoir is found at the sea–land interface, where tuff and sandstone layers develop, and it mainly comprises sedimentary clastic rocks and fractured tuff.

4.3. Cover Layer

Dense volcanic lava, volcanic tuff, mudstone, and muddy siltstone have developed in the Longjiang, Jiufengshan, and Ganhe Formations in Dayangshu Basin, with dense rock structures and undeveloped pores and fissures, which together constitute the oil and gas cover of the basin.

5. Spatial Distribution Characteristics of the New Strata

5.1. Physical Characteristics of the New Strata

5.1.1. Density Characteristics

Regarding the variation in the formation's density, the formation extends from old to new, and its density generally ranges from large to small (Figure 2). The strata can be divided into three density layers, which are Proterozoic–Late Paleozoic, Mesozoic (Triassic, Jurassic, Cretaceous), and Cenozoic (Quaternary), listed from bottom to top. On the whole, the densities of volcanic rocks with different lithologies in the Jurassic–Cretaceous are obviously different. The density gradually increases from acid rock to intermediate acid rock, intermediate rock, and basic rock. The density of sedimentary rocks gradually decreases from the Proterozoic to the Paleozoic, Mesozoic, and Cenozoic.

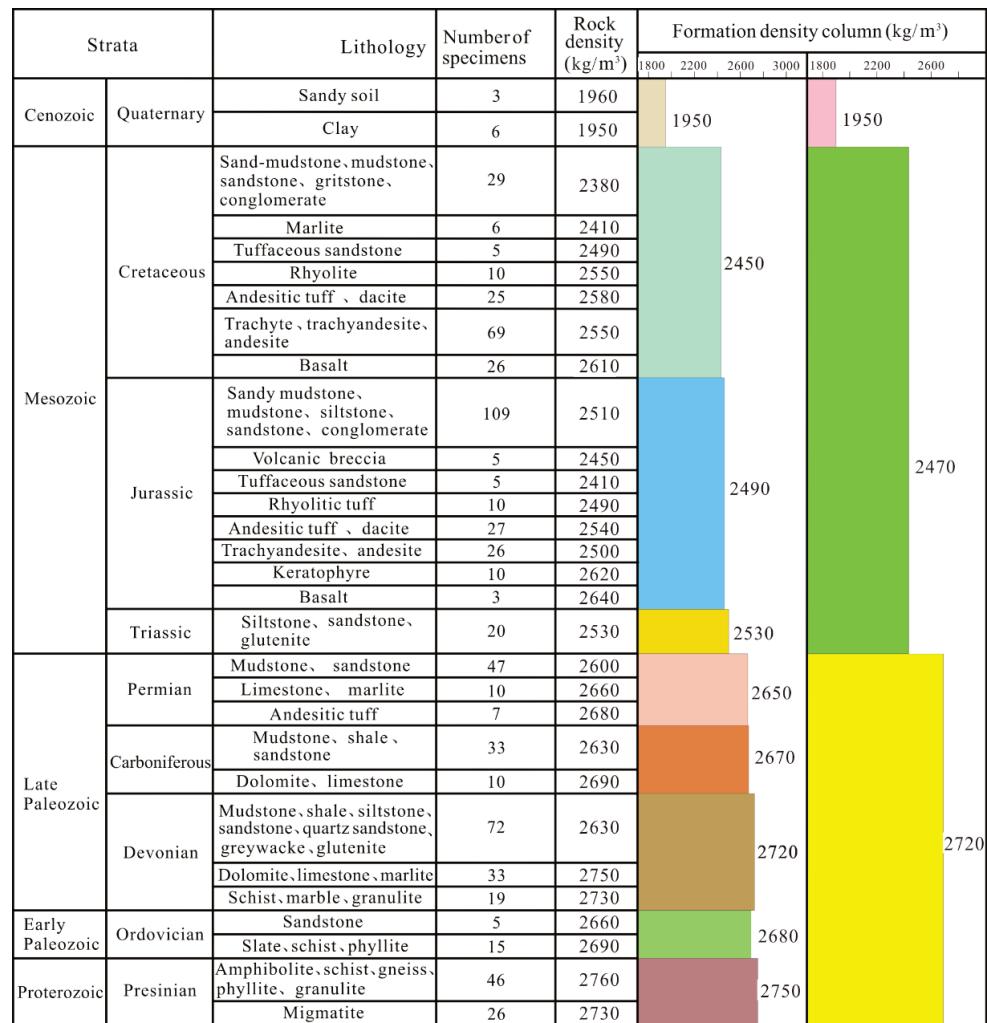


Figure 2. A density histogram of strata (rocks) in the study area and its surroundings.

5.1.2. Magnetic Characteristics

Regarding the magnetic difference, the magmatic rocks in the research area show strong magnetism, while the metamorphic rocks show weak magnetism, and the sedimentary rocks show the weakest magnetism (Figure 3). The main features include the following:

- (1) The weak magnetic layer is mainly composed of sedimentary clastic rocks, and the average magnetic susceptibility is 30×10^{-5} SI, which does not cause obvious positive magnetic anomalies;
- (2) The Cretaceous and Jurassic local distribution is a strongly magnetic layer, comprising thick but unstable intermediate–basic volcanic (clastic) rock types. Among these, the neutral volcanic rock’s magnetism is greatly affected by lithology, and its magnetic susceptibility ranges from 1340 to 1867×10^{-5} SI. The average magnetic susceptibility of basic rock is 2052×10^{-5} SI, and this often causes high-amplitude jump changes that manifest positive magnetic anomalies;
- (3) The Paleozoic regional distribution comprises a weak magnetic layer that is mainly composed of sedimentary rocks, with a magnetic susceptibility of less than 100×10^{-5} SI that does not cause obvious positive magnetic anomalies;
- (4) The Proterozoic medium-strong magnetic layer comprises a set of medium-strength magnetic metamorphic rock series, which cause certain gentle-amplitude positive magnetic anomalies.

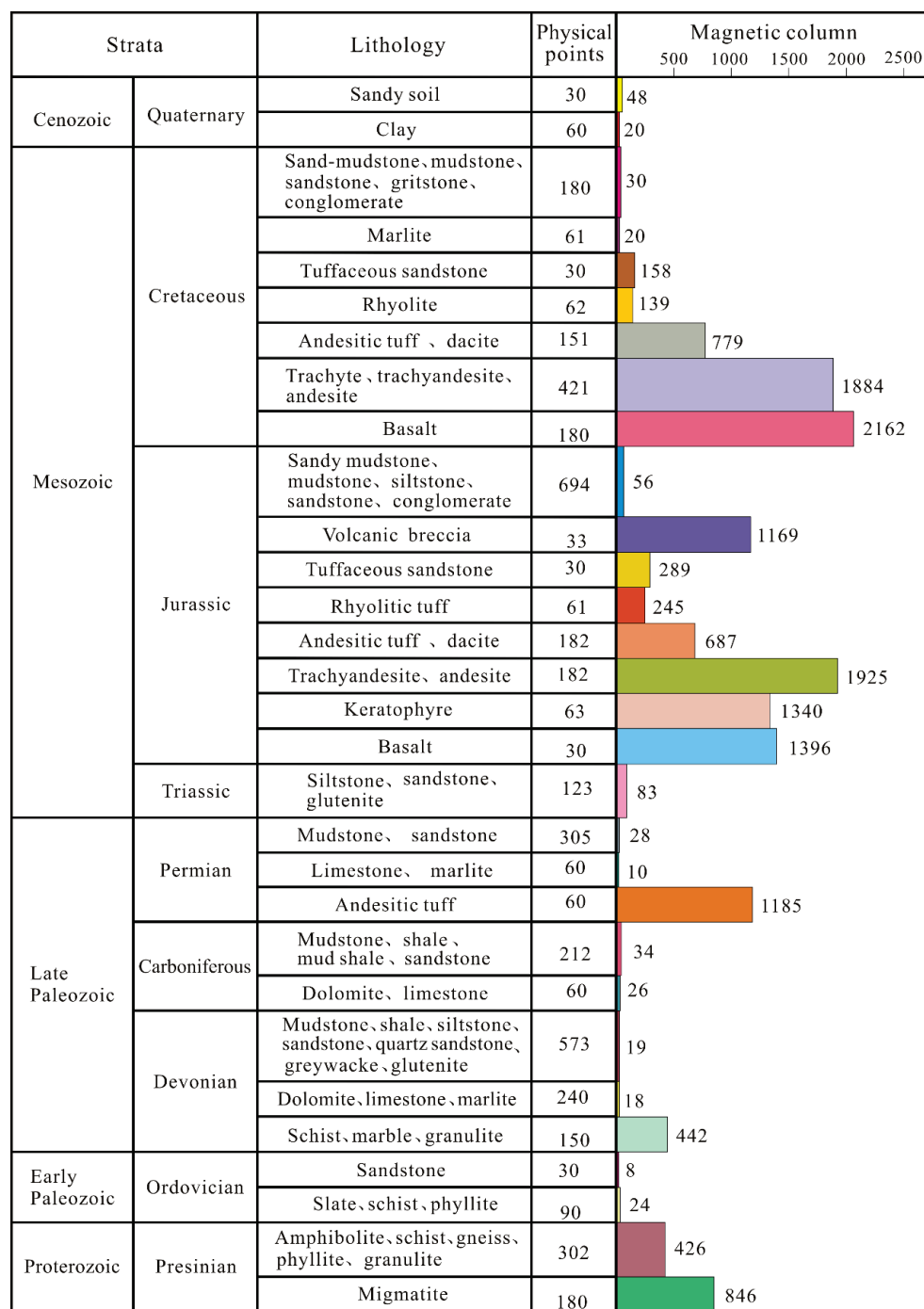


Figure 3. A magnetic susceptibility map of strata (rocks) in the study area and its surroundings.

5.2. Occurrence Characteristics of Deep New Strata

5.2.1. Upper Paleozoic Spreading Characteristics

Since the classic target layer of oil and gas exploration is the Mesozoic, there are relatively few data or results related to exploration in the deeper layers of the Upper Paleozoic, whether from drilling or seismic exploration. The thickness of the Upper Paleozoic has been calculated, and a thickness contour map has been drawn (Figure 4). It can be seen that the Upper Paleozoic in the study area has the following characteristics:

- (1) The Upper Paleozoic boundary mainly developed in the central and eastern parts of the study area, while the thickness of the Upper Paleozoic boundary in the western part of the study area is small and locally missing;

- (2) The thickness of the Upper Paleozoic boundary varies from 0 to 6000 m, and the development stage of the Upper Paleozoic boundary in different tectonic units varies significantly. The Upper Paleozoic boundary in the northern Dayangshu Basin is buried at a greater depth, and an obvious center of thickness can be seen in the northwest corner of the Pingyang Terrane (the thickness of the center is greater than 6000 m), which gradually increases as one moves from the surrounding terrane to the center. The depth of the central and south-central Longjiang Basin is about 2000–6000 m, and the three centers of thickness are located in the northeast and southeast of Longjiang Basin (the thickness value of the center is greater than 6000 m). The eastern part of the study area (the western slope of Songliao Basin) also shows a thickness characteristic of the Upper Paleozoic, and the thickness of deposition here is relatively stable, mostly around 3500–5000 m;
- (3) A series of thickness gradient zones have developed in the Upper Paleozoic, such as in the central and western parts of the study area where the thickness gradient is dense, and the distribution of the Upper Paleozoic is obviously controlled by the NWW-oriented F3 fracture. In the eastern part of the south of the study area, the Upper Paleozoic thickness gradient zone near the southern section of the F₁ fracture is more apparent, and the thicknesses of the upper and lower plates of the fracture vary significantly, indicating that the fracture structure controls the development of the Upper Paleozoic in this region;
- (4) In the same zone, the thickness of the Upper Paleozoic is relatively stable, without obvious local jump changes.

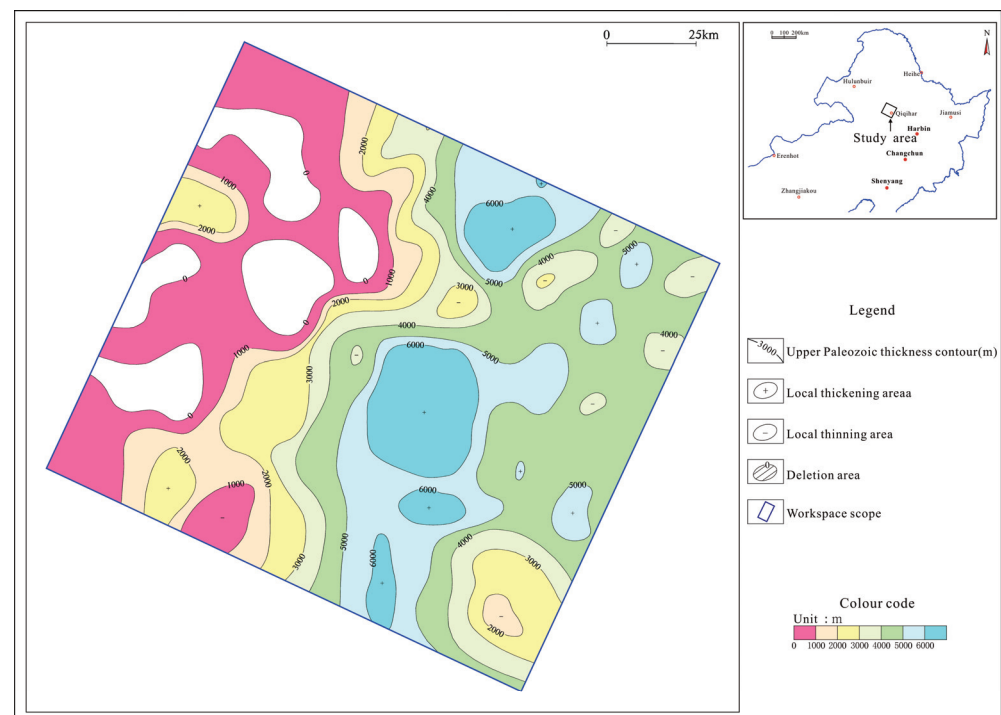


Figure 4. The thickness of the Upper Paleozoic in the study area.

5.2.2. Jurassic–Cretaceous Spreading Characteristics

Drilling and seismic data regarding the density of this set of strata locate them between the Cenozoic and pre-Jurassic strata. The characteristic features of the Jurassic–Cretaceous stratigraphic development in the study area are obvious (Figure 5).

- (1) Jurassic–Cretaceous stratigraphy is more developed.

It is preserved in several tectonic units in the northern, south-central, and eastern parts of the study area. In the west, the strata set is missing in most areas.

- (2) Jurassic–Cretaceous thickness zoning is obvious.

The thickness of the whole region varies from 0 to 3000 m and is greater in the central and southern parts. The thickness of the Mesozoic boundary in the western slope of Songliao Basin gradually increases from west to east, while the thickness of this boundary in the western Guangfeng Bulge and the western part of the southern Taikang Bulge is mostly 500–1500 m. The Mesozoic boundary in the eastern depressions is relatively thick, and its maximum depth exceeds 2000 m.

- (3) The Mesozoic bottom surface has distinct depth centers. They are at the northeast and southwest of the Liuhe Sag, the south of the Pingyang Terrane, the northeast and northwest of the northeastern depression of Longjiang Basin, the Shanquan Depression, the Fufu Depression, the gentle slope zone of the Heping Farm, the eastern part of the Yantongtun Depression, and the southwest of the Taikang Bulge, for a total of 10 depth centers.
- (4) Jurassic–Cretaceous depression boundaries are mostly fractured structures. For example, the Jurassic–Cretaceous system that has developed in the Liuhe Sag of Dayanshu Basin is sandwiched between the F₂₄ fault, the F₂₅ fault, and the F₂₆ fault, and the distribution of the Mesozoic boundary in this region is obviously controlled by the fault structure.

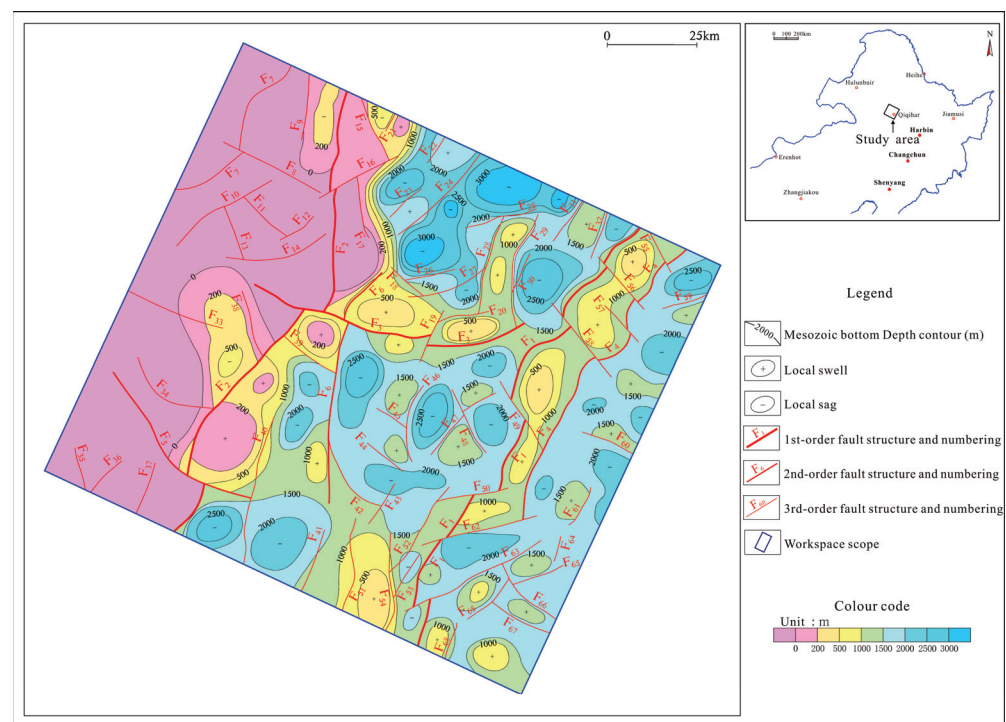


Figure 5. A bottom depth map of the Jurassic–Cretaceous system in the study area.

6. Oil and Gas Exploration Potential

6.1. Evaluation Methodology

Here, based on the Mesozoic and Upper Paleozoic ranges and their thicknesses, as illustrated by airborne gravity and magnetic data, combined with known drilling data, the prospective oil- and gas-bearing conditions in the study area were comparatively evaluated on the basis of production, storage, and cover combinations, as well as oil and gas transport, accumulation, and preservation conditions, and two categories of prospective oil and gas zones were delineated.

6.2. Division of Prospective Oil- and Gas-Bearing Areas

6.2.1. The Class I Prospective Oil- and Gas-Bearing Areas

The Class I prospective oil- and gas-bearing areas are the most favorable for oil and gas enrichment, and the most promising for oil and gas transport and gathering units in the study area. These areas are located in the western part of Dayangshu Basin, the eastern part of Longjiang Basin, and the southern part of the western slope of Songliao Basin, respectively. They contain three prospective oil- and gas-bearing areas, including Liouhe, Harakhai North, and Taikang (Figure 6).

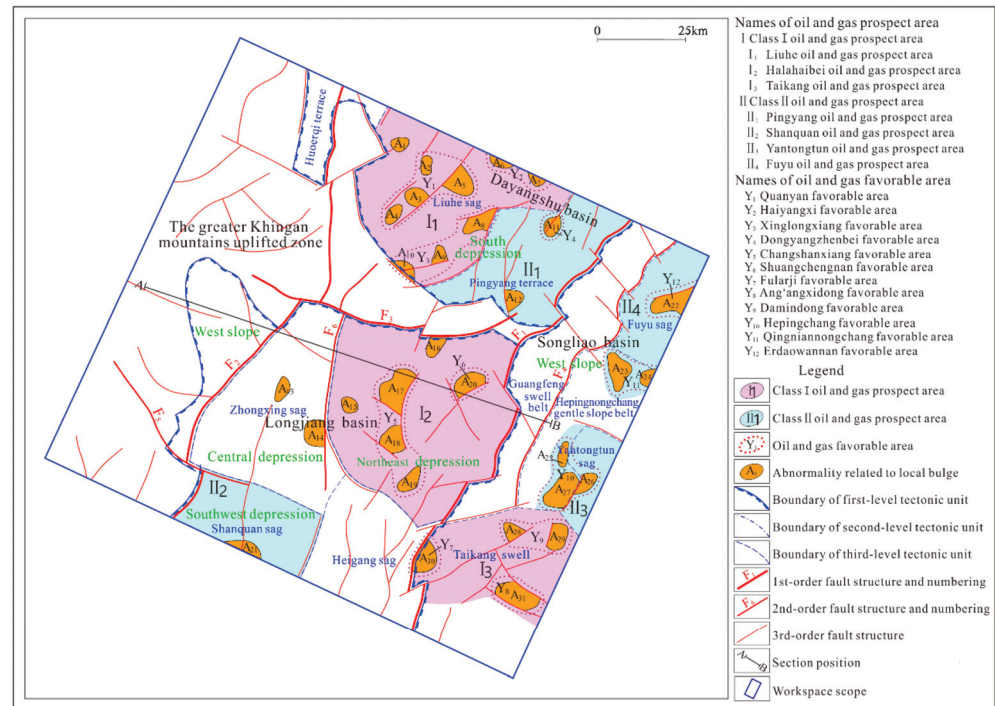


Figure 6. Prospective prediction of oil and gas in the study area.

- (1) The Liouhe prospective oil- and gas-bearing area basically corresponds to the Liouhe Sag in the western part of Dayangshu Basin, which covers a large area of about 1660 km² and is the main oil and gas generation and transport area in the region of interest. A Mesoproterozoic boundary of a certain thickness has been deposited in this area. In addition, the Upper Paleozoic boundary, with a thickness of about 1000–6000 m, is also deposited in this prospective area. Vertically speaking, this prospective area has a good configuration of raw reservoir and cover. Across the plane, there are sufficient oil and gas sources in the area, and the data on the parameter wells in the area show that oil and gas are visible here. In addition, a series of local high-gravity anomalies are apparent in the interior of the Liouhe Sag, mainly in the central, northwestern, and southern areas. These local high-gravity anomalies are mostly local structures within the depression, which provide good conditions for oil and gas accumulation and preservation.
- (2) The prospective oil- and gas-bearing area of Harahay North is located in the central part of the study area, which basically corresponds to the northeastern depression of Longjiang Basin, with an area of about 2403 km², and also has good conditions for oil and gas generation and transportation. The thickness of the Mesozoic boundary deposited in this area is relatively stable, with a varied range of about 1500–2500 m. Five Mesozoic depth centers can be seen in the prospective area, located in the northeast, center, southwest, and northwest of the prospective area. The aerial Bouguer gravity vertical one-guide anomaly map and the remaining anomaly map of the area show several local anomalies of small amplitude, which indicate storage sites in the

northeastern depression with sufficient oil and gas sources. The geomagnetic profile shows that this low-gravity and low-magnetic area is basically consistent with the distribution range of the larger low-resistance body (Figures 7–9). It is inferred that this area represents a relatively stable and continuous sedimentary depression, and the local gravity anomalies (Figure 8a–d) that have developed within the depression reflect the development of local structures, such as low swells and fault noses. The aeromagnetic anomaly maps and the related upward continuation maps (Figure 8e,f) indicate that the magmatic activity in this area is weaker compared to the surrounding area. A large range of negative magnetic anomalies indicates that a certain thickness of weakly magnetic sedimentary strata has developed in this area.

- (3) The Taikang prospective oil- and gas-bearing area is located in the southeast corner of the study area, roughly corresponding to the north-central part of the Taikang Bulge on the western slope of Songliao Basin. The depth of the Mesozoic boundary in this prospective area is mostly 1000–2000 m, with relatively little variation, and the depth center is located in the northwest. In addition to the Mesozoic boundary, an Upper Paleozoic boundary of a certain thickness also developed in this area. The thickness of the Upper Paleozoic boundary gradually increases from the southeast to the northwest. The local anomalies are mainly distributed in the northeast, southeast and western parts of the area, and can provide a place for oil and gas storage. Drilling data for the area show that local industrial oil flow has been registered.

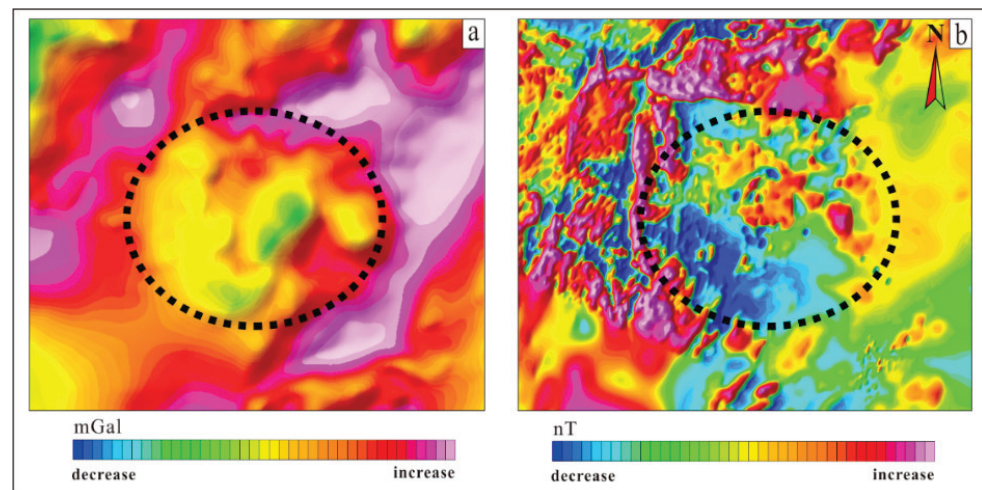


Figure 7. (a) A three-dimensional shadow map of the airborne gravity anomaly in the northeastern depression of Longjiang Basin; (b) a three-dimensional shadow map of the airborne magnetic anomaly in the northeastern depression of Longjiang Basin.

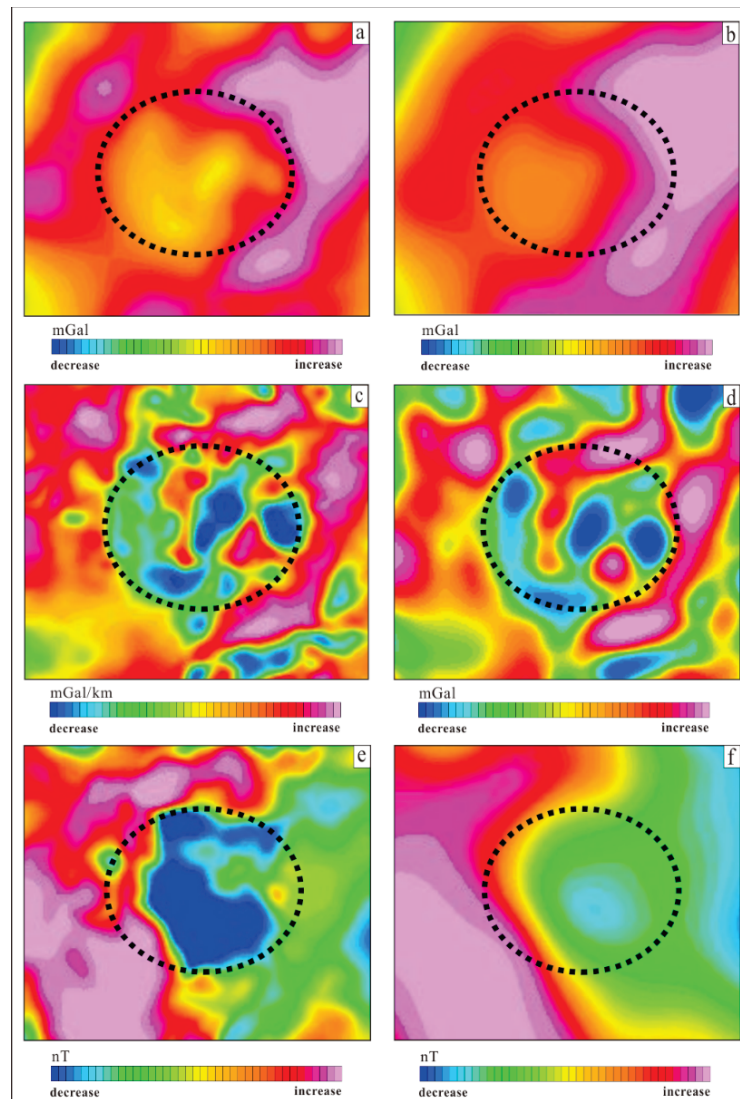


Figure 8. (a) Airborne Bouguer gravity anomaly extends upward for 3 km; (b) airborne Bouguer gravity anomaly extends upward for 15 km; (c) a vertical derivative map of airborne Bouguer gravity anomaly; (d) airborne Bouguer gravity residual anomaly; (e) airborne magnetic anomaly extends upward for 3 km; (f) airborne magnetic anomaly extends upward for 15 km.

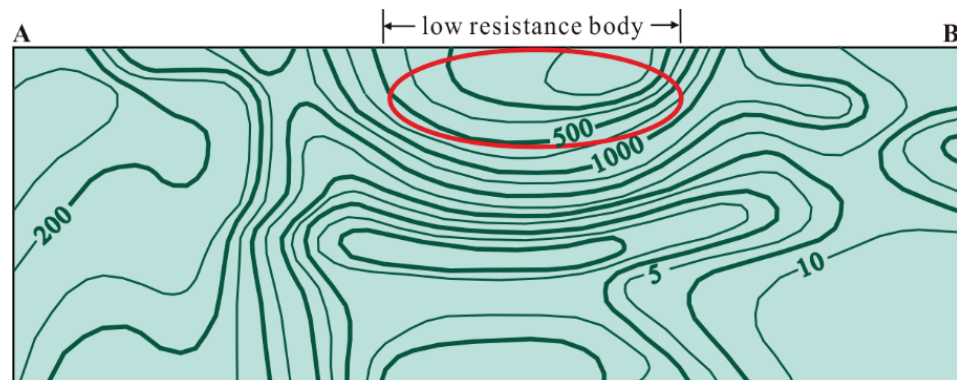


Figure 9. Geomagnetic bathymetric profile (over the northeastern depression of Longjiang Basin. The range in the red circle refers to low resistance body). AB: Section position shown in Figure 6.

6.2.2. The Class II Prospective Oil- and Gas-Bearing Areas

Class II prospective oil- and gas-bearing areas refer to the more oil- and gas-rich regions in the study area, the secondary oil- and gas-bearing and aggregating regions in the study area, or the areas that are closer to effective oil- and gas-bearing depressions, and which show certain prospects for oil and gas exploration. These are mainly located in the eastern part of Dayangshu Basin, the northern and central parts of the western slope of Songliao Basin, and the southern and western parts of Longjiang Basin.

- (1) The prospective oil- and gas-bearing area of Pingyang is located in the southern part of Dayangshu Basin, which basically corresponds to the Pingyang Terrace and covers an area of 1110 km². The Mesozoic boundary is more developed here, and has been deposited at a thickness of about 1500–2500 m. An obvious center of thickness can be seen in the southwest, with a maximum thickness value of more than 2500 m. The area also shows characteristics of the Upper Paleozoic, with a thickness value of about 3000–6000 m, and its maximum thickness (more than 6000 m) is detected in the northwest corner of Pingyang Terrace. A certain number of local anomalies have developed in the prospective area. The area is well-configured, with good reservoir cover, and should have good oil and gas prospects.
- (2) The Shanquan oil- and gas-bearing prospective area corresponds to the Shanquan Depression in Longjiang Basin, with an area of about 714 km². The Mesozoic boundary here is relatively developed, with a thickness of about 1500–2500 m, which is relatively stable. In addition, an Upper Paleozoic boundary of a certain thickness also developed in this prospective area, and the thickness of sediment here is about 1000–3000 m, showing a trend of gradually increasing from the northwest to the southeast. The reservoir cover in the area is well-configured, and it should have good oil and gas prospects.
- (3) The Yantongtun oil- and gas-bearing prospective area corresponds to the Yantongtun Depression and its western side. The two tectonic units contained in the area have deposited a Mesozoic boundary of a certain thickness—about 1500–2000 m. In addition, an Upper Paleozoic boundary with a thickness of about 4500–5000 m has also developed in this area. Its thickness center is located in the transition area between Yantongtun Depression and the gentle slope of Heping Farm. The Mesozoic and Upper Paleozoic boundaries are relatively thick and have a good reservoir cover configuration, which should yield good oil and gas prospects. According to the latest information derived from airborne physical prospecting, the Shenyang Geological Survey Center has implemented heavy, magnetic, electric, seismic, and drilling work in this prospect area, and encountered a Carboniferous–Permian system at 1370 m.

7. Conclusions

- (1) The Liuhe Sag in Dayangshu Basin, the northeastern depression in Longjiang Basin, and the northern part of the Taikang Bulge show good conditions for production, storage, and cover. The results of comprehensive high-precision airborne gravity and magnetic studies show that a series of local high-gravity anomalies have developed in the prospective area, and these anomalies mainly reflect the existence of bedrock bumps, including bedrock backslopes, subduction hills, and broken noses. These are mostly favorable local structures within the depressions and provide good sites for oil and gas accumulation and preservation. The new deep oil- and gas-bearing formations show a certain thickness and extension in the vertical direction; in the plane, the parameter data of wells in the Liuhe Sag and Taikang Bulge show that oil and gas have been found, and high-precision airborne heavy magnetic data combined with electrical, seismic, and drilling data have recently shown that the northeast depression of Longjiang Basin has low weight, low magnetism, and low resistance. The Mesozoic Depression is thus characterized by the “three lows”.
- (2) Using a combination of data conversion and processing, we can further reveal the spatial spreading pattern, tectonic control factors, main lithological composition, oil and

gas reservoir, and oil- and gas-bearing new formation system based on the analysis of oil and gas geological conditions in the study area. In this study, the thickness of the Upper Paleozoic and the depth of the Jurassic–Cretaceous base were calculated for the first time by using high-precision airborne gravity and magnetic inversion, which indicates that not only the Jurassic–Cretaceous (thickness 0–3250 m, mostly 1000–2500 m) but also the Upper Paleozoic (thickness 0–6500 m, mostly 2000–6000 m) are developed in the study area.

- (3) Based on the latest measured large-area high-precision aeromagnetic data, the favorable structural parts of new oil- and gas-bearing systems can be quickly screened. The high-precision aeromagnetic survey, combined with drilling, seismic, and electrical methods, and other auxiliary means, is one of the important ways to achieve an accurate, rapid, and efficient search for oil and gas resources.

Author Contributions: Data curation, Investigation, Writing—original draft, and Writing—review & editing, Y.L. (Yanxu Liu), Y.L. (Yanling Lai) and W.L.; Writing—review & editing, F.L., L.W., A.C., Z.J. and S.G. All authors have read and agreed to the published version of the manuscript.

Funding: This work was supported by the Geological Survey Project of China Geological Survey (No. DD20190028), the Geological Exploration Foundation Project of Hebei of China (No. 30001200000224097), and the Geological Survey Project of China Geological Survey (No. 1212011220563 and No. 12120114090401).

Data Availability Statement: Not applicable.

Conflicts of Interest: The authors declare no conflict of interest.

References

- Xing, J.S.; Yang, W.R.; Xing, Z.Y. Deep-seated structure characteristics of eastern China and its relation with metal mineralization-concentrated region. *Earth Sci. Front.* **2007**, *14*, 114.
- Li, W.Y.; Zhou, J.X.; Zhou, X.H.; Guo, Z.; An, Z.; Xu, J.; Li, B. Geological-genetic classification and prospecting significance on local anomaly of airborne gravimetry. *Adv. Earth Sci.* **2010**, *25*, 1061–1069.
- Zhao, Z.K.; Jiang, T.; He, J.L. The oil and gas exploration prospect of Carboniferous—Permian in Songliao basin, northeastern China. *Geol. Bull. China* **2011**, *30*, 221–227.
- Li, W.Y.; Zhou, J.X.; Xiong, S.Q.; Guo, Z.; Lu, W.; Xu, J.; Liu, Y. Effect and prospect of basic geological survey based on airborne gravimetry in China. *Acta Geol. Sin. Engl. Ed.* **2012**, *86*, 38–47.
- Zhu, R.K.; Zou, J.X.; Mao, Z.G. Characteristics and distribution of continental tight oil in China. *J. Asian Earth Sci.* **2019**, *178*, 37–51. [[CrossRef](#)]
- Li, W.Y.; Liu, Y.X.; Xu, J.C. Onshore Offshore Structure and Hydrocarbon Potential of the South Yellow Sea. *J. Asian Earth Sci.* **2014**, *90*, 127–136. [[CrossRef](#)]
- Liu, Y.X.; Li, W.Y. Interpretation of Local Anomalies of airborne gravity in the south yellow sea. *Prog. Geophys.* **2015**, *30*, 418–425.
- Du, J.H. Analysis of natural gas accumulation conditions and exploration perspective in the central paleo-uplift belt (north), Songliao basin. *China Pet. Explor.* **2017**, *22*, 1.
- Liu, Y.X.; Li, W.Y.; Cao, A.Q. Recognition of Tuquan basin structure based airborne gravity magnetic characteristics. *Geol. Surv. China* **2018**, *5*, 44–50.
- Guo, Q.L.; Wang, S.J.; Chen, X.M. Assessment on tight oil resources in major basins in China. *J. Asian Earth Sci.* **2019**, *178*, 52–63. [[CrossRef](#)]
- He, D.F.; Ma, Y.S.; Liu, B.; Cai, X.; Zhang, Y.; Zhang, J. Main advances and key Issues for deep-seated exploration in petroliferous basins in China. *Earth Sci. Front.* **2019**, *26*, 1–12.
- Liu, Y.X.; Li, W.Y.; Xu, J.C. The utilization of wavelet magnitude method of gravity anomaly in fault identification. *Geophys. Geochem. Explor.* **2014**, *38*, 96–99.
- Zhang, X.; Zhao, L.; Liu, T.Y.; Yang, Y.S. Multi—Scale wavelet separation of aeromagnetic anomaly and study of faults in Beijing area. *Acta Seismol. Sin.* **2006**, *19*, 542–551. [[CrossRef](#)]
- Liu, Y.X.; Li, W.Y.; Yang, D.H.; Lu, W.F.; Wang, S.M. Study on characteristics of aeromagnetic anomaly and prospecting in Tuchengzi, northwest Hebei province. *Prog. Geophys.* **2019**, *34*, 2301–2308.
- Jiang, W.L.; Tian, T.; Chen, Y.; Wang, X.; Zhang, J. Detailed crustal structures and seismotectonic environment surrounding the Su-lu segment of the Tan-lu fault zone in the eastern China mainland. *Geosci. J.* **2020**, *24*, 557–574. [[CrossRef](#)]
- Li, W.Y.; Liu, Y.X.; Lu, W.F.; Ma, G.Q.; Zhang, C.S.; Zhao, J.W. Characteristics of Zhangsanying-tongshanzi aeromagnetic anomaly zone and prospecting potential of iron deposits in northern Hebei, China. *Glob. Geol.* **2020**, *23*, 99–115.
- Achim, B.; Jia, J.L.; Susanne, A.I.S. Palaeo environmental conditions during deposition of the Upper Cretaceous oil shale sequences in the Songliao basin (NE China): Implications from geochemical analysis. *Org. Geochem.* **2012**, *46*, 76–95.

18. Wang, S.Y.; Cheng, Y.H.; Zeng, L.; Miao, P.; Jin, R.; Zhang, T.; Li, C.; Zhang, X. Thermal imprints of Cenozoic tectonic evolution in the Songliao basin, NE China: Evidence from apatite fission-track (AFT) of CCSD-SK1 borehole. *J. Asian Earth Sci.* **2020**, *195*, 104353. [[CrossRef](#)]
19. Bin, W.; Sun, D.S.; Chen, Q.C. Stress-state differences between sedimentary cover and basement of the Songliao basin, NE China: In-situ stress measurements at 6–7 km depth of an ICDP scientific drilling borehole (SK-II). *Tectonophysics* **2020**, *777*, 228–337.
20. Xu, M.; Li, Y.L.; Hou, H.S.; Wang, C.; Gao, R.; Wang, H.; Han, Z.; Zhou, A. Structural characteristics of the Yilan-yitong and Dunhua-mishan faults as northern extensions of the Tancheng-lujiang fault zone: New deep seismic reflection results. *Tectonophysics* **2017**, *706–707*, 35–45. [[CrossRef](#)]
21. Liu, X.F.; Zhong, G.F.; Yin, J.Y.; He, Y.; Li, X. GIS-based modeling of secondary hydrocarbon migration pathways and its application in the northern Songliao basin, China. *Comput. Geosci.* **2008**, *34*, 1115–1126. [[CrossRef](#)]
22. Liang, H.D.; Gao, R.; Hou, H.S.; Liu, G.X.; Han, J.T.; Han, S. Lithospheric electrical structure of the great Xing’an range. *J. Asian Earth Sci.* **2015**, *113*, 501–507. [[CrossRef](#)]
23. Wang, B.D.; Wang, L.Q.; Chung, S.L.; Chen, J.L.; Yin, F.G.; Liu, H.; Li, X.B.; Chen, L.K. Evolution of the Bangong-Nujiang Tethyan ocean: Insights from the geochronology and geochemistry of mafic rocks within ophiolites. *Lithos* **2016**, *245*, 18–33. [[CrossRef](#)]
24. Zhou, Z.; Yan, Y.P.; Ren, S.M.; Jiang, C.; Liu, G.; Yin, J. Prospects and strategy for shale oil exploration in Songliao basin, China. *China Min. Mag.* **2017**, *26*, 171–174.
25. Ji, Z.; Meng, Q.A.; Wan, C.B.; Ge, W.C.; Yang, H.; Zhang, Y.L.; Dong, Y.; Jin, X. Early Cretaceous adakitic lavas and a-type rhyolites in the Songliao basin, NE China: Implications for the mechanism of lithospheric extension. *Gondwana Res.* **2019**, *71*, 28–48. [[CrossRef](#)]
26. Li, C.L.; Cui, R.H.; Liu, Y.Z. Comprehensive geophysical prediction method of basement lithology-example of Binbei area, Songliao basin. *Chin. J. Geophys.* **2011**, *54*, 491–498. (In Chinese)
27. Wang, B.D.; Chen, J.L.; Xu, J.F.; Wang, L.Q. Geochemical and Sr-Nd-Pb-Os isotopic compositions of Miocene ultrapotassic rocks in southern Tibet: Petrogenesis and implications for the regional tectonic history. *Lithos* **2014**, *208–209*, 237–250. [[CrossRef](#)]
28. Wang, B.D.; Wang, L.Q.; Chen, J.L.; Yin, F.G.; Wang, D.B.; Zhang, W.P.; Chen, L.; Liu, H. Triassic three-stage collision in the Paleo-Tethys: Constraints from magmatism in the Jiangda–Deqen–Weixi continental margin arc, SW China. *Gondwana Res.* **2014**, *26*, 475–491. [[CrossRef](#)]
29. Wang, T.T.; Ramezani, J.; Wang, C.S.; Wu, H.; He, H.; Bowring, S.A. High-Precision U-Pb geochronologic constraints on the late Cretaceous terrestrial cyclostratigraphy and geomagnetic polarity from the Songliao basin, northeast China. *Earth Planet. Sci. Lett.* **2016**, *446*, 37–44. [[CrossRef](#)]
30. Wang, B.D.; Wang, L.Q.; Chen, J.L.; Liu, H.; Yin, F.G.; Li, X. Petrogenesis of Late Devonian–Early Carboniferous volcanic rocks in northern Tibet: New constraints on the Paleozoic tectonic evolution of the Tethyan Ocean. *Gondwana Res.* **2017**, *41*, 142–156. [[CrossRef](#)]
31. Zhu, Y. *Tangent and Diagram Methods for Analysis of Dip Magnetized Models*; Geological Publishing House: Beijing, China, 2012. (In Chinese)
32. Oldenburg, D.W. The inversion and interpretation of gravity anomalies. *Geophysics* **1974**, *39*, 526–536. [[CrossRef](#)]
33. Parker, R.L. The rapid calculation of potential anomalies. *Geophys. J. R. Soc.* **1973**, *31*, 447–455. [[CrossRef](#)]
34. Li, Y.G.; Oldenburg, D.W. 3-D inversion of gravity data. *Geophysics* **1998**, *63*, 109–119. [[CrossRef](#)]
35. Li, Y.G.; Oldenburg, D.W. Rapid construction of equivalent sources using wavelets. *Geophysics* **1998**, *75*, 51–59. [[CrossRef](#)]
36. Al-Zoubi, A.; Eppelbaum, L.; Abueladas, A.; Ezersky, M.; Akkawi, E. Methods for removing regional trends in microgravity under complex environments: Testing on 3D model examples and investigation in the Dead Sea coast. *Int. J. Geophys.* **2013**, *2013*, 341797. [[CrossRef](#)]
37. Eppelbaum, L.V. *Geophysical Potential Fields: Geological and Environmental Applications*; Elsevier: Amsterdam, The Netherlands, 2019; 467p.

Disclaimer/Publisher’s Note: The statements, opinions and data contained in all publications are solely those of the individual author(s) and contributor(s) and not of MDPI and/or the editor(s). MDPI and/or the editor(s) disclaim responsibility for any injury to people or property resulting from any ideas, methods, instructions or products referred to in the content.

Article

Coal Mine Goaf Interpretation: Survey, Passive Electromagnetic Methods and Case Study

Nan Wang ^{1,2,*}, Zijian Wang ², Qianhui Sun ³ and Jian Hui ⁴

¹ Beijing Key Laboratory of Network Culture and Digital Communication, Beijing Information Science and Technology University, Beijing 100192, China

² School of Computer Science, Beijing Information Science and Technology University, Beijing 100192, China

³ China Kunlun Engineering Co., Ltd., Beijing 100037, China

⁴ Hikvision Research Institute, Hangzhou Hikvision Digital Technology Co., Ltd., Hangzhou 310051, China

* Correspondence: wangnan8848@bistu.edu.cn

Abstract: Coal mine goaf detection remains confronted with the lack of fast, effective and low-cost exploration means, especially for the accurate prediction of mining threats primarily caused by hydraulic infiltration. The rapid popularization of passive electromagnetic methods has contributed greatly to improving the interpretation effects of different types of goafs. This paper, firstly, summarizes the pros and cons of various exploration methods in goaf detection. Then, the feasibility of goaf detection using novel passive electromagnetic methods (e.g., the super low frequency alternating magnetic component method (SLF) and audio frequency magnetotelluric method (AMT)) is proposed and further discussed. With well-designed geo-electrical goaf models, the theoretical results demonstrate that the semi-quantitative interpretation of SLF responses can be directly used for the delineation of the target layer in the estimated depth range. In contrast, 3D inversion provides more information about conductive targets with the appropriate initial model selection. Then, shallow, low-resistive targets can be more accurately allocated in the inversion maps. Moreover, the real data interpretation results from study areas demonstrate that the SLF method can utilize the magnetic component responses to effectively identify the fault structures, and indirectly contributes to judge the goaf collapse locations in favor of describing the potential distribution of fracture water infiltration. Combined with the three-dimensional (3D) resistivity inversion of AMT data, the low-resistive water-rich areas within the depth of 400 m were revealed. The inverted depth distributions are basically consistent with those of the water-filled goafs and surrounding layers, which were also confirmed by known logging data. The detailed delineations of water-control fracture zones can be inferred to relate to aquifers in some mining areas; this can reveal potential collapses that require successive mining planning. In specific working faces, goaf risks have been handled in advance by strengthening the continuous monitoring of the water level and water inflow. The above verification has laid a theoretical and practical foundation for passive electromagnetic interpretation methods for effectively predicting collapse-type risks or hydraulic threats in coal mine goafs.

Keywords: coal mine goaf; passive electromagnetic method; super low frequency alternating magnetic component method (SLF); audio-magnetotelluric (AMT); three-dimensional inversion



Citation: Wang, N.; Wang, Z.; Sun, Q.; Hui, J. Coal Mine Goaf Interpretation: Survey, Passive Electromagnetic Methods and Case Study. *Minerals* **2023**, *13*, 422. <https://doi.org/10.3390/min13030422>

Academic Editor: Paul Alexandre

Received: 9 February 2023

Revised: 9 March 2023

Accepted: 13 March 2023

Published: 16 March 2023



Copyright: © 2023 by the authors. Licensee MDPI, Basel, Switzerland. This article is an open access article distributed under the terms and conditions of the Creative Commons Attribution (CC BY) license (<https://creativecommons.org/licenses/by/4.0/>).

1. Introduction

In recent years, the increasing demand for coal resources in sustainable production has become one of the most important topics all over the world. However, pervasive water-collapse disasters, a form of mine accident which has not been effectively prevented, occur frequently, especially in coal mine goafs [1]. Goafs, roof floors, collapse columns and other potential aquifers are the main factors in coal mining disasters [2,3]. Therefore, it is necessary to comprehensively evaluate the characteristics of different geophysical methods and select appropriate detection methods according to the geological settings and buried depths of goaf targets [3,4].

At present, almost all traditional exploration methods, including seismic methods, gravity, logging, radiation and electromagnetic methods, have been applied in goaf interpretation, combined with drilling [5], drainage and production data, temperature changes or thermal anomalies [6]. Seismic methods, including the shallow seismic reflection method, scattered or diffraction wave method, surface wave method (or microseismic method), tomography technology, etc., are mainly built on the wave velocity and impedance differences between goafs and surrounding roof-floor rocks, if coal seams are mined with the goafs formed [7,8]. It is widely acknowledged that complete coal seams possess low density and low velocity, with strong reflection waves and stable seismic events. In contrast, mine goafs could lead to damaged strata, which accounts for a strong attenuation effect, with distorted or misplaced events, on the seismic reflection waves [9]. This effect is characterized by irregular or even disordered reflection wave deformations [10,11]. The aforementioned reflection methods are inapplicable when the width of a goaf is less than its lateral resolution; thus, the diffraction method, the Rayleigh method and the microtremor seismic method (SMS) are introduced [8]. In addition, seismic velocity tomography can be obtained by the joint interpretation of the travel time, amplitude and signal frequency, and pressure inversion can also be carried out [12]. In particular, the extraction and application of seismic attributes can greatly improve detection results with high signal-to-noise ratio seismic data [13]. The radioactive method is also applied because of high radon concentration anomalies in coal mine goafs or collapse areas. As radon elements migrate to the surface through the caving fracture zone in a goaf, the locations of the coal mine goaf can be accurately delineated. However, it is difficult to determine goaf depth [14]. Additionally, the vertical density changes of the collapses in the goaf zones account for negative gravity anomalies, and the gravity method is characterized by three-dimensional apparent density inversion and the boundary identification of gravity anomalies [15,16]. Meanwhile, electromagnetic methods, based on electrical differences in the properties between goafs and surrounding rocks, such as resistivity, polarization parameters and electromagnetic absorption parameters, have also been employed [17–19]. The high-density resistivity method is used to analyze water-rich goafs [20]. The dipole–dipole device is suitable for a goaf with an exploration depth [21]. Transient electromagnetic method is also mainly aimed at a water-filled low-resistive goaf, and the changes of horizontal component responses are more sensitive than those of vertical component responses [22–24]. For a shallow goaf, a general central loop source device can be used. A large fixed source loop device possesses the advantages of high efficiency and high resolution [25]. Additionally, the dual-frequency induced polarization (IP) method was introduced because IP and amplitude frequency characteristics are reduced if a goaf forms [26]. Due to goaf deformation, synthetic aperture radar interferometry (InSAR) is used to obtain cumulative settlement in a continuous time [27], in addition to the deformation rate and surface deformation of goafs [28,29]. All exploration methods are summarized in detail in Table 1.

The current coal mine goaf interpretation technology was developed in the following directions: the joint method, from “the half space”, or from “the whole space” [30,31]. However, the widespread adoption of these methods remains limited because of the complex technology, high cost and low exploration efficiency involved. Therefore, a fast and efficient natural source method, i.e., the passive electromagnetic method, is rapidly being developed and applied. This method is based on the electromagnetic induction principle using the natural source’s electromagnetic observation data to produce an image of the electrical structure of the subsurface medium. The classical passive methods, such as geomagnetic sounding (GDS) and magnetotelluric sounding (MT), have entered full development [32]. In order to effectively analyze the theoretical electromagnetic responses of underground media, the equations mentioned in the following sections can be obtained on the assumptions of one-dimensional, two-dimensional and three-dimensional geoelectric models. Commonly used numerical simulation methods mainly include the finite difference method, finite element method and integral equation method, which lay a foundation for subsequent inversion [33]. The measured data is further fitted with the responses of the theoretical models after the signal spectrum estimation [34]. Regularization constraints are introduced to reduce the multiplicity of inversion solutions [35]; this multiplicity has grad-

ually changed from one-dimensional and two-dimensional inversion to three-dimensional inversion [36]. Nowadays, the audio-frequency magnetotelluric method (AMT) has attracted greater attention because of its fast and economical exploration to a depth of less than 1000 m [37]. Predecessors used EH4 detection equipment (one popular AMT module) to preliminarily detect coal mine goafs [38] and to analyze water-rich distribution [39]. Additionally, passive electromagnetic component methods were applied [40]. To date, AMT inversion used for the effective interpretation of coal mine goafs has still not been explored and resolved. Passive electromagnetic methods mainly use the ratio of electric field and magnetic field components to obtain the impedances or magnetic ratio responses for resistivity inversion [41]. Although impedance calculation eliminates random fluctuation and time variation factors, it may weaken detailed changes, contained in electromagnetic components, related to underground structures [40,42]. In fact, natural source electric and magnetic components both contain detailed subsurface information [43].

Table 1. A summary of classical geophysical methods in coal mine goaf exploration.

Category	Methods	Detection Basis	Detection Capability	Advantage	Defects	References
Seismic class	Reflection wave method	Wave impedances	Buried depth of 50~200 m	Small site distance, high density of data collection, high-resolution continuous measurement.	High cost, complicated process, low efficiency, unable to determine the water-rich nature of the mining area; reduced feasibility when the width of the mining area is smaller than the lateral seismic resolution.	Xue et al. [2] Xue et al. [9] Zhang et al. [12]
	Face wave method	Frequency dispersion, low-speed anomaly of P-waves	-	Convenient, fast detection, strong anti-interference ability, low requirements for exploration sites.		Xue et al. [2] Yu et al. [8] Wu et al. [44] Zhu et al. [13]
	Tomography imaging	Velocity and amplitude	-	Close to the target layers, high resolution, visual imaging.		
Radiology	Radon measurement	Radon anomaly	-	Low cost, simple process, high efficiency, not affected by the terrain of the environment.	Qualitative analysis, low detection reliability, and the depth cannot be interpreted.	Zhou et al. [14]
Electromagnetic class	High-density resistivity method	Resistivity	Burial depth of 50~150 m	High lateral resolution, sensitive to shallow low resistive anomalies and water-bearing bodies.	Influenced by the terrain conditions.	Wu et al. [18] Bharti et al. [21] Bharti et al. [45]
	Transient electromagnetic method	Resistivity	Burial depth greater than 400 m	Versatile devices with large exploration depth, high efficiency, and low topographic influence.	Low work efficiency, easily affected by high conductors or power line interferences.	Chang et al. [22] Chang et al. [46] Wang et al. [47] Wang et al. [25] Wu et al. [18]
	Geological radar method	Travel time, amplitude, frequency, waveform change	Burial depth less than 50 m	High resolution, high efficiency, and no damage to the target body	Noise suppression challenges.	Xu et al. [19] Xue et al. [9]
	Controlled-source audio-magnetotelluric sounding (CSMAT)	Resistivity	Burial depth greater than 400 m	Excellent detection of conductive bodies, large detection depth.	Static displacement, and near-field effects	Xu et al. [38]
	Excitation polarization method	Dielectric constant, polarization parameters	-	-	Little practice.	Wang et al. [26]
	Very low frequency method (VLF)	Resistivity	Depth less than 1000 m	Low cost, portable and fast, easy devices to operate.	Little practice.	Xue et al. [9]
	Multisource remote sensing (RS)	Land subsidence, deformation rate	Near surface	Large scale.	Not suitable for a small area, weak deformation measurement.	Li et al. [27] Fan et al. [28] Li et al. [29] Yang et al. [31]
Gravity	Gravity method	Density	-	Fast gravity anomaly analysis, variations of thickness.	Unable to realize depth sounding.	Xiang et al. [15] Li et al. [16]

In this paper, the potential advantages of passive electromagnetic methods in coal mine goaf interpretation will be systematically explored. Among them, semi-quantitative SLF inversion in collapse-type mining goaf areas will be discussed and validated. The

stable 3D AMT inversion method is also proposed and examined by analyzing single-target and multi-target model results combined with types of initial models or data error bars. Preliminary field surveys could be subsequently accomplished using proposed electromagnetic methods with promising applications as tools to interpreting collapse-type risks or hydraulic threats in coal mine goafs.

2. Passive Electromagnetic Detection Mechanism of Coal Mine Goafs

2.1. Typical Structure and Physical Properties of Coal Mine Goafs

Coal mine goafs often form after the mining process when the overlying strata collapse due to gravity. Generally, three zones are shaped vertically: the caving zone (overburden collapse of coal seam), the fracture zone (bending fracture under shear stress), and bending zone (from the roof of the fracture zone to the ground, deformed but not broken). See Figure 1 for details.

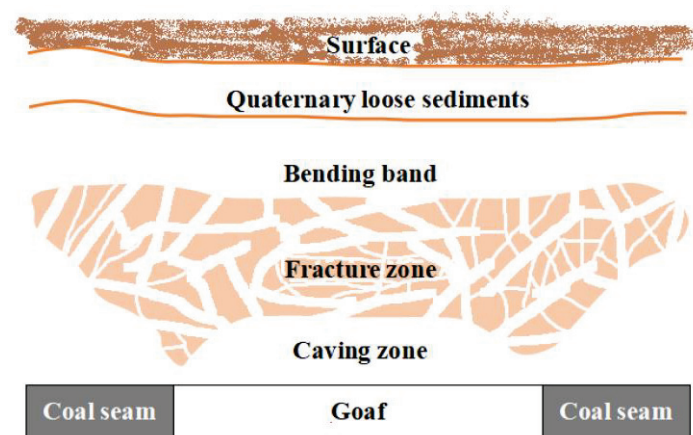


Figure 1. Sketch map of the vertical “three zones” in the coal mine goaf areas.

To facilitate the analysis of multiple types of coal mine goafs, for the purposes of this paper, two study areas were selected, as shown in Figure 2. These were located in the central part of Henan Province, China. Study Area 1 is bordered by Xinzheng City, Changge City and Yushi County, with a distance of 50 km from Zhengzhou City to the west of the city center. Study Area 2 is about 100 km away from Study Area 1. According to field investigation of the mining areas, the strata were deposited, from bottom to top, in the Paleozoic Cambrian and Middle Ordovician periods in the Upper Carboniferous Benxi Formation and, in the Taiyuan Formation, in the Permian and the Quaternary periods. The sedimentary sequence of coal seams is relatively clear and stable in the vertical direction and relatively uniform in the horizontal direction. The characteristics of resistivity parameters obtained from relevant sample tests are shown in Table 2. The resistivity value of coal seams is relatively high. After the resistivity value of coal seams, which was the highest found, the value of sandstone was second highest, and the value of clay rock was the lowest. Usually, the mineralization value of fractured water layers in the surrounding rocks of coal seams is up to 700–1100 mg/L, and aquifers often show abnormally low resistive distributions. In field surveys, coal mine goafs often form water-rich areas due to the groundwater infiltration or inflow through coal mine cracks. Taking typical structures and electrical characteristics into account, we designed theoretical models, as explained in the following sections.

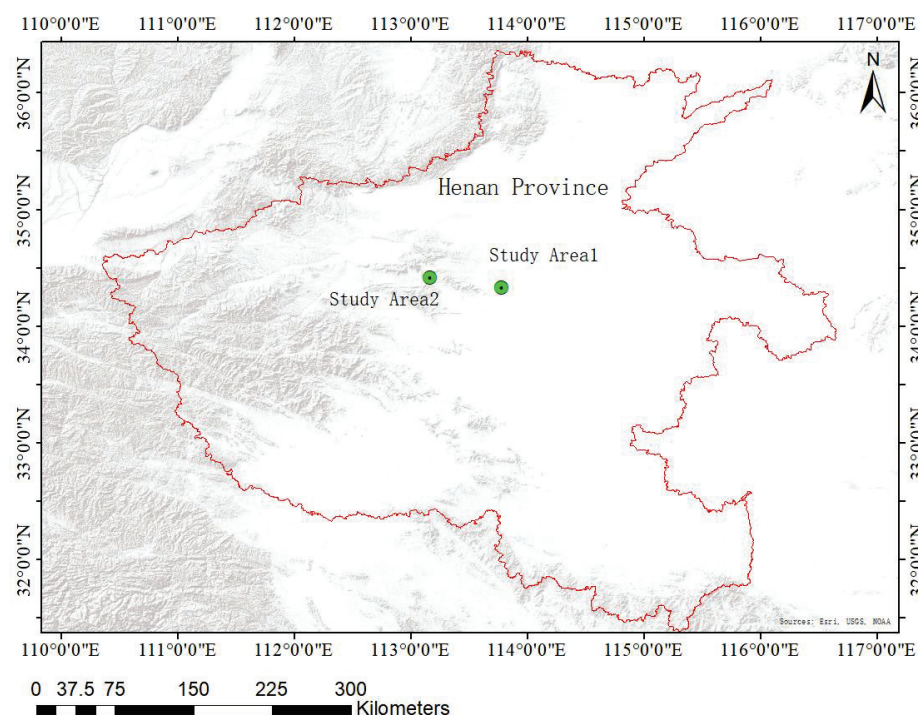


Figure 2. Geological map of two study areas (shown by the green dots).

Table 2. Electrical parameters and lithological properties revealed by drilling data.

Lithology	Resistivity Distribution ($\Omega \cdot m$)	Distribution Stratigraphic Code	Remarks
Clay	50–200	Q	Quaternary
Sandstone	100–600	Q, P ₁ s, C ₃ t	Quaternary, Upper Carboniferous Taiyuan Group, Permian
Mudstone	30–100	Q, P ₁ s, C ₂ b	Upper Carboniferous Benxi Formation, Permian
Limestone	900–3900	O ₂ f	Ordovician
Coal seams	1000–3000	P ₁ s, C ₃ t	Samples from the study area
Groundwater (mineralized water)	0.1–10		

Note: The parameter values are measured from stable rock samples, and if the rock formations change, the actual stratigraphic parameters will change significantly.

2.2. Semi-Quantitative Inversion of the SLF Method

As discussed above, electromagnetic inversion is the one of the key points of geo-electrical interpretation. For the SLF method, semi-quantitative inversion originates from the classical MT empirical formula, which accounts for how to realize frequency-depth transformation using magnetic component responses [32]. Firstly, Schmucker’s method describes the Schmucker impedance response by the first-order moment normalization of the induced current, and then completes the depth transformation according to the relationship between the impedance response itself and “apparent resistivity-phase”. However, this method is not valid for the case of a “low resistivity target layer + thick high resistivity basement”. Another classical empirical transformation, even more commonly used in the MT method, is Bostick inversion. As a semi-quantitative interpretation method, Bostick inversion is obtained following a mathematical transformation that analyzes the low-frequency asymptote of apparent resistivity under the conditions of both high-resistive

limit and low-resistive limit. Equations (1)–(4) are modified from the references [32,40]. The general form derived from the intersection of two asymptotes is:

$$\rho(H) = \rho_\alpha(\omega) \left[\frac{\pi}{2\varphi(\omega)} - 1 \right] \quad (1)$$

$$H = \sqrt{\frac{\rho_\alpha(\omega)}{\omega\mu}} \quad (2)$$

In Equations (1) and (2), $\rho(H)$ represents the inverted resistivity, and H represents the inversion depth. μ is the permeability, ω is the angular frequency. $\rho_\alpha(\omega)$ and $\varphi(\omega)$ are the apparent resistivity and phase at a certain angular frequency ω , respectively. Formula (2) is very similar to the exploration depth Formula (3) of the uniform half-space model [32]:

$$D = \sqrt{\frac{\rho}{\omega\mu}} \quad (3)$$

where D is the exploration depth, ρ is the uniform half-space resistivity.

In Equation (2), $\rho_\alpha(\omega)$ is the apparent resistivity of two asymptotes at the intersection of a certain frequency. Usually, the apparent resistivity calculation depends on the impedance calculation, and the impedance of each frequency point is contributed by the underlying stratum excluding the target layer [42]. ρ_α is the comprehensive resistivity of each layer at the depth of asymptote intersections. The target layer and its underlying stratum can be treated as a uniform body with its compromise resistivity set as the comprehensive resistivity ρ_g . ρ_α can be replaced with the comprehensive resistivity ρ_g . The influence of depth range measurement can be measured using the weight coefficient, so the exponential parameter (corresponding distance weight coefficient) of ω in Formula (3) can be dynamically selected [40]. The improved frequency-depth transformation can customize the exploration depth range and reasonably extract the layer thickness. In the international system of units, the expression is:

$$H = 356 * \frac{\sqrt{\rho_g}}{f^c} \quad (4)$$

In Equation (4), H is the estimated depth (m), ρ_g is the comprehensive resistivity ($\Omega \cdot m$), f is the frequency (Hz), and c is the adjustable exponential parameter (index), i.e., the weight coefficient. This frequency-depth transformation is actually an interpolation method with the depth as the weight, which reflects the “volume effect” in the electromagnetic methods [40].

With regards to the fact that the depth of coal mine goafs is less than 1000 m, a three-layer model was designed with specific parameters described as the caprock layer (variable thickness, resistivity of 100 $\Omega \cdot m$), the middle target layer (100 m thick, variable resistivity) and the basement (infinite depth with resistivity of 1000 $\Omega \cdot m$). Different models were obtained by changing the buried depths and resistivity distributions of the intermediate target layer. For example, in the case of an intermediate target layer 100 m thick with resistivity of 1 $\Omega \cdot m$ and a uniform half-space base of 1000 $\Omega \cdot m$, the comprehensive resistivity is set by test as 400 $\Omega \cdot m$, seen as a compromise between 1 $\Omega \cdot m$ and 1000 $\Omega \cdot m$. The index parameter is manually set at 0.5 following multiple attempts according to the geological settings. The SLF amplitude responses at the midpoint of the surface of each model are calculated using one-dimensional forward modeling, as shown in Figure 3. When the buried depth of the target layer changes from 200 m to 1000 m, the theoretical responses can be directly transformed as the curves in the depth domain. Compared with the trend line (shown by the straight line), the starting position of the upturned tail basically corresponds to the top buried depth of the target layer. As shown by the arrows, when the buried depth of the middle layer is 200 m, the tail tends to tilt up from 200 m, which basically demonstrates that the semi-quantitative frequency-depth transformation is suitable for the buried depth

estimation of the target layer. Meanwhile, the basement depth can also be reflected where the response tends to be gentle, around 2000 m. Therefore, the SLF response can be used for the delineation of the target layer in the estimated depth range.

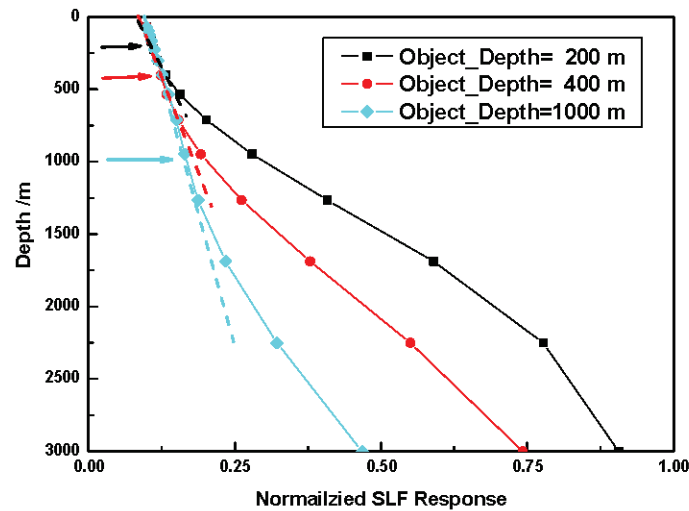


Figure 3. Three-layer model and theoretical responses using semi-quantitative frequency-depth transformation. The SLF responses in the depth domain (the second objective layers' top depths) are set as 200 m, 400 m and 1000 m. Different dotted lines represent the trend lines. The arrows are located at the intersection points of trend lines of the SLF responses.

2.3. Three-Dimensional Electromagnetic Inversion of the AMT Method

AMT inversion is also theoretically explored for its feasibility in interpreting coal mine goafs. In the past years, the two-dimensional inversion of three-dimensional (3D) models has primarily been discussed. With the distributed three-dimensional inversion program entering the industrialization stage, it is no longer difficult to realize 3D inversion of real data in AMT exploration [41]. Considering that coal mine goafs usually belong to two extreme types—either complete high-resistive air-rich areas or complete low-resistive water-rich areas—models can be designed with two types of target layers embodied, which can be used to evaluate the feasibility of three-dimensional AMT inversion. Shallow surface electrical bodies regarded as typical 3D electrical anomalies are also considered, which are often far smaller than the AMT exploration scale of several kilometers to tens of kilometers. The target layer is often only tens of meters thick, which can be regarded as a thin layer relative to the buried depth (assuming that the “depth-thickness” ratio is not less than 10). The target layer is usually distributed along the strike and can be regarded as a two-dimensional structure. The electrical properties of basement and overlying sedimentary rocks are relatively stable and can be regarded as a one-dimensional structure. The buried depth of the target layers designed in this way is generally 400 m~700 m, and the thickness of the target layer is generally 10 m~50 m. In contrast, the shallow anomalies are also tens of meters thick. In order to distinguish the abnormal response from different stratum, the resistivity values of shallow anomalies and target layers were set as $10 \Omega \cdot \text{m}$ and $1000 \Omega \cdot \text{m}$, respectively. The limestone basement was set as $3000 \Omega \cdot \text{m}$. Synthetic models of thin low and high-resistivity target layers are shown in Figure 4. In Figure 4a, y is the strike direction of the stratum. At the surface of $Z = 0$ in the XOY profile, the area of interest was $5 \text{ km} \times 3 \text{ km}$, of which the surface anomalies were set as a scale of $1 \text{ km} \times 1 \text{ km}$ with low resistivity ($10 \Omega \cdot \text{m}$) and high resistivity ($1000 \Omega \cdot \text{m}$). Along the XOZ section with $y = 0$, as shown in Figure 4b, the thickness of shallow abnormal bodies was 50 m. At a depth of 470 m, a two-dimensional anomalous body ($3000 \text{ m} \times 30 \text{ m}$, $1 \Omega \cdot \text{m}$) was designed as the exploration target layer extending infinitely along the strike Y direction. The high-resistive substrate at a depth of 50 m below the target layer was set as $3000 \Omega \cdot \text{m}$. As for the high-resistivity target layer model, the design was almost consistent

with that of the low-resistivity model, except that a two-dimensional high-resistive anomaly ($3000\text{ m} \times 30\text{ m}$, $1000\ \Omega\cdot\text{m}$) was present in the XOZ section at $y = 0$, shown in Figure 4c. As for the mining area, there are often multiple target layers (coal seams or goafs), and, therefore, two-layered target models were also designed with a particular depth distance. The first layer was set as a low-resistive layer and the second layer was set as a high-resistive or low-resistive layer; these models were also used to test the AMT 3D inversion, as shown in Figure 4d,e.

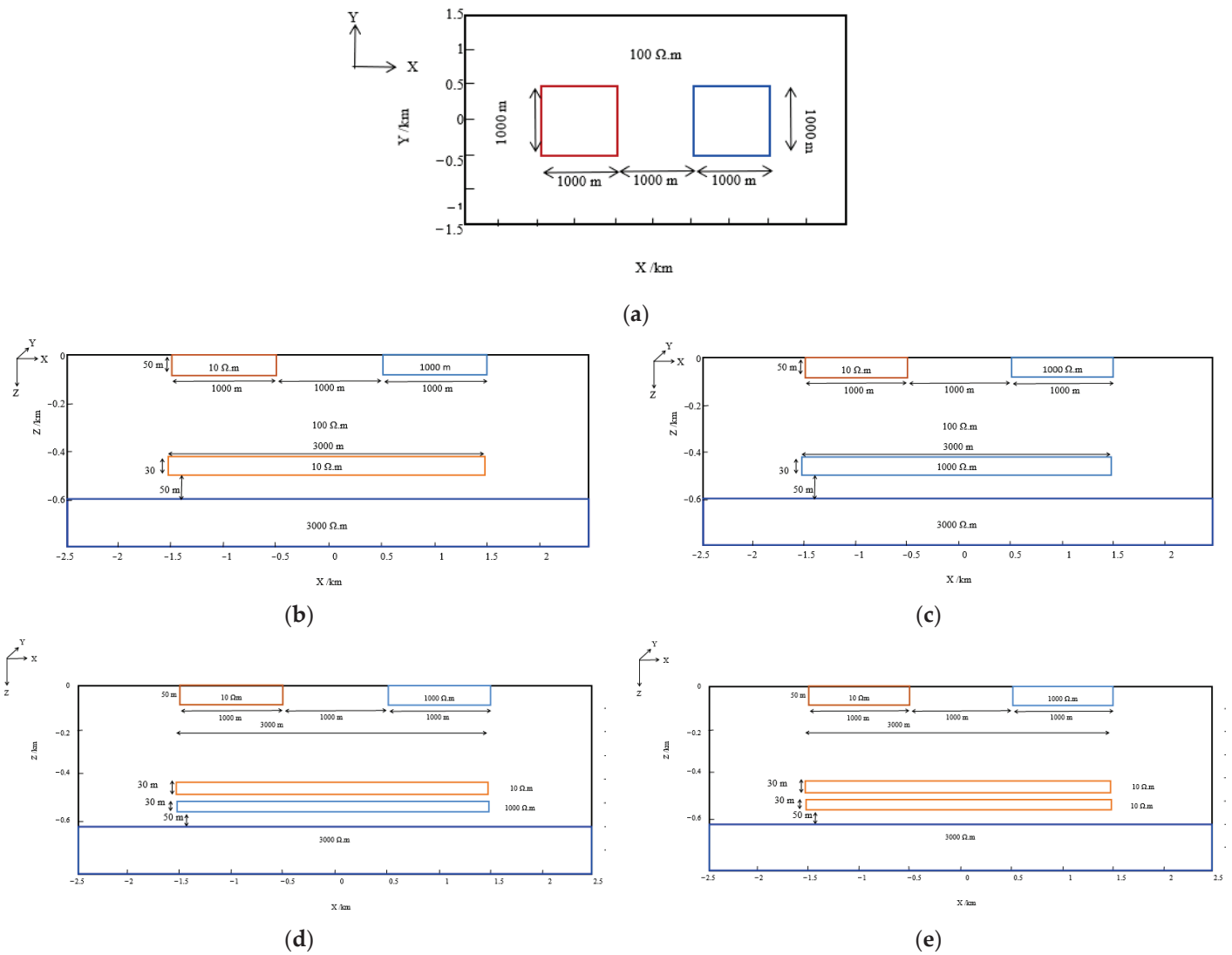


Figure 4. Profiles of the 3D synthetic models of single- or double-target layers from different perspectives. (a) Schematic diagram of XOY profiles at $Z = 0$ for both single-target models; (b) XOZ profile at $Y = 0$ for the low resistive target layer model; (c) XOZ profile at $Y = 0$ for the high resistive target layer model; (d) double-target layer model with the second target as high resistive; (e) double-target layer model with the lower layer set as low resistivity.

A typical measurement line, which strides over a shallow inhomogeneous body at $Y = 0$ in the XOY plane, as shown in Figure 5a, was selected. The impedance tensor responses of 20 points along the line were simulated by 3D forward modeling. For each response, 5% Gaussian random noise was added. The synthetic data were treated as the initial data file of the 3D inversion. Then, the 3D impedance tensor inversion of the line was performed using the ModEM inversion system [48]. Both the initial model and the priori model were set to a uniform half-space of $100\ \Omega\cdot\text{m}$. The 3D inversion grid was set to

$24 \times 32 \times 28$, and the air layer was divided into 7 grids. The horizontal grid profiles were carried out in 250 m steps in the region of interest. In the vertical Z-direction, the shallow surface and target layers were dissected in 10 m grid steps. Meanwhile, the surrounding layers were dissected at 25 m–100 m intervals, and so that the substrate depth meets the minimum frequency skinning depth and boundary conditions. The initial RMS of the 3D inversion was 10, on average, and the final RMS was about 1.5–2 after 80–100 iterations when the final iteration converged. The results of 3D tensor impedance inversion for all points of the same line are shown in Figure 5b–e, where all the superficial anomalies can be accurately circled. In Figure 5b, the low-resistive target body is clearly prominent. However, there are still some false anomalies in the vertical direction of the target layer, which may be related to the excessive thickness and the low-resistive influence of the surface anomalies. The model inversion procedure in the “high-resistive target layer” model is the same as that of the low resistive model in the previous section; the inversion results are shown in Figure 5c. Both the resistivity distribution and anomalous boundary can be accurately extracted for the shallow anomalies. However, it is very difficult to distinguish the high-resistive target layer from the background. This demonstrates that it is difficult to extract the high-resistive thin layer in the 3D impedance tensor inversion of the AMT method, and it is not suitable to use the high-resistive thin layer as the target. Therefore, taking into account the available computational resources, it is better to choose the 3D inversion of a thin low-resistive target layer in the AMT exploration, which can achieve the purpose of highlighting the targets as much as possible and reducing the influence of false anomalies.

The 3D inversion results of the “two target” models are further discussed in Figure 5d. When the first layer is low resistive, the high-resistive anomalies below will be completely masked. If the lower layer is a low-resistive anomaly, the inversion effect of the first layer will be enhanced, and it will be difficult to infer the lower anomaly, as shown in Figure 5e. All of the results show that it is almost always easier to completely invert the shallow anomalies. Although both the boundary and resistivity values of the target layer can be inverted, there is still a small vertical resistivity bias in the inversion. In the exploration depth range of the AMT method, the vertical distribution of the area of interest in models is 1000 m deep. As for the target layer at tens or hundreds of meters, the inversion results will be affected by the inversion algorithm, calculation accuracy and shallow surface anomalies. Even under ideal circumstances, it is very likely that electrical deviations of several meters or even a dozen meters from the target layer will be caused, which cannot be completely avoided in practical applications. Therefore, the AMT method is suitable for 3D inversion interpretation of single-layer conductive anomalies. In addition, we conducted a stability test of 3D inversion with different initial models and error bars, including full-information (impedance tensors + tippers) inversion. The results demonstrate that full-information 3D inversion does not provide more target information than that of impedance tensor inversion. Additionally, the initial model plays a key role in 3D inversion. However, there is not sufficient empirical evidence to demonstrate that the initial model would be better on the AMT sounding scale. In practice, the uniform half-space model is usually chosen as the initial model, or one-dimensional inversion is performed and interpolated based on real data [48].

Coal mine goafs often form water-rich areas due to groundwater infiltration or inflow, and low-resistive anomalies can be considered as targets. Through the theoretical analysis above, the aforementioned electromagnetic methods were also appropriately applied in our coal mine goaf areas. In the mining or coal retrieval areas, there is an urgent need to improve the geological discrimination of geological threats and water-rich damages, such as coal seams, fault positions and caves. In the following section, the actual application will be discussed in detail.

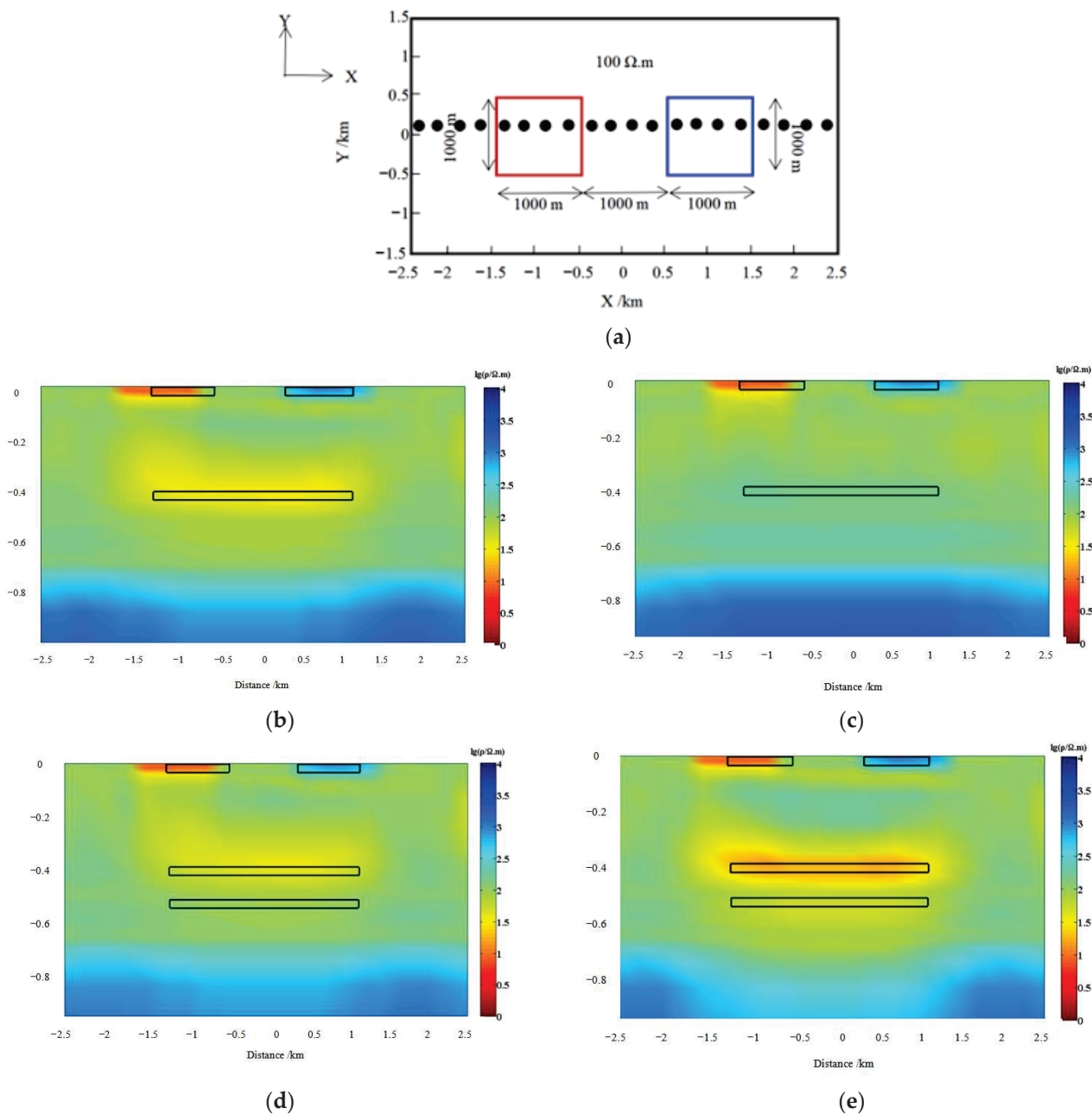


Figure 5. Schematic diagram of the theoretical measuring line and 3D inversion results of different models. (a) A typical profile in X-direction on the surface of one 3D model. The black dots represent the locations of the measurement points, the red boxes circle the shallow low-resistive target bodies ($10 \Omega \cdot m$), and the blue boxes circle the shallow high-resistive bodies ($1000 \Omega \cdot m$); from (b–e): three-dimensional impedance tensor inversion results of single- or double-target models—the black boxes show the positions of the real anomalies in each model, respectively.

3. Collapse-Type Coal Mine Goaf Interpretation

3.1. Overview of the Collapse-Type Mining Area

This area is located in Study Area 1 (shown in Figure 2), where the whole tectonic pattern is an incomplete asymmetric diagonal structure with an axial direction from NE to SW. For collapse-type mining area, two folds were distributed and about 82 faults with a drop greater than 5 m were identified, all of which were high-angle positive faults with a fault density of $1.48 \text{ faults}/\text{km}^2$. A field survey should be carried out to reveal the status of faults which lie concealed around coal mine goafs, as shown in Table 3. Additionally, the

stratigraphic formations, from old to new, revealed by boreholes, belong to the Ordovician's Majiagou Group, the Upper Carboniferous' Taiyuan Group, the Lower Permian's Shanxi Group and Lower Shi Box Group, the Upper Permian's Upper Shi Box Group and the Quaternary Formation. The Carboniferous and Permian formations are the main coal-bearing seams.

Table 3. Statistical characteristics of faults in collapse-type coal mine goaf area.

Fault ID	Fault Feature	Extension Length (m)	Bed Attitude			Stratigraphic Fall (m)	Corresponding Sites
			Strike	Dip	Dip Angle		
F ₁₃	Positive	1700	Near EW	S	65°	0~15	8–10
F ₁₂	Positive	>3600	NWW~SEE	NNE	65°	0~60	8–10
F ₁₁	Positive	4300	NWW~SEE	NNE	65°	0~175	13–15
F ₁₀	Positive	1050	NWW~SEE	SSW	65°	0~70	16–17

3.2. Stratigraphic Characteristics and Preliminary Exploration Basis

The coal-bearing strata in this area were mainly distributed in the Taiyuan Group, Shanxi Group, Lower Shi Box Group and Upper Shi Box Group, and the total thickness of coal seams was 8.14 m. The No. 2₁ coal seam is the main minable coal seam. At this location, it is scarcely possible to distinguish the mining area from the surrounding rocks. However, the overlying aquifer of the No. 2₁ coal seam forms the direct water filling source, and this may have a hydraulic connection with other strong aquifers and coal mine goafs. The fracture water enters the working faces as the mining process occurs; this can form a low-resistive zone. This zone was quite closely related to the faults, and the fracture water status and fault distributions in the collapsed mining area must be accurately measured before the successive mining plan is initiated.

3.3. The SLF Exploration Tests

High-quality detection data are important to improve SLF signal resolution and inversion accuracy. In recent years, a high-precision and portable device used in the SLF method has been developed; a workflow for the field survey is summarized in detail. For the acquisition of data in the SLF band, a BD-6 electromagnetic detector developed by us is mainly used [40]. The detector uses a high-precision magnetic sensor to receive a horizontal magnetic field component signal from 3 Hz to 3000 Hz. The system consists of three parts: a magnetic sensor, a host and a power supply. The magnetic sensor contains a magnetic rod, an amplification circuit, a programmable trap circuit, a high-speed acquisition circuit and other modules. The minimum received induced voltage value is 0.1 μ V, and the response of the weak varying magnetic field amplitude can be obtained sensitively. The sensor noise is very faint, and the preamplifier output gain can amplify the weak signal at micro-voltage level by 10^6 times, which provides hardware support for the effective signal identification. The host contains data acquisition, format conversion, storage and control units, and is capable of suppressing powerline noise (50 Hz) and its harmonics. The power supply unit can supply power to the host and the sensor for a long time. The equipment is portable, easy to use and highly efficient.

The workflow of the SLF method is shown in Figure 6. In a specific study area, suitable measurement points are selected according to real data, and the BD-6 detector is used for multiple, multi-angle data acquisitions. The data quality is evaluated after each acquisition; a high signal-to-noise ratio and good spectral repeatability are required. Through the averaging, normalization, filtering and denoising to suppress the powerline interference, the effective geological information is highlighted with semi-quantitative inversion. In fact, it is necessary to, firstly, evaluate the resistivity distributions of the target layer and the following strata from known geological and geophysical data. The empirical parameter of the improved frequency-depth transformation in Section 2.2 is often not more than 0.5 when the target layer is of low resistivity. In the study area, the electromagnetic detection test was

carried out for production monitoring from 27–28 April 2012. The detection depth, step size, magnification, probe orientation and wiring plan were initially determined according to the actual conditions. A total of 26 measurement sites were selected from north to south at intervals of about 20 m—as far as possible from the surrounding human noise.

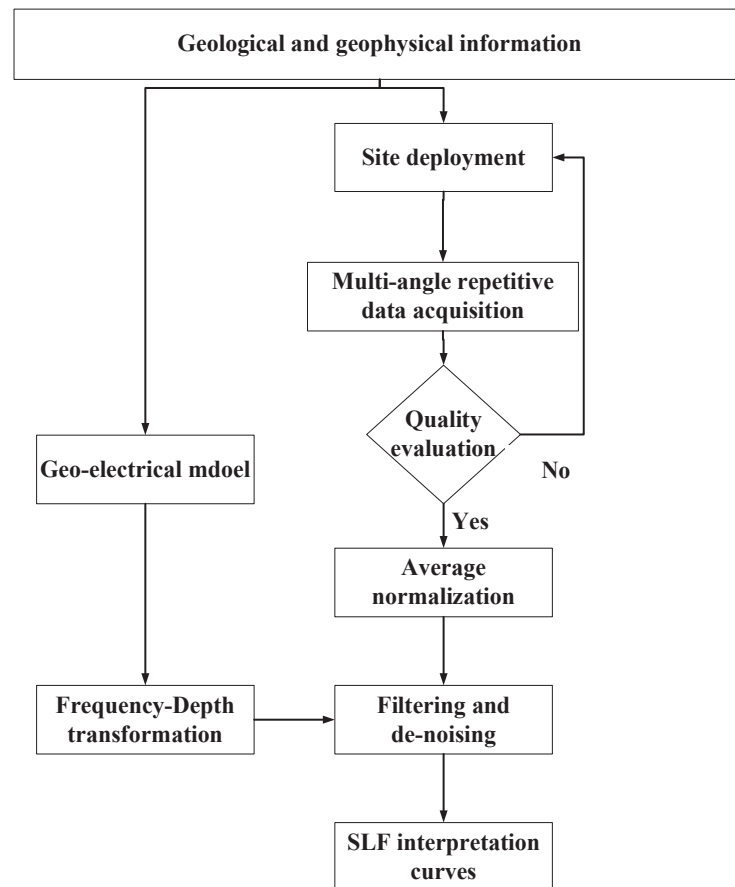


Figure 6. Workflow chart of the SLF electromagnetic method.

3.4. Result Interpretation and Comparative Validation

The semi-quantitative inversion profile of the SLF method was obtained from the left to the right of No. 8–16 sites, as shown in Figure 7a. The anomalous response in the curve was mainly around 900 m, which may be due to the conductive difference between the upper and lower layers. The response section demonstrated that there were indeed faults at measurement sites 08–10 and sites 13–16. The low-resistive layers in the different depths of 500–700 m formed because of faults, which led to the anomalous responses at dislocated depths. The drilling data show that the coal seam is located at a depth of 590–610 m, which is mostly consistent with the exploration results. Combined with the 2D seismic travel time profile (Figure 7b), the faults were also interpreted based on the distortion or misalignment of the reflection waves, corresponding to significant interruptions or disappearances of the coal seams. The profile showed that the stratum above the yellow line was horizontally distributed, and, meanwhile, the reflection waves below demonstrated a misalignment of the seismic events, where there are interruptions and disappearances at the faults. The reflection waves on the left and right sides were clearly different, which indicated that there were some electrical differences between two sides of the faults. The characteristics of the faults in the profile were similar to those of the SLF interpretation. The misalignment of F13 and F11 faults was consistent with the fault characteristics. In contrast, F12 and F10 were also further revealed in this SLF profile. Thus, the SLF method can feasibly reflect the hidden fault distribution with more details than that of the 2D seismic method.

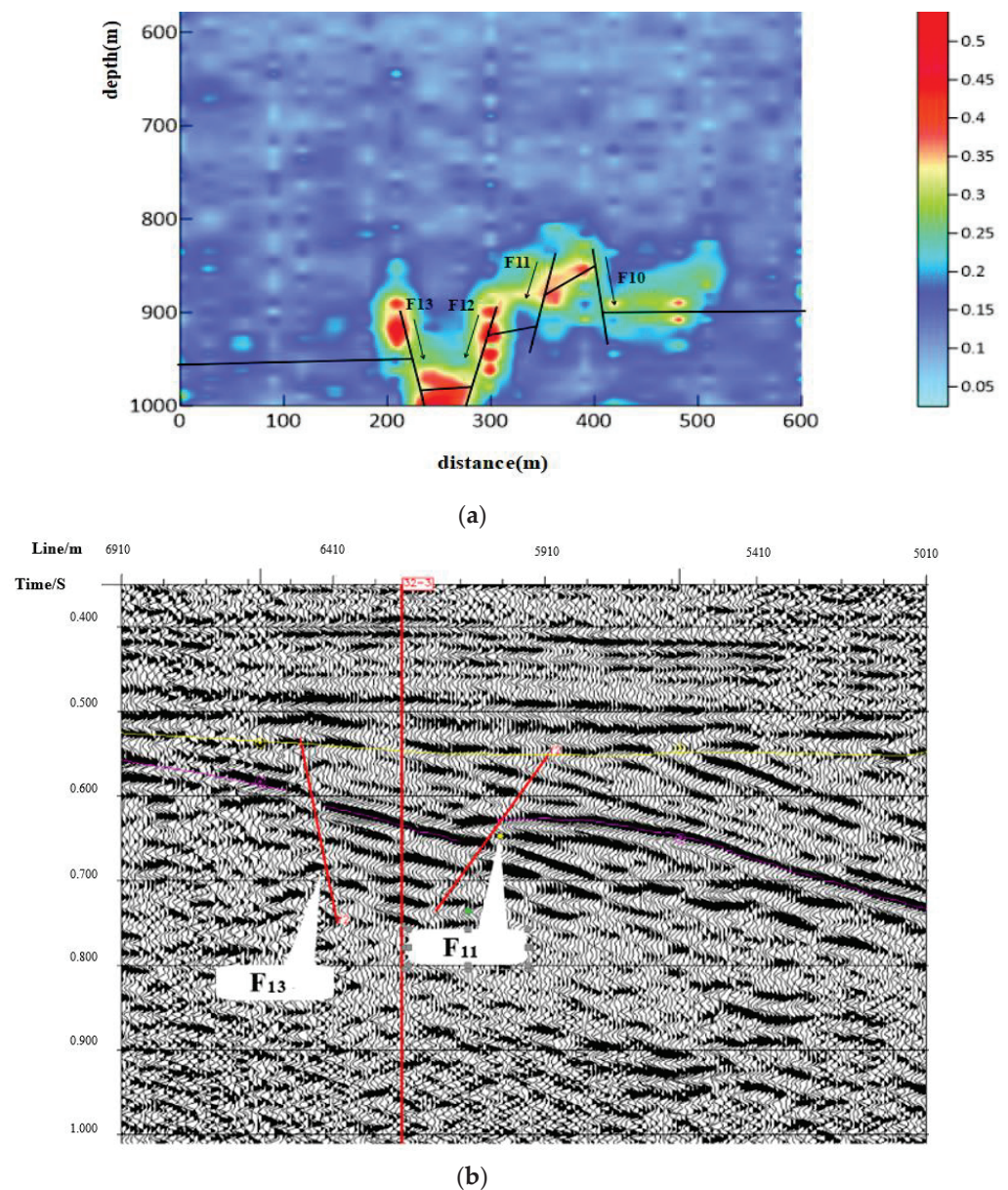


Figure 7. (a) The 2D semi-quantitative SLF inversion profile of the measurement sites No. 8–No. 16; (b) the corresponding seismic travel time profile.

According to the geological data of the study area, F12 is located north of F11, in the northwestern part of the study area. F11 starts from Xiaolianlou village in the west and passes through Xiaofanzhuang village in the north. F10 is located in the central part of the study area, starting from Lions Xing village in the west and ending at the F11 fault in the east, which is basically consistent with the SLF-interpreted distribution. The F13 fault is a positive fault with an extension of 1700 m, trending nearly east–west and tilting southward with a dip angle of 65° . It intersects with the positive F12 fault, which extends more than 3600 m, trending north–west–west with a maximum drop of 60 m. This shows that these two faults have been verified by the mine production units, and the distribution of faults at this location is indeed consistent with the predicted depth range. This shows that the SLF electromagnetic method is effective for the rapid estimation of collapse-type mining areas.

4. Water-Rich Type Coal Mine Goaf Interpretation

4.1. Overview of Hydraulic-Threat Coal Mining Areas

There are a few water-type coal mine goafs located in Study Area 2 (shown in Figure 2), where two mining areas were selected for AMT exploration tests. The stratigraphy of the No. 01 mining area is dominated by a sedimentary rock system, and the main geological structure is a broad and gentle anticline with a dip angle 3–15° and an axial NWW–SEE direction. This anticline controls coal seam production in the northern part of the mining area with some wide and gentle folds. Tens of kilometers away from area No. 01, the No. 02 mining area is sandwiched between two major anticlines: Songshan and Minshan anticlines. The structure is generally characterized by a broad and gently incomplete syncline. The northwest of coal mining area No.2 is generally high, but lower in the southeast, with a highest elevation of 470 m. The two coal mining areas face upwards with a high water-damage risk, which has resulted in great challenges for the coal mining process.

4.2. Stratigraphic Characteristics and Coal-Water Distribution

The stratigraphic development of the two coal mining areas is deposited, from bottom to top, from the Paleozoic Cambrian in the Ordovician Middle Majiagou Group, from the Carboniferous in the Upper Benxi Group, and, in the Taiyuan Group, from the Permian and the Quaternary, as shown in Figure 8. The main coal seams in the Permian Shanxi Group are mainly mined at a depth of 200–400 m, with an average seam thickness of 4.86 m. According to the field survey, the fissure water source in the mining area was mainly from the roof aquifer, and water bursts have occurred many times. The main water-bearing layers, with regards to the minable No. 2_1 coal seam, were as follows. Firstly, the Upper Carboniferous Taiyuan Group aquifer, consisting of 4 layers of limestone, from L1 to L4, with a thickness of 13.86–42.99 m. The average distance of this aquifer section from the bottom of the No. 2_1 coal seam was 40–60 m; this aquifer is an indirect water-filled aquifer. The roof-fractured aquifer of the No. 2_1 coal seam was initially stable because of the significant thickness of the overlying aquifer and large static storage capacity. However, the original status of the sliding tectonic zone was destroyed along with the mining of this coal seam, which directly led to a connection between the overlying caving zone and sandstone aquifers. In the later stage of mining, aquifuges can be greatly weakened by damage to the working face. This may pose a hydraulic threat to the mining of the working face, leading to the demand for detection of these weaknesses by the AMT method, as described in the following sections.

4.3. AMT Data Acquisition and 3D Inversion

The AMT module of the V8 multifunctional electromagnetic device from Phoenix Geophysics Ltd., Toronto, Canada has been used to fulfill the field survey of water-rich coal mine goafs. The data from the working face of the No. 1 mining area was collected in August 2013, and the survey was carried out to allow the measuring line to cover the main mining face. The observation time for each measurement site was one or two hours. In late June 2014, data collection was also carried out along the working area of the No. 2 mining area. The measurement sites were geographically distributed in a straight line. The surrounding area was mostly covered by farmland, with no interferences from the AMT module. The distance between the sites was basically from 30 m to 50 m. In Figure 9, the AMT's apparent resistivity and phase curves of a field survey site showed that a nearly consistent trend was similar to the responses of the one-dimensional stratified model. However, at the low frequency stage (below 10 Hz), it showed two-dimensional characteristics. In a word, the stratigraphic distribution in these areas is simple and homogeneous, but they need to be accurately interpreted by subsequent 3D inversion.

System		Group	Layer Thickness/m	Stratigraphic Status
Permian System (P)	Lower series P ₁	Lower Shihezi Formation P _{1x}	10.03	
			5.00	
			17.64	
			8.06	
		Shanxi Formation P _{1s}	13.12	
			7.00	
			12.00	
			14.23	
			1.37	
			17.00	
			8.00	
			5.27	
Carboniferous System (C)	Upper series C ₂	Taiyuan Formation C _{2t}	0.80	
			3.00	
			7.01	
			6.00	
			14.99	
			18.71	
			12.02	
			12.35	
			1.46	
			1.44	
		Benxi Formation C _{2b}	8.93	
Ordovician System (O)	Middle unification O ₂	Majiagou Formation O _{2M}	30.70	
			15.00	
			9.00	

Figure 8. The integrated geological drilling histogram of the water-rich type coal mining goaf areas (modified from the geological report of this study area).

4.4. Results and Discussions of the No. 01 Mining Area

The coal seam in the No. 01 mining area is relatively stable; No. 21041 is the first comprehensive mining face. The coal seam’s elevation is −190 to −120 m with a surface elevation from +225.3 to +296 m. The average coal thickness is 4.7 to 5.3 m. The water-bearing layer, 25 to 85 m thick, is 20 to 100 m high from the coal seam roof. The water richness of the aquifer is unevenly distributed in No. 21041, and the similar working face No. 21031 is located to the west. The measurement sites almost cover the two working faces as far as possible, as shown in Figure 10. In Figure 10a,b, the 3D inversion slices extracted from the E-W and N-S directions can be further cross-checked with each other. The inversion results also show that there is a clear low-resistive distribution in the depth range of 280 m to 400 m. Especially in the NE part of the working faces, the conductive area is characterized by larger thickness and lower resistivity, which is probably due to the presence of a hydraulic fracture zone. According to the drilling data, there is a heavily water-filled upper roof aquifer adjacent to No. 21041. Therefore, the roof fracture permeability is likely related to the surrounding hydraulic conductivity structures and has probably already posed a threat to coal mining in the past.

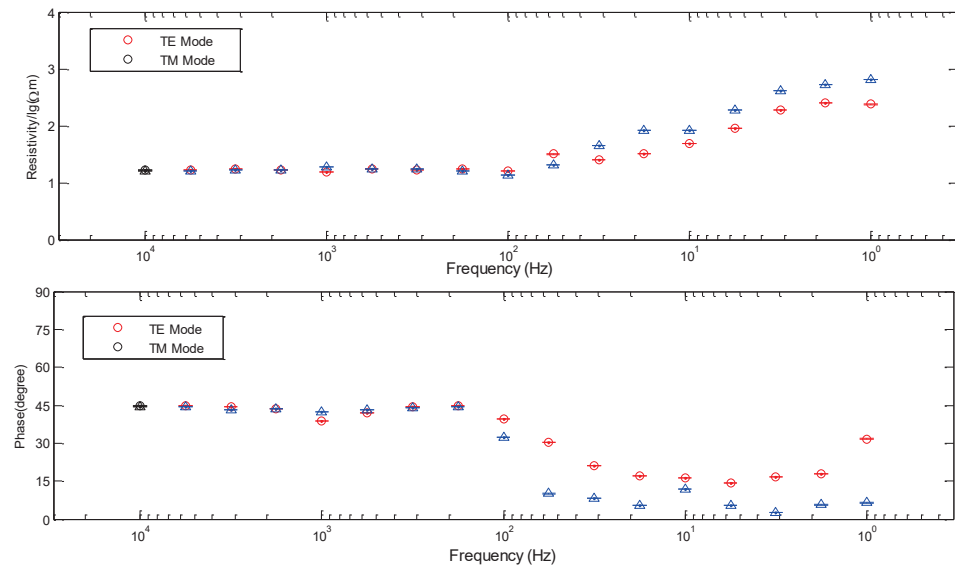


Figure 9. The processing results of collected data in one site in the water-rich coal mining goaf area. The red curve indicates the TE mode and the blue curve indicates the TM mode.

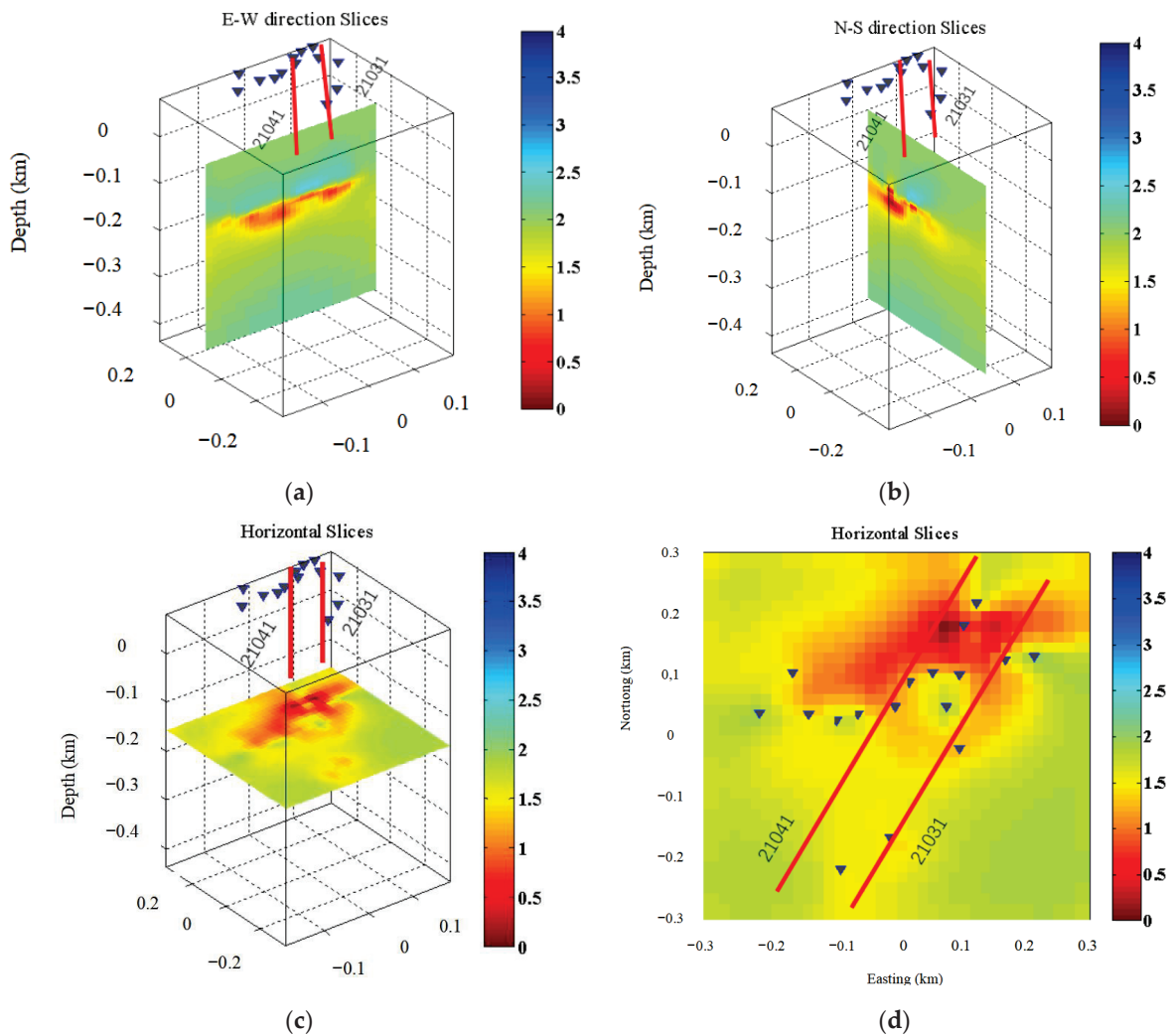


Figure 10. 3D inversion results of the No. 01 coal mining area. (a) Slices in the EW direction; (b) slices in the NS direction; (c) horizontal direction slice at the depths from 310 m to 320 m; (d) the horizontal view of the slice in (c). The resistivity data is lg(Ω·m).

In order to illustrate the detection results more clearly, we intercepted the resistivity cross-section slice of 310–320 m, as shown in Figure 10c,d. The No. 21041 comprehensive mining face is located in the middle of the profile, and the roof of the coal seam is water-rich with fissure water. The field survey demonstrates that the roof water has entered the coal mine goafs along the fissure zone during the mining process. This could also be verified by an in situ sampling test, revealing that the bottom slab of the coal seam was not affected and has been reinforced by grouting operations in recent years. Therefore, the water is deduced to originate from the roof fissures. The upper part of the cross-section, as shown in Figure 10d, shows a very clear low-resistive distribution. This likely indicates that the overlying fissure permeability zone of the goafs has been located; this is also consistent with the distribution of the No. 21041 and No. 21031 mine passages. Furthermore, this may cause a permeability hazard to subsequent mining. In the lower part of the profile, there is no hydraulically permeable area, which is also consistent with the actual mining situation. Additionally, the drilling data revealed that the main No. 2-1 coal seam distribution depth was 340 m–400 m, and the roof aquifer was located 20–100 m above it. This is also consistent with the low-resistive anomaly distribution from 250 m to 400 m indicated by 3D inversion, and the local distribution of suspected water-rich goafs also corresponds to the inferred depth range of the coal seam.

4.5. Result Analysis of the No. 02 Mining Area

The working face No. 12201 in the No. 02 mining area was selected as the main water-rich type goaf target. This working face involves Neoproterozoic strata, and the fallout fracture zone could reach the Neoproterozoic bottom “sand-gravel” aquifer. The distribution of the total thickness of the Neoproterozoic sandstone layer has been damaged by mining; fractures were found in the bottom 0–50 m of the rock. The working face spread towards the east through the fold axis, and the hydraulic permeability zone formed because of the gradually intensive fracture of the aquifers at the bottom of the Neoproterozoic system. This may cause water from the bottom of the Neoproterozoic system to enter the mining area, thus threatening the safety of mining operations.

The finite difference method was used for 3D forward modeling, and the resistivity sections of each depth layer were obtained by 3D inversion; the anomalies were sliced along the east–west, north–south and horizontal directions of the sectioning grid, as shown in Figure 11a–c. It can be seen that there is a clear distribution of low-resistive anomalies at the depths between 100 m and 200 m. Especially around sites circled in Figure 11c, the distribution of low-resistive anomalies was particularly obvious, with lower resistivity values and a wider distribution. As shown in Figure 11d, there was an obvious conductive area between measurement sites (circled in the black box). Considering that the working face is located in the axis of the Hutuo anticline, the coal seam is covered by the slightly water-rich Neoproterozoic aquifer. It can be inferred that the water source of the low-resistive area may come from the overlying zone. According to a comprehensive analysis, the No. 12211 working face caused the fractured zone to fall to the bottom of the Neoproterozoic aquifer at nearly 150 m depth, which resulted in the aquifer’s connection with the coal seam. Finally, a hydraulic connection between the Neoproterozoic aquifer and the coal seam formed. In order to reduce the damage from roof fracture and the damage of the lower Neoproterozoic aquifer, it is recommended to strengthen the monitoring of the roof water level and the water influx after mining, especially to prevent the formation of a suspected water-filled area (shown by the rectangle box) at depths between 100 m and 150 m. These exploration tests successfully guided the subsequent mining plan.

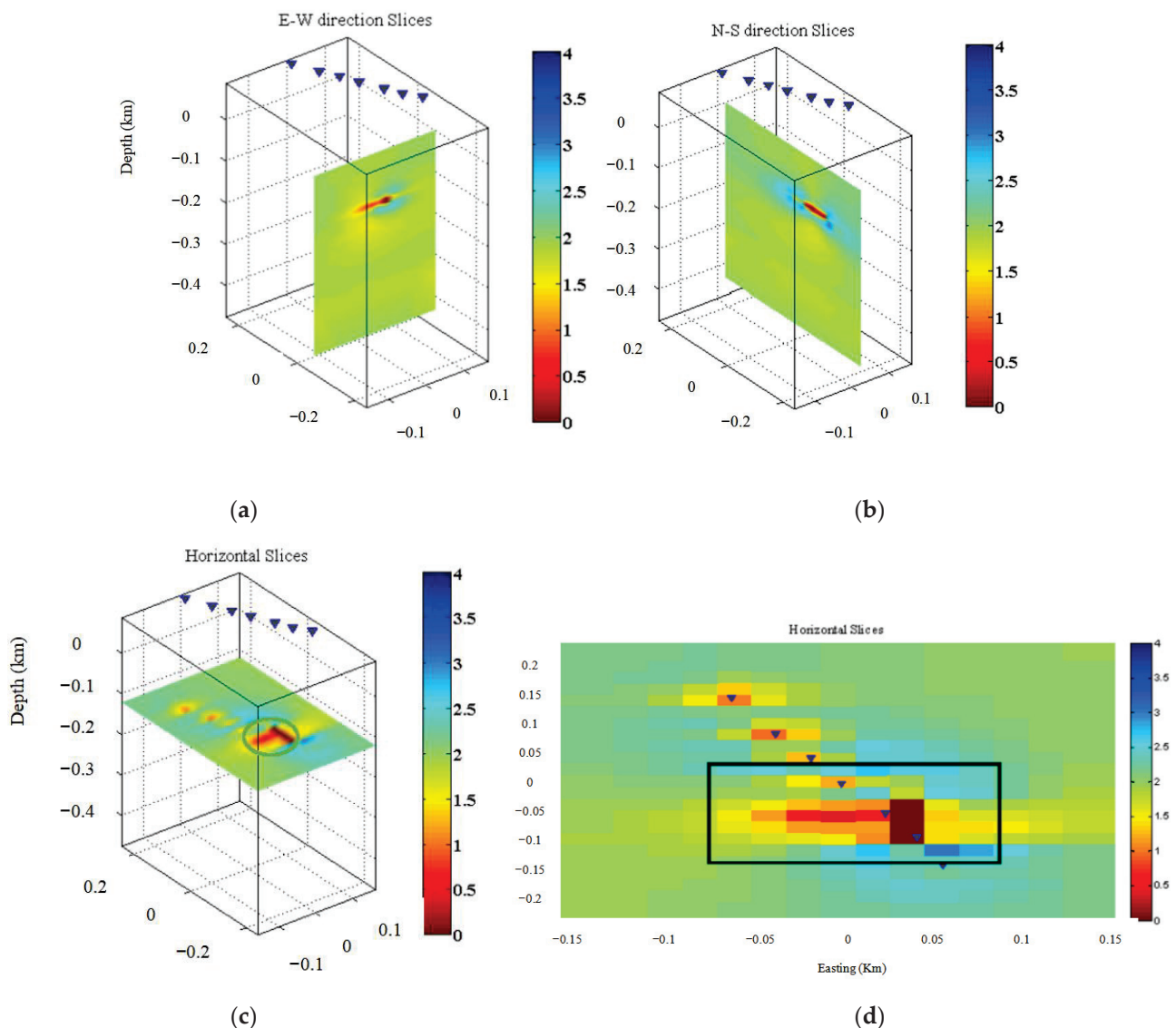


Figure 11. 3D AMT inversion results of the No. 02 coal mining area. (a) Slices in the EW direction; (b) slices in the NS direction; (c) horizontal direction slice at the depths from 120 m to 125 m; (d) the horizontal view of the slice in (c). The resistivity data is $\lg(\Omega \cdot m)$. AMT sites are shown by blue triangles in each figure.

5. Conclusions

This paper proposes and illustrates a goaf interpretation trend using passive electromagnetic methods (especially for the SLF method and the AMT method). The effectiveness of these methods has previously been validated in theory and practice, which lays a foundation for the future popularization of the electrical delineations of goafs. Some key concluding remarks:

- (1) Geo-electrical goaf models were designed and the theoretical feasibility of interpreting goaf targets was fully explored by developing forward modeling and inversion algorithms using the finite difference method (FDM).
- (2) Semi-quantitative inversion of the SLF method was fully explored with a three-layer electrical model, which can efficiently perform the vertical delineation of low-resistive bodies and facilitate fault structure identification.
- (3) Theoretical 3D inversion analysis of “single and double target” models has been discussed systematically, and this AMT method, with appropriate initial models

and data accuracy selections, was most appropriate for single low-resistive layer distribution at a depth range of 100 m–400 m.

- (4) In field surveys of goaf areas, the inverted depth distributions using both methods are basically consistent with the water-filled goafs and surrounding layers, as verified by known data. SLF interpretation was successfully applied in collapse-type mining goaf areas. In contrast, with regards to water-rich-type coal mine goafs, the AMT method, using stable 3D inversion, has the capability of revealing obvious low-resistive anomalies appropriate for determining the hydraulic tectonic area connected with fracture zones. These results can help industries to improve subsequent coal production.

In the future, a joint use of these passive electromagnetic methods should be investigated more thoroughly; a set of economic and rapid goaf evaluation methods should be the subject of greater practical attention for subsequent mining areas under study.

Author Contributions: N.W.: conceptualization, methodology, validation, original draft preparation, review and editing; Z.W.: data curation, inversion algorithms, editing; Q.S.: data processing, field survey and analysis; J.H.: modeling and discussions. All authors have read and agreed to the published version of the manuscript.

Funding: This work is supported by the National Science and Technology Major Project of China (2011ZX05034-02), Scientific Research Project of Beijing Educational Committee (KM202311232004), BISTU College Students' innovation and entrepreneurship training program (5112210832) and Beijing Information Science and Technology University Foundation (2021XJJ27).

Data Availability Statement: The datasets will be provided upon request.

Acknowledgments: We are very grateful to the authors who have contributed to this paper and the companies that have provided resources and methods. Resources of Peking University (PKU) and other companies were utilized and much appreciated. We extend great thanks to Qiming Qin and Guhuai Han for their support. We also express our thanks for constructive comments from Gary Egbert and Anna Kelbert at Oregon State University, USA. In addition, we thank Hao Dong at China University of Geosciences for his 3D visualization tool.

Conflicts of Interest: The authors declare no conflict of interest.

References

1. Gui, H.; Qiu, H.; Qiu, W.; Tong, S.; Zhang, H. Overview of Goaf Water Hazards Control in China Coalmines. *Arab. J. Geosci.* **2018**, *11*, 1–10. [[CrossRef](#)]
2. Guoqiang, X.; Hai, L.; Weiyang, C. Progress of Transient Electromagnetic Detection Technology for Waterbearing Bodies in Coal Mines. *J. China Coal Soc.* **2021**, *46*, 77–85.
3. Yin, Y.; Zhao, T.; Zhang, Y.; Tan, Y.; Qiu, Y.; Taheri, A.; Jing, Y. An Innovative Method for Placement of Gangue Backfilling Material in Steep Underground Coal Mines. *Minerals* **2019**, *9*, 107. [[CrossRef](#)]
4. Chlebowski, D.; Burtan, Z. Geophysical and Analytical Determination of Overstressed Zones in Exploited Coal Seam: A Case Study. *Acta Geophys.* **2021**, *69*, 701–710. [[CrossRef](#)]
5. Wang, Y.; Fan, X.; Niu, K.; Shi, G. Estimation of Hydrogen Release and Conversion in Coal-Bed Methane from Roof Extraction in Mine Goaf. *Int. J. Hydrogen Energy* **2019**, *44*, 15997–16003. [[CrossRef](#)]
6. Xinhai, Z.; Hui, Z. Prediction Method of Coal Mine Goaf Temperature and Its Practical Application. *IOP Conf. Ser. Earth Environ. Sci.* **2021**, *647*, 12008. [[CrossRef](#)]
7. Xie, H.; Gao, M.; Zhang, R.; Peng, G.; Wang, W.; Li, A. Study on the Mechanical Properties and Mechanical Response of Coal Mining at 1000 m or Deeper. *Rock Mech. Rock Eng.* **2019**, *52*, 1475–1490. [[CrossRef](#)]
8. Yu, C.; Wang, Z.; Tang, M. Application of Microtremor Survey Technology in a Coal Mine Goaf. *Appl. Sci.* **2023**, *13*, 466. [[CrossRef](#)]
9. Xue, G.Q.; Pan, D.M.; Yu, J.C. Review the Applications of Geophysical Methods for Mapping Coal-Mine Voids. *Prog. Geophys.* **2018**, *33*, 2187–2192. [[CrossRef](#)]
10. Zhang, S.; Sun, L.; Qin, B.; Wang, H.; Qi, G. Characteristics and Main Factors of Foam Flow in Broken Rock Mass in Coal Mine Goaf. *Environ. Sci. Pollut. Res.* **2022**, *29*, 47095–47108. [[CrossRef](#)]
11. Zhang, C.; Tu, S.; Zhao, Y.X. Compaction Characteristics of the Caving Zone in a Longwall Goaf: A Review. *Environ. Earth Sci.* **2019**, *78*, 1–20. [[CrossRef](#)]
12. Zhang, X.X.; Ma, J.F.; Li, L. Monitoring of Coal-Mine Goaf Based on 4D Seismic Technology. *Appl. Geophys.* **2020**, *17*, 54–66. [[CrossRef](#)]

13. Zhu, G.A.; Dou, L.M.; Cai, W.; Li, Z.L.; Zhang, M.; Kong, Y.; Shen, W. Case Study of Passive Seismic Velocity Tomography in Rock Burst Hazard Assessment During Underground Coal Entry Excavation. *Rock Mech. Rock Eng.* **2016**, *49*, 4945–4955. [[CrossRef](#)]
14. Zhou, B.; Deng, C.; Hao, J.; An, B.; Wu, R. Experimental Study on the Mechanism of Radon Exhalation during Coal Spontaneous Combustion in Goaf. *Tunn. Undergr. Sp. Technol.* **2021**, *113*, 103776. [[CrossRef](#)]
15. Xiang, Z.; Si, G.; Wang, Y.; Belle, B.; Webb, D. Goaf Gas Drainage and Its Impact on Coal Oxidation Behaviour: A Conceptual Model. *Int. J. Coal Geol.* **2021**, *248*, 103878. [[CrossRef](#)]
16. Li, L.; Qin, B.; Liu, J.; Leong, Y.-K.; Li, W.; Zeng, J.; Ma, D.; Zhuo, H. Influence of Airflow Movement on Methane Migration in Coal Mine Goafs with Spontaneous Coal Combustion. *Process Saf. Environ. Prot.* **2021**, *156*, 405–416. [[CrossRef](#)]
17. Yang, C.; Liu, S.; Wu, R. Quantitative Prediction of Water Volumes Within a Coal Mine Underlying Limestone Strata Using Geophysical Methods. *Mine Water Environ.* **2017**, *36*, 51–58. [[CrossRef](#)]
18. Wu, G.; Yang, G.; Tan, H. Mapping Coalmine Goaf Using Transient Electromagnetic Method and High Density Resistivity Method in Ordos City, China. *Geod. Geodyn.* **2016**, *7*, 340–347. [[CrossRef](#)]
19. Xu, X.; Peng, S.; Yang, F. Development of a Ground Penetrating Radar System for Large-Depth Disaster Detection in Coal Mine. *J. Appl. Geophys.* **2018**, *158*, 41–47. [[CrossRef](#)]
20. Bharti, A.K.; Singh, K.K.K.; Ghosh, C.N.; Mishra, K. Detection of Subsurface Cavity Due to Old Mine Workings Using Electrical Resistivity Tomography: A Case Study. *J. Earth Syst. Sci.* **2022**, *131*, 39. [[CrossRef](#)]
21. Bharti, A.K.; Pal, S.K.; Ranjan, S.K.; Kumar, R.; Priyam, P.; Pathak, V.K. Coal Mine Cavity Detection Using Electrical Resistivity Tomography—A Joint Inversion of Multi Array Data. In Proceedings of the 22nd European Meeting of Environmental and Engineering Geophysics, Near Surface Geoscience 2016, Barcelona, Spain, 4–8 September 2016. [[CrossRef](#)]
22. Chang, J.; Su, B.; Malekian, R.; Xing, X. Detection of Water-Filled Mining Goaf Using Mining Transient Electromagnetic Method. *IEEE Trans. Ind. Inform.* **2020**, *16*, 2977–2984. [[CrossRef](#)]
23. Zhang, L.; Xu, L.; Xiao, Y.; Zhang, N. Application of Comprehensive Geophysical Prospecting Method in Water Accumulation Exploration of Multilayer Goaf in Integrated Mine. *Adv. Civ. Eng.* **2021**, *2021*, 1434893. [[CrossRef](#)]
24. Chen, K.; Xue, G.Q.; Chen, W.Y.; Zhou, N.N.; Li, H. Fine and Quantitative Evaluations of the Water Volumes in an Aquifer Above the Coal Seam Roof, Based on TEM. *Mine Water Environ.* **2019**, *38*, 49–59. [[CrossRef](#)]
25. Wang, P.; Yao, W.; Guo, J.; Su, C.; Wang, Q.; Wang, Y.; Zhang, B.; Wang, C. Detection of Shallow Buried Water-Filled Goafs Using the Fixed-Loop Transient Electromagnetic Method: A Case Study in Shaanxi, China. *Pure Appl. Geophys.* **2021**, *178*, 529–544. [[CrossRef](#)]
26. Wang, C. Dual-Frequency Induction Polarization Electric Field Focusing Based on Intelligent Algorithm for Coal Mine Electric Exploration. *J. Phys. Conf. Ser.* **2021**, *2143*, 12012. [[CrossRef](#)]
27. Li, J.; Gao, F.; Lu, J. An Application of InSAR Time-Series Analysis for the Assessment of Mining-Induced Structural Damage in Panji Mine, China. *Nat. Hazards* **2019**, *97*, 243–258. [[CrossRef](#)]
28. Fan, H.; Li, T.; Gao, Y.; Deng, K.; Wu, H. Characteristics Inversion of Underground Goaf Based on InSAR Techniques and PIM. *Int. J. Appl. Earth Obs. Geoinf.* **2021**, *103*, 102526. [[CrossRef](#)]
29. Li, T.; Zhang, H.; Fan, H.; Zheng, C.; Liu, J. Position Inversion of Goafs in Deep Coal Seams Based on Ds-Insar Data and the Probability Integral Methods. *Remote Sens.* **2021**, *13*, 2898. [[CrossRef](#)]
30. Gui, X.; Xue, H.; Zhan, X.; Hu, Z.; Song, X. Measurement and Numerical Simulation of Coal Spontaneous Combustion in Goaf under Y-Type Ventilation Mode. *ACS Omega* **2022**, *7*, 9406–9421. [[CrossRef](#)]
31. Yang, Z.; Li, Z.; Zhu, J.; Yi, H.; Feng, G.; Hu, J.; Wu, L.; Preusse, A.; Wang, Y.; Papst, M. Locating and Defining Underground Goaf Caused by Coal Mining from Space-Borne SAR Interferometry. *ISPRS J. Photogramm. Remote Sens.* **2018**, *135*, 112–126. [[CrossRef](#)]
32. Chave, A.D.; Jones, A.G. *The Magnetotelluric Method: Theory and Practice*; Cambridge University Press: Cambridge, UK, 2012; pp. 1–584. [[CrossRef](#)]
33. Mackie, R.L.; Madden, T.R.; Wannamaker, P.E. Three-Dimensional Magnetotelluric Modeling Using Difference Equations—Theory and Comparisons to Integral Equation Solutions. *Geophysics* **1993**, *58*, 215–226. [[CrossRef](#)]
34. Jones, A.G. Static Shift of Magnetotelluric Data and Its Removal in a Sedimentary Basin Environment. *Geophysics* **1988**, *53*, 967–978. [[CrossRef](#)]
35. Newman, G.A.; Alumbaugh, D.L. Three-Dimensional Magnetotelluric Inversion Using Non-Linear Conjugate Gradients. *Geophys. J. Int.* **2000**, *140*, 410–424. [[CrossRef](#)]
36. Siripunvaraporn, W. Three-Dimensional Magnetotelluric Inversion: An Introductory Guide for Developers and Users. *Surv. Geophys.* **2012**, *33*, 5–27. [[CrossRef](#)]
37. Zhao, H.; Zhang, Q.; Tan, J.; Liu, Z.; Li, B. Research and Application of AMT in Tunnel Hidden Goaf under Complex Conditions. *IOP Conf. Ser. Earth Environ. Sci.* **2021**, *861*, 52085. [[CrossRef](#)]
38. Xu, J.; Yang, Z.; Zhang, Y. Application of EH4 Electromagnetic Imaging System in Goaf Detection. *IOP Conf. Ser. Earth Environ. Sci.* **2021**, *651*, 32086. [[CrossRef](#)]
39. Song, D.; Wang, E.; Li, Z.; Zhao, E.; Xu, W. An EMR-Based Method for Evaluating the Effect of Water Jet Cutting on Pressure Relief. *Arab. J. Geosci.* **2015**, *8*, 4555–4564. [[CrossRef](#)]
40. Wang, N.; Qin, Q. Natural Source Electromagnetic Component Exploration of Coalbed Methane Reservoirs. *Minerals* **2022**, *12*, 680. [[CrossRef](#)]

41. Wang, N.; Zhao, S.; Hui, J.; Qin, Q. Three-Dimensional Audio-Magnetotelluric Sounding in Monitoring Coalbed Methane Reservoirs. *J. Appl. Geophys.* **2017**, *138*, 198–209. [[CrossRef](#)]
42. Wang, N.; Zhao, S.; Hui, J.; Qin, Q. Passive Super-Low Frequency Electromagnetic Prospecting Technique. *Front. Earth Sci.* **2017**, *11*, 248–267. [[CrossRef](#)]
43. Wang, N.; Qin, Q.; Chen, L.; Bai, Y.; Zhao, S.; Zhang, C. Dynamic Monitoring of Coalbed Methane Reservoirs Using Super-Low Frequency Electromagnetic Prospecting. *Int. J. Coal Geol.* **2014**, *127*, 24–41. [[CrossRef](#)]
44. Wu, Z.; Pan, P.Z.; Konicek, P.; Zhao, S.; Chen, J.; Liu, X. Spatial and Temporal Microseismic Evolution before Rock Burst in Steeply Dipping Thick Coal Seams under Alternating Mining of Adjacent Coal Seams. *Arab. J. Geosci.* **2021**, *14*, 1–28. [[CrossRef](#)]
45. Bharti, A.K.; Pal, S.K.; Saurabh; Kumar, S.; Mondal, S.; Singh, K.K.K.; Singh, P.K. Detection of Old Mine Workings over a Part of Jharia Coal Field, India Using Electrical Resistivity Tomography. *J. Geol. Soc. India* **2019**, *94*, 290–296. [[CrossRef](#)]
46. Chang, J.H.; Yu, J.C.; Liu, Z.X. Three-Dimensional Numerical Modeling of Full-Space Transient Electromagnetic Responses of Water in Goaf. *Appl. Geophys.* **2016**, *13*, 539–552. [[CrossRef](#)]
47. Wang, P.; Wang, Q.; Wang, Y.; Wang, C. Detection of Abandoned Coal Mine Goaf in China’s Ordos Basin Using the Transient Electromagnetic Method. *Mine Water Environ.* **2021**, *40*, 415–425. [[CrossRef](#)]
48. Kelbert, A.; Meqbel, N.; Egbert, G.D.; Tandon, K. ModEM: A Modular System for Inversion of Electromagnetic Geophysical Data. *Comput. Geosci.* **2014**, *66*, 40–53. [[CrossRef](#)]

Disclaimer/Publisher’s Note: The statements, opinions and data contained in all publications are solely those of the individual author(s) and contributor(s) and not of MDPI and/or the editor(s). MDPI and/or the editor(s) disclaim responsibility for any injury to people or property resulting from any ideas, methods, instructions or products referred to in the content.

Article

Complex Resistivity Anisotropy Response Characteristics of Wufeng-Longmaxi Formation Shale in Southern Sichuan

Kui Xiang ¹, Liangjun Yan ^{1,*}, Gongxian Tan ¹, Yuanyuan Luo ¹ and Gang Yu ²¹ Key Laboratory of Exploration Technologies for Oil and Gas Resources, Yangtze University, Wuhan 430100, China² Bureau of Geophysical Prospecting, China National Petroleum Corporation, Zhuozhou 072751, China

* Correspondence: yljemlab@163.com

Abstract: Electrical exploration has become an important means of shale gas reservoir exploration and evaluation, and is expected to play a key role in the later stages of reservoir fracturing and development. At present, the research on the electrical response characteristics of shale gas reservoirs and their relationship with reservoir parameters is extensive and in-depth, but there is little research on their complex resistivity anisotropy characteristics and influencing factors, which restricts petrophysical modeling and reservoir parameter prediction, and reduces the reliability of shale gas exploration and reservoir evaluation by electromagnetic methods. In this paper, shale samples from the Longmaxi Formation and the Wufeng Formation of shale gas wells in southern Sichuan were collected, the complex resistivity of 34 shales in bedding direction and vertical bedding direction were measured, and the induced polarization (IP) parameters of shales were extracted by inversion. The electrical anisotropy response characteristics under different temperature and pressure conditions were analyzed, and the influencing factors and laws of complex resistivity anisotropy of shales were revealed. Combined with the test results of shale porosity and permeability, the evaluation model of resistivity, polarizability and porosity and permeability parameters was established. The research results have formed a set of testing methods and analysis techniques for electrical anisotropy of shale reservoirs, which are mainly based on complex resistivity parameter testing. It is helpful to understand the electrical anisotropy characteristics of shale gas reservoirs in southern Sichuan; this will provide the theoretical and physical basis for shale gas reservoir evaluation and fracturing monitoring by electrical exploration.

Keywords: shale; complex resistivity; anisotropic; polarizability

Citation: Xiang, K.; Yan, L.; Tan, G.; Luo, Y.; Yu, G. Complex Resistivity Anisotropy Response Characteristics of Wufeng-Longmaxi Formation Shale in Southern Sichuan. *Minerals* **2022**, *12*, 1395. <https://doi.org/10.3390/min12111395>

Academic Editor: Paul Alexandre

Received: 18 September 2022

Accepted: 28 October 2022

Published: 31 October 2022

Publisher's Note: MDPI stays neutral with regard to jurisdictional claims in published maps and institutional affiliations.



Copyright: © 2022 by the authors. Licensee MDPI, Basel, Switzerland. This article is an open access article distributed under the terms and conditions of the Creative Commons Attribution (CC BY) license (<https://creativecommons.org/licenses/by/4.0/>).

1. Introduction

As a high-quality clean energy, shale gas has attracted much attention in recent years. Many countries and regions represented by North America have successfully realized the exploration and large-scale production of shale gas. China has also realized the effective development of shale gas resources, and the output has continued to grow rapidly, opening up a new energy market and optimizing the energy consumption structure [1–3]. Shale gas has great potential in unconventional oil and gas in China. According to the evaluation results of oil and gas resources in the 13th Five-Year Plan, the accumulated proven shale gas resources in Sichuan Basin are $44.03 \times 10^{12} \text{ m}^3$, with the proven rate less than 4%, and the exploration degree is still low [4,5]. Up to 2015, four shale gas-rich areas, namely Fuling, Changning-Weiyuan, Zhaotong and Fushun-Yongchuan, have been discovered in the Wufeng-Longmaxi Formation of Sichuan Basin in the south, three national shale gas demonstration areas, namely Fuling in Chongqing, Changning-Weiyuan in Sichuan and Zhaotong in northern Yunnan and Guizhou, have been built, and industrial development has been successfully realized [6–9]. The main shale gas-producing horizon is the marine shale series from the Longmaxi Formation of the Lower Silurian to the Wufeng Formation of the Upper Ordovician [10,11].

Electrical prospecting has the advantages of low cost and high efficiency, and can play a key role in basin structure evaluation and deep target detection [12]. Moreover, this method has been effectively applied to the exploration of organic-rich shale strata in Sichuan Basin, and the effect is remarkable [13,14]. At the same time, the time-frequency electromagnetic method is applied to the study of electromagnetic characteristics and polarization mechanism of organic-rich shale, and the organic-rich shale series is delineated [15,16]. A wide-area electromagnetic method is used to find the distribution range of organic-rich mud shale from the Wufeng Formation of the Upper Ordovician to the Longmaxi Formation of the Lower Silurian in the target layer of eastern Chongqing [17]. The controlled source electromagnetic method has been applied and popularized in shale gas reservoir evaluation and fracturing monitoring in the Fuling area of Sichuan Basin [18].

Of course, the first step of exploration is to master the petrophysical response characteristics of shale gas reservoirs. Marine organic-rich shale usually has the response characteristics of low resistance and high polarization, and pyrite is the main reason for the high polarization of shale [19,20]. At the same time, the complex resistivity of shale is also affected by salinity, total organic carbon (TOC), mineral composition, pore structure, formation temperature and pressure, etc. [21–23]. Other test and research results show that the resistivity and polarizability of shale IP parameters are related to the TOC, pyrite content and brittleness index of shale, which provide the physical basis for shale gas exploration and evaluation [24,25]. In recent years, more and more research has been conducted on the complex resistivity characteristics of shale, and some important achievements and consensus have been achieved. However, the induced polarization response mechanism of oil and gas still needs to be further studied. The anisotropy of the earth's internal media exists objectively and cannot be ignored. A large number of petrophysical experiments show that shale reservoirs have strong anisotropy and complex geophysical responses, which cannot be ignored in the interpretation of electromagnetic exploration data, due to the influence of the sedimentary environment (stress change, mineral composition, etc.), hydrocarbon maturity, fractures and other factors [26–28]. The complex resistivity anisotropy of shale lays a foundation for the study of the relationship between IP parameters and reservoir parameters, and also provides the physical basis for shale gas electromagnetic exploration and data interpretation [29,30].

Based on the black shale of a shale gas well in southern Sichuan, this paper measured the complex resistivity of shale under different temperature and pressure conditions, revealed the anisotropic response characteristics, influencing factors and laws of shale complex resistivity, established the evaluation model of resistivity, polarizability and porosity and permeability parameters, and analyzed and discussed the electrical anisotropy characteristics of reservoir shale, which provided the physical basis for shale gas reservoir evaluation and fracturing monitoring by electrical exploration.

2. Collection and Preparation of Rock Samples

The research block is located in Gongxian County and Junlian County, Yibin City, Sichuan Province, next to Changning shale gas block, and the structural block is located in the southern edge of the low and steep fold belt in Tai 'ao, Sichuan Province. It mainly deposits marine and continental sedimentary assemblages, and marine black shale is the main gas source rock in the exploration area. The target strata of this study are the Wufeng Formation of the Upper Ordovician and the Longmaxi Formation of the Lower Silurian, which mainly develop shallow water-land shelf facies and deep water-land shelf facies, with large thickness, high organic carbon abundance and good preservation. The location of sampling wells is shown in Figure 1.

The shale samples are from a shale gas well in southern Sichuan Basin; information on rock samples is shown in Table 1. The target horizon of the study area is the southern marine shale, and the main source rock strata are the Silurian Longmaxi Formation and the Ordovician Wufeng Formation, all of which are black shale with high TOC content and rich brittle minerals, so they are favorable dessert areas for shale gas exploration and

development. According to the geological and geophysical data of the exploration area, the target shale of the Longmaxi Formation and Wufeng Formation has a resistivity range of 30–50 Ω·m, which belongs to a low resistivity layer.

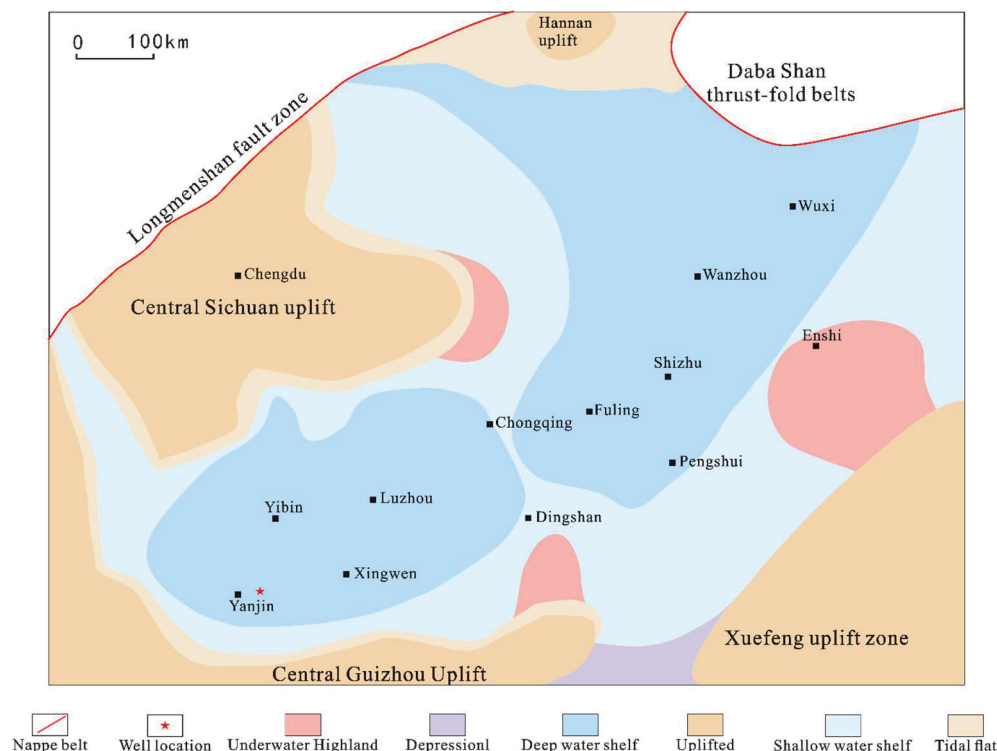


Figure 1. Sedimentary facies and shale distribution in the study area and its periphery.

Table 1. Information on shale gas well rock samples.

No.	Number	Depth (m)	No.	Number	Depth (m)
1	V-3	2385.46–2385.73	18	H-22	2481.09–2481.39
2	H-3	2385.46–2385.73	19	V-23	2481.92–2482.22
3	V-5	2388.16–2388.43	20	H-23	2481.92–2482.22
4	H-5	2388.16–2388.43	21	V-30	2489.48–2489.77
5	V-12	2469.77–2470.07	22	H-30	2489.48–2489.77
6	H-12	2469.77–2470.07	23	V-31	2490.28–2490.55
7	V-13	2471–2471.28	24	H-31	2490.28–2490.55
8	H-13	2471–2471.28	25	V-39	2498.44–2498.75
9	V-14	2472.19–2472.45	26	H-39	2498.44–2498.75
10	H-14	2472.19–2472.45	27	V-47	2507.40–2507.67
11	V-15	2472.93–2473.22	28	H-47	2507.40–2507.67
12	H-15	2472.93–2473.22	29	V-49	2509.22–2509.50
13	V-16	2473.72–2473.97	30	H-49	2509.22–2509.50
14	H-16	2473.72–2473.97	31	V-50	2510.38–2510.65
15	V-21	2480.34–2480.64	32	H-50	2510.38–2510.65
16	H-21	2480.34–2480.64	33	V-51	2511.42–2511.69
17	V-22	2481.09–2481.39	34	H-51	2511.42–2511.69

In the sample number, H represents that the drilling direction of the rock sample is horizontal (bedding direction), and V represents that the drilling direction of the rock sample is a vertical bedding direction. The coring direction and schematic diagram are shown in Figure 2.

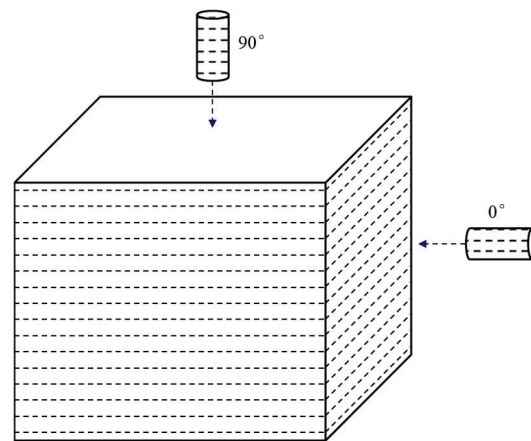


Figure 2. Schematic diagram of shale coring.

3. Complex Resistivity Experiment and Parameter Inversion of Shale

3.1. Complex Resistivity Test Method

In the experiment, Autolab1000 is combined with impedance analyzer 1260A, and the frequency range of complex resistivity is expanded by using the low frequency characteristic of 1260A. This time, the quadrupole method is used for observation. The measurement principle is shown in Figure 3, and the measurement frequency is 0.01 Hz~10 Hz. The experimental measurement temperature and pressure conditions are shown in Table 2.

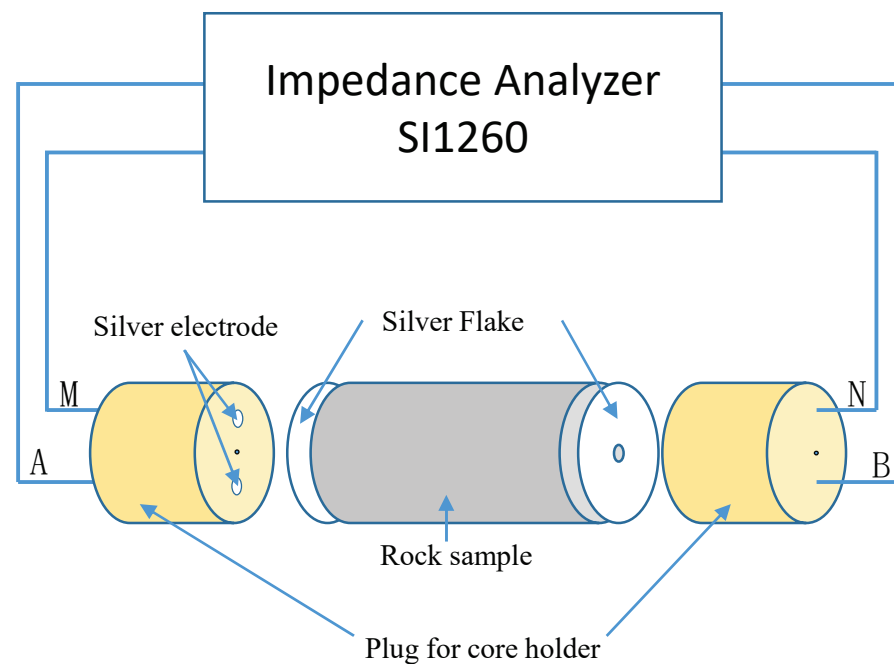


Figure 3. Schematic diagram of complex resistivity measurement.

Table 2. Temperature and pressure of complex resistivity experiment.

Measuring Condition	Temperature (°C)	Confining Pressure (MPa)	Pore Pressure (MPa)
normal temperature and pressure	25	0	0
stratigraphic conditions	85	55	20

3.2. Complex Resistivity Model

For mineralized rocks, its basic structural unit can be simplified to the structure shown in Figure 4a, and its equivalent circuit is shown in Figure 4b.

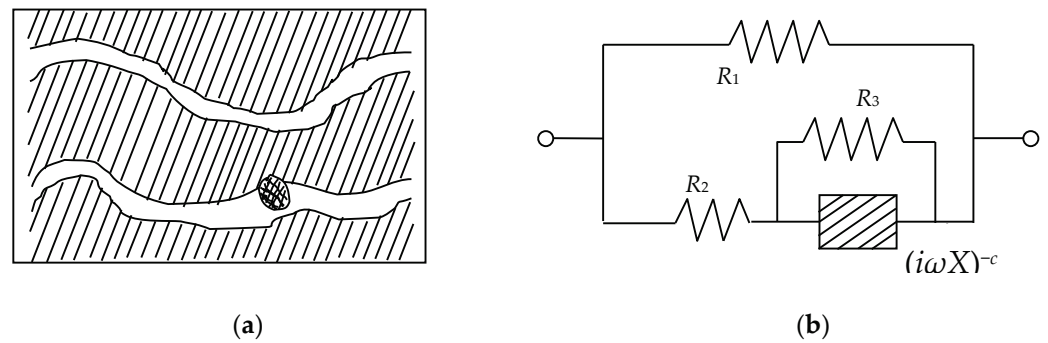


Figure 4. Schematic diagram of the basic structure of mineralized rocks and equivalent circuit. (a) Basic structure; (b) equivalent circuit.

The structural unit includes pore channels blocked by electronically conductive mineral particles and unblocked pore channels. R_1 in the equivalent circuit diagram represents the resistance of the solution in the unblocked pore channels, R_2 represents the sum of the resistance of the solution in the blocked pore channels and the resistance of the electronic conductor. The parallel combination of complex impedance $(i\omega X)^{-c}$ and R_3 represents the interface impedance between the electronic conductor and the ionic solution. The expression of the equivalent circuit complex impedance under this model is:

$$Z(\omega) = \frac{R_1 \left[R_2 + \frac{R_3}{1 + R_3(i\omega X)^c} \right]}{R_1 + R_2 + \frac{R_3}{1 + R_3(i\omega X)^c}} \tag{1}$$

Because:

$$\tau = X \left(\frac{(R_1 + R_2)R_3}{R_1 + R_2 + R_3} \right)^{1/c} \tag{2}$$

Therefore, by combining Equations (1) and (2), Equation (1) can be simplified as:

$$Z(\omega) = Z(0) \left[1 - m \left(1 - \frac{1}{1 + (i\omega\tau)^c} \right) \right] \tag{3}$$

This is called Cole-Cole impedance expression; $Z(0)$ represents the impedance at zero-frequency, m is the polarizability, τ is the time constant, and c is the frequency correlation coefficient, which is called the Cole-Cole parameter. The unit of $Z(0)$ is Ω , the unit of τ is s, and m and c are dimensionless. K.S.Cole and R.H.Cole first proposed the above model to describe the spectrum characteristics of complex dielectric constant, so it is called the Cole-Cole model. Pelton et al. borrowed a similar equivalent circuit to study the IP effect of rocks and carried out experimental measurements on rock and ore samples, describing the spectrum characteristics of the complex resistivity of rocks [31]. The Cole-Cole expression of complex resistivity can be obtained according to Equation (3):

$$\rho(\omega) = \rho_0 \left[1 - m \left(1 - \frac{1}{1 + (i\omega\tau)^c} \right) \right] \tag{4}$$

where ρ_0 is the zero-frequency resistivity, and m , τ and c are the polarizability, time constant and frequency correlation coefficient, respectively.

4. Results Are Discussed with Analysis

4.1. Porosity Measurement Results

In the experiment, the porosity and permeability are measured by the FYHK-2A rock overburden porosity and permeability testing system.

Porosity and permeability are important factors affecting the complex resistivity of rock samples. After the preparation of columnar shale samples, first wash oil, wash salt

and dry, and then measure porosity and permeability. The measurement results of porosity and permeability are shown in Table 3.

Table 3. Measurement results of shale porosity and permeability.

No.	Number	Permeability ($10^{-3} \mu\text{m}^2$)	Porosity (%)	No.	Number	Permeability ($10^{-3} \mu\text{m}^2$)	Porosity (%)
1	V-3	0.029	3.9	18	H-22	1.781	4.9
2	H-3	0.29	3.9	19	V-23	0.023	5.7
3	V-5	0.028	4.5	20	H-23	0.066	6.3
4	H-5	0.104	4.2	21	V-30	0.033	6.9
5	V-12	0.004	3.5	22	H-30	3.88	6.3
6	H-12	0.219	4.4	23	V-31	0.005	6.6
7	V-13	0.055	4	24	H-31	0.031	6.2
8	H-13	0.099	3.9	25	V-39	0.021	6.7
9	V-14	0.064	3.9	26	H-39	1.97	7.8
10	H-14	1.91	4.2	27	V-47	0.021	5.6
11	V-15	0.004	3.9	28	H-47	0.07	5.1
12	H-15	0.074	3.8	29	V-49	0.005	5.5
13	V-16	0.008	3.8	30	H-49	1.704	6.9
14	H-16	4.41	3.9	31	V-50	0.001	6.6
15	V-21	0.003	5	32	H-50	0.55	6.5
16	H-21	0.089	4.6	33	V-51	0.0028	6.6
17	V-22	0.017	4.9	34	H-51	1.43	5.9

4.2. Complex Resistivity Test Results

The complex resistivity of 34 shales was measured under the conditions of normal temperature and pressure, and then under high temperature and pressure. The amplitude and phase of resistivity are shown in Figures 5–8.

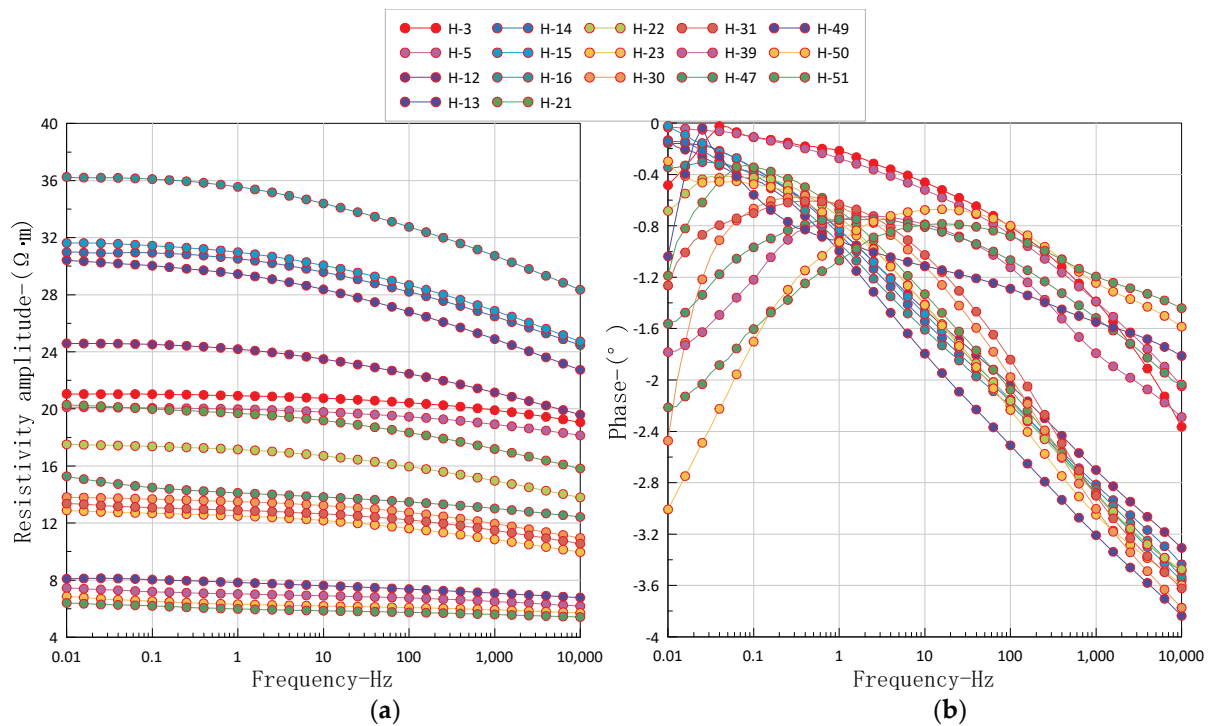


Figure 5. Amplitude and phase diagram of shale resistivity in H direction at normal temperature and pressure. (a) resistivity amplitude; (b) phase.

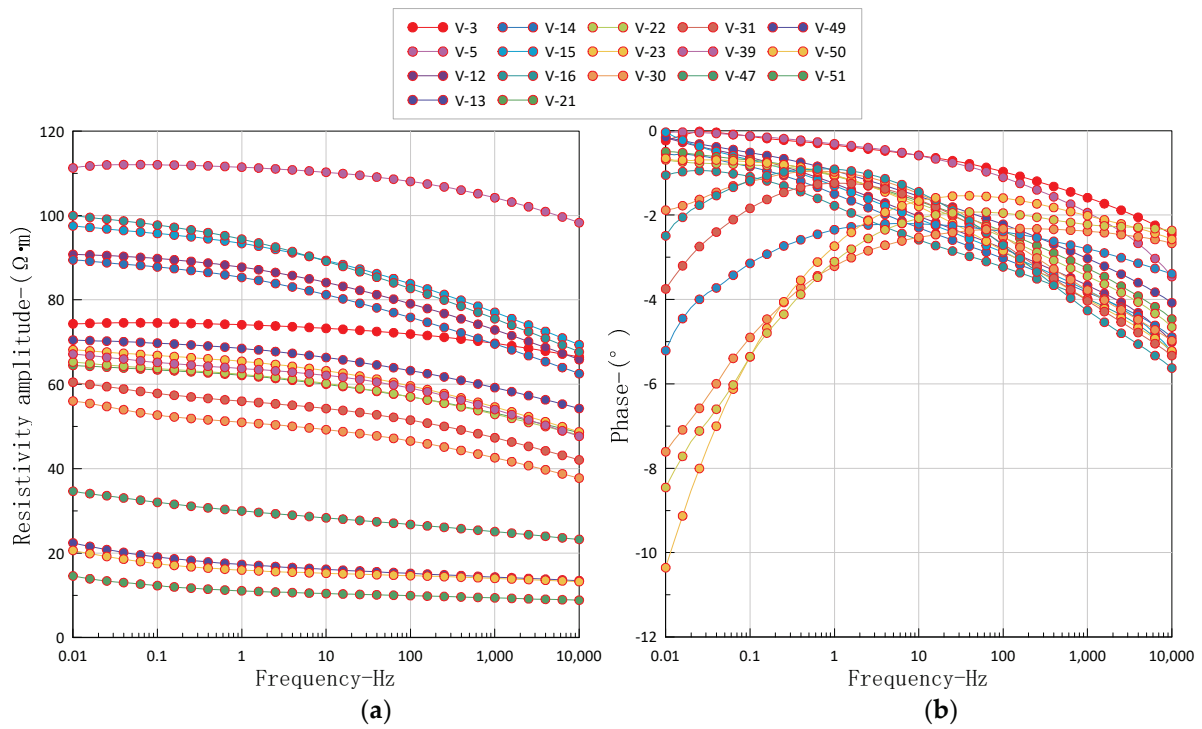


Figure 6. Amplitude and phase diagram of shale resistivity in V direction at normal temperature and pressure. (a) resistivity amplitude; (b) phase.

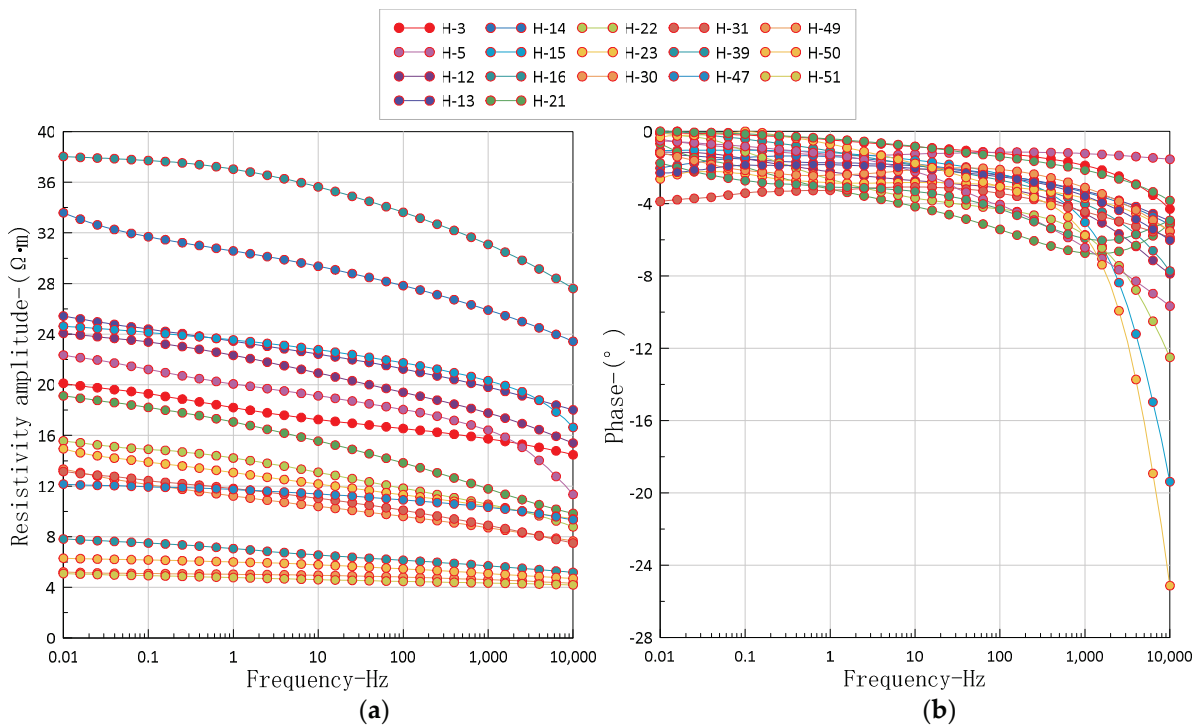


Figure 7. Amplitude and phase diagram of shale resistivity in H direction at high temperature and pressure. (a) resistivity amplitude; (b) phase.

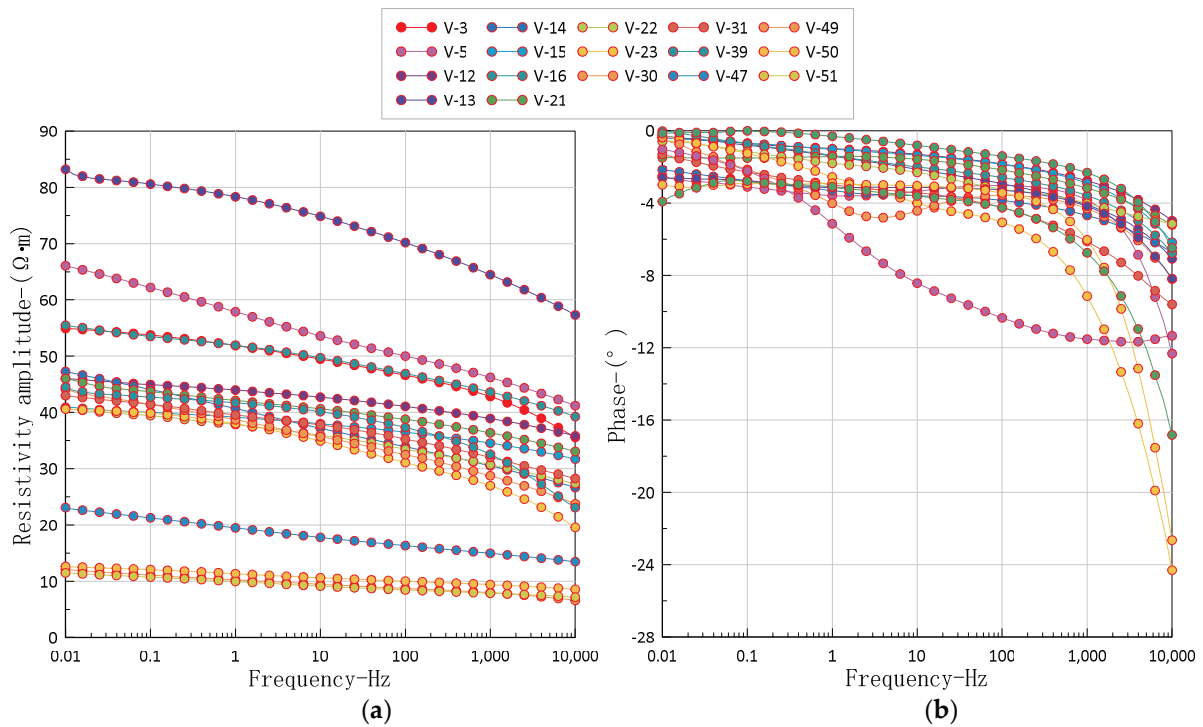


Figure 8. Amplitude and phase diagram of shale resistivity in V direction at high temperature and pressure. (a) resistivity amplitude; (b) phase.

The measurement results show that the amplitude of resistivity increases monotonically with the decrease of frequency, and the amplitude of phase changes complicatedly with the decrease of frequency. It can be seen that shale shows different degrees of induced polarization effect; especially with the increase in depth, the shale has high TOC and pyrite content in the gas-producing horizon, and its IP characteristics are more intense. On the whole, the resistivity amplitude of the rock samples in the H direction is smaller than that of the rock samples in the V direction. Of course, the shale resistivity will also be affected by factors such as fractures.

4.3. IP Parameter Inversion Result

According to the Cole-Cole model, the induced polarization parameters are extracted by inversion, and the results are shown in Tables 4 and 5. Two induced polarization parameters, the zero-frequency resistivity and polarizability, are emphatically analyzed and studied. According to the inversion results, the resistivity in the vertical bedding direction (V direction) is larger than that in the bedding direction (H direction). In addition, the resistivity of shale under high temperature and pressure is lower than that under normal temperature and pressure, while the polarizability under high temperature and pressure is higher than that under normal temperature and pressure.

Table 4. Inversion results of core IP parameters under normal temperature and pressure.

No.	Number	ρ_0 ($\Omega \cdot m$)	m (%)	No.	Number	ρ_0 ($\Omega \cdot m$)	m (%)
1	V-3	153.72	8.44	18	H-22	20.96	17.16
2	H-3	24.79	13.5	19	V-23	134.7	17.42
3	V-5	184.75	7.97	20	H-23	15.38	17.57
4	H-5	23.71	13.7	21	V-30	127.14	14.62
5	V-12	140.45	12.99	22	H-30	16.79	17.08
6	H-12	29.26	16.56	23	V-31	107.18	16.33

Table 4. Cont.

No.	Number	ρ_0 ($\Omega \cdot m$)	m (%)	No.	Number	ρ_0 ($\Omega \cdot m$)	m (%)
7	V-13	136.01	12.58	24	H-31	15.97	16.56
8	H-13	36.18	17.87	25	V-39	117.28	13.16
9	V-14	186.98	11.2	26	H-39	8.73	15.55
10	H-14	36.81	16.52	27	V-47	73.98	17.99
11	V-15	151.87	10.8	28	H-47	17.47	15.41
12	H-15	37.43	16.51	29	V-49	109.32	15.25
13	V-16	165.32	13.16	30	H-49	9.63	16.36
14	H-16	42.97	16.69	31	V-50	60.45	20.19
15	V-21	143.16	15.88	32	H-50	9.63	16.36
16	H-21	24.04	16.96	33	V-51	43.52	18.2
17	V-22	127.45	14.94	34	H-51	7.9	14.32

Note: ρ_0 is zero-frequency resistivity, m is polarizability.

Table 5. Inversion results of core IP parameters under high temperature and pressure.

No.	Number	ρ_0 ($\Omega \cdot m$)	m (%)	No.	Number	ρ_0 ($\Omega \cdot m$)	m (%)
1	V-3	64.73	17.76	18	H-22	19.86	28.37
2	H-3	23.57	19.83	19	V-23	52.61	26.03
3	V-5	77.78	21.53	20	H-23	18.14	25.76
4	H-5	21.64	22.09	21	V-30	53.96	24.74
5	V-12	46.16	14.66	22	H-30	16.75	28.46
6	H-12	29.79	24	23	V-31	50.74	19.13
7	V-13	52.39	14.15	24	H-31	16.48	27.23
8	H-13	30.09	20.08	25	V-39	52.08	18.08
9	V-14	96.51	17.3	26	H-39	9.61	24.61
10	H-14	39.42	19.63	27	V-47	27.46	24.21
11	V-15	57.63	25.34	28	H-47	14.4	17.34
12	H-15	29.33	18.3	29	V-49	14.87	26.25
13	V-16	46.81	14.46	30	H-49	6.1	15.46
14	H-16	45.28	17.66	31	V-50	14.77	19.49
15	V-21	51.97	15.95	32	H-50	7.64	20.05
16	H-21	25.78	34.05	33	V-51	13.79	23.29
17	V-22	48.14	19.01	34	H-51	5.94	16.94

Note: ρ_0 is zero-frequency resistivity, m is polarizability.

Figure 9 is the intersection diagram of zero-frequency resistivity, porosity and permeability at normal temperature and pressure. The resistivity decreases with the increase of porosity, but the shale porosity in H and V directions shows little difference. The horizontal permeability is higher than the vertical permeability, and the resistivity in the horizontal direction is lower than $40 \Omega \cdot m$ as a whole. In the zero-frequency resistivity and permeability diagram, the V direction data are in the upper left corner, with an average value of zero-frequency resistivity of $127.25 \Omega \cdot m$ and an average value of permeability of $0.019 \times 10^{-3} \mu m^2$. H direction data are in the lower right corner, with an average zero-frequency resistivity of $22.21 \Omega \cdot m$ and an average permeability of $1.099 \times 10^{-3} \mu m^2$. Generally, the average resistivity decreases with the increase in permeability. Therefore, the resistivity and permeability parameters of shale have strong directionality, which cannot be ignored in the process of reservoir evaluation.

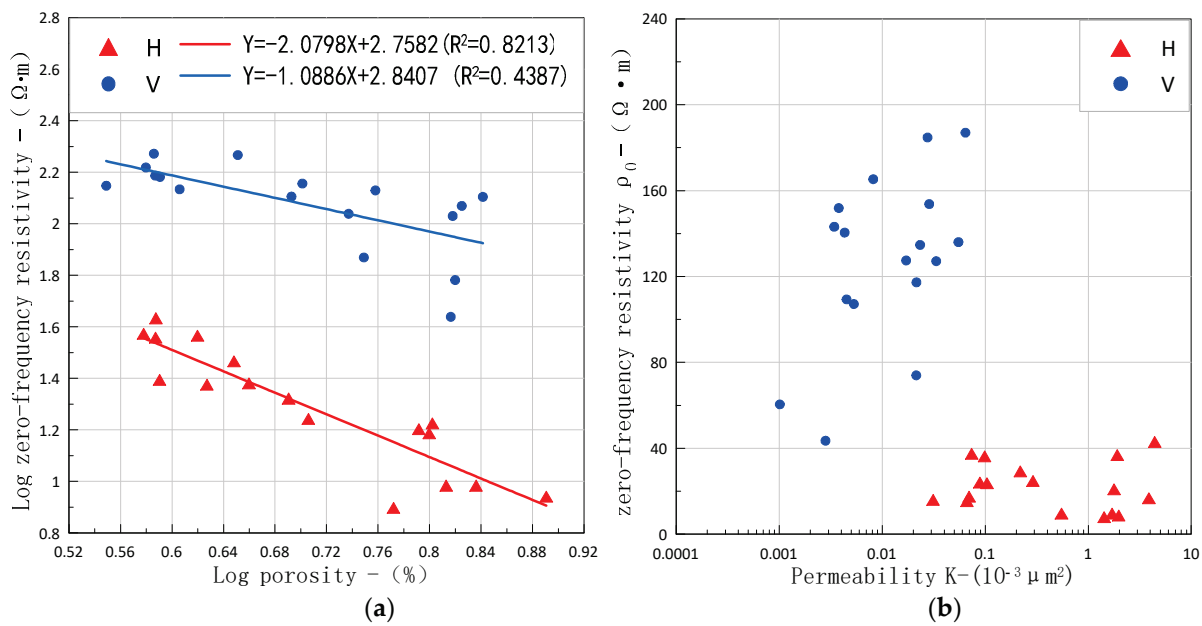


Figure 9. Intersection diagram of zero-frequency resistivity, porosity and permeability at normal temperature and pressure. (a) Zero-frequency resistivity and porosity; (b) zero-frequency resistivity and permeability.

4.4. Anisotropic Feature Analysis

4.4.1. Anisotropy Coefficient

The heterogeneity and anisotropy of rock are common phenomena, and are also important components of petrophysical research at present. The resistivity measurement direction of the sample includes two directions, a vertical bedding direction (direction perpendicular to plane A) and a bedding direction (direction perpendicular to plane B and C); the schematic diagram of resistivity measurement directions in different directions and the real samples of coring rock samples are shown in Figure 10. In the research process of this paper, the vertical bedding direction (ρ_a direction) and the bedding direction (ρ_b or ρ_c) are considered in the coring direction.

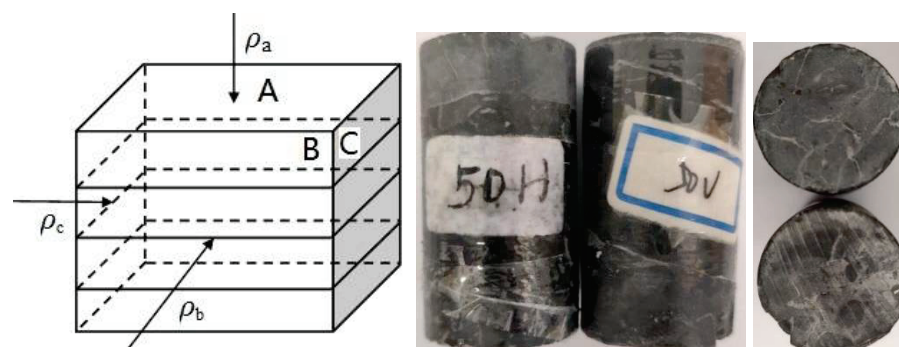


Figure 10. Schematic diagram of resistivity measurement orientation of rock sample and physical drawing of coring rock sample.

The electrical anisotropy of rock can be described by the anisotropy coefficient:

$$\lambda = \sqrt{\frac{\rho_n}{\rho_t}}, \tag{5}$$

where ρ_n is the resistivity in the vertical direction and ρ_t is the resistivity in the horizontal direction. Therefore, according to the schematic diagram of Figure 10, the anisotropy coefficient of shale can be defined as:

$$\lambda = \sqrt{\frac{\rho_a}{\rho_b}} \text{ or } \lambda = \sqrt{\frac{\rho_a}{\rho_c}}, \tag{6}$$

ρ_a —resistivity in vertical bedding direction, ρ_b, ρ_c —resistivity along bedding direction.

4.4.2. Analysis of Heterogeneity of Porosity and Permeability of Shale

Porosity and permeability parameters are two important parameters for shale gas reservoir evaluation. The results in Figure 11 show that the porosity in the V and H directions of reservoir shale is basically the same, and the average ratio of the two directions is 0.988, close to 1. However, the average ratio of the permeability along the bedding direction to the vertical bedding direction reaches 35, indicating that the permeability is directional.

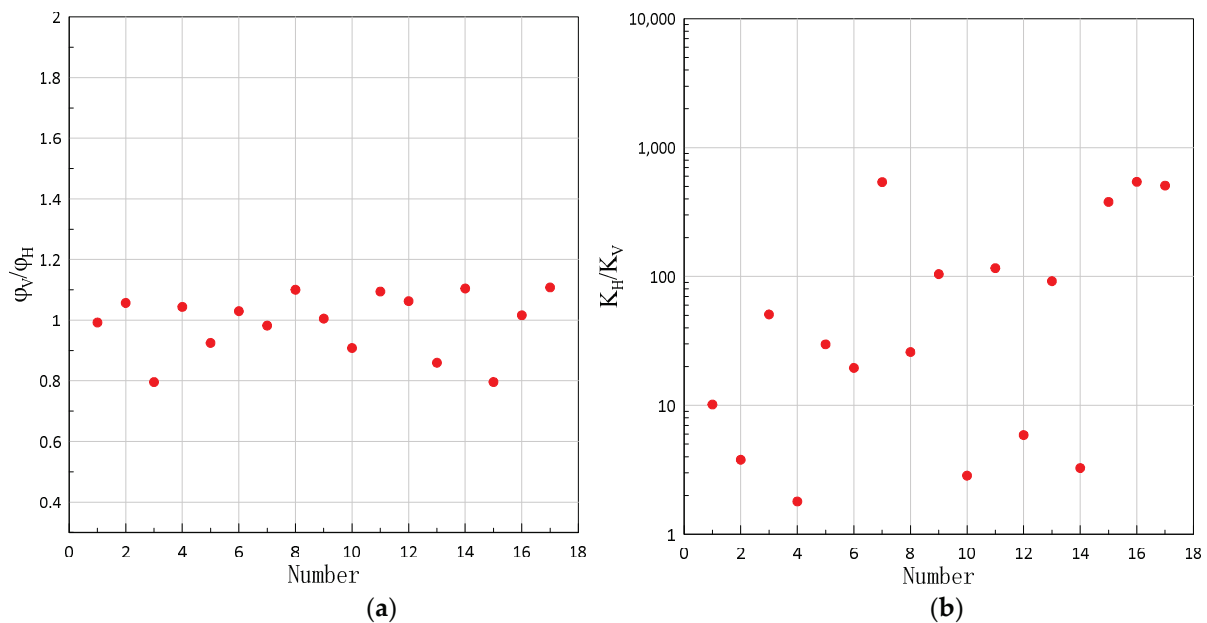


Figure 11. The heterogeneity of porosity and permeability. (a) Porosity; (b) permeability.

4.4.3. Influence of Temperature and Pressure on Electrical Anisotropy Coefficient of Shale

Under different temperature and pressure conditions, the distribution of complex resistivity anisotropy coefficients of shale is shown in Figure 12, and the complex resistivity parameters of shale from Wufeng Formation to Longmaxi Formation in southern Sichuan show strong anisotropy. The average resistivity anisotropy coefficient is 6.1 at normal temperature and pressure and 2.4 at high temperature and pressure. Therefore, it shows that the pores or fractures of shale are closed under the conditions of high temperature and pressure, which weaken its resistivity anisotropy. The average anisotropy coefficient of shale polarizability is 0.86 at normal temperature and pressure and 0.90 at high temperature and pressure, which is slightly increased, but both are close to 1.0, indicating that the anisotropy of polarizability is relatively weak.

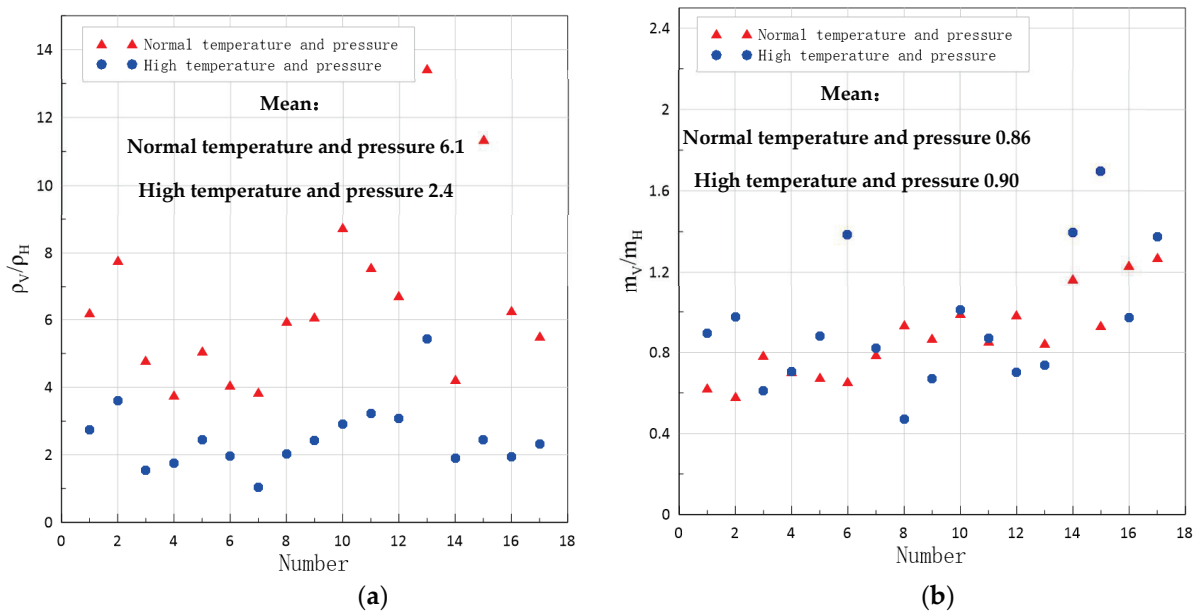


Figure 12. Anisotropy coefficient of resistivity and polarizability under normal temperature and pressure, high temperature and pressure. (a) resistivity; (b) polarizability.

4.4.4. Influence of Electrical Anisotropy of Shale on Actual Exploration

The electrical anisotropy of underground media is objective and universal. In recent years, the phenomenon of anisotropy has been paid more and more attention, and it has many applications in prospecting, the petroleum industry and so on. For example, through the study of resistivity anisotropy, it can be linked with the development direction of underground faults and the dominant position of in situ stress accumulation in order to understand the underground situation. Shale gas reservoirs usually have good stratification and obvious anisotropy, so it is feasible to apply resistivity anisotropy to shale gas reservoir exploration.

With the emphasis of oil and gas exploration and development in China gradually shifting to unconventional and steep structures in front of the mountain, the evaluation of reservoir anisotropy is particularly important. Anisotropy refers to some physical parameters of rock, such as acoustic velocity, electrical conductivity, permeability, etc. Its numerical value is directional; that is, the results measured in different directions are different. The grain structure arrangement in the rock, external temperature and pressure are the main reasons for the anisotropy, and its structural scale can range from a few microns to tens of kilometers.

The resistivity anisotropy system of shale is mainly related to the layered structure of shale, with good connectivity of pores parallel to the layered structure and poor connectivity of pores perpendicular to the layered structure. Saturated shale takes pore fluid as the main conductive body, so the resistivity decreases with the pore size increasing. Because of the layered structure of shale, the distribution of fluid channels in rocks has obvious directionality and demonstrates obvious anisotropy of the pore structure. Pressure and temperature also have influence on the resistivity of the sample, compressing and closing pores, thus increasing rock resistivity. Temperature rise will reduce the resistivity of fluid, thus reducing the resistivity of rock. There is a noticeable difference between the geoelectric field generated by the anisotropic medium and the geoelectric field generated by the isotropic medium, which leads to a great deviation in the interpretation of the observed data and even makes it difficult to explain them. Therefore, electrical anisotropy is one of the physical properties that must be considered in geological structure and natural energy exploration, and it is also one of the factors that affect the detection results. It is of great significance to find out the internal situation of underground structures and solve some puzzles in field exploration.

5. Conclusions and Cognition

The shale resistivity of the Nanwufeng Formation and Longmaxi Formation is obviously anisotropic.

Through testing and analyzing the complex resistivity, porosity and permeability of shale in the Wufeng Formation and Longmaxi Formation in southern Sichuan in two orthogonal directions (vertical bedding V and along bedding H), the following conclusions and understandings are obtained:

(1) In the middle and low measurement frequency band, the cores in shale gas wells show different degrees of induced polarization characteristics. The amplitude and phase curve of shale complex resistivity in two directions are basically the same, but the amplitude of complex resistivity is obviously anisotropic, and the amplitude of complex resistivity in V direction is significantly larger than that in H direction.

(2) There is a small difference between the porosity in H direction and V direction of shale, but the permeability in H direction is much larger than that in V direction, which indicates that the permeability parameters have obvious directionality and show strong anisotropy, which is different from the porosity.

(3) The resistivity parameters of shale show strong anisotropy. The average resistivity anisotropy coefficient is 6.1 under normal temperature and pressure and 2.4 under high temperature and pressure, while the average polarization anisotropy coefficient is 0.86 under normal temperature and pressure and 0.90 under high temperature and pressure, indicating that the resistivity has strong anisotropy and the polarization is relatively weak. In addition, the pores and fractures of shale contract under conditions of high formation pressure, which leads to the weakening of conductivity in H direction, the decrease in the resistivity anisotropy coefficient and the slight increase in the polarization anisotropy coefficient. Therefore, in the process of shale gas reservoir exploitation, the influence of reservoir pressure sensitivity and anisotropy on productivity cannot be ignored.

(4) The horizontal layered structure of shale reservoir leads to the strong heterogeneity and anisotropy of shale, and the fracture system has the characteristics of strong pressure sensitivity and anisotropy, which make the process of shale gas development and reservoir reconstruction extremely complicated. Therefore, the study of shale gas reservoir permeability anisotropy and shale electrical anisotropy has important guiding significance for improving the exploration and development effect of shale gas reservoirs.

Based on the shale complex resistivity experiment, this study has formed a set of testing methods and analysis techniques for electrical anisotropy of shale reservoirs. Combined with the analysis of two important reservoir parameters, porosity and permeability, it is found that shale resistivity and permeability parameters have strong anisotropy, which should be paid attention to in the process of reservoir evaluation. At the same time, the research results are helpful to understand the anisotropic characteristics of complex resistivity of shale gas reservoirs in southern Sichuan, and lay a foundation for shale gas reservoir evaluation and fracturing monitoring by electrical exploration.

Author Contributions: Conceptualization, K.X. and L.Y.; methodology, K.X.; validation, L.Y., G.T. and Y.L.; investigation, K.X.; resources, G.Y.; writing—original draft preparation, K.X.; writing—review and editing, L.Y. All authors have read and agreed to the published version of the manuscript.

Funding: This research was funded by the National Natural Science Foundation of China (Grant No. 42174083, 42030805 and 41874119).

Acknowledgments: We thank the department of geophysical and geochemical prospecting, BGP, CNPC, for supplying rock samples.

Conflicts of Interest: The authors declare that there are no conflict of interest.

References

1. Curtis, J.B.; Montgomery, S.L. Recoverable natural gas resource of the united states: Summary of recent estimates. *AAPG Bull.* **2002**, *86*, 1671–1678. [[CrossRef](#)]
2. Loucks, R.G.; Ruppel, S.C. Mississippian Barnett Shale: Lithofacies and depositional setting of a deep-water shale-gas succession in the Fort Worth Basin, Texas. *AAPG Bull.* **2007**, *91*, 579–601. [[CrossRef](#)]
3. Zou, C.; Zhao, Q.; Cong, L.; Wang, H.; Shi, Z.; Wu, J.; Pan, S. Development progress, potential and prospect of shale gas in China. *Nat. Gas Ind.* **2021**, *41*, 1–14. [[CrossRef](#)]
4. Zhang, J.; Nie, H.; Xu, B.; Jiang, S.; Zhang, P.; Wang, Z. Geological condition of shale gas accumulation in Sichuan basin. *Nat. Gas Ind.* **2008**, *28*, 151–156.
5. Li, G.; Yuan, B.; Zhu, H.; Yang, G.; Dai, X. Genesis of super-rich gas in the Sichuan Basin. *Nat. Gas Ind.* **2022**, *42*, 1–10. [[CrossRef](#)]
6. Zhao, W.; Li, J.; Yang, T.; Wang, S.; Huang, J. Geological difference and its significance of marine shale gases in South China. *Pet. Explor. Dev.* **2016**, *43*, 499–510. [[CrossRef](#)]
7. Potter, C.J. Paleozoic shale gas resources in the Sichuan Basin, China. *AAPG Bull.* **2018**, *102*, 987–1009. [[CrossRef](#)]
8. Ma, X. Enrichment laws and scale effective development of shale gas in the southern Sichuan Basin. *Nat. Gas Ind.* **2018**, *38*, 1–10. [[CrossRef](#)]
9. Liu, S.; Deng, B.; Sun, W.; Song, J.; Jiao, K.; Ye, Y.; Xie, G. May Sichuan Basin be a Super Petroliferous Basin? *J. Xihua Univ. (Nat. Sci. Ed.)* **2020**, *39*, 20–35. [[CrossRef](#)]
10. Zhang, J.; Tao, J.; Li, Z.; Wang, X.; Li, X.; Jiang, S.; Wang, D.; Zhao, X. Prospect of deep shale gas resources in China. *Nat. Gas Ind.* **2021**, *41*, 15–28. [[CrossRef](#)]
11. Nie, H.; Li, P.; Dang, W.; Ding, J.; Sun, C.; Liu, M.; Wang, J.; Du, W.; Zhang, P.; Li, D.; et al. Enrichment characteristics and exploration directions of deep shale gas of Ordovician-Silurian in the Sichuan Basin and its surrounding areas, China. *Pet. Explor. Dev.* **2022**, *49*, 648–659. [[CrossRef](#)]
12. Liu, L.; Zhang, M.; Wang, P.; Zhang, S.; Qiao, J.; Yu, H.; Huang, J. Construction of geophysical-geological structural models for complex basins: Application of interpretation of gravity, magnetic, electric and seismic data to exploration in the Chuxiong basin. *Chin. J. Geophys.* **2018**, *61*, 4921–4933. [[CrossRef](#)]
13. Zhang, C.; Liu, X.; He, L.; He, W.; Zhou, Y.; Zhu, Y.; Cui, Z.; Kuang, X. A study of exploration organic rich shales using Time-Frequency Electromagnetic Method (TFEM). *Chin. J. Geophys.* **2013**, *56*, 3173–3183. [[CrossRef](#)]
14. Zhang, C.; Liu, X.; Zhou, H.; He, L.; He, W.; Zhou, Y.; Zhu, Y. A step forward study for the exploration of organic-rich shale by using time-frequency electromagnetic method (TFEM). *Geophys. Prospect. Pet.* **2015**, *54*, 627–634. [[CrossRef](#)]
15. Zhou, Y.; Liu, X.; Zhang, C.; Zhu, Y. The TEEM technology for quick identification of ‘sweet spot’ of shale gas and its applications. *Geophys. Geochem. Explor.* **2015**, *39*, 60–63. [[CrossRef](#)]
16. Ma, Y.; Zhang, C.; Tian, Y.; Ma, Y. Research on identification of organic-rich shales using seismic constrained time-frequency electromagnetic method. *Prog. Geophys.* **2016**, *31*, 2618–2626. [[CrossRef](#)]
17. Meng, F.; Bao, S.; Chen, K.; Wang, P.; Li, L. The prediction of shale gas favorable area based on wide area electromagnetic method: A case study of Wushan area in northeast Chongqing. *Geophys. Geochem. Explor.* **2018**, *42*, 68–74. [[CrossRef](#)]
18. Yan, L.; Chen, X.; Tang, H.; Xie, X.; Zhou, L.; Hu, W.; Wang, Z. Continuous TDEM for monitoring shale hydraulic fracturing. *Appl. Geophys.* **2018**, *15*, 26–34. [[CrossRef](#)]
19. Xiang, K.; Hu, W.; Yan, L.; Zhang, H.; He, W.; Tang, X.; Liu, X. Complex resistivity dispersion characteristics of shale samples in Sichuan and Guizhou area. *Oil Geophys. Prospect.* **2014**, *49*, 1013–1019. [[CrossRef](#)]
20. Yan, L.; Xiang, K.; Li, P.; Wang, Z. Study on the induced polarization model in the exploration for shale gas in southern China. *SEG Tech. Program Expand. Abstr.* **2014**, 912–916. [[CrossRef](#)]
21. Zhao, W. Reservoir of Electricity of Silurian Longmaxi Shale in South Sichuan Area. Master’s Thesis, Chengdu University of Technology, Chengdu, China, 2015.
22. Huang, T.; Yu, G.; Wang, X.; Zhang, B.; He, Z.; Chen, J.; Zhu, H. Experiment research of the main influence factors of shale sample complex resistivity dispersion characteristics. *Comput. Tech. Geophys. Geochem. Explor.* **2016**, *38*, 167–174. [[CrossRef](#)]
23. Sun, B.; Tang, X.; Xiang, K.; Dou, C. The Analysis and Measure on Complex Resistivity Parameters of Shaly Sands in High Temperature and High Pressure. *J. Eng. Geophys.* **2016**, *13*, 277–284. [[CrossRef](#)]
24. Wang, X.; Zhang, B.; He, Z.; He, L.; Yang, K.; Huang, T.; Luo, F.; Tang, J.; Gan, L. Electrical properties of Longmaxi organic-rich shale and its potential applications to shale gas exploration and exploitation. *J. Nat. Gas Sci. Eng.* **2016**, *36*, 573–585. [[CrossRef](#)]
25. Xiang, K.; Yan, L.; Hu, H.; Hu, W.; Tang, X.; Liu, X. Relationship analysis between brittle index and electrical properties of marine shale in South China. *Geophys. Prospect. Pet.* **2016**, *55*, 894–903. [[CrossRef](#)]
26. Liu, Z.; Sa, L.; Yang, X.; Li, X. The demand of shale gas exploration and development for geophysical technology. *Oil Geophys. Prospect.* **2011**, *46*, 810–819. [[CrossRef](#)]
27. Wang, Y.; Yang, D.; Yin, C.; Gao, Y. Anisotropic geophysics and vector field. *Chin. Sci. Bull.* **2017**, *62*, 2594–2605. [[CrossRef](#)]
28. Liu, Y.; Yin, C.; Cai, J.; Huang, W.; Ben, F.; Zhang, B.; Qi, Y.; Qiu, C.; Ren, X.; Huan, X.; et al. Review on research of electrical anisotropy in electromagnetic prospecting. *Chin. J. Geophys.* **2018**, *61*, 3468–3487. [[CrossRef](#)]
29. Revil, A.; Woodruff, W.F.; Torres-Verdín, C.; Prasad, M. Complex conductivity tensor of anisotropic hydrocarbon-bearing shales and mudrocks. *Geophysics* **2013**, *78*, D403–D418. [[CrossRef](#)]

30. Cheng, L.; Wang, Y.; Zhang, C. Anisotropy of complex resistivity of the shale in eastern Guizhou province and its correlations to reservoir parameters of shale gas. *Chin. J. Geophys.* **2021**, *64*, 3344–3357. [[CrossRef](#)]
31. Pelton, W.H.; Ward, S.H.; Hallof, P.G.; Sill, W.R.; Nelson, P.H. Mineral Discrimination and Removal of Inductive Coupling with Multifrequency Ip. *Geophysics* **1978**, *43*, 588–609. [[CrossRef](#)]

Article

Imaging Karatungk Cu-Ni Mine in Xinjiang, Western China with a Passive Seismic Array

Peixiao Du ^{1,2}, Jing Wu ^{1,*} , Yang Li ^{1,2}, Jian Wang ³, Chunming Han ³,
Mark Douglas Lindsay ⁴ , Huaiyu Yuan ^{4,5} , Liang Zhao ^{1,2}  and Wenjiao Xiao ^{1,2}

¹ State Key Laboratory of Lithospheric Evolution, Institute of Geology and Geophysics, Chinese Academy of Sciences, Beijing 100029, China; dupeixiao17@mails.ucas.ac.cn (P.D.); liyang181@mails.ucas.ac.cn (Y.L.); zhaoliang@mail.iggcas.ac.cn (L.Z.); wj-xiao@mail.iggcas.ac.cn (W.X.)

² College of Earth Sciences, University of Chinese Academy of Sciences, Beijing 100049, China

³ Key Laboratory of Mineral Resources, Institute of Geology and Geophysics, Chinese Academy of Sciences, Beijing 100029, China; jianwang@mail.iggcas.ac.cn (J.W.); cm-han@mail.iggcas.ac.cn (C.H.)

⁴ Centre for Exploration Targeting, School of Earth Sciences, The University of Western Australia, Crawley, Western Australia 6009, Australia; mark.lindsay@uwa.edu.au (M.D.L.); huaiyu.yuan@gmail.com (H.Y.)

⁵ ARC Centre of Excellence for Core to Crust Fluid Systems, Department of Earth and Planetary Sciences, Macquarie University, North Ryde, NSW 2109, Australia

* Correspondence: wujing_js@mail.iggcas.ac.cn

Received: 8 June 2020; Accepted: 29 June 2020; Published: 1 July 2020



Abstract: Karatungk Mine is the second-largest Cu-Ni sulfide mine in China. However, the detailed structure beneath the mine remains unclear. Using continuous waveforms recorded by a dense temporary seismic array, here we apply ambient noise tomography to study the shallow crustal structure of Karatungk Mine down to ~1.3 km depth. We obtain surface-wave dispersions at 0.1–1.5 s by calculating cross-correlation functions, which are inverted for 3D shear-wave structure at the top-most (0–1.3 km) crust by a joint inversion of group and phase dispersions. Our results show that low-velocity zones beneath Y1 ore-hosting intrusion (hereafter called Y1) at 0–0.5 km depth and northwest of the Y2 ore-hosting intrusion (hereafter called Y2) at 0–0.6 km depth are consistent with highly mineralized areas. A relatively high-velocity zone is connected with a weakly mineralized area located to the southeast of Y2 and Y3 (hereafter called Y3) ore-hosting intrusions. Two high-velocity zones, distributed at 0.7–1.3 km depth in the northernmost and southernmost parts of the study area respectively, are interpreted to be igneous rocks related to early magma intrusion. Furthermore, the low-velocity zone at 0.7–1.3 km depth in the middle of the study area may be related to: a possible channel related to initial magma transport; mine strata or a potentially mineralized area. This study demonstrates a new application of dense-array ambient noise tomography to a mining area that may guide future studies of mineralized regions.

Keywords: Karatungk Mine; ambient noise tomography; dense array; mineralization

1. Introduction

Karatungk Mine, located on the southern margin of the Altay Mountains, is the second-largest Cu-Ni sulfide mine in China (Figure 1) [1–3]. The surface area of the mine is ~13 km², and the reserves of the mine were re-predicted to be 1,240,000 tons in 2005 [4]. This mine still has a relatively large stable mining value. Previous research suggests that there may be a large number of additional Cu-Ni sulfide orebodies hosted in ultramafic intrusions at depth, especially given that the geology mainly comprises mafic intrusions, although significant ultramafic intrusions are not exposed [5]. Moreover, as a basis for studying the sulfide mine, improved imaging of the 3D shallow structure helps to better understand

the spatial-temporal distribution of magmatism, mineralization, and evolution mechanisms, which are crucial in future mine planning and exploration.

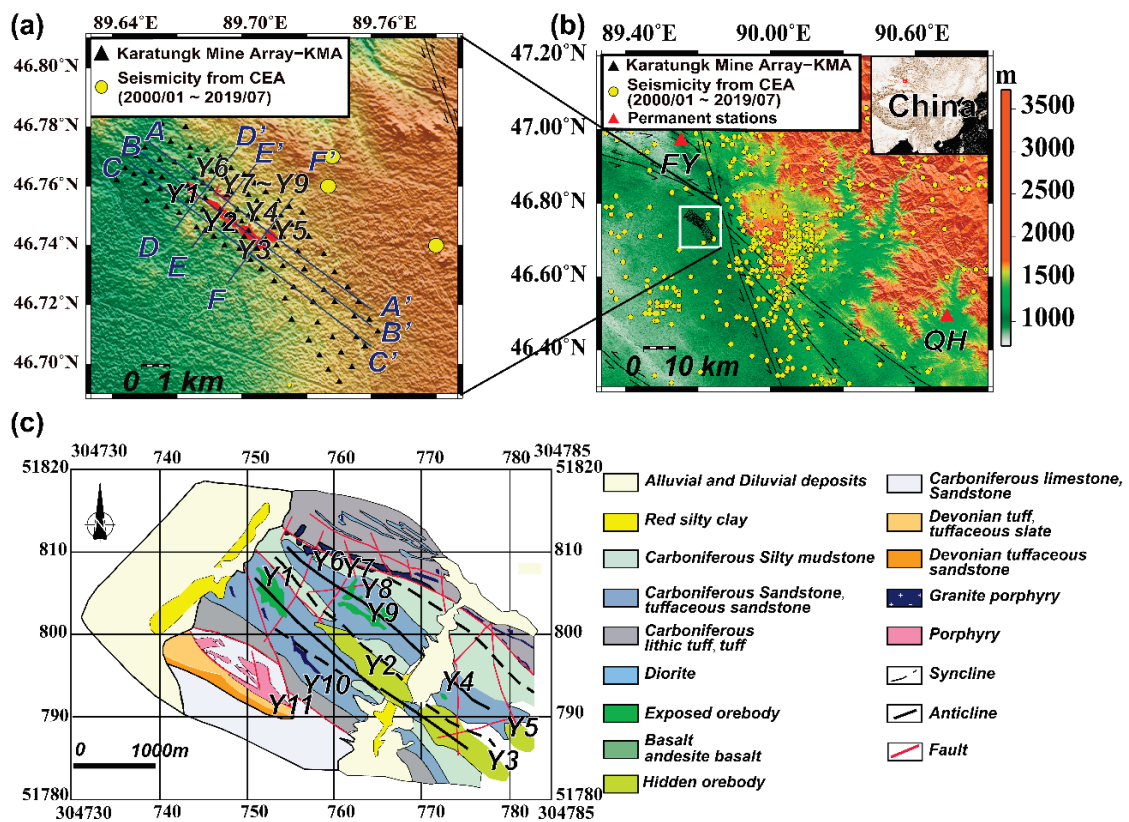


Figure 1. Karatungk Mine, local geological setting, and seismic array. (a) Topographic map and the Karatungk Mine array—KMA. The map shows the location of KMA (black triangles). Blue solid lines show the profiles across the mine on which velocity model is presented. Red areas represent the ore-hosting intrusions. White letters are the name of intrusions. (b) The regional map of Karatungk Mine: black lines are faults and red triangles show the permanent stations in Xinjiang Province, yellow circles show the seismicity from China Earthquake Network Center. The inset shows the geographic location of this map. The white rectangle shows the geographic location of (a). (c) Detailed distribution of ore-hosting intrusions (Y1–Y11) in Karatungk Mine, modified from [5]. Labels of horizontal and vertical axis are the location of the mine given in Geodetic coordinate system. Right panel shows detailed structural attributes.

The outcropping rocks in Karatungk Mine are mainly of Devonian or Carboniferous age, with parts being Ordovician, Jurassic, Tertiary, and Quaternary [2]. Northwest striking folds and thrusting faults are dominant structures in the mine (Figure 1b,c), and the intersection of folds and faults are favorable for intruding of ore-hosting intrusions [5,6]. From northwest to southeast, there are three major ore-hosting intrusions named Y1, Y2, and Y3, respectively (Figure 1c). Y1 is partially exposed to the ground and all rocks have been mineralized, Y2 is unexposed with high mineralization in the northwest and weak mineralization in the southeast, and Y3 is unexposed with weak mineralization, (Figure 1) [5]. In addition, there are another six ore-hosting intrusions with weak mineralization named Y4–Y9, distributed in the northeast of three main ore-hosting intrusions, in which Y4 and Y6–Y9 are exposed and Y5 is unexposed (Figure 1c) [5].

To date, previously discovered shallow structures have been largely usually revealed by active source seismic, gravity, and magnetic detection including both Time Domain Electromagnetic Method (TEM) and Wide-Field Electromagnetic Method (WFEM) [7,8]. Gravity and magnetic measurements typically reveal Cu-Ni sulfide orebodies in this area with higher magnetic, density and polarization

signatures and lower resistivity values relative to ore-hosting intrusions [9]. By combining TEM and exploration drilling, it is inferred that Y2 does not connect with Y5 and Y7–Y9 as there are steeply individual intrusions in the depth shallower than 0.7 km [5]. Application of seismic reflection imaging in this mine indicates that buried mafic intrusions may exist beneath Y3 and Y5 [5]. This speculation has been supported by borehole data, which found mafic intrusions (diorite, gabbro-diorite, and diorite porphyrite) at depths of 686–840 m and 1060–1140 m [10]. Unfortunately, the methods mentioned above are costly with some not environmentally friendly. Even though many studies have examined Karatungk Mine, the detailed structure beneath those ore-hosting intrusions remains unclear, which prevents us from better understanding of the origin of the intrusions, e.g., [5], deep ore genesis processes and their relationship to seismic structures.

Ambient noise tomography (ANT) provides a feasible, cost-effective, and environmentally friendly approach to study shallow velocity structures, where the resolution depends on array setup, interstation distance, and frequency content of surface-wave in the study area [11,12]. Therefore, in order to observe fine shallow velocity structures, a dense seismic array and high-frequency content are required to study mines like Karatungk where major orebodies are distributed within the topmost (~2 km) of the crust. Many studies have demonstrated that ANT can be used for retrieving the structures on local (~20 km) [13], regional (~100–1000 km) [14–16] and global scales (>1000 km) [17–19]. In recent years, ANT has been increasingly applied to highly dense arrays [12,13,20], for example, the array of 5204 seismometers in Long Beach, California [13], and the array of 1108 stations in the San Jacinto Fault Zone southeast of Anza, California [21]. These studies show that detailed structures at kilometeric, or much smaller scales (hundreds or even tens of meters, e.g., [21]), can be obtained by combining ANT and highly dense arrays. However, to our knowledge, few published studies have focused on mines by ANT using dense arrays.

In this paper, we apply ANT to a dense array with 100 single-component seismometers in Karatungk Mine in northeastern Xinjiang, China. We obtain 1838 group velocity and 2092 phase velocity dispersion curves respectively from 4950 cross-correlation functions using a matured ANT technique [16,22,23]. Using a direct surface wave tomography approach [24], we invert these dispersion measurements for the shear-wave structure at a depth of 0–1.3 km beneath the study area. We find that velocity heterogeneities spatially correlate well with the distribution of major ore-hosting intrusions and mineralization of ore-hosting intrusions. These intrusions tend to cause a decrease in its shear-wave velocity in our study area, which is sensitive to the ANT technique. We propose that a combined approach with the ANT and a dense array setup may be a potentially feasible tool to map Cu-Ni sulfide orebodies in mines. Ultimately, this may help to better understand the geological evolution of the region and identify other potential mineral targets located in the shallow crust that remain undiscoverable to conventional tools.

2. Data and Method

To investigate the 3D shallow velocity structure in Karatungk Mine, we deployed a dense array of 100 short-period vertical-component seismometers between June 19, 2018 and August 25, 2018 (Figure 1), which was named Karatungk Mine array (KMA). The full aperture of the KMA was ~12 km in length and ~3 km in width, with an average station spacing of ~500 m. The seismometer used was manufactured by Dynamic Technologies Cooperation Company (DTCC), with the natural frequency of 0.2 s. The recording sampling rate was 0.002 s.

2.1. Cross-Correlation Function

We followed the method outlined in [25] and procedures outlined in [26] to process the data. Procedures performed include waveform demeaning and de-trending, instrument response removal, data cutting into 1-hour segments, spectral whitening, and temporal normalization. The final inter-station cross-correlation functions (CCFs) for all station pairs of the KMA were calculated in the periods of 0.1–2 s. Figure 2 shows examples of CCFs in which clear fundamental Rayleigh surface

waves are present. On the positive and negative lag time of CCFs, we can see some differences in amplitude, which indicates directional heterogeneous noise sources in mine (Section S1).

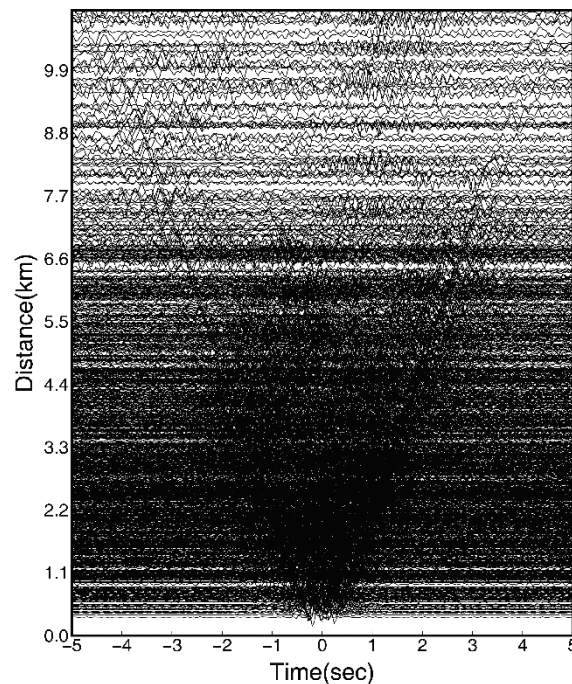


Figure 2. An example of cross-correlation functions (CCFs) used for dispersion measurements in the periods of 0.1–2 s. The CCFs of the total 58 days between 10 stations (named as XJ100~XJ109) and all the other stations of KMA. CCFs shown here are not symmetrized waveforms.

2.2. Rayleigh Wave Dispersion Measurement

Previous studies show that the CCFs of the ambient noise field between any station pairs is related to the Green's function of the selected stations [16]. Here we applied the frequency–time analysis method [16,22,23] that can solve several CCFs at a time and measure dispersion curves accurately. We stacked the negative and positive components of CCFs to suppress the influence of inhomogeneous source distribution of the noise sources (Figure S1) [13,17]. Luo et al. (2015) suggested that dispersion measurements at short interstation distance are stable if measured with a two- or three-wavelength rule [16,23,25,27]. We here chose one wavelength as the threshold for restriction on the inter-station distance [27] so that there were more dispersion points available for inversion while satisfying quality control of signal-to-noise ratio (SNR). Similar short wavelength rule has been used in other studies [13,27]. After filtering CCFs with a narrow band Gaussian filter [16], the dispersion curves were measured by setting the threshold of SNR >5. During the measurements, we firstly picked group velocity dispersion curves (Figure 3a) and then performed time-variable filtering to obtain the phase velocity dispersion curves in Figure 3b. In order to avoid the 2π ambiguity in phase velocity measurement, the group velocity dispersion curve was used as a reference for picking phase velocity dispersion curves, considering close trending in two dispersion curves. The group velocity and phase velocity dispersion curves obtained from the CCFs were in the periods of 0.1–1.5 s and 0.1–1.2 s, respectively (Figure S2). Figure 4 shows ray path density maps of the group and phase velocities at representative periods of 0.1, 0.5, 0.7, and 1.1 s, which suggests a dense and uniform coverage in the study area.

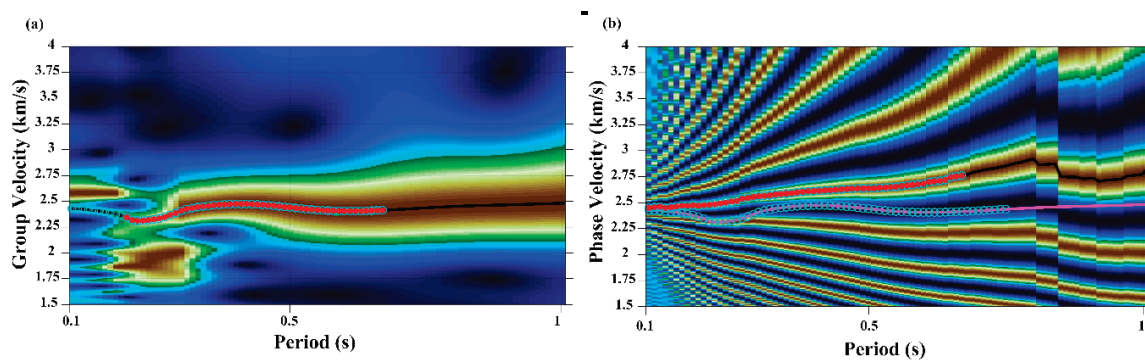


Figure 3. Rayleigh wave group (a) and phase (b) velocity dispersion curves analysis. Different color shows envelope amplitude at different period and velocity; blue presents lower amplitude and yellow brown show higher amplitude. (a) Rayleigh wave group velocity dispersion curves analysis. The horizontal axis is period (s) and the vertical axis is group velocity (km/s). Blue circles are the dispersion points satisfying the threshold of which only red-filled points are saved for inversion. The dark line is the dispersion curve which is predicted by the code. (b) Rayleigh wave phase velocity dispersion curves analysis. Horizontal axis is period (s) and vertical axis is group velocity (km/s). Pink line (bottom) shows the group velocity dispersion curves extracted in the previous step, which is used as a reference to guide picking of the corresponding phase velocity dispersion curve.

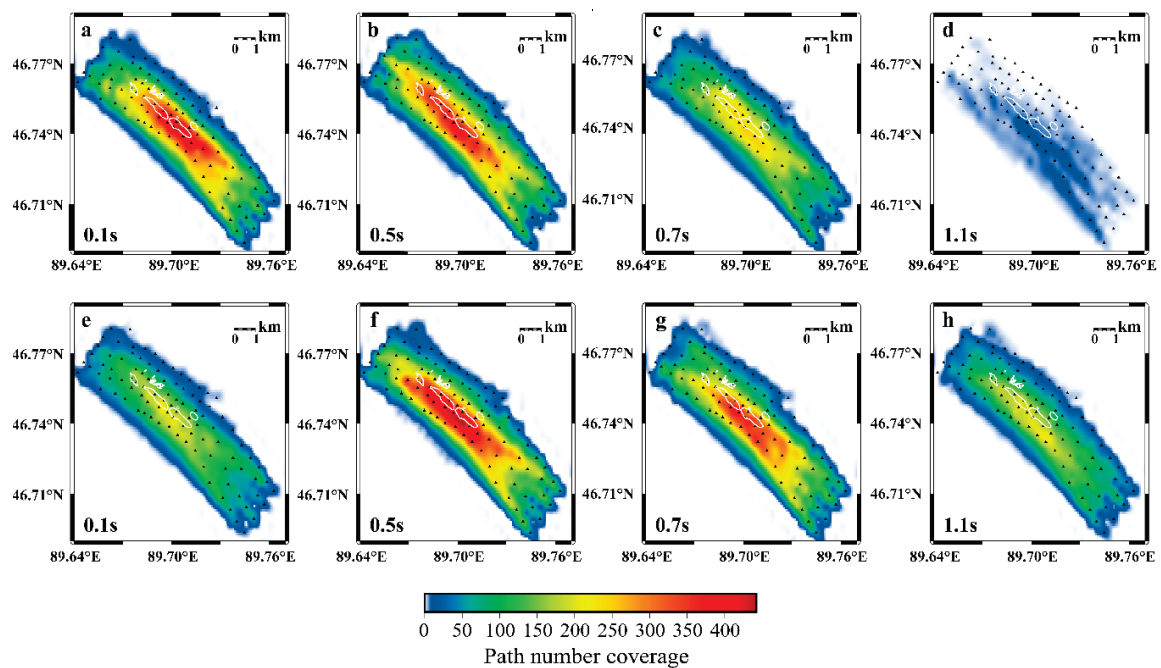


Figure 4. Ray path density maps of Rayleigh wave dispersion curves between all stations at various periods, and 0.1 s, 0.5 s, 0.7 s, 1.1 s are presented, respectively. (a–d) Ray path density maps of phase velocity; (e–h) Ray path density maps of group velocity.

2.3. Direct Surface Wave Tomography

Empirically proven relationships suggest that the fundamental mode Rayleigh-wave phase velocity is mostly sensitive to the shear-wave velocity at depths about one-third of its corresponding wavelength [24,28] and phase velocity is 0.92 of shear-wave velocity at a uniform half-space Poisson solid [28]. We constructed an initial 1D shear-wave velocity model and adjusted it according to CRUST 1.0 [29] (Figure S3). Then the *srfer96* program in Computer Programs in Seismology was used to solve the depth sensitivity kernels (Figure 5) depending on the input of the 1D shear-wave velocity model at a given frequency [30]. The sensitive kernel functions, corresponding to the selected periods

plotted in Figure 5, show that phase and group velocities are complementary in depth. In addition, when phase and group velocities are inverted simultaneously, uncertainties are significantly reduced at depths [31], suggesting that joint inversion of group velocity and phase velocity may help to increase the robustness of the inverted velocity model.

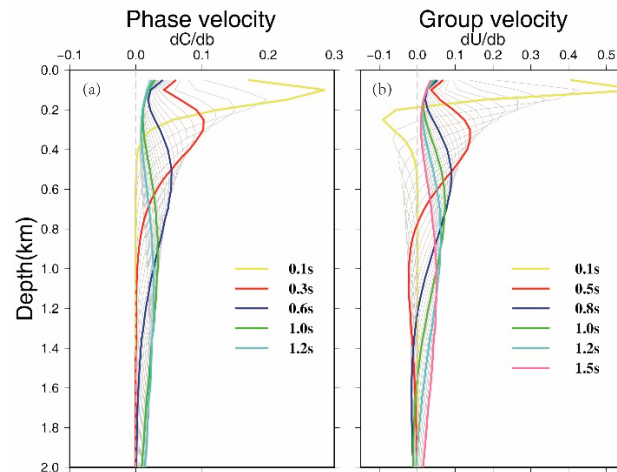


Figure 5. Rayleigh wave depth sensitivity kernels at different periods. (a) The sensitivity kernels of the phase velocity. (b) The sensitivity kernels of the group velocity. Gray curves show the kernels with 0.1 s increments in between the labeled periods.

We subsequently applied a direct inversion imaging technique [24] to invert both surface wave dispersions for the 3D shallow crustal shear-wave velocity structures beneath the mine. The method is based on 2D ray tracing instead of surface-wave propagating along the great-circle path, which is more suitable for complex situations in the shallow crust where large velocity variations usually cause strong non-linear effects. Next, a fast-marching method [32] was used to calculate Rayleigh-wave travel-time. Traditional inversion approaches do not usually update ray paths and sensitivity kernels for the updated 3D models, which may bias computation in wave propagation and thus invert velocity models in complex mediums [24]. In the computation of direct inversion imaging, the 3D wave speed model at each inversion step was used to obtain the 2D phase velocity maps and to construct new depth sensitivity kernels. Essentially these laterally varying depth kernels were updated with each iteration of inversion so that more accurate kernels were considered. Inversion parameters (e.g., weight factor between data misfit and model smoothing [24]) are tested at the beginning to obtain an optimal residual distribution [24,33]. Finally, we used all the parameters obtained from previous calculations to inverse for a 3D shear-wave velocity structure of Karatungk Mine.

3. Results

We jointly inverted group and phase velocity dispersion data to obtain the shallow crustal shear velocity structures. The study area was parameterized into a 36 by 36 grid points on the horizontal plane and 20 grid points along the depth direction. The grid size of the latitude and longitude in the horizontal plane are 0.0102° and 0.0147° , and in depth the grid interval varies from 50 m to 300 m within the depth of 1.3 km.

3.1. Resolution Tests

In order to test the robustness of the inversion results, we conducted a series of resolution tests (Figure S4). These tests illustrate that our dataset may reach a lateral resolution of ~ 1.0 km at shallow depth (< 0.2 km) and 1.3 km at deep depth, respectively. In Figure 6 we show the residual distribution of initial inversion and last inversion. After the iterative, non-linear inversion, the distribution of travel time residuals is more Gaussian-like, and the average and standard deviation of the residuals dropped

significantly from -0.022 s and 0.197 s in the initial model to 0.001 s and 0.076 s in the final model, respectively (Figure 6).

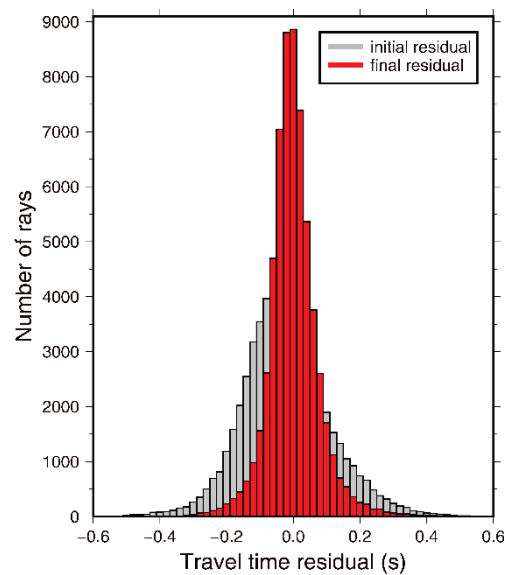


Figure 6. Distributions of surface wave travel-time residuals. Residuals before inversion are gray columns with the average $\mu = -0.022$ s and the standard deviation $\sigma = 0.197$ s. Residuals after inversion are red columns with $\mu = 0.001$ s and $\sigma = 0.076$ s.

3.2. Error Analysis

In order to improve the accuracy and stability of the inversion results for all dispersion curves, here we adopted a bootstrap resampling method with repeated sampling of dispersion curves [34], then multiple sets of dispersion curves can be used for inversion. We performed the bootstrap procedure in which 50 sets of resampled dispersion curves were generated and then inverted for 50 velocity models. We used the resulting mean and standard deviation of the velocity models as the final model and the approximated model error, respectively (Figure 7). There are only few ANT studies that deal with model errors at this step, e.g., [24,35]. Here the bootstrap procedure has the advantage to deal with real data errors without any assumptions, for example the distribution, the amplitude, and different sources of error that cannot be explained by an inversion problem. Figure 7 shows the velocity structure of the imaging results, in which the mean and standard deviation of the velocity structure were obtained by the bootstrap resampled datasets. We found that the bootstrapped average velocity structure is very close to the velocity structure inverted from the original data set (Figure S5). The model errors approximated by the standard deviation allow us to evaluate robust model regions for interpretation, for example, in most areas the approximated model errors are $< \sim 1.0\text{--}1.2\%$ level (Figure 7 and Figure S6). These measures provide confidence that the results are robust. The bootstrap procedure restricts the description of error to the dataset used in this study; thus, the error estimate described here is not transferrable to other regions or datasets. Nonetheless, the approach is transferrable to other regions and datasets in order to provide a useful measure from which robustness is represented to guide predictive endeavours. We stress that the model error obtained this way is not in the absolute sense, but this “approximated” approach helps us determine reliable model features.

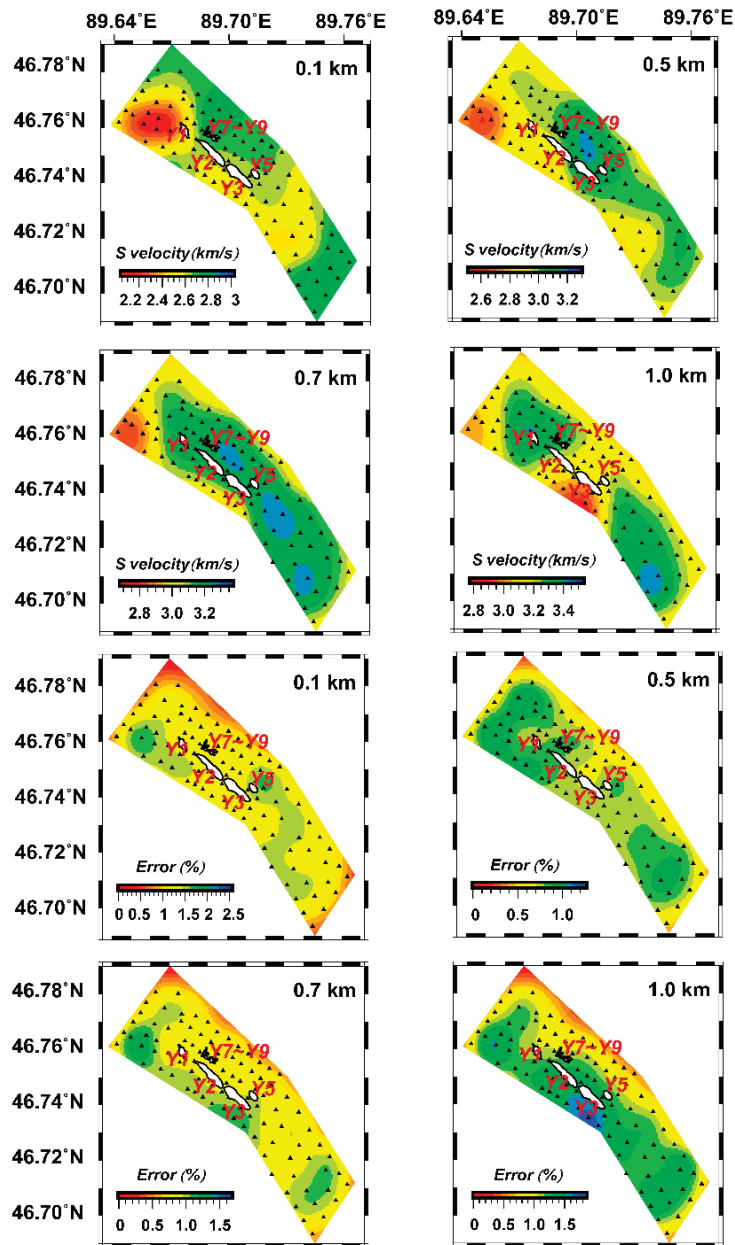


Figure 7. The Vs model and approximated model errors from the bootstrap inversion. The final Vs model is averaged from the 50 models inverted using bootstrapped datasets, and is shown at 0.1, 0.5, 0.7 and 1.0 km, respectively in the top panels. The model errors approximated from the standard deviation are plotted in the lower panels. The errors are in general in the range of ~0.2% to 2.7%. (Note outside the array there is no ray coverage. The <0.2% errors reflect smoothing and regularization in the effective regions and therefore may not be representative of robust regions). White areas with black solid lines represent the surface location of ore hosting intrusions Y1–Y9.

3.3. Shear-Wave Velocities

Figures 7–9 present the new features of our absolute shear-wave velocity model beneath Karatungk Mine. In the shallow section within 0.5 km depth, the shear-wave velocity maps show that prominent low velocities (<2.55 km/s) spatially correspond to the major ore-hosting intrusions Y1 and northwest of Y2 (Figure 8), while high velocities (2.7–3.3 km/s) are present in Y3 and southeast of Y2, which extends vertically to ~0.6 km depth (Figure 8). Another major feature is a low-velocity zone (LVZ) of 1.5–2 km width beneath Y2 and Y3 at a depth of 0.7–1.3 km (Figure 8). In this depth range, we also find

high-velocity zones (HVZs) in the northernmost and the southernmost sections of the study area at a depth of 0.7–1.3 km.

Depth cross-sections of the velocity structure are shown in Figure 9. The high-velocity anomalies (3.25–3.6 km/s) mentioned above are observed on sections A–A', B–B', and C–C'. The high-velocity anomalies are thinner in the middle of the section and thicker on both sides (Figure 9). In sections A–A' to C–C', the LVZs, locating in the middle of the mine, gradually expand horizontally from northeast to southwest and vertically expand from 1.0–1.3 km to 0.7–1.3 km. Additionally, a thin high-velocity anomaly, also located in the middle of the mine, is proximal to the LVZ beneath Y2 and Y3 at section B–B' (Figure 9). Profiles D–D', E–E', and F–F' in Figure 9 intersect Y1, Y2, and Y3, respectively. The HVZ beneath Y1 in D–D' is much thicker than the zone beneath Y2 in E–E', and the HVZ beneath Y3 in F–F' is estimated to be the thinnest among those proximal to Y3, Y2, and Y1 (Figure 9).

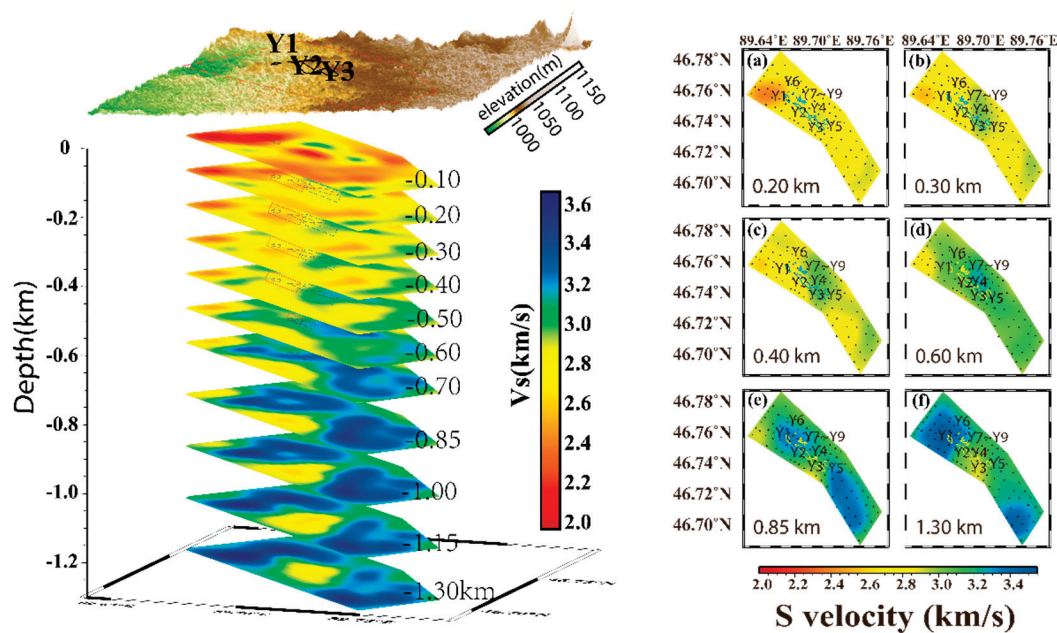


Figure 8. Left panel shows 3D shear wave velocity slices at the depth of 0.1, 0.2, 0.3, 0.4, 0.5, 0.6, 0.7, 0.85, 1.0, 1.15 and 1.30 km, respectively. Black lines at the left top panel of topographic pattern and black dotted lines at 0.1–0.7 km in the lower panel all show ore hosting intrusions. Red solid rectangles represent LVZs at Y1 and northwest of Y2. Blue dotted rectangles indicate HVZs southeast of Y2 and Y3. Right panel represents horizontal slices of shear wave velocity in the mine at the depth of 0.2, 0.3, 0.4, 0.6, 0.85 and 1.3 km (a–f). Areas circled by blue lines on the upper panel and yellow lines on the bottom panel are the ore-hosting intrusions Y1~Y9 in Karatungk mine.

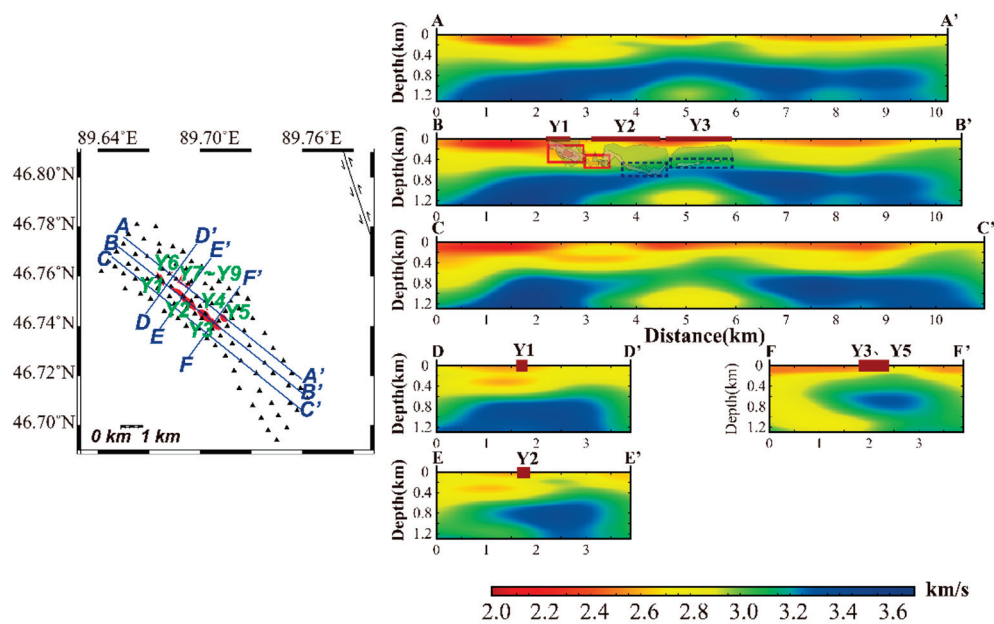


Figure 9. Vertical profiles of shear wave velocity and distribution of ore-body intrusions. Left: Surface distribution of ore-hosting intrusions and location of the profiles. Black triangles are station of KMA. Red areas are ore-hosting intrusions Y1–Y9 with names labeled in green. Along profile in B–B', D–D', E–E' and F–F' ore hosting intrusions are marked at the surface. Along B–B' the transparent zones with black lines are ore hosting intrusions with different mineralization [5]. Red solid rectangles along B–B' represent LVZs at Y1 and northwest of Y2, which have highest degree of mineralization. Blue dotted rectangles include HVZs southeast of Y2 and Y3, which have lower degree of mineralization.

4. Discussion

In this paper, we applied the ANT to the dense passive-source array data to image a mining area in northeastern Xinjiang, China. We found clear velocity heterogeneities in the study area that spatially coincide with the major ore-hosting intrusions. We attempt to interpret their geological meaning here (Figures 8 and 9). In the following section, we discuss the structure at depths 0–0.7 km and 0.7–1.3 km, respectively. The velocity structure is considered to be in two sections as the major ore-hosting intrusions are suggested by borehole observations to be distributed at 0–0.7 km depth [5,10] where the model errors are also considerably small (Figure S6). The deeper part (0.7–1.3 km), were considered as the source regions of these ore-hosting intrusions [36].

4.1. Seismic Structure within 0.7 km and Y1, Y2, Y3

The major pattern of the seismic structure at Karatungk Mine within 0.7 km is that three main ore-hosting intrusions present different velocity features (Figures 8 and 9). Y1 and northwest of Y2 present relatively LVZs (<2.55 km/s) at the depth of 0–0.5 km. Y3 and southeast of Y2 present HVZs (2.7–3.3 km/s) at a depth of 0–0.6 km. Horizontal checkerboard tests show that horizontal resolution of our measurements may reach ~1.0 km, indicating that Y1 and Y2 are distinguishable from each other. We performed vertical synthetic model tests by setting six velocity anomalies with different thickness in depth (Figure S7), each of which has the same distribution of synthetic anomalies, and its depth range is equal to the thickness of the anomalies. Vertical recoveries of tests (Figure S7) suggest that a depth resolution of 0.1 km in the region shallower than 0.4 km may be reasonably recovered, i.e., the tests in Figure S7 show that even vertical smearing of ~0.1 km may occur, the centers of the anomalies are well recovered at correct depths. This confirms the reliability of the LVZs distributed at Y1 and northwest of Y2 at depths of 0–0.5 km, and HVZs at southeast of Y2 and Y3 at depths of 0–0.6 km. We focus on the velocity features of Y1–Y3 here since imaging has limited resolutions near Y4–Y9 (Figure 1) and

most published works of Karatungk Mine relate to Y1–Y3. Figure S6 further illustrates that these three features are in very small model error regions (<1.0%).

Factors contributing to the velocity features nature of the feature Y1–Y3 mentioned above include lithology, water content, and degree of mineralization for the ore-hosting intrusions. The observed lithologies of Y1 are biotite gabbro, amphibolite, hyperite, and diabase gabbro; Y2 are bojite, norite, and gabbro; and Y3 are gabbro-diorite, bojite, and amphibolite [5]. Overall there is little difference in lithology compositions that would differentiate these bodies in velocity structure. According to lithology and composition, the ore-hosting intrusions comprise multiple hydrous minerals, which indicate early magma intrusion was relatively hydrous [37]. Considering that the hydrous minerals evolve under the same tectonic conditions, we reasonably deduce that water is not a predominant discriminating factor. According to previous geological studies and borehole data, the mineralization of three major ore-hosting intrusions indicates that Y1 and northwestern part of Y2 are strongly mineralized, while the southeast of Y2 has a weaker degree of mineralization, and Y3 presents weak mineralization [5]. Previous studies suggest a relationship between mineralization and velocity. For example, [10] suggest that compressional velocity decreases with an increase of mineralization of gabbroic rocks. Additionally, based on the results of borehole petrophysics experiments at Voisey's Bay Cu-Ni sulfide mine from [38], the highly-mineralized sulfide shows higher density but lower seismic wave velocity compared with the host rocks. Other studies, while not specifically describing Cu-Ni mineralization, do investigate similar styles of mineralization and report a similar relationship between sulfidation and velocity [39,40]. To summarize, the rock composition and water content of three ore-hosting intrusions show few differences. As levels of mineralization are consistent with changes in velocity features in our study, we speculate the spatial variations of the shear-wave velocity may be mainly related to the distribution of mineralization.

4.2. Seismic Structure at the Depth of 0.7–1.3 km

The major feature at the depths of 0.7–1.3 km is an LVZ of approximate width 1.5–2 km beneath Y2 and Y3 (Figure 8). Resolution tests show that our dataset can retrieve structures of similar size at the depth (Figure S3), although these structures are located in relatively large model error regions (up to 2%; Figure S6). We propose three candidates for the origin. First, we speculate that the LVZ beneath Y2 and Y3 may be the possible channel for initial magma transport. A continuous supply for magma suggests that the older host rocks of this area would cool earlier than the intrusions, and possibly exhibit higher velocities. The second speculation is inspired by the drilling data obtained from beneath Y3 and Y5, which show that siliceous rocks and a fragmentation zone exist at depths >1.1 km [10]. From results at 0–0.6 km depth, the tuff and weakly mineralized intrusive rocks would be indistinguishable in terms of shear-wave velocity. With the support of borehole data, we further realize that LVZ beneath Y2 and Y3 at the depth of 0.7–1.3 km may also correspond to the strata observed in the mine, of which are predominantly carbonaceous tuff, argillaceous tuff, and coarse-grained tuff. Since we do not have enough constraints for fault distribution in the mine, we are unable to correlate this velocity feature to a possible fragmentation zone beneath Y2 and Y3 without further drilling data. The last speculation is that the relative LVZ near the intrusive rocks might indicate a possible mineralized area according to the arguments presented in Section 4.1 linking mineralization and lower velocities [10,38].

We find HVZs in the northernmost and the southernmost sections of the study area at a depth of 0.7–1.3 km. Prior investigations of ore-hosting lithology in the mine indicate that main intrusive rocks are gabbro and hyperite of the middle-late Hercynian age. Laboratory measurements suggest that less mineralized gabbro has a higher velocity [9]. Thus we suggest that HVZs may be connected with un-mineralized intrusive rocks (e.g., gabbro, peridotite and gabbro-diorite) resulting from early magma intrusion.

4.3. Passive Observations Based on a Dense Array

This study demonstrates a new application of ANT to a dense array in a mine, trying to provide a general connection between seismic velocity, the seismic images and Cu-Ni sulfide orebodies. This relationship contributes to a better understanding of the shallow mineralization processes beneath Karatungk Mine. The major limitation of this study is the resolution of tomographic imaging. Resolution, however, can be improved by increasing the number of seismometers and reducing the station spacing.

Firstly, to demonstrate that increasing the number of stations can effectively improve the resolution of inversion results in the case of a specific study area, we used a jackknife-style resampling approach [41] to artificially select 50%, 70%, and 90% of stations from the original 100 stations. Then, we used dispersion curves corresponding to the selected stations for horizontal resolution tests. Theoretical model and inversion parameters used in the test are the same as those in Section 3.1. Figure 10 shows the comparison of resolution tests corresponding to different numbers of stations (50, 70, and 90) and various depths (0.1 km, 0.5 km, and 0.85 km) to the original data (100 stations). It is clear that for a grid size of $0.1^\circ \times 0.14^\circ$, using only 50 stations results in difficulties in recovering the input model for most regions. By increasing the number of stations, recovery of the input model at depths of 0.1, 0.5, and 0.85 km are improved systematically. When the number of samples reaches 90, the resolution tests show similar recovery of that from the original dataset (100 stations). This shows that under these conditions, increasing the number of ray paths, by deploying more stations, can improve the resolution to a certain degree.

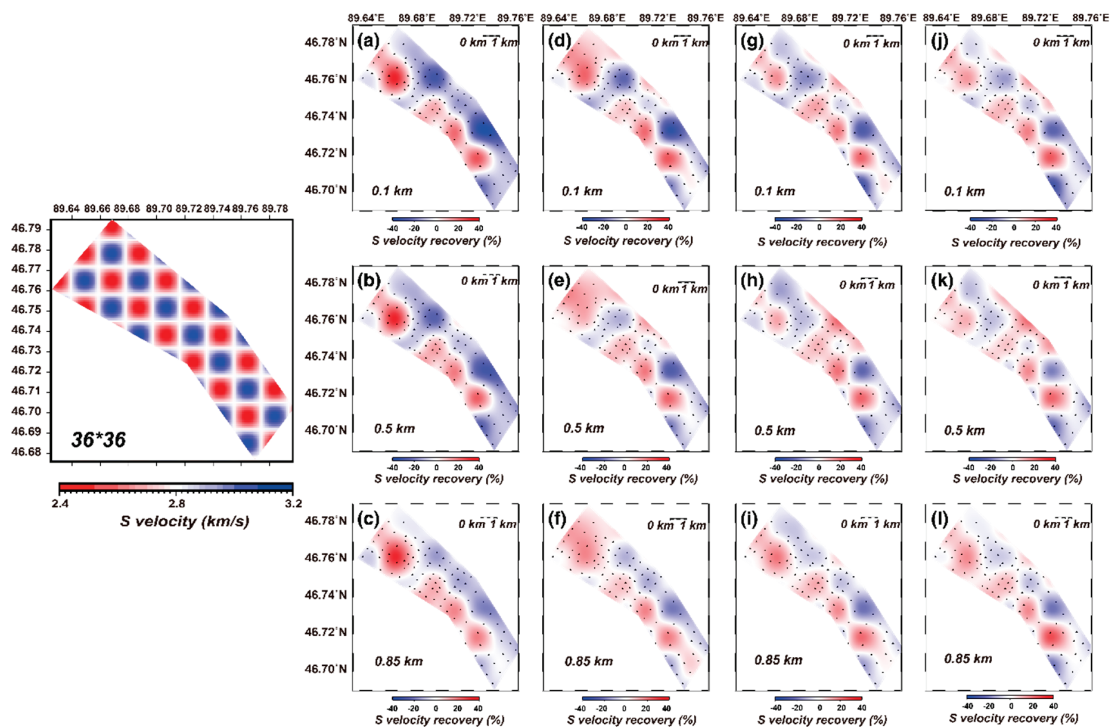


Figure 10. Horizontal resolution tests of numbers of stations. The left panel shows the synthetic model. (a–c) the model recoveries with 50 stations at depth of 0.1, 0.5 and 0.85 km in order. (d–f) the model recoveries with 70 stations at depth of 0.1, 0.5 and 0.85 km in order. (g–i) the model recoveries with 90 stations at depth of 0.1, 0.5 and 0.85 km in order. (j–l) the model recoveries with 100 stations at depth of 0.1, 0.5 and 0.85 km in order.

4.4. Potential of Seismic Observations in Deep Prospecting Work

Another major difficulty in this study, and indeed in many mining locations, is the complex structure of the ore bodies. The uneven mineralization distribution of ore-hosting intrusions and the different degrees of mineralization can result in various velocity characteristics. Thus, determining the distribution of Cu-Ni sulfide orebodies is not easily obtained by seismic imaging alone. Indeed, some geological control from direct observation or sampling will always be required to support interpretation of mineralized zones from geophysics. Furthermore, in Karatungk Mine, magnetic and gravity anomalies have a consistent surface correlation with the ore bodies (Y1 to Y9) inferred from earlier multi-disciplinary studies [5] (Figure 11a,b). These geophysical datasets, however, do not distinguish the orebodies' depth distribution, and mineralization extent of orebodies so far depends on more expensive surface and in-tunnel drilling data (Figure 11c). With limited spatial resolution, the seismic model here seems to favor a positive correlation between the two highly mineralized regions beneath Y1 and Y2 (red open blocks in Figure 11c) and the shallowing trending slow velocity (Figure 11d), and between the low mineralized regions beneath Y2 and Y3 (blue dashed open blocks) and the high velocities towards the bottom of the orebodies (Figure 11c,d). We conclude that complementary to expensive direct observation and sampling, less expensive reconnaissance surveys as described here can mitigate the risk of drilling activities. In the future, we may better solve this issue with the help of multiple geophysical observations; however, this technique demonstrates a feasible reconnaissance method that can provide useful initial images to better guide more expensive and invasive mineral exploration methods.

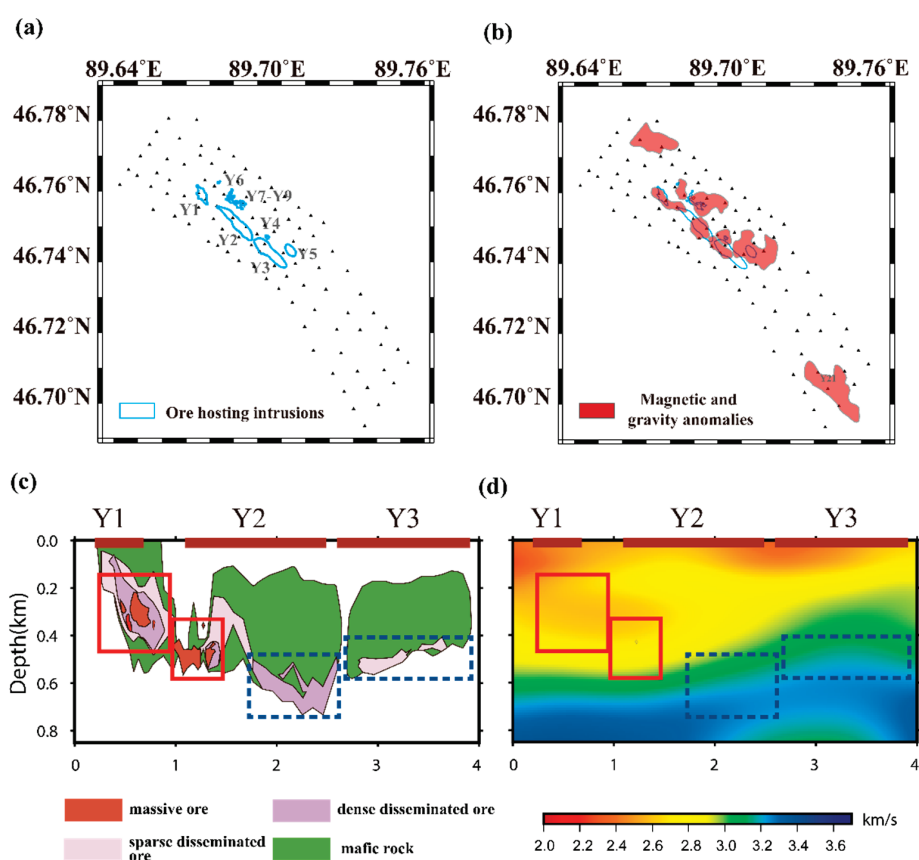


Figure 11. Potential of geophysical models in aiding deep prospecting work. (a) Surface distribution of orebodies. (b) Magnetic and gravity anomalies from [5]. (c) Locations of intrusions along the NW-SE profile across the three main ore bodies Y1 to Y3. The shapes of the intrusions were determined by drilling data from [5]. Red boxes are highly mineralized intrusions and blue boxes are much less mineralized. (d) Velocity model from ambient noise inversion.

5. Conclusions

We have demonstrated a technique to recover a shallow crustal shear-wave velocity structure beneath Karatungk Mine, Junggar Basin, using ANT based on KMA. We observe that low-velocity heterogeneities are mainly distributed near the Y1 ore-hosting intrusion and northwest of Y2 within ~0.5 km depth. In addition, high-velocity heterogeneities are mainly located at the southeast of Y2 and Y3 within ~0.7 km depth. We proposed that the spatial variations of the shear-wave velocity may mainly be related to the mineralization of three ore-hosting intrusions, which is supported by other studies and qualitative reasoning. We also observe that low velocities beneath Y2 and Y3 at depths of 0.7–1.3 km. We interpret that these low-velocity zones may indicate the presence of magmatic conduits, mine strata or mineralized regions. High-velocity anomalies displayed in the northernmost and southernmost sections of the mine at depths of 0.7–1.3 km are interpreted to relate to the intrusions of gabbro, peridotite, and gabbro-d diabase resulting from the early magmatism.

Our study demonstrates an applicable technique for using passive seismic imaging at the mine-scale for the first time, which can then help us to better understand the shallow structure of Karatungk Mine, and mining environments in general. ANT method using a dense array is shown to be a potentially efficient way to reveal detailed structure in mine areas. In this example, ore-hosting intrusions within 0.7 km in depth have been well-constrained and supported by borehole data observations. However, variable spatial distribution of mineralization and complex ore-body geometry can cause difficulties in determining the exact location of Cu-Ni sulfide orebodies. In addition, the spatial resolution of the results is still too low to solve the geometry of all Cu-Ni sulfide orebodies. However, we successfully demonstrate that a denser ANT array will obtain more detailed structure in the area.

Supplementary Materials: The following are available online at <http://www.mdpi.com/2075-163X/10/7/601/s1>, Section S1: Beamforming of Cross-Correlation Functions; Section S2: Resolution, Robustness Tests and Model Error Estimates; Figure S1: Distribution of ambient noise sources along different azimuths and slowness; Figure S2: Results of fundamental mode Rayleigh wave dispersion measurement; Figure S3: Starting 1D velocity model (red), which is also used for depth kernel computation; Figure S4: Horizontal resolution tests; Figure S5: Model comparison between models without (left) and with bootstrap approach (right); Figure S6: Same as the cross-sections in Figure 9 but for approximated model errors using the bootstrap procedure; Figure S7: Vertical synthetic model tests.

Author Contributions: Conceptualization, J.W., C.H., J.W., L.Z., and W.X.; methodology, P.D., J.W., and H.Y.; software, P.D.; data curation, P.D., J.W., Y.L., J.W., and C.H.; writing—original draft preparation, P.D. and J.W.; writing—review and editing, J.W., Y.L., M.D.L., H.Y., and L.Z.; supervision, J.W.; and project administration, J.W., L.Z., and W.X. All authors have read and agreed to the published version of the manuscript.

Funding: This research was funded by the National Key R&D Programs of China (Grant No.2017YFC0601206 and Grant No.2017YFC1500302), National Natural Science Foundation of China (Grant No.41574055), State Key Laboratory of Lithospheric Evolution, Institute of Geology and Geophysics, Chinese Academy of Sciences (Grant No.11731210).

Acknowledgments: Zhengfu Guo, Kezhang Qin, Yibo Wang and Dongmei Tang from the Institute of Geology and Geophysics and the Chinese Academy of Sciences, and Nishida Kiwamu from the Earthquake Research Institute, Tokyo University, provided great supports for this study. Thanks to Zhihai Li, Xiaomei Liu, Jujing Li, Shaojiang Wu, and Xianzhen Chen for their help in the field work. Group members of Crustal and Mantle Structure from State Key Laboratory of Lithospheric Evolution helped a lot on this study. Support from the Computer Simulation Lab, Institute of Geology and Geophysics, and the Chinese Academy of Sciences is appreciated. The figures are produced by GMT [42]. Mark Lindsay acknowledges the support from ARC DECRA Scheme project number DE190100431. HY acknowledges partial support from NSFC programs 91955210, 41625016 and CAS program GJHZ1776. This is Contribution 1514 from the ARC Centre of Excellence for Core to Crust Fluid Systems (<http://www.cfs.mq.edu.au>).

Conflicts of Interest: The authors declare no conflict of interest.

References

1. Han, C.; Xiao, W.; Zhao, G.; Qu, W.; Mao, Q.; Du, A. Re-Os isotopic analysis of the Kalatongke Cu-Ni Sulfide Deposit, Northern Xinjiang, NW China, and its geological implication. *Acta Petrol. Sin.* **2006**, *22*, 163–170. (In Chinese with English abstract)

2. Wang, J. The Minerogenesis and Metallogenic Potential of Kalatongke Nickel -Copper Sulfide Deposit, Xinjiang, China. Ph.D. Thesis, Chang'an University, Xi'an, China, 2010. (In Chinese with English abstract)
3. Wan, B.; Xiao, W.; Windley, B.F.; Yuan, C. Permian hornblende gabbros in the Chinese Altai from a subduction-related hydrous parent magma, not from the Tarim mantle plume. *Lithosphere* **2013**, *5*, 290–299. [[CrossRef](#)]
4. Gong, Y.; Wang, Y.; Wang, B. Exploration on resource prediction in karatungk Cu-Ni metallogenic belt. *Xinjiang Nonferrous Met.* **2005**, *A2*, 32–35. (In Chinese with English abstract)
5. Qin, K.; Tian, Y.; Yao, Z.; Wang, Y.; Mao, Y.; Wang, B.; Xue, S.; Tang, D.; Kang, Z. Metallogenic conditions, magma conduit and exploration potential of the kalatongk Cu-Ni orefield in Northern Xinjiang. *Geol. China* **2014**, *41*, 912–935. (In Chinese with English abstract)
6. Han, C.; Wenjiao, X.; Guochun, Z.; Wenjun, Q.; Andao, D. Re–Os dating of the Kalatongke Cu–Ni deposit, Altay Shan, NW China, and resulting geodynamic implications. *Ore Geol. Rev.* **2007**, *32*, 452–468. [[CrossRef](#)]
7. Ferguson, I.J.; Young, J.B.; Cook, B.J.; Krakowka, A.B.C.; Tycholiz, C. Near-surface geophysical surveys at the Duport gold deposit, Ontario, Canada: Relating airborne responses to small-scale geologic features. *Interpretation* **2016**, *4*, SH39–SH60. [[CrossRef](#)]
8. Malehmir, A.; Juhlin, C.; Wijns, C.; Urosevic, M.; Valasti, P.; Koivisto, E. 3D reflection seismic imaging for open-pit mine planning and deep exploration in the Kevitsa Ni-Cu-PGE deposit, northern Finland. *Geophysics* **2012**, *77*, 95–108. [[CrossRef](#)]
9. Tong, T.; Hu, X.; Liu, J. Study of Metallogenic Forecast and Geophysical Characteristics in Copper-nickel Mine of Kalatongke. *West-China Explor. Eng.* **2004**, *9*, 105–106. (In Chinese with English abstract)
10. Zhou, J.; Xu, M.; Liu, J.; Gao, J.; Wang, X.; Zhang, B. Application of seismic reflection imaging in the Karatungk Cu-Ni deposit of Xinjiang. *Geol. Explor.* **2016**, *52*, 0910–0917. (In Chinese with English abstract)
11. Lin, F.-C.; Ritzwoller, M.H.; Snieder, R. Eikonal tomography: Surface wave tomography by phase front tracking across a regional broad-band seismic array. *Geophys. J. Int.* **2009**, *177*, 1091–1110. [[CrossRef](#)]
12. Wang, Y.; Allam, A.; Lin, F.-C. Imaging the Fault Damage Zone of the San Jacinto Fault Near Anza With Ambient Noise Tomography Using a Dense Nodal Array. *Geophys. Res. Lett.* **2019**, *46*, 12938–12948. [[CrossRef](#)]
13. Lin, F.-C.; Li, D.; Clayton, R.W.; Hollis, D. High-resolution 3D shallow crustal structure in Long Beach, California: Application of ambient noise tomography on a dense seismic array. *Geophysics* **2013**, *78*, Q45–Q56. [[CrossRef](#)]
14. Sabra, K.G.; Gerstoft, P.; Roux, P.; Kuperman, W.A.; Fehler, M.C. Extracting time-domain Green's function estimates from ambient seismic noise. *Geophys. Res. Lett.* **2005**, *32*, L03310. [[CrossRef](#)]
15. Shapiro, N.M.; Campillo, M.; Stehly, L.; Ritzwoller, M.H. High-Resolution Surface-Wave Tomography from Ambient Seismic Noise. *Science* **2005**, *307*, 1615–1618. [[CrossRef](#)] [[PubMed](#)]
16. Yao, H.; Hilst, R.D.V.D.; Hoop, M.V.D. Surface-wave array tomography in SE Tibet from ambient seismic noise and two-station analysis—I. Phase velocity maps. *Geophys. J. Int.* **2006**, *166*, 732–744. [[CrossRef](#)]
17. Lin, F.-C.; Moschetti, M.P.; Ritzwoller, M.H. Surface wave tomography of the western United States from ambient seismic noise: Rayleigh and Love wave phase velocity maps. *Geophys. J. Int.* **2008**, *173*, 281–298. [[CrossRef](#)]
18. Saygin, E.; Kennett, B.L.N. Crustal structure of Australia from ambient seismic noise tomography. *J. Geophys. Res.* **2012**, *117*. [[CrossRef](#)]
19. Yang, Y.; Ritzwoller, M.H.; Levshin, A.L.; Shapiro, N.M. Ambient noise Rayleigh wave tomography across Europe. *Geophys. J. Int.* **2007**, *168*, 259–274. [[CrossRef](#)]
20. Keifer, I.; Dueker, K.; Chen, P. Ambient Rayleigh wave field imaging of the critical zone in a weathered granite terrane. *Earth Planet. Sci. Lett.* **2019**, *510*, 198–208. [[CrossRef](#)]
21. Roux, P.; Moreau, L.; Lecointre, A.; Hillers, G.; Campillo, M.; Ben-Zion, Y.; Zigone, D.; Vernon, F. A methodological approach towards high-resolution surface wave imaging of the San Jacinto Fault Zone using ambient-noise recordings at a spatially dense array. *Geophys. J. Int.* **2016**, *206*, 980–992. [[CrossRef](#)]
22. Yao, H.; Xu, G.; Zhu, L.; Xiao, X. Mantle structure from inter-station Rayleigh wave dispersion and its tectonic implication in Western China and neighboring regions. *Phys. Earth. Planet. In.* **2005**, *148*, 39–54. [[CrossRef](#)]
23. Yao, H.; Gouédard, P.; Collins, J.; McGuire, J.; van der Hilst, R.D. Structure of young East Pacific Rise lithosphere from ambient noise correlation analysis of fundamental- and higher-mode Scholte-Rayleigh waves. *Comptes Rendus Geosci.* **2011**, *343*, 571–583. [[CrossRef](#)]

24. Fang, H.; Yao, H.; Zhang, H.; Huang, Y.-C.; van der Hilst, R.D. Direct inversion of surface wave dispersion for three-dimensional shallow crustal structure based on ray tracing: Methodology and application. *Geophys. J. Int.* **2015**, *201*, 1251–1263. [[CrossRef](#)]
25. Bensen, G.D.; Ritzwoller, M.H.; Barmin, M.P.; Levshin, A.L.; Lin, F.; Moschetti, M.P.; Shapiro, N.M.; Yang, Y. Processing seismic ambient noise data to obtain reliable broad-band surface wave dispersion measurements. *Geophys. J. Int.* **2007**, *169*, 1239–1260. [[CrossRef](#)]
26. Yao, H.; Beghein, C.; van der Hilst, R.D. Surface wave array tomography in SE Tibet from ambient seismic noise and two-station analysis—II. Crustal and upper-mantle structure. *Geophys. J. Int.* **2008**, *173*, 205–219. [[CrossRef](#)]
27. Luo, Y.; Yang, Y.; Xu, Y.; Xu, H.; Zhao, K.; Wang, K. On the limitations of interstation distances in ambient noise tomography. *Geophys. J. Int.* **2015**, *201*, 652–661. [[CrossRef](#)]
28. Shearer, P.M. *Introduction to Seismology*, 2nd ed.; Cambridge University Press: New York, NY, USA, 2009.
29. Laske, G.; Masters, G.; Ma, Z.; Pasyanos, M. Update on CRUST1.0—A 1-degree global model of Earth’s crust. *Geophys. Res. Abstr.* **2013**, *15*, 2658.
30. Herrmann, R.B. *An Overview of Synthetic Seismogram Computation, Computer Programs in Seismology*; Saint Louis University: Baguio, Benguet, 2002.
31. Shapiro, N.M.; Ritzwoller, M.H. Monte-Carlo inversion for a global shear-velocity model of the crust and upper mantle. *Geophys. J. Int.* **2002**, *151*, 88–105. [[CrossRef](#)]
32. Rawlinson, N.; Sambridge, M. Wave front evolution in strongly heterogeneous layered media using the fast marching method. *Geophys. J. Int.* **2004**, *156*, 631–647. [[CrossRef](#)]
33. Liu, Y.; Zhang, H.; Fang, H.; Yao, H.; Gao, J. Ambient noise tomography of three-dimensional near-surface shear-wave velocity structure around the hydraulic fracturing site using surface microseismic monitoring array. *J. Appl. Geophys.* **2018**, *159*, 209–217. [[CrossRef](#)]
34. Efron, B.; Tibshirani, R. Bootstrap methods for standard errors, confidence intervals, and other measures of statistical accuracy. *Stat. Sci.* **1986**, *1*, 54–77. [[CrossRef](#)]
35. Li, T.; Zhao, L.; Wan, B.; Li, Z.X.; Bodin, T.; Wang, K.; Yuan, H. New crustal Vs model along an array in south-east China: Seismic characters and paleo-Tethys continental amalgamation. *Geochem. Geophys. Geosyst.* **2020**, *21*, e2020GC009024. [[CrossRef](#)]
36. Zhou, J. The application of seismic method in deep prospecting—take the case of the Cu-Ni deposit in Karatungk of Xinjiang Province. Ph.D. Thesis, China University of Geosciences, Wuhan, China, 2017. (In Chinese with English abstract)
37. Chai, F. Comparison on Petrologic Geochemistry of Three Mafic-ultramafic intrusions Associated with Ni-Cu Sulfide Deposits in Northern Xinjiang. Ph.D. Thesis, China University of Geosciences, Wuhan, China, 2006. (In Chinese with English abstract)
38. Duff, D.; Hurich, C.; Deemer, S. Seismic properties of the Voisey’s Bay massive sulfide deposit: Insights into approaches to seismic imaging. *Geophysics* **2012**, *77*, 59–68. [[CrossRef](#)]
39. Shetselaar, E.; Bellefleur, G.; Craven, J.; Roots, E.; Cheraghi, S.; Shamsipour, P.; Caté, A.; Mercier-Langevin, P.; El Goumi, N.; Enkin, R.; et al. *Geologically Driven 3D Modelling of Physical Rock Properties in Support of Interpreting the Seismic Response of the Lalor Volcanogenic Massive Sulphide Deposit, Snow Lake, Manitoba, Canada*; Geological Society: London, UK, 2017; Volume 453.
40. Dentith, M.; Enkin, R.J.; Morris, W.; Adams, C.; Bourne, B. Petrophysics and mineral exploration: A workflow for data analysis and a new interpretation framework. *Geophys. Prospect.* **2020**, *68*, 178–199.
41. Efron, B. Bootstrap Methods: Another Look at the Jackknife. *Ann. Stat.* **1979**, *7*, 1–26. [[CrossRef](#)]
42. Wessel, P.; Smith, W.H.F.; Scharroo, R.; Luis, J.; Wobbe, F. Generic Mapping Tools: Improved Version Released. *Eos Trans. Am. Geophys. Union* **2013**, *94*, 409–410. [[CrossRef](#)]



© 2020 by the authors. Licensee MDPI, Basel, Switzerland. This article is an open access article distributed under the terms and conditions of the Creative Commons Attribution (CC BY) license (<http://creativecommons.org/licenses/by/4.0/>).

Article

Mapping New IOCG Mineral Systems in Brazil: The Vale do Curaçá and Riacho do Pontal Copper Districts

Sérgio Roberto Bacelar Hühn ^{1,*}, Adalene Moreira Silva ², Francisco José Fonseca Ferreira ³ 
and Carla Braitenberg ⁴ 

¹ Department of Geology, Universidade Federal do Ceará-UFC-Campus do PICI, Fortaleza 60440-554, Brazil

² Instituto de Geociências, Universidade de Brasília, Brasília 70910-900, Brazil; adalene@unb.br

³ Laboratório de Geofísica Aplicada, Universidade Federal do Paraná, Curitiba 81531-980, Brazil; francisco.ferreira@ufpr.br

⁴ Department of Mathematics and Geosciences, University of Trieste, 34149 Trieste, Italy; berg@units.it

* Correspondence: sergio.bacelar@ufc.br

Received: 5 September 2020; Accepted: 24 November 2020; Published: 30 November 2020



Abstract: The Vale do Curaçá and Riacho do Pontal copper districts are located within the northern part of the Archaean São Francisco Craton and represent two pulses of mineralization. The copper districts have been identified as Iron-Oxide-Copper-Gold (IOCG) classes of deposits. An older metallogenic event associated with the Caraíba copper deposit, which is located in the Vale do Curaçá district, is related to Palaeoproterozoic (ca. 2 to 2.2 Ga) hydrothermal processes. A younger Neoproterozoic (ca. 750 to 570 Ma) episode of volcanism and associated plutonism is represented by the Riacho do Pontal mineral district. Seismic tomography data from across east-central Brazil show that the multiage Carajás province and Vale do Curaçá and Riacho do Pontal copper districts sit along either side of a prominent NW-trending upper lithospheric high-velocity zone. The edges of the high-velocity zone point to long-lived subparallel transcrustal structures that have been the focus of multiple reactivations and copper mineralization events. Regional gravity and magnetic maps show that the Vale do Curaçá copper district extends over an area greater than 110 km by 22 km. The magnetic and gravity values show significant variations correlated with this area. The district includes high gravity values associated with the Caraíba copper mine (>-35 mGal), which has a greater density (3.13 g/cm³) than the nonmineralized host rock density (2.98 g/cm³). The gravity anomaly signature over the Riacho do Pontal copper district is characterized by a 40-km long NW–SE trending Bouguer gravity low. The occurrences of the Riacho do Pontal copper district are situated in these regional low-gravity domains. Data from regional airborne magnetic and ground gravity surveys were inverted to obtain a 3D magnetic susceptibility and density model, respectively, for the known districts. The results show that the Caraíba deposit is characterized by a both dense and magnetic source showing structural control by thrust shear zones. The 2D and 3D geological models show two main NNW prospective trends. Trends I and II have a sigmoidal shear shape and are positioned in the contact zone between domains with high magnetic susceptibility ($SI > 0.005$) and density > 0 g/cm³). Trend I is 40 km \times 10 km in size and hosts the Caraíba, Surubim, and Vermelho copper mines and other minor deposits. The results obtained from the 3D magnetic inversion model for the region of the Riacho do Pontal district show weak magnetic anomaly highs extending along a NW–SE magnetic gradient trend. The gradient is related to mapped shear zones that overprint older and deeper NE–SW features of the São Francisco cratonic root. The area includes high gravity values associated with the Caraíba copper deposit, which has a greater density (3.13 g/cm³) than the nonmineralized host rock density (2.4 g/cm³).

Keywords: 3D data integration; IOCG; Palaeoproterozoic; gravimetric and magnetic inversion; Riacho do Pontal; Brazil

1. Introduction

World-class IOCG (Iron Oxide Copper-Gold) deposits express their metallogenic footprint in different tectonic settings through variable volumes of associated alteration and metal endowments, which can be geophysically sensed [1–4]. IOCG mineralization is often controlled by shear system zones and involves high concentrations of magnetite and/or hematite. Magnetic and gravity signatures related to magnetite- and hematite-rich copper ore zones have led the mining community and other researchers to use these data as an effective exploration tool to find new IOCG deposits [5–8]. Frequently, the geometry and structural control of mineralized trends are related to secondary structures and transtensional sites [9–11]. The orebodies are structurally controlled by stretching lineations associated with the shear zone. These important geologic features of IOCG mineralization are often expressed in physical property changes related to density, magnetization, and seismic velocities at a wide range of scales [1,5,10].

Geologic characteristics of the world-class Carajás IOCG deposits are distinct and show a complex interplay between geologic structures, fluid flows, and forms of hydrothermal alteration [12–24]. For example, the flow of mineralized fluids along regional shear zones is responsible for the “sigmoidal-shape” structural pattern and magnetic signature of the Carajás province and Vale do Curaçá district [6,14,20,25].

The Vale do Curaçá and Riacho do Pontal copper districts host copper as the primary commodity along with Au, Fe, and Cr and other metals [26,27]. Early studies characterized the copper deposits as magmatic. According to Lindenmayer et al. [13,14], mineralization is exclusively hosted in orthopyroxenite. High concentrations of sulfides, however, can also occur in norite- and biotite-rich shear rocks and in calcsilicate rocks. Recently, new geologic [24,26–29], tectonic [26,30], isotopic, and geochemical [27] studies have shown evidence that copper mineralization is related to the diverse family of IOCG deposits. In the last 10 years, high-resolution airborne geophysical surveys have been completed. This geophysical effort has motivated new exploratory campaigns in both districts. However, despite an increase in modern airborne geophysical coverage and geologic mapping, the rate of the discovery and identification of new IOCG deposits remains low. This low discovery rate is partly due to the absence of a modern mineral systems approach followed by a systematic exploration program that involves higher density exploration drilling. Additional challenges exist because shallower deposits have been discovered, and presently, major efforts are focused on deeper exploration below different types of cover. Outcrop deposits have already been discovered. The new targets are located deeper within and/or below the cover.

Both the Vale do Curaçá and the Riacho do Pontal copper districts can be considered among the most important areas for IOCG prospectivity in Brazil [24,26,27]. Globally, IOCG deposits are a significant source of base and precious metals, which is key to supporting and expanding economic growth. In particular, the Vale do Curaçá copper district, which occupies an area of approximately 2000 km², is one of the most significant mining districts in Brazil, having produced 30 kt of copper in 2018. Approximately 300 copper occurrences and prospects have been mapped. The district includes a total of 42.4 Mt @ 1.71% copper [30–32]. The most productive copper deposits in the Vale do Curaçá are Caraíba-Pilar (24.8 Mt @ 1.9% copper), Vermelhos (4.52 Mt @ 3.4% copper, underground) and Surubim (4.5 Mt @ 1.04% copper) [32].

Despite these important metal endowments, there is a lack of knowledge that would provide broad insight into how the deposits formed and concerning the larger mineral systems that were active during their emplacement. A previous study [24] used multiparameter geologic and geochemical remote sensing and airborne geophysical data to statistically identify new areas of IOCG prospectivity

related to shallow mineralization along the northern border of the São Francisco Craton (Figure 1). Areas of known mineralization and targets of new prospectivity were identified in a previous data integration study [24]. The study presented here expands on this previous work in three different ways. First, magnetic and gravity maps are interpreted in concert with new geologic information to map deep crustal and lithospheric controls on copper mineralization. Second, regional magnetic and gravity data are inverted to obtain 3D models of magnetic susceptibility and density, respectively, to understand the concealed geology related to physical property distributions and geometries underlying the districts. Third, seismic tomography data are analyzed to place the Vale do Curaçá and Riacho do Pontal IOCG districts within a tectonic and cratonic framework and to characterize potential lithospheric controls of the mineral provinces. Our objective is to use these approaches to obtain an advanced understanding of the mineral system(s) that controlled the emplacement of the NE Brazil IOCG mineral districts.

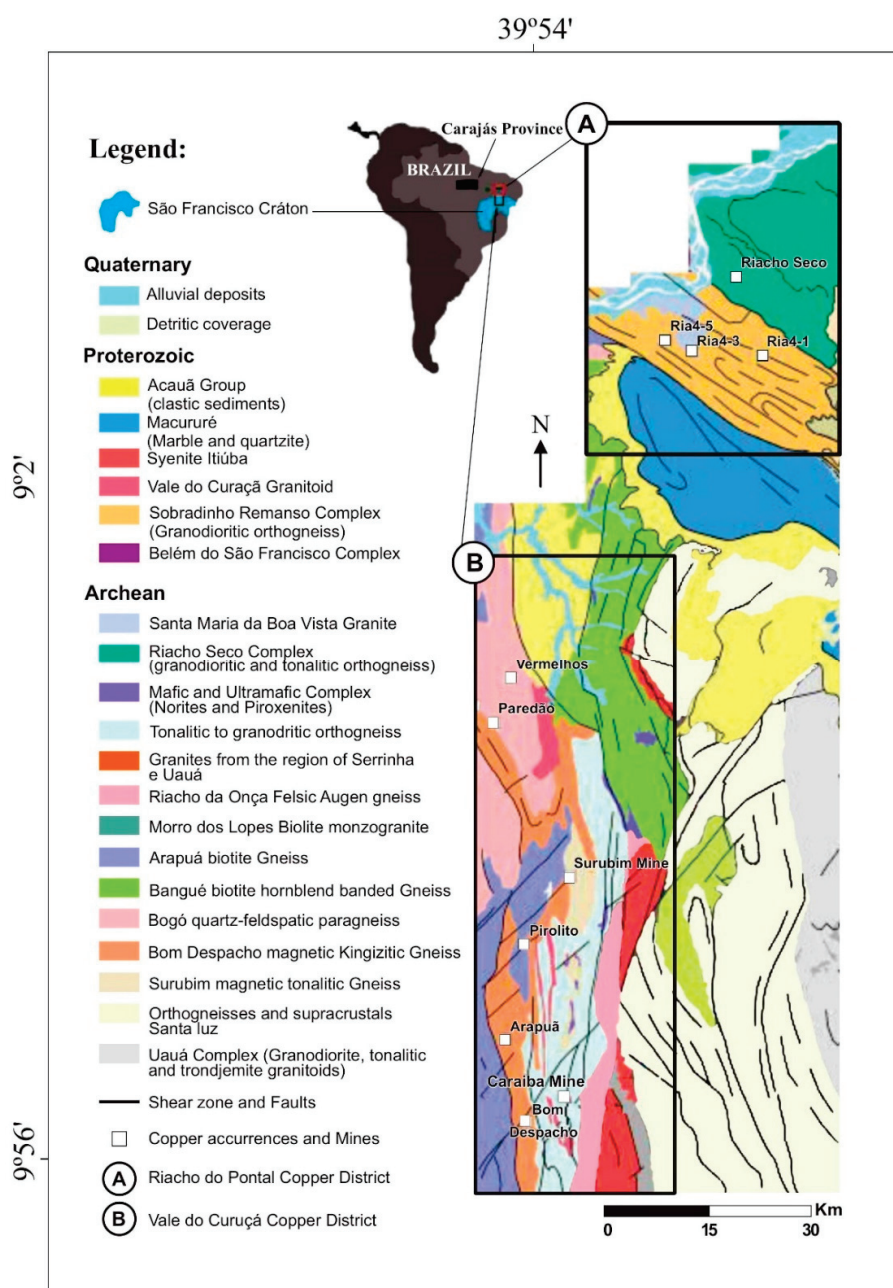


Figure 1. Geologic map showing the study location with (A) the Riacho do Pontal and (B) the Vale do Curaçá copper districts. Major copper mines and occurrences are shown [20,27,31].

Purpose and Scope

The purpose of our study is to synthesize available regional magnetic, gravity, and seismic tomography data with geologic information to evaluate the 2D and 3D geologic and tectonic setting of the Vale do Curaçá and Riacho do Pontal IOCG districts. An overarching goal of our study is to develop a better understanding of the deep crustal and lithospheric structural controls for Palaeoproterozoic and Neoproterozoic mineralization events.

2. Geologic Setting and Mineralization

2.1. Classification as IOCG Deposits

Early studies of the Caraíba copper mine within the Vale do Curaçá district emphasized orthomagmatic processes as responsible for the genesis of copper mineralization [13,14,30]. noted that the unusual aspects of the Caraíba deposit shared similarities with other copper deposits of magmatic origin [33], including (a) the presence of primary sulfides such as bornite and chalcopyrite; (b) the presence of large amounts (>50 wt %) of magnetite; (c) a high Cu/Ni ratio (~40); and (d) orthopyroxenites with abundant biotite related to shear zones. The importance of metasomatic processes in the genesis of the Caraíba deposit was initially suggested by Rocha et al. [34] and more recently confirmed by Teixeira et al. [20], who proposed that copper deposits in the Vale do Curaçá copper district are analogous to other IOCG deposits worldwide.

Early studies fulfilled by several authors [35,36] on the copper deposits in the Riacho do Pontal district show that they were characterized as the volcanogenic massive sulphide (VMS) type. In the region of Riacho Seco. The following criteria have been used to classify copper mineralization in the Riacho do Pontal district as IOCG deposits [24,28]: (a) strong association with potassic and albite alteration; (b) copper ore that is hydrothermal and epigenetic, which is closely associated with shear zones; (c) the presence of hydrothermal iron oxides spatially and temporally related to copper orebodies; (d) mineralization that is not spatially related to proximal granites; and (e) magnetite or hematite (hydrothermal iron > 10%; [7,8]).

2.2. Palaeoproterozoic Vale do Curaçá Copper District

Since the beginning of the last century, the Vale do Curaçá copper district (B in Figure 1) has been the focus of intense geologic mapping and exploration activity. During the 1970s, a mineral exploration boom occurred in this region. The focus of the exploration program was on copper in volcanic-hosted massive sulfide (VMS) mineralization [37,38] in greenstone belts and copper mineralization hosted in mafic-ultramafic layered complexes [14,31,39]. The exploration activities led to the discovery of the Caraíba mine, which is the largest mine in the district. In addition, a series of copper deposits and occurrences in the Vale do Curaçá district were discovered. Approximately 300,000 m of drilling has taken place in the mining district [40].

The geology of the Vale do Curaçá copper district (B in Figure 1) consists mainly of rocks belonging to the Itabuna-Salvador-Curaçá Orogen (ISCO). The ISCO is located east of the Gavião and Jequié blocks and west of the Serrinha block (Figure 2) and represents an 800 km long belt of Archaean to Palaeoproterozoic high metamorphic grade granulitic rocks [20,41]. These rocks were deformed and metamorphosed due to the collision of the Gavião, Jequié, and Serrinha blocks [20,41–43]. The ISCO is a Rhyacian to Orosirian orogenic belt resulting from the collision of Archaean blocks in the range of ca. 2 to 2.2 Ga [26,44]. This was followed by deformation with high metamorphic grade and syntectonic granites [45]. A SHRIMP U/Pb age of 2695 ± 12 Ma was obtained for granulitic rocks of the Caraíba complex [20] and a U/Pb age of 2072 Ma was found for the metamorphic event [45]. The mafic-ultramafic complex should have mafic-ultramafic intrusions of two different ages (2695 Ma and 2580 Ma).

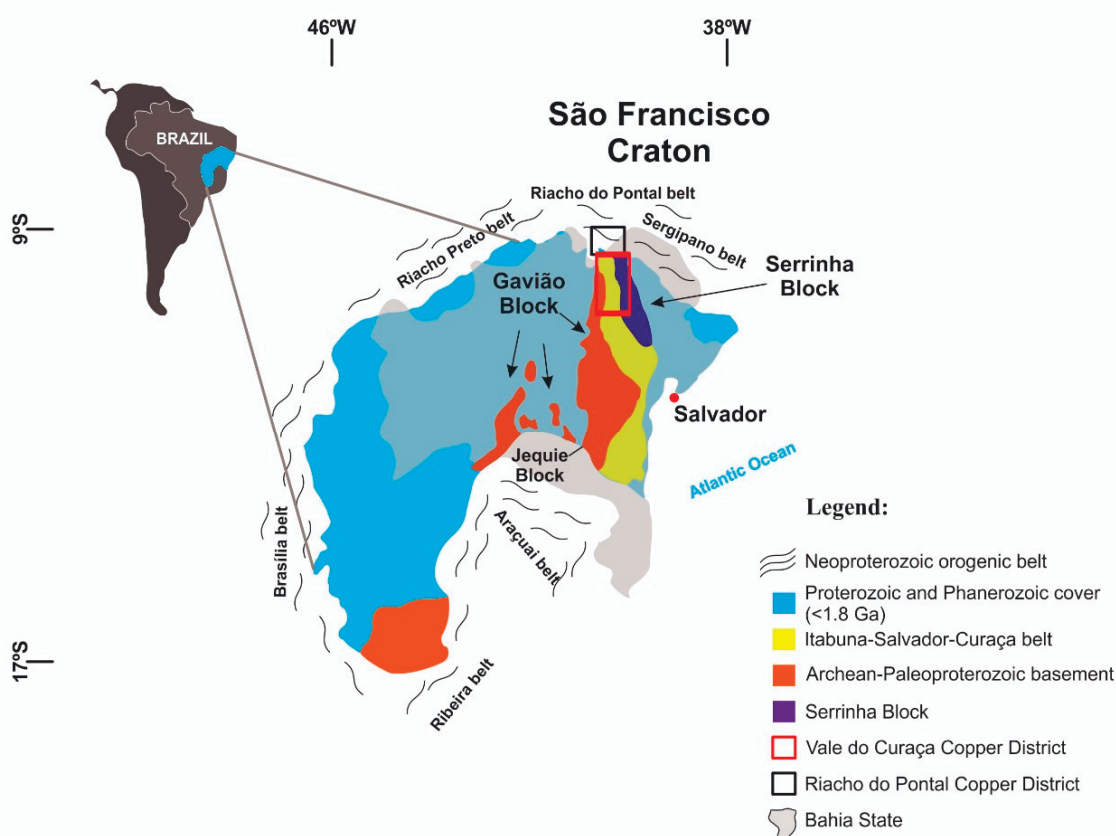


Figure 2. Simplified geologic map of the São Francisco Craton showing the locations of the Riacho do Pontal and Vale do Curaçá copper districts. Both districts are situated on the northern edge of the SFC in contact with Borborema province. (Modified from [26]).

The specific geology of the Curaçá copper district comprises the Tanque Novo and Caraíba complexes. The Tanque Novo complex consists of Bom Despacho, Arapuá, Surubim, and Bogó gneissic rocks [13] composed mainly of feldspathic quartz gneiss, cordierite-garnet-biotite gneiss, amphibolite, and magnetite (quartzite)-rich rocks. The Caraíba complex contains tonalite to granodiorite bodies. A series of mafic-ultramafic bodies individually intruded into the supracrustal rocks. These rocks have undergone episodes of deformation, metamorphism, and related granitic intrusion. The U/Pb SHRIMP ages of ultramafic rocks within the Caraíba mine show that the rocks formed at ca 2580 ± 10 Ma [45]. Field relationships show that the Itiúba syenite is younger than the Medrado gabbro. Importantly, Itiúba syenite is a syn tectonic to shear zone of 2084 ± 9 Ma. This age is also related to copper mineralization situated along shear zones [26,46].

Shear zones have been mapped along the Vale do Curaçá district and are often marked by intense biotite-rich rocks related to mylonitic rocks. These zones are characterized by two phases of progressive deformation [34,46]. (a) The first phase (D1) involved transpressive thrust structures showing convergence to the west. The associated metamorphism occurred in the amphibolite to granulite facies. (b) The D2 phase was related to strike-slip shear zones with N–S isoclinal folds and penetrative vertical shearing structures. Kinematic studies indicate that D1 was overprinted by sinistral strike-slip shear zones [26,47]. These shear zones were responsible for the positioning of mylonitized granites and the intense fluid flux. The shearing process destroyed the preexisting fabric. The foliation of shear zones has a strike of 350° and dips towards SE at 45° to 75° . The main mineralization event in the Vale do Curaçá district occurred between ca 2050 and 2010 Ma [26,29].

Geology of the Caraíba Mine

The geology of the Caraíba mine is well marked by the contact between orthogneiss (G2) and mafic-ultramafic rocks. Frequently, biotite has been mapped along N–S trending geologic contacts. The supracrustal rocks include banded gneiss, diopsidite, forsterite marbles, garnetiferous mafic granulite, biotite-schist, and iron formations [14].

The Caraíba orebody is hosted mainly in mafic-ultramafic complexes [20,34] with recognized hydrothermal calcic-ferric alteration related to copper-ore zones. More recent work shows early (2580 ± 10 Ma; [45]) orthomagmatic mineralization overprinted by a later hydrothermal event that produced IOCG mineralization at ca 2 Ga [20,29,36]. Studies conducted by [46–48] show evidence of structural control at the Caraíba mine.

Ore minerals at Caraíba include chalcopyrite, bornite, and chalcocite, which are usually associated with magnetite. Intercumulus crystals of disseminated chalcopyrite, bornite, and magnetite grown in the interstices of pyroxenes and amphiboles constitute the primary (magmatic) mineralization. Minerals associated with hydrothermal alteration include biotite, microcline, epidote, chlorite, magnetite, and quartz [36]. Ore often occurs as veining or magnetite hydrothermal breccia. Magnetite sometimes occurs in equilibrium with spinel. Frequently, ilmenite exhibits replacement by chalcopyrite, bornite, and magnetite, especially when the host rock is biotite mylonite. Magmatic ilmenite is replaced by ilmenite hydrothermal. The latter IOCG system is richer in copper, highly magnetic, and dense.

2.3. Geology of the Neoproterozoic Riacho do Pontal Copper District

More than twenty copper occurrences have been found in the Riacho do Pontal region (A in Figure 1; [26]). Geologically, these occurrences are mostly located in the contact zone between the Borborema province and the San Francisco craton (Figures 2 and 3). The area includes a small slab of the ca. 750 Ma to 570 Ma Brasiliano collisional zone, which developed during the convergence of Neo- to Mesoproterozoic terrains with the São Francisco craton. Copper occurrences are structurally controlled by shear zones (Figure 1). The Ria4 occurrences and Riacho Seco deposit (Figure 1) are the main copper occurrences in the district. The drill hole intercepted a mineralized zone (0–26 m) related to biotite-malachite (after cpy; 1–3%) parallel to mylonitic foliation.

Several alteration types related to hydrothermal processes have been identified in the Riacho do Pontal district [28]. Hydrothermal alteration has led to a pervasive calcic-potassic and calcic-ferric overprint of the host gneisses and migmatites. Early-stage sodic hydrothermal alteration is distal in relation to areas with calcic-potassic and potassic-ferric alteration with a higher strain rate. Hydrothermal alteration processes led to the replacement of metamorphic minerals within banded gneiss with a suite of minerals, including albite, biotite, hematite, and amphibole. These replacement minerals are spatially connected to penetrative shear deformation, and ore zones plunge parallel to stretching lineations along shear zones. Pyrite, chalcopyrite, and chalcocite are related to the main sulfide minerals found in ore zones. Magnetite and/or hematite typically occurs in association with copper ore minerals and constitutes less than 1% of the paragenesis [29].

The Riacho do Pontal belt was overprinted by two main shearing events: (a) D1-thrust shear zones with convergence to the north representing a series of northwest-trending parallel structures related to hydrothermal alteration and mineralization and (b) D2-dextral strike slip shear zones related to multiple reactivation responsible for the strong shearing of paragneissic and orthogneissic rocks. The foliation of shear zones is significantly tilted with a strike of 320° and a dip to the NE at 60° to 75° . Both events were related to transpressive structural regimes.

The Riacho do Pontal Copper District is located at the apex of three orogenic belts (the Riacho Preto, Riacho do Pontal, and Sergipana belts), which are located along the northern border of the São Francisco Craton (Figure 2). The area has been located within the Brasiliano collisional zone (from ca. 750 Ma to 570 Ma), which developed during the convergence of the Neo- to Mesoproterozoic terrains of Borborema Province (Figure 3) with the São Francisco Craton [49]. The suture is marked by a gravity anomaly heavily flanked by anomalous lows (Figure 4b). The positive anomaly corresponds to the

lower crustal uplift of the Borborema province, and the flanking negative anomalies correspond to lower density nappes pushed towards the craton [50,51]. According to [50], supracrustal rocks of the Riacho do Pontal and Sergipana belts were placed over the São Francisco Craton with displacements to the south of the order of 30–60 km [52]. This overlapping structure is observed in both magnetic and gravimetric data with the truncation and displacement of old N–S structures occurring along the border between the São Francisco Craton and Borborema terrain. According to [52], the collisional event was overprinted by transcurrent shear zones.

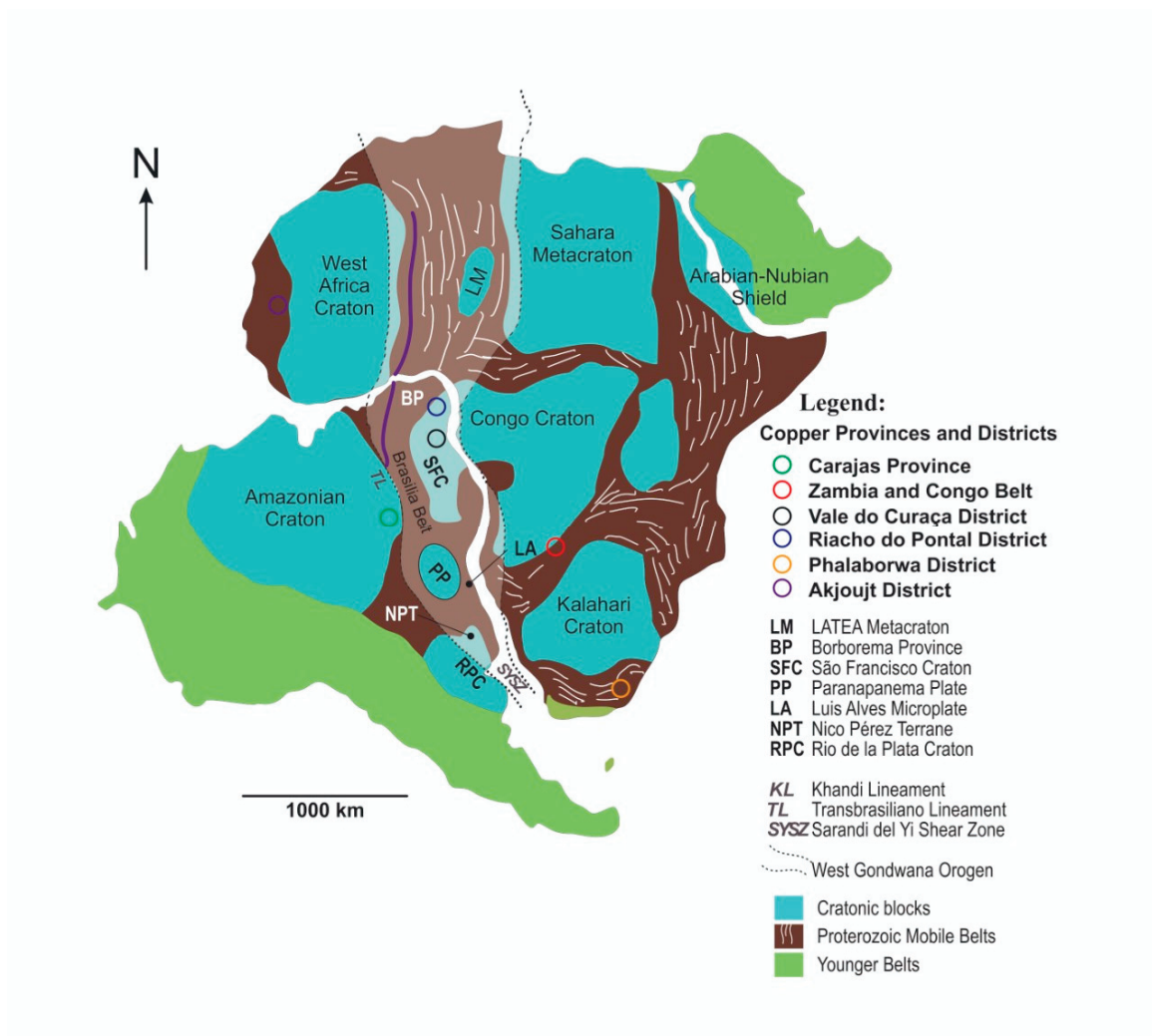


Figure 3. IOCG provinces and districts situated in Brazil and Africa: main crustal blocks and Neoproterozoic orogenic belts in South America and Africa, including locations of the West Gondwana Orogen (modified after [53–57]).

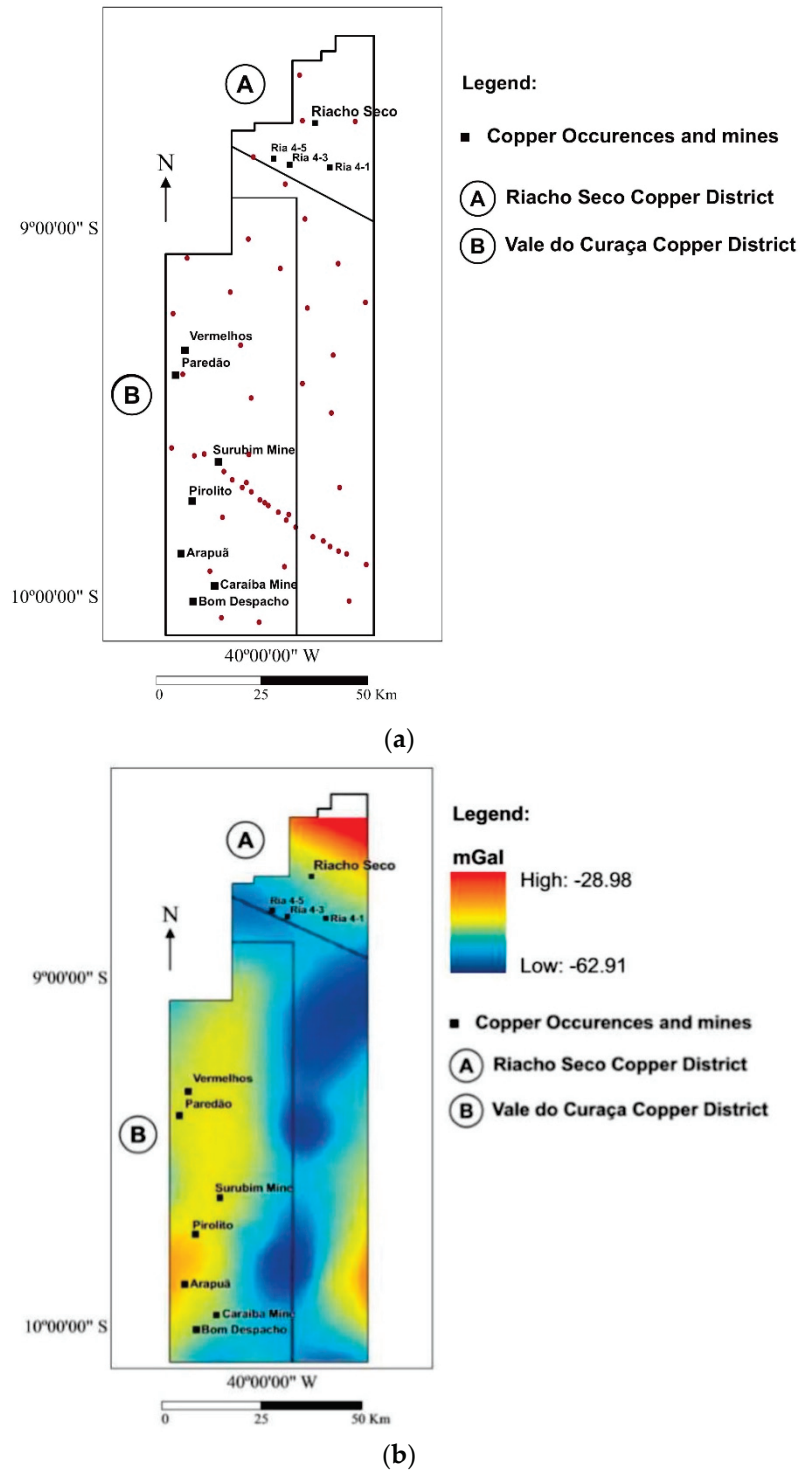


Figure 4. (a) Gravity stations and (b) Bouguer gravity map for the study area. Major copper occurrences and mines are shown. Block A: Riacho do Pontal district; block B: Vale do Curaça IOCG district.

3. Tectonic Setting

IOCG provinces and districts in Brazil and Africa are mainly situated along the borders of major crustal blocks and in Neoproterozoic orogenic belts (Figure 3). There are at least three IOCG metallogenic provinces with different ages in Brazil, which include the Carajás province (ca 2.72 Ga and ca 2.5 Ga), the Vale do Curaça district (ca 2 Ga), and the Neoproterozoic (ca 750 Ma–570 Ma) districts of Riacho do Pontal.

4. Data

4.1. Gravity and Magnetic Data

Gravity and magnetic anomaly data over an area of 7500 km² were extracted from public databases available from the Brazilian Geological Survey (CPRM) and the gravity data reduced to Bouguer gravity anomalies using procedures described in [50]. A total of 60 gravity points spaced an average of 8 to 15 km distance were extracted from the gravity database and used for this study (Figure 4a). Given the coarse spacing of the gravity data, we expect crustal density sources that occur at depths of 5 km and beyond to be effectively resolved. The gravity data were gridded by applying a minimum curvature algorithm to a 500 m grid (Figure 4b). The gravimetric signature is quite distinct in both districts while the Vale do Curaça Copper District is associated with a higher gravimetric signature, and the Riacho do Pontal Copper District is associated with a lower valued gravimetric domain (Figure 4b).

Airborne magnetic anomaly data were acquired in 2001 as part of the Riacho Seco and Andorinhas Project executed by the Brazilian Geological Survey [58]. Data were collected at a nominal height above ground of 100 m along N–S flight lines spaced 500 m with E–W tie lines every 10,000 m. A total of 48,641 km of magnetic data were collected. The total magnetic field (TMI) flight line data were gridded onto a 250 m grid (Figure 5). Given the flight-line spacing of the magnetic surveys and height at which the magnetic field measurements were observed, we expect to resolve crustal magnetic sources that lie at depths of 400 m and deeper [59]. The horizontal resolution is 200 m.

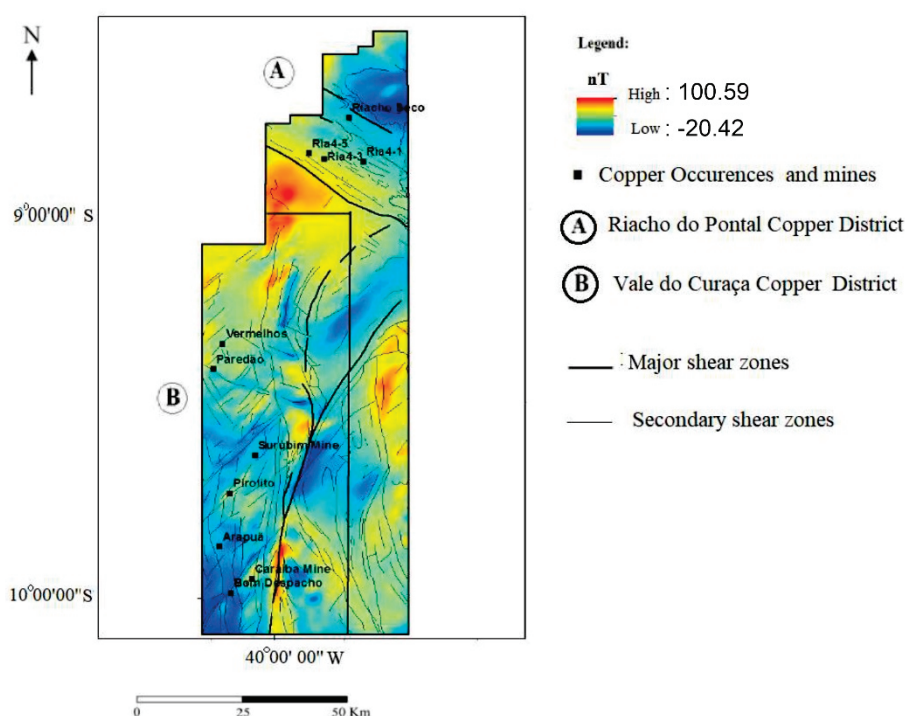


Figure 5. The reduced to pole (RTP) total magnetic intensity (TMI) data upward continued to 1000 m above ground. Major Cu mines and occurrences are shown. Block A: Riacho do Pontal district; block B: Vale do Curaça IOCG district.

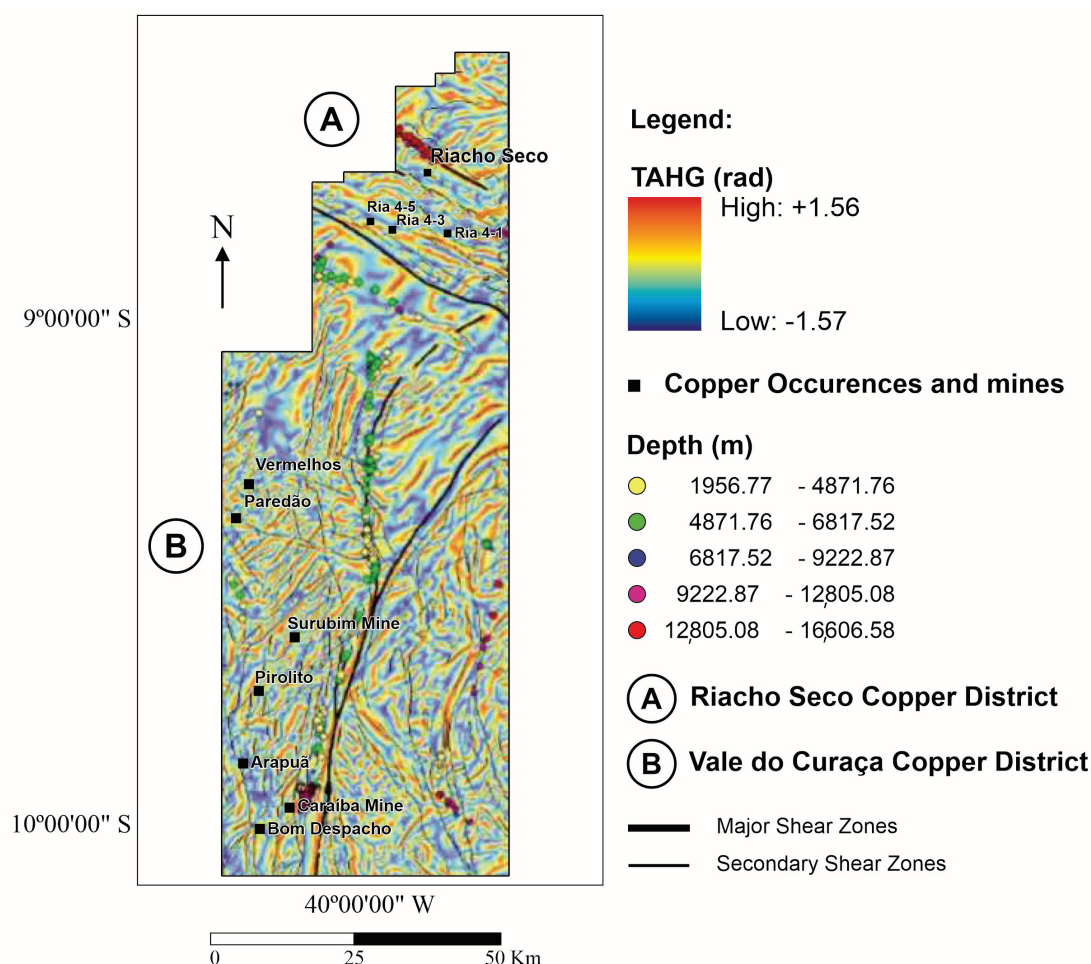
Gradient Functionals Calculated from the Magnetic Data

Several gradient quantities of the magnetic field were calculated from the grid of the TMI to enhance magnetic variations and lineations related to geologic structures, map magnetic signatures of altered and unaltered rocks, and identify magnetic signatures related to deep magnetic sources. The TMI data were reduced to the magnetic north pole (RTP) using an inclination of -20° and declination of -22.31° [60]. The RTP grid was continued upward to 1000 m above the terrain to reduce

noise caused by the low geomagnetic latitude and to enhance the magnetic signatures of deeper sources (Figure 5).

The grid of upward-continued RTP data was used to calculate the tilt angle of the total horizontal gradient (TAHG; [60]). The TAHG transform clearly identifies tracks of high anomaly gradients that map magnetic contrasts related to geologic structures at a range of depths (Figure 6a). Tracks of the TAHG ridgelines, marking major geologic structures, are shown relative to the gravity anomaly map (Figure 6b). The TAHG effectively identifies changes in the prevailing geologic structures as the northern limit of the SFC, where the main strike of the gradient changes from sub-NS orientations to SSW–NNE directions on the SFC and to SE–NW oriented strikes north of the SFC along the Sergipano foldbelt. The SE–NW strike farther north is replaced by more chaotic strike directions when moving northwards out of the foldbelt. Major copper mines Ria 1 to Ria 5 are located in the well-defined SE–NW striking magnetic field anomalies. The copper mineralizations are tied to shear movements and to magnetite and hematite occurrences. It is to be expected that the magnetic anomalies are correlated with the copper mines and have shearing strike directions.

Euler deconvolution solutions [61] were calculated from the grid of the magnetic anomaly data, and depths to magnetic source (structural index = 0) are shown along major shear zones. The structural index = 0 is adequate for detecting the top of a thick slab [62].



(a)

Figure 6. Cont.

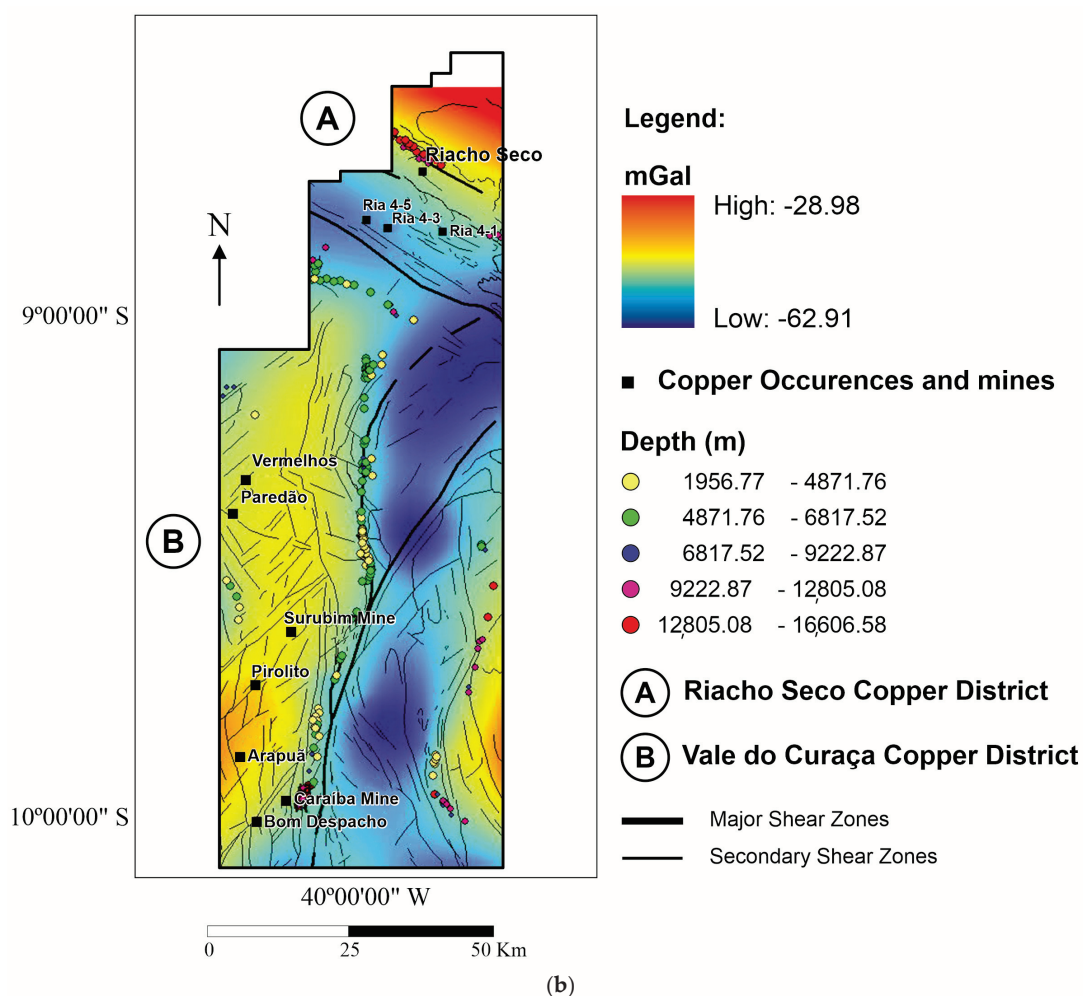


Figure 6. (a) Map showing the tilt angle of the horizontal gradient (TAHG) of the RTP magnetic anomaly data [60]. (b) Bouguer gravity anomaly map with major and secondary shear structures and TAHG tracks. Both maps include estimates of magnetic structures and their depths to the magnetic source as colored circles. Depths to the magnetic structures were calculated using the Euler deconvolution method [62]. Primary Copper Districts and occurrences are shown. Block A: Riacho do Pontal district; block B: Vale do Curaçá district. The detailed geology of the two studied districts is shown in Figure 1.

4.2. Petrophysical Data

Magnetic susceptibility and density data were acquired from drill cores and surface rock samples. Measurements are provided as susceptibility in SI (susceptibility intensity) $\times 10^{-3}$ and density in g/cm^3 . Magnetic susceptibility was measured using a KT10 PLUS S/C susceptibility meter, and rock density was measured by vacuum saturating the samples using a hydrostatic balance. During the field seasons, 33 drill core samples were investigated to determine density and susceptibility from samples collected in the Riacho do Pontal copper district, and 11 rock samples were collected from the outcrops and mines of the Vale do Curaçá copper district (Figure 7).

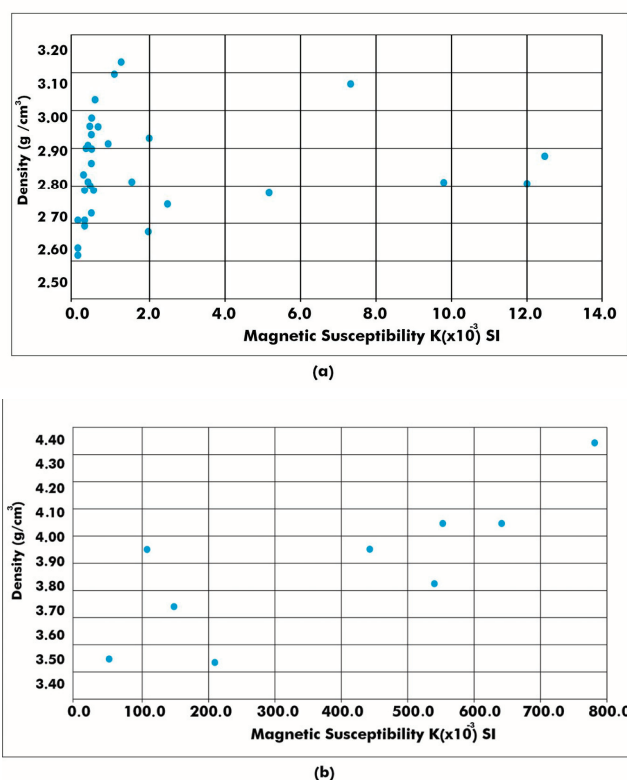


Figure 7. (a) Thirty-three samples measured for density and susceptibility taken from exploration drill holes in the Riacho do Pontal copper district, (b) 11 samples measured for density and susceptibility from rock samples collected from the outcrops and mines of Vale do Curaça copper district.

The densities found for the Riacho do Pontal copper district are representative of the rock types found in the boreholes, which are gneissic rocks (Table 1).

Table 1. Rock types and depths of samples from the Riacho do Pontal copper district sampled from two drill holes (PCB-RIA4-DH01 and PCB-RIA4-DH02).

PCB-RIA4-DH01	Depth (m)	Rock Type	PCB-RIA4-DH02	Depth (m)	Rock Type
PETRO-01	1.85	Quartz-magnetite-biotite mylonite	PETRO-21	2.75	Amphibole biotite gneiss
PETRO-02	5.50	Quartz vein	PETRO-22	10.60	Quartz vein
PETRO-03	8.70	Biotite mylonite	PETRO-23	14.30	Quartz vein
PETRO-04	10.70	Biotite mylonite	PETRO-24	26.30	Quartz vein
PETRO-05	13.00	Biotite mylonite	PETRO-25	31.80	Quartz vein
PETRO-06	21.00	Biotite mylonite	PETRO-26	45.69	Quartz vein
PETRO-07	25.50	Biotite mylonite	PETRO-27	60.00	Quartz vein.
PETRO-08	32.48	Quartz biotite gneiss	PETRO-28	73.10	Biotite quartz vein.
PETRO-09	67.70	Quartz biotite gneiss	PETRO-29	83.60	Quartz vein
PETRO-10	105.30	Quartz biotite gneiss	PETRO-30	103.50	Quartz vein.
PETRO-11	158.00	Quartz biotite gneiss	PETRO-31	137.00	Biotite quartz gneiss.
PETRO-12	167.80	Quartz biotite gneiss	PETRO-32	148.80	Biotite quartz gneiss
PETRO-13	173.60	Quartz biotite gneiss	PETRO-33	168.10	Biotite mylonite
PETRO-14	189.00	Quartz biotite gneiss	PETRO-34	265.10	Biotite quartz gneiss

The characteristic density and susceptibility values in the two districts are very different, as is the relation between the two quantities. The Riacho do Pontal copper district has quite standard crustal-rock-type densities, with values between 2.6 and 3.1 g/cm³. For all of the rock samples the magnetic susceptibility is proportional to density, but with two groups of proportionality. A first group is only mildly proportional, with susceptibility varying between 0 and 1.8·10⁻³ SI, and the other group is highly proportional, with susceptibility varying between 0 and 13·10⁻³ SI. For the second group the hydrothermal process was responsible for increase of magnetite. The Vale do Curaça

copper district has much higher densities between 3.5 and 4.4 g/cm³, with much higher proportionally varying susceptibilities values, ranging between 0 and 800·10⁻³ SI. The densities of the Vale do Curaçá copper district are typical of mafic and ultramafic rocks, rather than crustal type rocks. In the area the metamorphism has overprinted the ultramafic rocks, transforming them into granulites. The IOCG hydrothermal process in the shear zones increases the magnetization through deposition of magnetite in veins associated with copper mineralization.

4.3. Geologic Data

A compilation of data from the Brazil Geological Survey (CPRM) was used as a geological base map [20]. Supplemental geologic information, including structural and image interpretation data (Landsat 8), was collected for this study along secondary roads, resulting in an additional 300 geological observations [28]. Geologic sections along selected profiles were developed to better understand the structural setting of the area.

4.4. Seismic Tomography

Seismic tomography data have been collected for an area covering east-central Brazil [63,64]. The seismic velocity model which emerged from that study were provided to us by Minerals Targeting International Pty Ltd. and were extracted from a database produced as part of the Global Lithospheric Architecture Mapping (GLAM) Project [65] and refer to the methodology used for the model of [63]. The tomographic image shows the S-wave velocity (V_s) of the Carajás IOCG province, Riacho do Pontal and Vale do Curaçá copper districts in Brazil [63]. The data were used to determine seismic properties related to the lithosphere underlying major IOCG provinces in Brazil (Figure 8). The data represent a model of average seismic velocities at the depth slice of 0–100 km [63]. Our studied area is inboard of a relatively high velocity region, bordered eastwards by a low velocity region. The high-velocity region presumably indicates the cratonic area, with the lower velocity region demarcating the craton limit.

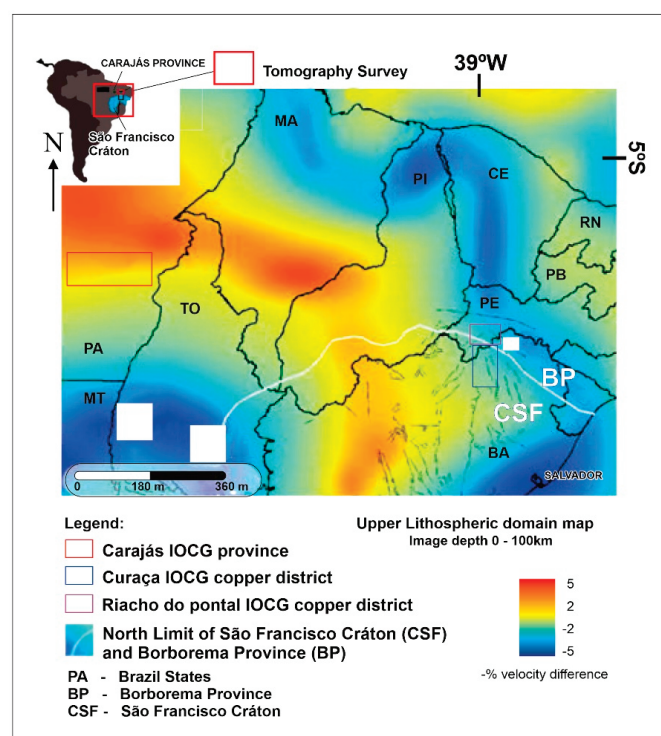


Figure 8. Tomographic image representing seismic S-wave velocity (V_s) of the Carajás IOCG province, Riacho do Pontal and Vale do Curaçá copper districts in Brazil [63–65]. The figure shows a 0–100-km tomographic depth slice. Red to orange colors denote high S-wave velocities (V_s), and blue-green colors denote low V_s values.

5. Methods

5.1. 3D Magnetic and Gravity Inversion Models

The magnetic potential method is sensitive to the magnetic properties of the rocks in terms of residual and induced magnetization. However, applications of this practice have been limited by conventional assumptions that rock magnetization is dominated by induced magnetization and that the magnetization direction is aligned with the geomagnetic field [66]. Modeling the magnetization vector direction and strength using magnetization vector inversion (MVI) has challenged these conventions, and MVI modeling has become an important exploration tool in the mining industry [66]. VOXI Earth Modelling is an Oasis Montaj cloud and clustered computing package that allows the inversion of geophysical data in 3D [66,67]. It uses a Cartesian Cut Cell (CCC) and the algorithm has been simplified by Ellis and MacLeod [67] in order to represent geological surfaces with better accuracy. VOXI Earth Modelling is an Oasis Montaj cloud and clustered computing package that allows the inversion of geophysical data in 3D [66,67]. It uses a Cartesian Cut Cell (CCC) and the algorithm has been simplified by Ellis and MacLeod [67] in order to represent geological surfaces with better accuracy.

Let us begin with the very general assumption that the magnetic properties of the earth can be represented by volume magnetization [68]. We make no assumptions about whether the source of this magnetization is induced or remanent [66,68].

Magnetic and gravity data were inverted to create 3D models of magnetic susceptibility and density, respectively, of selected areas of the two studied copper districts to better understand the anatomy of the crust underlying them. The three-dimensional models were integrated with other project data using a multicore cloud-based computing platform.

5.2. 3D Magnetic Inversion

The grid of total field magnetic anomaly data was inverted to create a 3D magnetic susceptibility model using the MVI method developed by [67] and employing software available from the Geosoft Oasis software package [66,68]. The MVI method is a particularly effective inversion methodology to use in areas of low geomagnetic latitude and in geologic environments where little is known about the remanent magnetization of the rocks under study [66].

No palaeomagnetic studies have been conducted on the rocks within these copper districts. The method assumes that the magnetic signal observed at the surface is associated both with varying susceptibility contrasts and with the varying direction of magnetic field magnetization, which allows one to verify the presence of remanence. In the end, we conclude that remanence is not present.

Voxels for the magnetic inversion were set to 250 m (x) × 200 m (y) × 250 m (z). Model inputs included petrophysical properties, surface geology, and structural information as qualitative constraints.

5.3. 3D Density Inversion

VOXI MVI modeling is a Geosoft Oasis Montaj cloud and clustered computing module used for the inversion of ground gravity data. The Geosoft package uses a cartesian cut cell (CCC) and an iterative reweighting inversion algorithm [67,68]. The algorithm has been simplified by [65,66] and represents geological surfaces with good accuracy. For the gravity models, voxels sized 250 m × 250 m × 250 m were used.

The model used topography to represent the top of the model and a 5000-m depth to constrain the bottom surface of the model. The Z voxel cell size follows a logarithmic progression with depth. The acceptable absolute error level for all models was set to 0.02 mGal. A linear trend background was removed from the input gravity grid to facilitate the modeling process and avoid generating erroneous results and undesirable edge effects. We use the Bouguer gravity field instead of the isostatic anomalies, because in the specific inversion areas, the topography is flat.

6. Results

6.1. Gravity and Magnetic Signatures

6.1.1. Vale do Curaçá District

Gravity anomaly signatures over the Vale do Curaçá copper district (Figure 6b) show that the district is underlain by rocks with high densities in contrast with those surrounding it. The district is located within an elongate 110 km × 22 km long N–S trending gravity high that occurs over rocks related to the Bom Despacho gneiss, Surubim gneiss, Banguê gneiss, mafic and ultramafic complex and tonalitic to granodioritic orthogneiss (Figure 1). In this study, density measurements were made from these units, including gneissic-granite, mylonitic, and pyroxenite rocks, which have average densities of 2.78, 3.1, and 3.3 g/cm³, respectively (Figure 7b). The lower gravity anomalies surrounding the gravity high are associated with the following units: Riacho da Onça augen gneiss and the Acauã Group. The densities measured from these units are generally lower and range from 2.65 to 3.0 g/cm³. The gravity low is hardly to be expected to be due to an isostatic compensation of topography, as there are little variations of topography.

The mines of Caraíba, Surubim, and Vermelhos and other copper occurrences are located in a region where rocks are widely affected by granulite-facies metamorphism, and strong hydrothermal processes which show a more positive gravimetric region situated on the eastern portion of the Vale do Curaçá.

The mines of Caraíba, Surubim, and Vermelhos and other copper occurrences are located in the eastern region of the Vale do Curaçá district, which includes a relatively higher gravimetric region. Density measurements taken from rocks sampled from ore zones within the Caraíba and Surubim mines show very high average densities of 3.5 to 4.35 g/cm³. Given the coarse gravity station spacing (Figure 4a), we do not expect anomalies associated with the high-density ore to be resolved in the gravity anomaly map. The ore is comprised of high-density rocks. The ore includes chalcopyrite, magnetite, and bornite associated with hornblende, biotite, apatite, and zircon. Chalcocite and ilmenite are rare [13].

The Vale do Curaçá district sits within a NS magnetic high positioned alongside sets of elongate magnetic lows that record major shear structural episodes and juxtaposed rocks with different magnetic susceptibilities. The magnetic anomaly lows are mapped as gneissic rocks and mafic and felsic dikes. These rocks exhibit weak levels of hydrothermal alteration as shown by outcrop and petrographic studies. Copper mineralization in the Vale do Curaçá district is associated with linear NS-trending magnetic anomalies located along the west side of the Itabuna-Salvador-Curaçá Belt (Figure 1). Late NW magnetic trends are related to hydrothermal alteration (Figures 5 and 6a). Late mafic and felsic dikes show the same trend.

The north- to northeast-trending magnetic anomalies of the Vale do Curaçá copper district correspond to anastomosed structures that have been geologically mapped throughout the district. The NS-trending structures have been overprinted by at least two cycles of shearing [34,46]. These later shear faults are recorded on the TAHG map (Figure 6a).

The copper occurrences and mines in this district, including areas of strong hydrothermal alteration, are associated with magnetic anomalies (TMIs) of ~25.98 to ~100.59 nT (Figure 5). Magnetic susceptibility ranges from 100 to 800 × 10⁻³ (Figure 7b). The magnetic susceptibility of ore zones of the Vale do Curaçá copper district is ten times higher than that of the Riacho do Pontal district (Figure 7a,b).

6.1.2. Riacho Do Pontal Copper District

The Riacho do Pontal district sits on a gravity gradient that separates a gravity high to the north from a NW-trending gravity low to the south (Figure 6b). The Bouguer anomaly low is likely related to low-density gneiss that partly outcrops in the Sobradinho Remanso and the southern portion of the Riacho Seco complex (Figure 1). Ria4 copper occurrences within the Riacho do Pontal district are

situated along the edge of the gravity gradient. Densities measured from rocks within the Ria4 mine show that the less altered rocks have densities of 2.7 to 2.78 g/cm³. Rocks that have been more heavily altered have densities that overlap with those of less altered rocks and range from 2.75 to 3.1 g/cm³ (Figure 7b).

The northwest trending Bouguer gravity low underlying the Riacho do Pontal district geologically corresponds to the collisional suture zone located between the higher density cratonic block and the lower density crust forming the Riacho do Pontal mobile belt [50,68]. Ophiolite bodies have been mapped in this region [52].

The northeast portion of the Riacho do Pontal copper district is characterized by a more positive gravimetric anomaly with values >−35 mgal. The gravity high corresponds to foliated orthogneissic rocks of the Riacho Seco complex. The Riacho Seco copper occurrences are situated along the gravity gradient, which likely marks a structure that has juxtaposed the denser crust of the craton against the lower density crust underlying the Riacho do Pontal mobile belt. The area of the gravity gradient includes biotite-garnet rich rocks, which occur along shear zones and host a small number of copper occurrences.

In the Riacho do Pontal Copper District, the copper occurrences (Ria4 and Riacho Seco) are not related to high magnetic anomalies. The Ria4 and Riacho Seco occurrences are hosted, respectively, in nonmagnetic gneiss of the Sobradinho Remanso and Riacho Seco complexes. The gneissic rocks are pervasively hydrothermally altered and have a range of magnetic susceptibility of 0.2×10^{-3} SI in less altered rocks to 12.2×10^{-3} SI in more hydrothermally altered rocks. On a regional scale, the NW–SE trending magnetic anomalies overprint longer wavelength NS trending anomalies related to older and deeper parts of the São Francisco Craton [69].

Copper deposits located in the belt of the Riacho do Pontal copper district are mainly situated in zones with or without weak magnetic anomalies (TMI) with intensities below 40 nT (Figure 5).

6.2. 3D Inversion Models

6.2.1. Vale do Curaçá Copper District

The 3D magnetic susceptibility model of the Vale do Curaçá copper district reveals magnetic features corresponding to numerous geologic structures that reflect episodic tectonic activity. The 3D interpretation was built using field geological and structural data. More than 150 geological points were visited, more than 50 thin sections were described, and at least 20 drill holes were observed. Structural data were systematically collected. A series of parallel magnetic trends aligned N–S and dipping 75–85° to the east are overprinted by at least two episodes of NS-trending shear faults (D1 and D2; [20,34,47]). The Caraíba mine is positioned along a NS-trending subvertical shear zone, showing an anastomosing shape in both the horizontal and vertical directions. A series of subparallel N–S shear structures have been active and responsible for multiple reactivation events. N–S shearing magnetic zones are related to thrust shear zones (D1) with convergence to the west and are overprinted by strike slip faults. The D1 and D2 events controlled the distribution of hydrothermal alteration and mineralization. The NE–SW late shear zones are subvertical [20,34,47].

The Caraíba mine bodies are strongly related to magnetic and gravimetric NS trends which are evident when analyzing the inversion results. In Figure 9, the inverted model is represented through the delineation of the body with high magnetic susceptibility, and high-density contrast. We have chosen a discriminant level that allows to represent the increased density and magnetization through positive density contrast values (>0 g/cm³) and susceptibility values above 0.005 SI. In a 3D rendering the model of these relatively high values is illustrated in Figure 9, where the known shear faults and the position of the Caraíba open pit mine has been included. A characteristic large-scale densification and increased susceptibility is found below the mine, as is expected considering the results concerning the rock properties we have described above, regarding the rocks that encase the IOCG mineralization (Figure 9). We find that the Caraíba mine and Paredão occurrences show a strong relationship to

magnetic anomalies. The other occurrences along the Vale do Curaçá district are not directly related to high gravimetric and magnetic anomalies.

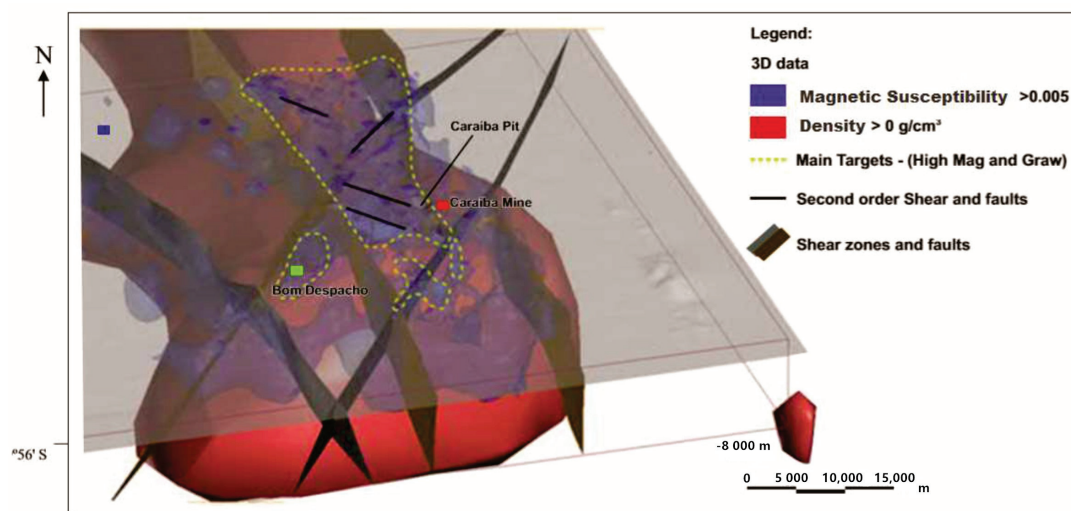


Figure 9. Draping structure and MVI magnetic ($SI > 0.005$) and density contrast ($>0 \text{ g/cm}^3$) inversion onto the terrain surface surrounding the Caraíba mine (Curaçá copper district). In the Vale do Curaçá district, a series of subparallel N–S magnetic trends were found. A great number of magnetic anomalies are related to geological units represented by mafic granulites and granulitic orthogneiss. The dashed yellow area denotes the main target with high potential to host new IOCG orebodies in the Vale do Curaçá district.

The host rocks of the Caraíba mine are granulitic orthogneiss and ultramafic bodies. The mine is situated approximately 1 km from the N–S shear zone that was displaced by NW–SE shear zones. Sodic and potassic hydrothermal alterations are mapped along shear zones [20,29]. To demonstrate the inversion results in more detail, we show a section of the model focused on the mine. In a 3D tectonic setting, the mine is intrinsically related to high magnetic susceptibility associated with a positive density anomaly (Figure 10). The orebodies are oriented in a subvertical direction and are controlled by stretching lineation [34]. The model resulting from the inversion of the potential field data is consistent and correlates with the outcropping geology and structural features mapped in the Caraíba mine. In Figure 10, we show a cross section through the model, centered on the mine, and extending 500 m on each side of the mine. The depth extent of the model reaches 8000 m. The blue model shows the relatively high susceptibility, with values being greater than 0.009 SI, whereas the mixed blue and red graph shows the superposition of susceptibility and positive density contrast. The black circle shows the location of the open pit of the Caraíba mine. Shown in grey is the topography, which is completely flat.

The magnetic trends (magnetic susceptibilities > 0.009 SI) are juxtaposed with shear structures and faults with different magnetism intensities (Figure 10). The Caraíba mine correlates with magnetic signatures higher than those of occurrences and deposits situated near the mine.

In Figure 11, the results from the gravimetric and magnetic inversions along an EW profile are shown, with the Caraíba mine in its eastern portion. Highly magnetic (>0.005 SI) and dense ($>3.20 \text{ g/cm}^3$) areas are related to rock properties at superficial depths. In the same profiles, at 3000 m depth, magnetization anomalies show continuity up to deeper zones (-8000 m), in the case of density anomalies, in deeper zones (-3000 m), the anomalies do not show continuity: this is interpreted geologically as graffitiated rocks that emerge at shallower depths and probably metasedimentary rocks at greater depths. We find that hydrothermal zones are related to magnetic zones in shear zones, opening the possibility for the continuity of mineralization in deeper zones.

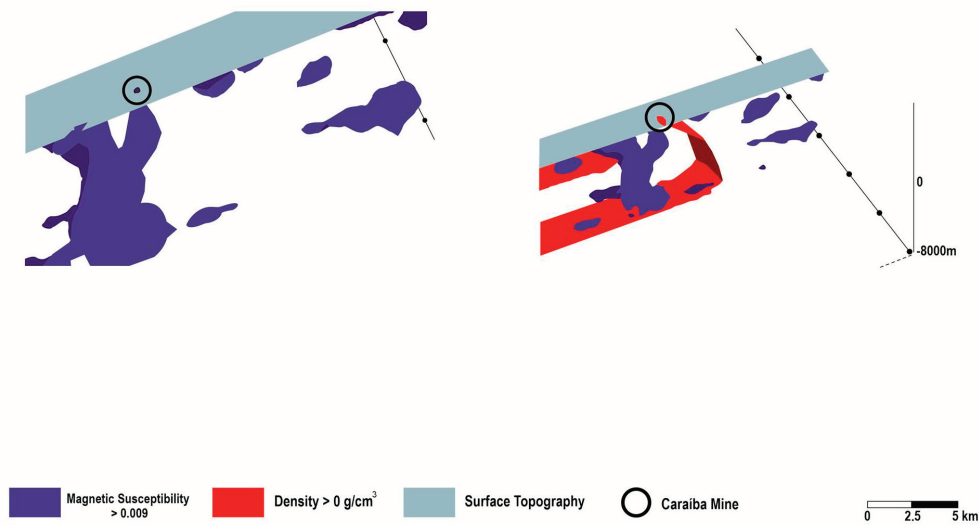


Figure 10. 3D representation of the results from magnetic (susceptibility in terms of >0.009 SI) and gravimetric (density > 0 g/cm^3) inversion integrated for the Caraíba mine. The Caraíba mine is strongly related to susceptibility and density anomalies. It shows potential for continuity in depth in ore zones related to susceptibility and density anomalies along shear traps.

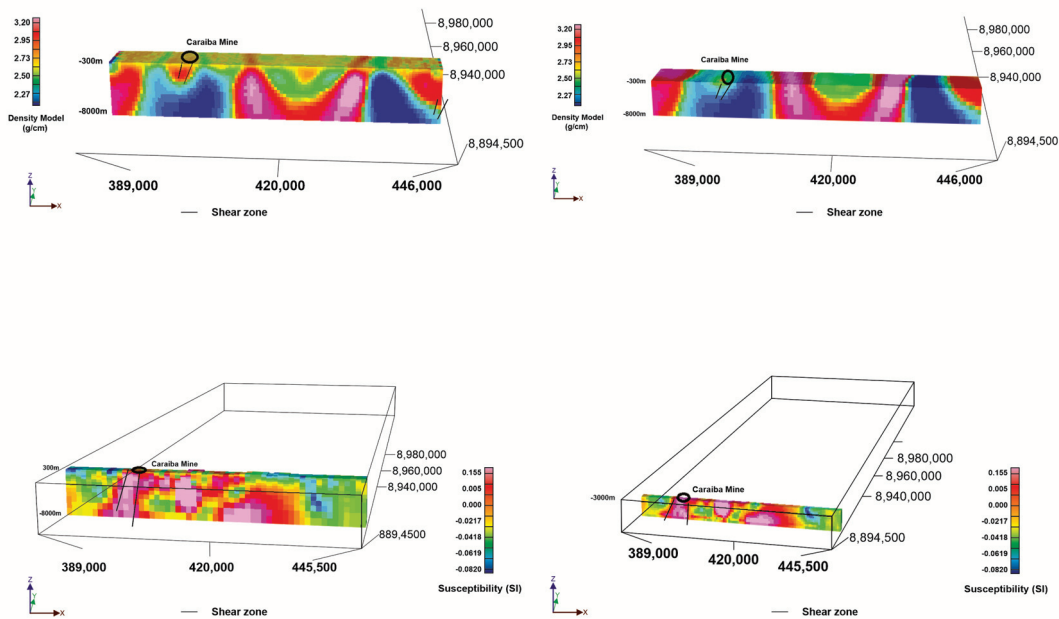


Figure 11. Density and magnetic susceptibility EW profiles in the southern portion of the Valley of the Curaça District, positioned between 300 m and 3000 m depth. Caraíba mine is located in the eastern portion of the area with high density and magnetization values up to 3000 m depth.

Geologically, the regional magnetic trends are related to more intense metamorphic granulitic processes overprinting geological units: the Bom Despacho gneiss and the Surubim, Banguê, and tonalitic to granodioritic orthogneiss. Late NE–SW shear zones are quite common, crosscutting N–S early magnetic trends [20,29,34]. Ore zones from the Caraíba and Surubim mines have a range of magnetic susceptibilities of 400×10^{-3} SI to 750×10^{-3} SI.

In Figure 12 we show the integrated model, with the gravimetric Bouguer values, overlaid on the inverted magnetic and density model. In the 3D view, the red domains are the increased magnetic susceptibility areas, and in grey the positive density contrast areas. Moreover, the faults

are shown. The Caraíba mine is associated with a shear structure, and a high density and magnetic susceptibility zone. It can be seen that the copper occurrences and mines are prevalently associated to increased susceptibility and increased density values. In fact, the occurrences align along the trend I in which we find structures and high density and susceptibility. Moreover, it is found that in the area Central North-East, these conditions are similar, but up to now no occurrences have been explored. In the future, this area should be studied in more detail.

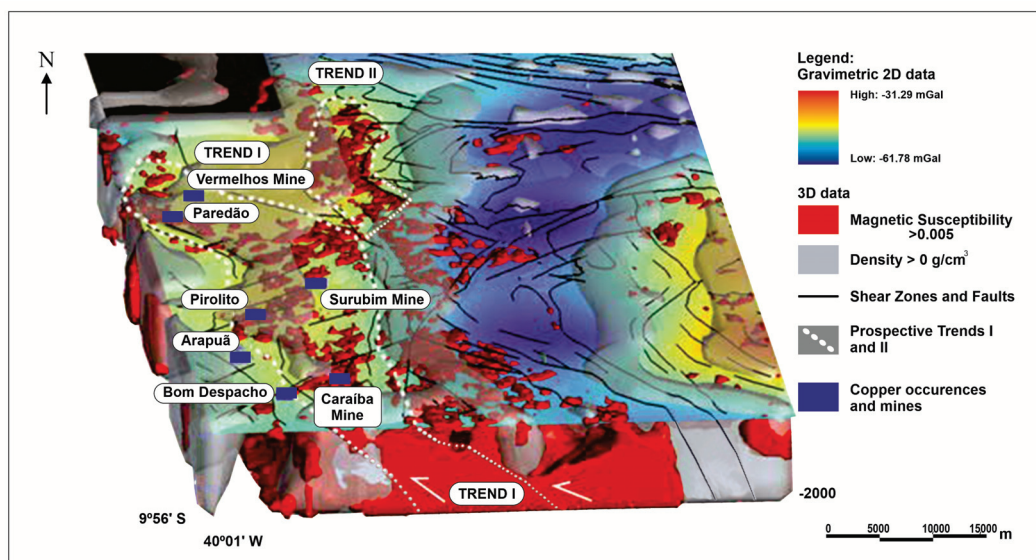


Figure 12. The IOCG mineral system in the region of the Vale do Curaçá Copper District, in regional terms, shows two main prospective trends. The trends are positioned in the contact zone between domains with high magnetic susceptibility (>0.005 SI) and density (>0 g/cm³) and show contrasts in density and magnetite content.

Three-dimensional magnetic and gravity inversions show two main NNW prospective trends, both with a sigmoidal shear shape. These trends are positioned in the zone of contact between domains with high magnetic (susceptibility > 0.005 SI) and density anomalies (density > 0 g/cm³) and show contrasts in dense rocks and magnetite content. The trends envelope granulitic rocks but are also the most hydrothermal rocks in the Vale do Curaçá district. Trend I is 40 km in length and 10 km in width, hosts the Caraíba, Surubim, and Vermelho mines and other deposits and is the most important trend for host IOCG deposits in the Vale do Curaçá Copper District. Trend II is 15 km in length and 5 km in width. Geologically, these trends are hosted mainly along points of contact between Surubim gneiss, tonalitic to granodioritic orthogneiss, and gabbronorite and/or norite bodies (Figure 12).

The alteration at the Vale do Curaçá copper district has a hydrothermal signature characterized by intense potassic-iron alteration indicative of a high temperature system [1,8,10].

Alteration and associated mineralization at the Vale do Curaçá Copper District are associated with magnetic and gravity anomalies as observed in other IOCG deposits from Carajás Mineral Province, Brazil; the Gawler Craton, Australia; Kiruna, Sweden; and the Great Bear Magmatic Zone, Canada [1,5,8,10].

6.2.2. Riacho do Pontal District

The 3D magnetic inversion over the Vale do Curaçá copper district shows that the Ria4 prospect and Riacho Seco deposit do not show a correlation with magnetic susceptibilities. Occurrences of copper in the region are positioned at magnetic lows. This observation is explained by the fact that the mineralized zone is related to hematite zones and iron oxide content is low ($<2\%$). The exploratory drilling program (Ria4-DH01) crosscut 32 m @ 1% copper [24,28].

In the Riacho do Pontal district, the copper occurrences are not associated to evident positive density and magnetic susceptibility values. This is coherent with the fact that the rock samples showed gneiss characteristics, with no evident density and susceptibility anomalies. The copper occurrences are associated to the shear faults, but not to increased density and magnetite content. Probably the mineralization and magnetization in the shear zone is much weaker compared to the Val do Curacao district.

The results obtained from magnetic inversions conducted in the region of the Riacho do Pontal copper district show weak magnetic anomalies along a NW–SE trend. The discrete linear magnetic features are related to shear zones. These NW–SE features overlap older and deeper NE–SW features. However, an analysis of Riacho do Pontal district magnetic anomalies in 3D in the Riacho Seco deposit shows a low magnetic anomaly close to the surface and a change in depth (>400 m) to an area with a high magnetic signature (>0.005 SI) (Figure 13). These results allow for the possible development of a continuous model for follow-up research on these deposits as related to deeper magnetic susceptibility anomalies.

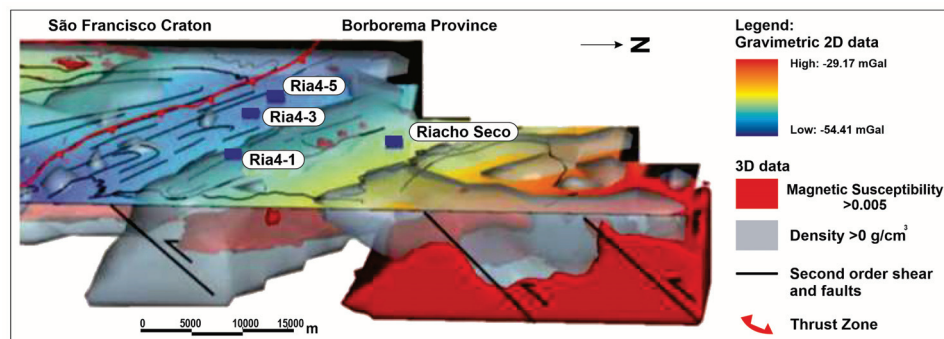


Figure 13. The MVI magnetic gravimetric inversions in the region of the Riacho do Pontal Copper District. Ria4-1, Ria4-3, Ria4-5 and Riacho Seco are the major occurrences at Riacho do Pontal Copper District. In the region of the Riacho Seco Deposit and Riacho do Pontal prospects, the magnetization and density anomalies are weaker ($SI > 0.005$ and density $> 0 \text{ g/cm}^3$) and deeper (>1.5 km).

7. Discussion

7.1. Vale do Curaçá and Riacho do Pontal District IOCG Mineral Systems

Understanding IOCG systems at different scales allows for tracing of some parameters leading to the formation of districts or fertile provinces [6,68,70–76].

More recently, a new generation of ore system exploration models has been developed to take advantage of the massive volume of data available to the exploration industry [76]. Improving exploration competitiveness will be necessary with the more sophisticated integration of different datasets. The challenge remains to decrease the size of exploration areas and increase the success rate of drilling programs [76,77]. Thus, for the Vale do Curaçá and Riacho do Pontal copper districts, the main footprint that shows the ore system signature was identified (Figure 13). The more important geological, structural, geochemical, mineralogical, and petrophysical parameters of these copper districts are summarized below and illustrated in Figure 13.

At a regional scale, large major lithospheric structures control the traps of IOCG mineralizing systems or heat magmas, or fluid flow is frequently evident in gravity and magnetic databases [4]. The outline of the inversion model for Riacho do Pontal obtained using these methods fits well with geological and structural features mapped in the field.

7.1.1. Lithospheric Setting Expressed by the Seismic Tomography Potential

The high zones (in red) on the tomographic map represent high-velocity domains that denote microcontinental blocks (mantle lithosphere domain). They are flanked by low velocity

domains interpreted as the refertilization of the subcontinental lithospheric mantle (SCLM) and/or higher temperatures along fault zones. Frequently, deposits are concentrated along prominent translithospheric structures, particularly in lower-velocity regions (blue) or on the flanks of velocity highs (courtesy of [63,64]).

A world map of the lithosphere produced through the integration of geophysical, geological, and geochemical data shows that approximately 70% of the existing SCLM may be of Archaean origin [63,64]. The implication for an Archaean SCLM is that most preserved Proterozoic crust overlies the older Archaean SCLM variably refertilized and metasomatized by mantle melts associated with convergent margin and mantle plume processes [63,78].

In general, seismic tomography images can show boundaries of cratons and discontinuities related to the SCLM. These discontinuities are favorable for the repeated ascent of magmas [76–78]. Preserved cratonic regions (SCLMs) can be mapped as areas of high seismic velocity. At a global scale, it has been shown that smaller volumes of magmas directly originating from the mantle are positioned at the craton edge (Figure 4).

Domains of high seismic velocity can represent ancient blocks of metasomatized SCLM within a discrete mantle lithosphere domain flanked by major faults [63,64]. The IOCG Carajás province and Vale do Curaçá and Riacho do Pontal copper districts are located in the transition zone between domains of high and low velocities (Figure 4) and may reflect the refertilization of the SCLM and/or zones of higher lithospheric and mantle temperatures. Ore deposits that originate from the mantle or from transition mantle/crust magmas such as diamond, platinum-group elements (PGEs), Ni-Cu-(PGE), copper porphyry and IOCG deposits are situated along cratonic edges and can be related to the tectonic evolution of the SCLM [63,64,78]. In this context, the extensive gradients flanking either side of the high velocity zone through east-central Brazil should be evaluated in more detail (Figure 4).

Craton edges are characterized by a thinning of lithosphere and are strongly tectonized zones creating transtensional or transpressional sites along translithospheric faults [62]. These major shear or fault zones are frequently used for melt introduction into the crust. For example, IOCG districts in Australia, including the world class Olympic Dam in the Gawler craton and within the Eastern Succession of Mount Isa Inlier in Australia, are related to the presence of large igneous provinces (LIPs) that may contain a considerable amount of intrusive felsic rocks [8,10,71,79–83].

Fertile provinces that lead to the formation of mantle-related world-class deposits require melting of the SCLM on the margins of cratons, which is responsible for magmatic ascent associated high heat flow and volatile flow [25,65]. The deposits occur in long-lived subparallel regional structures that have been the focus of multiple reactivation events [24,26,28,30,34,47]. In the Riacho do Pontal and Vale do Curaçá Copper Districts, structural interpretations show that early thrust zones are reused several times and are overprinted by strike-slip shear zones [47].

7.1.2. Structural Control

Sigmoidal or “SC-shaped” structures are indicative of major shear systems [18,23,25,74,75]. Fractal patterns that mimic “SC” structures are systematically repeated from macro- to microscales. These structures serve as critical pathways for the upward flux of fluids promoting interactions between fluid and rock. Duplex, shear band, and asymmetrical structures are quite common along the shear system. The structural controls and traps used for orogenic gold in shear zones are the same as those used for IOCG deposits [24]. The more important traps for host orebodies include (a) interconnection zones between “SC” structures; (b) fractal second- or third-order “C” structures; (c) bends along shear zones in both horizontal and vertical planes where high-grade breccia are typically hosted; (d) fault intersections highly favorable for host breccia ores; and (e) ductile shear zones reactivated by late brittle faults that enrich older zones and that can generate new mineralized bodies. The permeability and degree of fluid overpressure (where fluid pressure > lithostatic pressure) greatly influence the formation of brecciated zones along shear zones.

Frequently, lithological boundaries between units with different competencies are crucial for hosting high deformation corridors. In this way, zones of contact with competent rocks such as paragneiss, mafic granulite, granulitic orthogneiss, and banded iron formations (BIFs) are usually trapped for the percolation of hydrothermal fluids related to shear zones. In the Vale do Curaçá copper district, considering only the epigenetic IOCG mineralization process, the host rocks are predominantly mafic and felsic granulitic rocks.

The orebodies often assume a sigmoidal shape, as they are often hosted in shear zones [8,11,70]. Often, early, sin and late-tectonic breccia pipe zones are found along hydrothermal IOCG systems. The evolution of IOCG-rich systems entails development by the direct melting of the SLCM, positioning in shear zones initially as pipe breccia, and continuous reworking by shear deformation. Variation in the direction and dipping along shear zones, both horizontally and vertically, acts as a structural trap for both hydrothermal and pipe breccias. Typically, breccia-rich ores are situated in a central hydrothermal system zone in transtensional structures.

7.1.3. Geophysical Implications for Alteration

Hydrothermal alteration is characterized by early high-temperature Na (albite) alteration (500–700 °C; [84]) to lower-temperature K-Fe (< 350 °C) alteration [20,24,27–29]. High-temperature albite alteration can be linked to magmatic-hydrothermal systems [26,82,84,85]. Iron is highly soluble at high temperatures and in saline fluids and is enhanced by increasing H⁺ in the fluid system, resulting in more intense Fe fluxes [84].

Hydrothermal alteration is related to intermediate- to high-temperature fluids in the Riacho do Pontal and Vale do Curaçá districts. The alteration halo extends from 1 to 5 km in width, following the major shear zones. Sodic alteration is more distal and potassic, and calcic and ferric alterations are more proximal in both districts. The southern deposits and Sussuarana, Caraíba, and Surubim mines are related to deeper and high-temperature sodic/potassic hydrothermal alteration in contrast with the Vermelho deposit, in which hydrolytic alteration occurred in shallower zones in the IOCG hydrothermal system as initially described by [5,10]. Typically, a series of magnetic dipoles are linked to shear zones and hydrothermal halos.

The general hydrothermal zoning pattern for IOCG deposits is usually vertical from magnetite-dominant at depth to hematite-dominant at shallower levels [5,10,84–90]. Using this model, it is possible to interpret the Riacho do Pontal District as positioned in the shallowest portion of the IOCG system (Figure 14). Thus, additional work must be performed to identify deeper (or more eroded) areas of the IOCG system related to more magnetic and density targets, such as those identified in the Riacho Seco project.

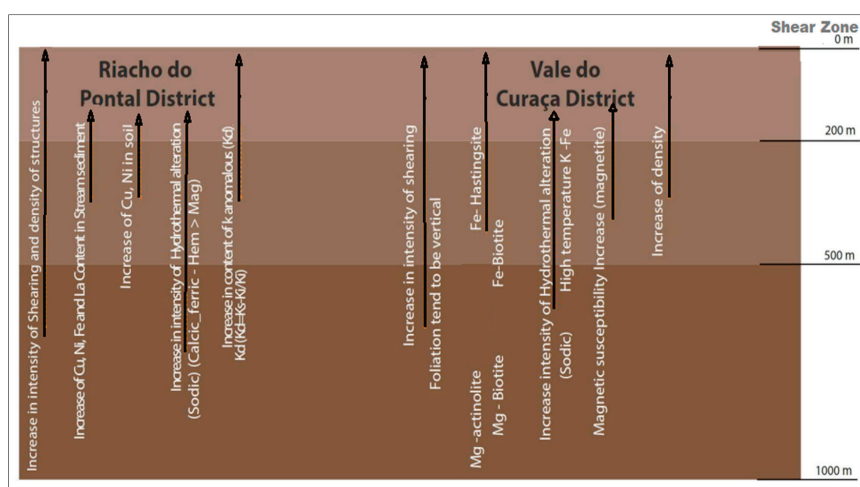


Figure 14. The main geological geochemical, structural, and geophysical vectors illustrating the footprint of the Vale do Curaçá and Riacho do Pontal Copper Districts (modified from [76]).

8. Exploration Potential

Through 2D and 3D mapping, it is possible to verify variation in these parameters with distance in the direction of mines, deposits, or occurrences. An increase or decrease in the intensity of these processes represents vectors towards the IOCG systems studied (Figure 14).

The main footprints of the two IOCG districts are described below:

Riacho do Pontal District:

- (a) Structural: increase in shearing intensity and in the density of structures in the direction of secondary structures. Foliation tends to be vertical. Regardless of the structural regime, most deposits in both districts are controlled by bends in the host rocks.
- (b) Stream sediment and soil: anomalies of Cu, Ni, Fe, and La in stream sediment and Cu (Ni, Ce and La) in soil.
- (c) Low magnetic anomalies related to Kd (Kd-anomalous potassium) and shear zones [24].
- (d) Low magnetic anomalies (abundant hematite related to ore zones).

Vale do Curaçá District:

- (a) The district of Vale do Curaçá is associated regionally with high gravimetric and magnetic anomalies corresponding with the portion west of the ISCO.
- (b) Our studied area is inboard of a relatively high velocity region, bordered eastwards by a low velocity region. The high-velocity region presumably indicates the cratonic area, with the lower velocity region demarcating the craton limit.
- (c) The Caraíba mine bodies are strongly related to magnetic and gravimetric NS trends interpreted to have susceptibility with >0.09 SI and density >0 g/cm³.

Hydrothermal alteration: an increase in the anomalies is related to hydrothermal processes:

- (i) distal sodic alteration and (ii) the mineralized zone intensely related to calcic-ferric alteration.
- (d) Increases in Fe actinolite FeOt/and Fe-biotite (towards more hydrothermalized altered zones (Figure 14).

However, an atypical paradigm remains in the Vale do Curaçá district: the selection of new targets not necessarily hosted in ultramafic rocks. The IOCG system can develop in any host rock at varying depths. A full understanding of the IOCG model for mining companies can greatly expand exploration in the districts via data integration and the processing of structural, geological, and geophysical databases [11,65].

9. Conclusions

Knowledge of the signature of IOCG deposits in Brazil shows that these deposits can be hosted in any type of rock with specific styles of hydrothermal alteration and at different depths. Three-dimensional geological modeling, when combined with geophysical and structural interpretation, can facilitate the spatial and temporal understanding of the hydrothermal systems of the Vale do Curaçá and Riacho do Pontal districts.

The main conclusions obtained from the present study of the Vale do Curaçá and Riacho do Pontal copper districts are as follows:

1. The Vale do Curaçá and Riacho do Pontal copper districts are hosted in distinct geological and tectonic settings, and an older IOCG mineralization event occurring within the São Francisco Craton is related to Palaeoproterozoic (ca 2 to 2.2 Ga) hydrothermal processes. A younger phase of IOCG mineralization in the Neoproterozoic (ca 750 to 570 Ma) has been recognized in the Brazilian mobile belt.
2. Both IOCG districts developed in an arc tectonic setting [50] overprinted by strike slip shear zones.

3. The interpretation of gravimetric and magnetic data shows different magnetic and gravimetric signatures for these two copper districts.
4. The Vale do Curaçá copper district is in a high regional gravimetric domain. It is 110 km in length and 22 km in width and shows a strong relationship with magnetic and gravimetric anomalies. The Caraíba, Surubim, and Vermelhos mines and some copper occurrences are positioned at this site.
5. The regional gravimetric signature of the Riacho do Pontal District is mainly related to a negative Bouguer NW–SE anomaly. This negative Bouguer anomaly represents the collisional suture between the cratonic block and mobile belt Riacho do Pontal. The IOCG occurrences of the Ria4 prospects are found in these low gravimetric signature domains. The rocks, slightly altered, have a density of 2.7–2.78 g/cm³, and the most heavily altered rocks show densities of 2.75–3.1 g/cm³.
6. The magnetic signatures are quite distinct. Copper corridors in the Vale do Curaçá copper district are associated with magnetic anomalies located in the western portion of the Itabuna-Salvador-Curaçá orogen. On the other hand, the copper deposits located in the belt of the Riacho do Pontal district are situated in zones with or without very weak magnetic anomalies.
7. MVI shows two main NNW prospective trends in the Vale do Curaçá district. Trends I and II have a sigmoidal shear shape. These trends are positioned in the contact zone between domains with high magnetization (susceptibility > 0.005 SI) and density anomalies (>0 g/cm³) and show a contrast in density and magnetite content. Trend I is 40 km in length and 10 km in width. It hosts the Caraíba, Surubim, and Vermelho mines and other deposits and is the most important trend for hosting IOCG deposits in the district.
8. The general hydrothermal zoning pattern for IOCG deposits is largely vertical from magnetite-dominant at depth to hematite-dominant in the upper levels. It is possible to interpret the Neoproterozoic Riacho do Pontal district as positioned in the shallowest portion of the IOCG system. Thus, additional work must be performed by searching for deeper (or more eroded) areas of the IOCG system related to more magnetic and dense areas (targets in the northern portion of the Riacho Seco target).
9. Large areas flanking the high-velocity seismic tomography image that already control, on a broad scale, the Carajás IOCG province and Riacho do Pontal and Vale do Curaçá copper districts in Brazil should be evaluated in more detail in a further exploratory program.

Author Contributions: Conceptualization, S.R.B.H. and A.M.S.; Methodology, A.M.S. and F.J.F.F.; Software, S.R.B.H.; Validation, A.M.S., C.B. and F.J.F.F.; Formal Analysis, C.B.; Investigation, S.R.B.H.; Resources, S.R.B.H.; Data Curation, A.M.S.; Writing-Original Draft Preparation, S.R.B.H.; Writing-Review & Editing, A.M.S. and C.B.; Visualization, S.R.B.H.; Supervision, A.M.S. and C.B.; Project Administration, A.M.S.; Funding Acquisition, A.M.S. All authors have read and agreed to the published version of the manuscript.

Funding: A.M. Silva gratefully acknowledges the National Council for Scientific and Technological Development (CNPq) for research grant 307177/2014-9.

Acknowledgments: The authors gratefully acknowledge Vale S. A. for supporting this study. We would like to thank the Vale exploration team for extensive discussions. We would also like to thank Victoria Basileu for providing special support in developing the figures.

Conflicts of Interest: The authors declare no conflict of interest related to the publication of this paper.

References

1. Hayward, N.; Corriveau, L.; Craven, J.A.; Enkin, R.J. Geophysical signature of the NICO Au-Co-Bi-Cu deposit and its iron oxide-alkali alteration system, Northwest Territories, Canada. *Econ. Geol.* **2016**, *111*, 2087–2109. [[CrossRef](#)]
2. Smith, R.J. Geophysics of iron oxide copper-gold deposits. In *Hydrothermal Iron Oxide Copper-Gold and Related Deposits*; Porter, T.M., Ed.; PGC Publishing: Adelaide, Australia, 2002; Volume 2, pp. 357–367.

3. Clark, D.A.; Geuna, S.; Schmidt, P.W. Predictive Magnetic Exploration Models for Porphyry, Epithermal and Iron Oxide Copper-Gold Deposits: Implications for Exploration, and Mining: Commonwealth Scientific and Industrial Research Organization (CSIRO) Exploration and Mining Report. 2013. 1073R. Available online: <https://confluence.csiro.au/download/attachments/26574957/Clark%20etal%202004%20P700%20CSIRO%201073Rs.pdf?version=2&modificationDate=1460597746010&api=v2> (accessed on 24 November 2020).
4. Clark, D.A. Magnetic effects of hydrothermal alteration in porphyry copper and iron-oxide copper-gold systems: A review. *Tectonophysics* **2014**, *624–625*, 46–65. [[CrossRef](#)]
5. Hitzman, M.W.; Oreskes, N.; Einaudi, M.T. Geological characteristics and tectonic setting of proterozoic iron oxide (Cu U Au REE) deposits. *Precambrian Res.* **1992**, *58*, 241–287. [[CrossRef](#)]
6. Pollard, P.J.; Taylor, R.G.; Peters, L.; Matos, F.; Freitas, C.; Saboia, L.; Huhn, S. 40Ar-39Ar dating of Archean iron oxide Cu-Au and Paleoproterozoic granite-related Cu-Au deposits in the Carajás Mineral Province, Brazil: Implications for genetic models. *Miner. Deposita* **2018**, *54*, 329–346. [[CrossRef](#)]
7. Barton, M.D. *Iron Oxide (-Cu-Au-REE-P-Ag-U-Co) Systems: Treatise on Geochemistry*, 2nd ed.; 2014; Volume 13, pp. 515–541. Available online: <https://doi.org/10.1016/B978-0-08-095975-7.01123-2> (accessed on 24 November 2020).
8. Groves, D.I.; Bierlein, F.P.; Meinert, L.D.; Hitzman, M.W. Iron oxide copper-gold (IOCG) deposits through earth history: Implications for origin, lithospheric setting, and distinction from other epigenetic iron oxide deposits. *Econ. Geol.* **2010**, *105*, 641–654. [[CrossRef](#)]
9. O’Driscoll, E.S.T. The application of lineament tectonics to the discovery of the Olympic Dam Cu-Au-U deposit at Roxby Downs, South Australia. *Glob. Tecton. Metallog.* **1985**, *3*, 43–57.
10. Hitzman, M.W. Iron oxide-Cu-Au deposits: What, where, when, and why. In *Hydrothermal Iron Oxide Copper-Gold and Related Deposits: A Global Perspective*; Porter, T.M., Ed.; Australian Mineral Foundation: Adelaide, Australia, 2000; pp. 9–25.
11. Groves, D.I.; Goldfarb, R.J.; Santosh, M. The conjunction of factors that lead to formation of giant gold provinces and deposits in non-arc settings. *Geosci. Front.* **2016**, *7*, 303–314. [[CrossRef](#)]
12. Hühn, S.R.B.; Nascimento, J.A.S. São os depósitos cupríferos de Carajás do tipo Cu-Au-U-ETR? In *Contribuições à Geologia da Amazônia*; Costa, M.L., Angélica, R.S., Eds.; FINEP.SBG-NO: Belém, Brazil, 1997; pp. 143–160.
13. Lindenmayer, Z.G. Evolução geológica do Vale do Rio Curaçá e dos corpos máfico-ultramáficos mineralizados a cobre (Orgs.). In *Geologia e Recursos Minerais do Estado da Bahia: Textos básicos*; In da, H.A.V., Marinho, M.M., Duarte, F.B., Eds.; SME: Salvador, Brazil, 1981; Volume 4, pp. 72–110.
14. Lindenmayer, Z.G. Evolução Geológica do Vale do rio Curaçá e dos Corpos Máfico-Ultramáficos Mineralizados a Cobre. Master’s Thesis, Universidade Federal da Bahia, Salvador, Brazil, 1982.
15. Requia, K.; Stein, H.; Chiaradia, M. Re-Os and Pb-Pb geochronology of the Archean Salobo iron oxide copper-gold deposit, Carajás mineral province, northern Brazil. *Miner. Depos.* **2007**, *38*, 727–738. [[CrossRef](#)]
16. Tallarico, F.H.B.; Figueiredo, B.R.; Groves, D.I.; Kositcin, N.; McNaughton, N.J.; Fletcher, I.R.; Rego, J.L. Geology and shrimp U-Pb geochronology of the Igarapé Bahia deposit, Carajás copper-gold belt, Brazil: An Archean (2.57 Ga) Example of Iron-Oxide Cu-Au-(U-REE) Mineralization. *Econ. Geol.* **2005**, *100*, 7–28. [[CrossRef](#)]
17. Dreher, A.M.; Xavier, R.P.; Taylor, B.E.; Martini, S.L. New geologic, fluid inclusion and stable isotope studies on the controversial Igarapé Bahia Cu–Au deposit, Carajás Province, Brazil. *Miner. Depos.* **2008**, *43*, 161–184. [[CrossRef](#)]
18. Monteiro, L.V.S.; Xavier, R.P.; De Carvalho, E.R.; Hitzman, M.W.; Johnson, C.A.; Filho, C.R.D.S.; Torresi, I. Spatial and temporal zoning of hydrothermal alteration and mineralization in the Sossego iron oxide-copper-gold deposit, Carajás Mineral Province, Brazil: Paragenesis and stable isotope constraints. *Miner. Depos.* **2008**, *43*, 129–159. [[CrossRef](#)]
19. Monteiro, L.V.S.; Caetano, J.; Souza, C.R.; Carvalho, E.R.; Hitzman, M.W. Mineral chemistry of ore and hydrothermal alteration at the Sossego iron oxide-copper-gold deposit, Carajás Mineral Province, Brazil. *Ore Geol. Rev.* **2008**, *34*, 317–336. [[CrossRef](#)]
20. Teixeira, J.B.G.; Silva, M.D.G.D.; Misi, A.; Cruz, S.C.P.; Sá, J.H.D.S. Geotectonic setting and metallogeny of the northern São Francisco craton, Bahia, Brazil. *J. S. Am. Earth Sci.* **2010**, *30*, 71–83. [[CrossRef](#)]

21. Xavier, R.P.; Rusk, B.; Emsbo, P.; Monteiro, L.V.S. Composition and source of salinity of ore-bearing fluids in Cu-Au systems of the Carajás Mineral Province, Brazil. In Proceedings of the 10th biennial meeting of the SGA, Townsville, Australia, 17–20 August 2009; Volume 1, pp. 272–274.
22. Xavier, R.P.; Monteiro, L.V.S.; Souza Filho, C.R.; Torresi, I.; Carvalho, E.R.; Dreher, A.M.; Wiedenbeck, M.; Trumbull, R.B.; Pestilho, A.L.S.; Moreto, C.P.N. The iron oxide copper-gold deposits of the Carajás Mineral Province, Brazil: An updated and critical review. In *Hydrothermal Iron Oxide Copper-Gold and Related Deposits: A Global Perspective, v3—Advances in Understanding of IOCG Deposits*; Porter, T.M., Ed.; PGC Publishing: Adelaide, Australia, 2010; pp. 285–306.
23. DeMelo, G.H.C.; Monteiro, L.V.S.; Xavier, R.P.; Moreto, C.P.N.; Santiago, E.S.B.; Dufrane, S.A.; Aires, B.; Santos, A.F.F. Temporal evolution of the giant Salobo IOCG deposit, Carajás Province (Brazil): Constraints from paragenesis of hydrothermal alteration and U-Pb geochronology. *Miner. Depos.* **2016**, *52*, 709–732. [[CrossRef](#)]
24. Hühn, S.R.B.; Silva, A.M. Favourability potential for IOCG type of deposits in the Riacho do Pontal Belt: New insights for identifying prospects of IOCG type deposits in NE Brazil. *Braz. J. Geol.* **2018**, *48*, 703–771. [[CrossRef](#)]
25. Holdsworth, R.; Pinheiro, R.V. The anatomy of shallow-crustal transpressional structures: Insights from the Archaean Carajás fault zone, Amazon, Brazil. *J. Struct. Geol.* **2000**, *22*, 1105–1123. [[CrossRef](#)]
26. Teixeira, J.B.G.; Silva, M.G.; Lindenmayer, Z.G.; Silva D’el-Rey, L.J.H.; Vasconcelos, P.M.; Reis, C.H.C.; Andrade, J.B.F. Depósitos de cobre do Vale do Rio Curaçá, Bahia. In *Modelos de Depósitos de Cobre do Brasil e Sua Resposta ao Intemperismo*; Brito, R.S.C., Silva, M.G., Kyumjian, R.M., Eds.; CPRM: Brasília, Brazil, 2010; p. 190.
27. Juliani, C.; Monteiro, L.V.; Fernandes, C.M.D. Potencial mineral: Cobre. In *Recursos Mineral do Brasil: Problemas e Desafios*; Academia Brasileira de Ciências: Rio de Janeiro, Brazil, 2016; pp. 134–153.
28. Huhn, S.R.B.; Sousa, M.J.; Filho, C.R.D.S.; Monteiro, L.V.S. Geology of the Riacho do Pontal iron oxide copper-gold (IOCG) prospect, Bahia, Brazil: Hydrothermal alteration approached via hierarchical cluster analysis. *Braz. J. Geol.* **2014**, *44*, 309–324. [[CrossRef](#)]
29. Garcia, P.M.D.P.; Teixeira, J.B.G.; Misi, A.; Sá, J.H.D.S.; Silva, M.D.G.D. Tectonic and metallogenic evolution of the Curaçá Valley Copper Province, Bahia, Brazil: A review based on new SHRIMP zircon U-Pb dating and sulfur isotope geochemistry. *Ore Geol. Rev.* **2018**, *93*, 361–381. [[CrossRef](#)]
30. D’el-Rey, L.J.H.; Oliveira, J.G.; Gaal, E.G. Implication of the Caraíba deposit’s structural controls on the emplacement Brazilian. *J. Geol.* **1996**, *2*, 309–324.
31. Delgado, L.M.; Souza, J.D. *Projeto Cobre Curaçá. Cobre no Vale do Rio Curaçá, Estado da Bahia, Departamento Nacional de Produção Mineral, Seção Geologia Econômica*; Geologia Econômica: Brasília, Brazil, 1981; pp. 7–149. (In Portuguese)
32. Mendonca, R.J. *Updated Mineral Resources and Mineral Reserves Statements of Mineração Caraíba’s Vale do Curaçá Mineral Assets, Curaçá Valley*; Curaca Technical Report: Bahia, Brazil, 2018; p. 284. Available online: https://www.miningdataonline.com/reports/Curaca_Technical_report_2018.pdf (accessed on 24 November 2020).
33. Maier, W.D.; Barnes, S.J. The origin of Cu sulfide deposits at Curaçá Valley, Bahia, Brazil: Evidence from Cu, Ni, Se and platinum—Group element concentrations. *Econ. Geol.* **1999**, *2*, 165. [[CrossRef](#)]
34. Rocha, A.M.R. *Metassomatismo Hidrotermal e Controle da Mineralização Aurífera na Área da Mina Futura, depósito de Caraíba, Bahia*. Ph.D. Thesis, Universidade Federal do Rio Grande do Norte, Natal, Brazil, 1999.
35. Companhia Baiana De Pesquisa Minerais—CBPM. *Informações Geológicas e de Recursos Minerais do Estado da Bahia*. 2011. Available online: <http://www.cbpm.com.br/igba> (accessed on 24 November 2020).
36. Garcia, P.M.P. *Metalogênese dos depósitos cupríferos de Caraíba, Surubim, Vermelhos e Sussuarana, Vale do Curaçá, Bahia, Brasil*. Master’s Thesis, Universidade Federal da Bahia, Salvador, Brazil, 2013.
37. Franklin, J.M.; Lydon, J.W.; Sangster, D.F. Volcanic associated massive sulfide deposits. In *Economic Geology, 75th Anniversary Volume*; Society of Economic Geologists: Denver, CO, USA, 1981; pp. 485–627.
38. Barrie, C.T.; Hannington, M.D. Introduction: Classification of VMS deposits based on host rock composition. In *Volcanic-associated massive sulfide deposits: Processes and Examples in Modern and Ancient Settings. Reviews in Economic Geology, n.8*; Society of Economic Geologists: Denver, CO, USA, 1999; pp. 2–10.
39. Delgado, L.M.; Sousa, J.D.; Projeto Cobre Curaçá. *Geologia Econômica do Distrito Cuprífero do Rio Curaçá. In Relatório Final*; CPRM: Salvador/Bahia, Brazil, 1975. Available online: <http://rigeo.cprm.gov.br/jspui/handle/doc/8838> (accessed on 24 November 2020).

40. Fraguas, S. Evolução da Mina Caraíba, Bahia. In *Simexmin: Novos Casos de Sucesso em Exploração Mineral e Desenvolvimento de Minas no Brasil*; CD-ROM, V Simpósio Brasileiro de Exploração Mineral (Simexmin): Ouro Preto/MG, Brazil, 2012.
41. Barbosa, J.S.F. *The Granulites of the Jequié Complex and Atlantic Coast Mobile Belt, Southern Bahia, Brazil—An Expression of Archean/Early Proterozoic Plate Convergence*; Springer: Dordrecht, the Netherlands, 1990; pp. 195–221. Available online: https://link.springer.com/chapter/10.1007/978-94-009-2055-2_11 (accessed on 24 November 2020).
42. Barbosa, J.S.F.; Dominguez, J.M.L. (Eds.) *Geologia da Bahia: Texto Explicativo*; SGM: Salvador, Brazil, 1996; p. 400.
43. Padilha, A.V.; Melo, R.C. 8th Chapter. Evolução Geológica. In *PLGB. Pintadas. Folha SC-24-Y-D-V. Texto Explicativo*; Melo, R.C., Ed.; Escala 1:100.000. DNPM: Brasília, Brazil, 1991; pp. 129–157.
44. Barbosa, J.; Sabaté, P. Archean and Paleoproterozoic crust of the São Francisco Craton, Bahia, Brazil: Geodynamic features. *Precambrian Res.* **2004**, *133*, 1–27. [[CrossRef](#)]
45. Oliveira, E.P.; Windley, B.F.; McNaughton, N.J.; Pimental, M.; Fletcher, I.R. Contrasting copper and chromium metallogenic evolution of terranes in the Paleoproterozoic Itabuna-Salvador-Curaçá orogen, São Francisco Craton, Brazil: New zircon (SHRIMP) and SmNd (model) ages and their significance for orogen-parallel escape tectonics. *Precambrian Res.* **2004**, *128*, 143–165. [[CrossRef](#)]
46. D’el-Rey, J.H.; Dantas, E.L.; Teixeira, J.B.G.; Laux, J.H.; Silva, M.G. U–Pb and Sm–Nd geochronology of amphibolites from the Curaçá Belt, São Francisco Craton, Brazil: Tectonic implications. *Gondwana Res.* **2007**, *12*, 454–467. [[CrossRef](#)]
47. Alves da Silva, F.C.; Chauvet, A.; Faure, M. Thrusting, wrench-type tectonics and granite emplacement during an early Proterozoic Basin closure: The example of the Itapecuru greenstone belt NE-Brasil. In *Anais II Simp. Geol. do Cráton do São Francisco*; Salvador. Soc. Bras. Geol: Núcleo Bahia/Sergipe, Brazil; pp. 63–66.
48. D’el-Rey, L.J.H. Geologia e controle estrutural do depósito cuprífero Caraíba, Vale do Curaçá, Bahia. *Geologia e Recursos Naturais do Estado da Bahia, SME*, 1985. *Série Textos Básicos* **1985**, *6*, 51–123.
49. Alkmin, F.F.; Brito Neves, B.; Castro, J.A. Arcabouço tectônico do Cráton São Francisco: Uma revisão. In *O Cráton do São Francisco*; Domingues, J.M.L., Misi, A., Eds.; SBG/SGM/CNPq: Salvador, Brazil, 1993; pp. 45–62.
50. Oliveira, R.G. Arcabouço geofísico, isostasia e causas do magmatismo cenozóico da Província Borborema e de sua margem continental (nordeste do Brasil). Ph.D. Thesis, Universidade Federal do Rio Grande do Norte, Natal, Brazil, 2008.
51. Jardim de Sá, E.F. A Faixa Seridó (Província Borborema, NE do Brasil) e o seu significado geodinâmico na Cadeia Brasileira/Pan-Africana. Ph.D. Thesis, Universidade de Brasília, Brasília, Brazil, 1994; 803p.
52. Jardim de Sá, E.F.; Macedo, M.H.F.; Fuck, R.A. Terrenos proterozóicos na Província Borborema e a margem norte do Cráton São Francisco. *Rev. Bras. Geociências* **1992**, *4*, 472–480.
53. Gray, D.R.; Foster, D.A.; Meert, J.G.; Goscombe, B.D.; Armstrong, R.; Trouw, R.A.J.; Passchier, C.W. A Damara orogen perspective on the assembly of southwestern Gondwana. In *West Gondwana: Pre-cenozoic Correlations across the South Atlantic Region*; Pankhurst, R.J., Ed.; Geological Society Special Publications: London, UK, 2008; p. 294.
54. Liégeois, J.-P.; Stern, R.J. Sr–Nd isotopes and geochemistry of granite-gneiss complexes from the Meatiq and Hafafit domes, Eastern Desert, Egypt: No evidence for pre-Neoproterozoic crust. *J. Afr. Earth Sci.* **2010**, *57*, 31–40. [[CrossRef](#)]
55. Neves, B.B.D.B.; Fuck, R.A. The basement of the South American platform: Half Laurentian (N–NW)+half Gondwanan (E–SE) domains. *Precambrian Res.* **2014**, *244*, 75–86. [[CrossRef](#)]
56. De Araujo, C.E.G.; Rubatto, D.; Hermann, J.; Cordani, U.G.; Caby, R.; Basei, M.A.S. Ediacaran 2500-km-long synchronous deep continental subduction in the West Gondwana Orogen. *Nat. Commun.* **2014**, *5*, 5198. [[CrossRef](#)]
57. Ganade, C.E.; Cordani, U.G.; Agbossoumounde, Y.; Caby, R.; Basei, M.A.S.; Weinberg, R.F.; Sato, K. Tightening-up NE Brazil and NW Africa connections: New U–Pb/Lu–Hf zircon data of a complete plate tectonic cycle in the Dahomey belt of the West Gondwana Orogen in Togo and Benin. *Precambrian Res.* **2016**, *276*, 24–42. [[CrossRef](#)]
58. Grainger, C.J.; Groves, D.I.; Tallarico, F.H.; Fletcher, I.R. Metallogenesis of the Carajás Mineral Province, Southern Amazon Craton, Brazil: Varying styles of Archean through Paleoproterozoic to Neoproterozoic base- and precious-metal mineralisation. *Ore Geol. Rev.* **2008**, *33*, 451–489. [[CrossRef](#)]

59. Companhia Baiana De Pesquisa Minerai—CBPM. *Levantamento aerogeofísico Projeto Riacho Seco Andorinhas*; Companhia Baiana De Pesquisa Minerai—CBPM: Salvador, Brazil, 2001; 80p.
60. Reid, A.B. Aeromagnetic survey design. *Geophysics* **1980**, *15*, 973–976. [CrossRef]
61. Ferreira, F.J.F.; De Souza, J.; Bongioiolo, A.D.B.E.S.; De Castro, L.G. Enhancement of the total horizontal gradient of magnetic anomalies using the tilt angle. *Geophysics* **2013**, *78*, 33–41. [CrossRef]
62. Thompson, D.T. EULDPH: A new technique for making computer-assisted depth estimates from magnetic data. *Geophysics* **1982**, *47*, 31–37. [CrossRef]
63. Hinze, W.J.; von Frese, R.R.B.; Saad, A.H. *Gravity and Magnetic Exploration: Principles, Practices, and Applications*; Cambridge University Press: Cambridge, UK, 2013.
64. Begg, G.C.; Griffin, W.L.; Natapov, L.M.; O'Reilly, S.Y.; Grand, S.; O'Neill, C.J.; Poudjom Djomani, Y.; Deen, T.; Bowden, P. The lithospheric architecture of Africa: Seismic tomography, mantle petrology and tectonic evolution. *Geosphere* **2009**, *5*, 23–50. [CrossRef]
65. Begg, G.C.; Ronsky, A.M.H.; Arndt, N.T.; Griffin, W.L.G.; O'Reilly, S.Y.; Hayward, N. Lithospheric, cratonic and geodynamic setting of Ni-Cu-PGE sulphide deposits. *Econ. Geol.* **2010**, *105*, 1057–1070. [CrossRef]
66. Griffin, W.L.; Begg, G.C.; O'Reilly, S.Y. Continental-root control on the genesis of magmatic ore deposits. *Nat. Geosci.* **2013**, *6*, 905–910. [CrossRef]
67. Macleod, I.N.; Ellis, R.G. *Magnetic Vector Inversion, a Simple Approach to the Challenge of Varying Direction of Rock Magnetization*; Australian Society of Exploration Geophysicists, Extended Abstracts: Melbourne, Australia, 2013; pp. 1–4.
68. Telford, W.M.; Geldart, L.P.; Sheriff, R.E. *Applied Geophysics*, 2nd ed.; Cambridge University Press: Cambridge, UK, 1990.
69. Ellis, R.G.; de MacLeod, W.B. Inversion of Magnetic Data for Remanent and Induced Sources. ASEG Extended Abstracts. 2012, pp. 1–4. Available online: <https://doi.org/10.1071/ASEG2012ab117> (accessed on 24 November 2020).
70. Oliveira, R.G.; Medeiros, V.C. Contrastes geofísicos e heterogeneidade crustal do terreno Pernambuco-Alagoas, Província Borborema, NE Brasil. In *SBG-Núcleo Nordeste. Simpósio de Geologia do Nordeste. 17*; Boletim: Recife, Brazil, 2000; Volume 16, p. 176.
71. Corriveau, L.; Mumin, A.H.; Setterfield, T. IOCG environments in Canada: Characteristics, geological vectors to ore and challenges. In *Hydrothermal Iron Oxide Copper-Gold & Related Deposits: A Global Perspective*; Porter, T.M., Ed.; Porter Geoscience Consultancy Publishing: Adelaide, Australia, 2010; Volume 4, pp. 311–344.
72. Potter, E.G.; Corriveau, L.; Kerswill, J.K. Potential for iron oxide-copper-gold and affiliated deposits in the proposed national park area of the East Arm, Northwest Territories: Insights from the Great Bear magmatic zone and global analogs. In *Mineral and Energy Resource Assessment for the Proposed Thaidene Nene National Park Reserve, East Arm of Great Slave Lake, Northwest Territories*; Wright, D.F., Ed.; Open File 7196; Geological Survey of Canada: Ottawa, ON, Canada, 2013.
73. Braitenberg, C. Exploration of tectonic structures with GOCE in Africa and across-continent. *Int. J. Appl. Earth Obs. Geoinf.* **2015**, *35*, 88–95. [CrossRef]
74. Haddad-Martim, P.M.; Carranza, E.J.M.; Filho, C.R.D.S. The Fractal Nature of Structural Controls on Ore Formation: The Case of the Iron Oxide Copper-Gold Deposits in the Carajás Mineral Province, Brazilian Amazon. *Econ. Geol.* **2018**, *113*, 1499–1524. [CrossRef]
75. Costa, I.A. *Aerogeofísica em Carajás pelo Serviço Geológico do Brasil*; CPRM Serviço Geológico do Brasil: Brasília, Brazil, 2017; p. 5. Available online: www.cprm.gov.br (accessed on 24 November 2020).
76. Leshner, M.; Hannington, M.; Galley, A.; Ansdell, K.; Astic, T.; Banerjee, N.; Beauchamp, S.; Beaudoin, G.; Bertelli, M.; Beyer, S.; et al. Integrated multi-parameter exploration footprints of the Canadian Malartic disseminated Au, McArthur River-Millennium unconformity U, and Highland Valley porphyry Cu deposits: Preliminary results from the NSERC-CMIC Footprints Research Network. In *Conference Proceedings for Exploration 17: Exploration in the New Millennium, Sixth Decennial International Conference on Mineral Exploration*; Tschirhart, V., Thomas, M.D., Eds.; Conferências Decenais de Exploração Mineral: University Avenue Toronto, ON, Canada, 2017; pp. 325–347.
77. Barnett, C.T.; Williams, P.M. A radical approach to exploration: Let the data speak for themselves. *Soc. Econ. Geol. Newsl.* **2012**, *1*, 12–17.

78. Cooke, D.R.; Baker, M.; Hollings, P.; Sweet, G.; Chang, Z.; Danyushevsky, L.; Gilbert, S.; Zhou, T.; White, N.C.; Gemmill, J.B.; et al. New advances in detecting the distal geochemical footprints of porphyry systems—Epidote mineral chemistry as a tool for vectoring and fertility assessments. *Soc. Econ. Geol. Spec. Publ.* **2014**, *18*, 127–152.
79. Griffin, W.L.; O'Reilly, S.Y.; Afonso, J.C.; Begg, G.C. The Composition and Evolution of Lithospheric Mantle: A Re-evaluation and its Tectonic Implications. *J. Pet.* **2008**, *50*, 1185–1204. [[CrossRef](#)]
80. Czarnota, K.; Hoggard, M.J.; White, N.; Winterbourne, J. Spatial and temporal patterns of Cenozoic dynamic topography around Australia. *Geochem. Geophys. Geosystems* **2013**, *14*, 634–658. [[CrossRef](#)]
81. Pirajno, F.; Bagas, L. A review of Australia's Proterozoic mineral systems and genetic models. *Precambrian Res.* **2008**, *166*, 54–80. [[CrossRef](#)]
82. McPHIE, J.; Kamenetsky, V.S.; Allen, S.; Courtney-Davies, L.; Agangi, A.; Bath, A. The fluorine link between a supergiant ore deposit and a silicic large igneous province. *Geology* **2011**, *39*, 1003–1006. [[CrossRef](#)]
83. Pirajno, F.; Hoatson, D.M. A review of Australia's Large Igneous Provinces and associated mineral systems: Implications for mantle dynamics through geological time. *Ore Geol. Rev.* **2012**, *48*, 2–54. [[CrossRef](#)]
84. Oliver, N.H.S. Modelling the role of sodic alteration in the genesis of iron-oxide copper-gold deposits, Eastern Mt Isa Block, Australia. *Econ. Geol.* **2004**, *99*, 1145–1176. [[CrossRef](#)]
85. Pollard, P.J. An intrusion-related origin for Cu–Au mineralization in iron oxide–copper–gold (IOCG) provinces. *Miner. Depos.* **2006**, *41*, 179–187. [[CrossRef](#)]
86. Williams, P.J. Iron mobility during synmetamorphic in the Selwyn Range area, NW Queensland: Implications for the origin of iron-stone-hosted Au–Cu deposits. *Miner. Depos.* **1994**, *29*, 250–260. [[CrossRef](#)]
87. McCafferty, A.E.; Phillips, J.D.; Driscoll, R.L. Magnetic and Gravity Gradiometry Framework for Mesoproterozoic Iron Oxide–Apatite and Iron Oxide–Copper–Gold Deposits, Southeast Missouri. *Econ. Geol.* **2016**, *111*, 1859–1882. [[CrossRef](#)]
88. Leão-Santos, M.; Li, Y.; Moraes, R. Application of 3D magnetic amplitude inversion to iron oxide-copper-gold deposits at low magnetic latitudes: A case study from Carajás Mineral Province, Brazil. *Geophysics* **2015**, *80*, B13–B22. [[CrossRef](#)]
89. Belperio, A.; Flint, R.; Freeman, H. Prominent Hill: A hematite-dominated, iron oxide copper-gold system. *Econ. Geol.* **2007**, *102*, 1499–1510. [[CrossRef](#)]
90. Skirrow, R. The Olympic IOCG province (Gaoler craton): Lithospheric to district-scale controls on ore formation, and targeting of IOCG mineral systems. In Proceedings of the Geoconferences IOCG Workshop, Perth, Australia, 29 May 2014; Available online: http://geoconferences.org.au/wp-content/uploads/PR_TeamWA_R_Skirrow.pdf (accessed on 24 November 2020).

Publisher's Note: MDPI stays neutral with regard to jurisdictional claims in published maps and institutional affiliations.



© 2020 by the authors. Licensee MDPI, Basel, Switzerland. This article is an open access article distributed under the terms and conditions of the Creative Commons Attribution (CC BY) license (<http://creativecommons.org/licenses/by/4.0/>).

Article

A Study on the Imaging Method for the Channel Wave Dispersion Curve Variability Function

Wei Wang ^{1,*} , Xing Gao ¹ and Yanhui Wu ²

¹ The State Key Laboratory of Resources and Environmental Information Systems, Institute of Geographic Sciences and Natural Resources Research, Chinese Academy of Sciences, Beijing 100101, China

² State Key Laboratory of Coal Resources and Safe Mining, School of Geoscience and Surveying Engineering, China University of Mining and Technology, Beijing 100083, China

* Correspondence: wang_wei@reis.ac.cn

Abstract: When the channel wave passes through the abnormal body, the dispersion curve appears interval, dislocation, and discontinuity, resulting in the non-standard and large error of the “velocity-frequency” pickup result of the transmitted channel wave dispersion curve, which directly leads to the inaccurate tomography. Therefore, aiming at this problem, the imaging method of dispersion curve variability function is proposed: (1) count the breakpoints of dispersion curve according to three types; (2) set the weighting factor for the breakpoint according to the spectrum curve; (3) the variability function is constructed for the dispersion curve, and the corresponding variation value is obtained; and (4) the variability value is back projected into the imaging grid space to obtain the abnormal body information in the detection area. The example verification results show that the imaging results of this method are accurate and stable, and non-convergence is caused by cyclic iteration, which provides a new imaging mode for the detection of complex structures in coal seams.

Keywords: channel wave; dispersion curve; variability function; imaging



Citation: Wang, W.; Gao, X.; Wu, Y. A Study on the Imaging Method for the Channel Wave Dispersion Curve Variability Function. *Minerals* **2023**, *13*, 50. <https://doi.org/10.3390/min13010050>

Academic Editor: Paul Alexandre

Received: 16 November 2022

Revised: 24 December 2022

Accepted: 25 December 2022

Published: 28 December 2022



Copyright: © 2022 by the authors. Licensee MDPI, Basel, Switzerland. This article is an open access article distributed under the terms and conditions of the Creative Commons Attribution (CC BY) license (<https://creativecommons.org/licenses/by/4.0/>).

1. Introduction

Channel wave seismic detection is a geophysical method that utilizes guided waves formed after multiple reflections in coal seams to detect coal seam structure and lithological changes [1,2]. It has advantages that include a large detection range, high precision, strong anti-interference, and easy recognition of waveform features. Therefore, the channel wave detection technique has gradually become an optimal choice for detecting abnormal bodies, such as faults, collapse columns, dirt bands, and others in underground coal mines [3,4]. There are two stages of progress in the application of channel wave seismic detection techniques in the 21st century. The first phase is the Feasibility Plan for Goaf Geophysical Detection launched by the United States in 2001 that included four research projects that focused on channel wave detection, which has greatly promoted the development of channel wave exploration [5]. The second phase is the key projects supported by the National Natural Science Foundation and led by Teng from 2012, which were critical in leading channel wave study in China, greatly promoting the development of channel wave forward modelling and dispersion curve characters, multiple tomographic imaging methods, applications for channel wave technology, and many other aspects [6–9].

Seismic waves usually travel slower in coal seams than in the surrounding upper and lower rocks. When seismic waves are excited in a coal seam, they spread into the surrounding rocks in the coal seam. As they travel faster in the surrounding rocks than in the coal seam, transmitted waves and reflected waves are generated when the wave rays encounter the interfaces between the coal seam and the surrounding rocks. When the incident angle exceeds the critical angle, total reflection occurs. The seismic waves then propagate and interfere with each other in the coal seam, thus forming channel waves with dispersion characteristics. Their dispersion curves are related not only to the

velocity in the upper and lower surrounding rocks and the velocity in and the thickness and density of the coal seams but also to the types, locations, sizes, and shapes of any abnormal bodies they pass through [10–12]. Yanhui Wu used the ellipse tangent method and transmission tomography information to obtain the interpretation results for channel waves and statistically analyzed the quantity, extended length, and direction of faults interpreted by structure development rules and 3D seismic techniques, further reasonably inferring internal and external distributions and the extended lengths of channel wave detection faults in the working faces [13]. Based on the homogeneity and isotropy condition of the coal seam, Cox and Mason used five different methods to analyze the dispersion of Schwalbach coal mine data and obtained the advantages and differences of different methods. At the same time, it has been proved that the slight discrepancy between theoretical and actual dispersion characteristics could be reduced by increasing the model's complexity [14]. Hu used wave equation reverse time migration imaging technology to image faults and voids in coal seams in 2D model data and to effectively distinguish fluids in mine voids from seismic data [15]. Ge made use of the wide frequency channel wave in the thin coal seam (1.4 m on average), with a frequency of 50 to 5000 Hz, and found that the Airy phase had a typical frequency range of 400–600 Hz with a fairly stable velocity of 975 m/s [16]. By using wavelet transform, the dispersion characteristics of channel wave velocity varying with frequency in thin coal seam are obtained, and the examples prove that the attenuation characteristics of channel wave low frequency can effectively identify goaf and faults in coal seam [17]. Hu analyzed the relationship between the depth and energy distribution of multi-order Love-type channel waves and the group velocity dispersion curve by time–frequency analysis and obtained the phase velocity dispersion curve based on the mathematical relationship between the group and phase velocities [18]. Ji found that the difference between the basic order Rayleigh dispersion curves of vertically anisotropic media and isotropic media is small by analyzing the model data, whereas the difference between the dispersion curves of higher-order modes is large. The difference between the horizontal transversely isotropic medium (HTI) and the isotropic medium is large [19].

Transmission detection usually adopts dispersion curves to determine the traveling velocity (travel time) tomography of the transmitted wave [20,21]. However, when dispersion curves are used for determining travel time or velocity, their shapes will be affected by the coal seam thickness and wave velocity and by any abnormal bodies on the ray path of channel waves [22–24]. When channel waves pass through an abnormal body, the dispersion curves have poorer continuity and are not smooth, making the accurate determination of the travel time impossible and leading to difficulty in determining the travel time based on a fixed frequency. In channel wave tomography, the travel time (velocity) of the Airy phase or the travel time (velocity) information of a certain frequency seismic phase is picked up from the dispersion curve. The inversion calculation algorithm using tomography is as follows [25–27]: Back projection method (BG), conjugate gradient method (CG), Least square QR-factorization (LSQR), Algebraic reconstruction technique (ART), simultaneous iterative reconstruction technique (SIRT), etc. The results of these inversion methods are only relative, and the result values are through to the velocity information of the dispersion curve within the thickness range of coal seam for theoretical inversion. However, it is difficult to determine the degree of influence of geological anomalies on the dispersion characteristics. In actual detection work, determining travel time on complex coal faces is an important link that causes issues for processing personnel. Lacking a unified standard for determining velocity, the imaging results are inconsistent and inaccurate [28–30]. To solve the aforementioned imaging problems, this paper proposes a function that is based on the quantitative description and calculates the variation degrees of dispersion curves and utilizes the tomography method to identify abnormal bodies.

2. Variability Function Method

2.1. Definition of Variability Function

A seismic wave that is excited in the low-velocity coal seam propagates in all directions, encountering the surrounding upper and lower high-velocity rock mass media, resulting in transmission and reflection. When the incident angle exceeds the critical angle, total reflection occurs, and the total reflection wave is reflected by the upper and lower surrounding rocks into the coal seam and propagates forward, forming a channel wave with dispersion characteristics [31,32]. When the channel wave propagates forward, it encounters abnormal bodies, such as collapse columns, faults, and goaves, resulting in changes in the total reflection conditions of the channel wave, leading to intermittent, erratic, and discontinuous channel wave dispersion curves, forming irregular dispersion curves [33,34] that are defined as variance dispersion curves, and the degree of variance is expressed in terms of variability. The number of discontinuity points of the dispersion curve and the corresponding velocity and frequency are used as independent variables to construct a variability function indicating the variation magnitude.

A dispersion curve can be extracted from the transmitted waves received in the underground roadway using narrow band filtering or wavelet transformation. When the transmitted channel wave does not pass through abnormal bodies, the dispersion curve is a continuous smooth curve, close to the theoretically calculated dispersion curve, as shown in Figure 1a. When the transmitted channel wave passes through abnormal bodies, the dispersion curve appears to be intermittent and is an irregular variation curve, as shown in Figure 1b. The velocity in the figure is the ratio of the ray path length to the travel time; thus, the distribution of the velocity values is unequal [35].

2.2. Breaking Point Classification

Comparing the variance dispersion curve with the theoretical dispersion curve (blue curve in Figure 2), the breaking points can be classified into three categories according to the discontinuity of the variance curve: Type I breaking point, in which the variance dispersion curve is intermittent (the frequency is not continuous) but is consistent with the shape of the theoretical dispersion curve (N1 in Figure 2); Type II breaking point, in which the variance dispersion curve is staggered vertically, but the frequency is continuous (N3 in Figure 2); and Type III breaking point, in which the variance dispersion curve is erratic vertically, and the frequency is not continuous (N2 in Figure 2). The dispersion curves are extracted for each transmission channel wave, and the breaking point type of all dispersion curves are identified and the total number of breaking points, N , is counted. Two frequency values are specified at each breaking point. Then, the corresponding frequency values at the i th breaking point are f_{2i-1} , f_{2i} , and $f_{2i-1} \leq f_{2i}$. The frequency at the breaking point and the corresponding velocity change information reflect the magnitude of the dispersion curve variability.

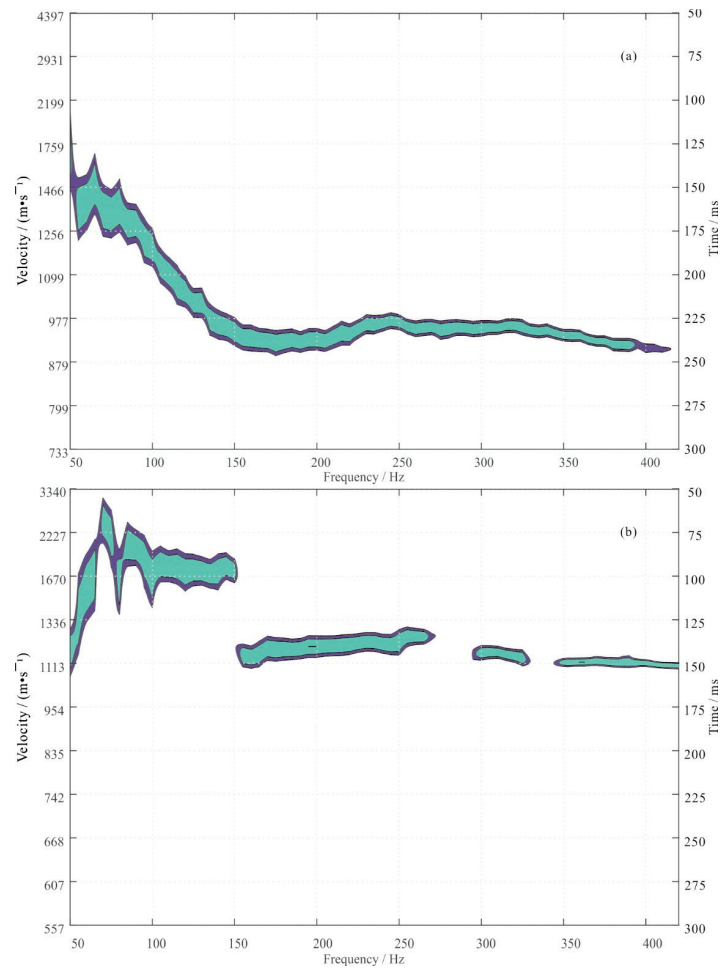


Figure 1. Dispersion curves: (a) continuous smooth dispersion curve and (b) irregular dispersion curve.

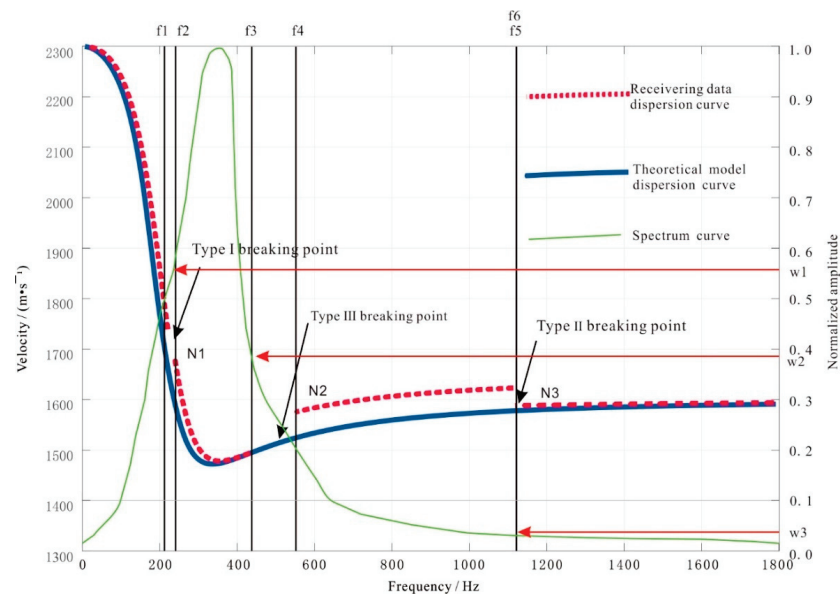


Figure 2. Dispersion curve breaking point classification and weighting factors.

2.3. Weighting Factor

In the variability function, the breaking point position is related to channel wave energy; thus, the normalized amplitude value corresponding to the breaking point position is set as a weighting factor. The Fourier transformation of the channel wave data is

performed, and the amplitudes are normalized to superimpose the spectral curve onto the dispersion curve (green spectral curve in Figure 2).

The three breaking points (N1, N2, N3) in the figure correspond to the three types of breaking points. N1 corresponds to the first type of breaking point and corresponds to two frequencies, f_1 and f_2 . The maximum value in the normalized amplitude of f_1 and f_2 in the spectrum curve is the weighting factor w_1 . Similarly, the weighting factors w_2 and w_3 corresponding to the breaking points N2 and N3 are obtained. That is, the maximum value in the spectrum corresponding to the two frequencies f_{2i-1} and f_{2i} in the i th breaking point of the actual dispersion curve is the weighting factor for that breaking point. From the spectrum curve, the main frequency of the channel wave f_m , and f_a and f_b , which are 0.1 times the amplitudes of the main frequency, are obtained. The difference between them is the spectrum band.

2.4. Construction of the Variability Function

Based on the definition of dispersion curve variability, Equation (1) for the variability for each transmitted channel wave is constructed as

$$d_{S_j R_k}(v, f, n) = \sum_{i=1}^N w_i \left| \frac{v'_{2i} - V_{2i}}{V} \right| + \sum_{i=1}^N w_i \left| \frac{f_{2i} - f_{2i-1}}{F} \right| \tag{1}$$

where d is the variability, R is the receiver point ($k = 1, 2 \dots, K$), S is the source point ($j = 1, 2, \dots, J$) (Figure 3), the total number of breaking points is N , i is the i -th breaking point, w is the weighting factor at the breaking point, V is the transverse wave velocity of the surrounding rock, F is the maximum frequency f_b corresponding to the main frequency interval, v_{2i} is the actual velocity value at frequency f_{2i} in the i th breaking point, and v'_{2i} is the theoretical calculated velocity value at frequency f_{2i} in the i th breaking point.

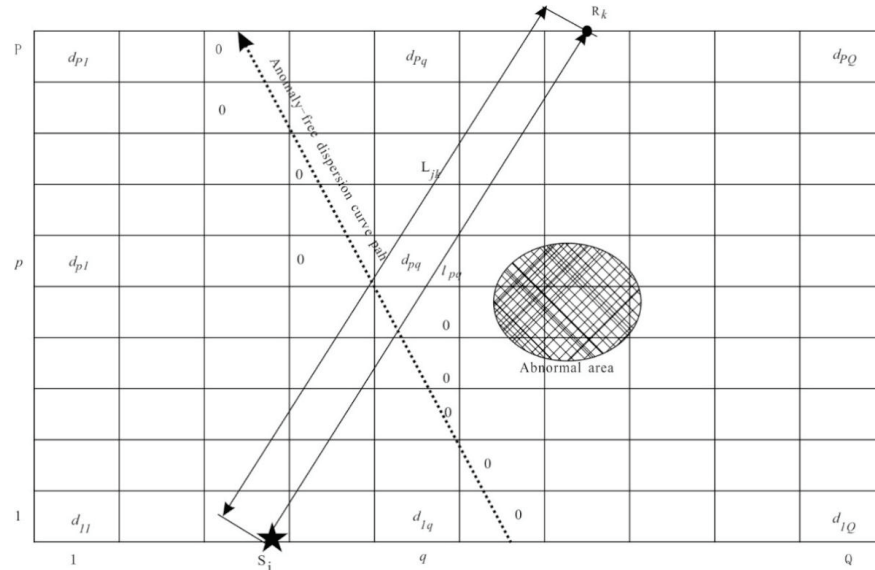


Figure 3. Variability gridding and variability projection.

The first term to the right of the equal sign in Equation (1) indicates the magnitude of the contribution of velocity (time) intermittency to the variability value, and the second term indicates the magnitude of the frequency intermittency contribution to the variability value.

According to the breaking point classification, the first and second terms in the equation take the values of the following:

In a Type I breaking point, the curve is consistent with the shape of the theoretical dispersion curve. Only the frequency f is intermittent and extended consistently with the theoretical frequency. According to the theoretical equation, f_{2i} corresponds to the velocity v'_{2i} ,

and $v'_{2i} = v_{2i}$, (v_{2i} is the velocity corresponding to the dispersion curve of the received data) when the first term in Equation (1) is 0, the second term is not 0.

In a Type II breaking point, the curve is erratic up and down, but the frequency f is continuous. According to the theoretical equation, f_{2i} corresponds to v'_{2i} , with $v'_{2i} \neq v_{2i}$ (v_{2i} is the maximum velocity of frequency f corresponding to the dispersion curve of received data), when the first term in the Equation (1) is not equal to 0, and the second term is 0.

In a Type III breaking point, the curve is erratic vertically, and the frequency f is intermittent. According to the theoretical equation, f_{2i} corresponds to v'_{2i} , with $v'_{2i} \neq v_{2i}$. At this time, the first and second terms in Equation (1) are not 0.

Equation (1) indicates that a greater number of breaking points leads to greater variability; a larger value for d leads to a greater variability value and a greater influence of geologically abnormal bodies, whereas a smaller d leads to less variability and less influence from geologically abnormal bodies. The variability value of the channel wave ray path is 0 when it does not pass through any abnormal bodies. The variability values for the channel wave data are calculated using Equation (1).

2.5. Variability Function Imaging

The detection area is dissected into a rectangular grid, as shown in Figure 3. In this figure, the receiver and source points are located in different lanes, and the channel wave ray path length is the distance L from the source point to the receiver point, and the variability is discretized by the grid. The theoretical dispersion curve variability value is determined by the length of the ray passing through the grid point and the grid point variability value, using Equation (2):

$$d_{jk}^t = \sum_{p=1}^P \left(\frac{l_{pq}^{jk}}{L_{jk}} \times d_{pq} \right), \tag{2}$$

where d_{jk}^t is the theoretical calculated value of the dispersion curve variability of the channel wave at the j th source point and the k th receiver point, L_{jk} is the length of the channel wave path at the j th source point and the k th receiver point, l_{pq}^{jk} is the length of the grid point in row p and column q through which the channel wave at the j th source point and the k th receiver point passes, and d_{pq} is the value of the grid point variability in row p and column q .

Each transmitted channel wave variability value and the theoretical calculated value form the system of Equation (3), and the system of binary linear equations is solved under the least squares conditions to obtain the grid point variability values.

$$\left\{ \begin{array}{l} d_{S_1R_1} = \sum_{p=1}^P \left(\frac{l_{pq}^{11}}{L_{11}} \times d_{pq} \right) \\ d_{S_1R_2} = \sum_{p=1}^P \left(\frac{l_{pq}^{12}}{L_{12}} \times d_{pq} \right) \\ \vdots \\ d_{S_jR_k} = \sum_{p=1}^P \left(\frac{l_{pq}^{jk}}{L_{jk}} \times d_{pq} \right) \\ \vdots \\ d_{S_jR_{k-1}} = \sum_{p=1}^P \left(\frac{l_{pq}^{jK-1}}{L_{jK-1}} \times d_{pq} \right) \\ d_{S_jR_K} = \sum_{p=1}^P \left(\frac{l_{pq}^{jK}}{L_{jK}} \times d_{pq} \right) \end{array} \right. . \tag{3}$$

As can be determined by the application of Equation (1), when the dispersion curve is smooth and continuous, its variance value is 0. Since the defined variability value is greater than or equal to 0, and the grid points through which the slotted wave rays pass have a variability value of 0, the variability value for this grid point in the corresponding initial model is 0, thus reducing the number of unknown solutions to Equation (3). The abnormal-free dispersion curve shown in Figure 3 has a variability value of 0 through the path grid. When using travel time (velocity) tomography, the velocity value magnitudes of the grid points on the same ray path vary, and the total ray travel time is obtained by accumulating the travel times of the grid points; thus, the initial model velocities are unknown. Theoretically, the variability function tomography has fewer unknowns and fewer equations and is computationally efficient.

The solution process: (1) according to the channel wave ray path, the variation value is allocated to the grid points passing by, the initial variation model is obtained, and the theoretical grid point variation value is calculated; thus, (2) calculate the variation correction amount of ray passing through each grid area; (3) add the above results to the initial variability to generate a new variability; (4) and the variation value shall be recalculated and compared with the actual variation value until the minimum error condition is met.

3. Example

3.1. Introduction to the Work Area and Data Collection

The above method was applied to a channel wave detection example. The work area of the channel wave seismic detection is a Mine 090606 working face (Figure 4) that has a stable coal seam thickness of 4.1–4.3 m. The working face roadway revealed five collapse columns in Figure 4 marked with red circles, plus one collapse column determined from 3D seismic speculation in Figure 4 marked with dotted line. The abnormal body detection target is the collapse column. According to the detection task, 27 source points and 24 receiver points were set up in the upper and lower lanes of the working face, respectively, with the source point distance being 10 m and the receiver point distance being 15 m. SUMMIT-II channel wave seismic recording and double-component velocity detectors were used for the receiver.

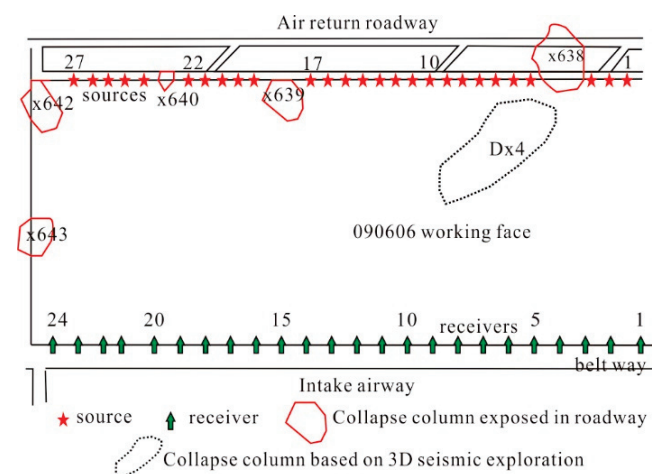


Figure 4. In-seam seismic observation system on the working face.

The red stars mark source point locations, and the green arrows mark the receiver point locations.

3.2. Data Processing

Direct P-wave, S-wave, and channel wave signals can be identified from the seismic records (Figure 5a). Dispersion analysis and spectral analysis of the channel waves were conducted by the dispersion curve variability method to determine the type of break-

ing point and its weighting factor in the spectral curve (Figure 5b). For the theoretical dispersion curve calculation, a smooth and continuous dispersion curve from the actual channel seismic record was used (Figure 5b red curve). In Figure 5b, the f_a is 110 Hz, f_b is 410 Hz, and the F is 300 Hz, the V is the S velocity, 2600 m/s. The path length is 198.8 m (shot No. 10 with receiver No. 18), and the variability parameters for the n th trace of the n th source are shown in Table 1.

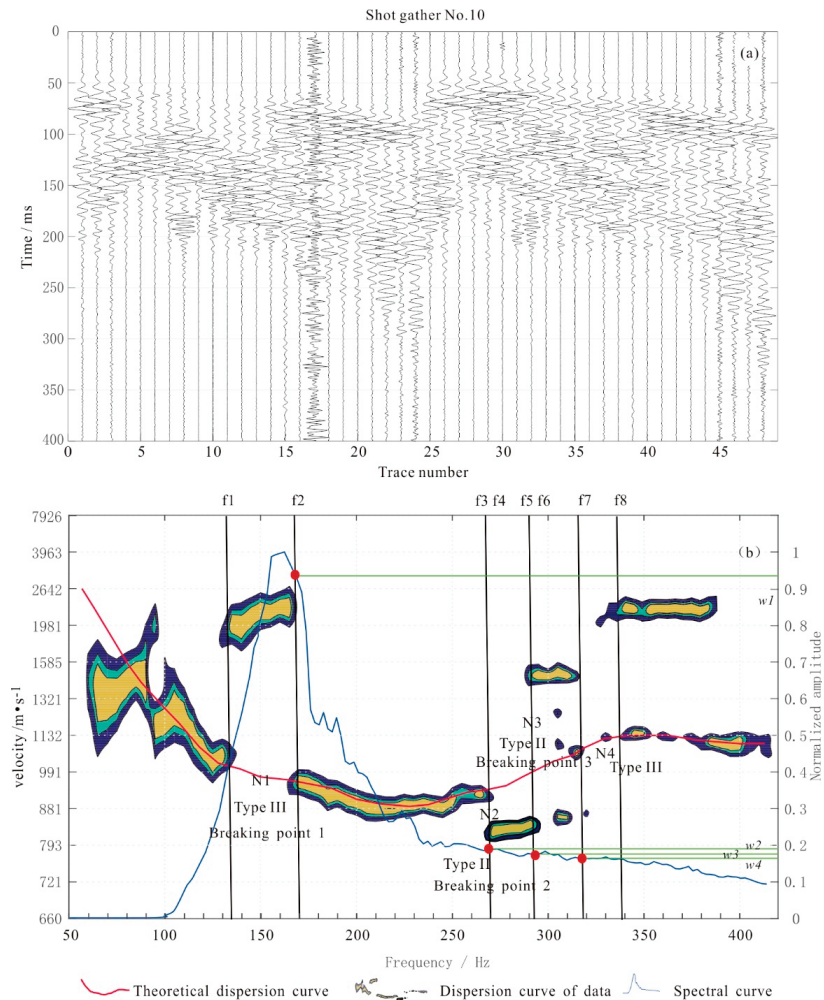


Figure 5. (a) Shot gather No. 10; (b) Signal dispersion curve for the 10th source point of the 18th receiver point; the theoretical dispersion curve (red curve), and the spectral curve (blue curve). Airy phase frequency, 230 Hz; velocity, approximately 900 m/s.

Table 1. Variability Parameters.

Breaking Point Number	Breaking Point Type	Theoretical Breaking Point Velocity (m/s) /Time (ms)	Practical Breaking Point Velocity (m/s) and Time (ms)	Breaking Point Frequency1 (Hz)	Breaking Point Frequency2 (Hz)	Weighting Factor
1	III	967/205.5	2298/86.5	135	170	0.935
2	II	929/214	808/246	270	270	0.190
3	II	947/210	824/241	292	292	0.175
4	III	1156/172	2185/91	319	349	0.160

In the actual calculation of the variation value, we do not need to identify the break-point type but only need to extract the frequency, velocity, normalized amplitude value of the corresponding frequency, and the velocity value at the breakpoint of the theoretical

dispersion curve, and we bring these parameters into the calculation Equation (1) for automatic identification and calculation.

3.3. Imaging Results

By incorporating the dispersion curve variability parameter in the table into Equation (1), the variability value (0.6842) of the channel wave in the source No. 10 and receiver No. 18 is obtained. Similarly, the variability values of all channel wave data were obtained and incorporated into Equation (3) to obtain the variability distribution in the detection area, as shown in Figure 6a, whereas Figure 6b shows the travel time imaging results.

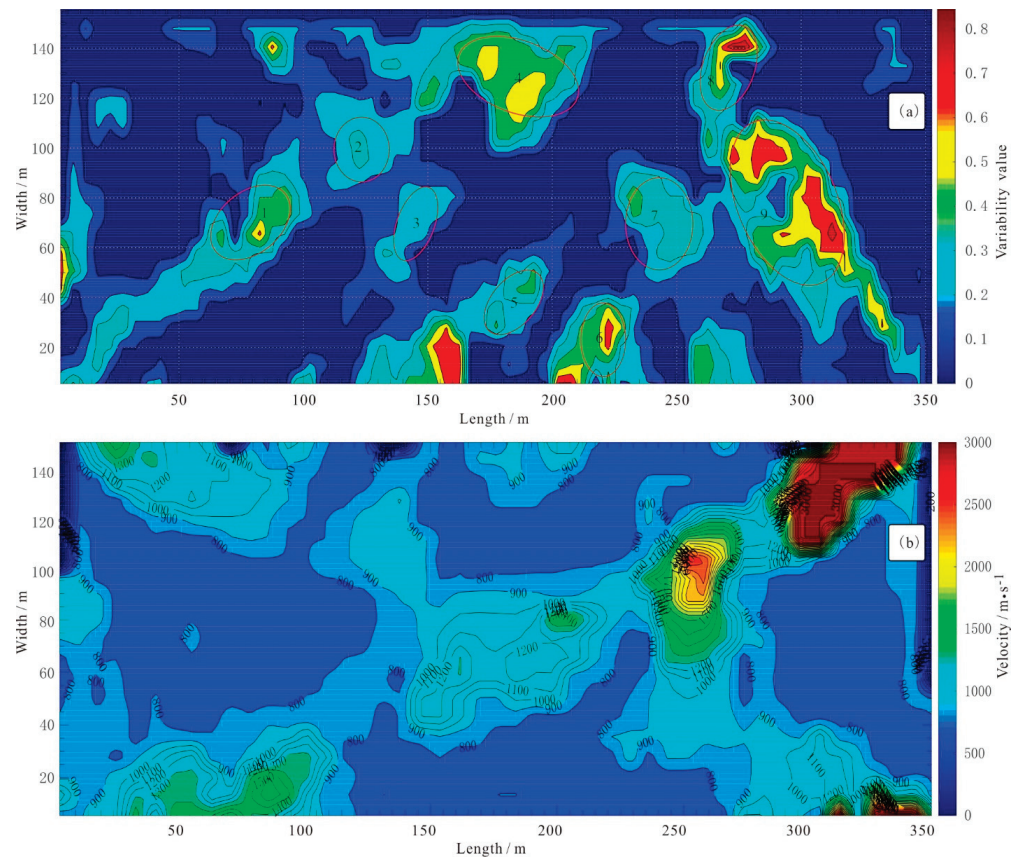


Figure 6. (a) Channel wave variability value distribution on Working Face 090606. Red circles indicate abnormal areas of collapse columns; (b) Travel time imaging results.

The CT imaging results of the variability function show that there are anomalies near the positions of the collapse columns X638, X639, X640, X639, and X640 exposed in the air return roadway and the laneway of the working face, and the variability coefficient is relatively high. At the same time, nine regions of variability anomalies are revealed in the working face, with different sizes and shapes of the anomalies. From left to right, the anomaly bodies are numbered 1–9. According to geological data, all 9 anomaly bodies are interpreted as collapse columns. The mining verifies that No. 1–9 collapse columns exist. Among them, No. 1, 2, 3, 5, 6, and 8 collapse columns are small in scale, with the long axis being less than 30 m. No. 4, 7, and 9 collapse columns are large in scale, with the long axis being greater than 40 m. Among them, No. 9 collapse column has a long axis of 70 m and a short axis of 40 m. The positions of No. 7, 8, and No. 9 collapse columns are close to the DX4 positions speculated by the surface 3D seismic, and the channel wave detection results are more accurate. Collapse pillars No. 1–9 were verified by back mining with a positional deviation of less than 5 m.

During travel time tomography, the travel time or velocity information picked up generally corresponds to a fixed frequency. When picking up travel time at a fixed frequency

of 125Hz, as shown in Figure 6b, the picking error is large, which affects the imaging results. The CT imaging results of velocity reveal that abnormal areas at the collapse pillars X638, X639, X640, X642, and X643 locations exposed in the working face return airways and laneway, with relatively high wave velocities (all greater than 1100 m/s), but the images are deviations from the correct positions. A number of abnormal areas with obvious high velocities were found within the working face and were errors with the verification results (Figure 6b).

It can be seen from the comparative analysis of Figure 6a,b as well as the mining verification results that the error of the variability function imaging method is small and more accurate. When the coal seam is stable, the inversion of the abnormal body is better than conventional tomography. The function construction can effectively reflect the combination characteristics of the time domain and frequency domain and carry out variance imaging through the constraint of theoretical velocity on actual and the breakpoint feature of the abnormal body, with errors being reduced and results more stable.

4. Conclusions

In this paper, based on the changes in the dispersion curve when the channel wave passes through an abnormal body, the variability imaging method is proposed. The variability is related not only to the number and type of breaking points in the dispersion curve but also to the velocity, frequency, and the corresponding spectral value of the breaking point position. Thus, the variability function imaging method has not only kinematic characteristics but also kinetic characteristics. The variability function tomography method effectively reduces the number of unknowns and improves computational efficiency. The method overcomes the disadvantage of the uncertainty of extracting travel time information in velocity tomography and quantitatively analyzes the breakpoints of the dispersion curve, which reduces the error caused by processors and makes the calculation result more stable. Through example calculations, the method is able to identify irregular collapse columns. The imaging result is more accurate to explain the location and shape of the DX4 anomaly area than the result delineated by 3D seismic, and the delineated collapse column anomaly is consistent with the recovery verification.

Author Contributions: Conceptualization, W.W.; methodology, W.W.; software, W.W.; validation, W.W., X.G. and Y.W.; formal analysis, W.W. and Y.W.; investigation, W.W., X.G. and Y.W.; Writing—original draft preparation, W.W. and Y.W.; Writing—review and editing, W.W. and Y.W.; Funding acquisition, W.W. All authors have read and agreed to the published version of the manuscript.

Funding: This research is supported by NSFC (grant no. 41641040).

Data Availability Statement: Data supporting the reported results can be found in the literature cited in the manuscript.

Conflicts of Interest: The authors declare no conflict of interest.

References

1. Evison, F.F. A Coal Seam as a Guide for Seismic Energy. *Nature* **1955**, *176*, 1224–1225. [[CrossRef](#)]
2. Krey, T.C. Channel Waves as a Tool of Applied Geophysics in Coal Mining. *Geophysics* **1963**, *28*, 701–714. [[CrossRef](#)]
3. Buchanan, D.J. The propagation of attenuated SH channel waves. *Geophys. Prospect.* **1978**, *26*, 16–28. [[CrossRef](#)]
4. Kerner, C.; Dresen, L. The influence of dirt bands and faults on the propagation of Love seam waves. *J. Geophys.* **1985**, *57*, 77–89.
5. MHA Quecreek #1 Mine Inundation Investigation Report; Mine Safety and Health Administration office of the Administrator Coal Mine Safety and Health: Philadelphia, PA, USA, 12 August 2003.
6. Wang, W.; Shi, L.; Gao, X. Research of LANCANG River Basin Data Information Sharing System Based on Metadata and Dataset Management. *J. Ind. Intell. Inf.* **2013**, *1*, 59–62. [[CrossRef](#)]
7. Qiao, Y.H.; Teng, J.W. Calculation method for the orerial dispersion curves of seismic channel waves considering variation of coal seam thickness and analysis of dispersion characteristics. *Chin. J. Geophys.* **2018**, *61*, 3374–3384. (In Chinese)
8. Wang, W.; Gao, X.; Li, S.Y.; Teng, J.W.; Li, Y.Y. Fault Detection in Coal Seam by the Channel Wave Method. *Sci. J. Earth Sci.* **2014**, *4*, 27–36.
9. Hu, G.Z.; Teng, J.W.; Pi, J.L.; Wang, W.; Qiao, Y.H. In-seam seismic exploration techniques—a geophysical method predicting coal-Mine disaster. *Prog. Geophys.* **2013**, *28*, 439–451. (In Chinese)

10. Wang, W.; Gao, X.; Li, S.Y.; Yue, Y.; Hu, G.Z.; Li, Y.Y. Channel wave tomography method and its application in coal mine exploration: An example from Henan Yima Mining Area. *Chin. J. Geophys.* **2012**, *55*, 1054–1062. (In Chinese)
11. Wang, B.; Liu, S.; Zhou, F.; Zhang, J.; Zheng, F. Diffraction Characteristics of Small Fault ahead of tunnel face in coal roadway. *Earth Sci. Res. J.* **2017**, *21*, 95–99. [[CrossRef](#)]
12. Feng, L.; Zhang, Y. Dispersion calculation method based on S-transform and coordinate rotation for Love channel waves with two components. *Acta Geophys.* **2017**, *65*, 757–764. [[CrossRef](#)]
13. Wu, Y.H.; Wang, W.; Teng, J.W.; Zhu, G.W.; Gao, X. Application and research on technology of channel wave seismic transmission and reflection method: An example from Shanxi Longquan mining area. *Prog. Geophys.* **2021**, *36*, 1325–1332. (In Chinese)
14. Cox, K.B.; Mason, I.M. Velocity Analysis of the Sh-Channel Wave in the Schwalbach Seam at Enseldorf Colliery1. *Geophys. Prospect.* **1988**, *36*, 298–317. [[CrossRef](#)]
15. Hu, Y.; Mcmechan, G.A. Imaging mining hazards within coalbeds using prestack wave equation migration of in-seam seismic survey data: A feasibility study with synthetic data. *J. Appl. Geophys.* **2007**, *63*, 24–34. [[CrossRef](#)]
16. Ge, M.; Wang, H.; Hardy, H.; Ramani, R. Void detection at an anthracite mine using an in-seam seismic method. *Int. J. Coal Geol.* **2008**, *73*, 201–212. [[CrossRef](#)]
17. Yang, Z.; Ge, M.-C.; Wang, S.-G. Characteristics of transmitting channel wave in a coal seam. *Min. Sci. Technol.* **2009**, *19*, 331–336. [[CrossRef](#)]
18. Hu, Z.; Zhang, P.; Xu, G. Dispersion features of transmitted channel waves and inversion of coal seam thickness. *Acta Geophys.* **2018**, *66*, 1001–1009. [[CrossRef](#)]
19. Ji, G.; Zhang, P.; Wu, R.; Guo, L.; Hu, Z.; Wu, H. Calculation method and characteristic analysis of dispersion curves of Rayleigh channel waves in transversely isotropic media. *J. Soc. Explor. Geophys.* **2020**, *85*, C187–C198. [[CrossRef](#)]
20. Wu, Y.; Zhu, G.; Wang, W. Precise prediction of the collapse column based on channel wave spectral disparity characteristics and velocity tomography imaging. *J. Geophys. Eng.* **2022**, *19*, 326–335. [[CrossRef](#)]
21. Wu, Y.H.; Zhu, G.W.; Wang, W.; Zhang, M.B.; Gao, Z. Quantitative Evaluation of Faults by Combined Channel Wave Seismic Transmission-Reflection Detection Method. *Minerals* **2022**, *12*, 1022. [[CrossRef](#)]
22. Mason, I.M.; Buchanan, D.J.; Booer, A.K. Channel wave mapping of coal seams in the united kingdom. *Geophysics* **1980**, *45*, 1131–1143. [[CrossRef](#)]
23. Buchanan, D. The Scattering of Sh-Channel Waves by a Fault in a Coal Seam. *Geophys. Prospect.* **1986**, *34*, 343–365. [[CrossRef](#)]
24. Wang, B.; Liu, S.; Zhou, F.; Hu, Z.; Huang, L.; Jiang, Y. Dispersion Characteristics of SH Transmitted Channel Waves and Comparative Study of Dispersion Analysis Methods. *J. Comput. Theor. Nanosci.* **2016**, *13*, 1468–1474. [[CrossRef](#)]
25. Hestenes, M.R.; Stiefel, E.L. Methods of Conjugate Gradients for Solving Linear Systems. *J. Res. Natl. Bur. Stand.* **1952**, *49*, 409–436. [[CrossRef](#)]
26. Gordon, R.; Bender, R.; Herman, G.T. Algebraic Reconstruction Techniques (ART) for three-dimensional electron microscopy and X-ray photography. *J. Theor. Biol.* **1970**, *29*, 471–481. [[CrossRef](#)]
27. Gilbert, P. Iterative methods for the reconstruction of three dimensional objects from their projections. *J. Theor. Biol.* **1972**, *36*, 105–117. [[CrossRef](#)]
28. Ji, G.; Li, H.; Wei, J.; Yang, S. Preliminary study on wave field and dispersion characteristics of channel waves in VTI coal seam media. *Acta Geophys.* **2019**, *67*, 1379–1390. [[CrossRef](#)]
29. Teng, J.W.; Li, S.Y.; Jia, M.; Lian, J.; Liu, G.D.; Wang, W.; Volker, S.; Feng, L.; Yao, X.S.; Wang, K.; et al. Research and application of in seam seismic survey technology for disaster a using potential geology anomalous body in coal seam. *Acta Geol. Sin. Engl. Ed.* **2019**, *94*, 10–26. [[CrossRef](#)]
30. Rader, D.; Schott, W.; Dresen, L.; Ruter, H. Calculation of Dispersion Curves and Amplitude-Depth Distributions of Love Channel Waves in Horizontally-Layered Media. *Geophys. Prospect.* **1985**, *33*, 800–816. [[CrossRef](#)]
31. Edward, S.A.; Asten, M.W.; Drake, L.A. P-SV wave scattering by coal seam inhomogeneities. *Geophysics* **1985**, *50*, 214–223. [[CrossRef](#)]
32. Cheng, J.Y.; Ji, G.Z.; Zhu, P.M. Love channel-waves dispersion characteristic analysis of typical coal models. *J. China Coal Soc.* **2012**, *37*, 67–72. (In Chinese with English Abstract)
33. Buchanan, D.J.; Jackson, P.J.; Davis, R. Attenuation and anisotropy of channel waves in coal seams. *Geophysics* **1983**, *48*, 133–147. [[CrossRef](#)]
34. Krey, T.; Arnetzl, H.; Knecht, M. Theoretical and practical aspects of absorption in the application of in-seam seismic coal exploration. *Geophysics* **1982**, *47*, 1645–1656. [[CrossRef](#)]
35. Wu, G.Q.; MA, Y.L. Research on the Interpretation Method of Channel Waves for Various Abnormal Bodies in Geologically Transparent Working Faces. *Coal Sci. Tech.* **2021**, *49*, 1–13.

Disclaimer/Publisher's Note: The statements, opinions and data contained in all publications are solely those of the individual author(s) and contributor(s) and not of MDPI and/or the editor(s). MDPI and/or the editor(s) disclaim responsibility for any injury to people or property resulting from any ideas, methods, instructions or products referred to in the content.

Article

Application of Historical Geophysical Materials in Searching for Cu-Ag Ore Deposits—A New Direction of Research

Stanisław Speczik ^{1,2}, Lidia Dziewińska ³, Waldemar Józwiak ² and Krzysztof Zieliński ^{2,*} 

¹ Department of Geology, University of Warsaw, Żwirki i Wigury 93, 02-089 Warsaw, Poland; s.speczik@uw.edu.pl

² Miedzi Copper Corp, Al. Jerozolimskie 96, 00-807 Warsaw, Poland; wjozwiak@miedzicopper.com

³ Geotechnology Division, Mineral and Energy Economy Research Institute of the Polish Academy of Sciences, J. Wybickiego 7A, 31-261 Kraków, Poland; lidiad@interia.pl

* Correspondence: kzielinski@miedzicopper.com; Tel.: + 48-22-256-3526

Received: 22 July 2020; Accepted: 16 August 2020; Published: 18 August 2020



Abstract: This paper presents a new instrument in geological exploration, which uses historical geophysical data for the indication of potential zones of the occurrence of Cu-Ag ore, based on the example of the newly discovered Nowa Sól deposit in south-western Poland. Basic historical seismic and gravimetric data were applied along with transformed maps. The new method of effective reflection coefficients (ERC) allowed the utilization of archival seismic records for a more precise determination of the most vaguely traced interfaces within the Permian Zechstein unit. Compared to an amplitude-based seismic section, an ERC section is characterized by its highly increased resolution of imaging. The tracing of changes in the facies and the tectonics of Zechstein sediments, particularly in a zone of their contact with Rotliegend rocks, along with the new ERC method, enabled the establishing of precise locations of prospecting boreholes. The combined use of ERC and historical well logs also allowed more precise identification of the shape of oxidized areas and the adjacent orebodies.

Keywords: Fore-Sudetic Monocline; the Nowa Sól copper and silver deposit; geophysical data processing; effective reflection coefficients; seismic survey; gravimetry

1. Introduction

A new direction of research involving the use of historical geophysical data for the indication of prospective zones of Cu-Ag ore is presented based on the example of the newly documented Nowa Sól deposit (Figure 1).

At the first stage of its exploration project in the Nowa Sól, Jany, Wilcze and Zatonie concession areas, Miedzi Copper Corp. (MCC, Vancouver, BC, Canada; with a local office in Warsaw, Poland) performed extended analyses of existing historical geophysical data. The quality of these abundant data did not allow their direct application to ore prospecting. Therefore, the new effective reflection coefficients (ERC) method was proposed as a means to trace the potential zones of Cu-Ag ore [1–3]. The locations of prospecting boreholes (Figure 2) were established after the reprocessing of geophysical data based on this new methodology. Comparison of the results of ERC and the drilled boreholes confirmed the usefulness of its application.

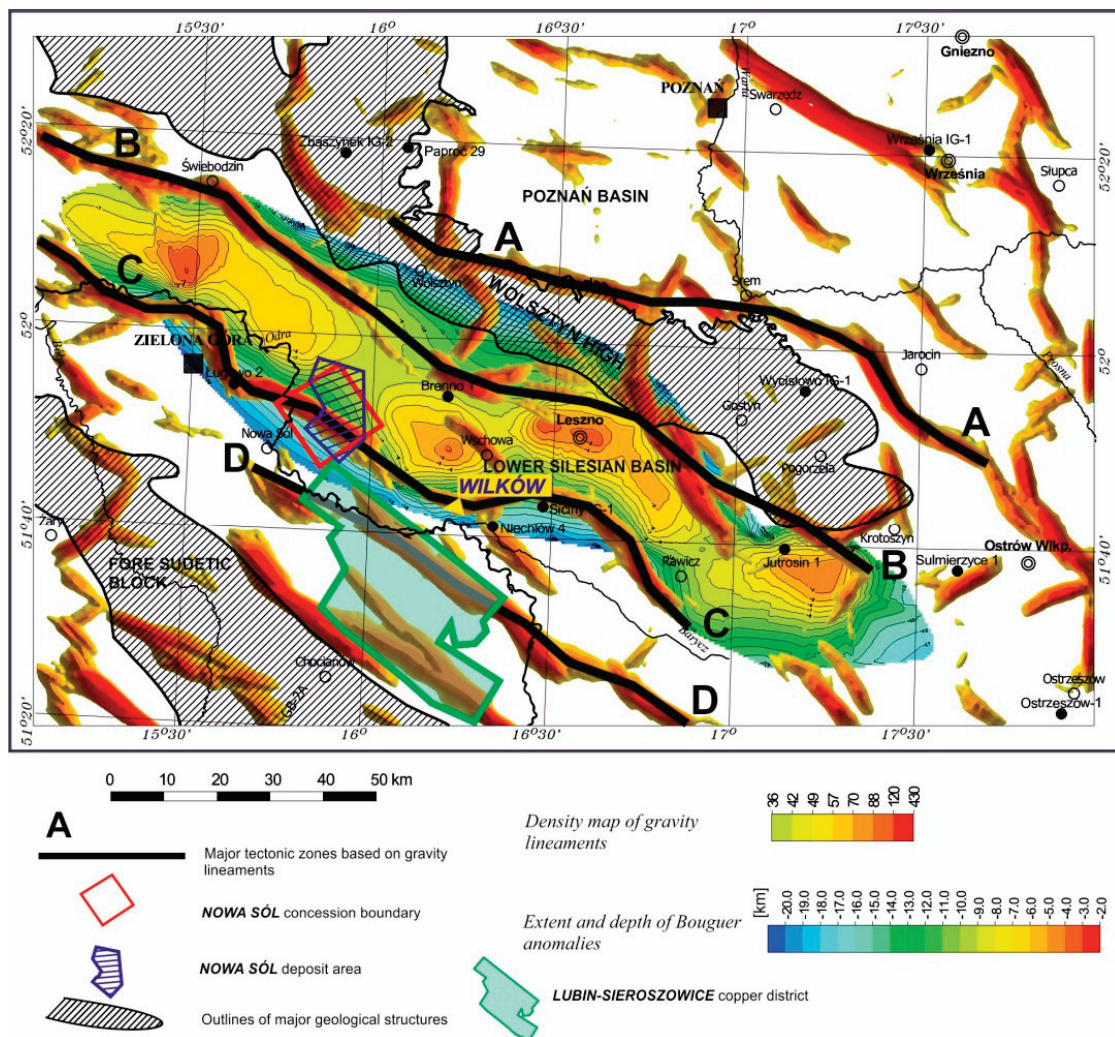


Figure 1. Interpretative gravity map presenting the surroundings of the Nowa Sól deposit.

In this study, the determination of the potential of copper and silver mineralization in the Zechstein copper-bearing series based on the demarcation of the most prospective, as well as possibly negative zones, focused on an area which had not been explored by drilling. The methods of gravimetry and seismic reflection were applied for the accomplishment of this task. An assessment of prospects in the region of the Fore-Sudetic Monocline and the selection of areas for the exploration of Cu-Ag ore, as well as the choice of optimal locations for the planned boreholes required the following steps:

1. The development and interpretation of gravimetric transformed maps of residual anomalies and maps presenting the directions of zones of tectonic and lithological discontinuities,
2. An analysis of the results of on-site work in terms of selecting seismic reflection lines for application of the new method of effective reflection coefficients (ERC),
3. For selected seismic profiles—application of the method of transforming two-way time wave-based sections into ERC sections, to obtain an image with higher resolution compared to a wave-based image, primarily for interfaces related to the Permian Zechstein sediments, in particular the basal Zechstein 1 (Werra) Kupferschiefer-limestone-anhydrite series.
4. Geophysical and geological interpretation of the resulting seismic sections in correlation with the results of geophysical borehole logging. Particular attention paid to the interval comprising Zechstein sediments (P2), including the zone of contact with Rotliegend sediments (P1). Correlation of drilling and ERC seismic data with data from lithological and parametric borehole logs.

5. An analysis of results with respect to the indication of potential zones of copper-silver orebodies in the Zechstein copper-bearing series, aimed at targeting exploration boreholes.

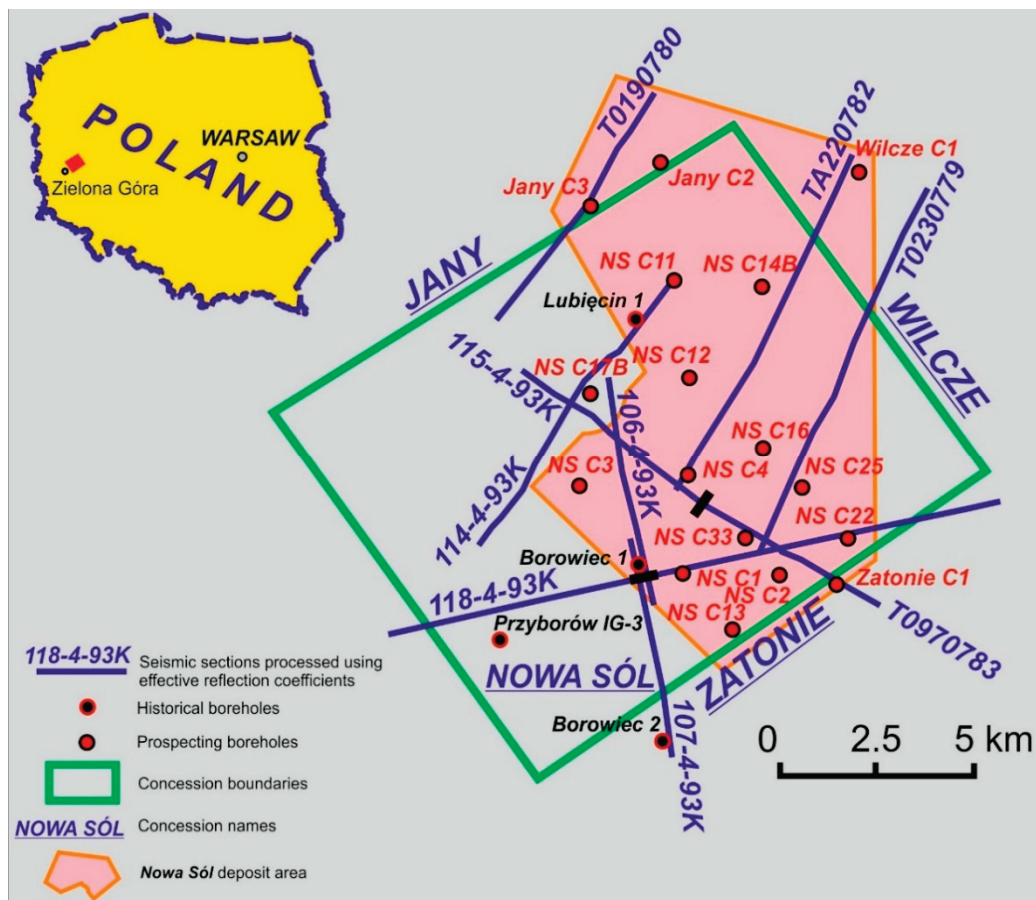


Figure 2. Location of seismic sections reinterpreted using the effective reflection coefficients (ERC) method, as well as historical and prospecting boreholes within the boundaries of the Nowa Sól concession area and deposit.

2. Geological Setting

The research area is located in Poland, in the south-western part of the Fore-Sudetic Monocline, on the southern slope of the Wolsztyn High (Figure 1). This region is interpreted as the eastern extension of the Rheno-Hercynian (RH) and Saxo-Thuringian (ST) zones demarcated within the Variscan orogen of Germany, as well as the Mid-German Crystalline Rise (MGCR) [4–6]. In Poland and Germany, these units are associated with the occurrence of mineral deposits [7–9].

The boundary between the Fore-Sudetic Monocline and the Fore-Sudetic block extends along the Middle Odra fault zone, delimited NE and SW by a complex system of tectonic discontinuities. These faults mark the boundaries of a horst located in the south, whose interior consists of crystalline rocks described as the Middle Odra Metamorphic Complex.

The Wolsztyn High is a Variscan structural palaeo-element, constituting a central part of fragmented tectonic elevations extending from Brandenburg in the west to the Pogorzela High in the south east. During the Permian, this pronounced tectonic structure separated two Rotliegend sedimentary basins—the Lower-Silesian Basin (of Zielona Góra) in the southwest from the Poznań Basin in the northeast, to which it delivered material during erosion [10]. These geological units represent deep structures forming a sub-Permian substrate of the Fore-Sudetic Monocline [4]. Information acquired from boreholes and the results of seismic surveys in the area of the monocline made it possible to distinguish the following structural complexes: Caledonian, comprising Cambrian, Ordovician and

Silurian rocks; Variscan, formed by Devonian and Carboniferous sediments; Permian and Mesozoic cover rocks; as well as Palaeogene, Neogene and Quaternary sediments. The direct substratum of the platform cover of the Fore-Sudetic Monocline consists of folded Carboniferous rocks. They represent a fragment of internal/external Variscan orogenic terranes [11] located between the fault zones of Middle Odra (to the south) and Dolsk (to the north), structures with a WNW-ESE direction.

Folded Variscan rocks are overlain by Rotliegend sediments (P1), consisting of sedimentary and volcanic series. The lower sedimentary series comprises mudstones and claystones with sandstone beds. Sandstones classified as the so-called Weissliegend occur in the top part. The rocks of P1 are overlain by carbonates, sulphates and salts of the Zechstein (P2), with a deepening trend of its bottom surface from the south to the north. Permian rocks are overlain by Mesozoic sediments—primarily Triassic. Sub-Permian Palaeozoic rocks are characterized by discontinuous tectonics. Compared to the tectonics of the Variscan unit, younger strata are characterized by their relatively undisturbed position and generally monoclinal dip towards the N and NE.

The Zechstein sediments in the area of the Fore-Sudetic Monocline are represented by four sedimentary cycles. The oldest, Werra, when present in its entirety, consists of the following units: the copper-bearing shale (Kupferschiefer), the Zechstein Limestone, the Lower Anhydrite, the Oldest Rock Salt and the Upper Anhydrite (Figure 3).

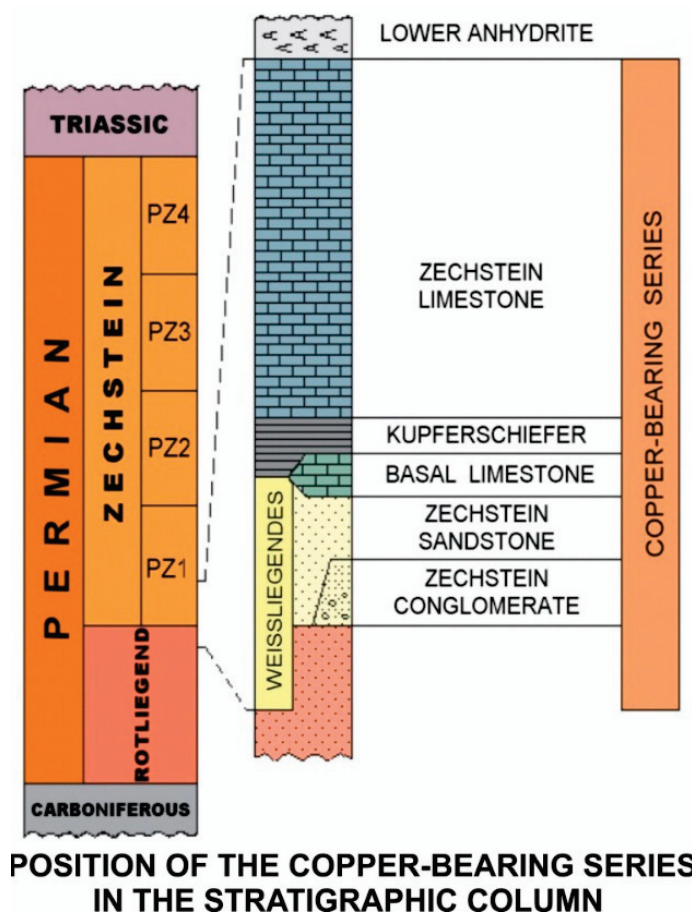


Figure 3. Lithostratigraphy of the Zechstein Copper-bearing Series.

The area of the Nowa Sól deposit was previously explored by drilling performed by the PGNiG Company. Two boreholes—Lubięcín-1 and Borowiec-1 ended in the rocks of P2. Rotliegend sediments were penetrated by one borehole Przyborów IG-3 located outside of the deposit, near its SW boundary (Figure 2).

3. The State of Geophysical Knowledge

The Cu-Ag deposits are categorized as epigenetic, created due to the influx of low-temperature hydrothermal solutions. Their migration pathways probably included regional and local tectonic zones. Fractures could be considered as channels for the convection of heat necessary for mineralizing processes [12,13]. Thermal characteristics indicate a considerable increase in the heat-flow rate density parameter in the SW Fore-Sudetic Monocline compared to those observed in the remaining parts of Poland [14,15], with its maximum values in the surroundings of the Sława IG-1 borehole (98.4 mW/m^3) [16,17].

A seismic image prepared for today's Nowa Sól deposit area by petroleum companies in 1980–1994 consisted of a grid of lines of varying quality, spaced 1–2 km apart. Major structures were identified in the prospective sediments of the Main Dolomite lithostratigraphic unit. Distinguishable zones are related primarily to changes in the lithology, facies and thickness of Zechstein cyclothem, in particular Stassfurt and Werra, as well as the occurrence of tectonically deformed regions.

Historical gravimetric surveys in the form of a semi-detailed image with a density of approximately 3.5 points/km^2 were performed in the area of the Nowa Sol deposit and its nearest surroundings. The uniform coverage of the whole area of the deposit with gravimetric data complements the degree of geophysical exploration, particularly in sites where information from seismic surveys is missing. The sets of gravitational values constituting a basis for the preparation of a Bouguer anomaly map were developed based on the IGSN71 system and a formula for calculating a normal gravitational force field for the WGS84 ellipsoid [18]. The resulting image is a superposition of gravimetric effects originating from Mesozoic and Palaeozoic complexes as well as the deep basement and it confirms the existence of distinct characteristic changes in the morphology and density of specific stratigraphic complexes.

Proper reinterpretation processes [3] allowed the identification of structural elements of the Palaeozoic substrate (Figure 1). The gravimetric map of Bouguer anomalies features a pronounced positive anomaly extending in the Lower-Silesian Basin between Zielona Góra and Leszno. The Wolsztyn High is located in an extensive gradient zone in the north-eastern limb of the anomaly. A positive anomaly identified in the area of the Lower-Silesian basin, present over the whole analyzed depth interval, is associated with a geological structure standing out due to its high values of density. In here, the possible existence of a complex with noticeably elevated density (approx. 2900 kg/m^3) relative to the surrounding rocks (2700 kg/m^3) is confirmed by the results of Deep Seismic Sounding (GBS) [19,20].

As a consequence, the Wolsztyn High can be interpreted as a branch of an anomaly associated with a structural unit in the Lower-Silesian Basin, with higher density contrasts which prevail in the surface image of Bouguer anomalies.

Distinguishable tectonic directions consisting of at least two or even three lines, mark a dislocation. It is particularly easy to trace tectonic zones (Figure 1) delimiting the Wolsztyn High (A and B), a positive anomaly in the Lower-Silesian basin (B and C), as well as faults in the vicinity of the Odra river (D). Relationships between fault zone C (the Bielawa Fault) based on gravimetry and a deep tectonic rupture are confirmed by the results of Deep Seismic Sounding (GBS) [20] and by the image of the magnetic field [21]. Over a considerable length, it overlaps with the NW boundary of a regional magnetic anomaly extending from south of Zielona Góra to the western border of Poland (the Gubin region) and further to Germany. The width of the anomaly indicates a relationship with the rupture zone of middle Odra, described as a system of deeply rooted faults, probably with a strike-slip nature [22]. This anomaly has its source in rock masses of the basement, with densities and magnetic properties elevated relative to the surroundings. They probably reflect the presence of volcanic rocks with enhanced magnetic properties. This may be due to elevated amounts of ferromagnetic minerals in zones of contact with substrate rocks of different densities or related to the migration of solutions in the fault zone.

4. The Methodology of Research

4.1. Compilation and Interpretation of Transformed Gravimetric Anomaly Maps

On the Bouguer gravity map, the Nowa Sól deposit occupies the north-eastern area of positive anomalies separated by a gradient zone from lower values in the southwest (Figure 4). The use of various methods for processing Bouguer anomalies allowed visualization of deep structural elements based on frequency filtration methods for density complexes, as well as gravimetric-tectonic maps presenting the directions of the zones of tectonic and/or lithological discontinuities. Gravimetric data is sufficient for the identification of anomalies related to Zechstein sediments and their substrate.

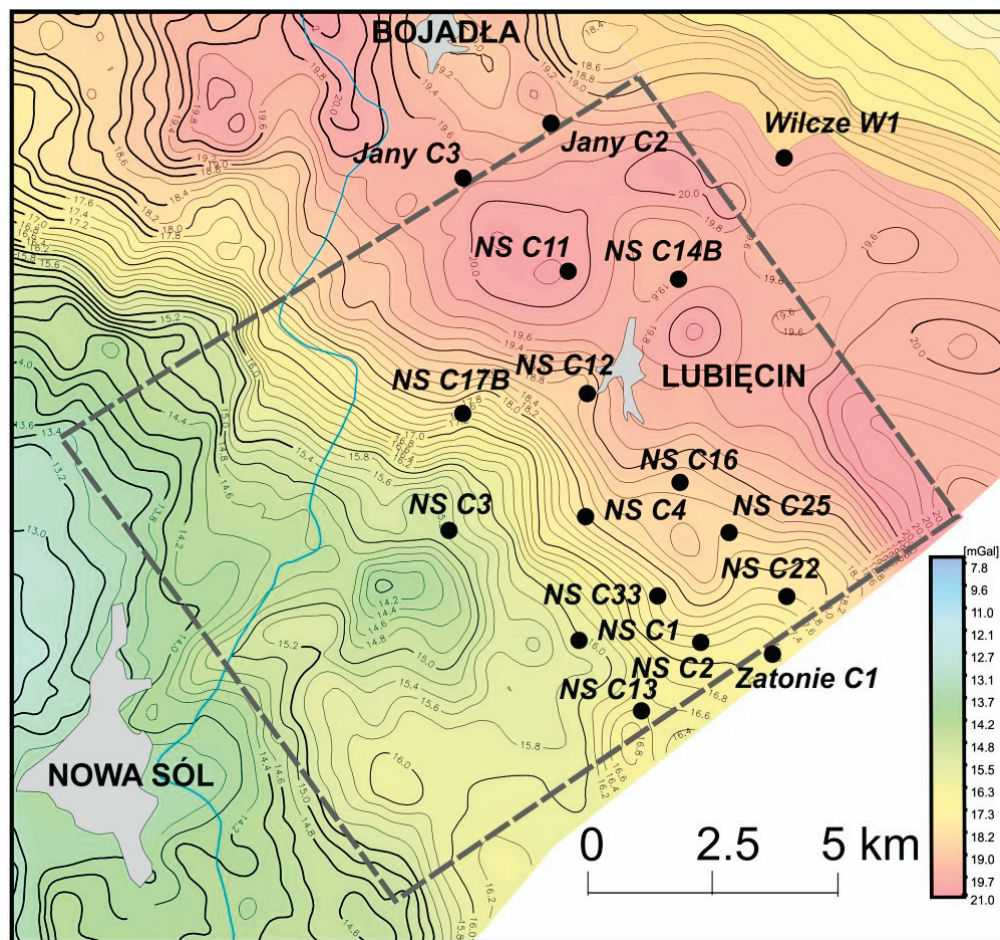


Figure 4. Bouguer gravity map of the Nowa Sól concession area showing the locations of prospecting boreholes; density in the reduction layer 2.25, reference level 0 mamsl.

One characteristic element of a map of residual anomalies for a depth interval of 2800–4000 m associated with sediments underlying the Zechstein involves its considerable similarity to the image of Bouguer anomalies, indicating the impact of basement rocks on the gravimetric image. These are the dense rocks of the older Palaeozoic or metamorphic rocks of the Wolsztyn-Pogorzela High [10]. Changes in the lithology and thickness of Zechstein sediments reflect the residual anomalies for shallower depth intervals, associated with salts and anhydrites of varying densities [2].

Various transformations of the image used the methods of frequency-based filtration. Along with an analysis of zones with increased gradients, this allowed tracing geological objects with elongated shapes, like faults or anticlines, as well as changes within analyzed depth intervals. On a horizontal gradient map according to Rosenbach (Figure 5), a zone of anomalies with a NW-SE direction, approximately parallel to the Wolsztyn High, demarcates a tectonic zone located close to its south-western limb.

For comparison, this map also presents geological faults and the boundary of an oxidized field interpreted based on later drilling results.

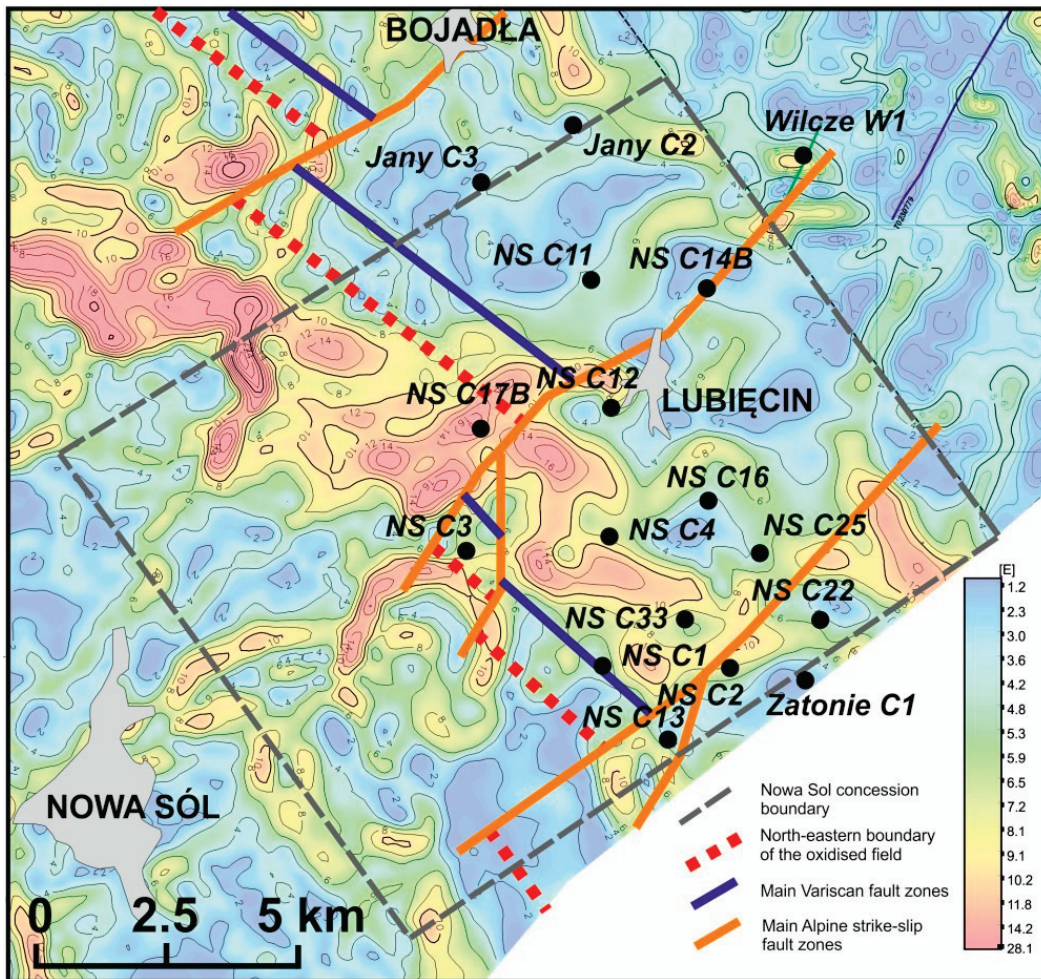


Figure 5. Gravity map of the Nowa Sól concession area - Horizontal gradient after Rosenbach against the distribution of prospecting boreholes. Geological faults and boundaries of the oxidized field interpreted from drilling data.

The map presented in Figure 6 provides a less ambiguous depiction of gravimetric linear elements in the form of axes of maximum horizontal gradient and lines of vertical density interfaces prepared for three depth intervals: 0–1600 m, 1600–2800 m and 2800–4000 m. This map is based on the combined data on horizontal gradient axes and vertical density interfaces. Attention should be paid to the main, regional line of discontinuities with a characteristic NW-SE direction, extending along anomalies visible on the horizontal gradient map. This zone primarily comprises depth intervals related to Zechstein sediments (1600–2800 m) and the basement (2800–4000 m)—dislocations ending in Permian rocks. In the surroundings of a regional fault zone, less pronounced zones of changes in linear elements were distinguished, also covering the shallowest depth interval. Information collected in the form of separate symbols for each depth interval enables the determination of the direction of inclination of fault planes, taking into account their association with stratigraphy.

In the gravimetric image one can also observe less pronounced lines of discontinuities, probably of a tectonic and/or lithological nature, with an NE strike direction. One of them, visible in the vicinity of Nowa Sól, intersects the abovementioned zone.

It should be noted that, although prepared prior to the initiation of the drilling program, the map of Figure 6 presents the same general directions of tectonic discontinuities as the Variscan and Alpine faults shown in Figure 5, which were interpreted based on drilling results.

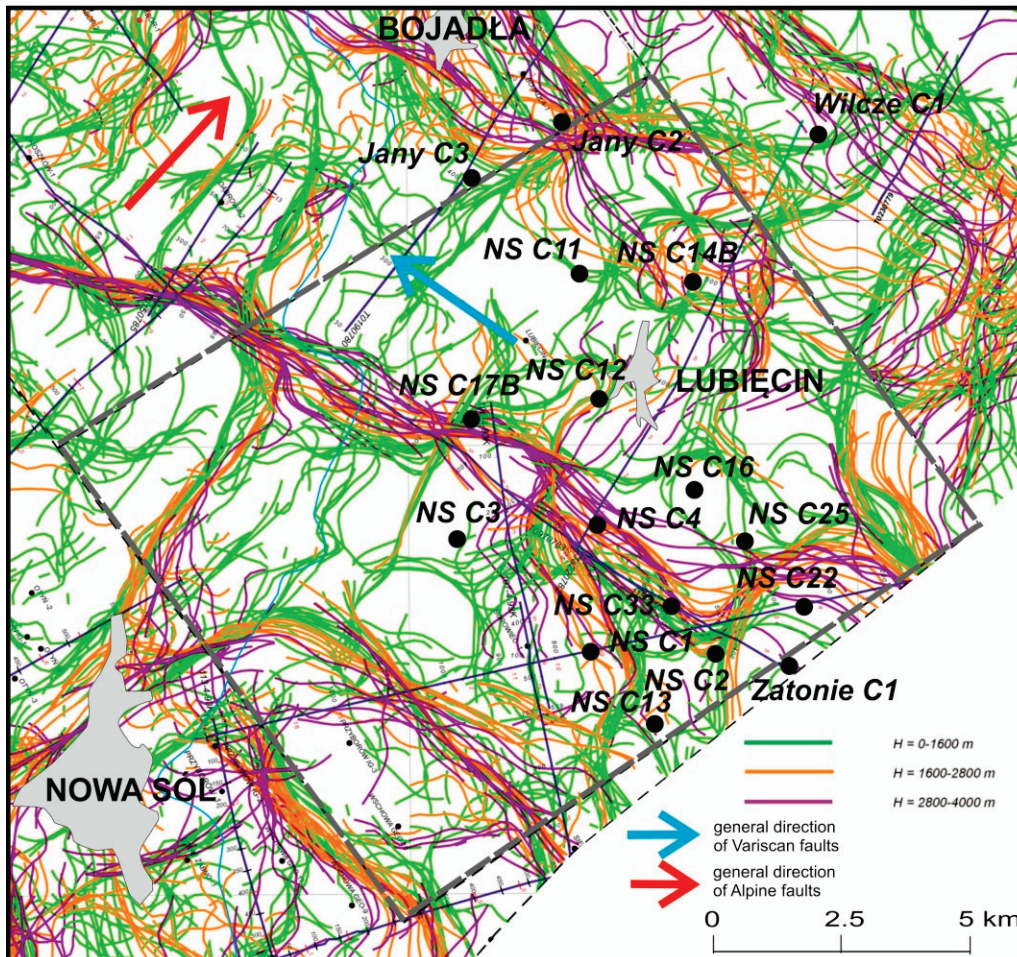


Figure 6. Gravity map of the Nowa Sól concession area—Axes of maximum horizontal gradient and vertical density interfaces in depth intervals of 0–1800 m, 1800–2800 m and 2800–4000 m and the locations of prospecting boreholes.

For a depth interval of 1600–2800 m, as the most representative one for Zechstein sediments and their contact with their direct substrate, the shapes of gravimetric zones and the related tectonic directions are also presented on a density map of gravimetric linear elements in the form of envelopes with specific contour lines (Figure 7). It is a graphically different form of visualizing tectonic information about an analyzed area. More pronounced gradient areas belong to tectonic zones covering a wider depth interval, while in the case of wedging out and changes in sedimentary facies, these contours are less distinguishable.

To sum up, the main purpose of gravimetric interpretation was to provide a certain degree of detail on the tectonic structure of the area. This included the areas of tectonic uplift and depressions, as well as the approximate locations and primary directions of geological faults, which would be subsequently presented on the ERC sections.

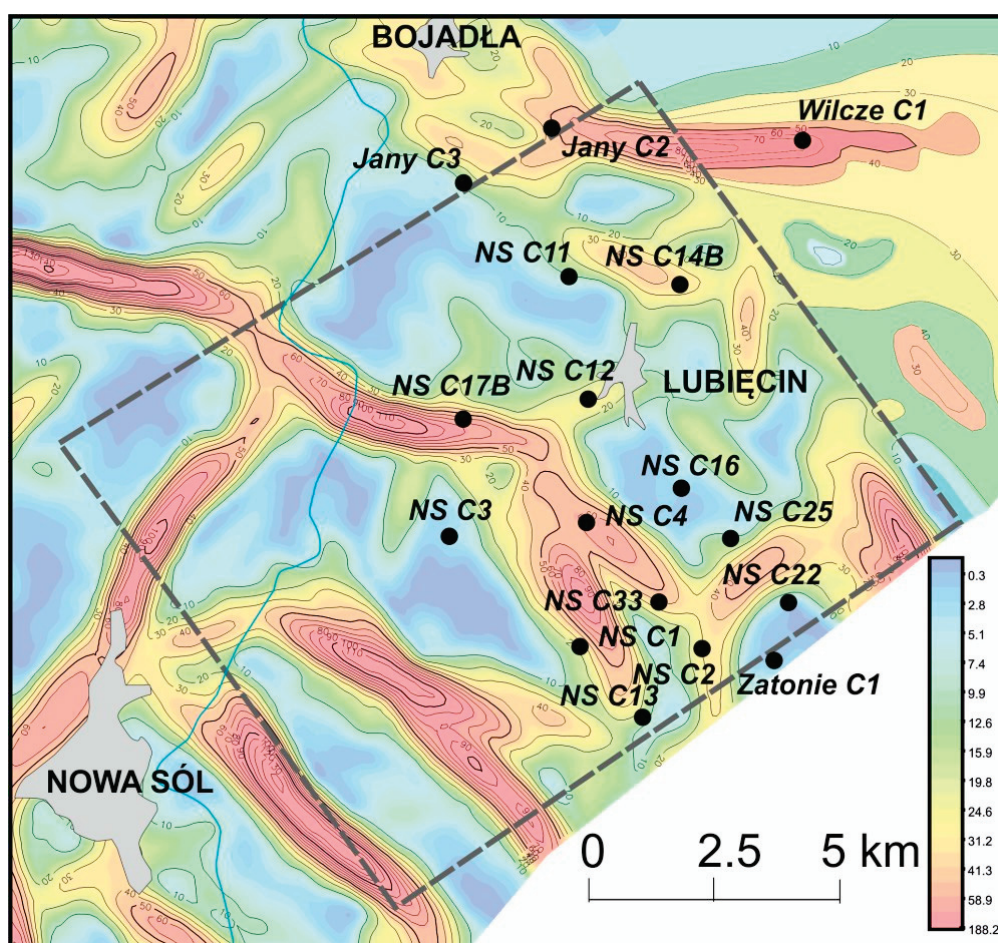


Figure 7. Gravimetric densities of linear elements in the Nowa Sól concession area in a depth interval of 1600–2800 m.

4.2. Processing of Seismic Data and Development of ERC Sections

The principles of the effective coefficient method were developed in “Sibgeo Novosibirsk” in the 1980s [23]. This method was modified and adjusted to the lithological and tectonic variability of Zechstein sediments by the authors of the present paper [1]. The calculations used historical seismic data of the petroleum industry (time records, seismic sections) retaining original amplitudes.

The calculation of effective reflection coefficients (ERC) enables the conversion of a waveform seismic image into an impulse form of seismic record, meaning a temporal sequence of reflection coefficients representing layers forming a geological structure. To this end, one of the most important features of a seismic image is used—the amplitude, its size being assumed as proportional to the reflection coefficient for a specific geological boundary.

The mathematical and physical model of a geological structure is a so-called convoluted model, according to which a seismic pathway is the result of combining the pathway reflection coefficients with the elementary seismic signal. The deconvolution of an amplitude-based seismic pathway allows obtaining a pathway in the form of a series of coefficients.

The pattern of processing includes three stages: determination of an elementary impulse, repeated mutual correlation of the impulse with a seismic pathway, as well as standardization (horizontal and vertical addition of the individual pathways) and the use of statistical treatment for the visualization of a seismic image.

The primary function of the system involves determining the shape of the elementary signal and establishing the impulse characteristics of the structure. The determination of an elementary

seismic impulse proceeds via the addition of subsequent groups of reflected waves for a given pathway presented for the same phase, as well as the combined time of recording. In this paper, particular attention was paid to the selection of a proper elementary impulse adjusted to the objective of research—used in the process of correlation for specific time intervals, as preceded by numerous tests. The determination of elementary signal can be validated using Fourier analysis. The function of correlation of the elementary signal with each seismic pathway enables conversion of a wave-based seismic pathway into temporal series of zero-phase amplitudes called the effective reflection coefficients. It determines the time-based points of maximum correlation of signal with reflected waves in the form of values of the coefficient and sign of the amplitude.

Sets of reflection coefficients undergo standardization and they are presented in the form of a seismic section which shows seismic pathways converted into an impulse form. The verification of effectiveness involves the performance of multiple mathematical processes, until it is concluded that the residual amplitude path consists only of disrupting waves.

The reflection coefficients present seismic interfaces conforming to actual boundaries. This coefficient is defined by layer-related velocities and rock density above and below a given seismic reflecting interface. Assuming that changes in density are relatively small compared to changes in velocity, it is accepted that the coefficient depends mainly on the latter. The resulting cross-sections have the form of horizontal and vertical graphical symbols. By using the relationship between the value and sign of the reflection coefficient and velocities in strata, this method facilitates the tracing of changes occurring at the interfaces generating reflections and in the lithology of strata along seismic sections. Diverse graphics on sections of the coefficients enhance the visualization of results. The direction of impulses facilitates the recording of changes occurring at interfaces. This method is particularly useful when identifying thin layers, small dislocations and tracing changes in the lithology of a given stratum, for example, porosity, along a seismic section. The lateral tracing of a sedimentary succession in the overall image of a seismic section is facilitated by relative changes in the values of reflection coefficients. Compared to a wave image, the elimination of interference signals enhances the ability to demarcate seismic interfaces (which for most rock masses correspond to strata with thickness of about a dozen meters).

An important feature of ERC sections involves the ability to identify a given velocity-based stratum along the seismic line. Software used for the interpretation of well logging data allows tracing individual lithological-stratigraphic successions along a seismic section based on the sign and value of the reflection coefficient. In the Nowa Sól deposit there are no deep historical boreholes with geophysical logging. Therefore, the well logging data which were used originated from nearby boreholes (Klenica-1, Jany-1, Zabór-1, Borowiec-2). The criterion for the selection of boreholes was based on the presence of measurements of average velocities, penetration of the Rotliegend sediments, as well as the assessment of the quality of the performed geophysical logging. In these boreholes, the following physical parameters of rocks were determined based on historical data: velocity, as well as density and porosity. Geophysical logging performed in boreholes enabled calculations of the values of parameters for strata exceeding 4 m in thickness. The correctness of calculations is ensured by correlation of results with sample density measurements and with the measurements of average velocities in boreholes. Individual parameters were attributed to strata with specific lithological profiles. The association of reflection coefficients with the lithological and parametric logging of a borehole enables the correlation of drilling and seismic, as well as stratigraphic data along seismic sections transformed into an impulse form. The determination of synthetic reflection coefficients related to parameters of the lithological profiles of boreholes allows relatively precise connection of correlated interfaces on seismic sections to Zechstein sediments distinguished by their physical parameters (Figure 8).

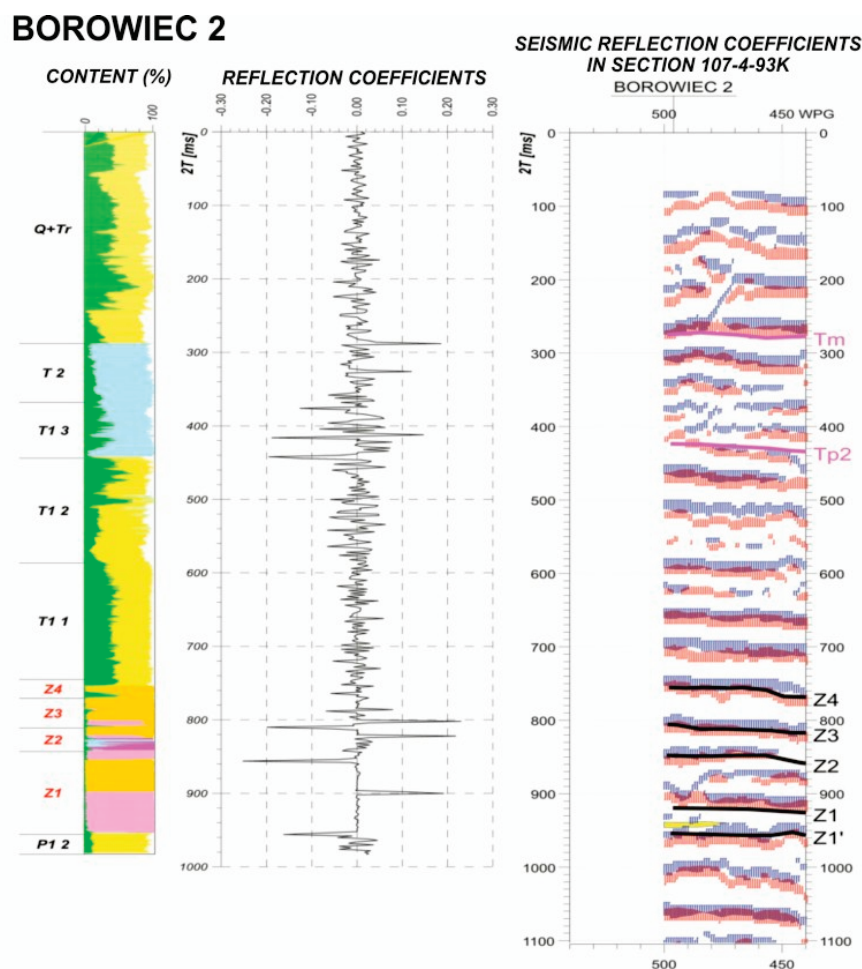


Figure 8. Lithological profile of the historical Borowiec 2 borehole relative to the geophysical section; geophysical parameters logged in this borehole included rock density and sonic velocity, suitable for seismic interpretation. Abbreviations: Q—Quaternary, Tr—Palaeogene + Neogene, T 2—Muschelkalk (Middle Triassic), T1 1 to T1 3—Lower to Upper Buntsandstein (Lower Triassic), Z1 to Z4—Zechstein sedimentary cycles (Permian), P1 2—Upper Rotliegend (Permian).

Due to the use of the attributes of an impulse section and the sign of the reflection coefficient, reflected wave intensity and the place of reflection, the efficiency of identification and correlation of seismic boundaries increases along with simultaneous characterization of the geometry of strata forming a given geological structure. Disruptions in the arrangement of strata are reflected by changes in the physical properties of individual layers. The reported higher number of distortions in the seismic image compared to those interpreted on wave sections results from the capabilities of the method and is linked to their diverse nature. The disruptions may be caused by the existence of tectonic features and/or changes in the lithology (lines of tectonic and/or lithological discontinuities).

The new ERC method combined with analyses of historical drilling logs from the vicinity of the deposit allowed better identification of the extent of the Zielona Góra oxidized field. This area is directly adjacent to the orebody, which forms a zone along its eastern edge, as confirmed by the historical Jany 1 borehole. The analysis also enabled the construction of a tectonic model of the area, consisting of several blocks separated by Variscan and Alpine faults (see Figure 5). It turned out that, due to tectonic displacements, the Zielona Góra field extended further to the north-east than previously expected. This resulted in a new location for the first borehole in the Nowa Sol area, which effectively discovered the Nowa Sól deposit. Further holes confirmed the existence of a zone of Zechstein ore-bearing sediments with a width of approximately 5 to 10 km, extending NW-SE

adjacent to the Zielona Góra field. The north-eastern extent of this oxidized field is shown in Figure 5, explaining why all prospecting boreholes in the Nowa Sol concession area were drilled in its NE half.

The ERC method was also applied successfully in Poland for solving a number of other issues, for example, the tracing of lithological changes in Carboniferous rocks of the Lublin Graben [24], mapping of Zechstein sediments in the NW rim of the Holy Cross Mountains [25] or the examination of geological structures selected for the storage of CO₂ (e.g., References [26,27]).

5. Results

5.1. Geophysical and Geological Interpretation of Seismic ERC Sections

The analysis and interpretation of results covered 9 selected seismic lines: T0970783, TA220782, T0190790, 115-04-93K, 106-04-93K, 107-04-93K, 118-04-93K, 114-4-93K and TA230782 (Figure 1) with a total length of 82.233 km.

The coefficients were calculated based on materials derived from historical seismic data having the form of sets of time- and amplitude-related seismic sections. When choosing data for further handling, the preferred materials included those whose actual amplitudes had been retained during processing.

Initially analyzed aspects included the degree of tectonic deformations (identification of tectonic elements) and morphology of the bedding of bottom Zechstein sediments (P2). Apart from seismic sections, the morphology of sub-Zechstein strata is documented by a structural map of the P2 bottom (Figure 9) prepared based on the results of reflection lines, including those developed in the ERC version, as well as deep drilling, providing important information about the predicted depth of planned boreholes. There is a visible consistent ascent of the P2 bottom from 2140 to 1440 m near the southern boundary of the area, accompanied by considerable diversity of substrate morphology which requires consideration when establishing the location of drilling. Near the 1800 m contour line there is a major zone of changes in the density of lines. This line, corresponding to an abrupt change in the inclination of P2 bottom, coincides with the prevalent tectonic zone which constitutes the southern boundary of an elongated gravitational anomaly interpreted as the already mentioned fault C (the Bielawa Fault). Changes in the morphology of the P2 bottom surface reflect the existence of a dislocation zone with a high amplitude in the substratum (a dislocation delimiting the Middle Odra rupture from the NE), separating two different geological settings. Its independent identification based on two geophysical methods confirms the proper direction of research.

The nature of the Middle Odra rupture zone is additionally shown by the Wilków Structure (a natural gas reservoir) located SE of the Nowa Sól deposit area (Figure 1). The presented cross-section (Figure 10) shows the effectiveness of using historical seismic sets applied in the form of effective reflection coefficients for identifying the structure of not only Zechstein sediments but also those of the Rotliegend, the Carboniferous and deeper ones from the area of a regional elevation in Rotliegend strata. The ERC section presents results along a line with a direction perpendicular to the structure. Sub-Permian rocks are characterized by discontinuous tectonics and the directions of faults form a distinct block-based system. The SW limb (slope) of the structure has a more monotonous nature and features gentler dipping compared to the NE limb, cut off by a fault with a higher amplitude. The seismic section indicates the dichotomy of the interpreted object in lower Zechstein, Rotliegend and Sub-Permian rocks. The tectonic discontinuity zone (within the range of fault C traced by gravimetry) extending near the central part of the structure and parallel to it in a surface image divides it into 2 parts (NE and SW). Interpretation of the Wilków Structure constitutes an example of the ability to correlate gravimetric tectonic zones with data from seismic surveying also below the bottom of Zechstein sediments, due to the use of information from a transformed wave image in the ERC system.

The main stage of interpretation involved lithological examination of the individual stratigraphic units of P2 along ERC sections, with particular emphasis on older Zechstein sediments which are potential copper-bearing strata, as well as an analysis of the mutual arrangement of seismic horizons along with the distribution of thickness of the traced strata and identification of zones of their

changes. The ultimate objective was to demarcate the probable zones of increased thickness of potential ore-bearing series. These zones are related to low values of the reflection coefficients at the Zechstein/Rotliegend boundary, identified along short segments of sections, which was possible due to high resolution of the method.

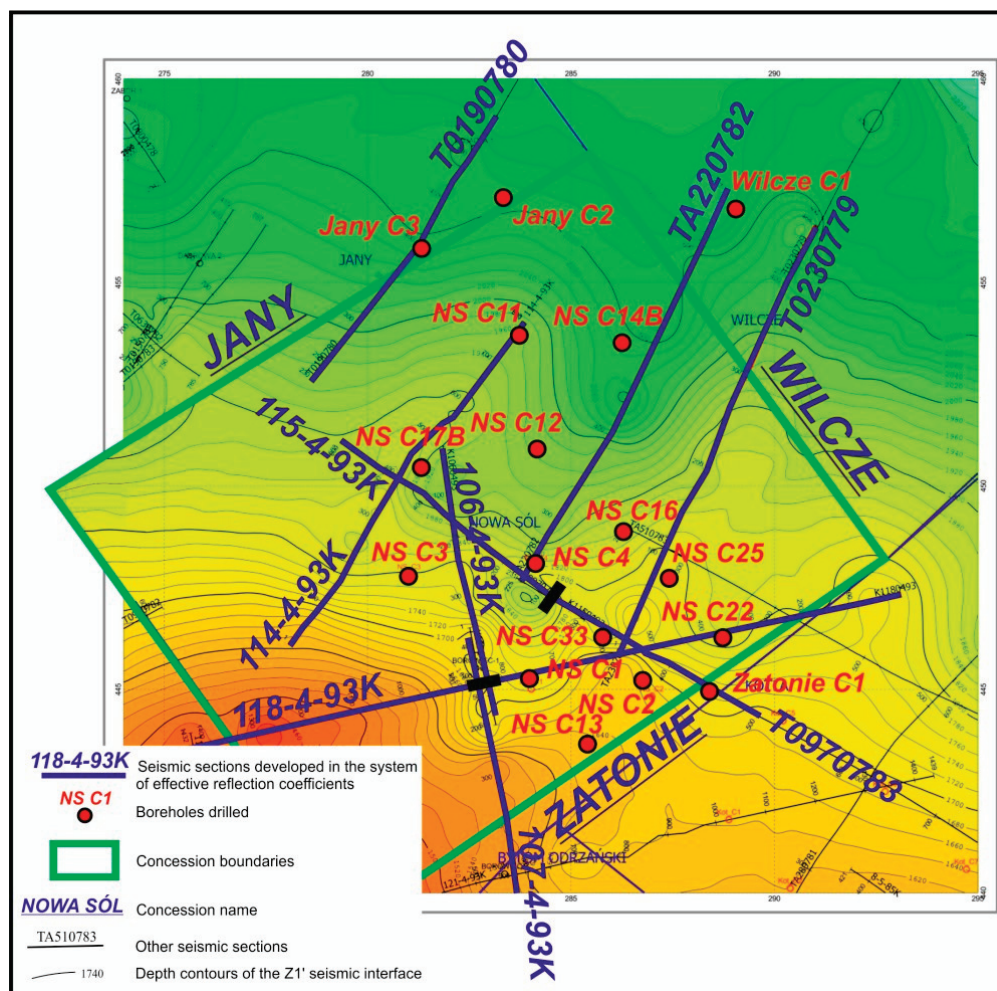


Figure 9. Seismic map of the Zechstein in the Nowa Sól concession area—depth of P2 bottom.

Compared to wave sections, ERC sections present a clearer and more unambiguous seismic image. The harmonization of data, as well as an improvement in the quality and resolution of the recorded interfaces, resulted in a much more precise and credible lithological, structural and tectonic image of the area in question, compared to earlier studies, which involves mainly Zechstein seismic horizons. The results allow the correlation of Triassic and Permian interfaces associated with the individual cyclothems of the Zechstein and with the top of the Rotliegend.

One characteristic feature is the arrangement of coefficients and zones of particular significance for predicting the occurrence of copper-bearing shales and the associated mineralized zones with the highest possible probability. On the seismic sections, particular attention was paid to the position of the boundary between Z1' and Z1. Due to its interferential nature, in previous research the Z1' interface presented uncertain correlation, as will be presented in Section 5.2.

Due to the abovementioned absence of deep boreholes in the area of the Nowa Sól deposit, the link to stratigraphy was established based on geological data from boreholes and geophysical logging originating mainly from adjacent concession blocks. Identification of the traced stratigraphic horizons is analogical to what is used traditionally in the Fore-Sudetic Monocline, as presented, for example, in Figure 10 above:

1. Tp2—interface reflecting the morphology of the top of Middle Buntsandstein (bottom of the Röt)—not presented in any of the figures due to their vertical scale
2. Z4—interface from the top of the Zechstein
3. Z3—interface from the top of the Main Anhydrite of the Leine cyclothem
4. Z2—interface from the top of the Basal Anhydrite of the Stassfurt cyclothem
5. Z1n—interface from the top of the Werra Salt—bottom of the Upper Anhydrite (difficult to trace; shown in Figure 10 above but not in the following figures)
6. Z1—interface from the bottom of the Werra Salt—top of the Lower Anhydrite
7. Z1' (or P1, see Figure 10 above)—interface formed at the contact between the bottom of the Zechstein and the top of the Rotliegend—it corresponds to a seismic interface associated with the bottom of the Basal Limestone of the Werra cyclothem and thus it characterizes the position and shape of the top surface of P1 sandy sediments
8. C—interface from the top of the Carboniferous.

The form of the Z1' interface associated with a negative reflection coefficient generated at the contact between high-velocity Werra sediments and sub-Zechstein rocks changes depending on the development of the near-roof parts of sub-Zechstein sediments. When the Zechstein is directly underlain by pure sandstones of sufficiently large thickness, the coefficients are clear due to the contrast of velocities between the overlying strata and the sandstones. On the other hand, when the bottom of the Zechstein is underlain by rocks with higher velocities compared to sandstones, the minimum associated with this interface is less pronounced.

Below these, there are clearly distinguishable seismic interfaces from the top part of P1, which are horizons probably corresponding to clayey and muddy insets within P1 rocks. The nature and magnitude of reflection coefficients indicate that Zechstein sediments may be underlain by insets of rocks characterized by much higher velocity compared to sandstones. The absence of drilling data and reflective interfaces along larger segments makes the interpretation more difficult. Considering the interfaces of velocity contrasts, the Tp2, Z4 and Z1' horizons were traced along negative reflection coefficients, while the remaining ones used positive values.

The Triassic and upper Zechstein rocks lie in general conformity with each other. No presence of tectonic disruptions was recorded in Triassic rocks. Tectonic deformations affected mainly the Zechstein sediments, especially older ones. The structure of complexes of the Stassfurt and Werra cyclothem is complicated due to dislocations, whose recorded numbers far exceeded those interpreted in wave sections in previous (historical) seismic reports. The seismic image of reflection coefficients shows that their nature is highly diverse. Some distortions are caused by the existence of small faults in areas of tectonic impact. Others, caused by small changes in thickness and/or lithology, are to be interpreted as lines of lithological discontinuities. Displacements within strata are frequently recorded in the zones of low amplitude faults. Fault zones in the Z1' horizon are associated with the diverse morphology of sub-Zechstein sediments. Most faults recorded in the Zechstein extend into older rocks, evidencing their deeper tectonic origins.

Zechstein sediments stand out on ERC sections due to boundaries with high values of the coefficients, documenting great lithological diversity of rocks which form series of salts, clays, as well as anhydrites and dolostones. The changes observed in the thickness of complexes between these horizons are caused mainly by changes in the thickness of the older salt of the Stassfurt cyclothem and the oldest salt and anhydrite of the Werra cyclothem. Based on the determined values and signs of the reflection coefficients recorded between these interfaces, it is also possible to estimate the thickness of the older and oldest rock salt in relation to the anhydrites.

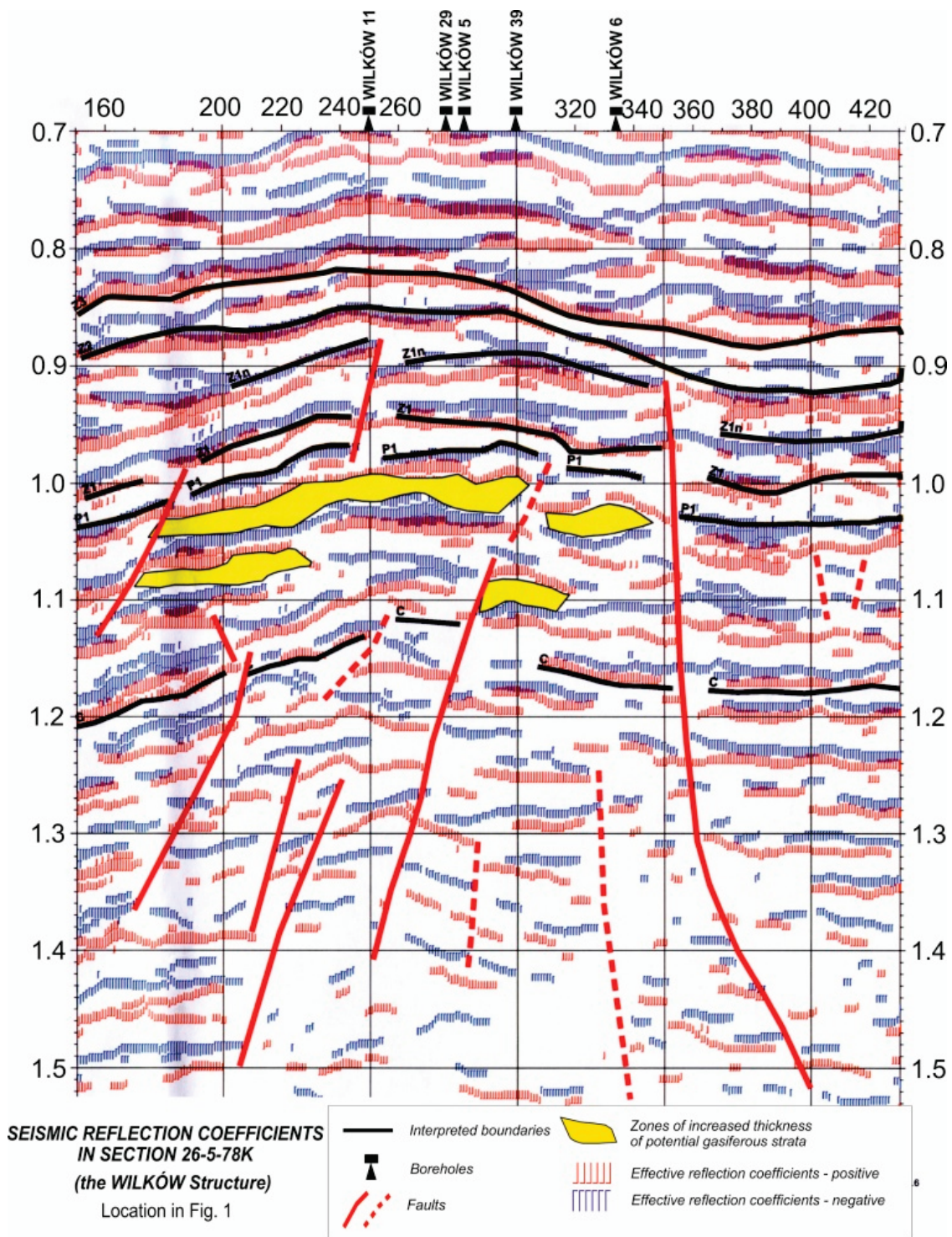


Figure 10. An example of using the ERC method. Additional symbols: C—top of the Carboniferous, P1—top of the Rotliegend, Z1—top of the Lower Anhydrite (Zechstein), Z1n—bottom of the Upper Anhydrite (Zechstein), Z2—top of the Basal Anhydrite (Zechstein), Z3—top of the Main Anhydrite (Zechstein).

5.2. Analysis of Seismic ERC Sections with Respect to Prediction of Ore Distribution

In the sediments of the Zechstein and its contact with the Rotliegend, there are distinguishable zones of lithological changes, layers with very characteristic values of the coefficients and low amplitude

faults, along with wedging out zones and those where the range of individual strata is delimited by tectonic or lithological changes (Figures 11–17). Considerable attention paid to the demarcation of the Z1' interface on ERC sections resulted from the need for the highest possible precision of depicting the top of Zechstein substrate in order to fulfil the prospecting objective—the use of an analysis of changes in reflection coefficients for the identification of mineralized zones. In the Zechstein Z1'–Z1 complex there are clearly visible boundaries originating from the individual strata from the lower series (Figure 3). Attention should be paid to the high-velocity complex of Zechstein sediments directly overlying the top of the Rotliegend and to the recorded changes in reflection coefficients. Drilling results indicate that rocks associated with the orebody are several meters thick and physical parameters characterizing these sediments: velocity, density and porosity, have values similar to the highly elastic thick structure present in their overburden, consisting of limestones, anhydrites and rock salts. The distinguishable relatively lower values of the reflection coefficients compared to those of the surrounding strata enable their correlation along short segments of seismic lines, wedging out or ended with low amplitude faults. Changes in the lithology of lowermost Zechstein sediments occur above the Z1' seismic interface as reflections with low values of the coefficients recorded in short segments of the profiles. They have been interpreted as “anomalous strata,” indicating the sites of potential mineralized zones.

The analysis of results performed in terms of the determination (demarcation) of the zones of potential occurrence of ore-bearing series is presented on ERC sections (Figures 11–17). The following commentary to the results shown on several selected sections illustrates the efficiency of the method for lines extending through various geological conditions, which is also summarized in Table 1.

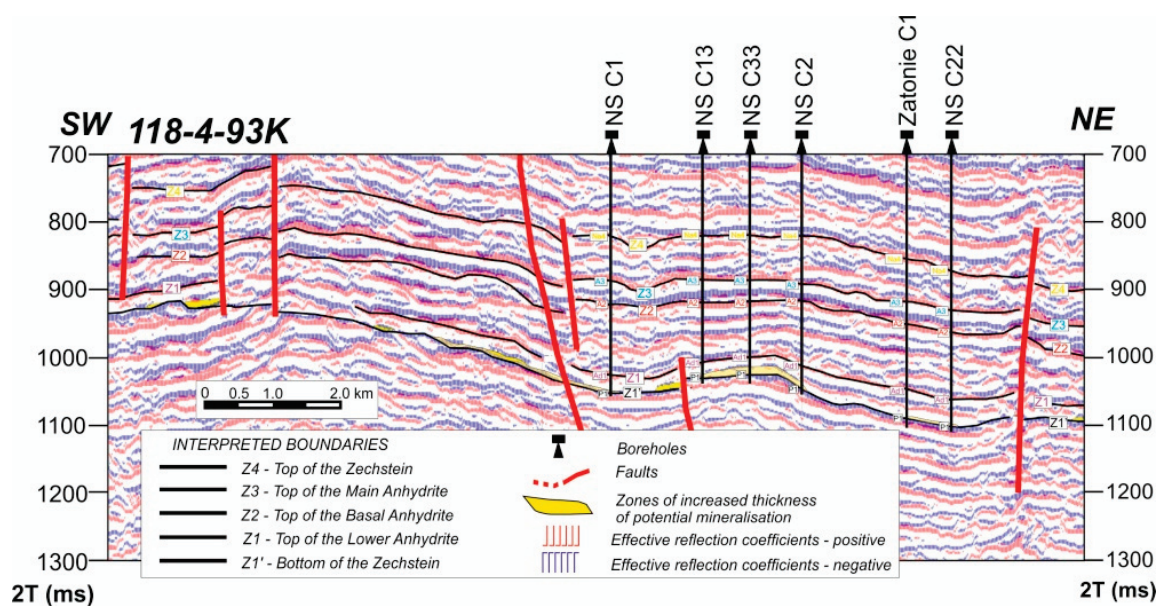


Figure 11. Time-converted seismic reflection coefficients in section 118-4-93K of a Zechstein deposit. Additional symbols: Na4—Youngest Rock Salt, A3—Main Anhydrite, A2—Basal Anhydrite, Ad1—Lower Anhydrite, P1—Rotliegend.

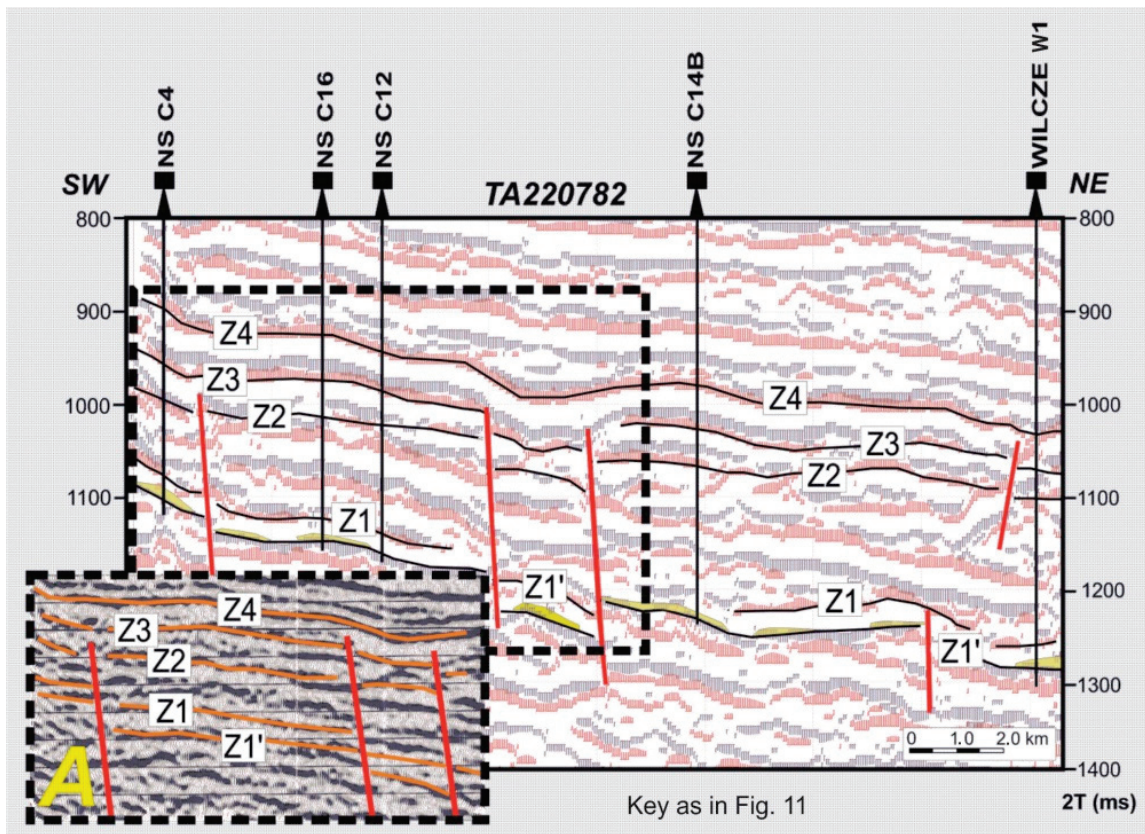


Figure 12. Time-converted seismic reflection coefficients in section TA220782 of a Zechstein deposit compared to a conventional wave-based image (A).

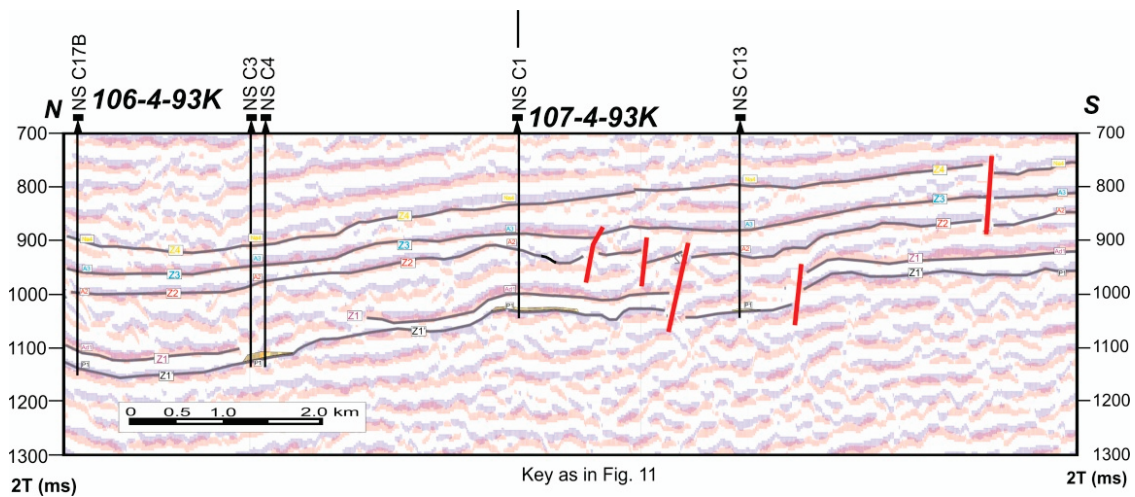


Figure 13. Time-converted seismic reflection coefficients in sections 106-4-93K and 107-4-93K of a Zechstein deposit.

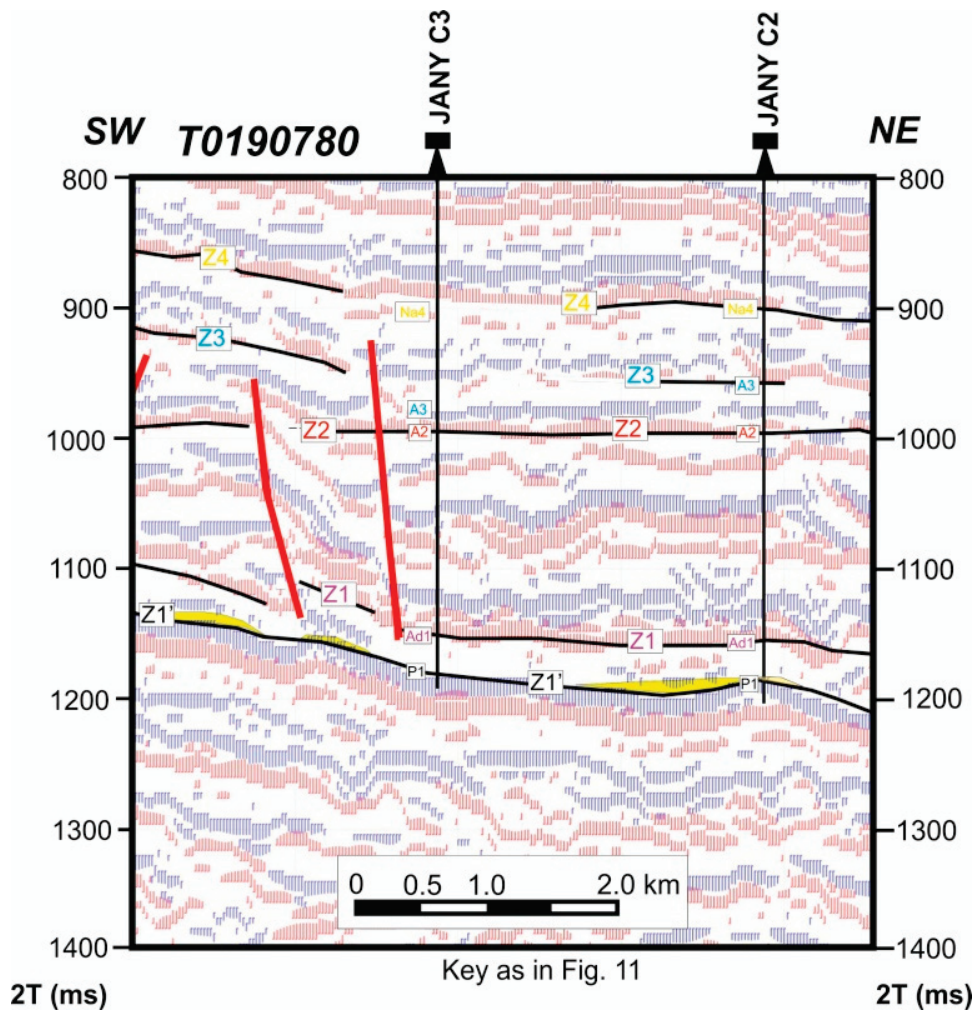


Figure 14. Time-converted seismic reflection coefficients in section T0190780 of a Zechstein deposit.

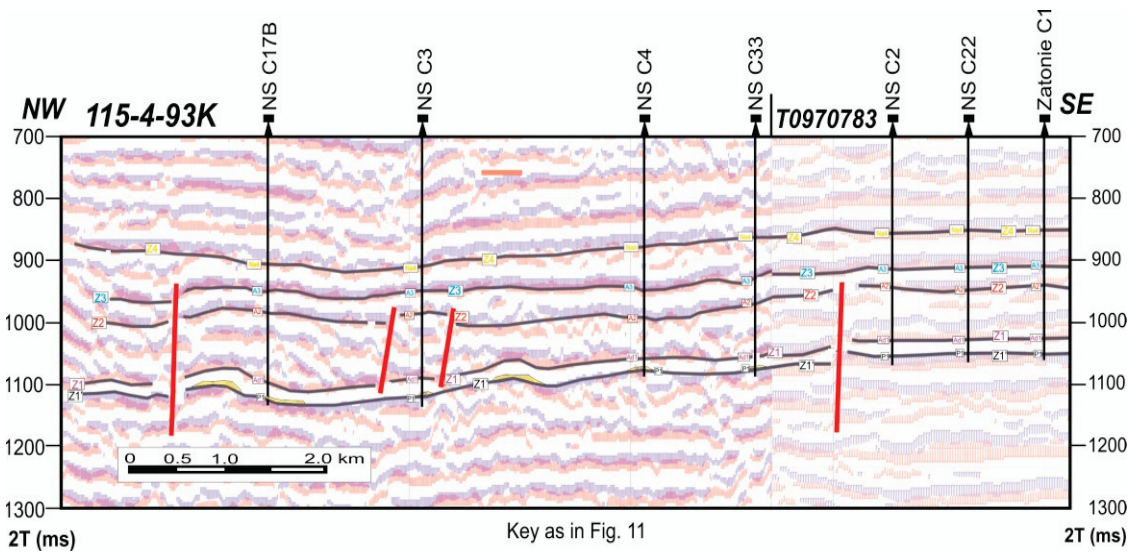


Figure 15. Time-converted seismic reflection coefficients in sections 115-4-93K and T0970783 of a Zechstein deposit.

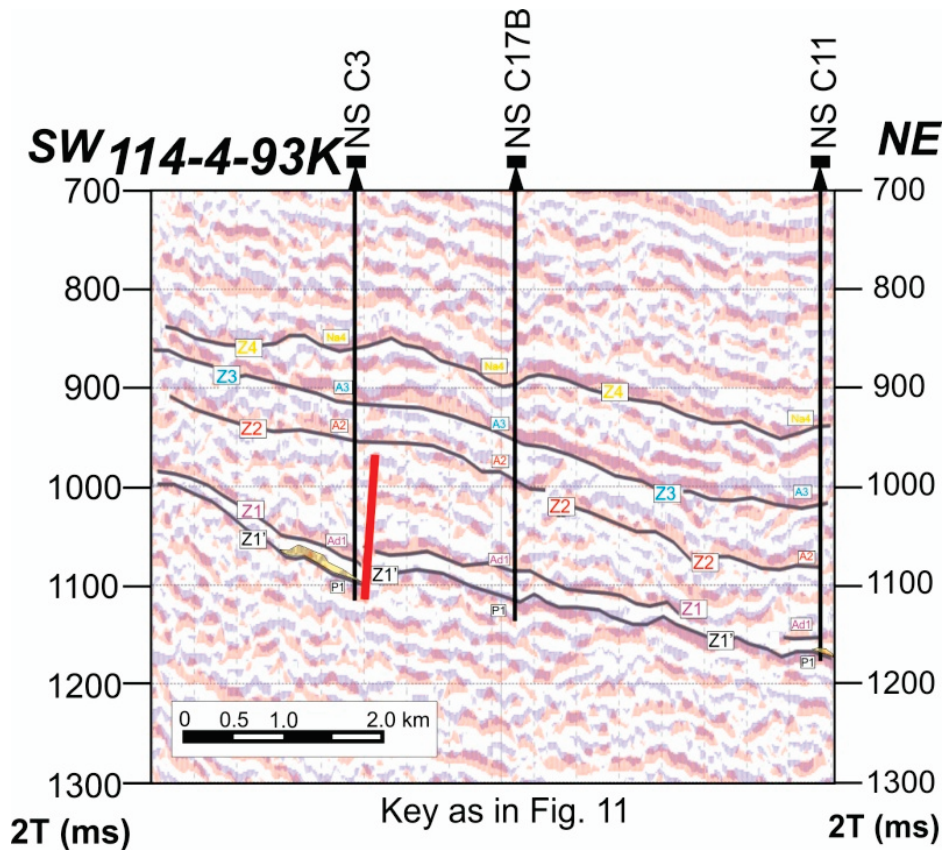


Figure 16. Time-converted seismic reflection coefficients in section 114-4-93K of a Zechstein deposit.

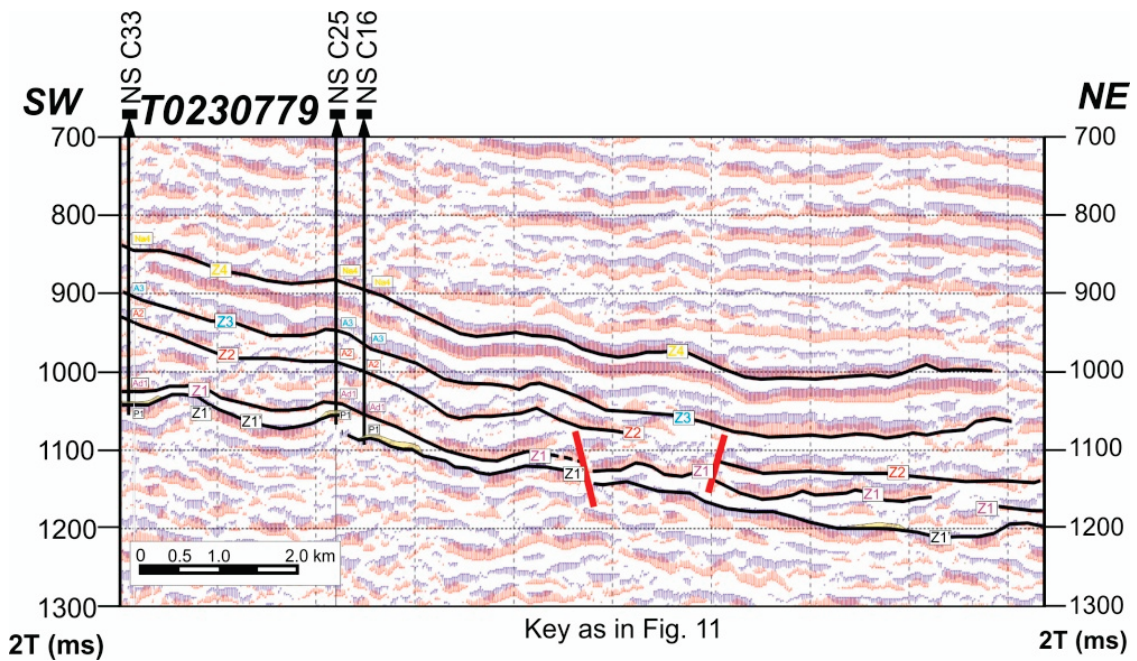


Figure 17. Time-converted seismic reflection coefficients in section T0230779 of a Zechstein deposit.

Table 1. Efficiency of the used ERC method.

Borehole Signature	Correlation with ERC Image	Seismic Section No.
NS C1	compliance	118-4-93K, 106-4-93K
NS C2	compliance	118-4-93K, T0970783
NS C3	no confirmation	118-4-93K, T0970783
NS C4	compliance	TA220782, 115-4-93K
NS C11	no confirmation	114-4-93K
NS C12	no confirmation	TA220782, 114-4-93K
NS C13	compliance	118-4-93K, 107-4-93K
NS C14B	compliance	TA220782
NS C16	compliance	TA220782, TA230782
NS C17B	compliance	115-4-93K, 114-4-93K, 106-4-93K
NS C22	compliance	118-4-93K, T0970783
NS C33	compliance	118-4-93K, T0970783

The table indicates that the ERC method proved to be effective in 75% of cases. The 25% failure may be caused by the fact that the resulting seismic images do not always perfectly represent the nature of detailed geological structure. This depends on the quality and number of available seismic sections. The higher the density of sections, the more precise the identification of geological structure, with a higher probability of pinpointing good drilling locations. It should be noted that the number of historical seismic sections from the Nowa Sól area was limited and that majority of the historical boreholes used for correlation were located outside that area.

Section 118-4-93K with a nearly latitudinal direction (Figure 11) is the most representative of all seismic sections selected for reprocessing. Along the Przyborów elevation and on its eastern slope, several anomalous zones were recorded at the boundary between the Zechstein and the Rotliegend, which due to the discontinuity of correlation were linked with Cu ore. Particular attention should be paid to the distinguished objects with a wider range, located between the zone of a tectonic and lithological discontinuity interpreted in the central part of the section, comprising the interval of P2 and deeper sediments and a tectonic line at the NE end. In here, a number of potential zones related to ore mineralization are located within local changes in the morphology of seismic horizons.

Section TA220782 (Figure 12) presents an undisturbed position of seismic interfaces dipping towards the NE. The interpreted potential orebodies are situated at the SW and NE ends of the section, in the central part of the line between two discontinuities delimiting a depression in the Zechstein horizon, including Z1', as well as directly east of them. This section was also chosen to present a comparison between an ERC image and a conventional (wave-based) image (marked with the letter A). The conventional image is characterized by much higher uncertainty of the Z1' interface.

A line with a direction resembling latitudinal consists of two profiles: 107-4-93K and 106-4-93K (Figure 13). The tectonically complex ERC image recorded in the southern section has numerous lines of lithological-tectonic discontinuities related to intra-stratum displacements in fault zones. Two interpreted zones of the occurrence of increased thickness of potential ore-bearing series are present between the individual lines of discontinuities, with one more in the location of the Borowiec 2 borehole. The P2 substrate dipping from the SW towards the NE is characterized by the monotonous structure of its northern section. An analysis of the ERC seismic record along the contact of P1 and P2 sediments indicates the lack of diversity in the distribution of reflection coefficients above an interface associated with the bottom of P2, which does not allow the identification of ore-bearing zones.

Section TO190780 (Figure 14) is characterized by its almost continuous Z1' interface dipping from the SW towards the NE and distinct block-based tectonics in the interval of Z1–Z2 horizons. Several zones of the occurrence of increased thickness of potential ore-bearing series were interpreted between the individual lines of lithological and tectonic discontinuities.

A relatively monotonous geological structure is presented on sections 115-4-93K and T0970783 (Figure 15). An analysis of the seismic record along the contact of Rotliegend and Zechstein sediments

indicates lack of variety in reflection coefficients above the Z1' interface, making the demarcation of ore-bearing zones much more difficult. Sections 114-4-93K (Figure 16) and T0230779 (Figure 17) present characteristic groups of reflective interfaces associated with Triassic and Zechstein rocks—the substrate of Zechstein is usually and are with no correlation between reflective interfaces along larger segments. Both seismic sections provide more detail about the structure of the north-eastern gradient zone in the top of the Rotliegend.

6. Conclusions

6.1. Usefulness of the ERC Method Applied for Establishing Drilling Locations as Part of an Exploration Programme for Cu-Ag Ore Deposits

Execution of the drilling program in the Nowa Sól deposit required very precise identification of interesting structural elements. Information which is particularly crucial to specialists performing exploration involves Zechstein tectonics, the development of the bottommost series of these sediments and information on the predicted stratigraphic profiles of the planned boreholes.

The transformation of archival seismic data into effective reflection coefficients (ERC) enabled the demarcation of Z1'-Z4 interfaces in Zechstein rocks. It also allowed the identification of tectonic features and the characteristic zones of lithological changes near the Z1' interface, which are possible hosts to orebodies. The individual elements of the seismic record were used to analyze the image recorded in Permian rocks, primarily Zechstein sediments and their contact with the Rotliegend. The bottom part of this complex usually hosts ore-bearing series, several meters thick, whose physical rock parameters do not differ significantly from values established for the whole complex. Because of this, the ore-bearing zones in the bottom parts of the Zechstein are difficult to trace in historical seismic data. Due to the high resolution of the used ERC method, the performed work resulted in the discernment of basic lithological complexes within P2, with the demarcation of its bottom surface, as well as the investigation of the geological structure—identifying the main tectonic zones and zones of smaller fractures, tracing the bottom of the shale and carbonate series Z1'. The presented assumptions and possibilities of depicting changes in mineralized zones along ERC sections have provided information about characteristic places associated with potential orebodies.

Professional interpretation of ERC sections resulted in establishing more precise locations of the planned prospecting boreholes.

In spite of the absence of characteristic anomalies associated with potential ore-bearing series on three interpreted ERC sections, the C17B borehole was drilled at the investor's request. The negative result of the drilling confirms the assessment implied by geophysical research. Summarizing the produced results, out of twelve prospective boreholes drilled, nine remain in compliance with the ERC image and three (C3, C11, C12) present a negative result of correlation. This proves the high validity of the performed interpretation of seismic sections in relation to drilling results and justifies the adopted course of research. The developed data were used in the planning of deep boreholes for prospecting work aimed at the identification of copper and silver orebodies in the bottom series of Zechstein sediments. Boreholes drilled close to or along the interpreted seismic sections confirmed the effectiveness of the ERC method in approximately 75%. Therefore, the resulting data are to be deemed necessary for the implementation of tasks related to the drilling program. Considering the complex geological conditions of the occurrence of orebodies and the small sizes of anomalies defining areas of copper concentration, the final outcomes documented by drilling results should be regarded as a major achievement.

6.2. Summary

According to available knowledge about relationships between ore-bearing zones and Zechstein bottom morphology, the prospecting boreholes planned as part of a copper project near the N slope of a zone of higher gradients in the P2 substratum proved to have been located correctly. The majority

of positive boreholes situated in the vicinity of the indicated C fault confirms the spatial relationship between more intense mineralization and regions with heavy tectonic deformations. This emphasizes the importance of tracing tectonic lines according to the assumption that deep tectonic roots had a primary impact on the development of Permian-Mesozoic rock series and as a consequence on the generation of ore deposits.

The completed drilling operations also confirmed the assumption about the position of lower Zechstein copper orebodies, forming a rather wide strip (5–10 km) placed in a zone extending NW-SE along the eastern range of the Zielona Góra oxidized field [28]. The Jany 1 borehole with abundant mineralization situated in a zone of lateral contact between reduced and oxidized sediments constituted a premise for the formulation of this pattern. However, before the beginning of the exploration program, drilling locations were modified as a result of the ERC method used in combination with analyses of historical well logs. It allowed better identification of the extent of the Zielona Góra field, which turned out to reach further to the north-east than previously expected.

Apart from conclusions related to the occurrence of potential ore-bearing zones, an additional result of reinterpretation of seismic data also involves more precise knowledge about the form and location of structural and tectonic objects present within the boundaries of the processed sections. Most of these structures have been defined by relatively minor amplitudes. The precision of the resulting information remains in a strict relationship with the number of processed seismic lines and drilled deep boreholes with geophysical logging. The identification of tectonic structures allowed the development of a new map of Variscan and Alpine faults in the area of the deposit, which was crucial to the determination of further drilling locations.

This study also has a methodical nature, showing the ability to use the impulse form of a seismic record for the identification of prognostic Cu and Ag resources, as confirmed by the results of prospecting drilling. The use of the sets of reflection coefficients in the form of ERC sections allows, for example, ongoing changes in parameters intended to present the most optimal image of the recorded section of coefficients. An increase in the density of the grid of reinterpreted seismic lines considerably affects the final result and as a consequence, the precision of outlining a potential Cu and Ag ore deposit. The high diversity of gravity field and the possibility to associate the demarcated anomalies with the identified density of specific geological series are of high significance in a comprehensive development of gravimetric and seismic data, as well as geophysical logging.

The results presented in this paper are based on historical data; therefore, they required relatively low financial expenses, with no need for costly on-site work. Proper interpretation of the prepared ERC sections allows efficient planning of other geological research, including drilling operations. This reduces the overall number of boreholes, specifically by increasing the ratio of those with positive results, which is also important in terms of environmental protection.

Author Contributions: Conceptualization, S.S. and W.J.; methodology, L.D.; validation, S.S. and K.Z.; formal analysis, K.Z.; investigation, W.J. and S.S.; resources, W.J. and S.S.; writing—original draft preparation, W.J. and L.D.; writing—review and editing, S.S. and K.Z.; visualization, K.Z.; supervision, S.S. All authors have read and agreed to the published version of the manuscript.

Funding: This research received no external funding.

Conflicts of Interest: The authors declare no known conflict of interest associated with this publication.

References

1. Speczik, S.; Dziewińska, L.; Pepel, A.; Józwiak, W. Możliwość wykorzystania impulsowej postaci zapisu sejsmicznego do rozpoznania złóż prognostycznych miedzi i srebra w północnej części monokliny przedsudeckiej. *Zesz. Nauk. IGSMIE-PAN* **2011**, *81*, 117–135.
2. Speczik, S.; Dziewińska, L.; Pepel, A.; Józwiak, W. Analiza i przetwarzanie danych geofizycznych jako instrument poszukiwań złóż Cu-Ag na monoklinie przedsudeckiej. *Biul. Państw. Inst. Geol.* **2012**, *452*, 257–286.

3. Dziewińska, L.; Pepel, A.; Tarkowski, R.; Żuk, Z. Nowe spojrzenie na wyniki badań geofizycznych monokliny przedsudeckiej w aspekcie poszukiwań surowców mineralnych. *Biul. Państw. Inst. Geol.* **2017**, *468*, 165–174.
4. Żelaźniewicz, A. *Rejonizacja Tektoniczna Polski*; Komitet Nauk Geologicznych PAN: Wrocław, Poland, 2011; 60p.
5. Grad, M.; Polkowski, M.; Ostaficzuk, S.R. High-resolution 3D seismic model of the crustal and uppermost mantle structure in Poland. *Tectonophysics* **2016**, *666*, 188–210. [[CrossRef](#)]
6. Nawrocki, J.; Becker, A. *Atlas Geologiczny Polski*; Polish Geological Institute: Warsaw, Poland, 2017.
7. Speczik, S.; Skowronek, C.; Fredrich, G.; Diedel, R.; Schumacher, C.; Schmidt, F.P. The environment of generation of some base metal Zechstein occurrences in central Europe. *Acta Geol. Pol.* **1986**, *36*, 1–36.
8. Franke, W.; Żelaźniewicz, A.; Porębski, S.J.; Wajsprych, B. The Saxothuringian zone in Germany and Poland: Differences and common features. *Geol. Rundsch.* **1993**, *82*, 583–599. [[CrossRef](#)]
9. Speczik, S. The Kupferschiefer mineralization of Central Europe: New aspects and major areas of future research. *Ore Geol. Rev.* **1995**, *9*, 411–426. [[CrossRef](#)]
10. Kiersnowski, H.; Peryt, T.M.; Buniak, A.; Mikołajewski, Z. From the intra-desert ridges to the marine carbonate island chain: Middle to late Permian (Upper Rotliegend-Lower Zechstein) of the Wolsztyn-Pogorzela high, west Poland. *Geol. J.* **2010**, *44*, 319–335. [[CrossRef](#)]
11. Żelaźniewicz, A.; Cwojdzinski, S.; England, E.W.; Zietara, P. Variscides in the Sudetes and the reworked Cadomian orogen: Evidence from the GB-2A seismic reflection profiling in southwestern Poland. *Geol. Q.* **1997**, *41*, 289–308.
12. Speczik, S. Metalogeneza podłoża podcechsztyńskiego monokliny przedsudeckiej. *Geol. Sudet.* **1985**, *20*, 37–96.
13. Piestrzyński, A. Historyczny rozwój poglądów na genezę złoża rud miedzi na monoklinie przedsudeckiej—dyskusja. *Biul. Państw. Inst. Geol.* **2007**, *423*, 69–76.
14. Speczik, S. Relation of Permian base metal occurrences to Variscan paleogeothermal field of the Fore-Sudetic Monocline; results of fluid inclusion studies and vitrinite rank determination. *Fort. Miner.* **1985**, *63*, 222.
15. Speczik, S.; Oszczepalski, S.; Nowak, G.; Karwasiecka, M. Cechsztyński łupek miedzionośny—poszukiwanie nowych rezerw. *Biul. Państw. Inst. Geol.* **2007**, *423*, 173–188.
16. Leszczyński, K. (Ed.) *Profile Głębokich Otworów Wiertniczych Instytutu Geologicznego*; Polish Geological Institute: Warsaw, Poland, 2015; p. 146.
17. Majorowicz, J.; Safanda, J. Lithosphere Thickness from New Heat-Flow Data of the Odra Variscan Area, SW Poland. *Pure Appl. Geophys.* **2018**, *175*, 4343–4354. [[CrossRef](#)]
18. Królikowski, C.; Petecki, Z. *Gravimetric Atlas of Poland 1:500,000 and 1:750,000*; Polish Geological Institute: Warsaw, Poland, 1995.
19. Cwojdzinski, S.; Młynarski, S.; Dziewińska, L.; Jóźwiak, W.; Zientara, P.; Baziuk, T. Pierwszy sejsmiczny profil głębokich badań refleksyjnych (GBS) na Dolnym Śląsku. *Przegląd Geol.* **1995**, *43*, 727–737.
20. Młynarski, S.; Pokorski, J.; Dziewińska, L.; Jóźwiak, W.; Zientara, P. Deep reflection seismic experiments in western Poland. *Geol. Q.* **2000**, *44*, 175–181.
21. Narkiewicz, M.; Petecki, Z. Basement structure of the Palaeozoic Platform in Poland. *Geol. Q.* **2017**, *61*, 502–520.
22. Kiersnowski, H.; Petecki, Z. Budowa geologiczna podcechsztyńskiego podłoża Legnicko-Głogowskiego Okręgu Miedziowego (LGOM) i jego otoczenia: Spojrzenie krytyczne. *Biul. Państw. Inst. Geol.* **2017**, *468*, 175–198.
23. Rudnickaja, D.I.; Danenberg, E.E.; Belozarov, V.B. Principy wydelenija sejsmociklitov v kontinentalnyh otlozhenijah jury Zapadno-Sibirskoj plity v svjazi s poiskami neantiklinalnyh zalezhej нефти i gaza. In *Prikladnye Voprosy Sedimentacionnoj Ciklichnosti i Neftegazonosnosti*; Nauka: Novosybirsk, Russia, 1987; pp. 67–72.
24. Dziewińska, L.; Jóźwiak, W. Zmiany litologiczne w utworach karbonu rowu lubelskiego w świetle interpretacji geofizycznej. *Biul. Państw. Inst. Geol.* **2000**, *39*, 5–48.
25. Dziewińska, L.; Petecki, Z. Kompleksowa interpretacja badań geofizycznych północnego obrzeżenia Gór Świętokrzyskich. *Instr. Metod. Badań Geol.* **2004**, *58*, 107.
26. Dziewińska, L.; Petecki, Z.; Tarkowski, R. Budowa geologiczna utworów permu struktury Wilków (monoklina przedsudecka) w świetle interpretacji sekcji współczynników odbicia. *Przegląd Gór.* **2011**, *67*, 64–72.

27. Dziewińska, L.; Tarkowski, R. Sejsmiczna interpretacja struktury Wierchowa dla potrzeb podziemnego składowania CO₂ z wykorzystaniem efektywnych współczynników odbicia. *Zesz. Nauk. IGSMIE-PAN* **2016**, *92*, 261–274.
28. Zieliński, K.; Speczik, S. Głębokie złoża miedzi i srebra szansą dla górnictwa metali w Polsce. *Biul. Państw. Inst. Geol.* **2017**, *468*, 153–164.



© 2020 by the authors. Licensee MDPI, Basel, Switzerland. This article is an open access article distributed under the terms and conditions of the Creative Commons Attribution (CC BY) license (<http://creativecommons.org/licenses/by/4.0/>).

Article

Handheld LIBS for Li Exploration: An Example from the Carolina Tin-Spodumene Belt, USA

Michael A. Wise¹, Russell S. Harmon^{2,*} , Adam Curry² , Morgan Jennings³, Zach Grimac⁴ and Daria Khashchevskaya²

¹ Department of Mineral Sciences, National Museum of Natural History, Smithsonian Institution, Washington, DC 20560, USA; wisem@si.edu

² Department of Marine, Earth and Atmospheric Sciences, North Carolina State University, Raleigh, NC 27695, USA; accurry3@ncsu.edu (A.C.); dkhashc@ncsu.edu (D.K.)

³ SciAps, Inc., 7 Constitution Way, Woburn, MA 01801, USA; mjennings@sciaps.com

⁴ Piedmont Lithium, Inc., 5706 Dallas Cherryville Highway, Bessemer City, NC 28016, USA; zgrimac@piedmontlithium.com

* Correspondence: rsharmon@ncsu.edu; Tel.: +1-919-588-0613

Abstract: Laser-induced breakdown spectroscopy (LIBS), which has recently emerged as tool for geochemical analysis outside the traditional laboratory setting, is an ideal tool for Li exploration because it is the only technique that can measure Li in minerals, rocks, soils, and brines in-situ in the field. In addition to being used in many products essential to modern life, Li is a necessary element for a reduced carbon future and Li–Cs–Ta (LCT) granitic pegmatites are an important source of Li. Such pegmatites can have varying degrees of enrichment in Li, Rb, Cs, Be, Sn, Ga, Ta>Nb, B, P, and F. We focus here on the LCT pegmatites of the Carolina Tin-Spodumene Belt (CTSB) situated in the Kings Mountain Shear Zone, which extends from South Carolina into North Carolina. The CTSB hosts both barren and fertile pegmatites, with Li-enriched pegmatites containing spodumene, K-feldspar, albite, quartz, muscovite, and beryl. We illustrate how handheld LIBS analysis can be used for real-time Li analysis in the field at a historically important CTSB pegmatite locality in Gaston County, N.C. in four contexts: (i) elemental detection and identification; (ii) microchemical mapping; (iii) depth profiling; and (iv) elemental quantitative analysis. Finally, as an example of a practical exploration application, we describe how handheld LIBS can be used to measure K/Rb ratios and Li contents of muscovite and rapidly determine the degree of pegmatite fractionation. This study demonstrates the potential of handheld LIBS to drastically reduce the time necessary to acquire geochemical data relevant to acquiring compositional information for pegmatites during a Li pegmatite exploration program.

Keywords: laser-induced breakdown spectroscopy; LIBS; Li analysis; LCT pegmatites; K/Rb-Li systematics



Citation: Wise, M.A.; Harmon, R.S.; Curry, A.; Jennings, M.; Grimac, Z.; Khashchevskaya, D. Handheld LIBS for Li Exploration: An Example from the Carolina Tin-Spodumene Belt, USA. *Minerals* **2022**, *12*, 77. <https://doi.org/10.3390/min12010077>

Academic Editor: Paul Alexandre

Received: 30 November 2021

Accepted: 4 January 2022

Published: 9 January 2022

Publisher's Note: MDPI stays neutral with regard to jurisdictional claims in published maps and institutional affiliations.



Copyright: © 2022 by the authors. Licensee MDPI, Basel, Switzerland. This article is an open access article distributed under the terms and conditions of the Creative Commons Attribution (CC BY) license (<https://creativecommons.org/licenses/by/4.0/>).

1. Introduction

Lithium is a metal widely used in the production of pharmaceuticals, glass, lubricants, and alloys; is present in most modern electronic devices; and used in many chemical processing and manufacturing processes [1]. It is also a critical element in the transition towards a low-carbon economy because it is central to the manufacture of the batteries that comprise energy storage systems and power electric vehicles. Because Li does not occur naturally as a native element, its current production comes from natural brines and granite-associated pegmatites in which Li concentrations have been strongly elevated above the average crustal abundance of 35 ± 11 ppm [2] to economically extractable levels. Brine deposits are the predominant source for Li at present (66%) and comprise the largest reserves but such deposits are geographically limited in distribution and face multiple production challenges. Pegmatite deposits (26%) will, therefore, remain an important source of Li because they are widespread globally and have a higher lithium concentration

compared to brines and clays [3–6]. Granitic pegmatites, in which Li typically occurs as a primary constituent in spodumene, petalite, and lepidolite, as well an important source of other important metals, including Be, Sc, Rb, Nb, Sn, Cs, Ta, REEs, Th, and U [7]. A particularly important type of granitic pegmatites is the Li–Cs–Ta (LCT) family [8,9].

2. Overview of LCT Granitic Pegmatites

LCT pegmatites are largely considered to be late magmatic products of extreme fractionation of peraluminous S-type granites [8], although the anatectic melting of supracrustal and mantle-related source lithologies has been proposed as an alternative process for the generation of some LCT pegmatite populations [10–12]. Granites parental to LCT pegmatites (i.e., fertile granites) often occur as texturally heterogeneous, zoned plutons that may include facies of (i) fine-grained biotite granite, (ii) two-mica granites, (iii) coarse-grained pegmatitic leucogranites, (iv) sodic aplites; and (v) highly mineralized pods and lenses of pegmatites in the apical portions of the pluton [13].

The population of LCT pegmatites cogenetic with fertile S-type granites ranges from barren bodies that lack significant rare-element mineralization to pegmatites that display varying degrees of enrichment in Li, Rb, Cs, Be, Sn, Ga, Ta > Nb, B, P, and F. This moderate to extreme fractionation of pegmatite melts typically results in rare-element mineralization that includes beryl, columbite-group minerals, the compositionally complex borosilicate tourmaline, and Li-minerals, such as triphylite-lithiophilite, amblygonite-montebbrasite, spodumene, petalite, and lepidolite.

In many districts and fields, granite-pegmatite suites show patterns of regional zoning where LCT pegmatites are situated within 10 km of their parental granite [14]. The exposed regional zoning pattern is rarely concentric, but instead is asymmetrical in most pegmatite fields and strongly influenced by the nature and structure of the host rock, by the shape of the parental intrusion, and the current erosional level of the granite–pegmatite system. In general, the least evolved and poorly mineralized bodies are found closest to the margins of the source granitic pluton, whereas the most chemically evolved Be-, Ta-, and Li-enriched pegmatites occur in distal areas relative to the parental pluton [15]. Spodumene- and petalite-bearing pegmatites typically occur the farthest away from their parental granite. This oversimplified sequence of pegmatite types extending outward from the margins of their parental granite is further characterized by progressive complexity of internal structural zones/units within individual pegmatite bodies, increasing diversity of mineral species, increasing degrees of metasomatic replacement, along with a gradual enrichment in Li, Rb, Cs, B, P, and F.

From an economic perspective, elemental abundance (e.g., Rb, Cs, Ta) and ratios (e.g., K/Rb, K/Cs, Nb/Ta) serve as valuable tools for the rapid assessment of the degree of rare-element fractionation in granite-pegmatite suites. Typically, low values of K/Rb (~2–400) and K/Cs (~20–2000) in K-feldspar, K/Rb (~1–50) and K/Cs (~10–1000) in muscovite, Na/Li (~2–20) in beryl, Fe/Mn in garnet (~0.007–2.0), Nb/Ta (~0.001–24) in columbite-group minerals, and Zr/Hf (~0.01–13) in zircon are encountered in pegmatites that have undergone moderate to extreme levels of fractionation and accumulation of rare lithophile elements [16,17]. These geochemical indicators of fractionation have been successfully used to identify parental granitoids, establish regional trends of rare-element enrichment in large pegmatite populations, and distinguish barren from mineralized pegmatites suitable for the extraction of potential rare-element ore minerals.

3. Geological Setting of the Carolina Tin-Spodumene Belt

The Carolina Tin-Spodumene Belt (CTSB) is of particular importance as a host of the most extensive and historically important Li pegmatite deposit in North America. Here, pegmatites of Carboniferous age [16] are concentrated in a belt across the Kings Mountain Shear Zone. This 0.5 to 3-km-wide, northeast-trending structure marks the boundary of the Inner Piedmont and Kings Mountain lithotectonic domains, with the shear zone extending approximately 60 km from Gaffney, South Carolina to Lincolnton, North Carolina (Figure 1).

Enclosed within the metamorphic rocks of the CTSB, which exhibit evidence of multiple periods of deformation, are hundreds of granitic pegmatite dikes, many containing spodumene and the tin oxide mineral cassiterite. Pegmatite intrusion occurred after major periods of deformation, but before the last of the tectonic movement [18,19]. The peraluminous 2-mica Cherryville granite lies just west of the CTSB in the Inner Piedmont belt and is considered by some investigators to be the source of the CTSB pegmatites, although derivation from the biotite-bearing High Shoals granite east of the CTSB has also been suggested [20–25].

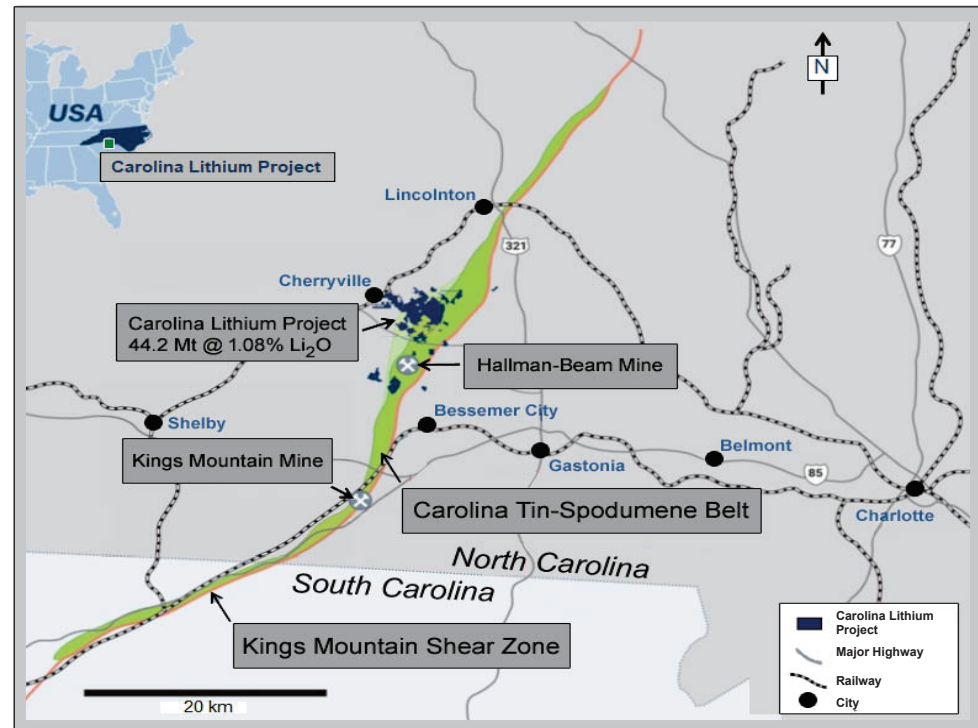


Figure 1. Carolina Tin-Spodumene Belt (green) showing the Kings Mountain Shear Zone (orange), the Kings Mountain and Hallman-Beam Li mines, and Piedmont Lithium’s Carolina Lithium Project (CLP) prospect in Gaston County, N.C. that has an estimated reserve of 44.2 Mt at 1.08 wt. % Li_2O (modified from map provided by Piedmont Lithium Inc. on 29 October 2021).

Different types of pegmatites have been identified within the CTSB that include (i) barren pegmatites containing primarily K-feldspar, oligoclase, quartz, with accessory muscovite, biotite, and garnet; (ii) barren pegmatites composed of K-feldspar, albite, quartz, and beryl; and (iii) lithium pegmatites bearing spodumene, K-feldspar, albite, quartz, and beryl [26]. Barren granitic pegmatites are most common within and near the Cherryville granite, whereas spodumene-bearing pegmatites are concentrated away from the granite body [27]. Accessory minerals in the pegmatites include beryl, garnet, titanite, cassiterite, zircon, Mn-bearing fluorapatite, triphylite, and columbite-group minerals [28,29].

Individual Li-bearing pegmatites are complex structures having typical surface dimensions of a few to a hundred meters in width and up to a kilometer in length that were intruded generally parallel to foliation in the surrounding country rocks [21]. Typically having a modal composition of ~20% spodumene, ~32% quartz, ~41% feldspar, and ~6% muscovite (Figure 2), these pegmatites are remarkably homogeneous, with minimal internal compositional zoning [23,28]. As illustrated in Figure 3, CTSB pegmatites can be quite coarse grained, with individual crystals > 1 m in length.

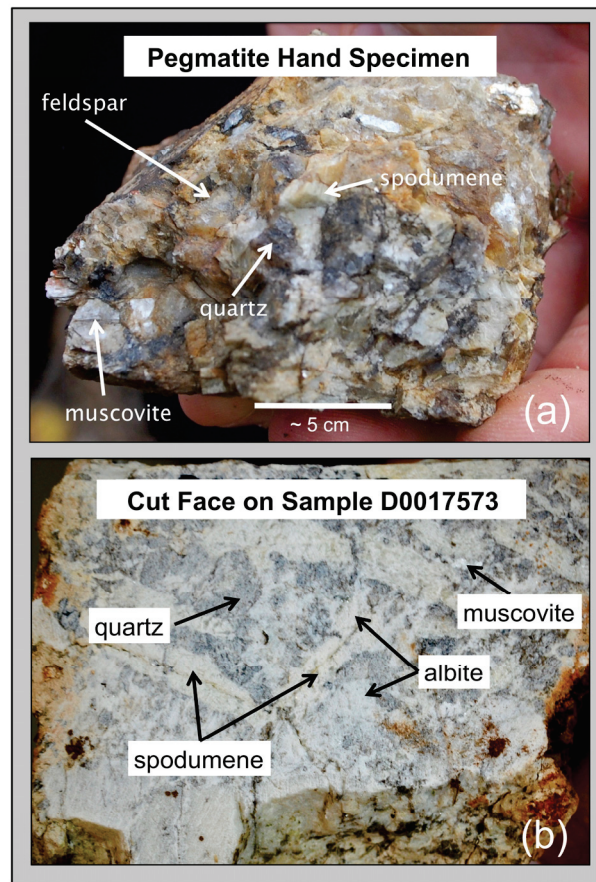


Figure 2. Two samples from the CLP in Gaston County, North Carolina: (a) hand specimen showing the typical mineralogy of spodumene, feldspar, quartz, and muscovite; (b) slab face of outcrop sample D0017573 showing a mineralogy of spodumene, quartz, albite, and muscovite.

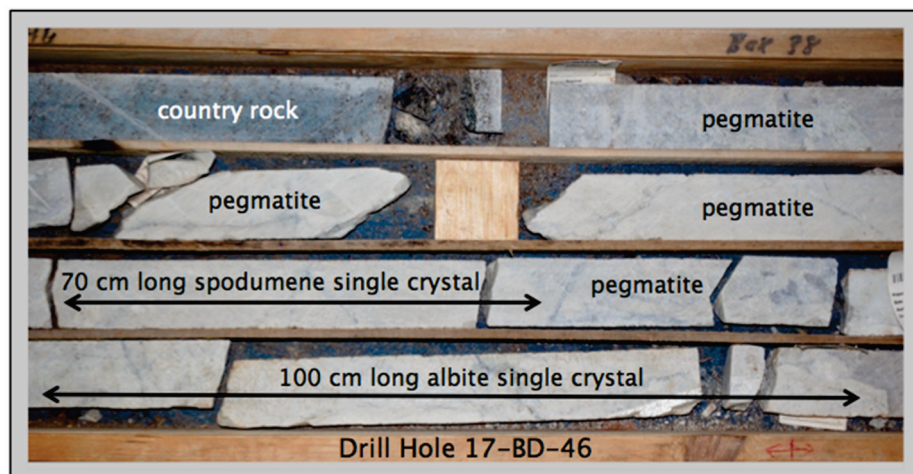


Figure 3. Carolina Lithium Project drill core 17-BD-46 between 107.51–110.21 m depth showing from top to bottom metamorphic country rock, and typical pegmatite containing a 70-cm-long crystal of spodumene and a 1-m-long albite crystal.

Estimates of Li reserves for the CTSB are large, >100 Mt averaging about 0.7% Li [30]. Active mining of spodumene was undertaken in the CTSB from the 1950s–1990s at two major mines: the Kings Mountain Mine operated by the Foote Mineral Company and the Hallman-Beam Mine operated by the Lithium Corporation of America (Figure 1). Recent

industrial demand for Li has resulted in renewed exploration activity across the CTSB, with the Piedmont Lithium's Carolina Lithium Project (CLP) presently assessing a large prospect in Gaston County near Bessemer City (Figure 1). The in-field LIBS analyses reported here were undertaken on drill core and at multiple outcrops across this prospect.

4. Laser-Induced Breakdown Spectroscopy

Laser-induced breakdown spectroscopy (LIBS) is a versatile form of atomic emission spectroscopy that can be used qualitatively for elemental detection or quantitatively for determination of elemental concentration [31,32] and references therein. In LIBS, a rapidly pulsed laser beam is focused onto a sample to ablate a minute amount of it and create a plasma on the sample surface in which constituent elements can be detected and identified through spectral analysis of emitted light. Because all elements have at least one emission line over the spectral range between 200–900 nm, any element can be analyzed by LIBS in situations where its abundance is above the limit of detection in the materials of interest [32]. As discussed by Harmon and Senesi [31], the rapid acquisition by LIBS of such information can be particularly useful to the mining industry for resource exploration and grade control during mining and ore beneficiation.

LIBS was one of many techniques restricted to chemical analysis in the laboratory or in industrial settings that have included mine and ore-processing sites [33] until the introduction of commercial handheld LIBS analyzers in 2016 [34]. Since that time, handheld LIBS has been used for a variety of geological applications that include the identification of elements and minerals; the discrimination of carbonate muds, limestone/dolomite stratigraphic sequences, volcanic rock suites, and meteorites; and natural resources exploration [35–49]. An important governing consideration with LIBS is the set of chemical and physical phenomena termed 'matrix effects' e.g., [31,50] and references therein, which determine the amount of mass ablated by an incident laser pulse. Chemical matrix effects occur when the emission behavior of one element in the plasma is interfered with by the presence of another element. By contrast, physical matrix effects arise from the nature of the sample. For example, there are a multiplicity of factors that determine the extent of laser–material coupling with geological materials, and therefore the resultant plasma character, which is primarily determined by the nature of the sample (e.g., its compositional homogeneity, degree of crystallinity or induration, hardness, grain size and porosity, surface texture and roughness, moisture and organic content, absorptivity and thermal conductivity, and optical transmissibility and reflectivity). Although full, broadband LIBS spectra may be used without preprocessing for elemental detection and applications, such as geochemical fingerprinting [50], the shot-to-shot variation that characterizes LIBS analysis of geological materials requires preprocessing that includes baseline correction of spectra and peak intensity normalization for development of calibration curves for quantitative analysis [51–55].

4.1. Laboratory LIBS Analysis of Li in Geological Materials

Li is an element effectively analyzed by LIBS because of its strong emissivity, which makes it readily detectable in geological materials, even when present at low ppm abundance levels. Analysis of Li in geological materials has been demonstrated in several studies over the past two decades using laboratory LIBS systems.

Fabre et al. [56] developed a quantitative calibration using 16 synthetic glasses and two micas that had a detection limit for Li of ~0.0005 wt. %. This calibration was then used to estimate the Li content of a suite of Li-bearing minerals that included spodumene and petalite with 6–8 wt. % Li from granite-associated pegmatites in Portugal, the glass (0.009–0.044 wt. %), and daughter minerals (up to 6.2 wt. % Li) for melt inclusions in quartz phenocrysts in a rhyolite from the Streltsovka caldera in the Transbaikalia region of eastern Russia, and in hydrothermal and diagenetic quartz (up to 0.034 wt. %) from the Sierra de Guadarrama in central Spain. McMillan et al. [57] observed strong Li emission in a LIBS survey of more than 96 beryls from 16 countries, and McManus et al. [58] determined that

Li was an important element for discriminating the provenance of beryl from pegmatite locations across the New England region of the northeastern United States.

Sweetapple and Tassios [59] demonstrated semi-quantitative mapping of Li, Be, and B in altered spodumenes and other Li-rich minerals from the Neoproterozoic Mt. Cattlin Li-pegmatite deposit in Australia and used this to discriminate spodumene; its accompanying sericitic alteration; and the matrix minerals, lepidolite, albite, and quartz. This study estimated a Li detection limit of ~0.024 wt. % based on Li-doped borosilicate glass as standards.

LIBS microchemical mapping and chemometric analysis was utilized by Romppanen et al. [60] to identify and discriminate the Li-bearing ore mineral spodumene from gangue minerals across the Kaustinen LCT pegmatite province of western Finland and to map sample texture. That same year, Janovszky et al. [61] undertook LIBS analysis of monzogranite from the Mórógy Granite Complex in the Eastern Mecsek Mountains of Hungary for the classification of constituent mineral grains and for Be and Li prospecting in granitoid rocks. This study demonstrated that valuable information about the distribution of elements in minerals can be obtained from LIBS elemental mapping, especially when combined with emission intensity data derived from matrix-matched calibrations.

Riberio et al. [62] used a portable XRF analyzer and a bespoke laboratory LIBS system to examine the same locations on quartz, montebrasite, and turquoise in a slab cut from a hydrothermal vein at the Argemela Tin Mine in Central Portugal. LIBS results demonstrated that montebrasite can be distinguished from turquoise because the turquoise did not contain Li. Micromapping by LIBS was successful in identifying minerals and their alteration products in a petrographically described thin section. The differences in spot size between XRF (5 mm) and LIBS (300 μm) resulted in a poorer performance by XRF in accurately identifying mixed minerals.

4.2. Li Analysis by Handheld LIBS

Senesi [39] described the potential for handheld LIBS analysis across the geosciences. Subsequently, Harmon et al. [37] described the use of a SciAps Z-300 handheld LIBS analyzer for quantitative Li analysis on-site during an exploration campaign at the Agua Fria Li prospect in the Sonora region of Mexico, where a Li-bearing hectorite clay and marl sequence is contained within the clastic sediments of an Oligocene to Miocene volcano-sedimentary basin sequence. The multielement composition of composite samples from 3 m intervals of the drill core was determined by ICP-MS analysis. LIBS measurements taking <3 seconds each to acquire for a 3×4 raster pattern at 12 locations on pressed pellets of each composite sample were averaged to produce a single-composite LIBS spectrum. The Li contents determined by handheld LIBS analysis agreed well with the laboratory results, with an R^2 observed of 0.86 for the suite of core samples analyzed.

Most recently, Fabre et al. [63] described the use of a SciAps Z-300 handheld LIBS instrument in the laboratory to acquire >4000 LIBS spectra for the Li-bearing minerals, including spodumene, petalite, lepidolite, zinnwaldite, amblygonite, or montebrasite, as well as various altered Li minerals and pegmatite samples from the Fregenda–Almendra pegmatite field that outcrops from the Guarda district in Portugal to the Salamanca province in Spain. These analyses were undertaken on minerals, rock thin sections, and pressed powder pellets and glasses prepared from pulverized minerals. The major elements observed were Al, Si, O, Mg, Ca, Li, Na, K, and Fe, with Be, Sr, Ba, Cs, Sn, Ta, and W being the most common minor and trace elements identified.

5. Analytical Methodology and Samples

Handheld LIBS is an attractive tool for undertaking geochemical measurements during exploration, drilling, or ore assessment campaigns because in-situ analytical results can be acquired rapidly under ambient environmental conditions with a minimum of sample preparation. Handheld LIBS analyzer has a unique capability to answer three questions in the field for the exploration geologist:

- What elements are present in a mineral, rock, or soil?
- How much of an element of interest is present?
- Is a sample compositionally homogeneous?

5.1. Samples

A wide variety of samples from the CLP prospect (Figure 1) were analyzed on site during 21–22 October 2021, either at the core storage facility (Figure 3) or at field outcrops (Figure 4) that included minerals in the drill core and outcrop, the pulverized drill core, and the soil. Minerals analyzed included spodumene, muscovite, quartz, albite, K-feldspar, tourmaline, and vivianite.



Figure 4. In-field LIBS analysis of pegmatite outcrops on the Carolina Lithium Project prospect in Gaston County, N.C., showing the use of the handheld LIBS analyzer for in-situ analysis (a) and examples of the different minerals analyzed—feldspar (b); feldspar, quartz, spodumene, and tourmaline (c); spodumene (d); and quartz (e).

5.2. Handheld LIBS Analysis

For this study, we used a SciAps Z-300 handheld LIBS analyzer (Figure 4). This instrument contains a Nd:YAG diode-pumped solid-state pulsed laser that generates a beam of focused laser light at 1064 nm that delivers a 5–6 mJ pulse of 1 ns pulse duration onto a 100- μ m area of the sample at a user-selected firing rate between 1 and 50 Hz. The instrument records light emission from the LIBS plasma, typically after a 650 ns delay over a 1-ms integration time, between the 190 to 950-nm spectral range, over which every element has at least one emission line. The Z-300 has the capability for the analysis to be conducted in Ar, which confines the plasma for enhanced emission, particularly in the deep ultraviolet portion of the LIBS emission between 190–300 nm. The light signal is collected and passed by fiber optic cable into three spectrometers with time-gated, charge-coupled

diode (CCD) detectors having respective spectral ranges and resolutions of 190–365 nm with a full-width half-maximum (FWHM) value of 0.18 nm, 365–620 nm with a FWHM value of 0.24 nm, and 620–950 nm with a FWHM value of 0.35 nm. This analysis produces composite LIBS spectra over the 23,432 channels of the spectrometer.

The sections that follow present examples of the *Element Pro*, *Geochem*, and *Geochem Pro* applications that are the on-board software programs facilitating the broad analytical capability of the Z-300 analyzer. Before our fieldwork, calibrations were prepared on the instrument in the laboratory for mica and bulk powdered pegmatite of known composition prior to using it at the CLP prospect to answer the three questions posed above. Four different analytical approaches were employed. First, for elemental identification using the *Element Pro* application, averages of four recorded spectra were collected after two cleaning shots at a laser firing rate of 50 Hz across a 4 × 3 grid. Next, microscale mapping with the *Geochem Pro* application was undertaken with a single laser shot at 256 locations over a 16 × 16 grid over 2 mm² areas of mineral surfaces to obtain distributions of elemental relative concentrations in the form of relative abundance ‘heat maps’. Then, elemental depth profiles were obtained by firing between 288–300 successive laser shots at single locations and recording 4-shot averages. Finally, quantitative analysis for Li was undertaken using the *Geochem* application by processing the average LIBS intensity values obtained from averaging of four spectra from 12 locations on a sample using the on-board calibrations.

The sections that follow present examples of the *Element Pro*, *Geochem*, and *Geochem Pro* applications described above. Before our fieldwork, calibrations were prepared on the Z-300 in the laboratory for mica- and bulk-powdered pegmatite of known composition, prior to using the handheld LIBS instrument at the CLP prospect to demonstrate its capability to answer the three questions posed above. Four different analytical approaches were employed, all of which used the option to undertake the LIBS analysis in an Ar atmosphere. First, for elemental identification using the *Element Pro* application, averages of four recorded spectra were collected after two cleaning shots at a laser firing rate of 50 Hz across a 4 × 3 grid. Next, microscale mapping with the *Geochem Pro* application was undertaken with a single laser shot at 256 locations over a 16 × 16 grid over 2 mm² areas of mineral surfaces to obtain distributions of elemental relative concentrations in the form of ‘heat maps’. Then, elemental depth profiles were obtained by firing between 288–300 successive laser shots at single locations and recording 4-shot averages. Finally, quantitative analysis for selected elements was undertaken using the *Geochem* application by processing the average LIBS intensity values obtained from averaging of four spectra from 12 locations on a sample using the calibration.

6. Application, Results, and Discussion

Exploration programs for rare-element granitic pegmatites typically utilize an integrated geological, mineralogical, and geochemical approach for identifying exposed and buried pegmatites of economic interest. Rock and mineral geochemistry has proven to be extremely effective in differentiating barren pegmatites lacking rare-element minerals from pegmatites that carry significant Be, Nb, Ta, Sn, or Li mineralization. The trace element content of pegmatite feldspars and micas have been proven to be useful markers for distinguishing chemically primitive pegmatites from moderately to highly evolved rare-element enriched pegmatites [16]. In a pegmatite field or district, where tens to hundreds of mineralogically diverse pegmatite bodies may be present, the inexpensive and rapid analysis of Li, K, Rb, and Cs in feldspar and muscovite by handheld LIBS can be a unique tool for identifying prospective Li-enriched pegmatites in the field during an exploration program.

The wallrock of some LCT pegmatites may develop exomorphic halos enriched in Li, Rb, Cs, B, and Be via interaction with pegmatite-derived fluids [64,65]. The occurrence of exomorphic minerals, such as holmquistite, biotite, tourmaline, and emerald, in amphibolitic and schistose wallrock surrounding pegmatites attest to episodes of metasomatic alteration, which have been shown in some cases to be a useful tool in pegmatite exploration. LIBS analysis of alteration assemblages in wallrocks surrounding rare-element-enriched peg-

matites has the potential to be an integral part of any pegmatite exploration program aimed at targeting Li-enriched pegmatites.

The geochemistry of soils and saprolite overlying pegmatite bodies has been shown to be successful in finding buried rare-element pegmatites [66]. Soils and saprolites that develop from weathered pegmatites can maintain low levels of trace elements inherent to the unweathered pegmatite body [67,68]. Because LIBS instruments can quickly detect low levels of Li and other trace elements, handheld LIBS is ideally suited for conducting soil surveys in pegmatite fields where outcropping bodies are scarce or absent.

6.1. Elemental Detection

For rapid qualitative analysis, the Z-300 is used in the *Element Pro* mode for element detection and identification. Relative emission strengths for each emission line in an acquired broadband LIBS spectrum are interrogated and compared with an onboard spectral library of selected elemental emission lines for the entire periodic table derived from the NIST atomic spectra database [69]. After each analysis, the list of elements identified in the sample is displayed (Figure 5), accompanied by a “likelihood” ranking that is a measure of the ratio of the number of elemental emission lines present in an acquired spectrum to the number of lines for each element in the spectral library and an estimated elemental “relative abundance” comparing how much of an element is present in the sample compared to other elements, with the caveat that there is no direct correlation between relative abundance and absolute element concentration. Used in this way, handheld LIBS analysis can be employed in the field to (i) detect the main elements present in a rock, mineral, or soil; (ii) rapidly distinguish between minerals of similar appearance; or (iii) identify an unknown mineral.

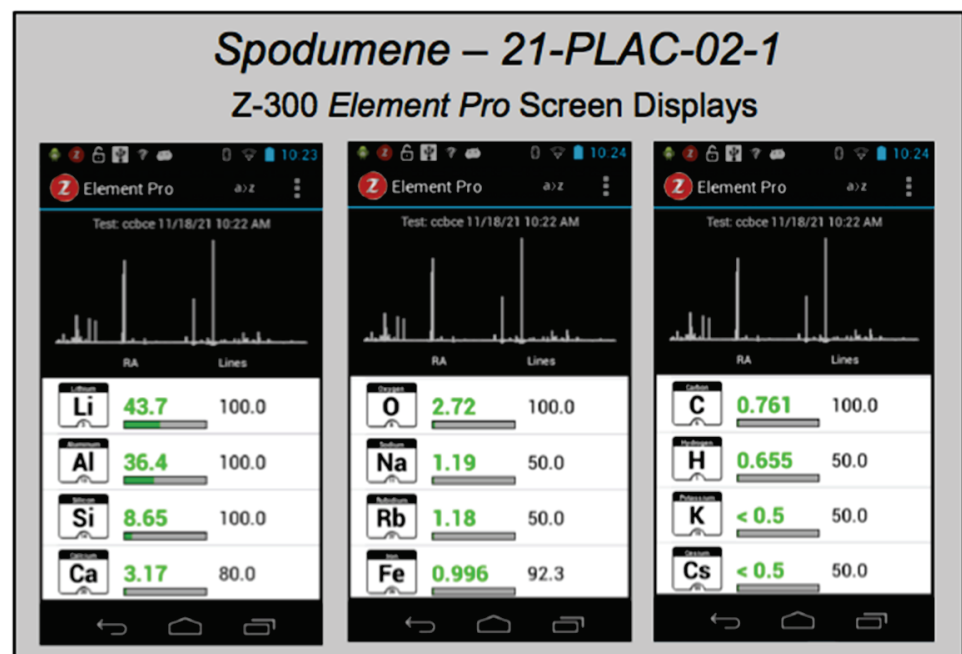


Figure 5. Z-300 screen shot sequence generated at the time of analysis showing the LIBS spectrum for spodumene in pegmatite outcrop 21-PLAC-02 on the Carolina Lithium Project prospect in Gaston County, N.C. and the 12 elements recognized with confidence in this sample—Li, Al, Si, Ca, O, Na, Rb, Fe, C, H, K, and Cs. The number in black text on the right-side column is the “likelihood” value, i.e., percentage of spectral lines in the on-board spectral library present in the LIBS spectrum, whereas the green number in the middle column is the “relative abundance” value. See text for discussion.

Analysis using the Z-300 handheld LIBS instrument identified 20 elements present in minerals of the pegmatite rock samples, drill cores, and outcrops analyzed across the CLP prospect above their different limits of detection (Table 1)—Al, B, Ba, Be, Ca, Cs, Fe, H, K,

La, Li, Mg, Mn, Na, O, P, Rb, Si, Sr, and V in some samples. Most elements are observed in the primary pegmatite minerals spodumene, quartz, feldspar, and/or muscovite; H and O are most pronounced in hydroxyl-bearing species; Be and La are only observed in the aluminosilicates; and P is only present in the phosphates (Figures 6–9). This is essentially the same set of elements recorded by Fabre et al. [63] in their handheld LIBS analysis of Li-bearing pegmatite minerals from the Fregenda–Almendra pegmatite field of the Iberian Peninsula.

Table 1. Emission lines for most common elements identified in pegmatite minerals from the Carolina Lithium Project prospect in Gaston County, North Carolina (USA).

Element	Wavelength (nm)	Wavelength (nm)	Wavelength (nm)	Element	Wavelength (nm)	Wavelength (nm)	Wavelength (nm)
Al	394.40	396.15	309.77	Li	670.79	610.36	460.29
B	249.77	249.68	-	Mg	279.53	282.27	285.22
Ba	455.40	553.55	493.41	Mn	257.61	260.57	356.95
Be	313.04	-	-	Na	589.00	589.59	-
Ca	393.37	396.85	422.67	O	777.20	-	-
Cs	852.11	894.35	257.80	P	213.62	214.95	-
Fe	259.94	438.35	371.99	Rb	780.03	794.76	-
H	656.28	-	-	Si	288.16	251.61	390.55
K	766.49	766.90	404.41	Sr	407.78	460.73	-
La	492.18	518.34	505.65	V	267.93	373.73	410.98

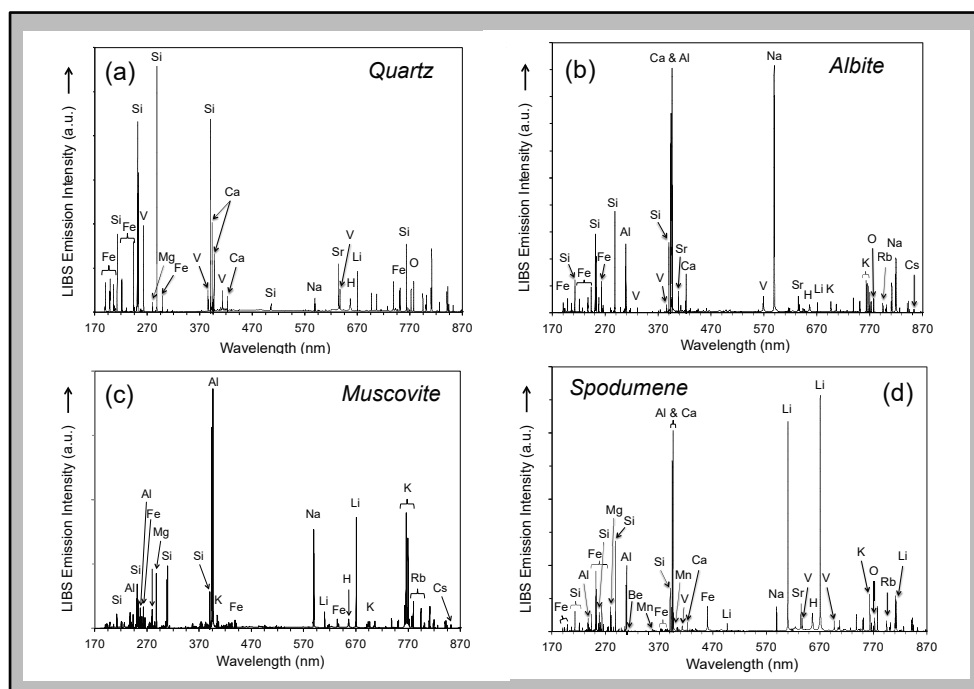


Figure 6. Handheld LIBS spectra for the primary pegmatite minerals quartz (a), albite (b), muscovite (c), and spodumene (d) from pegmatite outcrops on the Carolina Lithium Project prospect in Gaston County, N.C. The unlabeled peaks in the infrared portion of the spectrum between 700–870 nm are for the Ar purge gas used for the analysis.

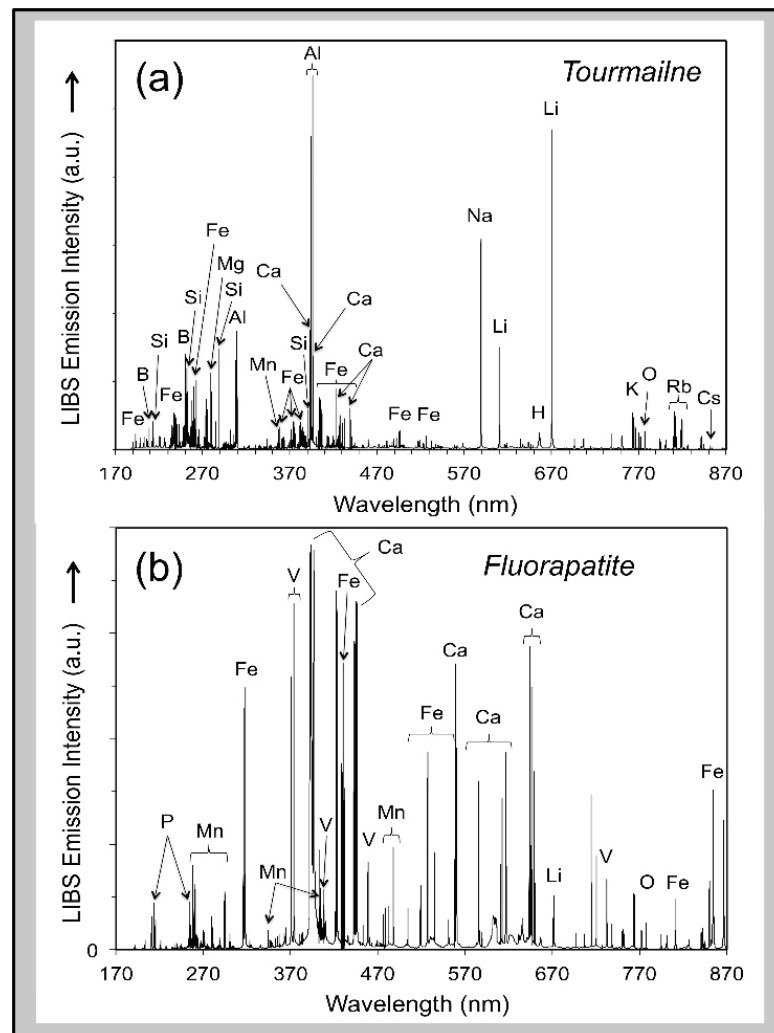


Figure 7. Handheld LIBS spectra between 170–870 nm for the pegmatite accessory minerals tourmaline (a) and fluorapatite (b) in pegmatite samples from the Carolina Lithium Project prospect in Gaston County, NC. The unlabeled peaks in the infrared portion of the spectrum between 700–870 nm are for the Ar purge gas used for the analysis.

Visually distinguishing between feldspar and spodumene or the micas muscovite and lepidolite rapidly in outcrops during an exploration campaign can sometimes be difficult but is immediately obvious by comparison of LIBS spectra based on the presence of the primary Li emission peaks at 610.36 nm and 670.79 nm in the Li-rich minerals (Figure 6). Similarly, phosphate minerals can be readily identified because the Z-300 analyzer records the ultraviolet region of the LIBS emission spectrum and, therefore, can observe the P emission lines at 213.62 nm and 214.95 nm (Figure 7). Non-metal elements, such as F, are particularly difficult to analyze by spectroscopic techniques, so it is notable that the two prominent molecular bands for CaF between 529–543 nm and 590–606 nm are present in the LIBS spectra for tourmaline and fluorapatite shown in Figure 7. Residual minerals in the regolith cover of the critical zone can be a useful guide to the presence of mineralized pegmatite at depth. For example, the presence of Li in detrital quartz in areas of deep soil cover lacking outcrop can be an important pathfinder to mineralization in the subsurface. Finally, under favorable circumstances, LIBS analysis can be helpful for rapid identification of accessory and uncommon minerals can be readily identified on site through a LIBS analysis (Figure 7).

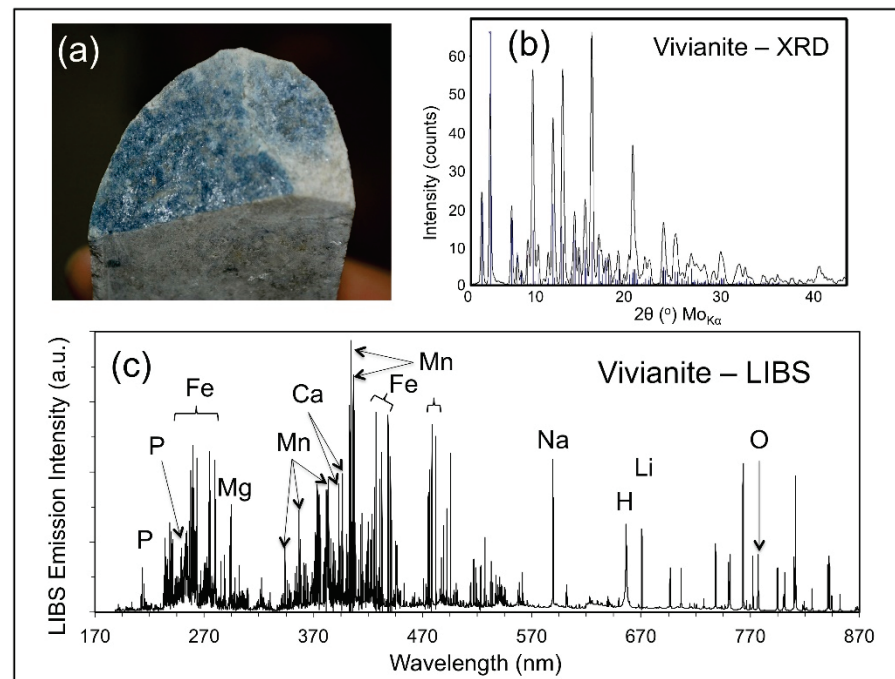


Figure 8. (a) Fine-grained vivianite $[\text{Fe}_3(\text{PO}_4)_2 \cdot 8\text{H}_2\text{O}]$ on a fracture in drill core 18-BD-288 from the Carolina Lithium Project prospect in Gaston County, N.C.; (b) X-ray diffraction pattern (Mo $K\alpha$ radiation) of vivianite after background subtraction (black), with International Centre for Diffraction Data pattern matches shown by vertical blue bars; and (c) handheld LIBS spectrum of vivianite showing the prominent P peaks at 213.62, 214.92, and 255.32 nm and the major Li peak at 670.79 nm. The suite of weak unlabeled peaks in the ultraviolet and visible portions of the LIBS spectrum between 234–278 nm and 404–441 nm are Fe emissions. The unlabeled peaks in the infrared portion of the LIBS spectrum between 700–870 nm are for the Ar purge gas used for the LIBS analysis. The very strong H peak at 656.3 nm in this spectrum, compared to those shown in Figures 6 and 7, indicate that this sample is a hydrated mineral and further supports its identification as vivianite.

Late-stage mineralization is common along fissures and fractures throughout the strongly tectonized and deformed CTSB. Figure 8 shows the occurrence of a blue-black, hypidiomorphic mineral along a fracture plane in a drill core (a) that was analyzed by X-ray diffraction analysis (b), and LIBS (c). LIBS analysis identified the presence of Fe, Li, and P, indicating that this mineral was either triphylite $[\text{LiFePO}_4]$ or vivianite $[\text{Fe}_3(\text{PO}_4)_2 \cdot 8\text{H}_2\text{O}]$ produced from the alteration of triphylite, with the latter attribution subsequently confirmed by the X-ray diffraction analysis.

6.2. Element Spatial Distribution

Whole-rock litho geochemistry of outcrop and drill core samples, together with microscale analysis of individual minerals, are two of the primary exploration tools for mapping the geochemical signature of ore systems. LIBS can be helpful in this context in two different ways. The Z-300 analyzer has a computer-controlled 3-D translational stage that permits rastering of the laser beam across the sample in the XY-direction at 12.5 μm steps over an area of up to $2 \times 2 \text{ mm}^2$, with the grid size and the number of laser shots fired at each point defined by the user. A user-selected number of non-analytical ‘cleaning’ shots can be performed prior to data collection. Therefore, compositional variation within a sample can be examined by the Z-300 analyzer at the $\sim 100 \mu\text{m}$ spatial scale of the LIBS analysis through either the microscale mapping feature where the laser is rastered over a 2 mm area of the sample surface or by depth profiling in which successive laser shots are undertaken at the same spot to ablate a sample to progressively greater depths.

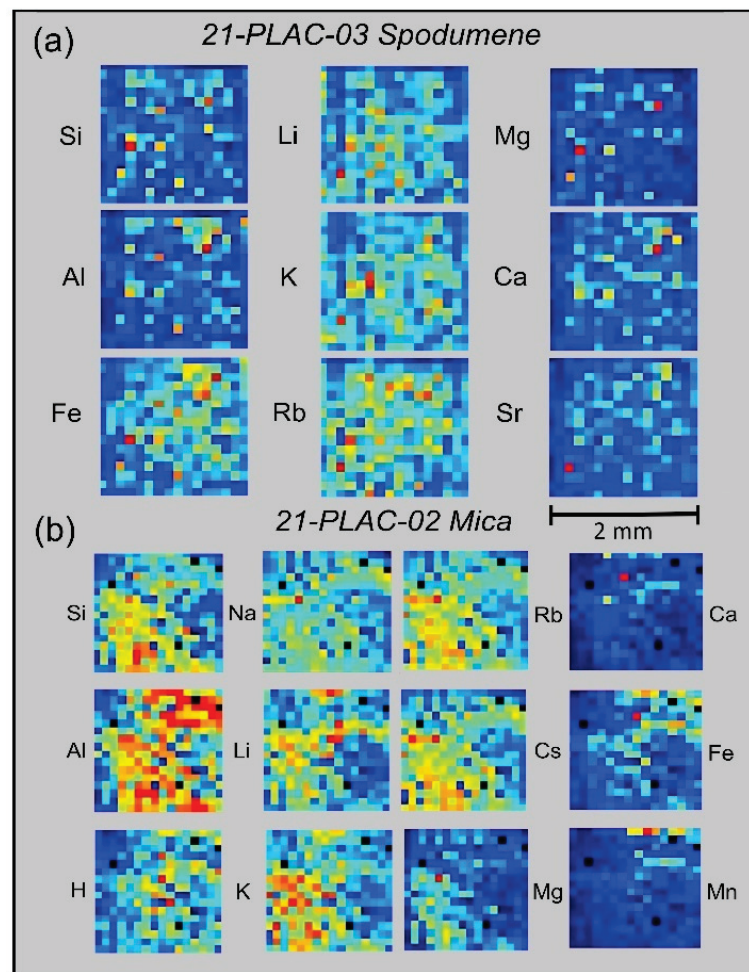


Figure 9. Elemental distribution ‘heat maps’ obtained by Z-300 raster scanning of a spodumene (a) and muscovite (b) specimens from outcrops on the Carolina Lithium Project prospect in Gaston County, N.C. Elemental emission intensity variations for different elements are shown in a gradient of colors that varies from red for high relative abundance to blue for low relative abundance. The spectral lines used for these microchemical maps are: Al = 396.15 nm, Ca = 393.37 nm, Cs = 852.11 nm, Fe = 438.35 nm, H = 656.28 nm, K = 766.49 nm, Li = 670.79 nm, Mg = 279.55 nm, Mn = 403.31 nm, Na = 588.99 nm, and Si = 288.16 nm.

For microscale mapping, the *Geochem Pro* mode of the Z-300 analyzer is used to identify spectral peaks and then generate relative concentration maps based on the recorded elemental intensities [37,46]. 2-D maps of relative emission intensity, commonly termed ‘heat maps’, are produced from individual laser shots spaced 12.5 μm across the surface of a sample over a 16×16 grid pattern. Examples from the CLP prospect are shown in Figure 9 for spodumene and muscovite crystals from two outcrop samples, 21-PLAC-03 and 21-PLAC-02. Such information can reveal whether a mineral is homogeneous at the spatial scale of the LIBS analysis and also can be helpful in understanding the geochemical behavior of different elements at a small spatial scale, which can provide insight into the process of pegmatite formation.

The panels in Figure 9a display the spatial distributions of variations in Si, Al, Fe, Li, K, Rb, Ca, Mg, and Sr abundances on the surface of a spodumene crystal in outcrop sample 21-PLAC-03, whereas those in Figure 9b show the spatial distributions of variations in Si, Al, H, Na, Li, K, Rb, Cs, Ca, Fe, and Mn abundances across a 2-mm domain on the surface of a muscovite crystal in outcrop sample 21-PLAC-02. Two features are of particular note across the $2 \times 2 \text{ mm}^2$ surface domains for the element distributions shown in Figure 9. The first is the general compositional homogeneity of the spodumene compared to the muscovite at

this spatial scale. By comparison to the nine ‘heat maps’ for 21-PLAC-03 spodumene, which are dominated by shades of dark and light blue, the individual ‘heat maps’ for 21-PLAC-02 muscovite exhibit the full range of color variation from almost entirely dark blue for Ca and Mn to domination by yellow and red colors for Al. The second is the coherent geochemical behavior of Li-K-Rb and Mg-Ca-Sr for the spodumene and Li-Na-K-Rb-Cs and Ca-Fe-Mn for the muscovite.

Figure 10 shows depth profiles for spodumenes in two outcrops. The profiles represent 4-shot averages of LIBS emission intensities of 10 spectral lines (Mg_{279.52}, Si_{288.16}, Be_{313.04}, Al_{309.27}, Ca_{422.67}, Na_{589.59}, Li_{610.36}, K_{766.49}, Rb_{794.76}, and Cs_{852.11}) for 300 successive laser shots at a single spot on sample 21-PLAC-03 and 288 successive laser shots at a single spot on sample 21-PLAC-04. These intensity variations are displayed on a logarithmic scale, as element intensities vary over five orders of magnitude for sample 21-PLAC-03 and four orders of magnitude for sample 21-PLAC-04. Thus, elements present in the samples at high abundance show subdued variation compared to elements of low concentration. Both depth profiles are characterized by significant variation over the first 5–6 depth intervals (i.e., 20–24 laser shots), which records decreases for some elements (e.g., Na, Mg, Ca) yet increases for others (e.g., Si, Al, Li, Rb, Cs). This behavior is interpreted to reflect the cumulative effect of surficial weathering of the spodumene that has caused elements of contrasting geochemical behavior being mobile to different extents. The other feature of note is the sharp increases in emission intensity for Na, Mg, Ca, K, and Be together with concomitant intensity decreases for Si, Al, Rb, and Cs observed for spodumene 21-PLAC-04 over the 40–45 laser shot depth interval. This compositional discontinuity likely reflects the encounter of the laser beam with an inclusion a few 10s of microns in size. Fabre et al. [56] have described how such inclusions can be probed and compositionally interrogated using a laboratory LIBS system.

6.3. Quantification

LIBS can measure the elemental abundance by measuring the intensity of the light captured at specific spectral wavelengths because the intensity of the plasma emission is proportional to the concentration of an element in a material of interest. Quantitative analysis by LIBS can be straightforward if the material being analyzed is compositionally homogeneous, as is the general situation for metal and alloy analysis where LIBS is well established and has been widely applied for a variety of industrial applications [33,40,70–75]. This is not generally the case for geological materials, which are intrinsically variable in terms of composition, crystallinity, and texture. Both the chemical composition of the matrix being analyzed by LIBS and its physical characteristics affect the measured abundance of an analyte present in the plasma [32] because these characteristics directly influence the excitation properties of the laser plasma produced by the ablation process [76] and, therefore, the emission line intensity measured for any element. Chemical matrix effects arise when the presence of an element of low ionization potential in the plasma elevates the plasma density and thereby inhibits the emission of other elements to decrease their abundance in the plasma [77]. Differences in material physical characteristics, such as crystallinity, hardness, opacity, grain size, coherence and texture, influence the degree of laser energy-material coupling so that elements of the same abundance in a dissimilar matrices will produce different emission intensities because of changes in the amount of sample ablated into the plasma with each laser pulse [78,79]. Further discussion of physical matrix effects is beyond the scope of this paper but has been described in detail in numerous previous studies, e.g., [31,36,78,80–88]. Chemical matrix effects are more readily ameliorated through optimization of the LIBS analytical system than physical matrix effects [32] which, therefore, present the greatest challenge to, and impediment for, quantitative analysis of geomaterials by LIBS. Despite these complications, quantitative analysis is possible by LIBS, but to do so requires careful selection of emission lines and creation of univariate or multivariate calibration curves using physically and compositionally similar matrix-matched standards.

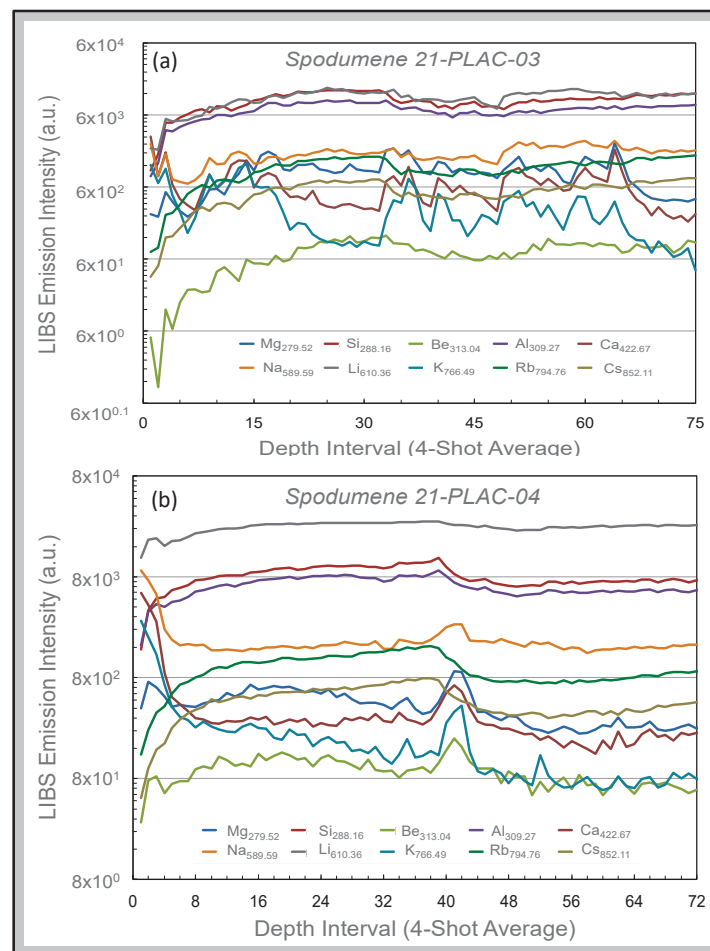


Figure 10. Depth profiles illustrating compositional variations just below the surface in two spodumene crystals from outcrops 21-PLAC-03 and 21-PLAC-04 on the Carolina Lithium Project prospect in Gaston County, N.C. Emission intensities are displayed for 10 elements (Mg, Si, Be, Al, Ca, Na, Li, K, Rb, and Cs) for 300 successive laser shots at a single spot on spodumene 21-PLAC-03 grouped into 4-shot averages (a) and 288 successive laser shots at a single spot on spodumene 21-PLAC-04 also grouped into 4-shot averages (b).

Quantitative analysis can be accomplished using *Geochem* mode of the Z-300 analyzer developed beforehand from the analysis of a set of matrix-matched reference materials using either single-element or multivariate calibration procedures. Two general calibrations curves are installed on Z-300 analyzers purchased for geoscience applications; a general geochemistry calibration (“geochem”) based on >70 different geological materials and NIST standards and an iron ore calibration (“Fe ore”) based on a smaller number of OREAS 400 series standard reference materials. Additionally, users can create bespoke calibration curves using the Z-300 *Profile Builder* PC-based software package as described in Harmon et al. [37].

Creating Z-300 calibrations utilizes a concentration versus intensity ratio approach that depends on two considerations: the number spectral lines for an element of interest and the presence of distinct emission lines that are not affected by overlap with lines from other elements present in the sample. Any LIBS calibration curve will perform best when developed for a specific matrix of interest. First, intensity values for elements are calculated after performing a Savitsky-Golay smoothing [89] on the LIBS spectrum, followed by a background subtraction, and finally integration of measured emission intensities across the defined spectral region of interest (ROI) to obtain a summed area under the peak value. Intensity ratios are then calculated by combining one or more summed peak intensity

values for the analyte element of interest in the numerator of the ratio and the denominator consisting either of the emission intensity for a single element or the sum of emission intensities of multiple elements for complex matrices. Ideally, elements used in the denominator comprise the bulk of the sample composition and remain relatively constant from sample to sample. Whilst concentration values are required for each of the target elements for which the calibration is being developed, they are not required for the elements in the denominator as elements of approximately constant composition (e.g., Al, Si and other major elements in silicate minerals) are used for this spectral intensity normalization. Once a set of calibration curves has been constructed, subsequent LIBS analysis using the Z-300 in the *Geochem* mode will calculate and display elemental concentrations for a test sample in real time.

As noted above, two provisional calibration curves have been developed on the Z-300 instrument from our initial work at the CLP prospect to illustrate this capability. These calibrations will be refined and enhanced, and new calibrations for other minerals developed, as our study continues and more samples of known composition are acquired. The first calibration (Figure 11) is for a set of mica samples with Li contents ranging from 0.014 to 2.59 wt. % from the collection of the U.S. Smithsonian Institution National Museum of Natural History that represent different LCT pegmatite subtypes and encompass a broad range of lithologies and geologic settings [90]. The second calibration (Figure 12) is for a suite of pressed pellets from 17 pulverized pegmatite core samples representing 1-m intervals in three drill holes on the CLP prospect previously analyzed by X-ray fluorescence (XRF) and inductively coupled plasma mass spectrometry (ICPMS). Low- and high-range calibration curves were developed for these samples, which ranged in Li content from 0.015 to 1.12 wt. %. Li contents measured for minerals, drill core, and soil from across the CLP prospect with the Z-300 handheld LIBS analyzer using these calibrations ranged from 0.005–2.672 wt. % (Table A3).

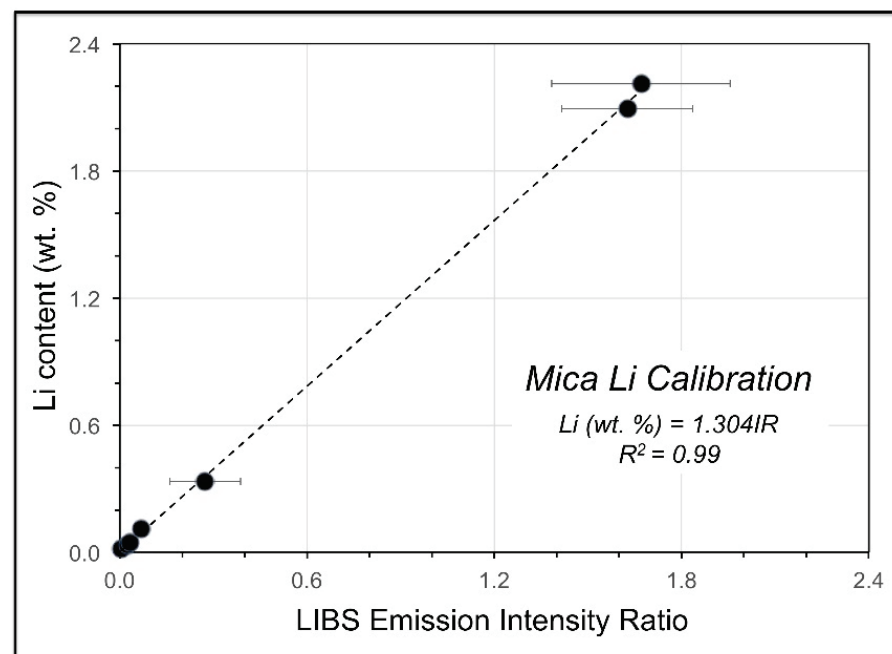


Figure 11. Handheld LIBS calibration curve for mica using the suite of nine mica specimens of known composition described in Table A1. The RMSE of the calibration is 0.0204%.

The calibration spectra were acquired with the same laser raster and pulse settings of 12 locations with two cleaning pulses and four data acquisition pulses per location. The laser was pulsed at a rate of 50 Hz and detector gating was used to avoid the collection of continuum light emitted early in the plasma lifetime, thus producing sharper spectra

with lower background. All 48 data pulses were averaged to produce a single spectrum for calibration use. Each sample was analyzed five times in this way and resulting intensity ratios were averaged. For the mica calibration, the Li intensity ratio consisted of the Li peak at 610.36 nm in the numerator and the sum of the peaks for Al at 394.40 nm, Ca at 396.85 nm, and Na at 819.48 nm in the denominator. The pegmatite powder calibration for our work at the CLP prospect used the intensity of Li nm peak at 610.36 nm in the numerator that was normalized to a combination of the intensities for the Al peak at 394.40 nm and the Fe peak at 438.35 nm.

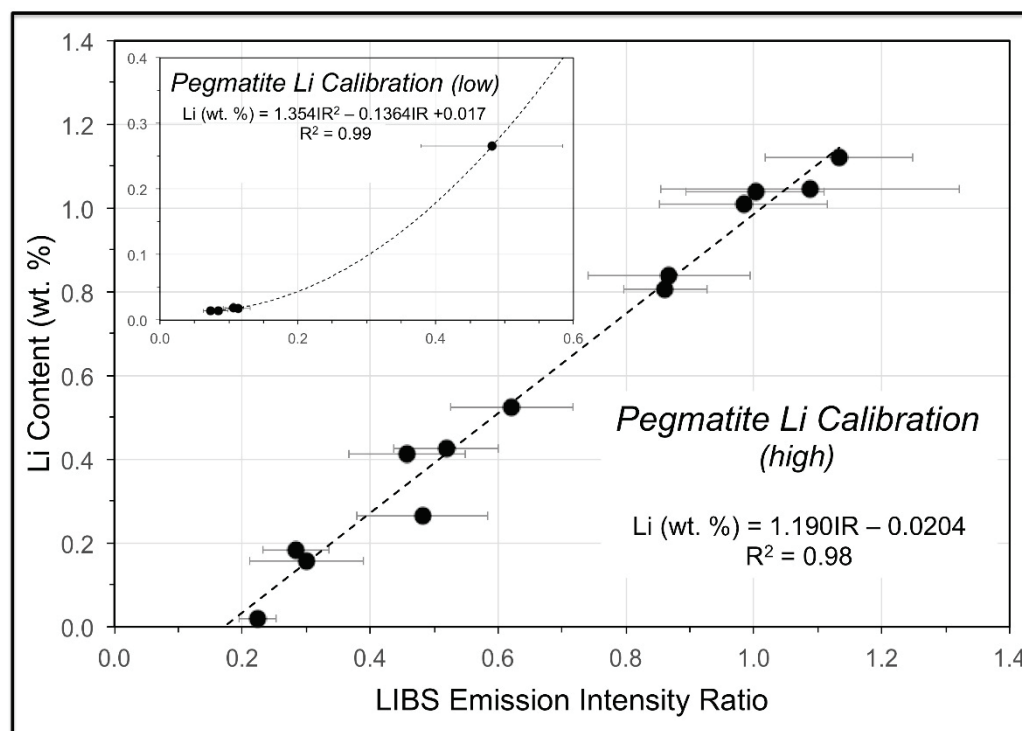


Figure 12. Handheld LIBS calibration curve developed from analysis of 18 pulverized pegmatite core samples from the CLP prospect described in Table A2. The RMSE values for the high and low calibrations are 0.0465% and 0.0021%, respectively.

Figure 13a shows the Z-300 *Geochem* mode screen display of LIBS spectra and sample Li composition of a muscovite from pegmatite outcrop sample 21-PLAC-02 and a surface exposure of the Cecil soil on the CLP prospect determined by comparison of an analyzed sample against the calibration that is provided to the analyst in real time.

The pegmatite powder calibration (Figure 12) was validated by analysis of a set of 14 pelletized powdered pegmatite samples from the Kleiber Oy Li deposit in Kaustinen-Kokkola area of central Ostrobothnia in western Finland, where Paleoproterozoic albite-spodumene pegmatites crosscut the Pohjanmaa schist belt situated between the Central Finland Granite and Vaasa Migmatite Complex of the Svecofennian Orogen [91,92]. Li contents for this validation suite range from 0.01–1.12 wt. % and, as shown in Table 2, analysis of the Kleiber Oy pegmatite powders against the calibration for the CLP pegmatite powders yielded Li contents very close to the assay values ($Li_{LIBS} = 0.941Li_{assay}$, $R^2 = 0.97$).

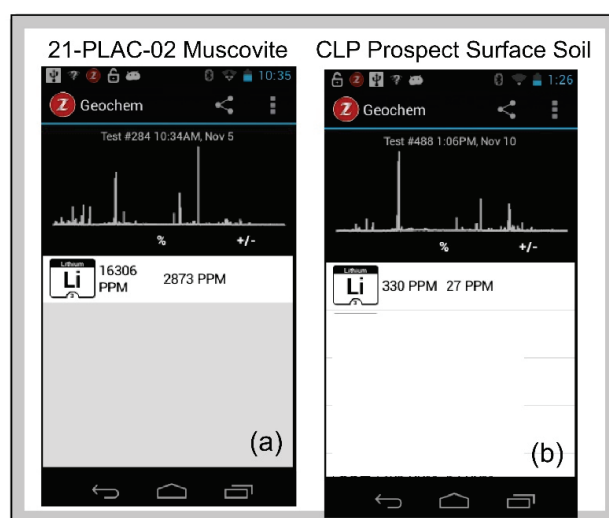


Figure 13. Screen shots from the Z-300 *Geochem* mode for a muscovite from Carolina Lithium Project prospect pegmatite outcrop sample 21-PLAC-02 (a) and a surface exposure of the Cecil soil on the CLP prospect (b). The Z-300 screenshots show the broadband LIBS spectrum recorded for each sample and estimated elemental abundances derived from the spectral emission line intensities. The Li content for the muscovite was determined from the mica calibration of Figure 11, whereas that for the Cecil soil was determined from the pegmatite powder calibration of Figure 12.

Table 2. Comparison of measured Li contents (wt. %) for pegmatite powders from the Kleiber Oy Li deposit, Finland with estimates using the CLP pegmatite powder calibration.

Sample #	KOP-21	KOP-22	KOP-23	KOP-24	KOP-25	KOP-26	KOP-27
Assay Li content	0.048	0.630	0.394	0.837	0.527	0.003	0.004
LIBS predicted Li content	0.046	0.703	0.322	0.856	0.484	0.002	0.003
Sample #	KOP-28	KOP-29	KOP-30	KOP-31	KOP-32	KOP-36	KOP-40
Assay Li content	0.214	0.746	0.251	0.863	1.016	0.608	0.009
LIBS predicted Li content	0.089	0.684	0.278	0.843	1.112	0.777	0.011

This example shows that calibrations for quantification can be developed using hand-held LIBS in situations of appropriate matrix matching between standards and samples. But what if that isn't possible? We considered this through analysis of a dozen samples from soil core 20-BD-359 from the CLP prospect drilled through the Cecil soil into saprolite. The Cecil soil is a well drained and moderately permeable soil derived from the deep weathering of felsic, igneous and high-grade metamorphic rocks on uplands throughout the Piedmont region of North Carolina [93] that is comprised primarily of Al and Fe oxyhydroxide minerals [94] rather than the aluminosilicate matrix on which the pegmatite powder calibration is based. The soil core samples, which were prepared as pressed pellets in exactly the same way as the pulverized pegmatites, were analyzed using both our pegmatite powder calibration and the SciAps general geochemistry calibration. Neither calibration produced the robust results shown in Table 2 for the Kleiber Oy pegmatite powders, but the latter yielded a more statistically significant relationship between Li assay values and LIBS abundance estimates than the former: $Li_{LIBS} = 0.828Li_{assay}$, $R^2 = 0.18$ using the pegmatite powder calibration versus $Li_{LIBS} = 0.368Li_{assay}$, $R^2 = 0.52$ using the Z-300 general geochemistry calibration. As illustrated in Table 3, soil Li abundances are closer to actual values for this general geochemistry calibration, which is based on >70 different geological materials that include a variety of soils, than for the calibration derived solely from the pegmatite powder which has an aluminosilicate matrix. A similar situation is observed when the suite of micas used to develop the mica calibration is analysed using

the pegmatite powder calibration (Table 4), with Li abundances lower using the pegmatite powder calibration than with the mica calibration. These two examples highlight the importance of matrix matching for quantitative LIBS.

Table 3. Comparison of Li analysis for a soil core on the Carolina Lithium Project prospect using different calibrations (CAL). PP = pegmatite powder, SAGG = SciAps General Geochemistry.

Z-300 ID	Sample Number	Li Assay (wt. %)	LIBS Li (wt. %)	CAL	Z-300 ID	Sample Number	Li Assay (wt. %)	LIBS Li (wt. %)	CAL
392	E00097886	0.023	0.009	PP	473	E00097886	0.023	0.014	SAGG
395	E00097887	0.049	0.018	PP	475	E00097887	0.049	0.032	SAGG
398	E00097888	0.035	0.018	PP	477	E00097888	0.035	0.022	SAGG
401	E00097889	0.043	0.02	PP	479	E00097889	0.043	0.031	SAGG
404	E00097890	0.030	0.008	PP	481	E00097890	0.030	0.025	SAGG
407	E00097891	0.039	0.015	PP	483	E00097891	0.039	0.049	SAGG
410	E00097892	0.022	0.006	PP	486	E00097892	0.022	0.024	SAGG
413	E00097893	0.030	0.012	PP	488	E00097893	0.030	0.033	SAGG
416	E00097894	0.036	0.012	PP	490	E00097894	0.036	0.035	SAGG
419	E00097895	0.029	0.012	PP	492	E00097895	0.029	0.031	SAGG
422	E00097896	0.033	0.013	PP	494	E00097896	0.033	0.030	SAGG
425	E00098117	0.033	0.005	PP	496	E00098117	0.033	0.011	SAGG

Table 4. Li analysis of mica using the mica (MC) and pegmatite powder (PP) calibrations.

Z-300 IDs	Sample Number	Li _{MC} (wt. %)	Li _{PP} (wt. %)
292 & 293	21-PLAC-02	0.091	0.007
306 & 307	Mt. Mica-11	1.357	1.159
341 & 342	Mt. Mica-56	0.052	0.005
361 & 362	Mt. Marie-15	0.052	0.004
376 & 377	Brown Derby Mine	1.943	1.437
433 & 434	Grosmont	1.842	1.75
456 & 457	Viitaniemi	2.202	0.008

6.4. Lithium Geochemistry for Exploration

Elevated values of Li in muscovite can suggest the presence of Li-bearing assemblages in LCT pegmatite populations. Lithium can substitute in the octahedral site of the muscovite structure via coupled substitutions involving Si, Al and vacancies [95,96]. The absolute value of Li in muscovite from granitic pegmatites can be as high as 3 wt. % Li, however, a minimal threshold of approximately 0.05 wt. % serves as a guide to prospecting for spodumene-bearing pegmatites [97]. Evolved muscovite compositions in LCT pegmatites generally show low K/Rb ratios and high Li contents with fractionation trends characterized by decreasing K/Rb with increasing Li contents.

Muscovite samples from the CLP prospect analyzed by the Z-300 handheld LIBS analyzer show reasonably high Li contents of 0.107–0.186 wt. % (Table A1), but does not reach the >1.5 wt. % levels observed for lepidolite [98]. K/Rb ratios calculated from the K_{766.43} and Rb_{779.97} spectral emission lines range from 3.0–8.6. As seen in Figure 14, our data for the CLP prospect plots within the mineralized field of granitic pegmatites and compares quite favorably to the domain of muscovite compositions from spodumene- and petalite-bearing pegmatites determined from other studies. The K/Rb and Li data for muscovites from the CLP prospect confirm the highly fractionated nature of these spodumene-bearing pegmatites. This approach to identifying fractionated LCT pegmatites has wide potential for rapidly identifying mineralized pegmatites by the exploration geologist in the field, as both Li content and K/Rb ratio can be calculated in real time by on-board software from a single LIBS mica analysis.

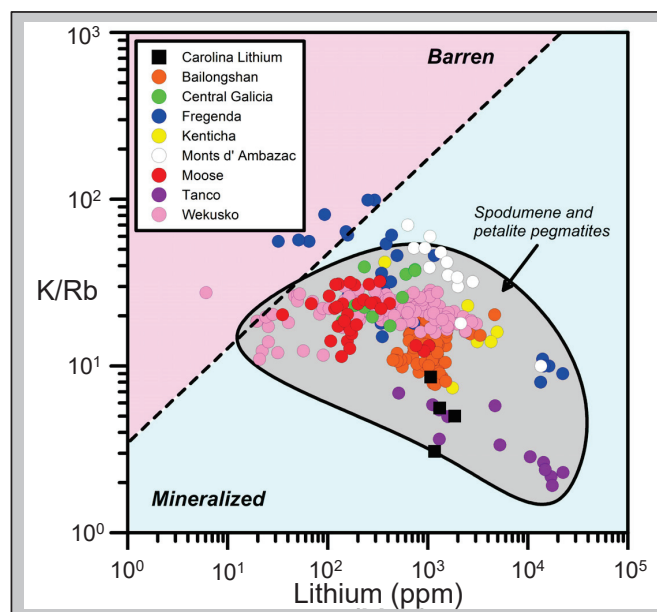


Figure 14. Comparison of muscovite K/Rb-Li (ppm) systematics for the CLP prospect with muscovite K/Rb-Li relationships for other Li-pegmatites worldwide: Bailongshan field, China [99]; Central Galicia field, Spain [100]; Fregenda area, Spain [101]; Kenticha pegmatite, Ethiopia [102]; Monts d' Ambazac field, France [103]; Moose pegmatite, Northwest Territories, Canada [104]; Tanco pegmatite, Manitoba, Canada [105]; and Dike 1, Wekusko Lake field, Manitoba, Canada [106].

7. Summary and Conclusions

LIBS is an analytical technique that has long been used for the analysis of ore minerals in laboratory [107–111] and, more recently, bespoke industrial LIBS systems have been developed for mineral exploration and exploitation [71,112–116]. The rapid acquisition of compositional data afforded by LIBS facilitates the interpretation of geochemical data in exploration, prospect evaluation, and ore processing contexts. Commercial handheld LIBS was developed in 2016 [34] and its potential for use in resources exploration was demonstrated shortly thereafter [37,46,48,117]. Here, we have described and illustrated the different analytical capabilities of handheld LIBS for mineral exploration, demonstrating elemental detection, microchemical mapping, depth profiling, and quantitative analysis with specific examples drawn from our analysis of soil, rocks, outcrops, and drill core from an active Li prospect in North Carolina (USA).

Using qualitative elemental analysis, the LIBS can differentiate minerals with similar field appearance such as muscovite and lepidolite and can identify accessory minerals like tourmaline and secondary minerals such as vivianite. Through microchemical mapping we illustrated how LIBS provides information about chemical homogeneity or heterogeneity at the 10s of micron spatial scale, yielding useful insights into coupled or decoupled behavior of elements within a sample. Similarly, the depth profiling ability of LIBS can be used to observe elemental distributions below the surface, allowing recognition of the effects of surficial weathering, a change in mineralogy, and presence of inclusions. Using laboratory-derived calibrations prior to fieldwork, quantitative chemical abundances in rocks, minerals, and soils can be readily measured in the field by handheld LIBS. Our new data both demonstrate the reliability of such calibrations and document the importance of having matrix matching when using a calibration. Finally, we illustrated the ability of handheld LIBS to effectively measure K/Rb and Li contents of muscovite, which has the potential for on-site recognition of the barren or fertile nature of the host pegmatite with regards to Li-enrichment. This is vital in an exploration or evaluation situation where spodumene might not be present on the surface outcrop of a pegmatite, but other minerals like muscovite are still available for chemical analysis. Overall, our study demonstrates

the ability of LIBS to provide rapid geochemical analyses in support of Li exploration of LCT pegmatites, which has the potential to save exploration endeavors money, time, and resources.

Author Contributions: M.A.W. and R.S.H. defined the study. R.S.H. and M.J. undertook the laboratory analyses prior to the fieldwork and developed the Li calibrations for the Z-300. A.C., R.S.H., and Z.G. conducted the LIBS analysis, with D.K. assisting with post-analysis spectral preprocessing. M.A.W., R.S.H., A.C. and M.J. prepared the paper with review from all co-authors. All authors have read and agreed to the published version of the manuscript.

Funding: Funding for the purchase of the Z-300 LIBS analyzer was provided to Professor Lewis A. Owen, Chair of the Department of Marine, Earth, and Atmospheric Sciences, by North Carolina State University.

Data Availability Statement: The LIBS spectra for all of the samples described in this paper are archived in the Li Pegmatite Project folder on the Open Science Framework at <https://www.osf.io/zhr9x/> (accessed on 2 January 2022).

Acknowledgments: Our appreciation is extended to Piedmont Lithium, Inc., specifically Lamont Leatherman, Michael Mason, and Gretchen Williams for logistical support, provision of geochemical data and for facilitating the in-field portion for this study, and to Lamont Leatherman and Patrick Brindle for internal review of the paper. This paper was improved by the thorough and insightful review received from Cécile Fabre (U Lorraine).

Conflicts of Interest: The authors declare no conflict of interest.

Appendix A

Table A1. Minerals analyzed by handheld LIBS on the Piedmont Lithium Carolina Lithium Project prospect, Gaston County, N.C. (USA).

Sample Number	Description
Mica	
PL_21-BD-490	Coarse muscovite rosette in barren pegmatite drill core
PL_S2L1_21-PLAC-01	Muscovite in East Pit Steep pegmatite outcrop
PL_S2L2_21-PLAC-03	Muscovite in pegmatite outcrop
Quartz	
PL_18-BD-228	Quartz crystal in pegmatite drill core
PL_21-BD-490	Quartz crystal in pegmatite drill core
PL_S2L2_21-PLAC-03	Quartz crystal in pegmatite outcrop
PL_S4L1	Quartz crystal in pegmatite outcrop
PL_S4L2_21-PLAC-06	Quartz crystal in pegmatite outcrop
Feldspar	
PL_21-BD-446	Albite crystal in pegmatite drill core
PL_17-BD-46	100 cm-long feldspar crystal in pegmatite drill core
PL_17-BD-62	Feldspar crystal in pegmatite drill core
PL_18-BD-228	Feldspar crystal in pegmatite drill core
PL_S2L1_21-PLAC-03	K-feldspar crystal in pegmatite outcrop
PL_S3L1	Feldspar crystal in pegmatite outcrop
PL_S3L2	K-feldspar crystal in pegmatite outcrop
PL_S3L2	Plagioclase crystal in pegmatite outcrop
PL_S3L2	Albite crystal in pegmatite outcrop
PL_S4L1	K-feldspar crystal in surface float
PL_S4L1	Albite crystal in surface float
Spodumene	
PL 21-BD-444	Spodumene in pegmatite drill core
PL 17-BD-46	70-cm spodumene in pegmatite drill core
PL hand specimen-1	Altered spodumene in saprolitic pegmatite
PL_D0017573	Spodumene in sample D0017573
PL_S2L1_21-PLAC-01	Spodumene in East Pit Steep pegmatite
PL_S2L2_21-PLAC-03-1	Spodumene in pegmatite outcrop
PL_S2L2_21-PLAC-03-2	Spodumene in pegmatite outcrop
PL-S2L3_21-PLAC-04	Spodumene in pegmatite outcrop
PL_S2L1	Spodumene in surface float
PL_S4L2_21-PLAC-06-1	Spodumene in pegmatite outcrop
PL_S4L2_21-PLAC-06-2	Spodumene in pegmatite outcrop
Other Minerals	
PL_18-BD-228	Vivianite on fracture surface in drill core
PL_21BD-490	Fluorapatite in in drill core
PL_S3L2	Tourmaline in pegmatite outcrop

Table A2. Chemical analyses for mica calibration and pegmatite powder calibration curves (values in wt. %).

LCT Pegmatite Micas		Element			
Sample ID	Locality	Li	K	Rb	Cs
Willis-7	Willis Warren, ME, USA	0.014			
Willis-2	Willis Warren, ME USA	0.033			
Mt Marie-15	Mt. Marie, Paris, ME, USA	0.042			
Mt Mica-56	Mt Mica, Paris, ME, USA	0.107			
Mt Mica-11	Mt Mica, Paris, ME, USA	0.334			
NMNH-165134	Bikita, Zimbabwe	1.779			
NMNH-105719	Brown Derby, CO, USA	2.088	8.388	1.712	0.071
NMNH-R11827	Vitaniemi, Eräjärvi, Finland	2.209	8.733	0.778	0.271
NMNH-128243	Grosmont, Western Australia, Australia	2.589	8.752	1.054	0.118

Drill Core Pegmatite Powders, Carolina Lithium Project Prospect									
Sample ID	Locality	Li	SiO ₂	Al ₂ O ₃	Fe ₂ O ₃	MgO	CaO	Na ₂ O	K ₂ O
20-BD-359 E00098037	Gaston County, NC (USA)	1.120	75.020	16.28	1.68	0.06	0.20	1.77	1.98
21-BD-413 F00097299	Gaston County, NC (USA)	1.046	75.920	16.18	1.21	0.01	0.20	2.88	1.90
21-BD-413 F00097290	Gaston County, NC (USA)	1.040	72.140	18.37	0.83	0.02	0.23	2.46	3.98
21-BD-398 F00098075	Gaston County, NC (USA)	1.010	74.490	15.89	1.40	0.09	0.25	1.91	2.40
21-BD-413 F00097297	Gaston County, NC (USA)	0.943	75.300	16.11	1.07	0.05	0.21	3.45	1.58
21-BD-413 F00097301	Gaston County, NC (USA)	0.839	73.640	16.69	0.95	0.04	0.30	3.98	1.89
20-BD-359 E00098047	Gaston County, NC (USA)	0.806	74.430	15.87	1.19	0.03	0.39	3.26	2.45
21-BD-398 F00098077	Gaston County, NC (USA)	0.526	74.170	15.16	1.25	0.09	0.44	3.64	2.62
20-BD-359 E00098045	Gaston County, NC (USA)	0.425	74.060	16.27	1.55	0.06	39.00	3.08	2.49
21-BD-398 F00098074	Gaston County, NC (USA)	0.441	74.510	15.55	0.96	0.05	0.29	5.19	2.06
20-BD-359 E00098043	Gaston County, NC (USA)	0.265	72.670	16.23	1.10	0.15	0.49	4.42	3.34
21-BD-398 F00098078	Gaston County, NC (USA)	0.185	75.020	15.08	0.93	0.06	0.31	5.40	1.75
20-BD-359 E00098033	Gaston County, NC (USA)	0.158	66.330	19.08	2.53	0.97	0.00	0.38	4.41
21-BD-413 F00097310	Gaston County, NC (USA)	0.021	72.700	15.44	0.92	0.16	1.53	6.90	0.98
21-BD-413 F00097275	Gaston County, NC (USA)	0.018	73.720	15.99	0.78	0.06	0.27	4.00	2.69
21-BD-413 F00097277	Gaston County, NC (USA)	0.018	73.000	15.78	0.66	0.07	0.52	5.70	2.95
21-BD-398 F00098065	Gaston County, NC (USA)	0.015	76.670	14.71	1.33	0.12	1.13	3.91	1.88
20-BD-359 E00098451	Gaston County, NC (USA)	0.014	72.830	15.92	1.03	0.19	0.60	3.54	6.38

Table A3. Li contents (wt. %) determined for minerals, drill core, and soil from the CLP prospect by handheld LIBS using the Z-300 handheld LIBS (M = mica calibration, PP = pegmatite powder calibration, GG = SciAps general geochemistry calibration).

Z-300 ID	Sample Description	Comment	Li (wt. %)	Cal
test 194	PL core—21-BD-490	mica in coarse mica rosette in barren pegmatite	0.118	M
test 196	PL core—21-BD-490	mica in coarse mica rosette in barren pegmatite	0.096	M
test 197	PL core—21-BD-490	mica in coarse mica rosette in barren pegmatite	0.137	M
test 200	PL core—21-BD-490	mica in mineralized pegmatite	0.204	M
test 202	PL core—21-BD-490	mica in mineralized pegmatite	0.189	M
test 203	PL core—21-BD-490	mica in mineralized pegmatite	0.205	M
test 204	PL core—hole 21-BD-444	spodumene in barren pegmatite	0.142	PP
test 205	PL core—hole 21-BD-444	spodumene in barren pegmatite	0.143	PP
test 206	PL core—hole 21-BD-444	spodumene in barren pegmatite	0.140	PP
test 207	PL core—hole 21-BD-444	mineralized pegmatite	0.298	PP
test 208	PL core—hole 21-BD-444	mineralized pegmatite	0.435	PP
test 213	PL core—hole 21-BD-444	mineralized pegmatite	0.282	PP
test 218	PL core 18-BD-228	quartz	0.053	PP
test 221	PL core 18-BD-228	quartz	0.418	PP
test 224	PL core 18-BD-228	quartz	0.117	PP
test 226	PL core 18-BD-228	feldspar	0.011	PP
test 227	large hand specimen	altered spodumene in saprolite	0.006	PP
test 230	PL core—21-BD-490	quartz	0.162	PP

Table A3. Cont.

Z-300 ID	Sample Description	Comment	Li (wt. %)	Cal
test 243	21-PLAC-01	mica; East Pit Steep	0.186	M
test 245	21-PLAC-01	spodumene; East Pit Steep	2.672	PP
test 246	21-PLAC-02	spodumene; East Pit Steep	1.603	PP
test 247	21-PLAC-02	spodumene; East Pit Steep	1.972	PP
test 248	21-PLAC-02	spodumene; East Pit Steep	0.984	PP
test 249	21-PLAC-02	spodumene; East Pit Steep	0.979	PP
test 250	21-PLAC-02	spodumene; East Pit Steep	1.153	PP
test 251	21-PLAC-03	Spodumene-1	2.671	PP
test 252	21-PLAC-03	Spodumene-2	1.377	PP
test 253	21-PLAC-03	Spodumene-2	1.505	PP
test 254	21-PLAC-03	large mica	0.126	M
test 255	21-PLAC-03	large mica	0.137	M
test 256	21-PLAC-04	spodumene	1.015	PP
test 257	21-PLAC-04	spodumene	1.573	PP
test 258	Stop 2	soil on road	0.006	PP
test 261	Stop 2	Na-feldspar float in soil	0.010	PP
test 263	Stop 2	quartz float in soil	0.021	PP
test 264	21-PLAC-06	spodumene	1.800	PP
test 472	PL core 20-SBD-017	soil core 1.2–2.4 m	0.009	PP
test 473	PL core 20-SBD-017	soil core 1.2–2.4 m	0.014	GG
test 474	PL core 20-SBD-017	soil core 2.4–4.0 m	0.017	PP
test 475	PL core 20-SBD-017	soil core 2.4–4.0 m	0.032	GG
test 476	PL core 20-SBD-017	soil core 4.0–5.5 m	0.018	PP
test 477	PL core 20-SBD-017	soil core 4.0–5.5 m	0.022	GC
test 478	PL core 20-SBD-017	soil core 5.5–8.5 m	0.020	PP
test 479	PL core 20-SBD-017	soil core 5.5–8.5 m	0.031	GG
test 480	PL core 20-SBD-017	soil core 8.5–10.0 m	0.008	PP
test 481	PL core 20-SBD-017	soil core 8.5–10.0 m	0.025	GG
test 482	PL core 20-SBD-017	soil core 10.0–11.5 m	0.059	PP
test 483	PL core 20-SBD-017	soil core 10.0–11.5 m	0.049	GG
test 485	PL core 20-SBD-017	soil core 11.5–13.1 m	0.006	PP
test 486	PL core 20-SBD-017	soil core 11.5–13.1 m	0.024	GG
test 487	PL core 20-SBD-017	soil core 13.1–14.6 m	0.018	PP
test 488	PL core 20-SBD-017	soil core 13.1–14.6 m	0.033	GG
test 489	PL core 20-SBD-017	soil core 14.6–16.2 m	0.012	PP
test 490	PL core 20-SBD-017	soil core 14.6–16.2 m	0.035	GG
test 491	PL core 20-SBD-017	soil core 16.2–17.6 m	0.012	PP
test 492	PL core 20-SBD-017	soil core 16.2–17.6 m	0.031	GG
test 493	PL core 20-SBD-017	soil core 17.7–19.2 m	0.013	PP
test 494	PL core 20-SBD-017	soil core 17.7–19.2 m	0.030	GG
test 495	PL core 20-SBD-017	soil core 19.2–20.7 m	0.005	PP
test 496	PL core 20-SBD-017	soil core 20.7–22.3 m	0.011	GG

References

1. USGS. *Mineral Commodity Summary 2011: Lithium*; U.S. Geological Survey: Reston, VA, USA, 2011. [\[CrossRef\]](#)
2. Teng, F.-Z.; McDonough, W.; Rudnick, R.; Dalpé, C.; Tomascak, P.; Chappell, B.; Gao, S. Lithium isotopic composition and concentration of the upper continental crust. *Geochim. Cosmochim. Acta* **2004**, *68*, 4167–4178. [\[CrossRef\]](#)
3. Gruber, P.W.; Medina, P.A.; Keoleian, G.A.; Kesler, S.E.; Everson, M.P.; Wallington, T.J. Global Lithium Availability: A constraint for electric vehicles? *J. Ind. Ecol.* **2011**, *15*, 760–775. [\[CrossRef\]](#)
4. Grosjean, C.; Miranda, P.H.; Perrin, M.; Poggi, P. Assessment of world lithium resources and consequences of their geographic distribution on the expected development of the electric vehicle industry. *Renew. Sustain. Energy Rev.* **2012**, *16*, 1735–1744. [\[CrossRef\]](#)
5. Kesler, S.E.; Gruber, P.W.; Medina, P.A.; Keoleian, G.A.; Everson, M.P.; Wallington, T.J. Global lithium resources: Relative importance of pegmatite, brine and other deposits. *Ore Geol. Rev.* **2012**, *48*, 55–69. [\[CrossRef\]](#)
6. Kavanagh, L.; Keohane, J.; Garcia Cabellos, G.; Lloyd, A.; Cleary, J. Global Lithium Sources—Industrial Use and Future in the Electric Vehicle Industry: A Review. *Resources* **2018**, *7*, 57. [\[CrossRef\]](#)

7. Linnen, R.L.; Van Lichtervelde, M.; Černý, P. Granitic Pegmatites as Sources of Strategic Metals. *Elements* **2012**, *8*, 275–280. [[CrossRef](#)]
8. Černý, P.; Ercit, S. The classification of granitic pegmatites revisited. *Can. Mineral.* **2005**, *43*, 2005–2026. [[CrossRef](#)]
9. Černý, P.; London, D.; Novak, M. Granitic pegmatites as reflections of their sources. *Elements* **2012**, *8*, 289–294. [[CrossRef](#)]
10. Simmons, W.; Falster, A.; Webber, K.; Roda-Robles, E.; Boudreaux, A.P.; Grassi, L.R.; Freeman, G. Bulk composition of Mt. Mica pegmatite, Maine, USA: Implications for the origin of an LCT type pegmatite by anatexis. *Can. Miner.* **2016**, *54*, 1053–1070. [[CrossRef](#)]
11. Barros, R.; Menuge, J.F. The origin of spodumene pegmatites associated with the Leinster Granite in southeast Ireland. *Can. Miner.* **2016**, *54*, 847–862. [[CrossRef](#)]
12. Fuchsloch, W.C.; Nex, P.A.; Kinnaird, J.A. Classification, mineralogical and geochemical variations in pegmatites of the Cape Cross-Uis pegmatite belt, Namibia. *Lithos* **2018**, *296–299*, 79–95. [[CrossRef](#)]
13. Černý, P.; Meintzer, R.E. Fertile granites in the Archean and Proterozoic fields of rare-element pegmatites: Crustal environment, geochemistry, and petrogenetic relationships. In *Recent Advances in the Geology of Granite Related Mineral Deposits*; Canadian Institute of Mining and Metallurgy: Montreal, QC, Canada, 1988; Volume 39, pp. 170–207.
14. Baker, D.R. The escape of pegmatite dikes from granitic plutons; constraints from new models of viscosity and dike propagation. *Can. Mineral.* **1998**, *36*, 255–263.
15. Černý, P. Characteristics of pegmatite deposits of tantalum. In *Lanthanides, Tantalum and Niobium*; Černý, P., Möller, P., Saupe, F., Eds.; Springer: Berlin/Heidelberg, Germany, 1989; pp. 195–239.
16. Černý, P.; Meintzer, R.E.; Anderson, A.J. Extreme fractionation in rare-element granitic pegmatites; selected examples of data and mechanisms. *Can. Mineral.* **1985**, *23*, 381–421.
17. Trueman, D.L.; Černý, P. Granitic pegmatites in science and industry. In *Short Course Handbook*; Mineralogical Association of Canada: Quebec City, QC, Canada, 1982; Volume 8, p. 463.
18. Kish, S.A.; Fullagar, P.D. Age and magmatic association of rare metal pegmatites; spodumene pegmatites, Kings Mountain, NC and Sn-Ta pegmatites, Rockford, Ala. *Geol. Soc. Am. Abstr. Programs* **1996**, *28*, A475.
19. Horton, J.W.; Butler, J.R. The Kings Mountain belt and spodumene pegmatite district, Cherokee and York Counties, South Carolina, and Cleveland County, North Carolina. In *Centennial Field Guide*; Neathery, T.L., Ed.; Southeastern Section of the Geological Society of America: Boulder, CO, USA, 1986; Volume 6, pp. 239–244.
20. Horton, J.W. Shear zone between the Inner Piedmont and Kings Mountain belts in the Carolinas. *Geology* **1981**, *9*, 28. [[CrossRef](#)]
21. Kesler, T. *The Tin-Spodumene Belt of the Carolinas, a Preliminary Report*; U.S. Government Printing Office: Washington, DC, USA, 1942; 269p. [[CrossRef](#)]
22. Kesler, T.L. The Kings Mountain area. In *Guides to Southeastern Geology*; Russell, R.J., Ed.; Geological Society of America Field Trip Guidebook: Boulder, CO, USA, 1955; pp. 374–387.
23. Kesler, T.L. Occurrence, development, and long-range outlook of lithium-pegmatite ore in the Carolinas. In *Lithium Resources and Requirements by the Year 2000*; Vine, J.D., Ed.; U.S. Geological Survey Professional Paper 1005; 1976; pp. 45–50.
24. Luster, G.R. Lithologic Variability of the Kings Mountain Pegmatite, North Carolina. Master's Thesis, Pennsylvania State University, University Park, PA, USA, 1977.
25. Hodges, R.A. A Petrologic Study of the Lithium Corporation of America Mine in the Tin-Spodumene Belt of North Carolina. Master's Thesis, University of North Carolina, Chapel Hill, NC, USA, 1983.
26. Griffiths, W.R.; Overstreet, W.C. Granitic rocks of the western Carolina Piedmont. *Am. J. Sci.* **1952**, *250*, 777–789. [[CrossRef](#)]
27. Kesler, T.L. Exploration of the Kings Mountain pegmatites. *Miner. Eng.* **1961**, *13*, 1062–1068.
28. White, J.S. Mineralogy of the Foote mine, Kings Mountain, North Carolina. In *Geological Investigations of the Kings Mountain Belt and Adjacent Areas in the Carolinas*; Horton, J.W., Butler, J.R., Milton, D.M., Eds.; Carolina Geological Society Field Trip Guidebook; South Carolina Geological Survey: Columbia, SC, USA, 1981; pp. 39–48.
29. Swanson, S.E. Mineralogy of spodumene pegmatites and related rocks in the tin-spodumene belt of North Carolina and South Carolina, USA. *Can. Miner.* **2012**, *50*, 1589–1608. [[CrossRef](#)]
30. Kesler, T.L. Raw lithium supplies. *Min. Eng.* **1978**, *30*, 283–285.
31. Harmon, R.S.; Senesi, G.S. Laser-Induced Breakdown Spectroscopy—A geochemical tool for the 21st century. *Appl. Geochem.* **2021**, *128*, 104929. [[CrossRef](#)]
32. Cremers, D.A.; Radziemski, L.J. *Handbook of Laser-Induced Breakdown Spectroscopy*, 2nd ed.; John Wiley & Sons: Chichester, UK, 2013.
33. Pedarnig, J.D.; Trautner, S.; Grünberger, S.; Giannakaris, N.; Eschlböck-Fuchs, S.; Hofstadler, J. Review of element analysis of industrial materials by in-line laser-induced breakdown spectroscopy (LIBS). *Appl. Sci.* **2021**, *11*, 9274. [[CrossRef](#)]
34. Connors, B.; Somers, A.; Day, D. Application of handheld laser-induced breakdown spectroscopy (LIBS) to geochemical analysis. *Appl. Spectrosc.* **2016**, *70*, 810–815. [[CrossRef](#)] [[PubMed](#)]
35. Harmon, R.S.; Hark, R.R.; Throckmorton, C.S.; Rankey, E.C.; Wise, M.A.; Somers, A.M.; Collins, L.M. Geochemical fingerprinting by handheld laser-induced breakdown spectroscopy. *Geostand. Geoanal. Res.* **2017**, *41*, 563–584. [[CrossRef](#)]
36. Harmon, R.S.; Throckmorton, C.S.; Hark, R.R.; Gottfried, J.; Wörner, G.; Harpp, K.; Collins, L. Discriminating volcanic centers with handheld laser-induced breakdown spectroscopy (LIBS). *J. Archaeol. Sci.* **2018**, *98*, 112–127. [[CrossRef](#)]

37. Harmon, R.S.; Lawley, C.J.; Watts, J.; Harraden, C.L.; Somers, A.M.; Hark, R.R. Laser-induced breakdown spectroscopy—An emerging analytical tool for mineral exploration. *Minerals* **2019**, *9*, 718. [[CrossRef](#)]
38. Harmon, R.S.; Khashchevskaya, D.; Morency, M.; Owen, L.A.; Jennings, M.; Knott, J.R.; Dortch, J.M. Analysis of rock varnish from the Mojave Desert by handheld laser-induced breakdown spectroscopy. *Molecules* **2021**, *26*, 5200. [[CrossRef](#)] [[PubMed](#)]
39. Senesi, G. Portable handheld laser-induced breakdown spectroscopy (LIBS) instrumentation for in-field elemental analysis of geological samples. *Int. J. Earth Environ. Sci.* **2017**, *2*, 17. [[CrossRef](#)]
40. Senesi, G.S.; Harmon, R.S.; Hark, R.R. *Field Portable and Handheld LIBS: In Laser Induced Breakdown Spectroscopy*; Singh, J.P., Thakur, S.Y., Eds.; Elsevier: Amsterdam, The Netherlands, 2020; pp. 537–560.
41. Senesi, G.S.; Manzari, P.; Consiglio, A.; De Pascale, O. Identification and classification of meteorites using a handheld LIBS instrument coupled with a fuzzy logic-based method. *J. Anal. At. Spectrom.* **2018**, *33*, 1664–1675. [[CrossRef](#)]
42. Senesi, G.; Manzini, D.; De Pascale, O. Application of a laser-induced breakdown spectroscopy handheld instrument to the diagnostic analysis of stone monuments. *Appl. Geochem.* **2018**, *96*, 87–91. [[CrossRef](#)]
43. Senesi, G.S.; Manzari, P.; Tempesta, G.; Agrosi, G.; Touchnt, A.A.; Ibhi, A.; De Pascale, O. Handheld laser induced breakdown spectroscopy instrumentation applied to the rapid discrimination between iron meteorites and meteor-wrongs. *Geostand. Geoanal. Res.* **2018**, *42*, 607–614. [[CrossRef](#)]
44. Pochon, A.; Desaulty, A.-M.; Bailly, L. Handheld laser-induced breakdown spectroscopy (LIBS) as a fast and easy method to trace gold. *J. Anal. At. Spectrom.* **2020**, *35*, 254–264. [[CrossRef](#)]
45. Defnet, P.; Wise, M.; Harmon, R.; Hark, R.; Hilferding, K. Analysis of garnet by laser-induced breakdown spectroscopy—Two practical applications. *Minerals* **2021**, *11*, 705. [[CrossRef](#)]
46. Lawley, C.J.; Somers, A.M.; Kjarsgaard, B.A. Rapid geochemical imaging of rocks and minerals with handheld laser induced breakdown spectroscopy (LIBS). *J. Geochem. Explor.* **2020**, *222*, 106694. [[CrossRef](#)]
47. Lemièrre, B.; Harmon, R.S. *XRF and LIBS for Field Geology: In Portable Spectroscopy and Spectrometry: Technologies and Instrumentation*; Crocombe, R., Leary, P., Kammrath, B., Eds.; John Wiley & Sons: Hoboken, NJ, USA, 2021; pp. 457–499.
48. Fabre, C.; Ourti, N.; Mercadier, J.; Cardoso-Fernandes, J.; Dias, F.; Perrotta, M.; Koerting, F.; Lima, A.; Kaestner, F.; Koellner, N.; et al. Analyses of Li-rich minerals using handheld LIBS tool. *Data* **2021**, *6*, 68. [[CrossRef](#)]
49. Rammelkamp, K.; Schröder, S.; Ortenzi, G.; Pisello, A.; Stephan, K.; Baqué, M.; Hübers, H.-W.; Forni, O.; Sohl, F.; Thomsen, L.; et al. Field investigation of volcanic deposits on Vulcano, Italy using a handheld laser-induced breakdown spectroscopy instrument. *Spectrochim. Acta Part B At. Spectrosc.* **2021**, *177*, 106067. [[CrossRef](#)]
50. Harmon, R.S.; Remus, J.; McMillan, N.J.; McManus, C.; Collins, L.; Gottfried, J.; DeLucia, F.C.; Miziolek, A.W. LIBS analysis of geomaterials: Geochemical fingerprinting for the rapid analysis and discrimination of minerals. *Appl. Geochem.* **2009**, *24*, 1125–1141. [[CrossRef](#)]
51. Tucker, J.; Dyar, M.; Schaefer, M.; Clegg, S.; Wiens, R. Optimization of laser-induced breakdown spectroscopy for rapid geochemical analysis. *Chem. Geol.* **2010**, *277*, 137–148. [[CrossRef](#)]
52. Zorov, N.B.; Gorbatenko, A.A.; Labutin, T.A.; Popov, A. A review of normalization techniques in analytical atomic spectrometry with laser sampling: From single to multivariate correction. *Spectrochim. Acta Part B At. Spectrosc.* **2010**, *65*, 642–657. [[CrossRef](#)]
53. Dyar, M.D.; Giguere, S.; Carey, C.; Boucher, T. Comparison of baseline removal methods for laser-induced breakdown spectroscopy of geological samples. *Spectrochim. Acta Part B At. Spectrosc.* **2016**, *126*, 53–64. [[CrossRef](#)]
54. Yi, C.; Lv, Y.; Xiao, H.; Ke, K.; Yu, X. A novel baseline correction method using convex optimization framework in laser-induced breakdown spectroscopy quantitative analysis. *Spectrochim. Acta Part B At. Spectrosc.* **2017**, *138*, 72–80. [[CrossRef](#)]
55. Guezenc, J.; Gallet-Budynek, A.; Bousquet, B. Critical review and advices on spectral-based normalization methods for LIBS quantitative analysis. *Spectrochim. Acta Part B At. Spectrosc.* **2019**, *160*, 105688. [[CrossRef](#)]
56. Fabre, C.; Boiron, M.-C.; Dubessy, J.; Chabiron, A.; Charoy, B.; Martin-Crespo, T. Advances in lithium analysis in solids by means of laser-induced breakdown spectroscopy: An exploratory study. *Geochim. Cosmochim. Acta* **2002**, *66*, 1401–1407. [[CrossRef](#)]
57. McMillan, N.J.; McManus, C.E.; Harmon, R.S.; De Lucia, F.C.; Miziolek, A.W. Laser-induced breakdown spectroscopy analysis of complex silicate minerals—Beryl. *Anal. Bioanal. Chem.* **2006**, *385*, 263–271. [[CrossRef](#)] [[PubMed](#)]
58. McManus, C.E.; McMillan, N.J.; Harmon, R.S.; Whitmore, R.C.; De Lucia, J.F.C.; Miziolek, A.W. Use of laser induced breakdown spectroscopy in the determination of gem provenance: Beryls. *Appl. Opt.* **2008**, *47*, G72–G79. [[CrossRef](#)]
59. Sweetapple, M.T.; Tassios, S. Laser-induced breakdown spectroscopy (LIBS) as a tool for in situ mapping and textural interpretation of lithium in pegmatite minerals. *Am. Mineral.* **2015**, *100*, 2141–2151. [[CrossRef](#)]
60. Romppanen, S.; Pölonen, I.; Häkkänen, H.; Kaski, S. Optimization of spodumene identification by statistical approach for laser-induced breakdown spectroscopy data of lithium pegmatite ores. *Appl. Spectrosc. Rev.* **2021**, 1–21. [[CrossRef](#)]
61. Janovszky, P.; Jancsek, K.; Palásti, D.J.; Kopniczky, J.; Hopp, B.; Tóth, T.M.; Galbács, G. Classification of minerals and the assessment of lithium and beryllium content in granitoid rocks by laser-induced breakdown spectroscopy. *J. Anal. At. Spectrom.* **2021**, *36*, 813–823. [[CrossRef](#)]
62. Ribeiro, R.; Capela, D.; Ferreira, M.; Martins, R.; Jorge, P.; Guimarães, D.; Lima, A. X-ray fluorescence and laser-induced breakdown spectroscopy analysis of Li-rich minerals in veins from Argemela Tin Mine, central Portugal. *Minerals* **2021**, *11*, 1169. [[CrossRef](#)]
63. Fabre, C. Advances in laser-induced breakdown spectroscopy analysis for geology: A critical review. *Spectrochim. Acta Part B At. Spectrosc.* **2020**, *166*, 105799. [[CrossRef](#)]

64. Shearer, K.C.; Papike, J.J.; Simon, B.S.; Laul, C.J. Pegmatite-wallrock interactions, Black Hills, South Dakota; interaction between pegmatite-derived fluids and quartz-mica schist wallrock. *Am. Mineral.* **1986**, *71*, 518–539.
65. Morgan, G.B.; London, D. Alteration of amphibolitic wallrocks around the Tanco rare-element pegmatite, Bernic Lake, Manitoba. *Am. Mineral.* **1987**, *72*, 1097–1121.
66. Galeschuk, C.; Vanstone, P. Exploration techniques for rare-element pegmatite in the Bird River greenstone belt, southeastern Manitoba. In Proceedings of the Exploration, 5th Decennial Conference on Mineral Exploration, Toronto, ON, Canada, 9–12 September 2007; Milkereit, B., Ed.; Volume 7, pp. 823–839.
67. Luecke, W. Soil geochemistry above a lithium pegmatite dyke at Aclare, Southeast Ireland. *Ir. J. Earth Sci.* **1984**, *6*, 205–211.
68. Marshall, B.T.; Herman, J.S. Trace element distribution in the soils above deeply weathered pegmatites, Virginia, U.S.A.: Implications for exploration. *Appl. Geochem.* **1986**, *1*, 681–690. [[CrossRef](#)]
69. Kramida, A.; Ralchenko, Y.; Reader, J.; NIST ASD Team. *NIST Atomic Spectra Database (Version 5.5.6)*; National Institute of Standards and Technology: Gaithersburg, MD, USA, 2021. Available online: <https://physics.nist.gov/asd> (accessed on 19 November 2021).
70. Noll, R.; Bette, H.; Brysch, A.; Kraushaar, M.; Mönch, I.; Peter, L.; Sturm, V. Laser-induced breakdown spectrometry—applications for production control and quality assurance in the steel industry. *Spectrochim. Acta Part B At. Spectrosc.* **2001**, *56*, 637–649. [[CrossRef](#)]
71. Noll, R.; Fricke-Begemann, C.; Brunk, M.; Connemann, S.; Meinhardt, C.; Scharun, M.; Sturm, V.; Makowe, J.; Gehlen, C. Laser-induced breakdown spectroscopy expands into industrial applications. *Spectrochim. Acta Part B At. Spectrosc.* **2014**, *93*, 41–51. [[CrossRef](#)]
72. Noll, R.; Fricke-Begemann, C.; Connemann, S.; Meinhardt, C.; Sturm, V. LIBS analyses for industrial applications—an overview of developments from 2014 to 2018. *J. Anal. At. Spectrom.* **2018**, *33*, 945–956. [[CrossRef](#)]
73. Sturm, V.; Vrenegor, J.; Noll, R.; Hemmerlin, M. Bulk analysis of steel samples with surface scale layers by enhanced laser ablation and LIBS analysis of C, P, S, Al, Cr, Cu, Mn and Mo. *J. Anal. At. Spectrom.* **2004**, *19*, 451–456. [[CrossRef](#)]
74. Legnaioli, S.; Lorenzetti, G.; Pardini, L.; Cavalcanti, G.H.; Palleschi, V. Applications of LIBS to the analysis of metals. In *Laser-Induced Breakdown Spectroscopy*; Musazzi, S., Perini, U., Eds.; Springer: Berlin/Heidelberg, Germany, 2014; Volume 182, pp. 169–193. [[CrossRef](#)]
75. Jochum, T.; Günther, J.U.; Bohling, C. Material analysis in fast industrial processes by LIBS: Technical and analytical solutions for inline process monitoring. *Photonics Views* **2019**, *16*, 56–59. [[CrossRef](#)]
76. Tognoni, E.; Palleschi, V.; Corsi, M.; Cristoforetti, G.; Omenetto, N.; Gornushkin, I.; Smith, B.W.; Winefordner, J.D. From sample to signal in laser-induced breakdown spectroscopy: A complex route to quantitative analysis. In *Laser-Induced Breakdown Spectroscopy (LIBS) Fundamentals and Applications*; Miziolek, A.W., Palleschi, V., Schechter, I., Eds.; Cambridge University Press: Cambridge, UK, 2006; pp. 122–170.
77. Russo, R.E.; Chan, W.-T.; Bryant, M.F.; Kinard, W.F. Laser ablation sampling with ICP-AES for the analysis of prototypic glasses. *J. Anal. At. Spectrom.* **1995**, *10*, 295–301. [[CrossRef](#)]
78. Eppler, A.S.; Cremers, D.A.; Hickmott, D.D.; Ferris, M.J.; Koskelo, A.C. Matrix effects in the detection of Pb and Ba in soils using laser-induced breakdown spectroscopy. *Appl. Spectrosc.* **1996**, *50*, 1175–1181. [[CrossRef](#)]
79. Gornushkin, S.I.; Gornushkin, I.B.; Anzano, J.M.; Smith, B.W.; Winefordner, J.D. Effective normalization technique for correction of matrix effects in laser-induced breakdown spectroscopy detection of magnesium in powdered samples. *Appl. Spectrosc.* **2002**, *56*, 433–436. [[CrossRef](#)]
80. Lepore, K.H.; Fassett, C.I.; Breves, E.A.; Byrne, S.; Giguere, S.; Boucher, T.; Rhodes, J.M.; Vollinger, M.; Anderson, C.H.; Murray, R.W.; et al. Matrix effects in quantitative analysis of laser-induced breakdown spectroscopy (LIBS) of rock powders doped with Cr, Mn, Ni, Zn, and Co. *Appl. Spectrosc.* **2017**, *71*, 600–626. [[CrossRef](#)] [[PubMed](#)]
81. Sallé, B.; Lacour, J.L.; Mauchien, P.; Fichet, P.; Maurice, S.; Manhes, G. Comparative study of different methodologies for quantitative rock analysis by laser-induced breakdown spectroscopy in a simulated Martian atmosphere. *Spectrochim. Acta Part B* **2006**, *61*, 301–313. [[CrossRef](#)]
82. Rauschenbach, I.; Lazic, V.; Pavlov, S.G.; Hübers, H.W.; Jessberger, E.K. Laser induced breakdown spectroscopy on soils and rocks: Influence of the sample temperature, moisture and roughness. *Spectrochim. Acta Part B At. Spectrosc.* **2008**, *63*, 1205–1215. [[CrossRef](#)]
83. Cousin, A.; Sautter, V.; Fabre, C.; Maurice, S.; Wiens, R.C. Textural and modal analyses of picritic basalts with ChemCam laser-induced breakdown spectroscopy. *J. Geophys. Res. Planets* **2012**, *117*, E10. [[CrossRef](#)]
84. Diaz, D.; Hahn, D.W.; Molina, A. Evaluation of laser-induced breakdown spectroscopy (LIBS) as a measurement technique for evaluation of total elemental concentration in soils. *Appl. Spectrosc.* **2012**, *66*, 99–106. [[CrossRef](#)]
85. Harmon, R.S.; Russo, R.E.; Hark, R.R. Applications of laser-induced breakdown spectroscopy for geochemical and environmental analysis: A comprehensive review. *Spectrochim. Acta Part B At. Spectrosc.* **2013**, *87*, 11–26. [[CrossRef](#)]
86. Rapin, W.; Bousquet, B.; Lasue, J.; Meslin, P.Y.; Lacour, J.L.; Fabre, C.; Wiens, R.C.; Frydenvang, J.; Dehouck, E.; Maurice, S.; et al. Roughness effects on the hydrogen signal in laser-induced breakdown spectroscopy. *Spectrochim. Acta Part B At. Spectrosc.* **2017**, *137*, 13–22. [[CrossRef](#)]
87. Popov, A.M.; Zaytsev, S.M.; Seliverstova, I.V.; Zakuskin, A.S.; Labutin, T.A. Matrix effects on laser-induced plasma parameters for soils and ores. *Spectrochim. Acta Part B At. Spectrosc.* **2018**, *148*, 205–210. [[CrossRef](#)]

88. Xu, W.; Sun, C.; Tan, Y.; Gao, L.; Zhang, Y.; Yue, Z.; Shabbir, S.; Wu, M.; Zou, L.; Chen, F.; et al. Total alkali silica classification of rocks with LIBS: Influences of the chemical and physical matrix effects. *J. Anal. At. Spectrom.* **2020**, *35*, 1641–1653. [[CrossRef](#)]
89. Gorry, P.A. General least-squares smoothing and differentiation by the convolution (Savitzky-Golay) method. *Anal. Chem.* **1990**, *62*, 570–573. [[CrossRef](#)]
90. Wise, M.A. Trace element chemistry of lithium-rich micas from rare-element granitic pegmatites. *Miner. Pet.* **1995**, *55*, 203–215. [[CrossRef](#)]
91. Nironen, M. Central Finland Granitoid Complex—Explanation to a Map. In *Report of Investigation 157*; Geological Survey of Finland: Espoo, Finland, 2003; pp. 1–45. (Finnish with English Summary)
92. Chopin, F.; Korja, A.; Nikkilä, K.; Hölttä, P.; Korja, T.; Zaher, M.A.; Kurhila, M.; Eklund, O.; Rämö, O.T. The Vaasa Migmatitic Complex (Svecofennian Orogen, Finland): Buildup of a LP-HT Dome during Nuna Assembly. *Tectonics* **2020**, *39*, e2019TC005583. [[CrossRef](#)]
93. Brewer, E.O. *Soil Survey of Catawba County, North Carolina*; US Department of Agriculture, Soil Conservation Service: Washington, DC, USA, 1975; 47p.
94. Hashimoto, Y. Citrate sorption and biodegradation in acid soils with implications for aluminum rhizotoxicity. *Appl. Geochem.* **2007**, *22*, 2861–2871. [[CrossRef](#)]
95. Foster, M. Interpretation of the composition of lithium micas. *U.S. Geol. Survey Prof. Paper* **1960**, *354-E*, 115–147. [[CrossRef](#)]
96. Hawthorne, F.C.; Černý, P.; The Mica Group. *Short Course Handbook*; Mineralogical Association of Canada: Quebec City, QC, Canada, 1982; Volume 8, pp. 63–98.
97. Černý, P.; Burt, D. Paragenesis, crystallochemical characteristics, and geochemical evolution in micas in granite pegmatites. In *Micas*; Bailey, S.W., Ed.; Reviews in Mineralogy; Mineralogical Society of America: Washington, DC, USA, 1984; Volume 13, pp. 257–297. [[CrossRef](#)]
98. Rosales, G.D.; Pinna, E.G.; Suarez, D.S.; Rodriguez, M.H. Recovery Process of Li, Al and Si from Lepidolite by Leaching with HF. *Minerals* **2017**, *7*, 36. [[CrossRef](#)]
99. Xing, C.-M.; Wang, C.Y.; Wang, H. Magmatic-hydrothermal processes recorded by muscovite and columbite-group minerals from the Bailongshan rare-element pegmatites in the West Kunlun-Karakorum orogenic belt, NW China. *Lithos* **2020**, *364–365*, 105507. [[CrossRef](#)]
100. Llera, A.R.; Fuertes-Fuente, M.; Cepedal, A.; Martin-Izard, A. Barren and Li–Sn–Ta Mineralized pegmatites from NW Spain (Central Galicia): A comparative study of their mineralogy, geochemistry, and wallrock metasomatism. *Minerals* **2019**, *9*, 739. [[CrossRef](#)]
101. Roda-Robles, E.; Perez, A.P.; Roldan, F.V.; Fontan, F. The granitic pegmatites of the Fregeneda area (Salamanca, Spain): Characteristics and petrogenesis. *Miner. Mag.* **1999**, *63*, 535–558. [[CrossRef](#)]
102. Küster, D.; Romer, R.L.; Tolessa, D.; Zerihun, D.; Bheemalingeswara, K.; Melcher, F.; Oberthür, T. The Kenticha rare-element pegmatite, Ethiopia: Internal differentiation, U–Pb age and Ta mineralization. *Miner. Depos.* **2009**, *44*, 723–750. [[CrossRef](#)]
103. Deveaud, S.; Millot, R.; Villaros, A. The genesis of LCT-type granitic pegmatites, as illustrated by lithium isotopes in micas. *Chem. Geol.* **2015**, *411*, 97–111. [[CrossRef](#)]
104. Anderson, M.; Lentz, D.; McFarlane, C.; Falck, H. A geological, geochemical and textural study of an LCT pegmatite: Implications for the magmatic versus metasomatic origin of Nb-Ta mineralization in the Moose II pegmatite, Northwest Territories, Canada. *J. Geosci.* **2013**, *58*, 299–320. [[CrossRef](#)]
105. Van Lichtenvelde, M.; Grégoire, M.; Linnen, R.L.; Béziat, D.; Salvi, S. Trace element geochemistry by laser ablation ICP-MS of micas associated with Ta mineralization in the Tanco pegmatite, Manitoba, Canada. *Contrib. Miner. Petrol.* **2008**, *155*, 791–806. [[CrossRef](#)]
106. Martins, T.; Linnen, R.L.; Fedikow, M.A.F.; Singh, J. Whole-rock and mineral geochemistry as exploration tools for rare-element pegmatite in Manitoba: Examples from the Cat Lake–Winnipeg River and Wekusko Lake pegmatite fields (parts of NTS 52L6, 63J13). *Manit. Geol. Survey Rep. Act.* **2017**, 42–51.
107. Grant, K.J.; Paul, G.L.; O'Neill, J.A. Quantitative elemental analysis of iron ore by laser-induced breakdown spectroscopy. *Appl. Spectrosc.* **1991**, *45*, 701–705. [[CrossRef](#)]
108. Death, D.; Cunningham, A.; Pollard, L. Multi-element analysis of iron ore pellets by laser-induced breakdown spectroscopy and principal components regression. *Spectrochim. Acta Part B At. Spectrosc.* **2008**, *63*, 763–769. [[CrossRef](#)]
109. Yaroshchuk, P.; Death, D.L.; Spencer, S.J. Comparison of principal components regression, partial least squares regression, multi-block partial least squares regression, and serial partial least squares regression algorithms for the analysis of Fe in iron ore using LIBS. *J. Anal. At. Spectrom.* **2011**, *27*, 92–98. [[CrossRef](#)]
110. Klus, J.; Mikysek, P.; Prochazka, D.; Pořízka, P.; Prochazková, P.; Novotny, J.; Trojek, T.; Novotný, K.; Slobodník, M.; Kaiser, J. Multivariate approach to the chemical mapping of uranium in sandstone-hosted uranium ores analyzed using double pulse Laser-Induced Breakdown Spectroscopy. *Spectrochim. Acta Part B At. Spectrosc.* **2016**, *123*, 143–149. [[CrossRef](#)]
111. Álvarez, J.; Velásquez, M.; Myakalwar, A.K.; Sandoval, C.; Fuentes, R.; Castillo, R.; Sbarbaro, D.; Yáñez, J. Determination of copper-based mineral species by laser induced breakdown spectroscopy and chemometric methods. *J. Anal. At. Spectrom.* **2019**, *34*, 2459–2468. [[CrossRef](#)]
112. Rosenwasser, S.; Asimellis, G.; Bromley, B.; Hazlett, R.; Martin, J.; Pearce, T.; Zigler, A. Development of a method for automated quantitative analysis of ores using LIBS. *Spectrochim. Acta Part B At. Spectrosc.* **2001**, *56*, 707–714. [[CrossRef](#)]

113. Gaft, M.; Sapir-Sofer, I.; Modiano, H.; Stana, R. Laser induced breakdown spectroscopy for bulk minerals online analyses. *Spectrochim. Acta Part B At. Spectrosc.* **2007**, *62*, 1496–1503. [[CrossRef](#)]
114. Cheng, X.; Yang, X.; Zhu, Z.; Guo, L.; Li, X.; Lu, Y.; Zeng, X. On-stream analysis of iron ore slurry using laser-induced breakdown spectroscopy. *Appl. Opt.* **2017**, *56*, 9144–9149. [[CrossRef](#)] [[PubMed](#)]
115. Khajehzadeh, N.; Haavisto, O.; Koresaar, L. On-stream mineral identification of tailing slurries of an iron ore concentrator using data fusion of LIBS, reflectance spectroscopy and XRF measurement techniques. *Miner. Eng.* **2017**, *113*, 83–94. [[CrossRef](#)]
116. Rifai, K.; Doucet, F.; Özcan, L.; Vidal, F. LIBS core imaging at kHz speed: Paving the way for real-time geochemical applications. *Spectrochim. Acta Part B At. Spectrosc.* **2018**, *150*, 43–48. [[CrossRef](#)]
117. Foucaud, Y.; Fabre, C.; Demeusy, B.; Filippova, I.; Filippov, L. Optimisation of fast quantification of fluorine content using handheld laser induced breakdown spectroscopy. *Spectrochim. Acta Part B At. Spectrosc.* **2019**, *158*, 105628. [[CrossRef](#)]

Article

Rapid Analysis of Muscovites on a Lithium Pegmatite Prospect by Handheld LIBS

Russell S. Harmon^{1,*}, Michael A. Wise², Adam C. Curry¹, Joshua S. Mistele¹, Michael S. Mason³ and Zach Grimač³

¹ Department of Marine, Earth, & Atmospheric Sciences, North Carolina State University, Raleigh, NC 27695, USA; accurry3@ncsu.edu (A.C.C.); joshua@mistele.com (J.S.M.)

² Department of Mineral Sciences, National Museum of Natural History, Smithsonian Institution, Washington, DC 20560, USA; wisem@si.edu

³ Piedmont Lithium, Inc., 5706 Dallas Cherryville Highway, Bessemer City, NC 28016, USA; mmason@piedmontlithium.com (M.S.M.); zgrimac@piedmontlithium.com (Z.G.)

* Correspondence: rsharmon@ncsu.edu

Abstract: Laser-induced breakdown spectroscopy (LIBS) is a technology for compositional analysis that is particularly effective for light elements, particularly Li, which is a critical commodity for emerging green technologies. This study undertook analysis by handheld LIBS of muscovite from the drill core, outcrop, and soil on the Carolina Lithium Prospect (CLP) in Gaston County, North Carolina (USA), which lies within the Carolina Tin-Spodumene Belt (CTSB). Abundances of the alkali elements Li, K, and Rb were determined for more than 130 muscovites from the Li-rich pegmatites to track the degree of pegmatite fractionation as a pathfinder for spodumene mineralization. Across the CTSB and including the CLP, muscovite Li contents vary over an order of magnitude, ranging from 0.04 to 0.74 wt. %, with their K/Rb ratios varying between 63 and 8, features that together document the highly evolved character of pegmatites within the CTSB district. On average, muscovite Li contents are greater in spodumene-bearing pegmatites at 0.21 ± 0.12 wt. % than for common quartz-feldspar pegmatites at 0.14 ± 0.08 wt. %. Although overlapping substantially in the middle portions of their distributions, muscovite K/Rb ratios are biased toward low values for spodumene-bearing pegmatites ($\bar{X} = 21 \pm 6$) compared to those for quartz-feldspar pegmatites ($\bar{X} = 33 \pm 9$). This study provides a framework for the use of LIBS analysis of muscovite in outcrop, drill core, and soil samples as an analytical tool for in-field and on-site geochemical analysis during Li pegmatite exploration and prospect evaluation.

Keywords: laser-induced breakdown spectroscopy; handheld LIBS; Carolina Tin-Spodumene Belt; LCT pegmatites; rapid geochemical analysis; muscovite K/Rb-Li systematics; geochemical exploration; prospect evaluation



Citation: Harmon, R.S.; Wise, M.A.; Curry, A.C.; Mistele, J.S.; Mason, M.S.; Grimač, Z. Rapid Analysis of Muscovites on a Lithium Pegmatite Prospect by Handheld LIBS. *Minerals* **2023**, *13*, 697. <https://doi.org/10.3390/min13050697>

Academic Editor: Paul Alexandre

Received: 26 April 2023

Revised: 15 May 2023

Accepted: 16 May 2023

Published: 19 May 2023



Copyright: © 2023 by the authors. Licensee MDPI, Basel, Switzerland. This article is an open access article distributed under the terms and conditions of the Creative Commons Attribution (CC BY) license (<https://creativecommons.org/licenses/by/4.0/>).

1. Introduction

Lithium (Li) is a strategic metal with a wide variety of industrial uses that include batteries, electronic devices, ceramics and glass, lubricating greases, polymer production, continuous casting, and air treatment. Recently, the demand for Li for batteries has grown at a rapid pace because rechargeable lithium batteries are used extensively in portable electronic devices, electric tools, electric vehicles, and energy grid storage applications. As discussed by Kesler et al. [1] and Bowell et al. [2], continental brines from salar and geothermal fields are the primary Li resource being exploited at present, but volcanic-sedimentary clays and granite-related pegmatites are other important sources. Presently pegmatite mining operations in Australia, a tailings reclamation operation in Brazil, and both pegmatite and brine extraction operations in Argentina and Chile, and China account for more than 90% of global Li production [3].

Li is also a lynchpin metal for the transition to a green future based on renewable energy. In 2020, the manufacture of Li-ion batteries accounted for 71% of total lithium consumption across the globe [4]. Presently, the global Li resource, which has increased substantially as a consequence of recent exploration activity, is estimated to be about 98 million metric tons [3]. Particularly noteworthy is the 75% production increase in global lithium production between 2016 and 2017 and the further increase by 23% from 2017 to 2018 [5]. Even given this rapid pace of recent production, a recent World Bank report considers that global Li production will have to rise by 500% to meet mid-century climate targets [6]. Given the present low level of commercial production in the US from a brine extraction operation in Nevada [3], there is an ongoing need for the identification and development of new domestic Li resources, particularly granite pegmatite, given the limited spatial extent of brine and potential geothermal sources.

Understanding the extent of parental melt fractionation and chemical evolution in granite pegmatites can contribute to the evaluation of regional and individual pegmatite prospects. Tracking abundance variations of the alkali trace elements Li, Rb, and Cs in muscovite provides one means of assessing the extent of pegmatite melt fractionation [7–10]. Exclusion of these elements from the structure of felsic rock-forming minerals during granite magma crystallization leads to their accumulation and enrichment in residual pegmatite-forming melts [11].

Muscovite is one of the most common minerals in granitic pegmatites, with both the Li abundance and K/Rb ratio serving as exploration guides to assess the potential for Li-aluminosilicate mineralization [7,11–16]. Building directly on the previous work of Wise et al. [17], we first undertook on-site measurements of the Li content in the drill core at the Carolina Lithium Prospect in Gaston County, NC, USA (Figure 1) in December 2022. We then determined the abundance of Li, K, and Rb in muscovite from outcrops in the field and additional drill core and pegmatite hand samples on site at the Piedmont Lithium field facility in March 2023 to illustrate how in-field analysis by handheld laser-induced breakdown spectroscopy (LIBS) can be used as an analytical tool in granite pegmatite exploration and for rapid prospect evaluation.

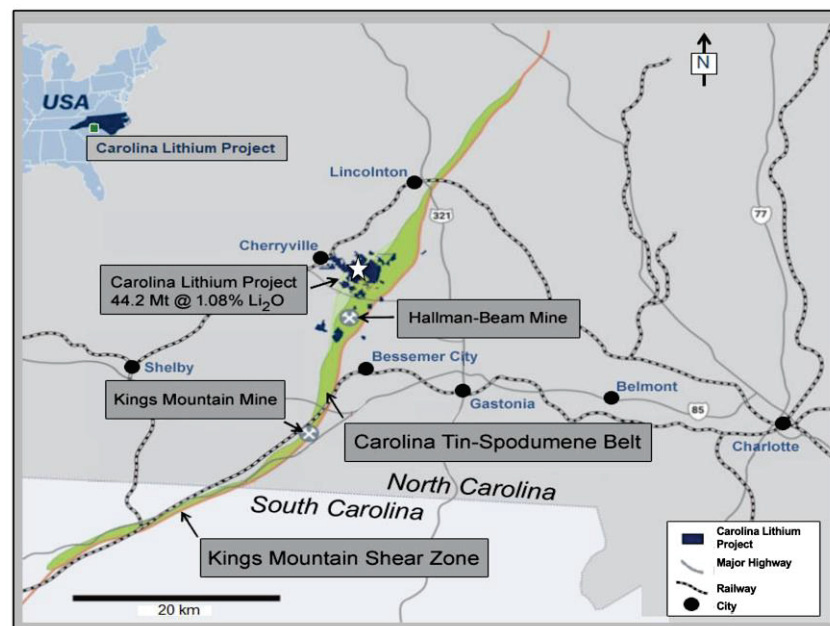


Figure 1. Carolina Tin-Spodumene Belt (green) showing the Kings Mountain Shear Zone (orange) along with the locations of the Kings Mountain Mine, the Hallman Beam Min, and Piedmont Lithium’s Carolina Lithium Project (CLP) prospect, which has an estimated reserve of 44.2 Mt at 1.08 wt. % Li_2O . The white star indicates the locations of the two drill cores that are a particular focus of this study.

2. Geological Setting

2.1. Carolina Tin-Spodumene Belt (CTSB)

The CTSB is a narrow domain of pegmatites of the Carboniferous age [18] located in the Inner Piedmont physiographic province [19] that host both cassiterite and spodumene. Concentrated in a belt across the Kings Mountain Shear Zone between Lincolnton, NC, and Gafney, SC (Figure 1), the CTSB was the most historically important Li pegmatite district in North America and is presently the focus of renewed exploration activity. This pegmatite mineralization lies just to the east of the Cherryville quartz monzonite, a complex intrusion of approximately the same age as both spodumene-bearing and common quartz-feldspar pegmatites across the CTSB, although existing age data are low-precision with the Cherryville and pegmatites overlapping within 10 Ma [20]. The ultimate source of CTSB pegmatites is not known. Some investigators have suggested that the CTSB pegmatites are associated with this peraluminous, 2-mica intrusion since spodumene-free pegmatite dikes extend eastward from the Cherryville granite with a strike that is sub-parallel to the northeast-trending Kings Mountain Shear Zone [21]. However, the biotite-bearing High Shoals granite east of the CTSB has also been suggested as a possible pegmatite source [22–24].

2.2. Previous Exploration and Mining Activity

The Li reserves for the CTSB are large, comprising more than 100 Mt at an average Li content of about 0.7% Li from Kesler's 1976 estimate [25]. Active mining of spodumene was undertaken in the CTSB from the 1950s to 1990s at two large mines (Figure 1), the Hallman-Beam Mine operated by the Lithium Corporation of America and the Kings Mountain Mine operated by the Foote Mineral Company, where reserves were estimated at 62.3 Mt averaging 0.67% Li and 45.6 Mt averaging about 0.7% Li, respectively [26].

Recent industrial demand for Li has resulted in renewed exploration activity across the CTSB, with Piedmont Lithium's Carolina Lithium Project (CLP) presently assessing a large prospect centered at UTM coordinates 473764 E, 3916209 N in Gaston County near Bessemer City (Figure 1). This area was of exploration interest in the past and trenched in places during the 1950s. The LIBS analyses reported here were undertaken on muscovite from drill core, outcrops, and soil on this prospect.

Li-pegmatite mineralization in the CTSB is of the albite-spodumene type defined by Černý [27], falling within the lithium-cesium-tantalum (LCT) family of Černý et al. [28] and the Group 1 type of Wise et al. [29]. Individual pegmatites across the CTSB are complex structures with surface dimensions of a few to a hundred meters in width and up to a kilometer in length that were intruded generally parallel to foliation in the surrounding country rocks [19,26]. Different types of pegmatites within the CTSB include (i) those comprised of K-feldspar, albite, quartz and beryl; (ii) those containing primarily K-feldspar, oligoclase, quartz, with muscovite, biotite, and garnet as accessory phases; and (iii) Li-bearing pegmatites composed of spodumene, K-feldspar, albite, quartz and beryl [30]. Pegmatites are texturally heterogeneous across the region, ranging from fine-grained aplite to very coarse-grained, but display little internal compositional zoning. Spodumene-bearing pegmatites typically have a modal composition of approximately 41% feldspar, 32% quartz, 20% spodumene, and 6% muscovite [26,31]. More than 50 accessory minerals occur in these pegmatites, including beryl, garnet, titanite, cassiterite, zircon, Mn-bearing fluorapatite, triphylite, and columbite-group minerals [19,31–34].

2.3. Pegmatites of the Carolina Lithium Prospect

Between 2017 and 2021, 542 drill holes comprising just over 80,000 m were completed on the CLP. The 511 assayed drill holes intersected >75 mineralized pegmatite bodies estimated to comprise the largest pegmatite resources in the United States at >44 Mt, having an average grade of 1.08 wt. % Li₂O [35].

As illustrated in Figure 2, this drilling has shown that pegmatite dikes in the CLP are interconnected by flat to shallow-dipping sills and inclined sheets that are encountered over broad lateral extents that only rarely outcrop at the surface. This pegmatite dike network is hosted in a country rock of (1) a fine- to medium-grained foliated biotite, hornblende, quartz-feldspar gneiss that is commonly referred to as ‘amphibolite’ and (2) metasedimentary rocks that include schists and metamorphosed mudstones. Massive to weakly foliated diabase dikes of the Triassic age are also present to a limited extent.

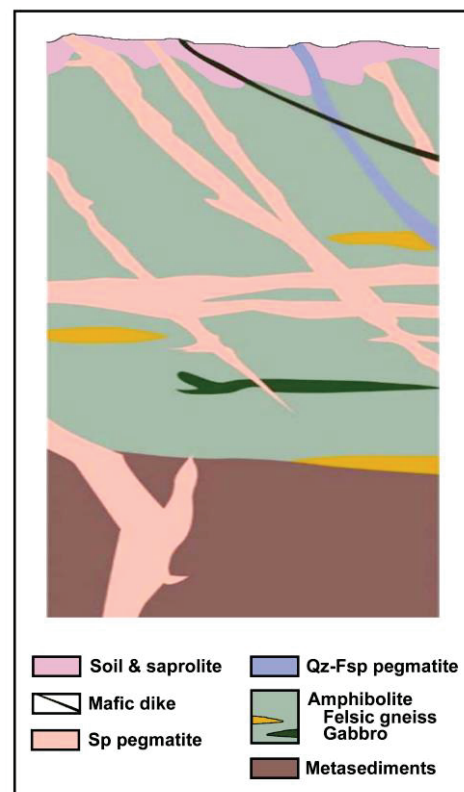


Figure 2. Idealized schematic geological section in the area of the CLP (after [35]).

CLP pegmatites are largely thin, sheet-like bodies [26] comprising composite structures of nearly uniform mineralogical character in which albite and quartz predominate over spodumene and K-feldspar. They vary from fine-grained to very coarse-grained in texture, with thin dikes of spodumene-bearing pegmatite cutting larger dikes of spodumene-free quartz-feldspar pegmatite or of aplite dikes cutting either spodumene-bearing or spodumene-free pegmatite [36]. The spodumene-free pegmatite dikes, which most commonly occur within and near the Cherryville intrusion [37], have variable orientations, with some having the same trend as the spodumene-bearing dikes, so they may represent either an early stage of weakly fractionated silicate melt or a later unmineralized pegmatite system.

The examination of surface outcrops and drill core has defined three varieties of pegmatite within the CLP—(i) common spodumene-free quartz-feldspar pegmatite, (ii) pegmatite in which spodumene is present but not dominant, and (iii) pegmatite having spodumene as the dominant constituent. Spodumene is the only Li-bearing ore mineral present in pegmatites on the CLP, with lath-shaped spodumene commonly oriented sub-normal to pegmatite contacts. Spodumene in the CLP pegmatites is dominated by white to light-green coarse-grain crystals, although medium- to fine-grained white spodumene is frequently present in subordinate proportions, and coarse-grained light-purple spodumene has been documented locally.

3. Methods

3.1. Laser-Induced Breakdown Spectroscopy (LIBS)

LIBS is an established form of atomic emission spectrometry with a capability for rapid and simultaneous multi-element analysis of geological materials. It is particularly suited to the analysis of the light elements (i.e., He, Li, Be, B, C, N, O, and Mg) that can be present in high abundance in geological materials but are difficult to determine by many other analytical techniques. LIBS has an attractive set of attributes that make it a suitable technology for geochemical analysis in the field. These include a simple analytical system architecture requiring only a laser, optics, detector/spectrograph, and computer that can be configured into a lightweight handheld device, rapid and simultaneous detection of most elements with a single laser pulse, minimal or no sample preparation, and a small sample size with only picograms (pg) and nanograms (ng) of material required for analysis.

In LIBS analysis, short-duration, pulsed laser light is tightly focused onto the sample to cause material 'breakdown', i.e., the conversion of a minute amount of sample by laser energy absorption into a vapor and particulate-bearing aerosol and generation of a high-temperature plasma [38]. Monitoring the wavelength and intensity of emission lines in the LIBS plasma provides information on both the chemical species present and their abundance because element abundances in the sample analyzed are reflected in the intensities of elemental emission lines measured in the LIBS emission spectrum. Simultaneous multi-element analysis by LIBS can be used for simple elemental detection or for quantitative analysis in real time through appropriate spectral preprocessing, careful selection of emission lines, and the creation of univariate or multivariate calibration curves using physically and compositionally similar matrix-matched reference samples.

The first handheld LIBS analyzer was introduced to the commercial market in 2015 and described in the literature shortly thereafter [39]. Utilizing recent advances in optics, compact laser sources, miniaturized high-resolution spectrometers, microelectronics, and computers, several manufacturers are presently producing lightweight battery-powered handheld LIBS analyzers that can be used by an individual in the field for several hours. These handheld instruments offer a real-time display of results, together with many features present in laboratory systems, including variable time gating, gas purging, rastering the laser beam across a sample, video targeting, and on-board data pre-processing and chemometric analysis.

3.1.1. Handheld LIBS Analysis

Lithium is an element effectively analyzed by LIBS because of its strong emissivity, which makes it readily detectable in geological materials, even when present at low concentrations. Previous quantitative LIBS analysis or compositional mapping related to Li-pegmatite mineralization has been undertaken using both laboratory LIBS systems [40–42], commercial LIBS drill core scanners [43,44], or handheld LIBS analyzers [17,45–48]. The work reported here utilized a SciAps Inc. (Woburn, MA, USA) Z-300 series handheld LIBS analyzer for the determination of Li, K, and Rb in muscovite either from outcrops in the field or drill core, pegmatite hand samples, and soil at the Piedmont Lithium field facility in the CLP.

This SciAps handheld LIBS analyzer employs an Android operating system with a graphic user interface and is powered by rechargeable Li-ion batteries that provide up to 8 h of operation. The instrument uses a proprietary pumped solid-state 1064 nm Nd-YAG pulsed laser that generates a 6 mJ laser pulse with a 50 μm beam size at a 1 nS pulse duration and has a built-in camera for beam targeting, a translational stage for 3-D beam rastering across the surface of a sample, and the capability to flow an inert gas across the sample surface for plasma confinement and signal enhancement. The 3-D translational stage is computer controlled for automatic adjustment of the laser focus at each sample location. Automated stage movement permits analysis over a 2 \times 2 mm area, with the raster pattern, spacing, and number of laser shots at each location determined by the user. A 4 \times 3 point grid pattern covering an area of approximately 1 mm \times 0.7 mm was employed for this study. Following two laser shots for sample surface cleaning, four laser shots for

data collection were taken at each point on five different raster grids on every sample and then averaged to produce a composite LIBS spectrum based on the 48 individual analyses. These five analyses were then averaged to generate the Li measurements and K/Rb ratios reported here.

The light signal from the plasma emission is collected, typically after a 650 ns delay over a 1 ms integration time, and passed by fiber optic cable into three spectrometers with time-gated, charge-coupled diode detectors having respective spectral ranges and resolutions of 190 to 365 nm with a full-width half maximum (FWHM) value of 0.18 nm, 365 to 620 nm with an FWHM value of 0.24 nm, and 620 to 950 nm with an FWHM value of 0.35 nm. This analysis produces composite LIBS spectra over the 23,432 channels of the spectrometer (Figure 3). A pre-loaded spectral library of element emission lines derived from the National Institute of Standards and Technology (NIST) Atomic Spectral Database (<https://www.nist.gov/pml/atomic-spectra-database> accessed on 14 May 2023) is used for element identification. Calibrations for quantitative analysis can be created on the Z-300 instrument for specific applications from the analysis of a set of matrix-matched reference samples of known composition.

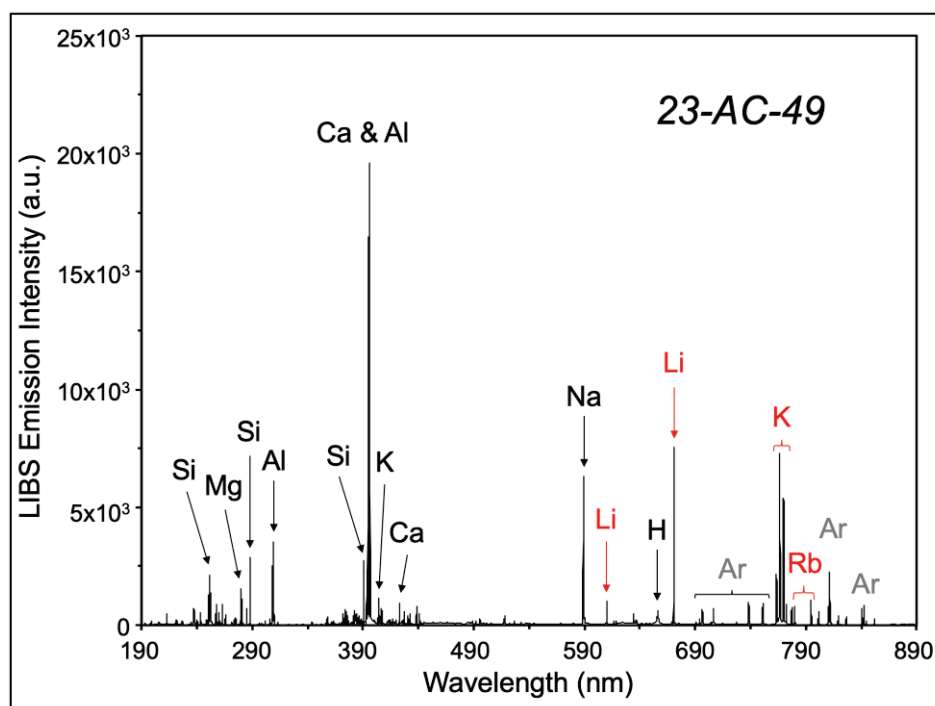


Figure 3. Representative LIBS spectra for a CLP muscovite sample showing emission lines for the elements of interest to this study (red arrows, brackets, and text), the Ar peaks in the infrared portion of the spectrum between 700 and 870 from the Ar purge gas used for the analysis (grey brackets and text), and other elements (black arrows and text).

3.1.2. Instrument Calibration

Quantitative analysis can be undertaken using the *Geochem* mode of the SciAps LIBS analyzers developed beforehand from the analysis of a set of matrix-matched reference materials using either single-element or multivariate calibration procedures using the *Profile Builder* PC-based software package. As described by Harmon et al. [47], this software utilizes a graphic user interface to facilitate the building of calibration curves via an established workflow that first selects the element suite of interest, next defines the element abundances in the reference samples, then acquires sets of reference spectra, and finally creates calibration models as concentration versus intensity ratio plots. These models can then be saved for subsequent quantitative testing to be performed by the handheld analyzer.

The creation of LIBS calibrations depends on two considerations—the number of spectral lines for an element of interest and the presence of distinct emission lines that are not affected by overlap with lines from other elements present in the sample. Any calibration curve will perform best when developed for a specific matrix of interest. Intensity values for elements are obtained after a background subtraction and integration of measured emission intensities across the defined spectral region of interest to obtain a summed area under the peak value. Intensity ratios are then calculated by combining one or more summed peak intensity or by normalizing to the full emission spectrum.

Two calibrations for the handheld LIBS analyzer were developed for this work (Figure 4), an initial one solely for Li in muscovite during the autumn of 2022 that was used for the analysis of CLP drill cores 21-BD-529 and 21-BD-531 in December 2022 and then a second expanded set of calibrations for Li, K, and, Rb prepared during February–March 2023 that was used in March 2023. LIBS analysis of mica in drill cores was undertaken at the Piedmont Lithium field facility, analysis of mica from pegmatite outcrops was carried out in the field at the site of collection, and soil muscovite was separated and analyzed at North Carolina State University.

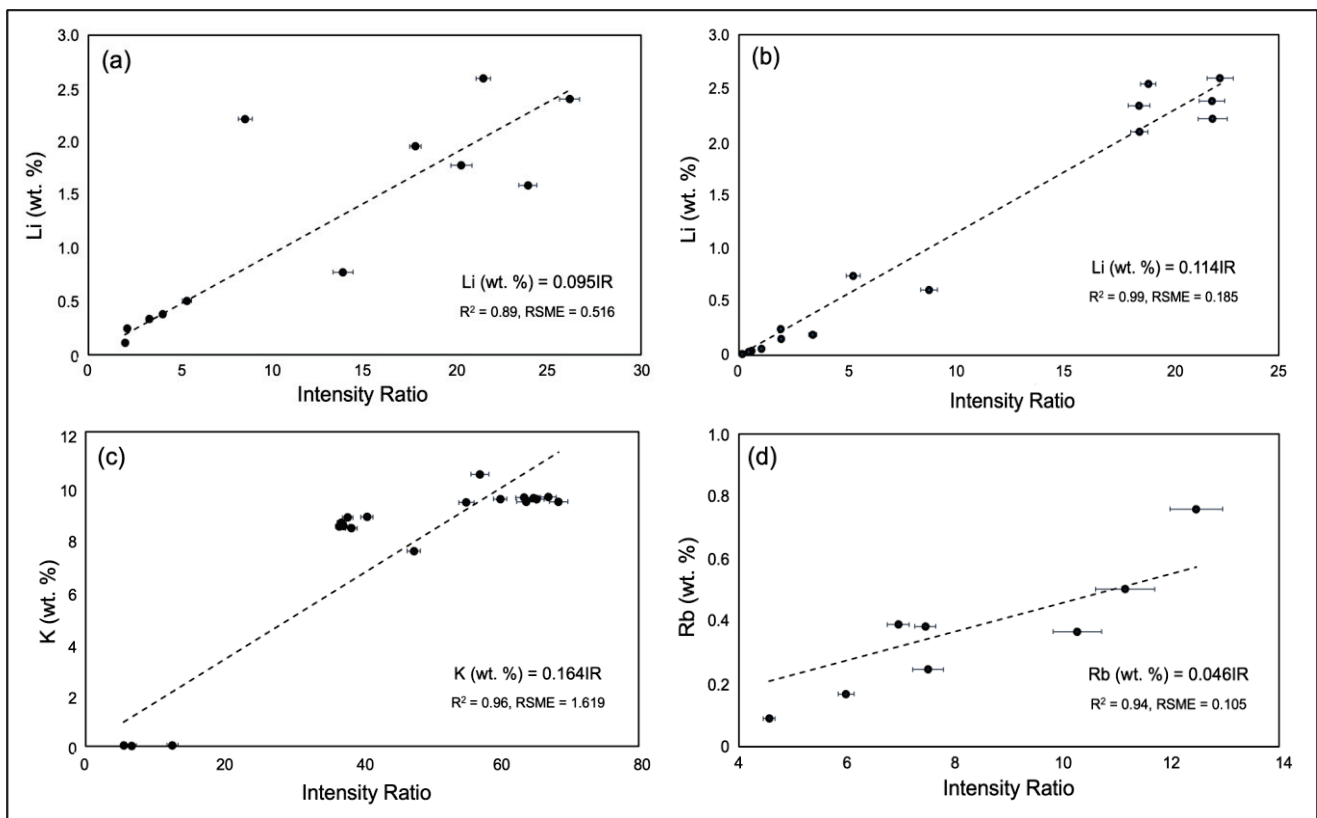


Figure 4. Handheld LIBS calibration curves developed for muscovite using the muscovite reference samples listed in Appendix A: (a) initial calibration curve for Li developed in the autumn of 2022, refined calibration curve for Li (b), and calibration curves for K (c) and Rb (d) developed in March 2023.

To develop our LIBS calibration models, a minimum of 20 spectra were acquired after spectral wavelength calibration in the *Profile Builder* software (SciAps proprietary) for elemental emission line(s) in three spectral regions of interest: (i) from 670 to 672 nm for the Li line at 670.7 nm, from 765 to 768 nm for the K line at 766.49 nm, and from 779 to 781 nm and 793 to 796 nm for the Rb lines at 780.03 and 794.76 nm (Figure 3) from each reference sample (Appendix A). Intensity ratios for the calibration plots were determined by full-spectrum normalization.

As physical matrix effects produce differences in laser-material coupling and, consequently, shot-to-shot differences in the observed elemental emission intensity, the individual spectra of the calibration set were sorted into a range of results for which the total emission intensity variation was <15%. From this point of the calibration workflow, curves can be generated and fit to the data by selecting a number of options, including the normalization approach, zero forcing, and curve order. An equation for each calibration curve and its root mean square error (RMSE) is provided by the proprietary SciAps *Profile Builder* software.

3.2. Electron Probe Microanalysis (EPMA)

Major and minor element contents of muscovite were determined by electron probe microanalysis (EPMA) using (Peabody, MA, USA) at Virginia Polytechnic Institute and State University. The standard minerals quartz (Si), diopside (Ca), rutile (Ti), albite (Al, Na), olivine (Mg), pyrope (Fe), rhodonite (Mn), orthoclase (K), benitoite (Ba), and fluorite (F) were used for microprobe calibration and analyzed periodically during each session for quality assurance. The probe used an acceleration voltage of 15 kV, a 10 nA probe current, and a 5 µm beam diameter for mineral analysis.

4. Results

The focus of this study was to ascertain if LIBS analysis of muscovite could be used as a pathfinder for spodumene mineralization within the CLP, across the CTSB, and potentially in other LCT pegmatite districts. Muscovite occurs in the Qtz-Fsp pegmatites and Spd-bearing pegmatites of the CLP as small isolated grains, aggregates of crystals, and as large books a centimeter or greater in size, but has only rarely been observed in Spd-pegmatites.

Four types of muscovite have been observed from exploration fieldwork and the logging of more than 500 drill cores from across the CLP. These different types represent a progression from pristine to weathered mica as follows:

- (i) transparent to semi-transparent book of muscovite with a green hue;
- (ii) opaque muscovite with a silvery color occurring as books or individual grains;
- (iii) muscovite with weak to moderate oxidation rims and clear, unaltered interiors;
- (iv) muscovite exhibiting ragged edges, an inhomogeneous color with mottled textures, and strong oxidation deep into the mica.

Type (i) muscovites occur in only the most pristine rocks. Type (ii) muscovites that exhibit little to no rim alteration are the most common type in CLP pegmatites. Type (iii) muscovites are most frequently observed in pegmatite surface outcrops and in residual soils. Type (iv) muscovites, which may have a residual unaltered core, occur in highly weathered rocks. All of the muscovites analyzed in this study are of types (i) and (ii) except for a few type (iii) muscovites from surface samples and soils.

Major-element analysis for mica from both barren and spodumene-mineralized pegmatites across the district confirms that CLP muscovites are found near end-member compositions (Figure 5, Appendix B). The respective K₂O and FeO contents range from 8.6 to 11.1 wt. % and 0.5 to 2.8 wt. %, the abundances of MgO, Na₂O, and BaO are below 1.1 wt. %, and the F contents are low (<0.5 wt. %). The five muscovite analyses reported by Swanson [34] for CSTB pegmatites and aplites are comparable to our 26 analyses (Appendix B).

Our LIBS analysis of muscovites within the CLP and from across the CTSB is discussed in Sections 4.1–4.3 below. The 130 samples analyzed comprised 65 in situ analyses of pegmatite muscovite in drill core, 49 analyses of muscovite from pegmatite outcrops, hand samples, and soils, and 16 specimens whose lithological context is not certain. These data are presented in Appendix C. The calibration curves shown in Figure 4 are appropriate for the analysis of muscovite containing 0–3 wt. % Li, 0–12 wt. % K, and 0–1 wt. % Rb and enable the handheld LIBS analyzer to be used for the real-time quantitative analysis of muscovite in the field.

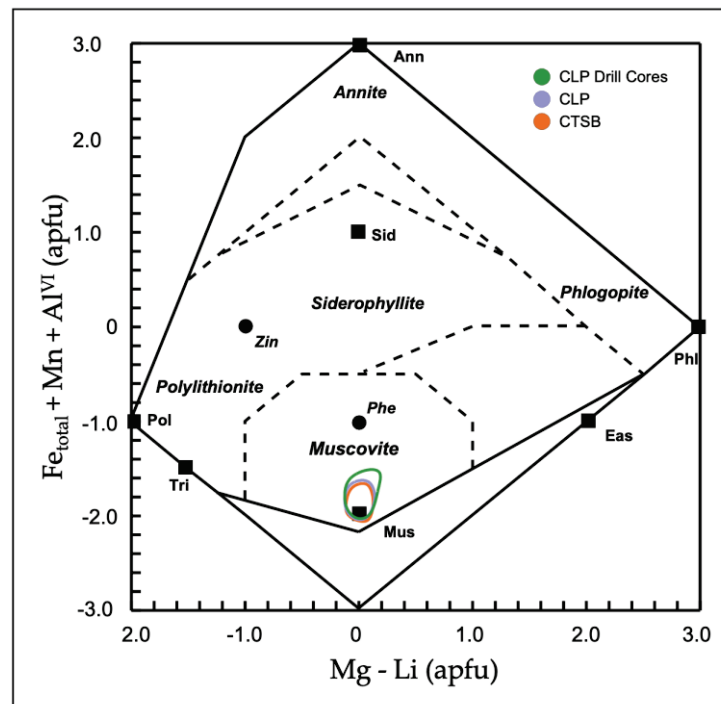


Figure 5. Plot of Mg-Li versus $(\text{Fe} + \text{Mn} + \text{Ti}) - \text{Al}^{\text{VI}}$ according to Tischendorf et al. [49] for micas from the Carolina Tin-Spodumene Pegmatite Belt. Black squares represent ideal end-member compositions of annite (Ann), eastonite (Eas), muscovite (Mus), phengite (Phe), phlogopite (Phl), polyolithionite (Pol), siderophyllite (Sid), trilithionite (Tri), and zinnwaldite (Zin). Respective compositional ranges for mica from the CTSB, CLP, and CLP drill cores 21-BD-529 and 21-BD-531 are shown by the red, blue, and green outlined fields.

4.1. CLP Drill Core Analysis

One way in which handheld LIBS analysis can be used for pegmatite prospect evaluation is for the rapid assay of Li in drill cores at the time they are acquired and logged. Core drilling by Piedmont Lithium on the CLP [50] uses standard wireline core-drilling techniques. All drill holes are started and recovered from the surface as HQ-sized (96 mm) drill core. Once the drill has passed through the saprolite to bedrock transition, the core size is reduced to NQ (75.7 mm) until the end of the hole is reached. As drilling proceeds, the drill core is retrieved from the hole, boxed, and delivered to a secure core logging facility.

The two complete drill cores that were analyzed in this study were obtained from an area outside of the defined resource of the CLP. The first core, 21-BD-529 (UTM coordinates 472194 E, 3915918 N), is a 151 m core that penetrated an initial 42 m section of soil and saprolite before encountering multiple spodumene-free pegmatite sequences intruded into the amphibolite country rock. A 4 m-thick spodumene-bearing pegmatite is present between 86.3 and 90.5 m depth, with 13 spodumene-free pegmatite horizons present above and below this mineralized section. The second core, 21-BD-531 (UTM coordinates 472160 E, 3915999 N), is a 160 m core that penetrated an initial 60 m section of soil and saprolite before encountering amphibolite penetrated by two spodumene-bearing pegmatites between 70.7 and 79.7 m depth and then transitioned into a lower section of spodumene-free pegmatite and altered pegmatite. A representative illustration of the different lithologies encountered in the two cores is provided in Figure 6. Their description and muscovite Li contents are given in Figure 7, and the chemical character of the different core lithologies is compared in Figure 8. The LIBS analyses of the two cores were undertaken on-site at the Piedmont Lithium field facility in December 2022 using the Li calibration shown in panel (a) of Figure 4.

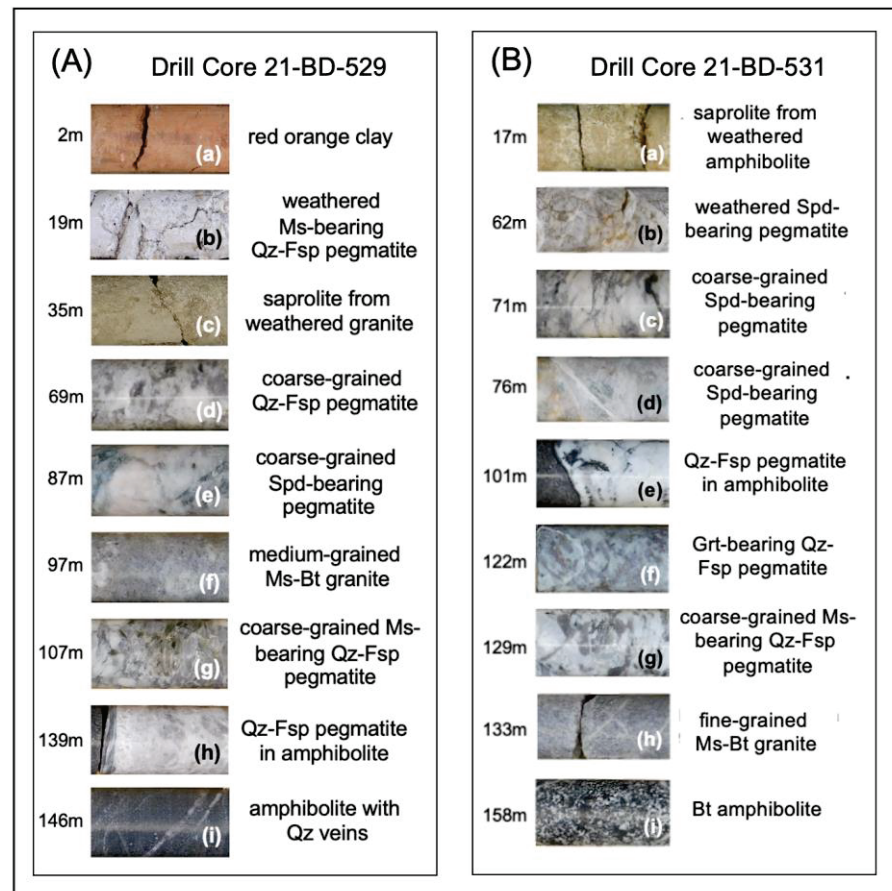


Figure 6. Photographs showing the textural character and mineralogy of selected portions of CLP cores 21-BD-529 and 21-BD-531. Bt = biotite, Fsp = feldspar, Grt = garnet, Ms = muscovite, Qz = quartz, Spd = spodumene.

Our LIBS Li assay of the 310 m of the 21-BD-529 and 21-BD-531 drill cores was undertaken on-site at the Piedmont Lithium field and core handling facility in December 2022 over the course of two days, with 34 analyses of micas from core 21-BD-529 and 31 analyses from core 21-BD-531. Li contents of muscovite for the saprolite intervals in each core are generally lower than for muscovite from pegmatite intervals. The Li content of saprolite muscovite ranges from 0.02 to 0.10 wt. % versus 0.05 to 0.25 wt. % in pegmatite muscovite for core 21-BD-529, and 0.023 to 0.120 wt. % (saprolite) versus 0.038 to 0.228 wt. % (pegmatite) for core 21-BD-531. The highest Li contents in both cores, 0.25 wt. % in 21-BD-249 and 0.23 in 21-BD-251, are displayed by muscovite from the spodumene-bearing intervals.

The average major- and trace-element composition of lithologies of drill cores 21-BD-529 and 21-BD-531 are presented in Appendix D. Pegmatite and ‘granite’ horizons of both cores are similar in their major element compositions. They are both peraluminous with A/CNK (molar $\text{Al}_2\text{O}_3/\text{CaO}+\text{Na}_2\text{O}+\text{K}_2\text{O}$) ranging between 1.13 and 1.36 and are characterized by high average SiO_2 (~72 to 75 wt. %) and Al_2O_3 (~14.3 to 15.4 wt. %) values. The average Na_2O and K_2O values are low regardless of the rock type, with Na_2O typically being higher than K_2O , likely reflecting a higher abundance of albite relative to microcline and muscovite. The bulk composition of the spodumene-bearing dikes compares favorably to spodumene-bearing pegmatites from other areas of the world (Table 1).

(a) CLP Core 21-BD-529

Depth (m)	Primary Lithology	Texture	Unit Description
0 - 4.5	SOIL		red-orange clay
4.5 - 18.5	SAP		heavily weathered red-orange to light brown SAP derived from AMP
18.5 - 19.5	PEG	VCG	weathered Qz-Fsp with coarse-grained Ms books, all Fsp weathered to clay
19.5 - 31.9	SAP		heavily weathered light brown to gray-black SAP derived from amphibolite
31.9 - 34.5	GRAN	MG	slightly to moderately weathered GRAN, most Fsp partially weathered to clay
34.5 - 41.9	SAP	MG	moderately weathered gray to light brown SAP derived from granite
41.9 - 51.4	PEG	VCG	slightly weathered Qz-Fsp PEG and PEG-SAP, differentiated from the GRAN by the presence of VCG Qz, Fsp, and Ms
51.4 - 66.7	PEG	VCG	Qz-Fsp PEG with variously-sized sub-intervals (20-70 cm) of MG GRAN
66.7 - 73.7	PEG	VCG	Qz-Fsp PEG delineated from GRAN by the absence of Bt and the presence of CG Ms books; interval occasionally contains VCG K-Fsp (5-10 cm)
73.7 - 79.9	GRAN	MG	equigranular grey Ms+Bt GRAN, Ms predominant over Bt, Bt appears slightly weathered
79.9 - 80.6	PEG	VCG	Qz-Fsp PEG containing large (0.5-2 cm) Ms books
80.6 - 82.7	GRAN	MG	equigranular grey Ms+Bt GRAN
82.7 - 85.3	PEG	VCG	Qz-Fsp PEG, interval contains a 15 cm AMP xenolith
85.3 - 86.3	AMP	MG	black AMP
86.3 - 90.5	SPEG	VCG	SPEG containing about 13% Sp, interval contains MG-CG Sp (0.5-5 cm) with occasional VCG crystals (20-25 cm) oriented with their long axis parallel to core axis, small (5-10 cm) patches of slight Ms and clay alteration present in interval
90.5 - 91.1	AMP	MG	black AMP
91.1 - 91.7	PEG	VCG	Grt-bearing Qz-Fsp PEG, interval contains 5 cm amphibolite xenolith
91.7 - 93.3	AMP	MG	black AMP
93.3 - 94.6	PEG	VCG	Grt-bearing Qz-Fsp PEG, interval includes large MS books
94.6 - 94.9	AMP	FG-MG	equigranular AMP
94.9 - 96.9	PEG	VCG	Qz-Fsp PEG becoming fine-grained with depth and having a gradational contact with the underlying GRAN, units distinguished by the presence of Bt in GRAN
96.9 - 99.1	GRAN	MG	equigranular Ms+Bt GRAN, Ms predominant over Bt, GRAN similar to overlying PEG but contains Bt and has a finer grained texture
99.1 - 100.4	AMP	MG	black AMP
100.4 - 107.2	GRAN	CG	interval is predominantly a CG version of the Ms+Bt granite present throughout the drillhole, remainder consists of small (10-35 cm) sections of Qz-Fsp PEG
107.2 - 107.7	PEG	VCG	Qz-Fsp PEG containing large (1-4 cm) Ms books, lower contact is 7 cm of weakly silicified clay matrix supporting angular breccia clasts of underlying GRAN
107.7 - 113.4	GRAN	MG	equigranular Ms+Bt GRAN, Ms predominant over Bt, GRAN is similar in appearance to the surrounding PEG but contains Bt and overall is of a much finer texture
113.4 - 115.3	PEG	VCG	Qz-Fsp PEG containing large (1-4 cm) MS books and several large Fsp crystals (10-15 cm) having perthitic texture, interval also contains a 20-cm AMP xenolith
115.3 - 119.0	GRAN	MG	equigranular Ms+Bt GRAN, Ms predominant over Bt, GRAN is similar in appearance to the surrounding PEG but contains Bt and overall is of a much finer texture
119.0 - 120.5	PEG	VCG	Grt-bearing Qz-Fsp PEG containing very coarse-grained (5 cm) mica books
120.5 - 127.2	AMP	MG	black AMP, interval contains several small (1-2 cm) Qz veins
127.2 - 132.7	GRAN	MG	equigranular Ms+Bt GRAN, Ms predominant over Bt
132.7 - 151.0	AMP	MG	black AMP, interval contains several (5-20 cm) Qz-Fsp PEG veins with thin (1-3 cm) Qz veinlets common, a single ALTPPEG vein that originally was 8-10% SPEG present at 139 m

Figure 7. Cont.

(b) CLP Core 21-BD-531			
Depth (m)	Primary Lithology	Texture	Unit Description
0 - 3.0	SOIL		brown to red clay, no original rock texture present
3.0 - 66.0	SAP		red-orange-brown AMP-derived SAP with some original rock texture present, interval contains some thin(<10 cm) Qz-Fsp PEG veins and Qz veins where fractured
66.0 - 70.8	AMP	FG	Fsp-rich AMP containing some thin Qz veins and 20 cm SAP in middle of interval
70.8 - 72.3	SPEG	MG-CG	Spd-bearing PEG originally 12% Spd, but much Spd and Fsp altered to clay
72.3 - 76.1	AMP	FG-MG	AMP containing thin healed fractures with clay alteration; 8 cm Qz-Fsp PEG vein near top of interval
76.1 - 79.7	SPEG	CG	Spd-bearing PEG originally 8-10% Spd, Spd with light green color, many small healed fractures with dark mineral. Some Grt present
79.7 - 101.3	AMP	FG-MG	AMP containing many healed fractures/veins, some large (5-15 cm) Qz-Fsp PEG veins present in the interval
101.3 - 102.6	PEG	FG-CG	Gt-bearing Qz-Fsp PEG with FG areas having more of a granitic texture and containing Bt
102.6 - 103.3	AMP	FG	AMP containing thin Qz veins
103.3 - 107.3	ALTSPEG	MG-CG	micaceous ALTSPEG in which all Spd altered to Ms, FG felsic segment containing Qz, Fsp, Ms, & Bt; fine-grained pink Grt present throughout interval
107.3 - 108.2	AMP	FG	AMP with abundant Grt near base, interval contains two felsic veins
108.2 - 109.3	ALTSPEG	MG-CG	ALTSPEG in which all Spd altered to Ms, some Tur present, top of interval begins in Ms+Bt GRAN
109.3 - 122.4	AMPH	FG-MG	AMP, 10 cm SPEG vein at 114 m containing altered
122.4 - 127.2	ALTSPEG	CG	micaceous ALTSPEG in which all Sp altered to Ms, interval contains abundant Grt and graphic texture produced by Qz-Fsp intergrowth, interval also contains segments that grade into Ms+Bt GRAN
127.2 - 128.6	AMP	FG-MG	AMP, interval contains thin Qz-Fsp PEG and Ms+Bt granite veins
128.6 - 133.4	PEG	CG	strongly micaceous Grt-bearing Qz-Fsp PEG cut by veins of Ms+ Bt GRAN and in thick books, 2-mica schist grades into PEG at beginning of interval
133.4 - 147.6	GRAN	FG	Ms+Bt GRAN containing thin Qz-Fsp PEG veins
147.6 - 149.9	AMP	FG-MG	typical AMP
149.9 - 152.1	GRAN	FG	Ms+Bt GRAN containing thin Qz veins qtz veins and greenish aplite
152.1 - 160.0	AMP	FG-MG	typical AMP containing many thin (<5cm) Qz-Fsp veins

Figure 7. Depth profiles and logging descriptions of CLP drill cores 21-BD-529 (a) and 21-BD-531 (b). Abbreviations as follows: rocks—SAP = sapolite, PEG = pegmatite, SPEG = spodumene-bearing pegmatite, ALTSPEG = altered spodumene-bearing pegmatite, GRAN = granite, AMP = amphibolite; minerals—Qz = quartz, Fsp = feldspar (undifferentiated), Kfs = potassium feldspar, Bt = biotite, Grt = garnet, Ms = muscovite, Tur = tourmaline, Spd = spodumene; Texture—FG = fine grained, MG = medium grained, CG = coarse grained, VCG = very coarse grained.

Spodumene-free pegmatite and ‘granite’ on the CLP are impoverished in Li, Be, Ga, Rb and Cs relative to the spodumene-bearing layers which are notably enriched in Li, Rb, Cs and Be. The degree of fractionation in the two CLP drill cores, as expressed by the K/Rb ratio, is generally low for the ‘granite’ (K/Rb = 183 to 105) and spodumene-free pegmatites (K/Rb = 94 to 84) whereas the highest level of chemical evolution occurs in the spodumene pegmatites (K/Rb = 43 to 42). The modest level of rare-element fractionation in the CLP drill cores is characterized by Li values that are comparable to other highly evolved Li-rich pegmatites (e.g., Tanco, Harding), which also host significant quantities of beryl, lepidolite, pollucite, columbite-tantalite, wodginite, cassiterite, or microlite. However, despite the elevated levels of Li, the CLP spodumene pegmatites lack similar levels of Rb and Cs enrichment as other Li-rich pegmatites and are noticeably poor in Be, Cs and Ta minerals.

Table 1. Compositional comparison of highly evolved, Li-rich granite pegmatites.

	CLP 21-BD-529 ¹	CLP 21-BD-531 ¹	Peg Claim, Maine, USA ²	INCO, Manitoba, Canada ³	Harding, New Mexico, USA ⁴	Tanco, Manitoba, Canada ⁵	Rubicon, Namibia ⁶	Mt. Mica, Maine, USA ⁷	Segura, Portugal ⁸
Pegmatite type *	Alb-Spd	Alb-Spd	Alb-Spd	Alb-Spd	Spd	Pet	Pet	Lep	Lep
SiO ₂	73.57	72.08	73	73.70	75.24	76.04	76.29	72.08	74.81
Al ₂ O ₃	15.44	15.61	17	16.53	14.42	13.62	14.40	17.33	13.83
Fe ₂ O ₃	1.06	0.81	n.d.	0.18	0.14	0.00	1.01	1.18	0.34
MgO	0.10	0.05	n.d.	0.05	0.01	0.00	0.04	0.15	n.d.
CaO	0.67	1.37	n.d.	0.13	0.20	0.15	0.19	0.48	0.49
Na ₂ O	4.23	5.25	3.4	3.78	4.23	3.81	6.00	5.35	3.95
K ₂ O	2.90	2.51	2.6	1.73	2.74	2.96	1.40	2.08	2.90
TiO ₂	0.01	0.03	n.d.	0.01	0.05	0.01	0.02	0.07	n.d.
MnO	0.14	0.11	n.d.	0.16	0.18	0.18	0.14	0.04	0.04
P ₂ O ₅	0.25	0.30	n.d.	<0.01	0.13	0.86	0.21	0.20	2.23
Li	3893	990	6968	6549	3019	3417	1178	511	1080
Be	122	158	n.d.	n.d.	n.d.	168		24	
Ga	28	26	n.d.	n.d.	n.d.	74	42.4	34	35
Rb	617	504	1829	3292	1737	5244	1545	636	1502
Cs	69	34	66	283	472	2649	106.2	99.9	
K/Rb	43	42	11.8	4.4	13.1	4.7	9.8	27.1	16.0
A/CNK	1.36	1.13	2.02	1.99	1.40	1.40	1.23	1.45	1.31

* Pegmatite type based on the classification of Černý and Ercit [51]. n.d.—not determined. Mineral symbols used: Spd—spodumene, Ptl—petalite, Lpd—lepidolite, Ab—albite. References: ¹—This study, ²—Sundelius [52], ³—Chackowsky [53], ⁴—Burnham and Jahns [54], ⁵—Stilling et al. [55], ⁶—Ashworth et al. [56], ⁷—Simmons et al. [57], and ⁸—Antunes et al. [58]. Li, Rb and Cs ppm values of the Peg Claim, INCO and Harding pegmatites was calculated from their wt. % oxide values.

Muscovite from highly mineralized portions of two other CLP drill cores was analyzed at the Piedmont Lithium field facility in March 2023. The multielement mica calibrations shown in Figure 4b–d were used for this analysis.

Drill core 18-SS-001 contains a significant interval of fine- to coarse-grained spodumene pegmatite from 62.5 to 83.4 m (20.9 m at 1.42% bulk Li₂O). There are several distinct textures within this interval, including fine-grained spodumene + quartz aplite and typical medium- to very coarse-grained pegmatite. These textures are nearly ubiquitous within large (>10 m wide) spodumene pegmatites in the CLP. Within this large drill intercept, there is a smaller zone from approximately 67 to 69 m that is visually distinct from the rest of the intercept. It lacks K-feldspar and contains columbite, which is not seen in other portions of the interval. Two muscovite grains from the columbite-bearing interval have Li contents of 0.98 and 0.168 wt. % and low K/Rb ratios of 21.5 and 19.5.

Drill core 19-CT-014 contains a significant intercept of fine- to very coarse-grained spodumene pegmatite from 69.8 to 113.0 m (43.2 m at 1.73% bulk Li₂O). The distinct fine- and medium-grained spodumene + quartz aplite plus medium- to very coarse-grained pegmatite textures in this intercept are characteristic of the strongly spodumene-bearing pegmatites of the CLP. Within this intercept, there is a smaller interval between 101 and 104 m (Figure 8) that is distinct from the rest of the intercept that contains (i) significantly more spodumene in larger, more equant crystals exhibiting a random orientation, (ii) far less albite and other feldspars than other portions of the intercept, and (iii) several infrequent yet distinct crystals of both columbite and apatite. Ten muscovite grains from the columbite-bearing core interval between a 71 and 111 m interval have high Li contents of 0.220 and 0.424 wt. % and the lowest K/Rb ratios of 18.0 and 7.7 observed in the CLP.

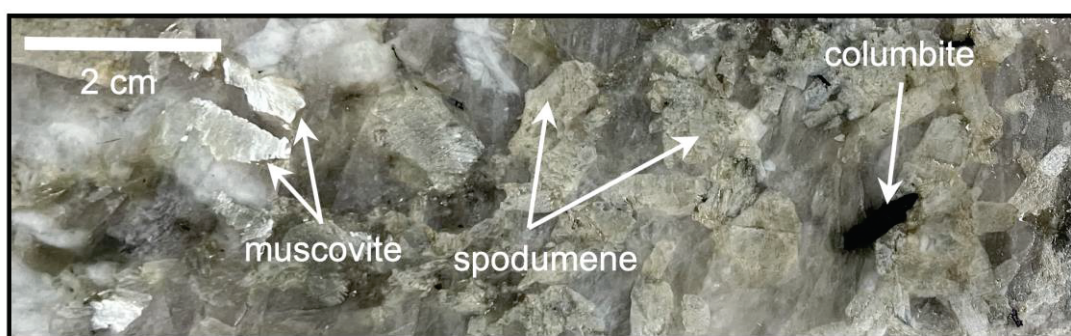


Figure 8. Photograph of a section of drill core 19-CT-014 that is representative of the highly fractionated and mineralized pegmatites of the CLP. This zone between 103 and 104 m depth contains columbite, apatite (not shown), tabular spodumene, and muscovite with 0.29 wt. % Li and a K/Rb ratio of 8.7.

4.2. Analysis of Muscovite in CLP Outcrops

A second way in which handheld LIBS can be utilized in an exploration and prospect context is for the real-time analysis of outcrops in the field. During our field campaign in March 2023, we analyzed muscovite from multiple CLP outcrops in one area characterized by spodumene-free pegmatites and also from multiple outcrops in three areas containing mineralized, spodumene-bearing pegmatites. Single muscovite grains from 27 pegmatite outcrops were pried loose with a knife, affixed to black tape, and presented to the handheld LIBS instrument for real-time, in-field analysis. Five LIBS analyses were made on each individual muscovite grain. These analyses are summarized in Table 2. Although the ranges of Li and K/Rb variation and the average Li contents of the spodumene-free and spodumene-bearing outcrops overlap, there is a clear distinction in their average K/Rb ratios, with muscovite from the three spodumene-bearing groups being distinctly lower (23.5 ± 4.1 , 21.4 ± 2.6 , 23.6 ± 3.5) than for the spodumene-free group (30.7 ± 2.3).

Table 2. Li abundance and K/Rb ratio by LIBS analysis for muscovite from CLP outcrops.

		#	Li (wt. %)	K/Rb
CLP Area 1 Spd-bearing pegmatites	range	10	0.088–0.308	17.6–30.6
	$\bar{X} \pm 2\sigma$			
CLP Area 2 Qz-Fsp pegmaties	range	7	0.104–0.376	28.2–35.6
	$\bar{X} \pm 2\sigma$			
CLP Area 3 Spd-bearing pegmatites	range	5	0.131–0.489	19.0–24.5
	$\bar{X} \pm 2\sigma$			
CLP Area 4 Qz-Fsp pegmaties	range	5	0.062–0.182	21.0–30.8
	$\bar{X} \pm 2\sigma$			

4.3. Analysis of Soil Muscovite

A particular exploration challenge in granite pegmatite is prospect evaluation in the absence of an outcrop. The third way in which handheld LIBS can be utilized in an exploration context is for the analysis of soil in the field. In such a situation, the real-time analysis of soil muscovite in the field would be especially helpful. LIBS is ideally suited for this task.

The red clay soil ubiquitously present across the Piedmont region of North Carolina and encountered in all drill cores from the CLP belongs to the Cecil series, a fine-grained and moderately permeable kaolinitic soil typically occurring on ridges and side slopes of the Piedmont uplands that formed in residuum weathered from felsic igneous and high-grade metamorphic rocks [59]. Having formed from weathered residuum, the red clay soils across the CLP frequently contain muscovite. As part of a LIBS Li survey across an upland area of the CLP where a Cecil series soil is inferred to overlie multiple buried pegmatite dikes, we separated muscovite from four soil cores augered to about a 50 cm depth along a 430 m NW-SE trending traverse centered at UTM coordinates 474796 E, 3917083 N for handheld LIBS analysis, with five measurements taken for each muscovite grain. The average Li contents and K/Rb ratios for these muscovites range from 0.097 to 0.164 wt. % and 17.1 to 25.9, respectively (Table 3), indicating that the muscovites analyzed were derived from spodumene-bearing pegmatites and illustrating how LIBS analysis of soil muscovite can be used to infer the subsurface presence of mineralized pegmatite.

Table 3. Li abundance and K/Rb ratio by LIBS analysis for soil-derived muscovite.

Sample #	Li (wt. %)	K/Rb
22-AC-133	0.097	22.5
22-AC-135	0.146	17.1
22-AC-142	0.145	19.7
22-AC-144	0.164	25.9

4.4. Li Abundances and K/Rb-Li Systematics

Li is a strongly incompatible element that becomes enriched in residual melts during the magmatic differentiation of granitic magmas. The K/Rb ratio is considered to be a reliable indicator of the extent of compositional fractionation of the melt from which muscovite crystallizes [11,13,60,61] and decreases with the progressive crystallization of a granitic magma due to the incompatible nature of Rb. Considered together, the K/Rb-Li systematics of muscovite reflects the extent of compositional evolution attained by a crystallizing magma, as the abundance of Li should increase in a fractionating melt as K/Rb decreases [60–65]. Thus, the binary plot of K/Rb versus Li can be used to gauge the degree of rare-element fractionation and geochemical evolution from poorly fractionated common pegmatites to extremely fractionated rare-element pegmatites. Consideration of K/Rb-Li has also been used as a tool for evaluating potential Li-mineralization in granitic pegmatites [66].

In general, common pegmatites, which lack rare-element mineralization such as beryl, columbite-group minerals, lithium phosphates, and lithium aluminosilicates, are impoverished in rare-alkalis (e.g., Be, Li, Rb, Cs), high-field strength elements (e.g., Nb, Ta, Sn) and volatile components (e.g., B, F). These pegmatites tend to have high K/Rb ratios and low concentrations of Li, Rb and Cs in their muscovite and K-feldspar. Specifically, muscovite from common pegmatites generally has K/Rb from roughly 65 to 40 with Li concentrations typically <200 ppm. Muscovite from Be-Nb-Ta-P-enriched pegmatites has a Li content that mostly varies between 20 and 1000 ppm with an associated K/Rb of 45 to 10. Highly fractionated pegmatites, enriched in Li and Cs, may host muscovite with K/Rb varying between 40 and 2 with Li contents ranging from 0.5 to nearly 2 wt. %.

Distributions of muscovite Li contents and K/Rb ratios from across the CTSB are displayed in Figure 9, with muscovite K/Rb-Li systematics illustrated in Figure 10. Overall, across the CTSB, the muscovite Li contents in pegmatites vary over an order of magnitude, extending from 0.04 to 0.74 wt. %, and K/Rb ratios vary between 63 to 8. Li contents for spodumene-bearing pegmatites, ranging from 0.0359 to 0.736 wt. % compared to 0.036 to 0.376 for common quartz-feldspar pegmatites (Figure 10). On average, Li contents are greater in spodumene-bearing pegmatites ($\bar{X} = 0.21 \pm 0.12$) than in the common quartz-feldspar pegmatites ($\bar{X} = 0.14 \pm 0.08$). Respective Li contents and K/Rb ratios for pegmatite

muscovite range from 0.61 to 0.74 wt. % and 61.0 to 17.3 across the CTSB, excluding the CLP (Figure 10a), from 0.26 to 0.49 wt. % and 45.4 to 14.1 within the CLP (Figure 10b), and 0.04 to 0.42 and 62.6 to 7.7 for the CLP drill cores (Figure 10c). Although distributions overlap substantially, K/Rb ratios for common quartz-feldspar pegmatites ($\bar{X} = 33 \pm 9$) are biased toward high values compared to those for spodumene-bearing pegmatites ($\bar{X} = 21 \pm 6$).

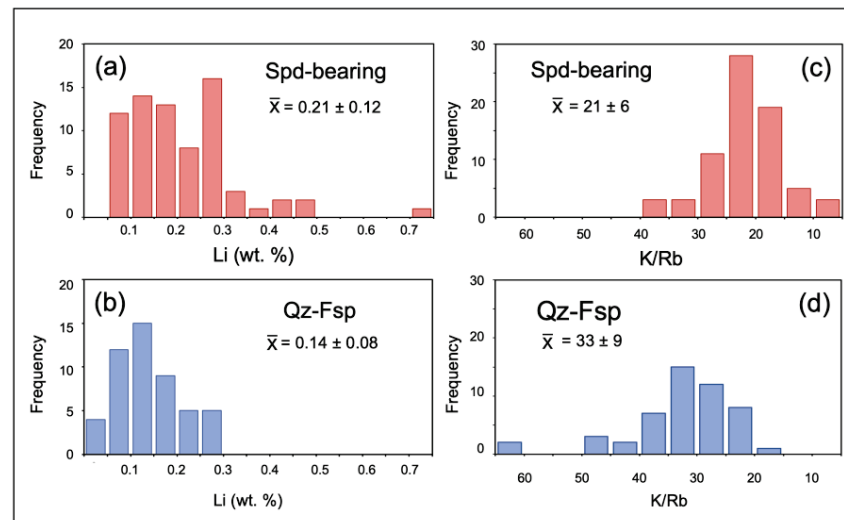


Figure 9. Distribution of Li abundances (a,b) and K/Rb ratios (c,d) in 65 muscovites from Spd-bearing pegmatites (Li = 0.059–0.739 wt. %, average = 0.210 ± 0.119 wt. %) and 64 muscovites from Qz-Fsp pegmatites (Li = 0.036–0.376 wt. %, average = 0.146 ± 0.095 wt. %) across the CTSB.

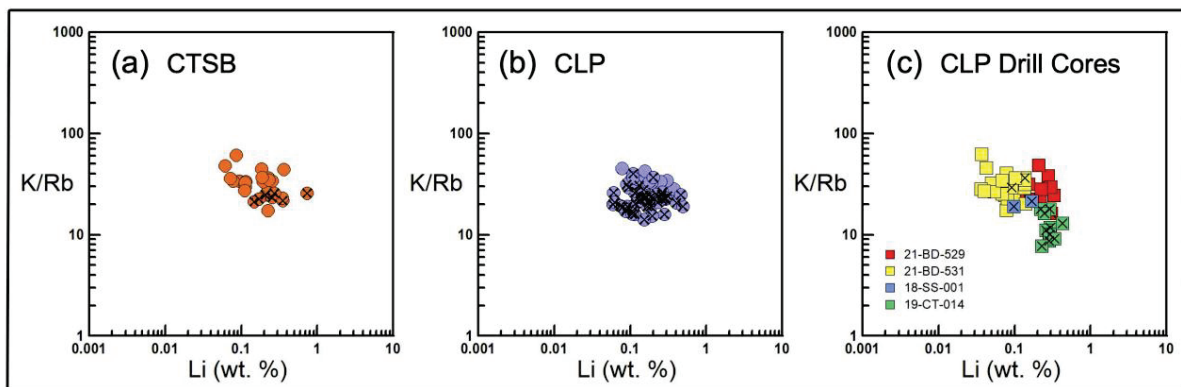


Figure 10. Plots of K/Rb versus Li for muscovite from pegmatites of the CTSB (a), CLP (b), and CLP drill cores (c) analyzed in this study by handheld LIBS. Symbols containing an ‘x’ denote spodumene-bearing pegmatites.

It is notable that muscovite in the highly fractionated and strongly mineralized pegmatite of drill core 19-CT-014 exhibits the lowest K/Rb ratios determined for the CTSB (Figure 10c). These values are comparable to muscovite from Li-rich pegmatites from other worldwide localities and confirm the highly fractionated nature of the CTSB pegmatites. While the K/Rb and Li values of muscovite from the spodumene-bearing CTSB pegmatites are comparable to muscovite from spodumene-bearing pegmatites of the Bailongshan field, China [67], the Leinster pegmatite field, Ireland [68], and the Black Hills of South Dakota, USA [69], the CTSB pegmatites do not reach the level of extreme fractionation displayed by muscovite from the Tanco pegmatite in Manitoba, Canada [70], or the Bikita pegmatite in Zimbabwe [71], arguably two of the most evolved Li-rich pegmatites in the world. It is worth noting that the common quartz-feldspar pegmatites of the CTSB have significantly

lower K/Rb ratios and higher Li values than many other common pegmatites found elsewhere, e.g., Cap de Creus, Spain [72]; Cross Lake, Manitoba, Canada [73]; and Yellowknife pegmatite field, Northwest Territories, Canada [74]. This could suggest that the CT SB pegmatites may carry hidden rare-element mineralization in other parts of the pegmatite domain that were not sampled and analyzed in this study.

5. Summary and Conclusions

Lithium is a key element for the transition from a carbon-based energy economy to a low-carbon energy economy of the future. Although Li brine deposits currently account for most of the mined Li in the world, the abundance of unmined Li-rich pegmatites in the world will be exploited in the coming years to meet the continually rising demand for Li. With this in mind, exploration for Li-rich, ore-grade pegmatite deposits is essential. The focus of this study is the analysis of muscovite in Li-rich pegmatites of the CT SB, particularly at the CLP in Gaston County, NC. Muscovite in CLP pegmatites has K₂O and FeO contents ranging from 8.6 to 11.1 and 0.5 to 2.8 wt. %; MgO, Na₂O, and BaO contents below 1.1 wt. %; and low F contents (<0.5 wt. %).

With its capability for real-time compositional analysis, handheld LIBS can be a valuable addition in the toolbox of the exploration geologist, particularly given its unique ability for the analysis of Li outside the conventional laboratory setting. By developing element-specific calibrations in the laboratory, handheld LIBS can be used in the field for quantitative element analysis of rocks, mineral, and soils during mineral exploration and prospect evaluation campaigns. Using a handheld LIBS analyzer calibrated for Li, K, and Rb in muscovite, this paper provides a framework for maximizing the efficiency during exploration for Li pegmatite ore bodies and the evaluation of identified pegmatite prospects. Because muscovite is a common constituent of Li-rich pegmatites, the determination of K/Rb ratios can provide a mineralization vector mineral for Li exploration.

LIBS analysis of drill core muscovites shows that the Li contents are highest and K/Rb ratios are lowest in the most fractionated, spodumene-bearing sections. The LIBS analyses of muscovite pegmatite outcrop yielded the same results, in agreement with the known presence or absence of spodumene in that outcrop. Based on these LIBS measurements in drill core and outcrop samples of a known spodumene character (i.e., present or absent) in this field area, we hypothesize that LIBS analyses of muscovite in soils can be a reliable predictor of spodumene-bearing pegmatites at depth because of the elevated Li contents and low K/Rb ratios of their detrital mica, respectively, 0.097 to 0.164 wt. % and 17.1 to 25.9 for the few soil micas analyzed.

Quantitative analysis of muscovites from the CT SB by handheld LIBS yields results that mimic geochemical characteristics of Li-rich pegmatites from around the world, showing high Li contents and low K/Rb ratios throughout the CT SB pegmatite belt. Within the CLP, and across the CT SB, muscovite Li contents vary over an order of magnitude, ranging from 0.04 to 0.74 wt. %, and their K/Rb ratios vary between 63 and 8. On average, mica Li contents are greater in spodumene-bearing pegmatites ($\bar{X} = 0.21 \pm 0.12$, than in quartz-feldspar pegmatites at ($\bar{X} = 0.14 \pm 0.08$). Although overlapping substantially in the middle portions of their distributions, muscovite K/Rb ratios for spodumene-bearing pegmatites ($\bar{X} = 21 \pm 6$) are biased toward low values compared to those for quartz-feldspar pegmatites ($\bar{X} = 33 \pm 9$), documenting the highly evolved character of the pegmatites within the CT SB district. Our results indicate that with a sufficient number of LIBS analyses, spodumene-bearing pegmatites can be successfully differentiated from spodumene-free pegmatites in the field in real-time using muscovites from the drill core, outcrop, and soil. This has important implications for Li exploration efforts, the most obvious being the reduction in time needed for quantitative geochemical analysis to vector towards ore bodies and subsequently to plan cost-effective drilling campaigns.

Author Contributions: R.S.H. defined and led the study. M.S.M. described the four drill cores analyzed. Z.G. planned and led the fieldwork. R.S.H. and J.S.M. undertook LIBS analysis of samples in the field. A.C.C. undertook the EPMA analyses. R.S.H., M.A.W. and A.C.C. prepared the paper with input and review from all co-authors. A.C.C. acquired the funding for the project. All authors have read and agreed to the published version of the manuscript.

Funding: Piedmont Lithium Funding for this research was provided by North Carolina Policy Collaboratory grant #207586-50004 and Piedmont Lithium contract #573984 to North Carolina State University.

Data Availability Statement: The data from this study, available on request, are provided in Appendices B–D.

Acknowledgments: Our appreciation is extended to Piedmont Lithium, Inc., particularly Chief Geologist Lamont Leatherman, for facilitating the fieldwork portion of the study and providing the lithological and geochemical data for the drill cores analyzed. We thank the U.S. National Museum of Natural History and the Peabody Museum of Yale University for providing the reference micas used for the development of the mica calibrations on the LIBS handheld analyzer. We also thank Lowell Moore at the Electron Microprobe Laboratory in the Department of Geosciences at Virginia Tech for his assistance with the microprobe analysis.

Conflicts of Interest: The authors declare no conflict of interest.

Appendix A

Mica specimens used in the development of mica calibration curves shown in Figure 4 (Lpd = lepidolite, Mrg = margarite, Ms = muscovite, Phl = plogopite); nd = not determined.

Specimen ID	Type	Location	Li (wt. %)	K (wt. %)	Rb(wt. %)
BB #7-6	Ms	BB #7 Pegmatite, Maine (USA)	0.613	9.439	0.759
Cole-13	Ms	Cole Pegmatite, Maine (USA)	0.153	9.489	0.247
Heinrich-222	Ms	Dike #3	0.745	10.376	nd
GE3-9	Ms	GE Pegmatite, Maine (USA)	0.246	9.306	0.391
Hayes-1	Ms	Hayes Pegmatite, Maine (USA)	0.195	9.331	0.503
Hibbs-4	Ms	Hibbs Pegmatite, Maine USA)	0.060	9.514	0.169
Mt. Marie-15	Ms	Mount Marie Pegmatite, Maine (USA)	0.044	9.431	0.090
NMNH-48633	Mrg	Laurel Creek, Maryland (USA)	nd	0.002	nd
NMNH-103041	Lpd	Varuträsk, Vasterbotten (Sweden)	2.537	2.539	1.900
NMNH-105719	Lpd	Brown Derby, Colorado (USA)	2.091	8.388	1.712
NMNH-115326	Phl	Talcville, NC (USA)	nd	7.445	nd
NMNH-128243	Lpd	Grosmont, Western Australia (Australia)	2.592	8.752	1.055
NMNH-128418	Lpd	Hoydalen, Tordal (Norway)	2.379	8.321	2.249
NMNH-144860	Lpd	Minas Gieras (Brazil)	2.334	8.403	1.616
NMNH-R4485	Mrg	Unionville, Pennsylvania (USA)	nd	0.025	nd
NMNH-R11827	Lpd	Vitaniemi, Eräjärvi (Finland)	2.211	8.733	0.780
Willis-2	Ms	Willis Warren Pegmatite, Maine (USA)	0.035	9.339	0.368
Willis-7	Ms	Willis Warren Pegmatite, Maine (USA)	0.015	9.472	0.385
YPM MIN-023948	Mrg	Chester, Massachusetts (USA)	nd	0.018	nd

Appendix B

Handheld LIBS Li and major element EMPA analyses of muscovite in drill cores 21-BD-529 (a) and 21-BD-531 (b).

(a) Drill Core 21-BD-529															
Sample Depth	Primary Lithology	LIBS	Li	SiO2	TiO2	Al2O3	MgO	FeO	MnO	CaO	Na2O	K2O	BaO	F	Total
		(wt %)													
12.6	SOIL														
15.0		0.039													
16.5	SAP	0.023													
17.0		0.025													
18.0		0.031													
19.0	PEG	0.021													
20.0	SAP	0.054													
	GRAN	0.026													
36.0	SAP	0.048													
39.0		0.103													
43.5		0.174													
49.3	PEG	0.102	44.99	0.09	35.16	0.53	2.07	0.05	0.01	0.57	10.63	0.03	0.27	94.35	
50.6		0.128	44.64	0.03	35.56	0.43	2.05	bd	0.04	0.52	10.65	0.02	0.28	94.18	
51.0		0.113													
52.0		0.106													
53.0		0.105													
54.0		0.114	44.25	0.07	35.43	0.38	2.08	0.06	0.02	0.49	10.74	0.04	0.11	93.57	
55.0		0.124													
55.9	PEG	0.146	45.57	0.06	34.41	0.48	2.27	bd	na	0.49	10.85	bd	0.34	94.46	
58.5		0.113													
61.1		0.172													
64.3		0.135													
66.0		0.124													
67.0		0.212													
71.0	PEG	0.149	45.42	0.04	35.12	0.47	2.26	0.03	na	0.57	10.57	0.02	0.20	94.72	
73.0		0.235													
	GRAN														
	PEG														
	GRAN														
84.0	PEG	0.210													
	AMP														
88.0	SPEG	0.249													
	AMP														
93.5	PEG	0.136													
	AMP														
94.5	PEG	0.099													
	AMP														
	PEG														
	PEG														
	AMP														
100.5	GRAN	0.079													
103.4		0.093													
107.4	PEG	0.088	45.14	0.02	36.38	0.30	1.82	0.05	0.01	0.66	10.56	0.01	0.14	95.07	
113.4	GRAN	0.093													
	PEG														
	GRAN														
120.0	PEG	0.069	45.19	0.06	36.02	0.29	1.79	0.03	0.01	0.62	10.66	0.01	0.12	94.79	
	AMP														
	GRAN														
	AMP														

(b) Drill Core 21-BD-531															
Sample Depth	Primary Lithology	LIBS	Li	SiO2	TiO2	Al2O3	MgO	FeO	MnO	CaO	Na2O	K2O	BaO	F	Total
		(wt %)													
2.8	SOIL	0.017													
22.5	SAP	0.032													
23.4		0.023	44.95	0.05	36.30	0.27	1.12	na	0.01	1.16	9.56	0.02	0.08	93.44	
	AMP														
26.8		0.043													
27.2	SAP	0.035													
28.5		0.025													
34.3		0.039													
49.5		0.054													
50.9	SAP	0.095	44.48	0.08	35.40	0.44	1.57	na	0.02	1.10	9.75	0.04	0.07	92.89	
54.0		0.120													
61.5		0.069													
62.8		0.071													
64.5		0.058													
	AMP														
70.9		0.228													
71.5	SPEG	0.145	45.00	0.02	36.46	0.04	1.33	0.07	0.02	0.59	10.57	0.03	0.17	94.27	
71.9		0.046	45.07	0.03	37.21	0.05	1.16	0.08	0.04	0.56	10.53	0.03	0.18	94.86	
72.3			44.46	0.02	37.02	0.03	0.80	na	bd	0.65	10.10	0.04	0.08	93.14	
	AMP														
73.0		0.091													
77.0		0.083													
77.5	SPEG	0.171	44.88	0.09	35.39	0.27	2.22	0.04	0.01	0.63	10.52	0.02	0.19	94.23	
78.0		0.149													
78.7		0.080	44.93	0.02	35.92	0.09	2.06	0.09	0.01	0.65	10.48	0.02	0.19	94.39	
	AMP														
99.0	PEG	0.244													
	AMP														
101.3	PEG	0.069	45.19	0.06	35.37	0.45	2.05	0.04	0.01	0.55	10.73	0.03	0.17	94.57	
102.5			45.21	0.04	35.18	0.49	2.09	0.03	0.02	0.53	10.87	0.03	0.10	94.49	
	AMP														
104.8			45.46	0.07	35.32	0.41	1.84	0.05	0.02	0.48	10.87	0.02	0.10	94.58	
105.8	ALTPEG		45.91	0.20	34.39	0.81	2.25	0.06	0.01	0.40	10.86	0.07	0.14	94.95	
106.6			43.82	0.03	36.82	0.01	0.88	na	0.02	0.68	10.25	0.08	0.13	92.59	
	AMP														
108.8	ALTPEG	0.038	45.32	0.03	36.49	0.25	1.35	0.03	0.05	0.56	10.74	0.09	0.12	94.89	
	AMP														
122.5		0.045													
124.2	ALTPEG	0.044	44.55	0.05	35.68	0.45	1.96	0.03	0.03	0.55	10.77	0.03	0.14	94.12	
126.7		0.046	44.75	0.07	35.80	0.36	1.72	0.06	0.01	0.59	10.65	0.03	0.08	94.04	
127.0		0.040	45.01	0.02	36.23	0.25	1.69	0.03	0.01	0.65	10.44	0.04	0.15	94.44	
	AMP														
129.4		0.052	45.82	0.09	35.48	0.38	1.87	0.03	0.02	0.48	10.81	0.03	0.11	94.94	
132.0	PEG		45.49	0.13	35.73	0.35	1.82	0.01	0.02	0.58	10.71	0.05	0.11	94.91	
133.3		0.047	45.03	0.06	35.67	0.28	1.76	0.08	0.00	0.51	10.87	bd	0.10	94.31	
142.0	GRAN	0.144													
	AMP														
	GRAN														
	AMP														

Appendix C

Li, K, and Rb abundances (wt. %) and K/Rb ratios in muscovite from pegmatites and soils within the Carolina Lithium Prospect and Carolina Tin Spodumene Belt determined by handheld LIBS (measured values and uncertainties in wt. %, Spd = spodumene, Y = spodumene-bearing pegmatite, N = spodumene-free pegmatite, NK = not known, NA = not analyzed). Mineral abbreviations as follows: Qz = quartz, Fsp = feldspar.

Carolina Lithium Prospect											
Sample ID	Description	Spd	UTM N	UTM E	Li	$\pm 2\sigma$	K	$\pm 2\sigma$	Rb	$\pm 2\sigma$	K/Rb
22-AC-00	Pegmatite hand specimen	Y	NK	NK	0.106	0.021	10.548	0.912	0.660	0.117	16.0
22-AC-01	Pegmatite outcrop #1	N	472603	3916672	0.192	0.038	10.454	1.227	0.319	0.048	32.7
22-AC-02	Pegmatite outcrop #2	N	472615	3916697	0.115	0.025	10.812	1.138	0.326	0.042	33.2
22-AC-23	Pegmatite outcrop #3	Y	473502	3914841	0.282	0.055	9.082	1.183	0.572	0.123	15.9
22-AC-24	Pegmatite outcrop #4	Y	473807	3915372	0.153	0.027	10.127	0.805	0.451	0.071	22.4
22-AC-06	Pegmatite outcrop #5	Y	473429	3916466	0.074	0.010	9.846	1.009	0.511	0.086	19.3
22-AC-07	Pegmatite outcrop #6	Y	473245	3916139	0.193	0.037	10.966	0.939	0.717	0.128	15.3
22-AC-10	Pegmatite float boulder	Y	472788	3915926	0.105	0.021	10.996	0.739	0.641	0.121	17.2
22-AC-11	Pegmatite outcrop #7	Y	472704	3915929	0.109	0.019	10.620	0.723	0.266	0.039	39.9
22-AC-13	Pegmatite outcrop #8	Y	472720	3915951	0.087	0.014	10.728	0.980	0.629	0.129	17.1
22-AC-14	Pegmatite outcrop #9	Y	472852	3916157	0.090	0.013	10.329	0.901	0.328	0.049	31.5
22-AC-16	Pegmatite dike	Y	472346	3915109	0.153	0.027	11.494	0.706	0.814	0.120	14.1
22-AC-17	Pegmatite outcrop #10	N	472350	3915056	0.122	0.020	11.288	1.043	0.318	0.048	35.6
22-AC-18	Pegmatite outcrop #11	N	472350	3915056	0.109	0.036	11.175	1.284	0.309	0.048	36.2
22-AC-51	Pegmatite outcrop #12	Y	473100	3915210	0.263	0.036	12.309	0.744	0.466	0.062	26.4
22-AC-52	Mica Pit Road	NK	470235	3908800	0.156	0.032	11.436	0.778	0.268	0.031	42.7
22-AC-53	Mica Pit Road	NK	470235	3908800	0.078	0.015	9.402	0.800	0.207	0.022	45.4
22-AC-130	Mica Pit	NK	470235	3908800	0.201	0.037	11.266	0.798	0.495	0.061	22.8
22-AC-133	Soil traverse NCS-2, D00176585	NK	474860	3916990	0.097	0.017	11.453	0.595	0.511	0.033	22.5
22-AC-135	Soil traverse NCS-4, D00176024	NK	474830	3917032	0.146	0.043	10.561	0.768	0.662	0.048	17.1
22-AC-142	Soil traverse NCS-10, D00176581	NK	474885	3916951	0.145	0.015	10.794	0.680	0.547	0.022	19.7
22-AC-144	Soil traverse NCS-10, D00176581	NK	474817	3917056	0.164	0.041	11.297	0.452	0.437	0.023	25.9
23-AC-21	Pegmatite specimen (#751)	N	473041	3915775	0.157	0.019	9.851	1.620	0.267	0.055	36.8
23-AC-66	Pegmatite outcrop #13, grain #1	Y	471040	3911384	0.079	0.017	11.161	0.847	0.596	0.067	18.7
23-AC-66	Pegmatite outcrop #113 grain #2	Y	471040	3911384	0.222	0.034	11.095	0.803	0.428	0.071	25.2
23-AC-67	Pegmatite driveway outcrop #1	Y	472830	3916280	0.288	0.029	12.083	0.964	0.525	0.085	23.0
23-AC-68	Pegmatite driveway outcrop #2	Y	472830	3916280	0.201	0.030	10.433	0.645	0.283	0.035	36.8
23-AC-69	Pegmatite driveway outcrop #3	Y	472830	3916280	0.174	0.042	9.151	1.890	0.438	0.114	21.0
23-AC-70	Pegmatite driveway outcrop #4	Y	472830	3916280	0.460	0.189	12.376	0.914	0.503	0.073	24.8
23-AC-71	Pegmatite outcrop at core shed	N	471070	3911410	0.178	0.022	10.133	0.463	0.302	0.033	33.5
22-AC-20	Pegmatite #1, CLP Outcrop Area 1	Y	474086	3916608	0.115	0.020	11.086	1.098	0.699	0.143	15.9
23-AC-17	Pegmatite #2, grain #1,CLP Outcrop Area 1	Y	474150	3916700	0.088	0.028	12.905	0.543	0.731	0.106	17.6
23-AC-17	Pegmatite #2, grain #2, CLP Outcrop Area 1	Y	474150	3916700	0.092	0.025	12.701	1.322	0.673	0.106	18.9

Carolina Lithium Prospect											
Sample ID	Description	Spd	UTM N	UTM E	Li	$\pm 2\sigma$	K	$\pm 2\sigma$	Rb	$\pm 2\sigma$	K/Rb
23-AC-18	Pegmatite #3 (0744), CLP Outcrop Area 1	Y	474086	3916608	0.114	0.049	11.059	0.396	0.424	0.052	26.0
23-AC-38	Pegmatite #4, grain #1, CLP Outcrop Area 1	Y	474086	3916608	0.130	0.059	10.362	0.630	0.339	0.041	30.6
23-AC-38	Pegmatite #4, grain #2, CLP Outcrop Area 1	Y	474086	3916608	0.151	0.041	10.243	0.698	0.367	0.037	27.9
23-AC-39	Pegmatite boulder #1, CLP Outcrop Area 1	Y	474086	3916608	0.162	0.032	11.312	1.268	0.480	0.063	23.6
23-AC-40	Pegmatite float boulder #2, CLP Outcrop Area 1	Y	474086	3916608	0.168	0.020	12.695	1.140	0.666	0.081	19.1
23-AC-41	Pegmatite float boulder #2, CLP Outcrop Area 1	Y	474086	3916608	0.259	0.024	11.426	0.978	0.452	0.041	25.2
23-AC-42	Pegmatite float boulder #3, CLP Outcrop Area 1	Y	474086	3916608	0.292	0.019	10.610	0.870	0.473	0.053	22.4
23-AC-43	Pegmatite float boulder #4, CLP Outcrop Area 1	Y	474086	3916608	0.308	0.018	12.223	1.268	0.502	0.059	24.3
23-AC-44	Pegmatite outcrop #1, CLP Outcrop Area 2	N	472729	3916866	0.178	0.013	12.027	1.123	0.396	0.038	30.4
23-AC-45	Pegmatite outcrop #2, grain 1, CLP Outcrop Area 2	N	472718	3916908	0.111	0.012	12.401	0.428	0.398	0.033	33.2
23-AC-45	Pegmatite outcrop #2, grain 2, CLP Outcrop Area 2	N	472719	3916981	0.175	0.034	12.079	1.342	0.365	0.058	33.0
23-AC-46	Pegmatite outcrop #3, CLP Outcrop Area 2	N	472693	3917024	0.104	0.014	11.629	0.601	0.327	0.028	35.6
23-AC-47	Pegmatite outcrop #4, CLP Outcrop Area 2	N	472664	3916978	0.376	0.065	11.728	0.888	0.416	0.051	28.2
23-AC-48	Pegmatite outcrop #5, CLP Outcrop Area 2	N	472574	3916953	0.173	0.035	11.212	0.971	0.348	0.073	32.2
23-AC-49	Pegmatite outcrop #6, CLP Outcrop Area 2	N	472659	3916769	0.304	0.040	11.615	0.826	0.340	0.033	34.1
23-AC-50	Pegmatite outcrop #7, CLP Outcrop Area 2	N	470605	3908798	0.249	0.049	13.282	1.453	0.396	0.070	33.6
23-AC-51	Pegmatite dike trending W-NW, CLP Outcrop Area 2	Y	470605	3908798	0.185	0.025	13.332	0.936	0.696	0.065	19.0
23-AC-52	Pegmatite boulder, CLP Outcrop Area 3	Y	470605	3908798	0.405	0.078	11.880	0.741	0.571	0.054	20.8
23-AC-53	Pegmatite outcrop #1 with large mica books, CLP Outcrop Area 3	Y	470630	3908799	0.260	0.077	12.723	0.676	0.519	0.047	24.5
23-AC-54	Pegmatite outcrop #2, CLP Outcrop Area 3	Y	470630	3908799	0.131	0.010	13.674	0.966	0.577	0.091	23.7
23-AC-55	Pegmatite outcrop #3, CLP Outcrop Area 3	Y	NK	NK	0.489	0.038	10.678	0.509	0.560	0.039	19.1
22-AC-123	Pegmatite #1, Outcrop Area 4	Y	NK	NK	0.158	0.024	10.465	1.013	0.445	0.066	23.5
22-AC-124	Pegmatite #2, Outcrop Area 4	Y	NK	NK	0.185	0.040	10.643	0.899	0.452	0.057	23.5
22-AC-125	Pegmatite #3, Outcrop Area 4	Y	NK	NK	0.116	0.024	10.826	0.809	0.537	0.053	20.2

Carolina Lithium Prospect											
Sample ID	Description	Spd	UTM N	UTM E	Li	$\pm 2\sigma$	K	$\pm 2\sigma$	Rb	$\pm 2\sigma$	K/Rb
22-AC-126	Pegmatite #4, Outcrop Area 4	Y	NK	NK	0.265	0.041	10.426	0.849	0.467	0.059	22.3
22-AC-127	Pegmatite #6, Outcrop Area 4	Y	NK	NK	0.149	0.027	11.218	1.066	0.467	0.073	24.0
22-AC-128	Pegmatite #6.5, Outcrop Area 4	Y	NK	NK	0.059	0.011	11.340	0.746	0.571	0.062	19.9
23-AC-22	Pegmatite dike #1, Outcrop Area 4	Y	NA	NA	0.134	0.026	12.257	1.261	0.563	0.076	21.8
23-AC-23	Pegmatite dike #2, Outcrop Area 4	Y	NA	NA	0.062	0.013	10.669	0.869	0.507	0.075	21.0
23-AC-31	Pegmatite dike #3, Outcrop Area 4	N	NA	NA	0.094	0.020	10.724	0.597	0.366	0.039	29.3
23-AC-32	Pegmatite dike #4, Outcrop Area 4	N	NA	NA	0.114	0.043	12.039	0.668	0.391	0.049	30.8
23-AC-33	Pegmatite outcrop with large mica books, Outcrop Area 4	Y	NA	NA	0.182	0.060	12.319	1.889	0.535	0.093	23.0

Appendix D

Compositional comparison of CLP drill cores 21-BD-529 (top) and 21-BD-531 (bottom).

Drill Core 21-BD-529					
	Qz-Fsp Pegmatite	Spd-Pegmatite	Altered Pegmatite	Granite	Amphibolite
(wt. %)	$n = 4$ SiO ₂ = 69.1–73.8	$n = 6$ SiO ₂ = 70.4–73.0	$n = 7$ SiO ₂ = 69.1–73.8	$n = 4$ SiO ₂ = 71.1–76.5	$n = 4$ SiO ₂ = 70.7–73.5
SiO ₂	72.47 ± 2.53	72.08 ± 0.84	73.51 ± 1.12	73.53 ± 1.32	72.73 ± 1.33
Al ₂ O ₃	15.04 ± 1.17	15.61 ± 0.59	15.06 ± 0.44	14.39 ± 0.47	15.13 ± 0.96
Fe ₂ O ₃	1.18 ± 0.20	0.81 ± 0.23	1.16 ± 0.24	1.58 ± 0.33	1.09 ± 0.41
MgO	0.12 ± 0.05	0.05 ± 0.02	0.12 ± 0.06	0.27 ± 0.14	0.17 ± 0.09
CaO	0.92 ± 0.53	1.37 ± 0.37	0.67 ± 0.27	1.08 ± 0.47	0.92 ± 0.39
Na ₂ O	3.89 ± 1.86	2.51 ± 0.82	3.62 ± 1.51	3.80 ± 0.89	4.11 ± 1.38
K ₂ O	4.38 ± 1.35	5.25 ± 0.87	4.50 ± 0.81	3.52 ± 0.33	4.22 ± 1.38
MnO	0.12 ± 0.03	0.11 ± 0.03	0.10 ± 0.06	0.03 ± 0.01	0.06 ± 0.03
P ₂ O ₅	0.32 ± 0.03	0.30 ± 0.19	0.28 ± 0.03	0.27 ± 0.05	0.27 ± 0.04
Li (ppm)	50 ± 16	990 ± 764	61 ± 24	87 ± 27	nd
Be (ppm)	39 ± 26	158 ± 81	18 ± 10	9 ± 4	nd
Ga (ppm)	19 ± 1	26 ± 2	18 ± 2	18 ± 1	nd
Rb (ppm)	343 ± 145	504 ± 173	234 ± 89	171 ± 30	nd
Cs (ppm)	16 ± 5	34 ± 16	10 ± 3	11 ± 2	nd
K/Rb	94 ± 30	42 ± 5	128 ± 21	183 ± 23	nd

Drill Core 21-BD-531					
	Saprolite	Qz-Fsp Pegmatite	Spd-Pegmatite	Granite	Amphibolite
(wt. %)	<i>n</i> = 3 SiO ₂ = 74.6–76.3	<i>n</i> = 24 SiO ₂ = 66.7–89.9	<i>n</i> = 5 SiO ₂ = 72.4–74.1	<i>n</i> = 22 SiO ₂ = 71.0–84.5	<i>n</i> = 2 SiO ₂ = 51.2–51.4
SiO ₂	75.62 ± 0.92	74.49 ± 4.40	73.57 ± 0.71	75.01 ± 2.48	51.75 ± 0.92
Al ₂ O ₃	13.85 ± 0.59	14.67 ± 2.36	15.44 ± 0.56	14.27 ± 1.62	18.66 ± 0.11
Fe ₂ O ₃	1.34 ± 0.17	1.13 ± 0.61	1.06 ± 0.28	1.13 ± 0.25	10.49 ± 0.06
MgO	0.25 ± 0.01	0.18 ± 0.18	0.10 ± 0.05	0.19 ± 0.10	3.94 ± 0.62
CaO	0.30 ± 0.15	0.64 ± 0.49	0.67 ± 0.31	0.54 ± 0.28	6.14 ± 1.07
Na ₂ O	2.27 ± 0.28	4.86 ± 1.00	4.23 ± 1.67	4.42 ± 0.90	2.06 ± 0.31
K ₂ O	4.40 ± 0.23	2.86 ± 1.13	2.90 ± 1.82	3.36 ± 0.85	2.05 ± 0.54
MnO	0.02 ± 0.01	0.09 ± 0.06	0.14 ± 0.07	0.05 ± 0.04	0.24 ± 0.02
P ₂ O ₅	0.15 ± 0.09	0.32 ± 0.14	0.25 ± 0.06	0.30 ± 0.07	0.36 ± 0.03
Li (ppm)	87 ± 4	125 ± 68	3893 ± 2492	134 ± 77	nd
Be (ppm)	125 ± 68	24 ± 26	122 ± 54	13 ± 8	nd
Ga (ppm)	16 ± 0.3	19 ± 5	28 ± 3	25 ± 21	nd
Rb (ppm)	219 ± 9	302 ± 172	617 ± 235	276 ± 123	nd
Cs	10 ± 1	27 ± 16	69 ± 17	23 ± 16	nd
K/Rb	21 ± 2	84 ± 24	43 ± 6	105 ± 24	nd

References

1. Kesler, S.E.; Gruber, P.W.; Medina, P.A.; Keoleian, G.A.; Everson, M.P.; Wallington, T.J. Global lithium resources: Relative importance of pegmatite, brine and other deposits. *Ore Geol. Rev.* **2012**, *48*, 55–69. [\[CrossRef\]](#)
2. Howell, R.J.; Lagos, L.; de los Hoyos, C.R.; Declercq, J. Classification and characteristics of natural lithium resources. *Elements* **2020**, *16*, 259–264. [\[CrossRef\]](#)
3. USGS. *Mineral Commodity Summaries 2023*; US Geological Survey: Reston, VA, USA, 2023; p. 214.
4. *Geoscience Australia, Australian Critical Minerals Prospectus*; Australian Trade and Investment Commission, Department of Industry, Science, Energy and Resources: Canberra, Australia, 2022; p. 82.
5. Tabelin, C.B.; Dallas, J.; Casanova, S.; Pelech, T.; Bournival, G.; Saydam, S.; Canbulat, I. Towards a low-carbon society: A review of lithium resource availability, challenges and innovations in mining, extraction and recycling, and future perspectives. *Miner. Eng.* **2021**, *163*, 106743. [\[CrossRef\]](#)
6. World Bank. *Minerals for Climate Action: The Mineral Intensity of the Clean Energy Transition*; World Bank Report: Washington, DC, USA, 2020; p. 110.
7. Jolliff, B.; Papike, J.; Shearer, C. Fractionation trends in mica and tourmaline as indicators of pegmatite internal evolution: Bob Ingersoll pegmatite, Black Hills, South Dakota. *Geochim. Et Cosmochim. Acta* **1987**, *51*, 519–534. [\[CrossRef\]](#)
8. Selway, J.; Breaks, F.; Tindle, A. A review of rare-element (Li-Cs-Ta) pegmatite exploration techniques for the Superior Province, Canada, and large worldwide tantalum deposits. *Explor. Min. Geol.* **2005**, *14*, 1–30. [\[CrossRef\]](#)
9. Martins, T.; Roda-Robles, E.; Lima, A.; De Parseval, P. Geochemistry and evolution of micas in the Barroso-Alvaõ Pegmatite Field, Northern Portugal. *Can. Mineral.* **2012**, *50*, 1117–1129. [\[CrossRef\]](#)
10. Hulsbosch, N.; Hertogen, J.; Dewaele, S.; André, L.; Muchez, P. Alkali metal and rare earth element evolution of rock-forming minerals from the Gatumba area pegmatites (Rwanda): Quantitative assessment of crystal-melt fractionation in the regional zonation of pegmatite groups. *Geochim. Et Cosmochim. Acta* **2014**, *132*, 349–374. [\[CrossRef\]](#)
11. Černý, P.; Meintzer, R.E.; Anderson, A.J. Extreme fractionation in rare-element granitic pegmatites: Selected examples of data and mechanisms. *Can. Mineral.* **1985**, *23*, 381–421.
12. Trueman, D.L.; Černý, P. Exploration for rare-element pegmatites. In *Granitic Pegmatites in Science and Industry*; Short Course Handbook; Černý, P., Ed.; Mineralogical Association of Canada: Winnipeg, Canada, 1982; Volume 8, pp. 463–493.
13. Černý, P.; Burt, D. Paragenesis, crystallochemical characteristics, and geochemical evolution of the micas in granite pegmatites. *Rev. Mineral.* **1984**, *13*, 257–297.
14. Smeds, S.-A. Trace elements in potassium-feldspar and muscovite as a guide in the prospecting for lithium- and tin-bearing pegmatites in Sweden. *J. Geochem. Explor.* **1992**, *42*, 351–369. [\[CrossRef\]](#)

15. Beurlen, H.; Thomas, R.; da Silva, M.R.R.; Müller, A.; Rhede, D.; Soares, D.R. Perspectives for Li- and Ta-mineralization in the Borborema Pegmatite Province, NE-Brazil: A review. *J. South Am. Earth Sci.* **2014**, *56*, 110–127. [[CrossRef](#)]
16. Maneta, V.; Baker, D.R. The potential of lithium in alkali feldspars, quartz, and muscovite as a geochemical indicator in the exploration for lithium-rich granitic pegmatites: A case study from the spodumene-rich Moblan pegmatite, Quebec, Canada. *J. Geochem. Explor.* **2019**, *205*, 106336. [[CrossRef](#)]
17. Wise, M.A.; Harmon, R.S.; Curry, A.; Jennings, M.; Grimac, Z.; Khashchevskaya, D. Handheld LIBS for Li exploration: An example from the Carolina Tin-Spodumene Belt, USA. *Minerals* **2022**, *12*, 77. [[CrossRef](#)]
18. Kish, S.A.; Fullagar, P.D. Age and magmatic association of rare metal pegmatites; spodumene pegmatites, Kings Mountain, NC and Sn-Ta pegmatites, Rockford, Ala. *Geol. Soc. Am. Abstr. Programs* **1996**, *28*, A475.
19. Kesler, T.L. *The Tin-Spodumene Belt of the Carolinas: A Preliminary Report*; US Geological Survey Report 936; United States Government Printing Office: Washington, DC, USA, 1942; p. 269.
20. Kish, S.A. Geochronology of plutonic activity in the Inner Piedmont and Kings Mountain belt in North Carolina. In *Field Guides for Geological Society of America, Southeastern Section Meeting, Winston-Salem, North Carolina*; Burt, E.R., Ed.; North Carolina Department of Natural and Economic Resources: Raleigh, NC, USA, 1977; pp. 144–149.
21. Kesler, T.L. The Kings Mountain area. In *Guides to Southeastern Geology*; Field Trip Guidebook; Russell, R.J., Ed.; Geological Society of America: Boulder, CO, USA, 1955; pp. 374–387.
22. Luster, G.R. Lithologic Variability of the Kings Mountain Pegmatite, North Carolina. Master's Thesis, Pennsylvania State University, University Park, PA, USA, 1977.
23. Horton, J.W. Shear zone between the Inner Piedmont and Kings Mountain belts in the Carolinas. *Geology* **1981**, *9*, 28–33. [[CrossRef](#)]
24. Hodges, R.A. A Petrologic Study of the Lithium Corporation of America Mine in the Tin-Spodumene Belt of North Carolina. Master's Thesis, University of North Carolina, Chapel Hill, NC, USA, 1983.
25. Kesler, T.L. Raw lithium supplies. *Min. Eng.* **1978**, *30*, 283–285.
26. Kesler, T.L. Occurrence, development, and long-range outlook of lithium-pegmatite ore in the Carolinas. In *Lithium Resources and Requirements by the Year 2000*; U.S. Geological Survey Professional Paper; Vine, J.D., Ed.; Superintendent of Documents; U.S. Government Printing Office: Washington, DC, USA, 1976; pp. 45–50.
27. Černý, P.; London, D.; Novák, M. Granitic pegmatites as reflections of their sources. *Elements* **2012**, *8*, 289–294. [[CrossRef](#)]
28. Černý, P. Geochemical and petrogenetic features of mineralization in rare-element granitic pegmatites in the light of current research. *Appl. Geochem.* **1992**, *7*, 93–416.
29. Wise, M.A.; Müller, A.; Simmons, W.B. A proposed new mineralogical classification system for granitic pegmatites. *Can. Mineral.* **2022**, *60*, 229–248. [[CrossRef](#)]
30. Griffiths, W.R.; Overstreet, W.C. Granitic rocks of the western Carolina Piedmont. *Am. J. Sci.* **1952**, *250*, 777–789. [[CrossRef](#)]
31. White, J.S. Mineralogy of the Foote Mine, Kings Mountain, North Carolina. In *Geological Investigations of the Kings Mountain Belt and Adjacent Areas in the Carolinas*; Carolina Geological Society Field Trip Guidebook; Horton, J.W., Butler, J.R., Milton, D.M., Eds.; South Carolina Geological Survey: Columbia, SC, USA, 1981; pp. 39–48.
32. Marble, L.; Hanahan, J. The Foote minerals the Foote Quarry in Kings Mountain, North Carolina is one of the premier micromount localities. *Rocks Miner.* **1978**, *53*, 158–173. [[CrossRef](#)]
33. Hanahan, J. The Foote Quarry, King Mountain, North Carolina revisited 1984. *Rocks Miner.* **1984**, *60*, 76–82. [[CrossRef](#)]
34. Swanson, S.E. Mineralogy of spodumene pegmatites and related rocks in the tin-spodumene belt of North Carolina and South Carolina, USA. *Can. Mineral.* **2012**, *50*, 1589–1608. [[CrossRef](#)]
35. Piedmont Lithium. *Technical Report Summary of a Definitive Feasibility Study of the Carolina Lithium Project in North Carolina, 18605-REP-GE-002*; Piedmont Lithium Ltd.: Belmont, NC, USA, 2022; p. 232.
36. Griffiths, W.R. *Beryllium Resources of the Tin-Spodumene Belt of North Carolina*; U.S. Geological Survey Circular: Washington, DC, USA, 1954; Volume 309, p. 12.
37. Kesler, T.L. Exploration of the Kings Mountain pegmatites. *Miner. Eng.* **1961**, *13*, 1062–1068.
38. Russo, R.E.; Mao, X.; Yoo, J.H.; Gonzalez, J. Laser ablation. In *Laser-Induced Breakdown Spectroscopy*; Singh, J.P., Thakur, S.N., Eds.; Elsevier: Amsterdam, The Netherlands, 2008; pp. 49–82.
39. Connors, B.; Somers, A.; Day, D. Application of handheld laser-induced breakdown spectroscopy (LIBS) to geochemical analysis. *Appl. Spectrosc.* **2016**, *70*, 810–815. [[CrossRef](#)]
40. Sweetapple, M.T.; Tassios, S. Laser-induced breakdown spectroscopy (LIBS) as a tool for in situ mapping and textural interpretation of lithium in pegmatite minerals. *Am. Mineral.* **2015**, *100*, 2141–2151. [[CrossRef](#)]
41. Romppanen, S.; Pölonen, I.; Häkkänen, H.; Kaski, S. Optimization of spodumene identification by statistical approach for laser-induced breakdown spectroscopy data of lithium pegmatite ores. *Appl. Spectrosc. Rev.* **2021**, *58*, 297–317. [[CrossRef](#)]
42. Ribeiro, R.; Capela, D.; Ferreira, M.; Martins, R.; Jorge, P.; Guimarães, D.; Lima, A. X-ray fluorescence and laser-induced breakdown spectroscopy analysis of Li-rich minerals in veins from Argemela Tin Mine, central Portugal. *Minerals* **2021**, *11*, 1169. [[CrossRef](#)]
43. Müller, S.; Meima, J.A. Mineral classification of lithium-bearing pegmatites based on laser-induced breakdown spectroscopy: Application of semi-supervised learning to detect known minerals and unknown material. *Spectrochim. Acta Part B At. Spectrosc.* **2022**, *189*, 106370. [[CrossRef](#)]

44. Rifai, K.; Constantin, M.; Yilmaz, A.; Özcan, L.Ç.; Doucet, F.R.; Azami, N. Quantification of lithium and mineralogical mapping in crushed ore samples using laser induced breakdown spectroscopy. *Minerals* **2022**, *12*, 253. [[CrossRef](#)]
45. Fabre, C.; Ourti, N.E.; Mercadier, J.; Cardoso-Fernandes, J.; Dias, F.; Perrotta, M.; Koerting, F.; Lima, A.; Kaestner, F.; Koellner, N.; et al. Analyses of Li-rich minerals using handheld LIBS tool. *Data* **2021**, *6*, 68. [[CrossRef](#)]
46. Fabre, C.; Ourti, N.E.; Ballouard, C.; Mercadier, J.; Cauzid, J. Handheld LIBS analysis for in situ quantification of Li and detection of the trace elements (Be, Rb and Cs). *J. Geochem. Explor.* **2022**, *236*, 106979. [[CrossRef](#)]
47. Harmon, R.S.; Lawley, C.; Watts, J.; Harraden, C.L.; Somers, A.M.; Hark, R.R. Laser-induced breakdown spectroscopy—An emerging analytical tool for mineral exploration. *Minerals* **2019**, *9*, 718. [[CrossRef](#)]
48. Dias, F.; Ribeiro, R.; Gonçalves, F.; Lima, A.; Roda-Robles, E.; Martins, T. Calibrating a Handheld LIBS for Li Exploration in the Barroso–Alvão Aplite-Pegmatite Field, Northern Portugal: Textural Precautions and Procedures When Analyzing Spodumene and Petalite. *Minerals* **2023**, *13*, 470. [[CrossRef](#)]
49. Tischendorf, G.; Forster, H.J.; Gottesmann, B.; Rieder, M. True and brittle micas: Composition and solid-solution series. *Mineral. Mag.* **2007**, *71*, 285–320. [[CrossRef](#)]
50. Piedmont Lithium. Core logging procedures for Piedmont Lithium Beaverdam Project. In *Core Logging Manual Internal Technical Report*; Piedmont Lithium Ltd.: Belmont, NC, USA, 2017; p. 16.
51. Černý, P.; Ercit, T.S. The classification of granitic pegmatites revisited. *Can. Mineral.* **2005**, *43*, 2005–2026. [[CrossRef](#)]
52. Sundelius, H.W. The Peg claims spodumene pegmatites, Maine. *Econ. Geol.* **1963**, *58*, 84–106. [[CrossRef](#)]
53. Chackowsky, L.E. Mineralogy, Geochemistry and Petrology of Pegmatitic Granites and Pegmatites at Red Sucker Lake, Northeastern Manitoba. Master's Thesis, University of Manitoba, Winnipeg, MB, Canada, 1983.
54. Burnham, C.W.; Jahns, R.H. A method for determining the solubility of water in silicate melts. *Am. J. Sci.* **1962**, *260*, 721–745. [[CrossRef](#)]
55. Stilling, A.; Černý, P.; Vanstone, P.J. The Tanco pegmatite at Bernic Lake, Manitoba. XVI. Zonal and bulk compositions and their petrogenetic significance. *Can. Mineral.* **2006**, *44*, 599–623. [[CrossRef](#)]
56. Ashworth, L.; Kinnaird, J.A.; Nex, P.A.M.; Harris, C.; Müller, A.B. Origin of rare-element-mineralized Damara Belt pegmatites: A geochemical and light stable isotope study. *Lithos* **2020**, *372*, 105655. [[CrossRef](#)]
57. Simmons, W.; Falster, A.; Webber, K.; Roda-Robles, E.; Boudreaux, A.P.; Grassi, L.R.; Freeman, G. Bulk composition of Mt. Mica pegmatite, Maine, USA: Implications for the origin of an LCT type pegmatite by anatexis. *Can. Mineral.* **2016**, *54*, 1053–1070. [[CrossRef](#)]
58. Antunes, I.M.H.R.; Neiva, A.M.R.; Ramos, J.M.F.; Silva, P.B.; Silva, M.M.V.G.; Corfu, F. Petrogenetic links between lepidolite-subtype aplite-pegmatite, aplite veins and associated granites at Segura (central Portugal). *Geochemistry* **2013**, *73*, 323–341. [[CrossRef](#)]
59. Brewer, E.O. *Soil Survey of Catawba County, North Carolina*; US Department of Agriculture, Soil Conservation Service: Washington, DC, USA, 1975; p. 47.
60. Roda Robles, E.; Pesquera Perez, A.; Velasco Roldán, F. Micas of the muscovite-lepidolite series from the Fregeneda pegmatites (Salamanca, Spain). *Mineral. Petrol.* **1995**, *55*, 145–157. [[CrossRef](#)]
61. Pesquera, A.; Torres-Ruiz, J.; Gil-Crespo, P.P.; Velilla, N. Chemistry and genetic implications of tourmaline and Li-F-Cs micas from the Valdeflores area (Caceres, Spain). *Am. Mineral.* **1999**, *84*, 55–69. [[CrossRef](#)]
62. Shaw, D.M. A review of K-Rb fractionation trends by covariance analysis. *Geochim. Cosmochim. Acta* **1968**, *32*, 573–601. [[CrossRef](#)]
63. Foord, E.E.; Černý, P.; Jackson, L.L.; Sherman, D.M.; Eby, R.K. Mineralogical and geochemical evolution of micas from miarolitic pegmatites of the anorogenic Pikes Peak batholith, Colorado. *Mineral. Petrol.* **1995**, *55*, 1–26. [[CrossRef](#)]
64. Wise, M.A. Trace element chemistry of lithium-rich micas from rare-element granitic pegmatites. *Mineral. Petrol.* **1995**, *55*, 203–215. [[CrossRef](#)]
65. Roda, E.; Keller, P.; Pesquera, A.; Fontan, F. Micas of the muscovite–lepidolite series from Karibib pegmatites, Namibia. *Mineral. Mag.* **2007**, *71*, 41–62. [[CrossRef](#)]
66. Steiner, B.M. Tools and workflows for grassroots Li–Cs–Ta (LCT) pegmatite exploration. *Mineral* **2019**, *20*, 499. [[CrossRef](#)]
67. Xing, C.M.; Wang, C.Y.; Wang, H. Magmatic-hydrothermal processes recorded by muscovite and columbite-group minerals from the Bailongshan rare-element pegmatites in the West Kunlun-Karakorum orogenic belt, NW China. *Lithos* **2020**, *364*, 105507. [[CrossRef](#)]
68. Barros, R.; Kaeter, D.; Menuge, J.F.; Škoda, R. Controls on chemical evolution and rare element enrichment in crystallising albite-spodumene pegmatite and wallrocks: Constraints from mineral chemistry. *Lithos* **2020**, *352*, 105289. [[CrossRef](#)]
69. Jolliff, B.L.; Papike, J.J.; Shearer, C.K. Petrogenetic relationships between pegmatite and granite based on geochemistry of muscovite in pegmatite wall zones, Black Hills, South Dakota, USA. *Geochim. Et Cosmochim. Acta* **1992**, *56*, 1915–1939. [[CrossRef](#)]
70. Van Lichtenvelde, M.; Grégoire, M.; Linnen, R.L.; Béziat, D.; Salvi, S. Trace element geochemistry by laser ablation ICP-MS of micas associated with Ta mineralization in the Tanco pegmatite, Manitoba, Canada. *Contrib. Mineral. Petrol.* **2008**, *155*, 791–806. [[CrossRef](#)]
71. Shaw, R.; British Geological Survey, Environmental Science Centre, Nicker Hill, Keyworth, Nottingham NG12 5GG, UK. Personal communication, 2023.

72. Serrano, J. Origine des Pegmatites du Cap de Creus: Approche Intégrée de Terrain, Pétrologie et Géochimie. Ph.D. Thesis, Université Paul Sabatier-Toulouse III, Toulouse, France, 2019.
73. Anderson, A. The Geochemistry, Mineralogy and Petrology of the Cross Lake Pegmatite Field, Central Manitoba. Master's Thesis, University of Manitoba, Winnipeg, MB, Canada, 1984.
74. Meintzer, R.E. The Mineralogy and Geochemistry of the Granitoid Rocks and Related Pegmatites of the Yellowknife Pegmatite Field, Northwest Territories. Ph.D. Thesis, University of Manitoba, Winnipeg, MB, Canada, 1987.

Disclaimer/Publisher's Note: The statements, opinions and data contained in all publications are solely those of the individual author(s) and contributor(s) and not of MDPI and/or the editor(s). MDPI and/or the editor(s) disclaim responsibility for any injury to people or property resulting from any ideas, methods, instructions or products referred to in the content.

Article

Gold Exploration in Two and Three Dimensions: Improved and Correlative Insights from Microscopy and X-Ray Computed Tomography

Joshua Chisambi ^{1,2,*}, Bjorn von der Heyden ¹ , Muofhe Tshibalanganda ³  and Stephan Le Roux ³

¹ Department of Earth Sciences, Stellenbosch University, Private Bag X1, Matieland, Stellenbosch 7602, South Africa; bvon@sun.ac.za

² Department of Mining Engineering, University of Malawi, the Polytechnic, Private Bag 303, Chichiri, Blantyre 3, Malawi

³ Central Analytical Facility, Stellenbosch University, Private Bag X1, Matieland, Stellenbosch 7602, South Africa; muofhe@sun.ac.za (M.T.); lerouxsg@sun.ac.za (S.L.R.)

* Correspondence: jjchisambi@gmail.com or jchisambi@poly.ac.mw

Received: 3 April 2020; Accepted: 12 May 2020; Published: 23 May 2020



Abstract: In this contribution, we highlight a correlative approach in which three-dimensional structural/positional data are combined with two dimensional chemical and mineralogical data to understand a complex orogenic gold mineralization system; we use the Kirk Range (southern Malawi) as a case study. Three dimensional structures and semi-quantitative mineral distributions were evaluated using X-ray Computed Tomography (XCT) and this was augmented with textural, mineralogical and chemical imaging using Scanning Electron Microscopy (SEM) and optical microscopy as well as fire assay. Our results detail the utility of the correlative approach both for quantifying gold concentrations in core samples (which is often nuggety and may thus be misrepresented by quarter- or half-core assays), and for understanding the spatial distribution of gold and associated structures and microstructures in 3D space. This approach overlays complementary datasets from 2D and 3D analytical protocols, thereby allowing a better and more comprehensive understanding on the distribution and structures controlling gold mineralization. Combining 3D XCT analyses with conventional 2D microscopies derive the full value out of a given exploration drilling program and it provides an excellent tool for understanding gold mineralization. Understanding the spatial distribution of gold and associated structures and microstructures in 3D space holds vast potential for exploration practitioners, especially if the correlative approach can be automated and if the resultant spatially-constrained microstructural information can be fed directly into commercially available geological modelling software. The extra layers of information provided by using correlative 2D and 3D microscopies offer an exciting new tool to enhance and optimize mineral exploration workflows, given that modern exploration efforts are targeting increasingly complex and low-grade ore deposits.

Keywords: gold exploration; X-ray computed tomography; correlative science

1. Introduction

Gold exploration continues to attract a vast proportion of the global minerals exploration budget (e.g., ~50% of the \$10.1 billion exploration budget for 2018 [1]). Much of this gold has been won from ‘orogenic’ classes of gold mineralization [2,3], which generally form in metamorphic terranes associated with accretionary or collisional orogenies [4]. These geological settings are typically characterized by a high level of structural complexity, in which gold mineralization may be multi-stage or may

be overprinted or remobilized during progressive stages during the evolving orogenic cycle [5]. This high degree of geological complexity complicates modern day gold exploration efforts, which are already compromised by the fact that most easily-mined near-surface gold deposits have already been discovered and/or mined out [6,7].

To address this challenge, geoscientists are continually looking to develop and apply robust exploration techniques which can better constrain the spatial distribution of ore minerals within the host rocks and within mineralized structures [8]. Once ore bodies have been identified and drilled, the conventional approach towards understanding mineral textures and parageneses has predominantly been limited to two-dimensional analytical protocols (e.g., optical microscopy [9], scanning electron microscopy (including automated technologies, Quantitative Evaluation of Minerals by Scanning Electron Microscopy (QEMSCAN) technologies), electron microprobe micro-analysis [10], (synchrotron) X-ray Fluorescence Mapping [11], Laser induced breakdown spectroscopy, Raman spectroscopy and to a lesser extent, Laser Ablation Inductively Coupled Plasma Mass Spectroscopy (LA-ICP-MS) mapping [12]). Although these protocols provide detailed 2D textural, chemical and mineralogical information, they are inherently limited in that they fail to fully consider the mineralogical, textural, and structural heterogeneity extending into the third dimension. The advent and proliferation of bench-scale X-ray computed tomography (XCT) analytical protocols enables 3D information of ore samples to be able now to be routinely obtained [13,14]. This non-destructive XCT technology measures X-ray attenuation as an X-ray beam passes through a rotating ore sample (i.e., 360° measurement), where the X-ray attenuation varies as a function of mineral density and atomic number [15,16]. Because of their relatively high density, ore minerals (e.g., sulphides and gold) can easily be identified and distinguished from a matrix of less dense silicate (rock-forming) minerals [14]. Importantly for orogenic gold studies, gold is characterized by an exceedingly high density ($19.3 \text{ g}\cdot\text{cm}^{-3}$) and thus, a high X-ray attenuation coefficient, which ensures that even very small grains can be distinguished and measured using XCT [17].

A growing body of scientific literature has realized the advantages of XCT based techniques for understanding the 3D internal structure of ore samples [17–23]. For example, [24] demonstrated the use of XCT as an analytical tool to quantify tungsten ore mineral content and ore grade. Similarly, [21] used lab-based XCT to characterize 3D textural settings of orogenic gold where they used combination of 3D visualization and mineral quantification methods to decipher spatial characteristics of ore-forming processes. Likewise, the authors in [25] investigated the distribution of sulphides using X-ray computed tomography to better understand how the base metal sulphides and gold formed in the Bushveld Igneous Complex, South Africa and Stillwater Complex, Montana, USA. Inasmuch as these examples serve to highlight the unique affordances of XCT in providing 3D textural (and to an extent mineralogical) data, the true power of XCT can only be fully realized if it is combined with the detailed chemical information supplied by more conventional 2D technologies (e.g., optical- and electron-microscopies, microprobes, etc.). In this contribution, we highlight a correlative approach, in which 3D XCT data are combined with 2D mineralogical and chemical data to understand a complex orogenic gold mineralization system in the Kirk Range (southern Malawi). Of special importance to orogenic gold deposits in which the siting of mineralization often has a strong structural control, we demonstrate the power of contextualizing observed 2D structural features in a 3D volume. We posit that export of this geometrically (XCT) contextualized structural data directly into geological databases and models will meaningfully contribute to the depth of data obtained during orogenic gold exploration programs, and foresee that correlative XCT-microscopic approaches will in future become a more prominent component of the gold exploration workflow.

2. Materials and Methods

Four drill core samples (extracted from borehole JJ-01: 100.20 to 100.50 m, 120.5 to 120.10 m depth, coordinates 15.31721° S, 34.83958° E and borehole JJ-02: 60.5 to 60.20 m, 80.1 to 80.8 m depth, coordinates 15.30666° S, 34.84301° E) were selected from the gold bearing mineralized quartz veins from the Manondo-Choma gold prospect for XCT and correlative microscopy analyses. Three

dimensional structures and semi-quantitative mineral distributions were evaluated using XCT and this was augmented with textural, mineralogical and chemical imaging using Scanning Electron Microscopy (SEM) and optical microscopy. Gold grades within the core samples were quantified using standard fire assay protocols [26].

2.1. High Resolution X-Ray Computed Tomography (XCT)

In order to understand the distribution of gold mineralization in mineralized drill core samples, four segments of the core sample (45 mm diameter; lengths respectively: 15, 3, 5 and 7 cm) were scanned using the Electric Phoenix VTomeX L240 micro X-ray Computed Tomography scanner system at the Central Analytical Facility (CAF), Stellenbosch University (South Africa), manufactured by General Electric Sensing and Inspection Technologies/Phoenix X-ray (Wunstorf, Germany). The XCT facility is described in more detail in [27]. To optimize scanning of gold-sulphide ores, the scanning parameters were set to 100 kV and 100 μ A and the X-ray beam was filtered using a 0.5 mm Cu filter. Images were acquired using a dwell time of 500 ms. Each scan took about 4 h and the resulting model had a voxel size of 35 μ m. Furthermore, a small subsample (dimensions 5 mm in diameter) cut from the original core sample JJ01 was also scanned at a high resolution using phoenix Nanotom S nanoCT scanner, manufactured by Phoenix X-ray (Wunstorf, Germany), the scanning parameters were set to 150 kV and 200 μ A and the X-ray beam was filtered using a 0.5 mm Cu filter. Images were acquired using a dwell time of 500 ms. The resulting model had a voxel size of 10 μ m.

These models were reconstructed using a filtered back projection algorithm built into the GE Datos 2.1 reconstruction package [27]. Subsequent data evaluation and visualization was conducted using Volume Graphics VGStudio Max 3.3, Heidelberg, Germany [28].

2.1.1. The XCT Thresholding Procedure for Gold in the Core Samples.

Thresholding is a process of material segmentation in X-ray computed tomography [16], in which materials or features of interest are mathematically separated from a background by distinguishing XCT model voxels according to threshold grey-scale values. To distinguish between voxels that represent gold, voxels that represent sulphides and voxels that represent matrix silicate minerals, we employed the global segmentation technique reported in [24]. Briefly, the global segmentation operation evaluates the grey-scale histogram of the entire core sample, identifies the main peaks in the histogram and defines the vertical segmentation line at the grey-scale value that marks the dip between the adjacent peaks. However, this method has a limitation of point spread function (PSF) [29]. Therefore, this threshold value is subsequently refined using a local threshold gradient search, in which the VGStudio Max 3.3 software identifies the sharpest change in grey value around the initial region of interest [24].

Figure 1 documents the grey value histograms for samples JJ01, JJ02, JJ04 and JJ05, wherein the automated global and local segmentation thresholding techniques have defined three main peaks. Based on the mineral densities and model mineral X-ray attenuation coefficients for the minerals that we have identified in our core samples (Table 1), we assume that the left peak denotes the less dense bulk silicate mineral matrix, the middle peak represents the sulphides, and the right peak denotes the much denser gold. Gold grains were defined using the minimum grey value threshold of 59,868. The peak of gold shifts a bit among the samples, but we still use the same threshold value for all the samples because the variation is not much. Sulphides were defined using the minimum threshold of CT number 49,774. These histogram-derived threshold values represent mathematical transformations of the original X-ray data, which were collected across 16 bit grey values. Because of the closeness between X-ray attenuation coefficients between the different sulphide minerals (Figure 1e), the XCT grey value alone could not distinguish between the different sulphide phases. The validity of these peak assignments was confirmed by comparing the grey value distributions in XCT image slices to correlated polished surfaces that were evaluated using optical microscopy and scanning electron microscopy (SEM). Notably, the SEM images revealed that many of the gold grains were much smaller than the 35 μ m XCT scanning resolution. This partial volume effect is one reason for the broadness

of the gold peaks (Figure 1), and although these partial volumes still allow identification of where gold is preferentially sited (by raising the voxel grey value), it does mean that the XCT-based approach should be acknowledged as being semi-quantitative. Using the thresholded data, we could visualize mineral grain size distribution and textures in 3D space. Furthermore, the thresholded data enabled us to generate volumes for each of the mineral phases (which were then used to calculate masses by considering known densities (Table 1)).

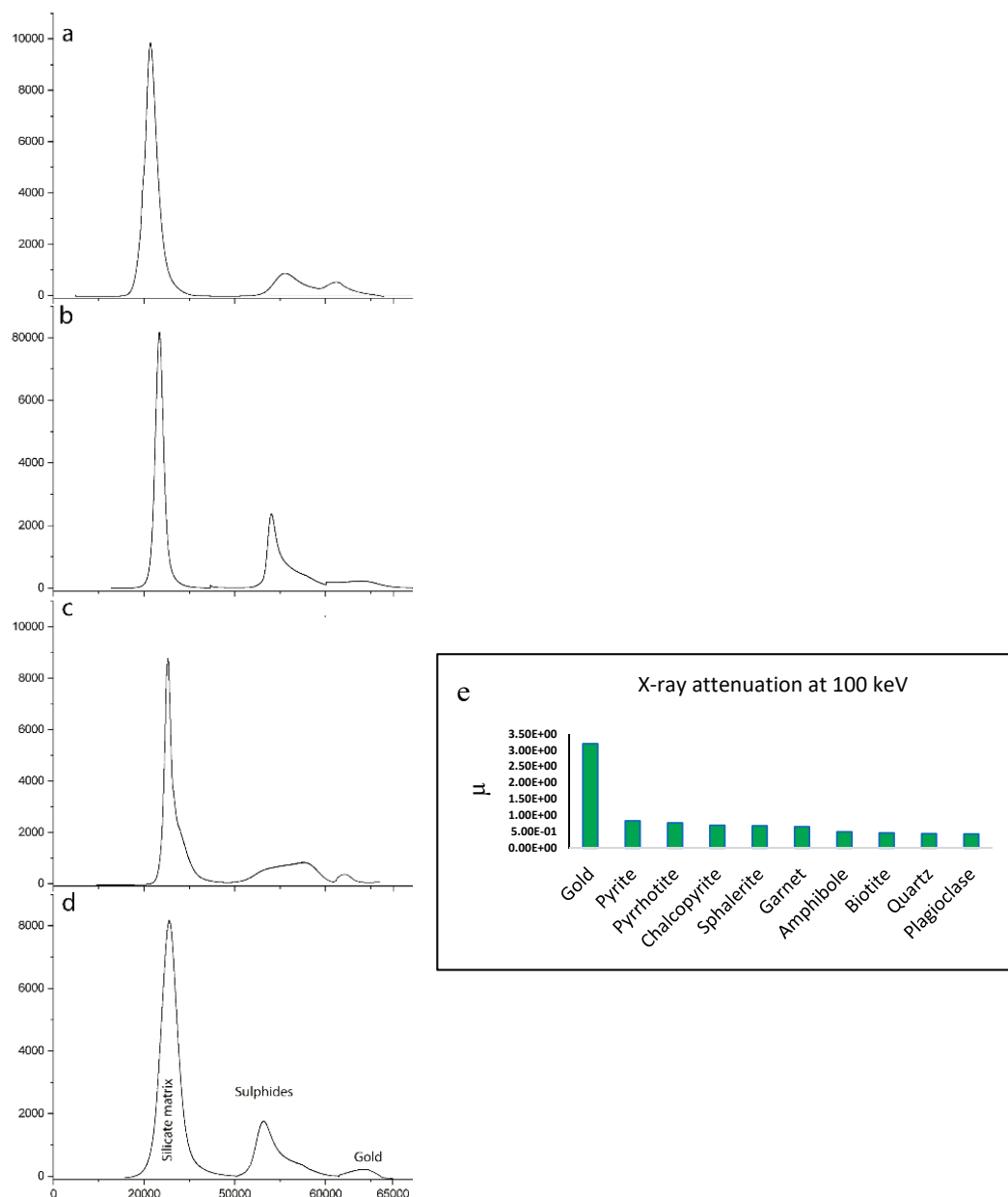


Figure 1. (a–d): Histograms of the core samples from grey value mapping used in thresholding. The histograms distinguish three dominant peaks. The left peak denotes the less dense bulk silicate mineral matrix, the middle peak the sulphides and the right peak denotes the much denser gold mineral. Samples JJ01, JJ02, JJ04 and JJ05, x axis denotes grey values and y axis frequency. (e): X-ray attenuation coefficient at 100 keV [30]. The graph indicates that at 100 KeV energy, gold will have the highest attenuation by a large margin. The XCT technique could not resolve different sulphides from one another as their density range is narrow, but clearly distinguishes gold as high atomic number phases distinct from the sulphides.

Table 1. Density range and X-ray attenuation coefficients of minerals present in the core samples. Density data are collected from [31] and X-ray attenuation coefficients are calculated using an Excel sheet developed by [32].

Mineral	Density g/cm ³	X-Ray Attenuation Coefficient
Gold	19.3	3.20 E ⁰⁰
Pyrite	5.01	8.32 E ⁻⁰¹
Pyrrhotite	4.65	7.72 E ⁻⁰¹
Chalcopyrite	4.19	6.96 E ⁻⁰¹
Sphalerite	4.1	6.81 E ⁻⁰¹
Garnet	3.93	6.52 E ⁻⁰¹
Amphibole	3	4.98 E ⁻⁰¹
Biotite	2.8	4.65 E ⁻⁰¹
Quartz	2.65	4.40 E ⁻⁰¹
Plagioclase	2.61	4.33 E ⁻⁰¹

2.1.2. Calibration of the XCT Thresholding Procedure for Gold in the Core Samples

To empirically verify that the small peak is indeed gold and is not confused with other minerals, gold grains identified in XCT (brightest and most dense spots) were intersected and proved in reflected light microscopy. We cut the core at an appropriate location and made thick sections. Reflected light microscopy identifies ubiquitous gold grains within the core samples, which proves that the dense minerals identified in XCT are indeed gold (Figure 2). Furthermore, in Figure 2c, the gold grain identified in XCT is proved in the reflected light microscopy in Figure 2d. This empirically proves that the dense minerals found in our samples are gold. In addition, we extracted grey values representing 100% gold, grey values representing 100% sulphides and grey value representing 100% silicates. Extracted XCT grey values for gold brightest spot grains range in 61,586–65,000, falling within the small peak on the histogram; those for sulphides range in 50,000–59,000, falling within the sulphide peak; and those for silicates range in 1600 and 49,771, falling within the silicate peak. This shows that our segmentation method is correct. However, grey values obtained from different scanners may differ, which would make comparison of the data difficult. To standardize this, grey values need to be correlated with Hounsfield units. This can be achieved by plotting the linear attenuation coefficient of the minerals in the core samples against grey values to provide a linear fit and a regression equation. The linear attenuation coefficient for each mineral at 100 keV energy can be converted to CT numbers' Hounsfield units (HU) using the equation $HU = (\mu_{\text{material}} - \mu_{\text{water}}) / (\mu_{\text{water}}) \times 1000$, where μ_{material} = linear attenuation coefficient of material and μ_{water} = linear attenuation coefficient of water. This can make the data comparable and has been demonstrated by the authors in [33].

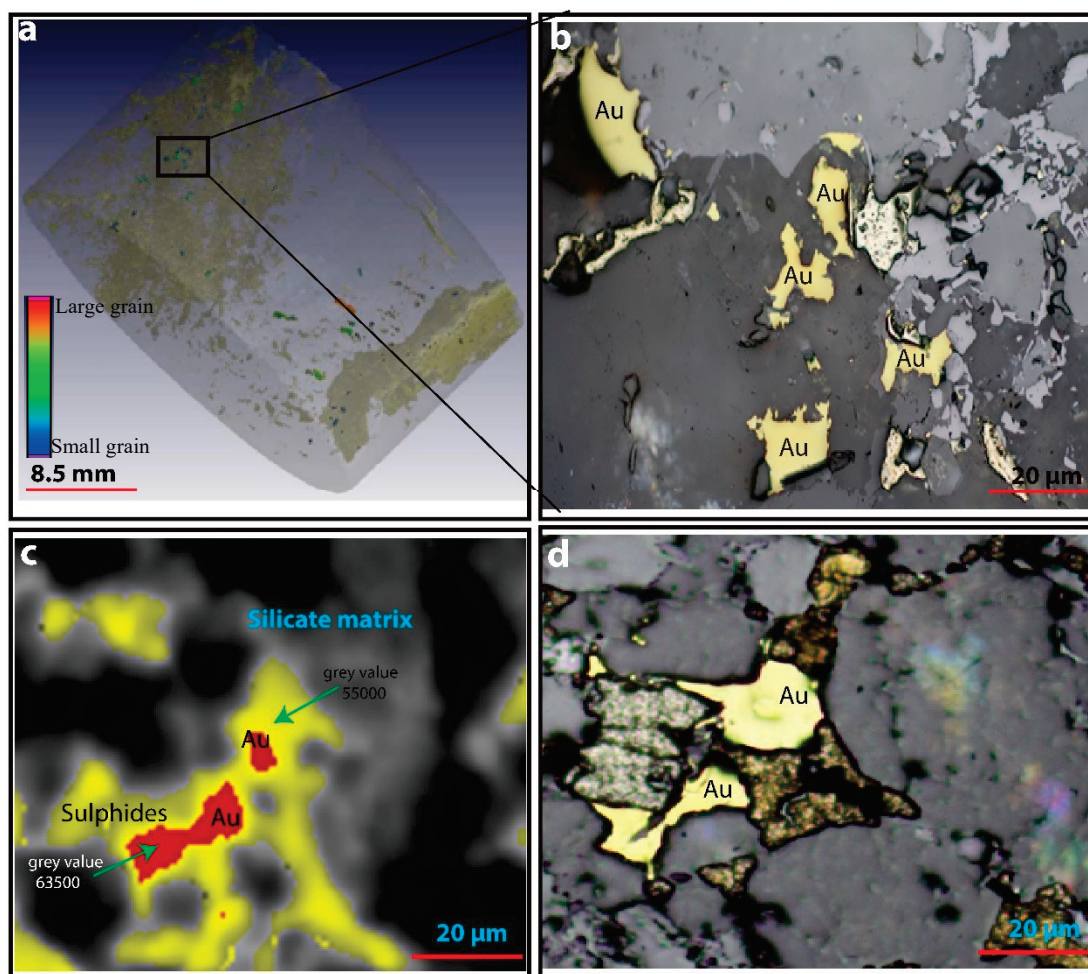


Figure 2. X-ray computed tomography and reflected light images indicating gold grains identified in XCT and gold grains identified in reflected light microscopy. (a) The drill core was cut on the rectangle shown to make thick sections. Grey colour in the drill core is the silicate matrix, the yellow colour indicates sulphides and other colours represent gold, distributed according to gold grain volume (warm colours = large grains, cold colours = smaller grains). (b) Reflected light microscopy shows ubiquitous presence of gold, which proves that the dense minerals we see in XCT are indeed gold. (c,d) Gold grain in XCT, same grain in reflected light microscopy. In Figure 2c, the yellow colour indicates sulphides, dark colour indicates silicate matrix and red colour indicates gold. Figure 2c is coloured according to density (warm colours = most dense gold grains, yellow colours = medium density sulphides, dark/grey colour = less dense silicate matrix).

2.2. Thin and Polished Section Photo Montages

Based on the gold distribution information provided by XCT data, we physically cut the cores samples at appropriate positions to intersect the identified gold and made thin and thick sections. The appropriate surfaces were polished and subjected to reflected and transmitted light microscopy. Thin and thick sections were described using a Nikon Eclipse E 200 petrological microscope at Stellenbosch University; digital photomicrographs were captured and stitched to make image mosaic of the thin and thick sections using PT GUI software. The 2D optical microscopy image was compared with the 3D XCT image for a specific region of the samples. The XCT data and microscopy data were aligned manually by visually aligning prominent features using commercially available Volume Graphics software [28]. Correlative microscopies in other geoscience studies (e.g., fluorescence microscopy + SEM [34]) have proven to be more precise and can expose the physical and chemical character of ore minerals at a better spatial resolution and analytical precision [35].

2.3. SEM Mapping

Scanning Electron Microscopy combined with an Electron Dispersive Spectrometer (SEM-EDS) was utilized to provide further insights into the mineralogy, textures and distribution of gold in the evaluated samples. Polished blocks, previously evaluated using reflected light optical microscopy, were coated with carbon to prevent localized charging and any resultant distortions or reflections of the electron beam. The SEM/EDS analyses were conducted at the Electron Microscopy Unit of the Central Analytical Facility (Stellenbosch University, South Africa) using a Zeiss EVO MA15VP Scanning Electron Microscope. SEM/EDS analyses were carried out in a nitrogen atmosphere at pressures from 65 to 96 Pa, voltages from 20 to 30 kV, working distance for EDS analyses of 8.5 mm and magnifications ranging between 1000× and 5000×.

2.4. Fire Assay

Fire assay analyses were conducted on subsamples of each of the cores that were scanned using XCT. Each subsample sent for fire assay was sectioned both physically and in the corresponding XCT reconstructed model. This ensured that the assayed gold grades could be accurately compared to calculated gold grades, which were derived from the XCT gold volumes generated after the thresholding procedure described in Section 2.1.1. The remaining core sample was reserved for future analytical work. Fire assay analyses were conducted at the ALS mineral services laboratory (Johannesburg, South Africa). Gold was assayed using fusion process at temperatures of 1200 °C to obtain the lead button that was then subjected to cupellation. Full details for this analytical technique are reported in reference [26].

3. Results

3.1. Thresholding and Quantification using XCT Data

The histogram of the measured grey values (Figure 1) provides a clear indication that the core sample contains mineral material from three markedly different density (or more correctly; X-ray attenuation coefficient) fractions viz. the silicate matrix, the sulphide paragenesis, and a distinctly high density material that we assume to largely represent gold. Other mineral phases that could be present with such high X-ray attenuation coefficients include galena, barite and native silver; however, none of these minerals were identified in the follow-up petrographic investigations.

The silicate mineralogy is quantitatively dominant throughout the core samples evaluated and have grey values ranging between 1600 and 49,771. Detailed interrogation of the XCT data revealed that we can see foliation within the silicates (Figure 3a) and pick out some garnet porphyroblasts (Figure 3b). Garnet porphyroblasts (density 3.93 gcm³) have relatively high grey values in the range 42,000 to 47,000, which are close to the grey value range expected for sulphides (Table 1). Thin sections made from the core prove the presence of garnet (Figure 3c). Due to the closeness of garnet grey values and those of sulphides, there could be a possible overlap of garnet with sulphides' peak. Immediately adjacent to the bright sulphides vein, there is a change in grey values, which may be an indicator of hydrothermal alteration (Figure 3b), followed by a dark silicate matrix with grey values less than 20,000. From the silicate matrix, we can see three phases, garnets, hydrothermally alteration adjacent to the vein and the dark silicate minerals that cannot be differentiated due to close density ranges. From microscopy, these dark silicate minerals are quartz, feldspars, amphiboles and biotite (Table 1).

The sulphide mineral paragenesis is represented in the XCT data by grey values ranging between 49,774 and 59,868. From reflected light microscopy, this assemblage includes minor amounts of chalcopyrite, sphalerite and pyrrhotite, with pyrite as the dominant (>80% modal proportion among sulphide minerals) sulphide phase. The density for these sulphides range between 4.1 and 5.01 g/cm³ (Table 1), and it is thus, not possible to discern between the different sulphide minerals using XCT alone (highlighting the need for correlative microscopies in order to derive additional detailed mineralogical information (Section 4.2)). In the core samples evaluated, the grey values representing the sulphides

are generally distributed along planar features which reflect the main vein network, and which in turn is structurally controlled in response to the regional stresses experienced by the geology during its deformational history. By considering the number of voxels ascribed to sulphide minerals through our thresholding approach and by deriving a weighted average density for the sulphide paragenesis, the mass of sulphide could be estimated for each of the core samples. These estimated masses ranged between 1.15 and 5.3 g (Table 2).

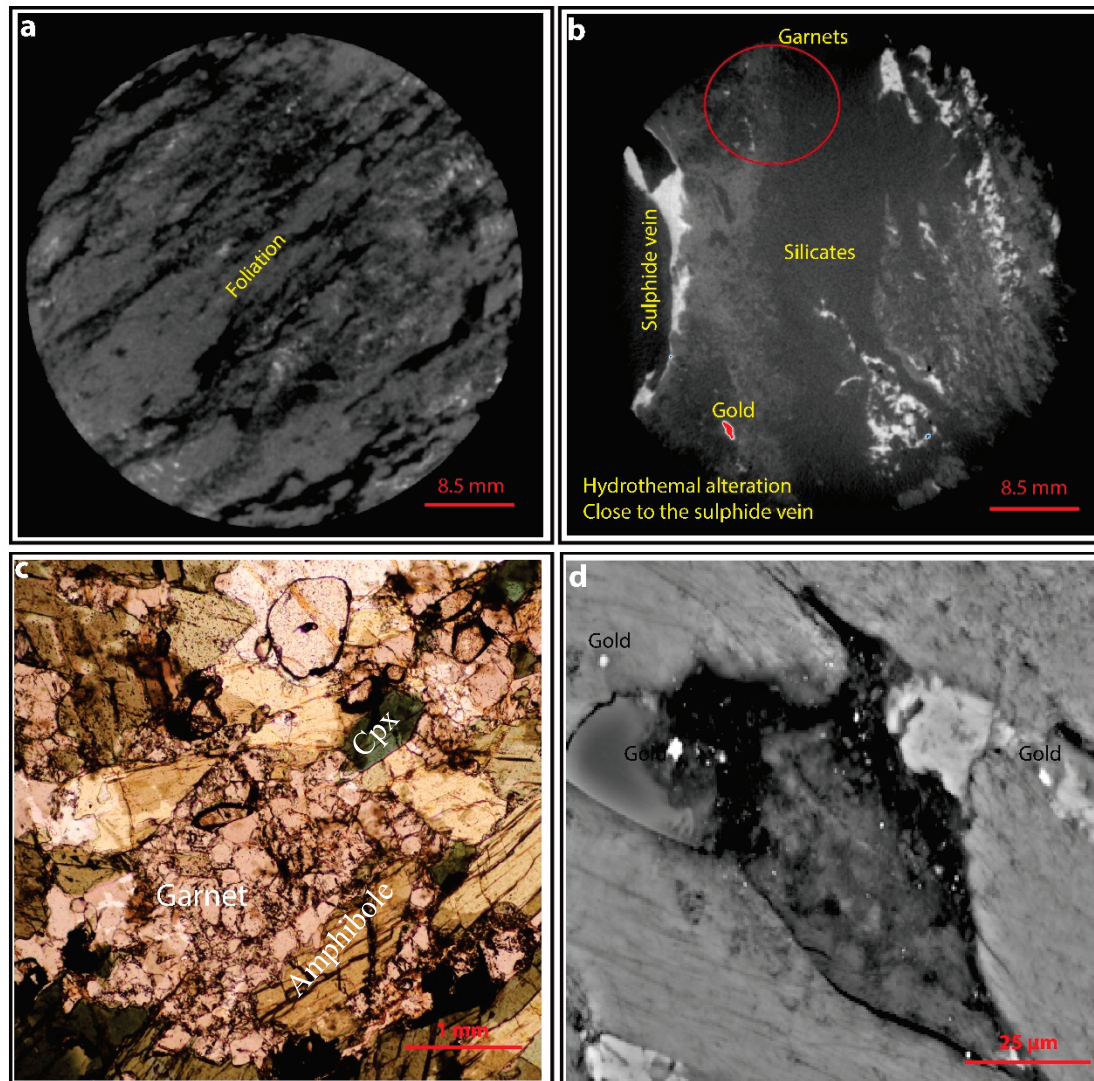


Figure 3. (a) Foliation within the silicates in the XCT image slice; the foliation is attributed to minerals biotite, amphibole, garnet, muscovite, quartz and feldspar. (b) XCT image slice of silicate matrix minerals bright pixels in red circle depicts garnet porphyroblasts identified as small round white dots. (c) Thin section made from the core proving the presence of garnet. (d) Backscattered gold elemental map obtained from the SEM analysis of the 2D cut surface of the core. The bright spots represent the spots where gold was found. Gold grains are small in SEM due to partial volume effect. Sample JJ01 and JJ02.

Gold in the core samples was identified by using a minimum grey value threshold value of 59,868. This represents the brightest pixels in the XCT images (Figure 4), since gold has the highest X-ray attenuation coefficient of all the minerals identified in the cores (Figure 1e). The presence of gold in our samples was confirmed using reflected light microscopy, Scanning Electron Microscopy (Figures 2 and 3d), and traditional fire assay. Voxels representing gold were predominantly found in association with the sulphides in the vein network, although a small proportion of these voxels were

also located in the silicate host rock, particularly in close proximity to the vein network (Figure 4a,b). The identified gold grains ranged in size between less than 0.14 to 0.7 mm in diameter, and a calculation based on the volume of the gold voxels and the known density of gold ($19.32 \text{ g}\cdot\text{cm}^{-3}$) estimates that the mass of gold in each sample ranges between 0.095 and 0.25 g, corresponding to a calculated gold grade of between 0.03 and 0.14 ppm (Table 2).

Table 2. Distribution of gold and sulphides in analysed drill core samples. Average density of sulphides was calculated by averaging the densities of individual sulphides identified in 2D microscopy.

Sample	Weight of Core (g)	Gold Volume (mm^3)	Density (g/cm^3)	Mass of Gold(g)	Gold Grade XCT (ppm)
JJ 01	136.17	4.93	19.30	0.10	0.07
JJ 02	384.70	7.18	19.30	0.14	0.04
JJ 04	89.56	6.70	19.30	0.12	0.14
JJ 05	919.05	13.32	19.30	0.26	0.03

Sample	Weight of Core (g)	Sulphide Volume (cm^3)	Avg. Density g/cm^3	Mass of Sulphides (g)	Concentration of Sulphides %
JJ 01	136.17	0.26	4.48	1.15	0.84
JJ 02	384.7	1.17	4.48	5.26	1.37
JJ 04	89.56	0.72	4.48	3.24	3.62
JJ 05	919.05	0.34	4.48	1.52	0.17

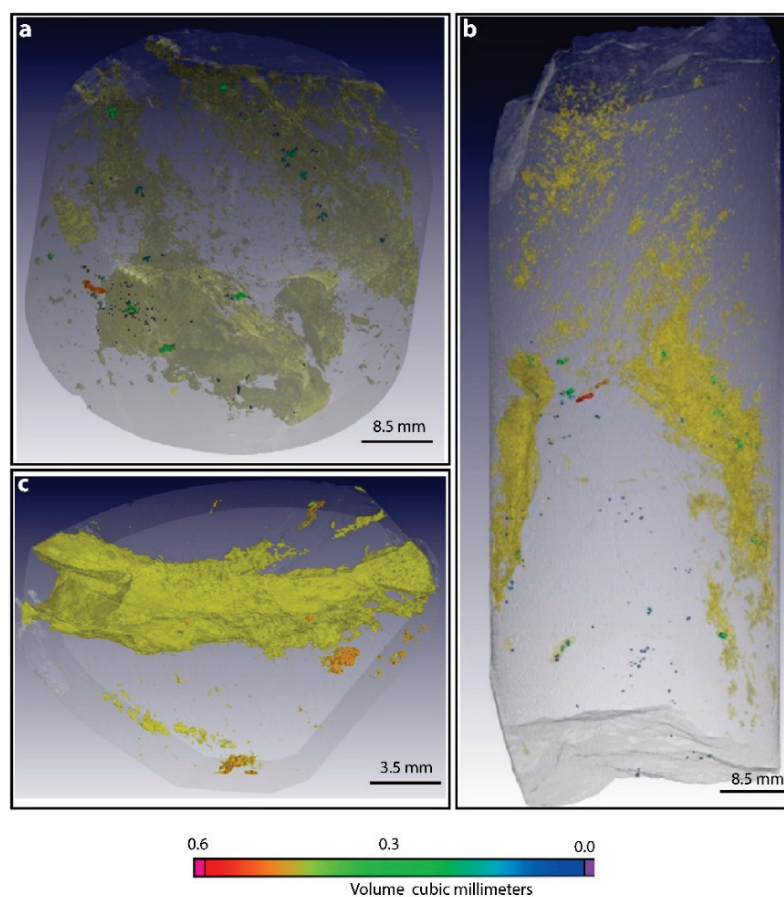


Figure 4. (a,b) XCT images showing 3D distribution of gold in mineralized drill core samples from gold-rich hydrothermal veins. The grey colour is the silicate matrix, the yellow colour indicates sulphides and the other colours represent gold, distributed according to gold grain volume (warm colours = large grains, cold colours = smaller grains). Samples JJ01 and JJ05 (c) is a thick section made from sample JJ04.

3.1.1. Fire Assay to Calibrate XCT Threshold Values

Fire assay analyses were conducted to confirm the presence of gold in our samples and to calibrate the calculated gold grades derived from XCT data. The fire assay analyses were conducted on quarter cores derived from the original scanned cores, and these data compared to calculated gold grades for the corresponding quarter of the core, which was sectioned digitally from the 3D XCT model (Figure 5). Fire assay data reveal that the gold grades for the respective cores in ppm are 0.03 (JJ1), 0.02 (JJ2), 0.01 (JJ4) and 0 (JJ5), (Table 3). The fire assay shows a strong and positive linear relationship with the gold grades calculated from our XCT thresholding protocol (Figure 6a: $y = 0.5888x - 0.0011$; $r^2 = 0.5$). The linear best-fit line has a slope that is less than the 1:1 line, indicative that the XCT protocol generally overestimates the mass of gold present in the core samples.

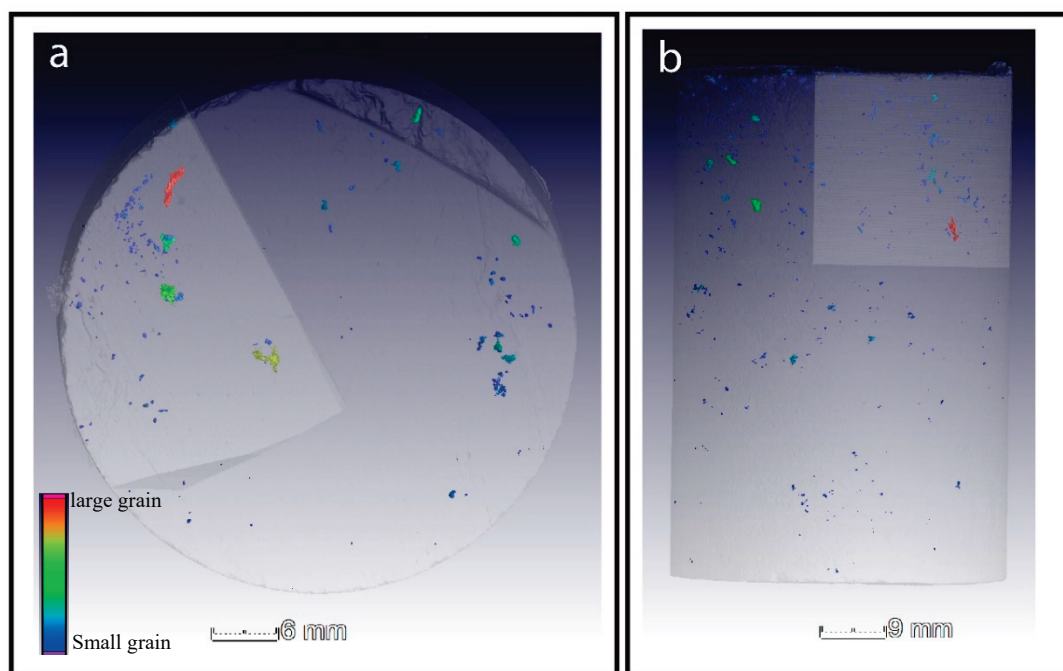


Figure 5. (a,b) Quarter cores that were sent for fire assay analysis cut from the whole cores. The grey colour in the drill core is the silicate matrix and other colours represent gold, distributed according to gold grain volume (warm colours = large grains, cold colours = smaller grains). Samples JJ01 and JJ02.

The equation of the best-fit line does however provide a useful internal calibration for the XCT data. Figure 7 compares the distribution of gold from the XCT model data using the original threshold value derived from the global segmentation protocol 59,868, to a threshold value that has been selected to ensure that the XCT calculated gold grades fall on the 1:1 line with fire assay gold grades. This exercise reveals that calibrating XCT values based on fire assay to the threshold grey value in our case, of 63,000, other dense minerals disappear, and gold is only present in the vein and not necessarily in the wall rock (Figure 7b) and is ~1:1 with fire assay (Figure 6c, Table 3), disregarding the JJ05 sample in which the assayed gold grades were below the detection limit. If we take grey values below 63,000, we have more gold grains making XCT to generally overestimate the mass of gold present in the core sample (Figure 7a).

A final test was conducted on the calibrated XCT core models in order to comment on the in situ nugget effect that may be induced by only assaying a quarter core. Quarter cores have relatively high gold values than the whole core due to the nugget effect (Table 3), except sample JJ04. The nugget effect is attributed to the heterogeneous distribution of gold grains in the core samples. Some regions of the core are rich in gold and others are not. This is so because vein systems typically contain both barren and mineralized segments with gold grade varying laterally, vertically and across the core.

Furthermore, finer grained gold mineralization usually has a high geological nugget effect [36]. Hence, some of the quarter cores have high gold values compared to the whole core (Table 3).

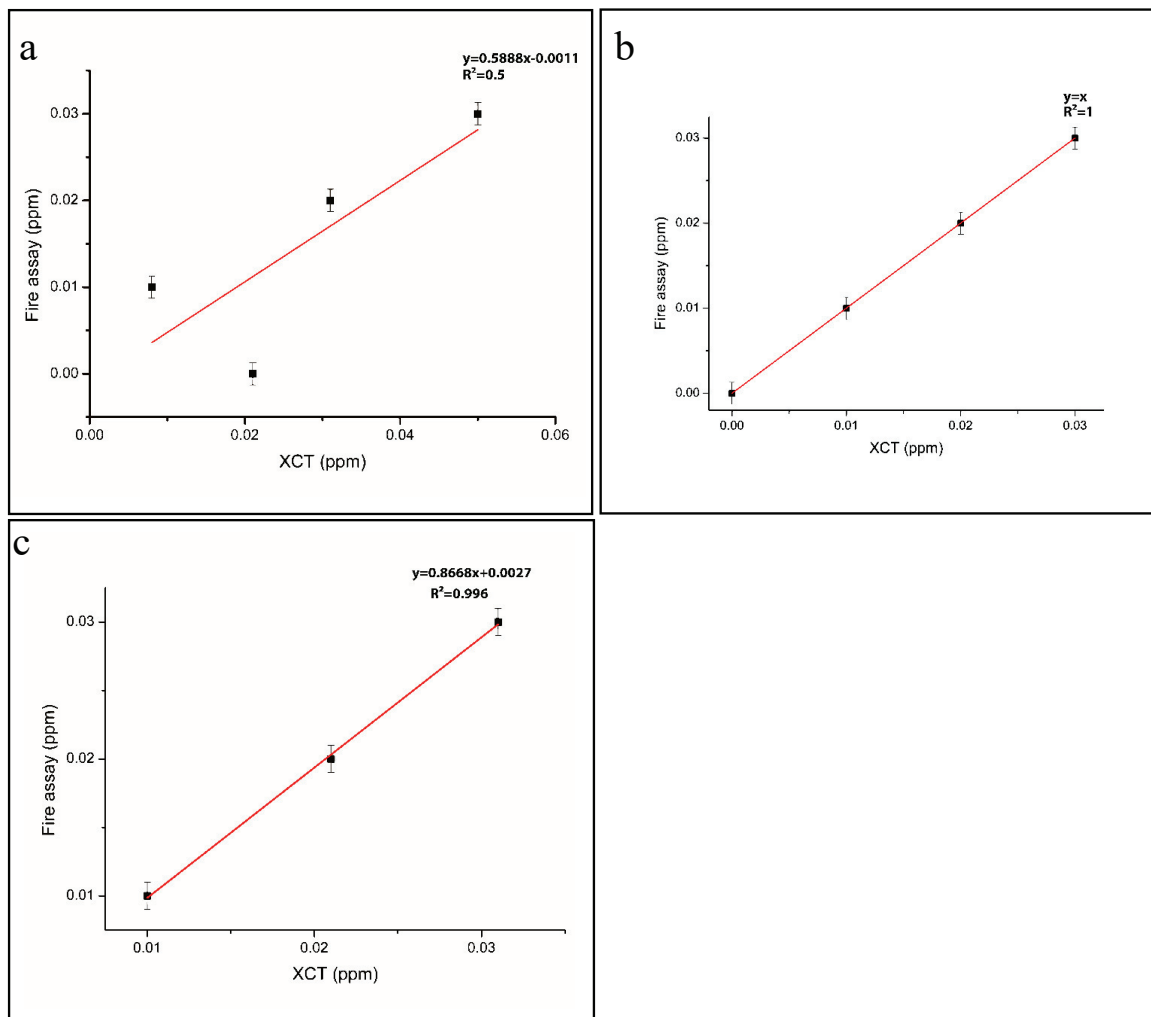


Figure 6. Correlation between XCT and Fire assay data. (a) Correlation between XCT and fire assay of quarter core before calibration. (b) 1:1 linear best fit line of XCT and fire assay. (c) Correlation between XCT and fire assay of quarter core after calibration. Error bar ± 0.001 .

Table 3. (Top) Gold grade of the scanned core samples calculated by XCT analysis and gold grade obtained by fire assay. (Middle) Calculated gold grade after calibrating using fire assay at threshold grey value of 63,000. (Bottom) comparison of gold grades before and after calibration.

Sample	Weight of Core (g)	Gold Volume (cm ³)	Mass Gold (g)	Gold Grade XCT (ppm)	Gold Grade Fire Assay (ppm)
JJ 01	50.56	0.0013	0.025	0.050	0.03
JJ 02	50.085	0.0008	0.015	0.031	0.02
JJ 04	60.175	0.00025	0.005	0.008	0.01
JJ 05	55.205	0.0006	0.012	0.021	0
JJ 01	50.56	0.0008	0.015	0.031	0.03
JJ 02	50.085	0.00054	0.010	0.021	0.02
JJ 04	60.175	0.0003	0.006	0.010	0.01

Table 3. Cont.

Sample	Gold Grade before Calibration (Quarter Core) XCT (ppm)	Gold Grade after Calibration (Quarter Core) XCT (ppm)	Gold Grade Fire Assay (Quarter Core) (ppm)	Gold Grade Whole Core after Calibration XCT (ppm)	% Difference between Calibrated Whole Core Gold XCT Data and Fire Assay
JJ 01	0.05	0.031	0.03	0.02	−0.04
JJ 02	0.031	0.021	0.02	0.004	−0.04
JJ 04	0.008	0.01	0.01	0.043	0.03
JJ 05	0.021	0.01	0	0.01	0.01

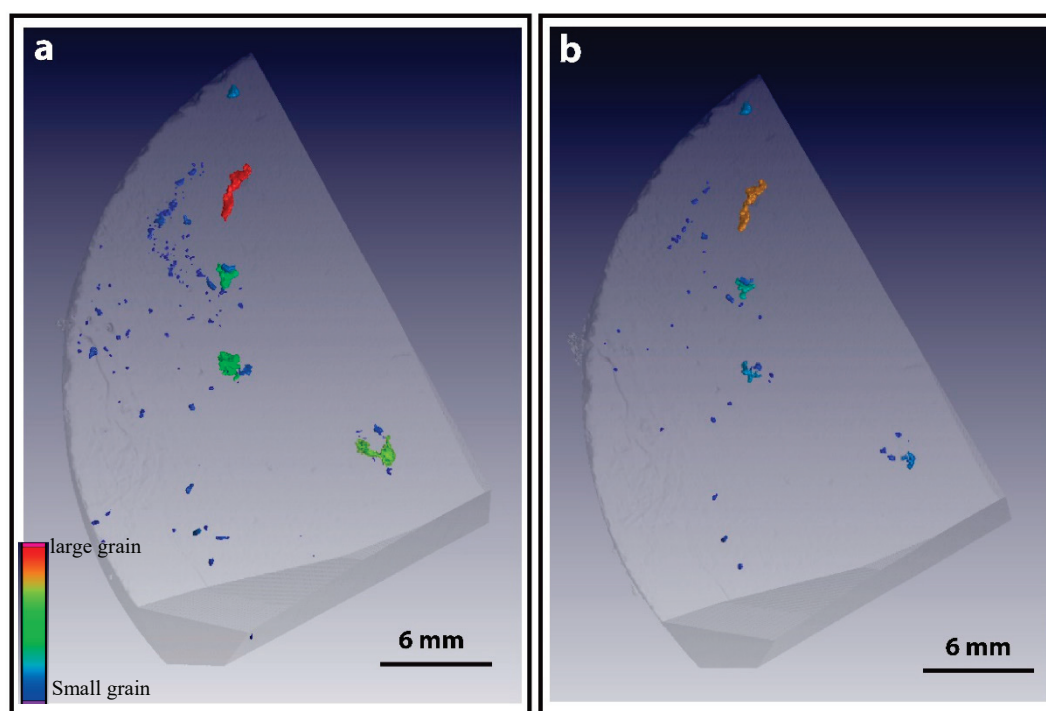


Figure 7. (a,b): Distribution of gold grains in the core after segmenting using a threshold value of 59,868 and 63,000 grey values respectively, at 59,868 XCT generally overestimate the mass of gold present in the core sample. The grey colour is the silicate matrix and other colours represent gold, distributed according to gold grain volume (warm colours = large grains, cold colours = smaller grains). Sample JJ01.

3.2. Textural and Mineralogical Correlations between 2D and 3D Study Approaches

The preceding section highlights the utility of XCT towards understanding and semi-quantitatively analysing gold distributions in three dimensional reconstructions of exploration borehole core samples. When used independently however, this approach fails to discern between different sulphide minerals in the assemblage and poorly resolves microstructural features that may have important implications for the exploration efforts. It is thus imperative to combine 3D XCT analyses with conventional 2D microscopies in order to derive the full value out of a given exploration drilling program. Figure 8 compares a montage of 2D optical (reflected light) microscopy images with the corresponding image slice extracted from an XCT model. The correlation was conducted manually by visually aligning prominent features using the commercially available Volume Graphic software. An artefact of this imperfect overlap is depicted in Figure 8a, in which a notable gold grain is intersected in the image slice but was either slightly below the polished surface or was above the polished surface and was subsequently cut and polished away. Indeed, when preparing polished sections of finely disseminated

gold mineralization, intersection of discrete gold grains can only be fortuitous if cutting and polishing is not guided by prior XCT analysis.

Figure 8b further contrasts the level of mineralogical detail that is achieved in the XCT image slice versus the petrographic montage. The XCT model provides a three-dimensional overview of the sulphide spatial distribution, reveals low-level textural information (e.g., mineral stretching along the shear plane is clearly evident), and enables a truer representation of the mineral size distributions (2D approaches provide apparent mineral sizes). However, it clearly lacks in its ability to discern between different sulphide mineral phases. In comparison, the 2D reflected light petrographic montage enables that the individual sulphide mineral phases can be identified, their paragenetic relationships can be more deeply investigated, and additional microstructural details (e.g., mica fish, rotated porphyroblasts) can be used to augment and enrich the understanding of the structural controls on the mineralization. Some disadvantages of the 2D petrographic study approaches include that they are destructive to the original core sample, the samples require preparation (i.e., cutting and polishing may be time-consuming), selection of sub-samples for thin/thick sectioning may introduce unconscious bias into the ultimate dataset, true mineral sizes cannot be discerned, and the 3D kinematics associated with the structural controls cannot be fully studied. These results (summarized in Table 4) clearly highlight that there is extra information that can be obtained from microscopy that cannot be obtained from XCT, and vice versa. Hence, from an optimized exploration perspective, it is important that these techniques should be used correlatively.

Table 4. Summary on information that can be obtained from combined approach.

2D Petrography	3D Computed Tomography	Combined and 2D and 3D Correlative Approach
Apparent size	True size and orientation	True size
Relative sense of motion (e.g., sinistral vs. dextral) associated with structural features	Absolute 3D orientation of major structures	Deeper understanding of orientation of major structures
Resolution determined by lenses on microscope	35 μm voxel resolution	Enables that 2 μm resolution can be spatially constrained within a 35 μm voxel size theoretical XCT model
Observation of microstructural features e.g., mica fish, rotated porphyroblasts, mineral stretching, etc.	Only major structures observed, possible identification of mineral stretching in dense gold samples	Microstructural details can be positioned in 3D space given x, y, z coordinates
Identification of individual mineral phases	Broad categorization of mineral phases based on X-ray attenuation coefficients	A better and more comprehensive understanding of mineral phases. Identified mineral phases can be quantified and positioned in 3D space

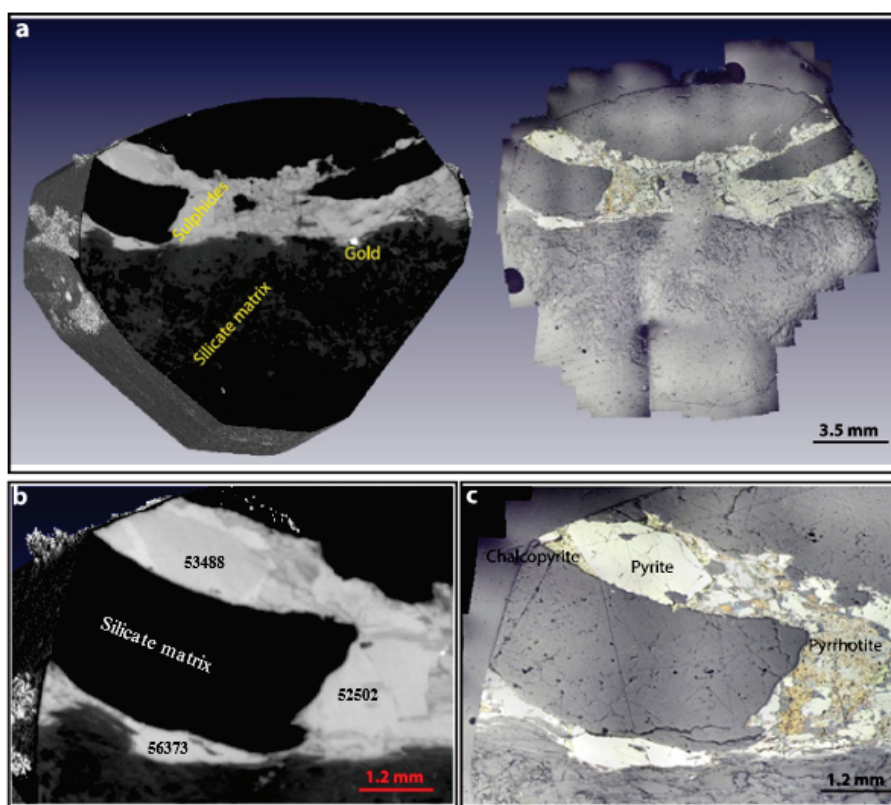


Figure 8. (a): Precise overlay of thin section and XCT scan images in 3D. The correlation was conducted manually by visually aligning prominent features using Volume Graphic software. A notable gold grain is intersected in the XCT image slice but was either slightly below the polished surface or was above the polished surface and was subsequently cut and polished away. The high-resolution X-ray computed tomography and microscopy analyses indicate that gold and accessory sulphides are not randomly distributed but rather follow specific orientation. They are distributed along shear fracture planes rather than disseminated throughout the cores. This suggests that gold was precipitated along the shear plane together with the sulphides during the ore-forming processes. The bright gold grain is not seen in reflected light microscopy, but it is easily seen in XCT image. (b) Zoomed in image of sulphides from XCT indicating that they cannot be differentiated due to a narrow density range. (c) The sulphide mineral assemblage comprises pyrite, pyrrhotite and chalcopyrite determined from detailed 2D examination of polished sections. Thick section cut from sample JJ04.

4. Discussion

The use of XCT in combination with microscopy provides an excellent tool for understanding gold mineralization, which is often nuggety and difficult to study because of its ppm-level grades. Although the application of this combined approach is not yet widespread, this approach overlays complementary datasets from 2D and 3D analytical protocols, thereby allowing a better and more comprehensive understanding on the distribution and structures controlling gold mineralization. In order to investigate the feasibility of the combined approach and its practical utility, we consider an example from the Manondo-Choma gold prospect (southern Malawi).

4.1. Advantages of Correlative Approaches to Exploration: Case Study from the Manondo-Choma Mineralization (Malawi)

4.1.1. Geological Context

The Kirk Range is a medium- to high-metamorphic grade mobile belt which is related to the Southern Irumide orogeny and which is located in south-central Malawi [37]. It is situated approximately

40 km north-west of Blantyre and lies between latitudes 15.30° S to 15.31° S and the longitudes 34.82° E to 34.85° E, near to the western border between Malawi and Mozambique. The major lithologies in the area comprise a suite of NE trending gneissic rocks that underwent amphibolite-granulite facies metamorphism [38]. These lithological units are characterized by polyphase deformation showing evidence of reworking possibly by the pan-African orogeny (800–550 Ma) [39].

Gold mineralization at the Manondo-Choma prospect has recently been described by the authors in [38]. Briefly, the gold is hosted predominantly in biotite schists and gneisses and is associated with a sulphide mineral paragenesis. Regional structures as well as mineralized quartz-sulphide vein sets exhibit a NE–SW trend, which is consistent with the deformation fabrics associated with the southern Irumide orogeny [40–42]. Textural and microstructural observations reveal that the vein sets have experienced subsequent deformation and overprinting, which has likely led to transposition of the primary gold mineralization on a regional scale [38].

4.1.2. Correlated 2D and 3D Insights into Gold Mineralization at the Manondo-Choma Prospect

Four segments of drill core were selected for detailed scanning and modelling using XCT and correlative reflected and transmitted light microscopies. The XCT reconstructions reveal that the gold is hosted primarily in sub-vertical vein structures that strike in a NE–SW direction (Figure 9b). The fine-grained gold flakes are sub-rounded in texture, range in size between 0.01 and 0.04 mm, and are typically elongated parallel to the direction of the strike of the host vein (Figure 9c). Gold grades for the different core segments range between 0.01 and 0.03 ppm from fire assay and 0.01–0.031 ppm calculated from XCT (Table 3; after corrections to account for nugget effects inherent in gold mineralization (see Section 3.1.1.)) and show good agreement with the gold grades measured using fire assay analytical protocols. The gold is strongly associated with sulphide minerals which also orientate preferentially in the NE–SW strike direction. Minor gold is also associated with the wall rock, perhaps reflecting a second-order lithological or geochemical control on the siting of the mineralization [38]. Although the XCT image slices show subtle differences in the grey values among different sulphide minerals, these grey values could not be used to unequivocally determine sulphide speciation and did not allow detailed comment on the textural and temporal relationships within the ore paragenesis.

Thus, to augment the gold spatial, size and shape distribution data, correlative 2D petrographic analyses were conducted on selected sub-samples of the core segments. These sub-samples were best selected based on prior evaluation of the 3D XCT models, whereby gold-rich regions of the core segment were targeted for the further detailed petrographic work. Reflected light microscopy revealed that the sulphide mineral assemblage is dominated by pyrite (~80% modal proportion), with the remaining 20% of the sulphides represented by chalcopyrite, sphalerite and pyrrhotite. Early formed pyrrhotite showed the strongest mineral stretching, which was parallel to both the stretching identified in the gold flakes and to the orientation of the main vein structure. Transmitted light microscopy enabled that microtextures and shear sense indicators could be identified within the silicate mineralogy associated with the vein structure. For example, 2D microscopy indicates the presence of shear in the silicate mineralogy within the vein structure defined by grain size reduction (Figure 9e) and display flow structures that indicate ductile deformation of the core (Figure 9f,g). In standard 2D petrography, this information can give insights into whether the mineralized vein experienced a dextral or sinistral sense of shear (i.e., X–Y directionality). However, by considering this information in light of the known orientation of the vein from prior XCT work, the kinematics can further constrained with reference to the Z-direction. Furthermore, the correlative approach allows the microstructures observed in polished sections to be confidently positioned in X, Y, Z space (using the known depth of sub-sampling down an orientated drill string). To advance exploration efforts, these orientated and positioned microstructural data can be pulled directly into implicit modelling software as an additional layer of information which could be readily analysed and iterated to finalize geological or grade interpretations.

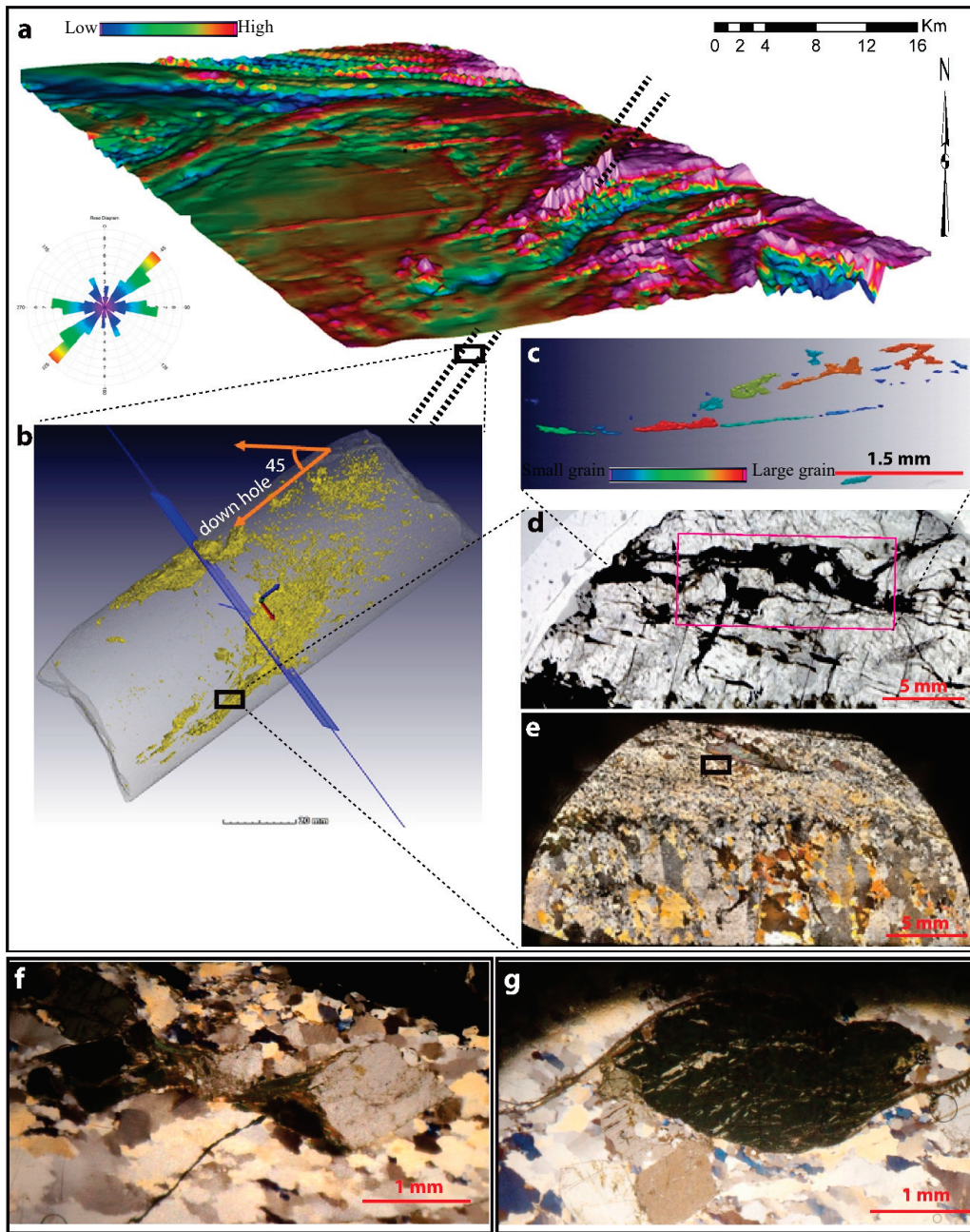


Figure 9. Nature of gold mineralization. (a) Structures (faults, fractures, shear zones and dykes) that were derived from interpretation of airborne magnetic data. The magnetic data show prominent lineaments that represent faults and shear zones. The faults and fractures and shear zones are thought to have acted as conduits for mineralizing hydrothermal fluids. Rose diagram show the dominant trend of structures to be NE–SW. (b) Drill core drilled from the indicated hole show that the mineralized vein system and the sulphide distribution also show the same trend; the distribution of the sulphides show that the sulphide minerals occur as an interconnected subvertical network and have preferred orientation. The orientation of sulphides is consistent with dominant structures in the field. The grey colour is the silicate matrix and the yellow colour indicates sulphides. (c) XCT scanned image of the thin section made from indicated rectangle shows gold grains have been elongated/stretched in this dominant NE orientation along the shear plane, (warm colours = large gold grains, cold colours = smaller gold grains). (d,e) Milled grains and stretched minerals in thin section from the drill core cut along the rectangle indicated on the drill core indicating shearing. (f,g) Shear sense indicators observed from thin section e above on the shear plane using a 50× objective lens. Sample JJ05.

The outcomes from this correlative study conducted at the Manondo-Choma gold prospect thus highlight that the gold is intimately associated with sulphide mineralization in NE–SW trending SE-dipping quartz-sulphide vein structures that show a dextral sense of shear. These structures were identified by considering the complementary 2D and 3D datasets, and the orientations are found to match those of the regional NE–SW magnetic trends identified using geophysics [32] (Figure 9a), and which are tentatively related to the southern Irumide orogeny. In addition to the value that the correlative approach unlocks for exploration at the front end of the mine value chain, it also reveals vital information that can assist during later processing and beneficiation of the ore assemblage. For example, XCT scanning provides definitive information on the size, distribution and mineralogical association of the gold, all of which can control the liberation efficiencies during minerals processing. Similarly, the distribution and semi-quantitative evaluation of the sulphide minerals (Table 2), offers a unique methodology to predict acid mine drainage capacity associated with an ore prospect, especially given that sulphide concentrations are difficult to measure using standard XRF quantification approaches [43]. Related to this, the complementary petrographic information related to sulphide speciation further has important implications for the presence of metal ‘sweeteners’ (e.g., Cu, Zn) that may add additional economic value to an ore prospect, and for the presence of any deleterious elements (e.g., As) that may require special consideration to ensure that the environmental impacts of downstream mining are minimized.

4.2. Recommendations for Further Development

The use of correlative microscopies in minerals exploration has not yet reached its full maturity, yet the example from the Manondo-Choma gold prospect clearly indicates its high potential for incorporation in routine minerals exploration workflows. This is especially pertinent for gold exploration endeavours given the nuggety distribution of the ore within mineralized vein sets. As bench-scale XCT machines become increasingly commercially available, it is anticipated that the approach will be adopted more extensively among exploration practitioners. However, in order to optimize the approach, the following recommendations apply:

- Need for automated alignment algorithms based on optical image analysis methodologies to match 2D montages to their positioning in XYZ space. This will help as it will require minimal initial user input. The manual approach can take 4 h.
- Need to develop software interfaces that allow XYZ positioned and orientated microstructural and mineralogical data (mapped in 3D space in XCT software) directly into common implicit and explicit geological modelling software.
- Need to optimize voxel sizes to match fine grained gold mineralization.
- Need to optimize the scanning parameters, or resolution of the sensors to better discern between different sulphide moieties using XCT technologies (and between gold and other dense minerals with high X-ray attenuation coefficients such as barite, galena, etc.).
- Opportunities to develop other computed tomography techniques to provide detailed mineralogical, chemical and valence distributions in 3D space (synchrotron XRD computed tomography [44], synchrotron XRF CT [45], and synchrotron XANES CT respectively [46]).

5. Conclusions

We have highlighted a correlative approach in which 3D XCT data are combined with 2D mineralogical and chemical data to understand a complex orogenic gold mineralization. The use of XCT in combination with microscopy provides an excellent tool for understanding gold mineralization. Contextualizing 2D structural features in a 3D volume enables a deeper understanding of the structures that control mineralization and characterize the distribution of gold. Given that modern exploration efforts are targeting increasingly complex and low-grade ore deposits, the extra layers of information provided by using correlative 2D and 3D microscopies offer an exciting new tool to enhance and

optimize minerals exploration workflows. It is anticipated that the approach will be adopted more extensively among exploration practitioners. Although the approach is especially well suited to gold mineralization (nuggety textures, high density and X-ray absorption coefficients of Au), it can also be applied to a range of other mineralization styles (e.g., disseminated sulphide mineralization, tungstate mineralization in skarns, etc.).

Author Contributions: Formal analysis, S.L.R. and M.T.; Supervision, B.v.d.H.; Writing—original draft, J.C. All authors have read and agreed to the published version of the manuscript.

Funding: Funding for the project was supported in part through grants to J. Chisambi (World Bank, Skills Development Project), and to B. von der Heyden (National Research Foundation of South Africa: Grant #106006, and additional support from DST-NRF CIMERA).

Conflicts of Interest: The authors declare no conflict of interest.

References

1. Ferguson, M. *World Exploration Trends 2018*; S&P Global Market Intelligence: New York, NY, USA, 2019.
2. Phillips, G. Australian and global setting for gold in 2013. In *Proceedings of the World Gold 2013*, Brisbane, Australia, 26–29 September 2013.
3. Gaboury, D. Parameters for the formation of orogenic gold deposits Parameters for the formation of orogenic gold deposits. *Appl. Earth Sci.* **2019**, *128*, 124–133. [[CrossRef](#)]
4. Groves, D.I. Gold Deposits in Metamorphic Belts: Overview of Current Understanding, Outstanding Problems, Future Research, and Exploration Significance. *Econ. Geol.* **2003**, *98*, 1–29. [[CrossRef](#)]
5. Augustin, J.; Gaboury, D. Multi-stage and multi-sourced fluid and gold in the formation of orogenic gold deposits in the world-class Mana district of Burkina Faso—Revealed by LA-ICP-MS analysis of pyrites and arsenopyrites. *Ore Geol. Rev.* **2019**, *104*, 495–521. [[CrossRef](#)]
6. Goldfarb, R.; Groves, D.; Gardoll, S. Orogenic gold and geologic time: A global synthesis. *Ore Geol. Rev.* **2001**, *18*, 1–75. [[CrossRef](#)]
7. Groves, D. The crustal continuum model for late-Archaeon lode-gold deposits of the Yilgarn Block, Western Australia. *Miner. Depos.* **1993**, *374*, 366–374. [[CrossRef](#)]
8. Popov, O.; Talovina, I.; Lieberwirth, H.; Duryagina, A. Quantitative Microstructural Analysis and X-ray Computed Tomography of Ores and Rocks—Comparison of Results. *Minerals* **2020**, *10*, 129. [[CrossRef](#)]
9. Asadi, H.H.; Voncken, J.H.L.; Kühnel, R.A.; Hale, M. Petrography, mineralogy and geochemistry of the Zarshuran Carlin-like gold deposit, northwest Iran. *Miner. Deposita* **2000**, *35*, 656–671. [[CrossRef](#)]
10. Pašava, J.; Svojtka, M.; Jana, Ď.; Drábek, M.; Halodová, P.; Haluzová, E. Laser ablation ICPMS study of trace element chemistry in molybdenite coupled with scanning electron microscopy (SEM)—An important tool for identification of different types of mineralization. *Ore Geol. Rev.* **2016**, *72*, 874–895. [[CrossRef](#)]
11. Stromberg, J.M.; Van Loon, L.L.; Gordon, R.; Woll, A.; Feng, R.; Schumann, D.; Banerjee, N.R. Applications of synchrotron X-ray techniques to orogenic gold studies; examples from the Timmins gold camp. *Ore Geol. Rev.* **2019**, *104*, 589–602. [[CrossRef](#)]
12. Butler, I.B.L.; Nesbitt, R.W. Trace element distributions in the chalcopyrite wall of a black smoker chimney: Insights from laser ablation inductively coupled plasma mass spectrometry (LA-ICP-MS). *Earth Planet Sci.* **1999**, *167*, 335–345. [[CrossRef](#)]
13. Godel, B. High-Resolution X-Ray Computed Tomography and Its Application to Ore Deposits: From Data Acquisition to Quantitative Three-Dimensional Measurements with Case Studies from Ni-Cu-PGE Deposits. *Econ. Geol.* **2013**, *108*, 2005–2019. [[CrossRef](#)]
14. Kyle, J.R.; Ketcham, R.A. Application of high resolution X-ray computed tomography to mineral deposit origin, evaluation, and processing. *Ore Geol. Rev.* **2015**, *65*, 821–839. [[CrossRef](#)]
15. Baker, D.; Mancini, L.; Polacci, M.; Higgins, M.; Gualda, G.A.R.; Hill, R.; Rivers, M. An introduction to the application of X-ray microtomography to the three-dimensional study of igneous rocks. *Lithos* **2012**, *148*, 262–276. [[CrossRef](#)]

16. Fatima, A.; Venkatesh, A.S.; Mukherjee, R.; Agrawal, A.K.; Singh, B.; Sarkar, P.S.; Shripathi, T. 3D spatial distribution of ore mineral phases using high resolution synchrotron micro-computed tomography (μ CT) combined with optical microscopy 3D spatial distribution of ore mineral phases using high resolution synchrotron micro-computed tomography (μ CT) combined with optical microscopy. *Appl. Radiat. Isot.* **2019**, *148*, 49–59.
17. Kyle, J.R.; Mote, A.S.; Ketcham, R.A. High resolution X-ray computed tomography studies of Grasberg porphyry Cu-Au ores, Papua, Indonesia. *Miner. Deposita* **2008**, *43*, 519–532. [[CrossRef](#)]
18. Naudé, G.; Hoffman, J.; Theron, S.J.; Coetzer, G. The use of X-ray computed tomography in the characterisation of coal and associated char reductants. *Miner. Eng.* **2013**, *52*, 143–154. [[CrossRef](#)]
19. Elangovan, P.; Hezel, D.C.; Howard, L.; Armstrong, R.; Abel, R.L. Computers & Geosciences PhaseQuant: A tool for quantifying tomographic data sets of geological specimens. *Comput. Geosci.* **2012**, *48*, 323–329.
20. Díaz, D.; Hahn, D.W.; Molina, A. Quantification of gold and silver in minerals by laser-induced breakdown spectroscopy. *Spectrochim. Acta Part B* **2017**, *136*, 106–115. [[CrossRef](#)]
21. Sayab, M.; Suuronen, J.-P.; Molnar, F.; Villanova, J.; Kallonen, A.; O'Brien, H.; Lahtinen, R.; Lehtonen, M. Three-dimensional textural and quantitative analyses of orogenic gold at the nanoscale. *Geology* **2016**, *44*, 739–742. [[CrossRef](#)]
22. Maire, E.; Withers, P.J.; Maire, E.; Withers, P.J. Quantitative X-ray tomography. *Int. Mater. Rev.* **2013**, *59*, 1–43. [[CrossRef](#)]
23. Zhang, P.; Lee, Y.; Zhang, J. A review of high-resolution X-ray computed tomography applied to petroleum geology and a case study. *Micron* **2019**, *124*, 102702. [[CrossRef](#)] [[PubMed](#)]
24. Le Roux, S.; Du Plessis, A.; Rozendaal, A. The quantitative analysis of tungsten ore using X-ray microCT: Case study. *Comput. Geosci.* **2015**, *85*, 75–80. [[CrossRef](#)]
25. Godel, B.; Barnes, S.-J.; Maier, W.D. 3-D Distribution of Sulphide Minerals in the Merensky Reef (Bushveld Complex, South Africa) and the J-M Reef (Stillwater Complex, USA) and their Relationship to Microstructures Using X-Ray Computed Tomography. *J. Pet.* **2006**, *47*, 1853–1872. [[CrossRef](#)]
26. ALS. *ALS Geochemistry Service*; ALS Laboratory: Johannesburg, South Africa, 2013.
27. Du Plessis, A.; Le Roux, S.; Guelpa, A. The CT Scanner Facility at Stellenbosch University: An open access X-ray computed tomography laboratory. *Nucl. Instrum. Methods Phys. Res. Sect. B* **2016**, *384*, 42–49. [[CrossRef](#)]
28. Volume Graphics GmbH. *VG Studio Max 3.1 User's Manual*; Volume Graphics GmbH: Heidelberg, Germany, 2001.
29. Ketcham, R.A. Resolution-invariant measurements of small objects in polychromatic CT data. In Proceedings of the Developments in X-Ray Tomography XII. International Society for Optics and Photonics, San Diego, CA, USA, 8–12 March 2019; Volume 11113, p. 111130B. [[CrossRef](#)]
30. Berger, M. XCOM: Photon Cross Sections Database. In *National Bureau of Standards*; Center for Radiation Research: Washington, DC, USA, 1998.
31. Density of Minerals. Available online: www.webminerals.com (accessed on 23 March 2020).
32. Bam, L. Developing Protocols for XCT Scanning of Dense Mineral Ore Samples with Applications to Geology and Minerals Processing. Ph.D. Thesis, Stellenbosch University, Stellenbosch, South Africa, 2019.
33. Reeves, T.; Mah, P.; McDavid, W. Deriving Hounsfield units using grey levels in cone beam CT: A clinical application. *Dentomaxillofacial Radiol.* **2012**, *41*, 500–508. [[CrossRef](#)]
34. Gazley, M.F.; Duclaux, G.; A Fisher, L.; De Beer, S.; Smith, P.; Taylor, M.; Swanson, R.; Hough, R.M.; Cleverley, J.S. 3D visualisation of portable X-ray fluorescence data to improve geological understanding and predict metallurgical performance at Plutonic Gold Mine, Western Australia. *Appl. Earth Sci.* **2011**, *120*, 88–96. [[CrossRef](#)]
35. Cook, N.J.; Cook, N.J.; Courtney-Davies, L.; Slattery, A.D.; Verdugo-Ihl, M.R.; Courtney-Davies, L.; Gao, W. Advances and Opportunities in Ore Mineralogy. *Minerals* **2017**, *7*, 233. [[CrossRef](#)]
36. Dominy, S.C.; Edgar, W.B. Approaches to reporting grade uncertainty in high nugget gold veins. *Appl. Earth Sci.* **2012**, *121*, 29–42. [[CrossRef](#)]
37. Bloomfield, K.; Garson, M.S. *The Geology of the Kirk Range-Lisungwe Valley Area*; Ministry of Natural Resources. Geological Survey Department. Bulletin No.17; Government Printer: Zomba, Malawi, 1965.
38. Chisambi, J.; von der Heyden, B. Primary gold mineralization at Manondo–Choma area, Kirk range, Southern Malawi. *S. Afr. J. Geol.* **2019**, *122*, 505–518. [[CrossRef](#)]

39. De Waele, B.; Fitzsimons, I.; Wingate, M.T.D.; Tembo, F.; Mapani, B.; Belousova, E. The geochronological framework of the Irumide Belt: A prolonged crustal history along the margin of the Bangweulu Craton. *Am. J. Sci.* **2009**, *309*, 132–187. [[CrossRef](#)]
40. De Waele, B.; Kampunzu, A.; Mapani, B.; Tembo, F. The Mesoproterozoic Irumide belt of Zambia. *J. Afr. Earth Sci.* **2006**, *46*, 36–70. [[CrossRef](#)]
41. Boyd, R.; Nordgulen, O.; Thomas, R.J.; Bingen, B.; Bjerkgård, T.; Grenne, T.; Henderson, I.H.C.; Melezhik, V.; Often, M.; Sandstad, J.S.; et al. The Geology And Geochemistry Of The East African Orogen In Northeastern Mozambique. *S. Afr. J. Geol.* **2010**, *113*, 87–129. [[CrossRef](#)]
42. Bingen, B.; Jacobs, J.; Viola, G.; Henderson, I.H.C.; Skår, Ø.; Boyd, R.; Thomas, R.J.; Solli, A.; Key, R.; Daudi, E. Geochronology of the Precambrian crust in the Mozambique belt in NE Mozambique, and implications for Gondwana assembly. *Precambrian Res.* **2009**, *170*, 231–255. [[CrossRef](#)]
43. Czerewko, M.A.; Cripps, J.C.; Reid, J.M.; Duffell, C.G. Sulfur species in geological materials—sources and quantification. *Cem. Concr. Compos.* **2002**, *25*, 657–671. [[CrossRef](#)]
44. Leißner, T.; Diener, A.; Löwer, E.; Ditscherlein, R.; Krüger, K.; Kwade, A.; Peuker, U.A. 3D ex-situ and in-situ X-ray CT process studies in particle technology—A perspective. *Adv. Powder Technol.* **2020**, *31*, 78–86. [[CrossRef](#)]
45. De Samber, B.; Silversmit, G.; Evens, R.; De Schamphelaere, K.; Janssen, C.; Masschaele, B.; Van Hoorebeke, L.; Balcaen, L.; Vanhaecke, F.; Falkenberg, G.; et al. Three-dimensional elemental imaging by means of synchrotron radiation micro-XRF: Developments and applications in environmental chemistry. *Anal. Bioanal. Chem.* **2007**, *390*, 267–271. [[CrossRef](#)]
46. Meneses, C.T.; Macedo, M.A.; Vicentin, F.C. LixMn₂O₄ thin films characterization by X-ray, electrical conductivity and XANES. *Microelectron. J.* **2003**, *34*, 561–563. [[CrossRef](#)]



© 2020 by the authors. Licensee MDPI, Basel, Switzerland. This article is an open access article distributed under the terms and conditions of the Creative Commons Attribution (CC BY) license (<http://creativecommons.org/licenses/by/4.0/>).

Article

The INOVMineral Project's Contribution to Mineral Exploration—A WebGIS Integration and Visualization of Spectral and Geophysical Properties of the Aldeia LCT Pegmatite Spodumene Deposit

Joana Cardoso-Fernandes ^{1,2}, Douglas Santos ^{1,2}, Cátia Rodrigues de Almeida ^{1,2,3}, Julia Tucker Vasques ¹, Ariane Mendes ¹, Ricardo Ribeiro ^{1,2}, Antonio Azzalini ¹, Lia Duarte ^{1,2}, Rui Moura ^{1,4}, Alexandre Lima ^{1,2,*} and Ana C. Teodoro ^{1,2,*}

- ¹ Department of Geosciences, Environment and Land Planning, Faculty of Sciences, University of Porto, Rua Campo Alegre 687, 4169-007 Porto, Portugal; joana.fernandes@fc.up.pt (J.C.-F.); douglas.santos@fc.up.pt (D.S.); up201600831@fc.up.pt (C.R.d.A.); up201900694@up.pt (J.T.V.); ariane.mendes@fc.up.pt (A.M.); ricardo.ribeiro@fc.up.pt (R.R.); antonio.azzalini@fc.up.pt (A.A.); liaduarte@fc.up.pt (L.D.); rmmoura@fc.up.pt (R.M.)
- ² ICT (Institute of Earth Sciences)—Porto Pole (Portugal), Rua Campo Alegre, 4169-007 Porto, Portugal
- ³ Centro de Investigação de Montanha (CIMO), Polytechnic Institute of Bragança (IPB), Campus de Santa Apolónia, 5300-253 Braganza, Portugal
- ⁴ INESC TEC CRAS—Centre for Robotics and Autonomous Systems, Superior Institute of Engineering of Porto (ISEP), 4249-015 Porto, Portugal
- * Correspondence: allima@fc.up.pt (A.L.); amteodor@fc.up.pt (A.C.T.)



Citation: Cardoso-Fernandes, J.; Santos, D.; Almeida, C.R.d.; Vasques, J.T.; Mendes, A.; Ribeiro, R.; Azzalini, A.; Duarte, L.; Moura, R.; Lima, A.; et al. The INOVMineral Project's Contribution to Mineral Exploration—A WebGIS Integration and Visualization of Spectral and Geophysical Properties of the Aldeia LCT Pegmatite Spodumene Deposit. *Minerals* **2023**, *13*, 961. <https://doi.org/10.3390/min13070961>

Academic Editor: Paul Alexandre

Received: 20 June 2023

Revised: 13 July 2023

Accepted: 15 July 2023

Published: 19 July 2023



Copyright: © 2023 by the authors. Licensee MDPI, Basel, Switzerland. This article is an open access article distributed under the terms and conditions of the Creative Commons Attribution (CC BY) license (<https://creativecommons.org/licenses/by/4.0/>).

Abstract: Due to the current energetic transition, new geological exploration technologies are needed to discover mineral deposits containing critical materials such as lithium (Li). The vast majority of European Li deposits are related to Li–Cs–Ta (LCT) pegmatites. A review of the literature indicates that conventional exploration campaigns are dominated by geochemical surveys and related exploration tools. However, other exploration techniques must be evaluated, namely, remote sensing (RS) and geophysics. This work presents the results of the INOVMINERAL4.0 project obtained through alternative approaches to traditional geochemistry that were gathered and integrated into a webGIS application. The specific objectives were to: (i) assess the potential of high-resolution elevation data; (ii) evaluate geophysical methods, particularly radiometry; (iii) establish a methodology for spectral data acquisition and build a spectral library; (iv) compare obtained spectra with Landsat 9 data for pegmatite identification; and (v) implement a user-friendly webGIS platform for data integration and visualization. Radiometric data acquisition using geophysical techniques effectively discriminated pegmatites from host rocks. The developed spectral library provides valuable insights for space-based exploration. Landsat 9 data accurately identified known LCT pegmatite targets compared with Landsat 8. The user-friendly webGIS platform facilitates data integration, visualization, and sharing, supporting potential users in similar exploration approaches.

Keywords: geological exploration; UAV; LiDAR; radiometry; geophysics; remote sensing; Landsat 9; GIS; lithium

1. Introduction

Considering the European Commission's environmental measures that have resulted in an increasing demand for lithium (Li) and other critical materials [1], there is a current need for new geological exploration technologies to discover and evaluate possible European deposits. This need and possible ways to address it have been discussed in previous works [1–3]. Studies focused on methodologies for locating and prospecting pegmatites are increasingly relevant, given their importance for the energy market in a scenario where new sources need to be identified.

Müller et al. [3] delineated the goals of the ongoing Horizon 2020 GREENPEG project to develop exploration toolsets to identify buried pegmatites of both Li–Cs–Ta (LCT) and Nb–Y–F (NYF) chemical types. According to the authors, distinct exploration techniques are being tested at several scales, including (i) remote sensing approaches, (ii) helicopter-borne, drone-borne, and ground-based geophysics (radiometry, magnetometry, electromagnetics, piezoelectric spectrometry, ground-penetrating radar, gravimetry, and resistivity), and (iii) geochemical surveys (soil Ah and C-horizon mapping, stream sediment mapping, lithochemical mapping, and quartz element-trace mapping).

Steiner [4] presented a review of exploration techniques for LCT pegmatites and a resulting workflow was proposed. The workflow starts with (i) literature and desktop studies followed by (ii) target selection under a Geographic Information System (GIS); in the selected targets, (iii) follow-up field campaigns are conducted and, if favorable evidence is found, (iv) drilling campaigns are eventually employed [4]. However, most of the exploration methods reviewed in this work for field campaigns are related to traditional geological mapping approaches or with geochemical surveys, namely, rock geochemistry, and soil and stream sediment sampling campaigns.

The earlier work of Galeschuk and Vanstone [5] already demonstrated the importance and success of geochemical exploration methods such as rock lithochemical and selective leach soil geochemistry to identify buried LCT pegmatites in the Bird River Belt, Manitoba, Canada. Similar approaches have been conducted in recent years [6–11]. For example, geochemical analysis of stream sediment samples allowed the identification of anomalies and new prospects for LCT pegmatites in several areas in Ireland, Iran, and Portugal, especially when employing multi-element statistical analysis, and subsequently determined geochemical pathfinders [6–9]. Errandonea-Martin et al. [10] presented a detailed lithochemical study that demonstrated that the LCT pegmatites from Fregeneda–Almendra (Iberian Peninsula) generated metasomatic haloes on their metasedimentary host rocks, with the magnitude of such haloes controlled by the degree of magmatic differentiation of pegmatitic melts. The authors demonstrated that Li and Cs display the greatest haloes which can serve as proxies for mineral exploration in fresh outcrops. Recently, Keyser et al. [11] analyzed the concentrations of pegmatite-related trace elements in quartz for LCT pegmatites in Austria and Ireland, concluding that such trace element concentrations in quartz can serve as reliable proxies for Li mineralization, besides presenting crucial information to assess primary pegmatite chemical signatures.

Besides geochemical approaches, other exploration techniques have been evaluated. In 2010, Trueman [12] conducted a study in which he considered the use of geophysical methods in the prospection of pegmatites. Taking into account that the minerals contained in pegmatites are not responsive to these methods, he concluded that electromagnetic and gravimetric methods are favorable for outlining the structures and contacts between the pegmatites and host rock. However, the radiometric method was considered a poor alternative because the studied pegmatites had low uranium (U) and thorium (Th) concentrations. In 2016, Thomas et al. [13] presented a study where the authors successfully employed radiometric data to define the pegmatitic zone. They used radiometric data from the Bird River belt, Manitoba, where numerous pegmatites outcrop, with Tanco pegmatite being one of them.

In parallel, remote sensing (RS) approaches have been fine-tuned to detect both surface LCT and NYF pegmatites [14–16]. The potential of RS data and image processing techniques and subsequent data integration in GIS for mineral exploration purposes was extensively reviewed by Rajesh [17], while limitations and difficulties related to pegmatite exploration have also been identified [18]. Rajesh [17] highlighted the importance of imaging spectrometry, also known as hyperspectral RS, to delineate prospective areas of interest using distinct absorption features that occur in most minerals. One methodology to analyze absorption features and understand the composition of the rock is to use reflectance spectroscopy, which can be measured in the field or in the laboratory [19–21]. This technique, associated with the pre-processing and processing and use of satellite images, can corroborate the

presence of critical minerals enriched in Li and related Li pegmatites. Several methodologies can be employed to identify the target minerals, such as comparing spectral data obtained in situ with theoretical reference spectral curves. The United States Geological Survey (USGS) [22] and ECOSTRESS [23] spectral libraries provide some reference spectral curves; however, they are not focused on providing spectra for all Li minerals [24].

Therefore, the joint use of RS, geophysical and geochemical data/techniques, and GIS analysis contributes to improving the knowledge of potential areas, reducing possible local impacts, and allowing the establishment of priorities with implications (i) on the investment to be carried out in the stages before the start of exploration; (ii) in the selection of the most eco-efficient technologies for blasting and ore treatment, preferably with no waste production; (iii) in the life cycle of the mining operation; (iv) in the value chain of extracted raw materials, respecting the Cleaner Production (CP) principles; and (v) in the selection of methodologies to be used either in the monitoring of environmental impacts or in their mitigation or remediation [17,25,26].

The work presented in this study is within the scope of the project INOVMINERAL4.0, funded by Portugal2020, Compete2020, Lisbon2020, and the European Regional Development Fund, whose overall objective is the innovation and reorientation of the industrial models that sustain the Mineral Resources Sector through the development of advanced technologies, new products, and software that respond to the entire value chain: prospecting and mineral research, integrated valorization of mineral resources, and gains in market share (<https://inovmineral.pt/>; accessed on 12 July 2023).

Specifically, this study focuses on the Aldeia LCT pegmatite dykes, located in the Barroso–Alvão pegmatite field, one of the most economically important fields in Iberia and Europe [1,27]. Considering the inherent costs of field campaigns to identify targets in situ, this study presents alternatives to traditional geochemical exploration, focusing on a preliminary evaluation of the spectral signature of targets, the subsequent RS approach, and geophysical surveys at a specific site to serve as an added value for future exploration studies. The large amount of data generated under the INOVMINERAL4.0 project require the development of an open-source GIS framework to spatially present all the information collected in the project. In recent decades, webGIS applications have been widely developed to dynamically represent variables [28]. In this work, the implementation of a webGIS platform was crucial for data storage, organization, and integration (<https://gis.fc.up.pt/INOVMIneral/index.html>; accessed on 12 July 2023).

Taking this into account, the following objectives were delineated: (i) evaluate the potential of high spatial resolution elevation data for subsequent exploration works; (ii) test geophysical exploration methods, namely, radiometry, and evaluate the potential to discriminate LCT pegmatites; (iii) present a methodology for obtaining reflectance spectral data on rock samples, culminating in the construction and availability of a spectral library that can be used in laboratory validation of field data, consequently stimulating the creation of other open access databases, in other locations; (iv) compare the spectra obtained with a satellite data from Landsat 9, evaluating the potential of this new satellite for mineral exploration; and (v) present a webGIS implementation under the INOVMINERAL4.0 project, to spatially represent the data acquired in the project and disseminate them to the public.

Therefore, several research questions were delineated in this study: (i) how is the acquisition of high spatial resolution elevation data relevant to pegmatite exploration?; (ii) is radiometry a useful geophysical exploration tool for LCT pegmatites?; (iii) can reflectance spectroscopy data be used as validation of an RS approach?; and (iv) is the new Landsat 9 data suitable for the identification of surface LCT pegmatites?

1.1. Study Area

The research area is located in the Ribeira de Pena region (Portugal), in an area known as Aldeia, where Li-bearing pegmatite resources are under study. The pegmatites are hosted by Silurian-age mica-schist in northern Portugal, more specifically within the Galicia-Trás-

os-Montes zone (Figure 1) [29–31]. These deposits have an inferred and indicated resource of almost 45,000 t of Li₂O [32].

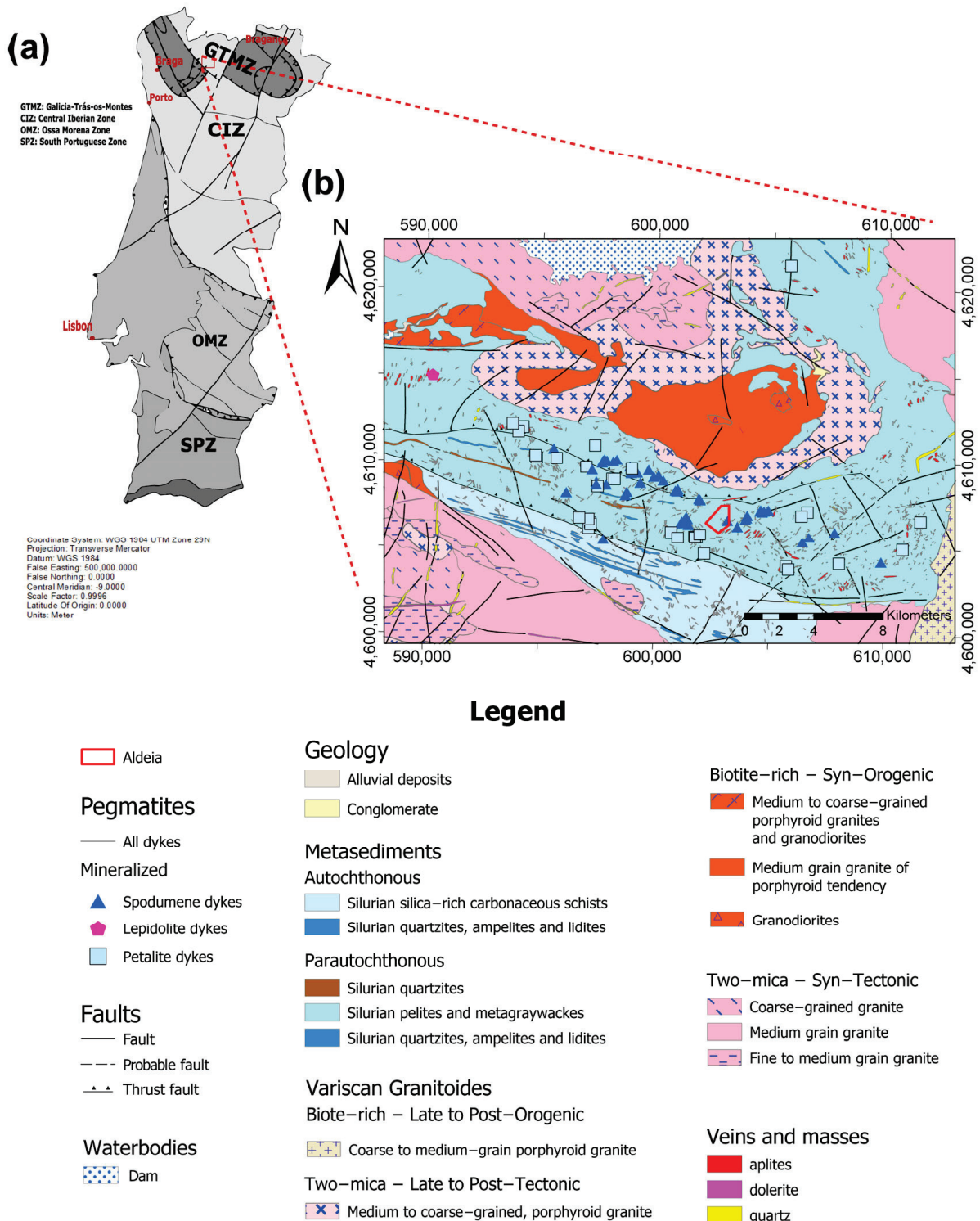


Figure 1. (a) The geotectonical map of Portugal, demonstrating that the study area belongs to the Galicia–Trás–os–Montes zone [29]; (b) geological setting of the study area from the Geological Map of Portugal at the scale 1:2,000,000, sheet 2 (<https://www.lneg.pt/en/product/geological-map-of-portugal-scale-1200-000/>; accessed on 28 May 2023).

The aplite–pegmatite dykes of the Barroso–Alvão pegmatite field were classified by Martins [33] and Dias [34] using the concepts of Černý and Ercit’s [35] classification as

belonging to the LCT family, subdivided into the complex type, spodumene sub-type, and petalite sub-type. The first type, namely, the spodumene complex type, is characterized by relatively high pressure (roughly 3 to 4 bar) crystallization, containing a significant amount of Li aluminosilicates and representing the most common category of the pegmatite complex type. The LCT family comes from a fractionated melt fractionation enriched in Li, Rb, Cs, Be, Ta, and Nb (Ta > Nb) and in large part in B, P, and F. There are three main sources for the LCT parental melt: (i) anatexis of metasedimentary and metavolcanic protoliths of the upper to the middle-underplated crust, (ii) a low percentage anatexis of meta-igneous rocks from the basement, or (iii) a mix of both [35,36].

A few thousand pegmatite bodies can be found at the Barroso–Alvão pegmatite field. Most of these bodies intrude on metasedimentary rocks, but barren ones can also be found intruding on the two mica granites and the biotite granites. The aplite–pegmatite bodies have different characteristics that enabled defining them into different groups [33]: (i) intragranitic pegmatites (the only group found intruding on granitic rocks); (ii) quartz–andalusite dykes, (iii) barren pegmatites, (iv) spodumene pegmatites, (v) petalite pegmatites, and (vi) lepidolite pegmatites, all intruding on metasedimentary rocks.

In general, the dykes are vertical, flat, or with a variable dip. They can appear as lenticular or with elongated shapes, in some cases outcropping more than 500 m along their strike. All aplite–pegmatite bodies are spatially associated with the two-mica peraluminous granites and Lima [30], which are considered syn-to-late-tectonic two-mica granites from the Cabeceiras de Basto complex and are genetically related to the Li aplite–pegmatite bodies [37].

The Li mineralization at the Barroso pegmatite field, which involves the Aldeia pegmatite (Figure 1), among others, occurs predominantly in the form of spodumene-bearing pegmatites, which are hosted by metapelites and mica schists.

The Aldeia pegmatite dyke corresponds to a moderately west-dipping tabular body defined over an area of 250 m N–S with a dip extent of 340 m [32]. At depth, the body appears to bifurcate. The thickness varies from 10 m to 45 m, mineralized across the full width. The main pegmatite extends to the surface and is visible in an outcrop over a portion of the deposit. The pegmatite is also exposed in a quarry in the central portion of the mine where the geometry of the main pegmatite is visible, allowing the use of RS data and techniques to acquire its spectral signature.

Regarding the petrographic study conducted by Vasques [31], it is generally possible to observe certain characteristics in the drill hole samples. Specifically, the white mica textures in the samples were lepidoblastic, suggesting a low-grade mylonite. Additionally, the andalusite had a poikilitic texture, indicating the possibility of rotation during growth, and apatites were located near the contacts with the pegmatite and had a detrital background.

2. Materials and Methods

2.1. Sample Collection

After careful selection, a total of 11 samples, representative of the pegmatite outcrops and metasedimentary host rocks, were collected on a field campaign between 19 and 20 of April 2021, performed on the Canedo-Covas Mining Lease Application integrated in the Savannah Resources PLC Barroso Lithium Project. The focus was the validation of the LCT–pegmatite Aldeia petrographic studies [31], specifically the spodumene mineralization on the target. The samples were collected where outcrops were accessible as shown in Figure 2, with two sampling profiles: the first with a northwest–southeast trend, and the second more along a northeast–southwest path.

The samples were divided into seven classes, including both pegmatite and metasedimentary host rocks, namely: (i) aplite–pegmatite; (ii) aplite–pegmatite with iron oxides; (iii) muscovite-schist; (iv) andalusite-schist; (v) metamorphic exudation quartz; (vi) aplite with iron oxides; and (vii) pegmatite with iron oxides. As aplite–pegmatite rocks of this region are very heterogeneous, sample types (i), (ii), (vi), and (vii) are representative of the pegmatite’s internal structure.

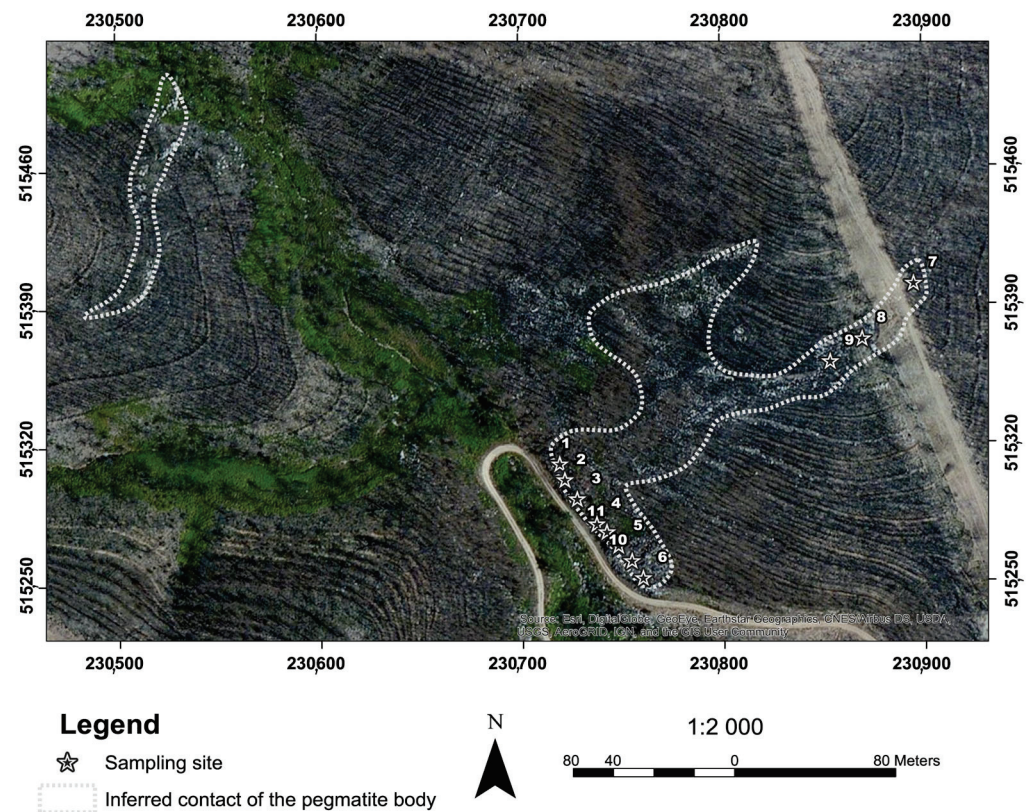


Figure 2. The zoomed map of the sampling area within the Aldeia pegmatite on the Mina do Barroso concession. The numbers represent the sample numbering.

2.2. Data Acquisition and Data Processing

2.2.1. Unmanned Aerial Vehicle (UAV) Surveys

A DJI Matrice 300 RTK Unmanned Aerial Vehicle (UAV) with a DJI L1 Light Detection and Ranging (LiDAR) sensor on board was used to acquire more detailed terrain information. LiDAR is an active remote sensing method that allows the acquisition of a point cloud through a sensor that scans targets using a pulsed laser acting as a transmitter, and an optics system that collects the reflected light and focuses it on a detector [38]. The UAV has an incorporated GPS (Global Positioning System)-RTK (Real Time Kinematic) sensor to estimate the position of the UAV/sensor system in real time. The system architecture consists of two or more satellite data receivers, with one of them being a stationary GNSS (Global Navigation Satellite System) station and the other a rover GNSS station, both sharing data via a radio channel to perform real-time positioning corrections. The technique is based on carrier-phase differential GPS positioning [39]. The Portuguese government, through a public institution called Direção-Geral do Território (DGT), created the ReNEP (Rede Nacional de Estações Permanentes GNSS), a public GPS/GNSS network of receivers installed across the country. In this study, the drone with the RTK was connected to the ReNEP Boticas GNSS station (closest ReNEP station), which uses a Leica GRX1200GG Pro receiver with a Leica AX1202GG antenna. To improve the positioning accuracy of the measurements, the L1 LiDAR has an Inertial Measurement Unit (IMU) integrated with an update frequency of 200 Hz.

2.2.2. Geophysical Surveys

To conduct the geophysical investigation, an Exploranium GR-320 enviSPEC Gamma Ray Spectrometer with a GPX-21A detector (SIAC Exploranium, Mississauga, ON, Canada) was used to measure the following levels: (i) total counts (ToT), (ii) potassium (K%), (iii) equivalent uranium (eU ppm) and, (iv) equivalent thorium (eTh ppm) emitted by the pegmatites and metasediments (mainly schists) in the study area. The system utilizes 256 or

516 channels and a high sensitivity 76 mm × 76 mm (3" × 3") detector with a NaI (Tl) (sodium iodide (thallium)) crystal and a resolution better than 9.0% FWHM (full width at half maximum) for Cesium-137. For each station, three measurements of 60 s were made, and the stations have a spacing of approximately five meters.

2.2.3. Spectral Data Acquisition and Processing

To build the spectral library, the 11 samples collected were previously dried at 50 °C in a muffle furnace for 24 h. The spectral data were collected on different faces of each sample, considering the visible changes in its composition [24].

The FieldSpec® 4 (ASD Inc., Boulder, CO, USA) spectroradiometer was used for data acquisition, with a wavelength range of 300 to 2500 nm, and a data collection time of 0.2 s per spectrum through a 1.5 m optic fiber beam with a 25° bare field of view that results in a 10 mm spot size when employing a contact probe with an internal light source. The equipment model has a spectral resolution of 3 nm @ 700 nm and 10 nm @ 1400/2100 nm. Before commencing the measurement, the spectroradiometer was turned on for 30 min due to the different temperature-related sensitiveness of the detectors, and the contact probe lens was sanitized with alcohol. To calibrate the equipment, a white reflectance plate was measured both at the beginning of the measurements and during the process (whenever the ASD ViewSpec Pro™ software (version 6.2., (ASD, Inc., Boulder, CO, USA) indicated this need.

In each analyzed sample point, an average of five measurements were performed with the ASD ViewSpec Pro™ software [40] to increase the signal-to-noise ratio, totaling 47 final (raw) spectra in the end. Moreover, for each analysis point, a photographic record was made together with a description of its characteristics.

Finally, each spectrum was submitted to a quality check through visual inspection using the SpectraGryph software (version 1.2) [41] and was subsequently processed with a Python routine to remove the continuum and extract the absorption features [24]. All results were inputted into the spectral library and the database was generated using the Microsoft Access (version 2108, Microsoft Corporation, Redmond, DC, USA) software.

2.3. Integration of Spectral Data through Satellite Image Processing

To validate the importance and added value of the spectral library built in this study, for mineral exploration, satellite data and image processing techniques were used to compare the spectra obtained in the laboratory and information obtained from RS data. By superimposing the satellite sensors' bands on key spectra, it is possible to identify the main absorption features and reflectance peaks in the visible and near-infrared (VNIR) and shortwave infrared region (SWIR) cross-referencing laboratory data with the spectral range of each satellite band and thus determine the most suitable ones to be used in satellite image processing.

Several satellite products are available for geological applications and pegmatite detection [18]. ASTER data were highly employed for mineral and lithological mapping, but due to failure in the SWIR module, only images acquired before 2008 can be used. Sentinel-2 data are being increasingly used, with the advantage of a medium-high spatial resolution, but with no thermal bands. In this study, Landsat satellite imagery, one of the most common satellites used for mineral exploration, was processed to identify possible pegmatite outcrops in the Aldeia pegmatite vicinities. Landsat 8 Operational Land Imager (OLI) was launched on 11 February 2013; it has 11 spectral bands including two thermal-infrared bands. The spatial resolution is 15 m and 30 m for the panchromatic and multispectral bands, respectively, while the spatial resolution of the thermal-infrared (TIR) bands is 100 m [42]. Landsat 9 data were also selected to assess the potential of this space dataset for mineral exploration, in general, and for pegmatite exploration, in particular. Landsat 9 has collected images of the Earth's surface since 31 October 2021. With a radiometric resolution of 14 bits, Landsat 9 can differentiate 16,384 shades of grey, allowing the sensors to detect more subtle differences on the Earth's surface. This radiometric improvement

makes Landsat 9 a powerful tool for lithological studies. Table 1 exemplifies the radiometric difference between Landsat 7 Enhanced Thematic Mapper Plus (ETM+), 8 (OLI), and 9 (OLI 2). Thus, Landsat data present a good compromise between spatial and spectral resolution and there is the opportunity to assess the differences between Landsat 8 and 9.

Table 1. Comparison of Landsat 9 with previous satellites of the Landsat program [26,43].

Parameter	Landsat 7 (ETM+)	Landsat 8 (OLI)	Landsat 9 (OLI 2)
Radiometric resolution (bit)	8 (256 shades)	12 (4096 shades)	14 (16,384 shades)
Temporal resolution (day)	16	16 *	16 *
Spatial resolution (m)	30 (VNIR)	30 (VNIR)	30 (VNIR)
	60 (TIR)	100 (TIR)	100 (TIR)
	15 (Panchromatic-PAN)	15 (PAN)	15 (PAN)
Number of bands	8	11	11

* The two satellites (Landsat 8-9) operating together increases the temporal resolution to 8 days.

Landsat images are available for download through the USGS Earth Resources Observation (Earth Explorer portal) and Science (EROS) Center [43].

Originally, this study intended to work only with the Landsat 8 image; however, the Landsat 8 image, acquired on 21 August 2018, was outdated compared with the mining exposition surface at the time of the fieldwork. Therefore, the Landsat 9 image, acquired on 28 January 2022, is more faithful to the current reality of the study area. As seen in Table 2, Landsat 8 and 9 have the same spatial (30 m ground sample distance, GSD) and spectral resolutions. The objective of image processing in this study was to practically demonstrate the applicability of spectral analysis in image processing.

Table 2. Information about the downloaded Landsat 8 and 9 images.

	Landsat 8	Landsat 9
Date acquired	2018/08/21	2022/01/28
Land cloud cover	0.03%	3.23%
Data type	OLI_TIRS_L1TP	OLI_TIRS_L1TP
Product map projection	UTM	UTM
DATUM	WGS84 Zone 29 N	WGS84 Zone 29 N

Among the available images, the ones with less cloud cover (less than 10%) were chosen for download. The images were pre-processed using the Semi-Automatic Classification Plugin (SCP) plugin (version 7.10.6) available in the QGIS software (version 3.22.1). The atmospheric correction method used was the Dark Object Subtraction (DOS 1) algorithm [44].

Regarding the methodological proceedings, first, the main absorptions and reflectance peaks were identified and analyzed based on the laboratory data, and the spectral mineralogy was identified by expert and literature-based knowledge [45,46]. After that, the main absorptions and reflectance features were compared with the spectral range of the satellite bands. Only the most significant spectrum of each sample was used in the analysis, totaling 10 spectra selected.

The processing method chosen to be applied in this study was the Principal Component Analysis (PCA), a multivariate statistical technique for dimensionality reduction, used to enhance and separate target spectral signatures from the background [47,48]. The number of components used to perform PCA depends on the objective criteria of the study or research. According to Johnson and Wichern [49], several criteria may be suggested regarding the number of components to retain in PCA, but no criterion is satisfactory for all situations. As the selective PCA on two components achieved the best results in previous studies of mineral exploration [50,51], for this work PCA was tested with two-band subsets. The criteria chosen to select the most adequate bands was a combination of a band with higher pegmatite reflectance and a band with lower pegmatite reflectance. Thus, the bands

used in this method were selected according to their spectral response compared with the rock samples from Aldeia pegmatite, namely: (i) PCA of bands 3 and 7; and (ii) PCA of bands 6 and 7. Taking into consideration that the host rock in the study area corresponds to schists and that this rock has a high reflectance in band 4 and a strong absorption in band 7 due to the Al-OH absorption feature at 2.20 μm , a third PCA of bands 4 and 7 was computed specifically for schist [52].

The step-by-step methodological processes and their integration for the identification of target minerals are explained in Figure 3.

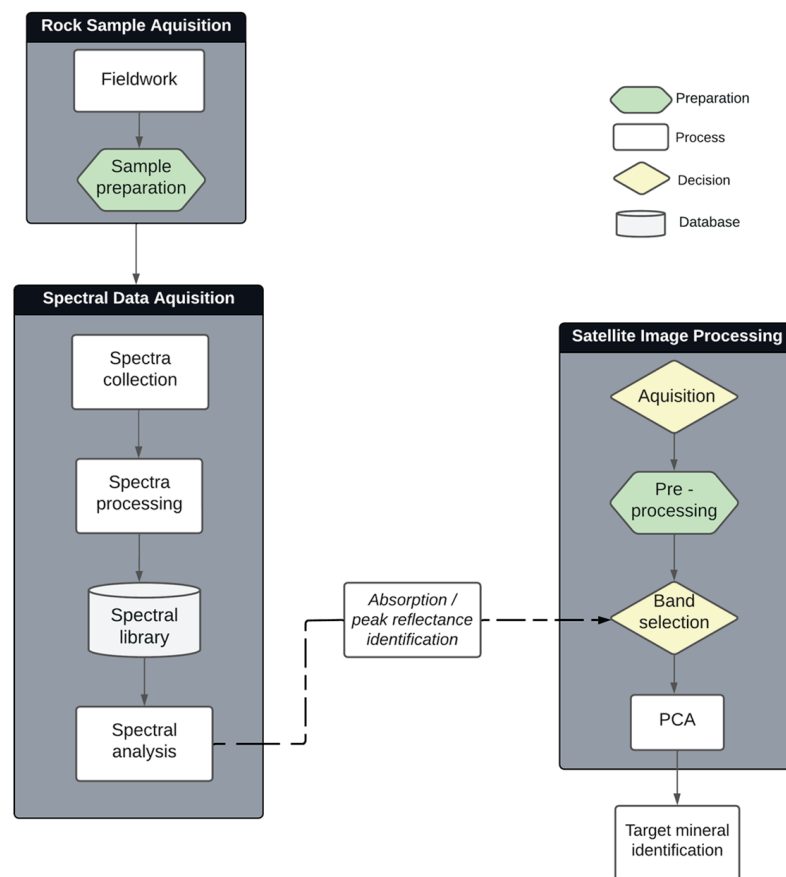


Figure 3. Methodology workflow, with methodological processes and their integration for the identification of target minerals.

3. Data Integration and Visualization in a WebGIS Platform

3.1. WebGIS

The webGIS platform was created using a web server (XAMPP), a popular PHP development environment (<https://www.apachefriends.org/>, accessed on 6 November 2022) that includes MariaDB, PHP, and Perl. XAMPP is an easy-to-install program in an open-source package [53]. To build interactive maps, Leaflet, an open-source JavaScript library designed for mobile-friendly maps was used (<https://leafletjs.com/>, accessed on 14 March 2023). Also, several Leaflet plugins hosted in GitHub were used, such as leaflet.ajax, which enables the retrieval of JSON data (<https://github.com/calvinmetcalf/leaflet-ajax>, accessed on 14 March 2023). These plugins allowed to insert geospatial information in the form of GeoJSON files, a format for encoding a variety of geographic data structures (<https://geojson.org/>, accessed on 14 March 2023). Thus, in this study, the vector files were displayed as GeoJSON files. For JavaScript functionality, jQuery, a user-friendly library compatible with multiple browsers was employed (<https://jquery.com/>, accessed on 14 March 2023). To ensure responsive and mobile-first design, we utilized Bootstrap, a

widely-used framework for developing websites (<https://getbootstrap.com/>, accessed on 14 March 2023).

The vector information in the platform was displayed as GeoJSON files in the World Geodetic System 1984 (WGS84; EPSG: 4326) coordinate system. Raster layers were integrated into the platform through the leaflet-geoserver-request plugin (<https://github.com/iamtekson/leaflet-geoserver-request>, accessed on 14 March 2023). The spectral library was represented as a points layer, where each point corresponds to a set of samples with valuable information. The point shapefile was converted to GeoJSON format using the L.geoJSON plugin from Leaflet. The properties of each point, including sample IDs, attributes, and photographs, are accessed and displayed through a popup tab created using HTML and JavaScript functions.

The webGIS is composed of five tabs: (i) the “webGIS” tab where the geospatial information is presented under a base map that can be chosen by the user; (ii) the “About the project” tab which presents some information about the project; (iii) the “Team” tab composed of information about the researchers of the project; (iv) the “Publications” tab with a list of publications (and respective links) produced under the project; and (v) the “Contacts” tab with a form to contact the researchers (Figure 4). It is also composed of standard tools, installed from the third-party leaflet plugins database (<https://leafletjs.com/plugins.html>, accessed on 14 March 2023), such as zoom in and out; search bar; measure tool; and the layers tab, which allows to activate or deactivate the visualization of the layers under a base map (Open Street Map, Topo Map, Imagery, or Watercolor; Figure 4).

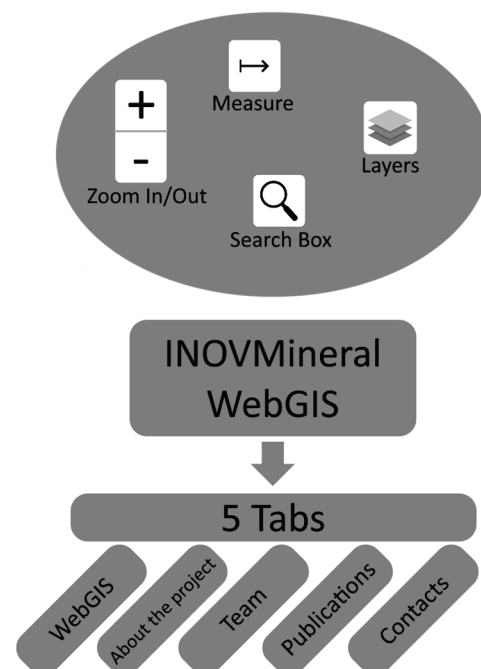


Figure 4. Flowchart with all the programming languages and libraries used in the webGIS implementation.

3.1.1. Digital Elevation Model (DEM)

The resulting LiDAR-derived ground points were used to create a Digital Elevation Model (DEM) with a 0.2 m spatial resolution. The RAW data generated by the sensor are in a DJI proprietary file format and was processed on the DJI Terra software to generate the LAS typical file format used in point clouds generated with laser scanning.

The raw point cloud obtained was in LAS format and had 245.620.454 points. The first processing step was to compress the LAS file into an LAS compressed format file (LAZ), which turned the 7.77 GB LAS point cloud into a 2.09 GB LAZ file using the las2las tool from LAStools software [54]. The resulting compressed point cloud was then processed with lasground and las2dem tools that are part of the software. The lasground tool uses an

algorithm proposed by Axelsson [55] for ground classification and bare-earth extraction. The las2dem tool uses Delaunay triangulation to convert the LAZ file into a temporary Triangular Irregular Network (TIN) and rasterizes the ground-resulting points using linear interpolation [56]. A hillshade model was generated from the DEM to better visualize the terrain. For public distribution and ease of visualization in the WebGIS platform, the original DEM was resampled to 10 m of spatial resolution.

3.1.2. Radiometry Data

Based on the radiometric measurements obtained, it was possible to generate maps of K, eTh, and eU, and the ratios eU/K, eTh/U, and eTh/eU. To produce those maps, the data were inserted into the ArcGIS Pro (Esri, Redlands, CA, USA) software. In the Geostatistical Wizard, the Simple Kriging algorithm was used to interpolate the data. Then, the Geostatistical Layer (GA Layer) for each element and ratios were exported to a contour layer and a 50 m buffer from each station was applied. To enhance visualization and to better integrate the data in the WebGIS, a GeoTiff was created with a spatial resolution of 2.5 m.

3.1.3. Spectral Data

The generated/processed products were organized in the spectral library, as described in Table 3. Considering the generated products, it is possible to perform several analyses, both on the raw spectrum and continuum removed spectra to identify the main absorption features and reflectance peaks. The database was intended to be freely used by researchers and industry professionals alike, as well as by any other mining or exploration stakeholders, and is distributed in the Zenodo platform [57].

Table 3. Description of the information contained in the spectral library [57].

Field Name	Description
ID	Primary key generated from Access software.
Sample_nr	Identification of the sample, represented by numbers from 1 to 11, for example: "INOV01", (...), "INOV11".
Spectrum_nr	Spectrum identification. The number indicated after the "_" represents the spectrum measured in each sample, for example, in sample "INOV01" four spectra were obtained, represented by "INOV01_1", (...), and "INOV01_4".
Locality	Place where the sample was obtained.
Sample_description	Geological description of the sample, considering visual aspects.
WGS84_Zone	UTM zone where the sample was extracted.
Latitude	Coordinate WGS84, where the sample was extracted (latitude).
Longitude	Coordinate WGS84, where the sample was extracted (longitude).
Preparation	Indication of the sample preparation routine.
Analysis	Equipment that was used in the spectrum collection.
Stored	Localization of the laboratory where the collection was carried out and where the samples are kept.
Face_color	Surface staining of the sample (visual observation).
Face_type	Type of sample face (visual observation). Ex.: exposed and sawn.
Photo	Photo indicating the area of the sample where the spectrum was collected (.jpg).
Raw_spectra	Raw spectrum collected (.txt and .pdf).
Processed_spectra	Processed spectrum, with removed continuum (.txt and .pdf).
Spectra_absorptions	Main absorption features automatically extracted (.png).
Spectral_mineralogy	Description of the sample considering the spectrally active minerals/compounds identified.

Because the data can be analyzed by different people with different backgrounds and potential uses, we prioritized data storage in a database, namely, a .accdb Access format (Microsoft Office), which holds files with different extensions (jpeg, .pdf, .txt, and .png, for example) as attachments, all within a single file. The database can be later connected to a Geographic Information System.

The database's structure logic allows representing each measured spectrum to be equivalent to a line, which details the storage of data/inclusion of more than one file in

each defined criterion and for the systematized/dynamized view of the characteristics of each sampled location. Therefore, all attributes related to each spectrum are represented as distinct database columns.

The spectral library was structured considering the analysis of two geologists who acted independently (to minimize subjectivity as much as possible) and by analytical results obtained from the spectroradiometer.

A first analytical approach was carried out based on the coloration of the sample, which allows for inferring possible mineralogical compositions. The results were compared with the spectroradiometer data and spectral curves were referenced, which show the expected trend in the spectral response of certain minerals [46]. Additionally, knowledge about the geological formation of the study area was considered to ratify the results obtained. This methodological systematization ensures that the available data resultant from this study are corroborated through different validation sources, minimizing the analytical subjectivity and allowing users to complement studies with new analysis criteria, if necessary.

4. Results and Discussion

4.1. UAV LiDAR

Processing the LAZ point cloud with *lasground* to classify ground points took 759.472 s on an AMD Ryzen 5 3600 6-Core Processor 3.60 GHz with 64 Gb of RAM and a Radeon RX 6700 XT MECH 2x 12G OC graphics card. The point cloud density was calculated using *lasinfo* (LAsTools) and resulted in a 636.55 points/m² density and an average distance between points of 0.04 m for the original point cloud file. The processed point cloud that was used to generate the DEM had a point density of 57.11 points/m² and an average distance between points of 0.13 m.

The resultant hillshade model is compared with the satellite imagery of the study area in Figure 5. It is possible to observe the topographic depression caused by a stream crossing the study area in green color (Figure 5b). The access road and the small exploration at the base of the hill are also visible, highlighting the mine face wall, expanding to the hill, below the drill core platforms, and a small portion of pegmatite outcrop in positive relief in the area where the access road bifurcates in the base of the hill. The minimum and maximum altitudes of the point cloud were 548.05 m and 650.07 m, respectively.

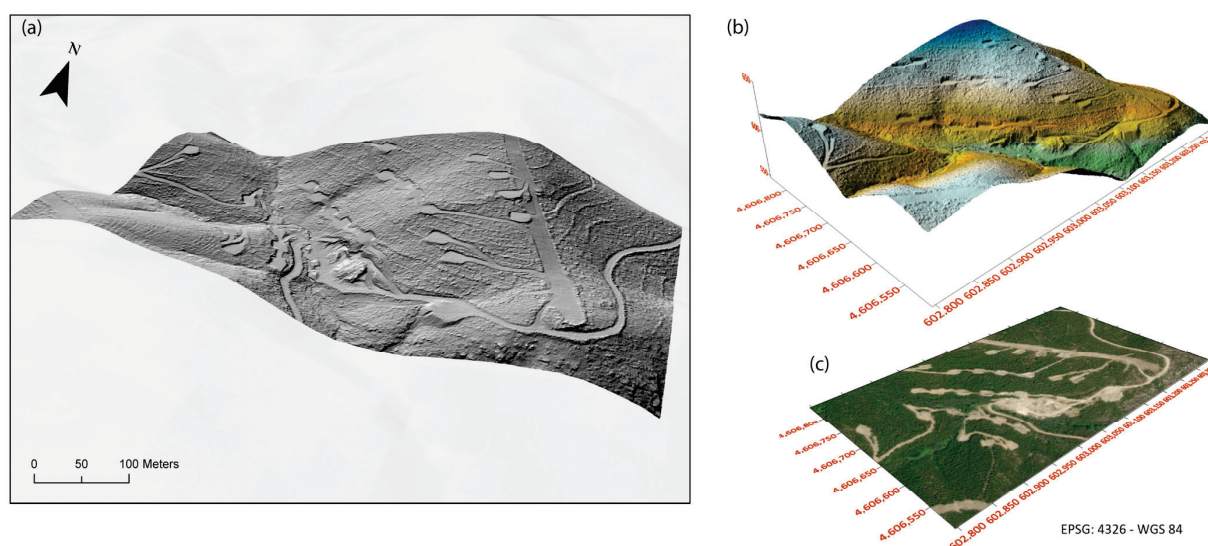


Figure 5. Stacked images created with ArcGIS Pro (version 3.0.0) and Surfer® (Golden Software, LLC, Golden, CO, USA): (a) hillshade image of the area draped over the terrain; (b) hillshade showing a slight coloration with the highest altitudes in blue color, lowest altitudes in green color, and intermediate areas in yellowish/orange color; and (c) ArcGIS World Imagery Basemap for comparison.

Although LiDAR sensors are a relatively new option for UAVs, this technology has been used since the 1960s [58]. The possibility of attaching the LiDAR sensor to a UAV provides a cost-effective way to carry out low-scale high-resolution laser altimetry in areas where airborne laser scanning would not be possible. In the case of this study, approximately 20 hectares of land were covered in under 15 min of flight, which highlights the advantages of using UAV-LiDAR.

4.2. Radiometry

After processing all radiometric data, it was possible to produce three maps. Figure 6 shows the eU map, Figure 7 the eTh map, and Figure 8 the eTh/eU ratio. The eU map shows higher concentration areas, which correspond with the pegmatites at the surface. The lower concentration corresponds to the host rock. The eTh map shows the opposite behavior, where the higher concentration corresponds to the host rock and the lower concentration corresponds to the pegmatites. The eTh/eU ratio allows us to better define the differences between the pegmatites (lower ratio) and the host rock (higher ratio).

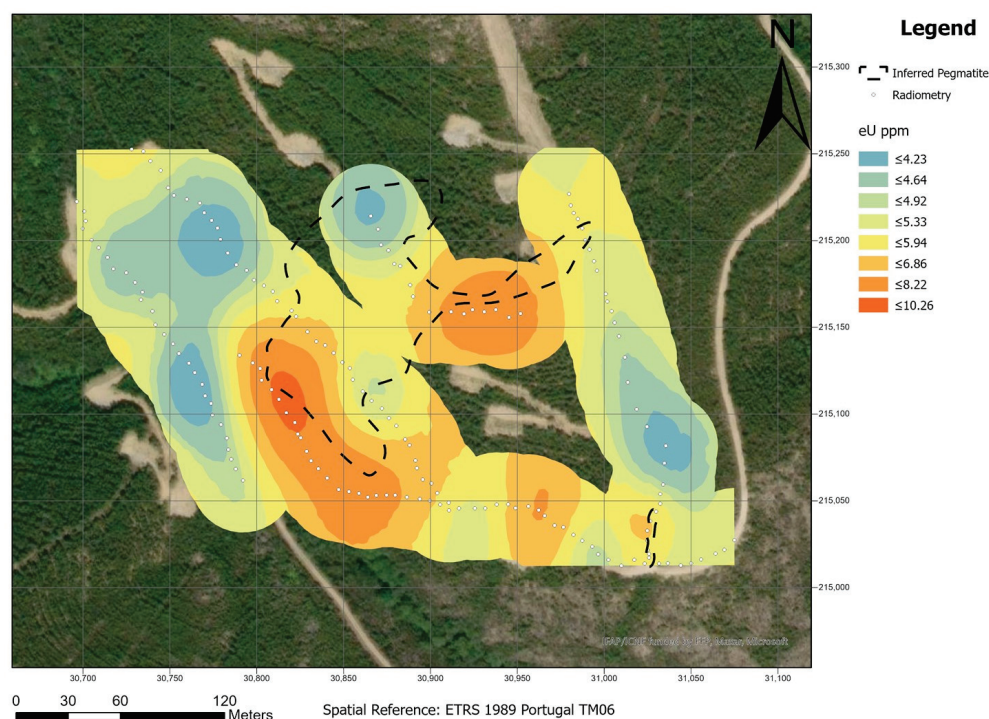


Figure 6. Map of equivalent uranium (eU) concentration in the Aldeia area. A 30 m buffer was applied to the Kriging interpolation.

In summary, the eTh map showed the worst correlation, while the eTh/eU ratio showed a good correlation with some of the outcropped pegmatites. The eU map presented the best results, where lower concentrations of eU are correlated with pegmatites.

The resolution in the depth of this method depends essentially on the energy, size, and charge of the different emission products and the density of the material that passes through. Gamma rays have the particularity that have no charge or mass, being able to penetrate much further. Even so, 90% of the gamma radiation detected via a radiometric survey will come only from 20 to 30 cm depth, and only 10% will come from below 50 cm [59,60]. Considering the results obtained in the Aldeia area, it is possible to say that radiometric data can be a good approach to complement other geological and geophysical studies. This is in agreement with previous findings in the Bird River belt, Manitoba [13]. However, the ability to discriminate the pegmatites from their host rocks depends primarily on the different lithologies found in the study area. Thus, as advised by Trueman [12], for this exploration method to be successful, a significant contrast between the U and Th contents

must exist. In the Aldeia area, the best radiometric responses are from the Th and the Th/U ratio. In the future, the potential of other geophysical methods for pegmatite detection will be tested in this region and in other European pegmatite fields.

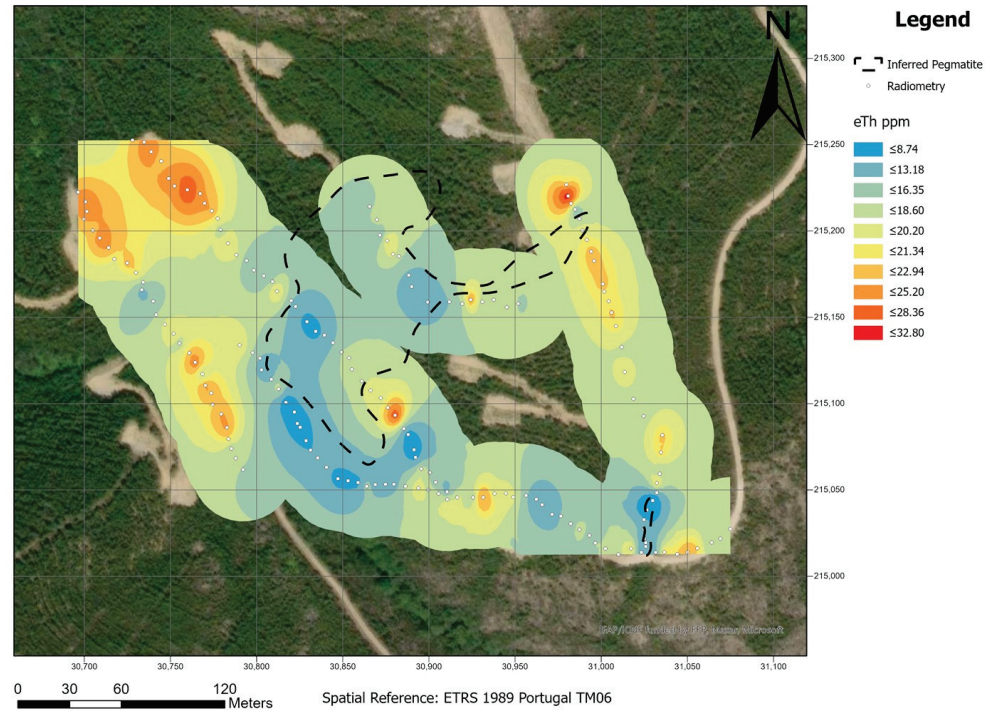


Figure 7. Map of equivalent thorium (eTh) concentration in the Aldeia area. A 30 m buffer was applied to the Kriging interpolation.

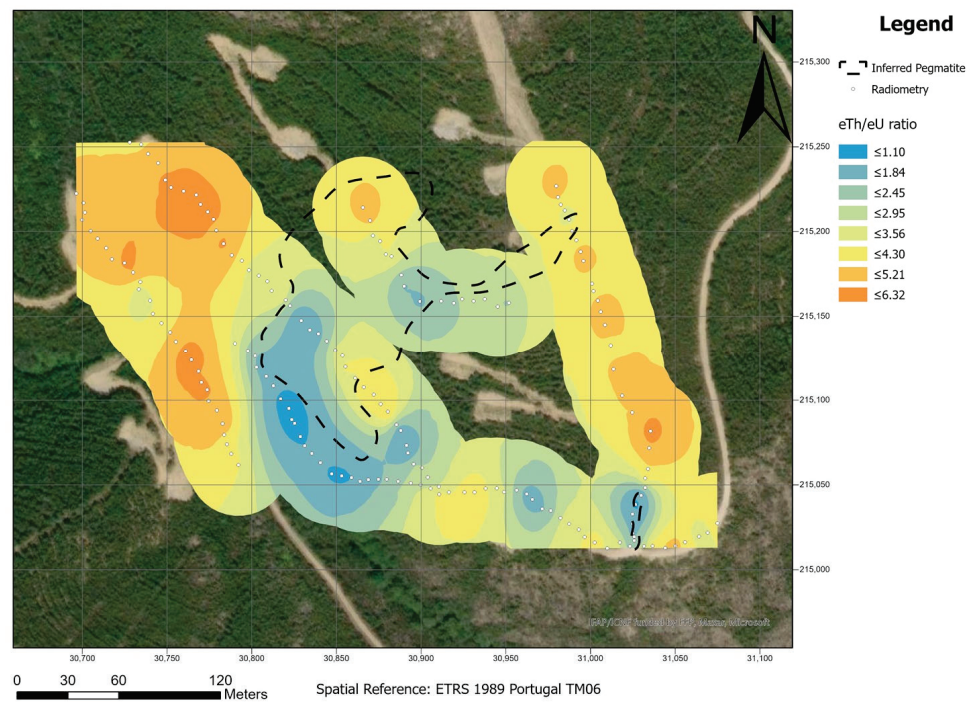


Figure 8. Map of equivalent thorium–equivalent uranium (eTh/eU) ratio on the Aldeia area. A 30 m buffer was applied to the Kriging interpolation.

4.3. Spectral Library

In the library created it is possible to access several files in different formats, including (i) a photograph of the location where the spectrum was collected within the sample (47 files in .jpeg format); (ii) the (raw) collected spectra consisting of the spectra for each sample, without any previous treatment (94 files with the same information, 47 of them in .txt format to import in any desired software and 47 in .pdf format for a quick preview of the resultant spectra, but in a vector format allowing the user to personalize the spectra plots); (iii) the processed spectra, consisting of the continuum removed files after computer processing (94 files with the same information, 47 in .txt and 47 in .pdf formats); and (iv) the extracted spectra absorptions, corresponding only to the most prominent (deep) features, resulting in 173 files in .png format with the different absorption bands of the samples. All the information recorded in the spectral library as well as a brief description of each field can be found in Table 3. Figure 9 shows an example of the graphical products available in the spectral library for consultation and analysis.

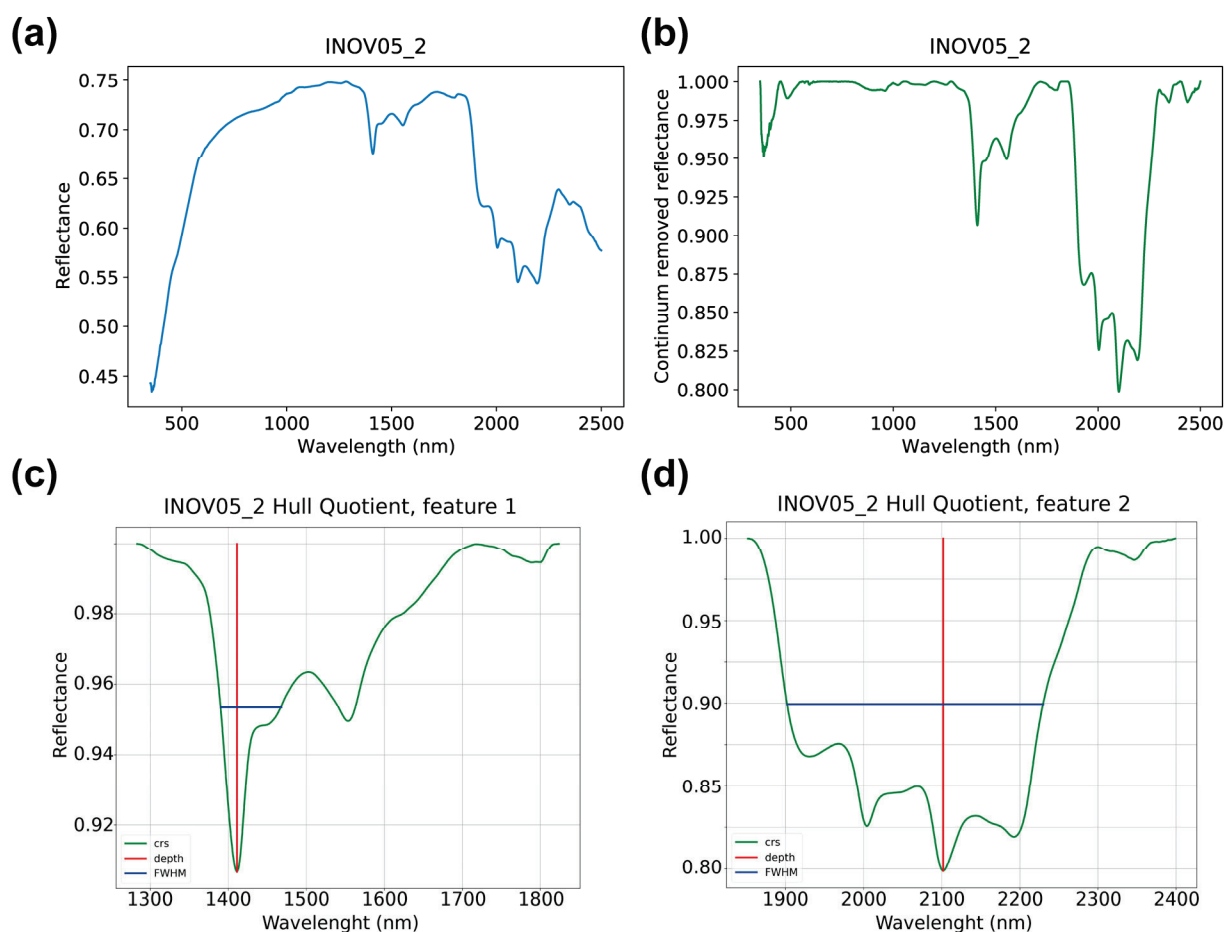


Figure 9. Example of the graphical products of the spectra INOV5_2, available in the spectral library, for consultation and analysis: (a) Raw_spectra; (b) Processed_spectra (with removed continuum); and (c,d) Spectra_absortions, with different wavelengths and depths, where crs is the continuum removed spectra, depth is the absorption depth, and FWHM is the full width at half maximum.

First, the user can preview and import to the software the (raw) original reflectance spectrum (Figure 9a). Then, the user can preview and import the already continuum-removed spectra represented in Figure 9b. In the end, for each spectrum, all major absorption features (continuum removed reflectance below 0.93) were automatically identified and extracted (Figure 9c,d) and provided in the database. In the case of Figure 9, the spectrum

was collected in an aplite–pegmatite sample, with the most prominent absorptions around ~1400 nm and ~2100 nm.

Considering the appearance of the sample, a first subjective analysis was performed to identify the minerals present in each sample, totaling seven classes as aforementioned (Table 4). Of the 47 spectra, 28 (59.57%) correspond to aplite–pegmatite samples with muscovite, plagioclase, and quartz in their composition; 9 spectra (19.15%) correspond to aplite–pegmatite samples with muscovite, plagioclase, quartz, and iron oxides identified; and 5 spectra (10.64%) were collected in aplite samples with plagioclase, quartz, spodumene, and iron oxides. These three classes alone represent 42 (89.36%) of all spectra collected and the minerals identified are congruent with those expected in the region, considering the local geological setting (Section 1.1).

Table 4. Sample and analysis following the content of the spectral database.

Sample Description	Number of Spectra	% of Spectra
Aplite–pegmatite with muscovite, plagioclase, and quartz	28	59.57
Aplite–pegmatite with muscovite, plagioclase, quartz, and iron oxides	9	19.15
Aplite with plagioclase, quartz, spodumene, and iron oxides	5	10.64
Muscovite-schist	2	4.26
Andalusite-schist	1	2.13
Exudation quartz	1	2.13
Pegmatite with iron oxides	1	2.13

4.3.1. Spectral Analysis

All 47 spectra were processed and analyzed to identify the most prominent absorption features and the corresponding spectral mineralogy. The spectral interpretation was achieved by analysis and comparison with the available literature [20–22,45,59]. In this study, the most representative spectra of each class were selected to exemplify the results. As can be observed in Figure 10, all spectra have one AIOH absorption feature around 2190 nm and two features around 2340 nm and 2440 nm. These features are present in the white mica group minerals, more specifically, in muscovite and illite. It is the presence of the AIOH secondary absorptions that, together with the symmetry and sharpness of the main AIOH absorption and absence of water features, are decisive for the distinction of these minerals.

The spectrum INOV09_03 has two iron features (680 nm and 880 nm), in addition to a reflectance peak at ~730 nm, indicating the possible presence of hematite in this sample (Figure 10a). Similar to the previous example, the spectrum INOV09_2 has the same absorptions and reflectance peak diagnostic of the presence of hematite (Figure 10b). The spectrum INOV09_01 (Figure 10c) also has diagnostic absorption features and reflectance peaks that indicate the presence of hematite (in the VNIR region). The weak to absent water absorption (~1904 nm), together with the AIOH absorption (~2194) and the double AIOH secondary absorptions at ~2340 nm and ~2430 nm, can confirm the presence of muscovite in this sample (Figure 10a,c). This is expected in spectra b and c (Figure 10b,c) since the schist hosting the pegmatites is expected to be more pelitic than psammitic, due to muscovite being an important rock constituent mineral. When looking at the sample photograph corresponding to spectra INOV09_03, it is possible to understand that due to the large 10 mm spot size, muscovite layers affected the overall spectral signature.

The spectra INOV11_2 (Figure 10d), INOV11_1 (Figure 10e), INOV08_2 (Figure 10f), and INOV04_3 (Figure 10g) have a more pronounced, asymmetric water absorption shorter than the main AIOH absorption that, together with the double AIOH secondaries at ~2340 nm and ~2430 nm, indicate the presence of illite in these samples. However, the similarity of characteristic absorptions of minerals from the white mica group in these mixed spectra made distinguishing between illite and muscovite challenging. Within the white mica group, muscovite was identified from the absence of other characteristic absorptions that are diagnostic to identify illite, such as the absence or very weak water

features [20,21,61]. On the other hand, illite shows a water absorption with a depth close to 1/3 of the depth of the main AIOH feature (Figure 10d,f) [20,21,61]. According to the analysis of the results, illite and muscovite can often appear mixed together (Figure 10g); or mixed with clays such as montmorillonite (Figure 10e) or kandite group minerals, due to the higher depth of the water feature when compared with the main AIOH absorption feature, or to the presence of an AIOH secondary triplet, respectively. In this spectrum, INOV04_3 (Figure 10g), the occurrence of iron oxides is confirmed by the presence of iron features in the VNIR region (~375 nm and ~500 nm). Furthermore, the spectral curve is characteristic of the presence of orthoclase, with the two absorptions, ~1410 nm and 1912 nm, possibly indicative of the presence of aqueous fluid inclusions [21].

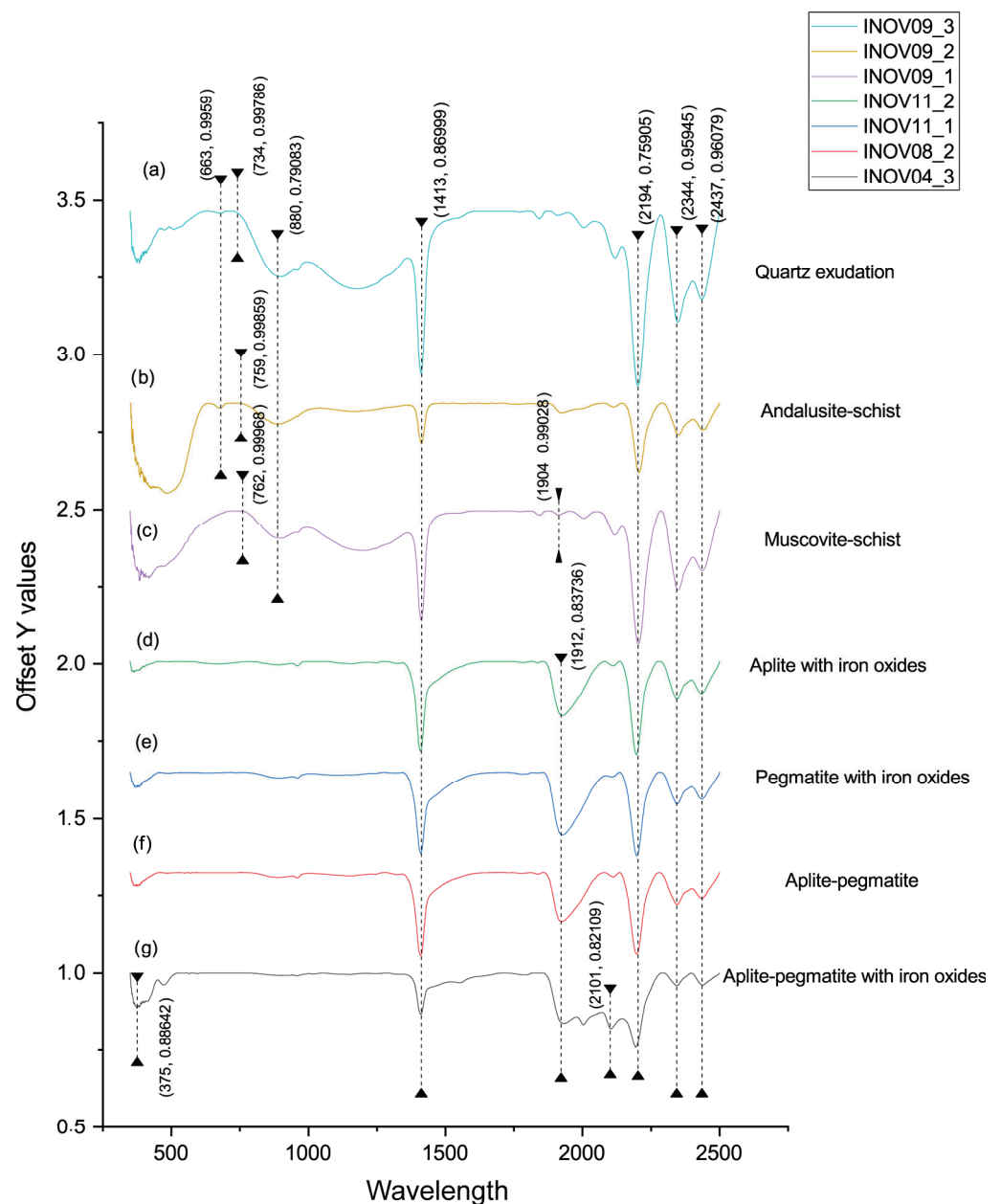


Figure 10. Diagnostic absorptions of the spectra of each class: (a) quartz exudation; (b) andalusite-schist; (c) muscovite-schist; (d) aplite with iron oxides; (e) pegmatite with iron oxides; (f) aplite-pegmatite; and (g) aplite-pegmatite with iron oxides.

The only Li-bearing mineral identified through its spectral features was cookeite, a Li-chlorite, due to the existence of two OH⁻ absorptions located at ~1574 nm and ~1834 nm, and a broad, asymmetric Mg-OH feature at ~2355 nm [20,21,61].

In general, the aplite-pegmatite samples can be well discriminated from the host rocks since the latter show very well developed and pronounced iron features in the VNIR region diagnostic of hematite.

4.3.2. Comparison of the Laboratory Spectra and Satellite Imagery

A comparison was made between the built spectral library and the Landsat 8 and 9 spectral resolution. This analysis was conducted in OriginPro software [62] (version 2022). Figure 11 shows an example using three aplite-pegmatite samples' spectra. This class was chosen because it is the most representative of the samples studied. It was observed that the laboratory spectra have three main absorption features located around 1400 nm, 1925 nm, and 2200 nm. This last absorption feature around 2200 nm is the most prominent, as it is the only one covered by a Landsat band (band 7, SWIR 2). Regarding the reflectance peaks, the most relevant band is band 6 (SWIR 1), which covers a faint reflectance peak occurring around 1600 nm. However, band 3 (green) and band 4 (red) also match with the high reflectance of the target under study. After this analysis, bands 3, 4, 6, and 7 were selected and assigned in the method described in the following steps.

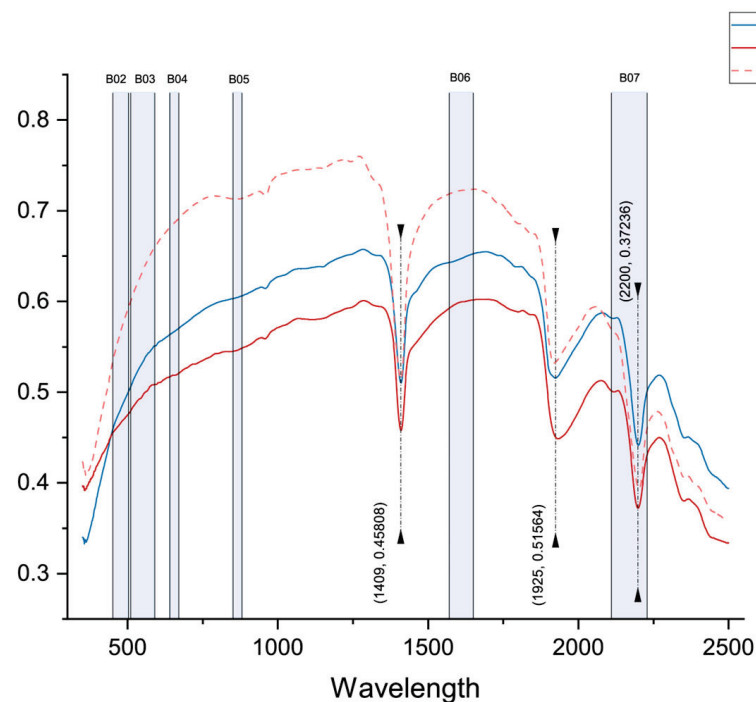


Figure 11. Absorption features and reflectance peaks of reference spectra from the samples of the Aldeia pegmatite. Three aplite-pegmatite spectra were used as examples. The blue rectangles represent the spectral range of the Landsat 8 and 9 bands superimposed on the raw spectra.

The available spectra (raw and with the continuum removed) allow the user to establish a relationship between the expected theoretical spectral curve and the empirical data obtained, which can favor more assertive prospecting processes through the selection of key satellite bands.

4.3.3. Principal Components Analysis (PCA)

To validate the spectral library built in the scope of INOVMINERAL4.0, information from the new Landsat 9 satellite was analyzed to evaluate its possible use for the delineation of LCT pegmatite prospective areas. The results confirm the high added value of such a

spectral database in the identification of outcropping pegmatites and the success of the combined approach presented in this work. Thus, the satellite data allowed for complementary analyses that can assist in the identification of LCT pegmatites, decreasing in situ campaigns, and optimizing human and financial resources and time. It is worth noting that there are limitations in the use of satellite data, especially concerning their spatial resolution (30 m GSD), which limits areas with low exposure to be captured in at least one sensor pixel, together with a high vegetation cover, and the fact that pegmatite bodies many times are smaller than the pixel size. However, the proposed method is extremely well adapted and can be applied to other study areas. The results can be used for several exploration purposes such as the identification of new points of interest for exploration. Nonetheless, the mentioned limitations, especially when it comes to spatial resolution, can be complemented with more specific methodologies, such as the use of UAVs.

The tested PCA two-band subsets highlight the pixels of aplite–pegmatite with high values which are represented in bright white color. The other elements of the study area like vegetation and water are represented in shades of grey. In previous studies [15,63], PCA stood out for being able to identify the areas of interest with fewer false positives than other classical processing methods such as RGB combinations and band ratios.

Taking this into account, PCA 6,7 was able to identify the other mining areas of the Barroso–Alvão pegmatite field, namely Lousas, NOA, and Alijó. Those are known LCT-pegmatite targets within a radius of 10 km of the Aldeia deposit. But the method was not successful in identifying the area of the Aldeia pegmatite. The PCA 3,7 and 4,7 methods obtained very similar results and were able to highlight the known pegmatites in the study area including the Aldeia pegmatite (Figure 12). False positives occur on some roads and in urban areas for all PCA methods tested, but PCA 3,7 has fewer false positives.

The respective eigenvalues and eigenvectors are represented in Tables 5–7. If the eigenvector values are positive in the highly reflective bands and negative in the absorption bands, the target is identified by bright pixels [25,64]. When the eigenvector values are inverted, i.e., when the band that should reflect is negatively valued in the matrix and the band that absorbs is positively valued, it is possible to multiply the image by (-1) . This makes the targets appear in bright pixels instead of dark [47,65]. The PCA that needed to be multiplied by (-1) was the PC2 resultant from the PCA of bands 6 and 7 for both Landsat 8 and 9 satellites.

Of all PCA methods tested in this work, the first PC (PC1) is the one that explains the most variance percentage contained in the results. The highest variance, i.e., the highest percentage of information belongs to PC1 of Landsat 9 bands 6 and 7 (99.25%). Similar to Landsat 9, the PCA with the highest variance result for Landsat 8 is PC1 from bands 6 and 7 (98.38%). When comparing the results of the two satellites, it is possible to see that Landsat 9 achieved higher variance values than Landsat 8.

Figure 12a,e represents the raster result of the PC1 generated from the PCAs. As we can see, the PCA of bands 6 and 7, besides obtaining the highest variance, also managed to highlight points of known pegmatites in bright colors and with little false positives in relation to the background. It is notable that in all PCAs tested, in both satellites, the Aldeia pegmatite has very similar values to roads and urban areas. This generates false positives that can interfere negatively with the result analysis. To further highlight the pegmatites in the study area a categorization can be carried out, where red is assigned to the pixel value range of the known pegmatite areas (Figure 13).

In the end, the adopted methodology served to evaluate the potential of the Landsat 8 and 9 satellites, with the PCA results, based on the subsets resultant from the comparison with the laboratory reference spectra, proving that this new satellite can be efficient for LCT pegmatite exploration. This potential use and the success of the combined approach are corroborated by the correct identification of known LCT pegmatite targets. However, considering the available spatial resolution of the satellite data (e.g., the Landsat 8/9 spatial resolution), the LCT pegmatites must present a good explosion so that this approach is relevant for other users and mining stakeholders. Nevertheless, it is notable that despite

the limitation in spatial resolution of the data, the method was able to identify the Aldeia pegmatite which does not have large dimensions when compared with the Landsat 8/9's pixel size. Regarding the spatial limitation, it can be avoided using spectral unmixing-based methods [66] or minimized considering the combination of complementary techniques, using a combined approach with other sensors with higher spatial resolution, such as UAV, and in situ data collection, depending on the financial and human resources for its execution.

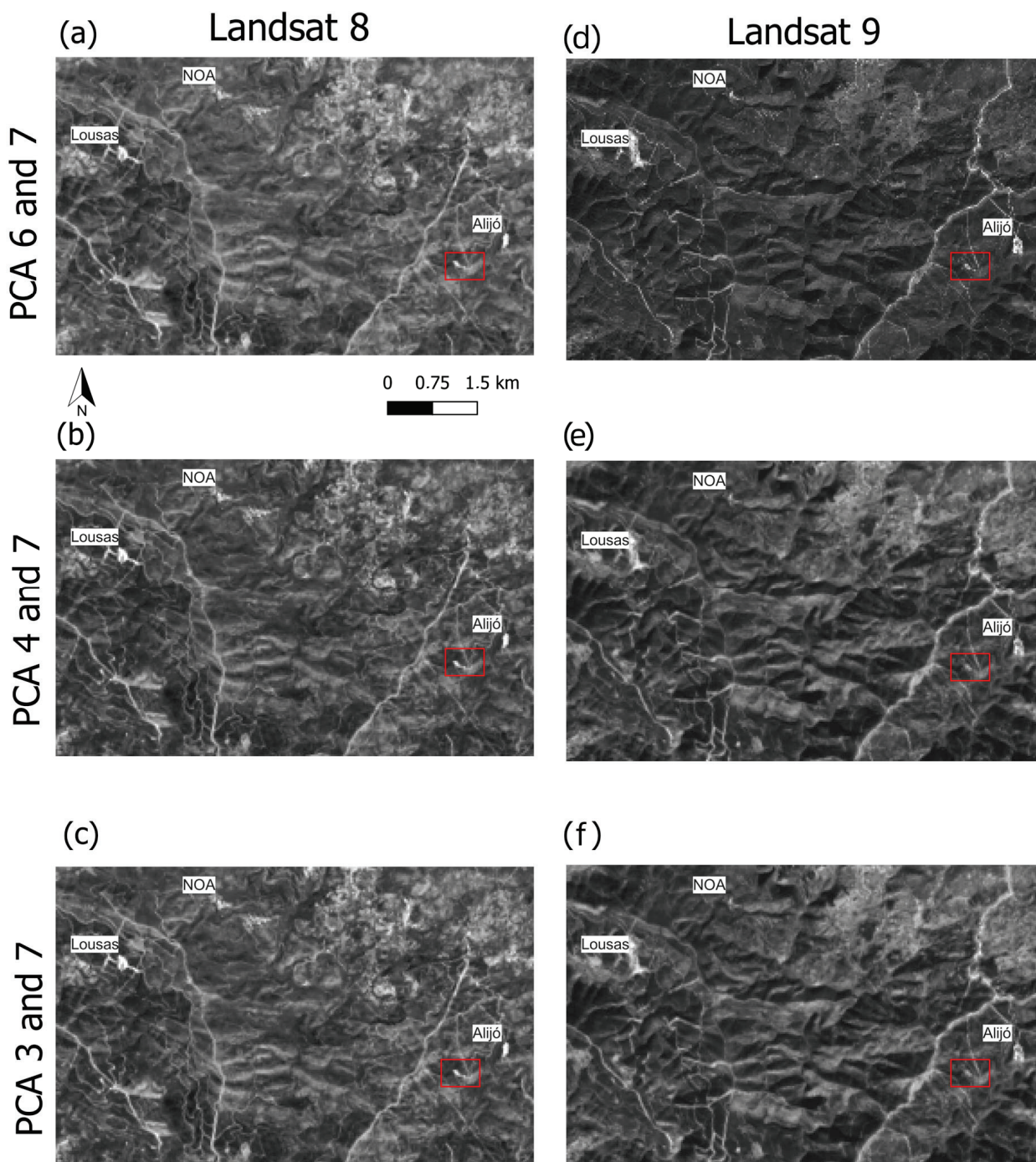


Figure 12. PCA result for Landsat 8 and 9. The Aldeia pegmatite is highlighted by the red rectangle. (a) PCA of bands 6 and 7 for Landsat 8. (b) PCA of bands 4 and 7 for Landsat 8. (c) PCA of bands 3 and 7 for Landsat 8. (d) PCA of bands 6 and 7 for Landsat 9. (e) PCA of bands 4 and 7 for Landsat 9. (f) PCA of bands 3 and 7 for Landsat 9. Other pegmatite occurrences are highlighted in the figure.

Table 5. Matrix of eigenvectors extracted after calculating the PCA on bands 6 and 7.

	LC08		LC09		Variance (%)	
	Band 6	Band 7	Band 6	Band 7	LC08	LC09
PC 1	−0.806750	0.590892	−0.835940	0.548820	98.38	99.25
PC 2	−0.590892	−0.8067501	−0.548820	−0.835940	1.61	0.75

Table 6. Matrix of eigenvectors extracted after calculating the PCA on bands 3 and 7.

	LC08		LC09		Variance (%)	
	Band 3	Band 7	Band 3	Band 7	LC08	LC09
PC 1	0.278870	−0.96032	0.278979	−0.960297	98.27	98.80
PC 2	0.960328	0.278870	0.960297	0.278979	1.72	1.20

Table 7. Matrix of eigenvectors extracted after calculating the PCA on bands 4 and 7.

	LC08		LC09		Variance (%)	
	Band 4	Band 7	Band 4	Band 7	LC08	LC09
PC 1	0.434049	−0.900889	0.398671	−0.917093	97.73	98.45
PC 2	0.900889	0.434049	0.917093	0.3986717	2.27	1.55

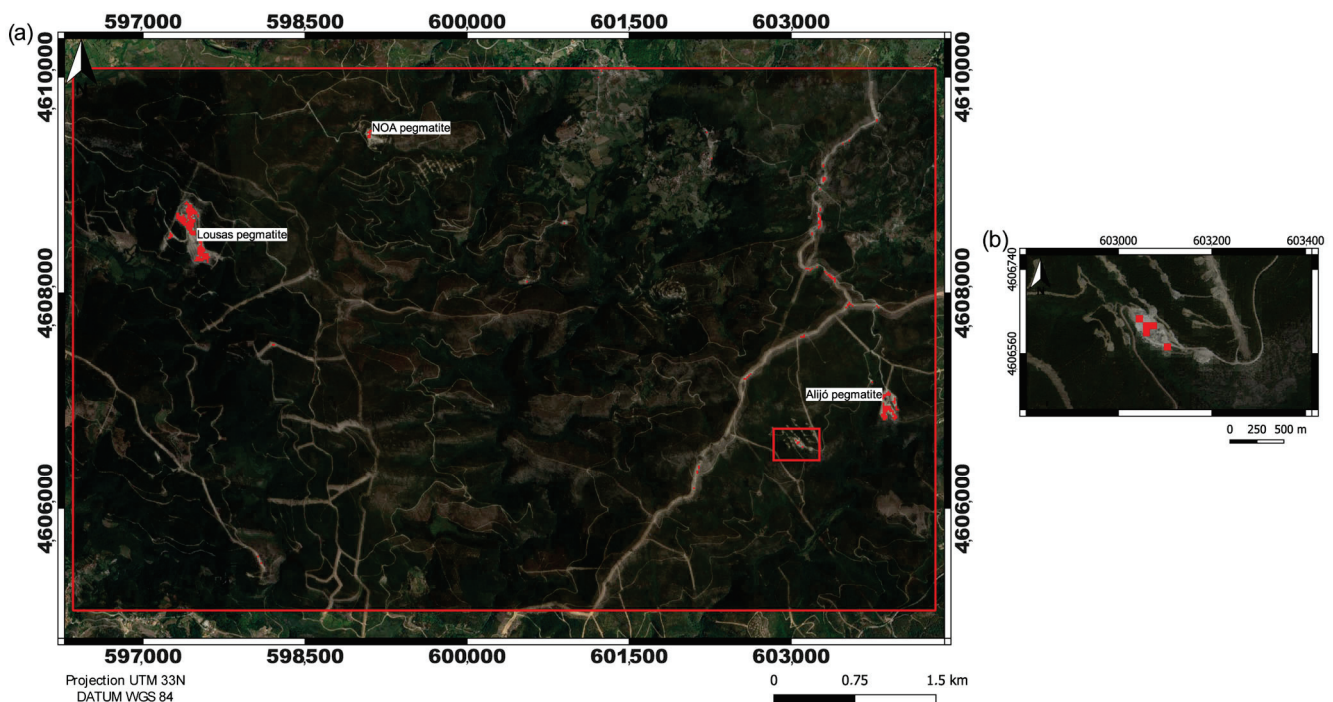


Figure 13. Result for PCA on bands 3 and 7 for Landsat 9. (a) The Aldeia mining area is highlighted by the red rectangle. The pixels of aplite–pegmatite are highlighted in red, showing that the method was accurate in other known target locations apart from the training area (e.g., Lousas, NOA, and Alijó). (b) Aldeia mining area in focus. Pixels of aplite–pegmatite are highlighted in red.

4.4. WebGIS

In this study, the results were presented in a new and intuitive webGIS developed under the scope of the INOVMINERAL4.0 project (<https://gis.fc.up.pt/INOVMIneral/index.html>; accessed on 12 July 2023). The data can be disseminated to any user, with tools that can help to analyze the information provided. The webGIS platform provides free access to any user and can help with management decision making.

The webGIS platform is composed of five tabs (Figure 14): (i) the “webGIS” tab where the geospatial information is presented under a base map; (ii) the “About the project” tab which presents some information about the project; (iii) the “Team” tab composed of information about the researchers of the project; (iv) the “Publications” tab with a list of publications (and respective links) produced under the project; and (v) the “Contacts” tab with a form to contact the researchers.

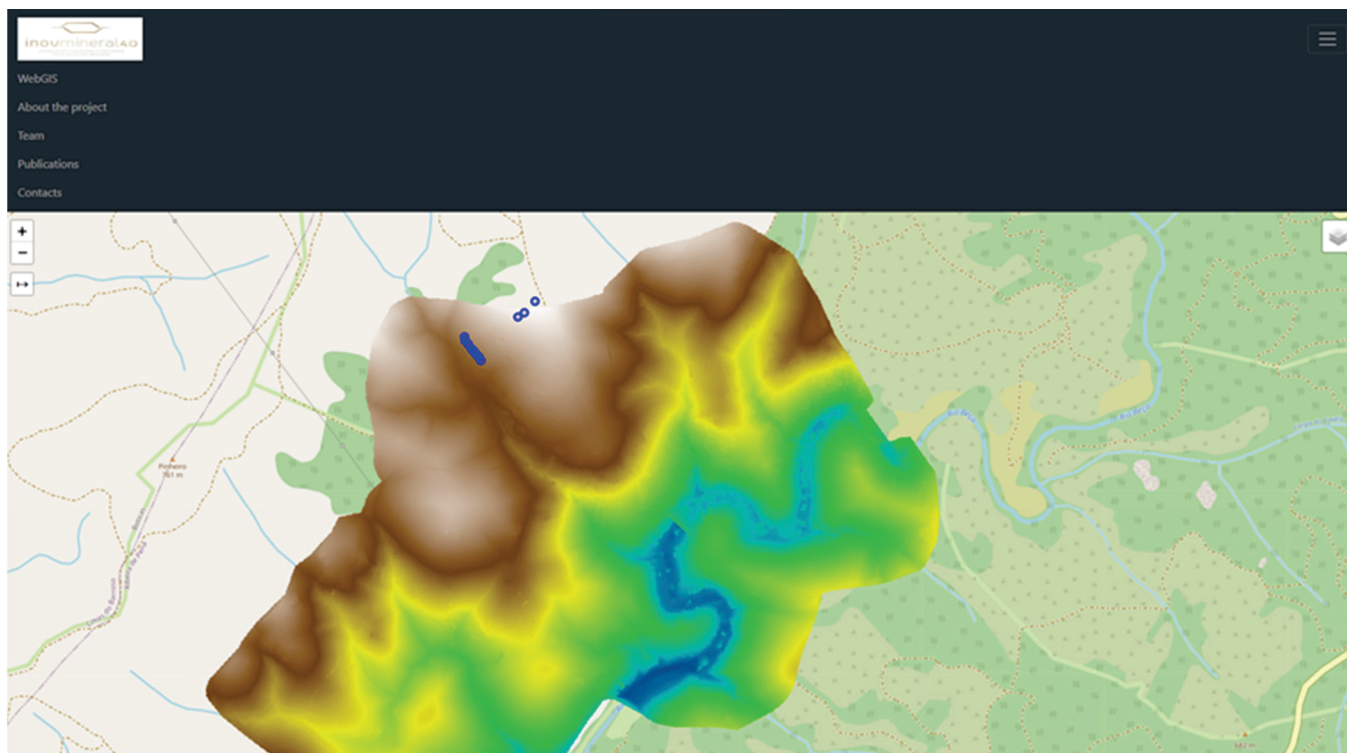


Figure 14. Preview of the webGIS interface and respective tabs (top left corner). The map view shows the created DEM with an elevation ramp (low altitude in blue; high in light brown) and the sampling sites (blue dots) previously shown in Figure 2. For each spot, the content of the spectral database can be previewed in an interactive way (Figure 15).

The development of a user-friendly webGIS platform allows users to dynamically visualize and analyze the data related to (i) LiDAR-derived DEM of the area; (ii) gamma-ray spectrometry maps; (iii) reflectance spectroscopy data of the Aldeia pegmatite and host rocks; and (iv) processed satellite images for LCT pegmatite exploration. Figure 15 presents the content of the spectral library provided interactively through popups in the webGIS platform.

In the future, the webGIS platform will incorporate more tools to manipulate the data as well as implement a better and more effective presentation of the spectral library.

1	2	3	4	5
---	---	---	---	---

ID: 1

Sample Number: INOV01

Spectrum Number: INOV01_1

Face Color: White and yellowish

Face Type: Exposed

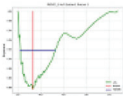
Sample_description: Aplite-Pegmatite/ muscovite, plagioclase, quartz

Spectral_m: Sericite/white mica

Photo:



Spectra_ab:



Spectra_1:

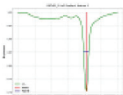


Figure 15. Example of the popup interface of the spectral library. This example corresponds to ID1 from sample number 1 (composed of 5 IDs, each ID respects a different spot analyzed within the sample).

5. Conclusions

The present research summarizes the contributions of the INOVMINERAL4.0 project for LCT pegmatite exploration by studying the spectral and geophysical properties of the Aldeia pegmatite in one of the most important pegmatite fields in Iberia and Europe. After data interpretation and result integration in a GIS environment, with enhanced visualization through the implementation of a webGIS platform, it was possible to evaluate the potential of non-destructive exploration techniques such as geophysical radiometrics and remote sensing. Thus, the objectives of this study were accomplished, namely:

- i. The obtention of high spatial resolution elevation data, such as a LiDAR-derived DEM, can be very helpful in understanding pegmatite outcrop distribution and is a fundamental base layer to overlay other kinds of data.
- ii. The acquisition of radiometric data through geophysical techniques can be a good approach to discriminate pegmatites and their host rocks, if their radiometric differences occur in a magnitude sufficient to be detected. Future studies must evaluate the penetration depth of this technique to detect buried pegmatites. Other geophysical techniques should be applied.

- iii. A successful methodology was proposed to structure the reflectance spectroscopy data into a spectral library, with freely available public access data that can even serve as a source of validation in new scientific studies.
- iv. The spectral library proposed in this study proved to be of high added value for space-based exploration. The superposition of the Landsat 9 bands over the selected reference spectra of distinct aplite–pegmatite samples allowed the selection of the best satellite bands for further testing.
- v. The performance of Landsat 9 and Landsat 8 data were compared. At the same time, the potential use of the spectral library and the success of the combined approach (comparison with satellite data spectral resolution) were positively evaluated with the correct identification of known LCT pegmatite targets.
- vi. The development of a user-friendly webGIS platform allowed data integration and visualization, as well as data sharing and dissemination to aid potential users in similar approaches.

It is intended that the data generated in this study, both those available in the spectral library and webGIS platform or the proposed multidisciplinary methodology, will stimulate scientific production elsewhere and contribute to meeting the available data needs regarding LCT pegmatite exploration. Nonetheless, it should be noted that in-depth and strategic knowledge of the methodology may be critical for expanding the study to other sites and detecting more LCT dykes.

Author Contributions: Conceptualization, J.C.-F., A.L., D.S., C.R.d.A. and A.C.T.; methodology, J.C.-F., D.S., C.R.d.A., R.R., A.A., L.D., R.M., A.L. and A.C.T.; software, J.C.-F., D.S. and L.D.; validation, J.T.V., A.M., D.S., C.R.d.A. and J.C.-F.; formal analysis, J.C.-F., D.S., C.R.d.A., R.M., R.R., A.A., J.T.V. and A.M.; investigation, J.C.-F., D.S., C.R.d.A., R.R., A.A., J.T.V. and A.M.; resources, A.L., R.M., J.T.V., R.R., A.A. and A.C.T.; data curation, J.C.-F. and C.R.d.A.; writing—original draft preparation, J.C.-F., D.S., C.R.d.A., R.R., A.A., J.T.V., A.M. and L.D.; writing—review and editing, J.C.-F., D.S., C.R.d.A., A.L. and A.C.T.; visualization, D.S., C.R.d.A., R.R., A.A., J.T.V., L.D. and J.C.-F.; supervision, R.M., A.L., A.C.T. and J.C.-F.; project administration, A.L. and A.C.T.; funding acquisition, A.L. All authors have read and agreed to the published version of the manuscript.

Funding: The authors acknowledge the support provided by Portuguese national funds through the FCT—Fundação para a Ciência e a Tecnologia, I.P. (Portugal) projects UIDB/04683/2020 and UIDP/04683/2020 (Institute of Earth Sciences), and through ANI and COMPETE 2020, as well as European funds through the European Regional Development Fund (ERDF) with the POCI-01-0247-FEDER-046083 INOVMINERAL project. Douglas Santos was financially supported by Portuguese national funds through FCT (Grant: UI/BD/154412/2023). Ricardo Ribeiro is financially supported by FCT within the compass of his Ph.D. thesis, ref. SFRH/BD/140266/2018. C.R.d.A. was financially supported by Portuguese national funds through FCT (Grant: PRT/BD/153518/2021). The spectroradiometer equipment was purchased under the European Commission’s Horizon 2020 innovation programme under grant agreement no. 869274, project GREENPEG New Exploration Tools for European Pegmatite Green-Tech Resources.

Data Availability Statement: The spectral library is publicly archived and published in the Zenodo platform <https://doi.org/10.5281/zenodo.7313964> (accessed on 5 June 2023) under a Creative Commons Attribution 4.0 International License. The raw Landsat 9 images are available upon querying at the Earth Explorer portal, a USGS data portal to obtain Satellite Earth imagery across existing geospatial data types available at <https://earthexplorer.usgs.gov/> (accessed on 14 January 2023). The processed Landsat 9 images presented in this research are available upon request during the first stage of the project and then publicly available at the end of the project in a WebGIS platform. The satellite image was processed using the QGIS open-access software, licensed under a Creative Commons Attribution-ShareAlike 3.0 license (CC BY-SA). Spectra continuum removal and absorption extraction were accomplished with a Python routine publicly available at <https://www.mdpi.com/2306-5729/6/3/33/s1> (accessed on 13 July 2023), © Copyright 2021 by Cardoso-Fernandes, J.; Silva, J.; Dias, F.; Lima, A.; Teodoro, A.C.; Barrès, O.; Cauzid, J.; Perrotta, M.; Roda-Robles, E.; and Ribeiro, M.A., under a Creative Commons Attribution (CC BY) license, based on the PySptools open-source Python library, © Copyright 2013–2018, Chris-

tian Therien, licensed under an Apache License Version 2.0. and available on GitHub repository <https://github.com/ctherien/pysptools> (accessed on 10 January 2023).

Acknowledgments: The authors thank Savannah Resources PLC for access to the Aldeia pegmatite and for providing the samples used in this study.

Conflicts of Interest: The authors declare no conflict of interest. The funders had no role in the design of the study; in the collection, analyses, or interpretation of data; in the writing of the manuscript; or in the decision to publish the results.

References

- Gourcerol, B.; Gloaguen, E.; Melleton, J.; Tuduri, J.; Galiegue, X. Re-assessing the European lithium resource potential—A review of hard-rock resources and metallogeny. *Ore Geol. Rev.* **2019**, *109*, 494–519. [\[CrossRef\]](#)
- Blengini, G.A.; Latunussa, C.E.L.; Eynard, U.; Torres de Matos, C.; Wittmer, D.; Georgitzikis, K.; Pavel, C.; Carrara, S.; Mancini, L.; Unguru, M.; et al. *Study on the EU's List of Critical Raw Materials Final Report*; European Commission: Brussels, Belgium, 2020.
- Müller, A.; Reimer, W.; Wall, F.; Williamson, B.; Menuge, J.; Brönnner, M.; Haase, C.; Brauch, K.; Pohl, C.; Lima, A.; et al. GREENPEG—Exploration for pegmatite minerals to feed the energy transition: First steps towards the Green Stone Age. *Geol. Soc. Lond. Spec. Publ.* **2022**, *526*, SP526-2021-189. [\[CrossRef\]](#)
- Steiner, B.M. Tools and Workflows for Grassroots Li–Cs–Ta (LCT) Pegmatite Exploration. *Minerals* **2019**, *9*, 499. [\[CrossRef\]](#)
- Galeschuk, C.R.; Vanstone, P.J. Exploration techniques for rare-element pegmatite in the Bird River greenstone belt, south-eastern Manitoba. In Proceedings of the Exploration 07: Fifth Decennial International Conference on Mineral Exploration, Toronto, ON, Canada, 9–12 September 2007; pp. 823–839.
- Kaeter, D.; Menuge, J.F.; Harrop, J. Stream sediment geochemistry for regional prospectivity analysis: Tin, cesium, tantalum and tungsten anomalies in Leinster, Southeast Ireland. In Proceedings of the 15th SGA Biennial Meeting, Glasgow, UK, 27–30 August 2019; pp. 1228–1231.
- Fyzollahi, N.; Torshizian, H.; Afzal, P.; Jafari, M.R. Determination of lithium prospects using fractal modeling and staged factor analysis in Torud region, NE Iran. *J. Geochem. Explor.* **2018**, *189*, 2–10. [\[CrossRef\]](#)
- Saadati, H.; Afzal, P.; Torshizian, H.; Solgi, A. Geochemical exploration for lithium in NE Iran using the geochemical mapping prospectivity index, staged factor analysis, and a fractal model. *Geochem. Explor. Environ. Anal.* **2020**, *20*, 461–472. [\[CrossRef\]](#)
- Cardoso-Fernandes, J.; Lima, J.; Lima, A.; Roda-Robles, E.; Köhler, M.; Schaefer, S.; Barth, A.; Knobloch, A.; Gonçalves, M.A.; Gonçalves, F.; et al. Stream sediment analysis for Lithium (Li) exploration in the Douro region (Portugal): A comparative study of the spatial interpolation and catchment basin approaches. *J. Geochem. Explor.* **2022**, *236*, 106978. [\[CrossRef\]](#)
- Errandonea-Martin, J.; Garate-Olave, I.; Roda-Robles, E.; Cardoso-Fernandes, J.; Lima, A.; Ribeiro, M.d.A.; Teodoro, A.C. Metasomatic effect of Li-bearing aplite-pegmatites on psammitic and pelitic metasediments: Geochemical constraints on critical raw material exploration at the Fregeneda—Almendra Pegmatite Field (Spain and Portugal). *Ore Geol. Rev.* **2022**, *150*, 105155. [\[CrossRef\]](#)
- Keyser, W.; Müller, A.; Knoll, T.; Menuge, J.F.; Steiner, R.; Berndt, J.; Hart, E.; Fegan, T.; Harrop, J. Quartz chemistry of lithium pegmatites and its petrogenetic and economic implications: Examples from Wolfsberg (Austria) and Moylisha (Ireland). *Chem. Geol.* **2023**, *630*, 121507. [\[CrossRef\]](#)
- Trueman, D.L. Exploring for a Tanco type pegmatite. In Proceedings of the International Workshop on the Geology of Rare Metals, Victoria, BC, Canada, 9–10 November 2010.
- Thomas, M.D.; Ford, K.L.; Keating, P. Review paper: Exploration geophysics for intrusion-hosted rare metals. *Geophys. Prospect.* **2016**, *64*, 1275–1304. [\[CrossRef\]](#)
- Gao, Y.; Bagas, L.; Li, K.; Jin, M.; Liu, Y.; Teng, J. Newly Discovered Triassic Lithium Deposits in the Dahongliutan Area, North West China: A Case Study for the Detection of Lithium-Bearing Pegmatite Deposits in Rugged Terrains Using Remote-Sensing Data and Images. *Front. Earth Sci.* **2020**, *8*, 591966. [\[CrossRef\]](#)
- Santos, D.; Cardoso-Fernandes, J.; Lima, A.; Müller, A.; Brönnner, M.; Teodoro, A.C. Spectral Analysis to Improve Inputs to Random Forest and other Boosted Ensemble Tree-Based Algorithms for Detecting NYF Pegmatites in Tysfjord, Norway. *Remote Sens.* **2022**, *14*, 3532. [\[CrossRef\]](#)
- Gemusse, U.; Lima, A.; Teodoro, A. Pegmatite spectral behavior considering ASTER and Landsat 8 OLI data in Naipa and Muiane Mines (Alto Ligonha, Mozambique). In Proceedings of the SPIE, SPIE Remote Sensing, Berlin, Germany, 10–13 September 2018; Michel, U., Schulz, K., Eds.; SPIE: Bellingham, WA, USA, 2018.
- Rajesh, H.M. Application of remote sensing and GIS in mineral resource mapping—An overview. *J. Mineral. Petrol. Sci.* **2004**, *99*, 83–103. [\[CrossRef\]](#)
- Cardoso-Fernandes, J.; Teodoro, A.C.; Lima, A.; Perrotta, M.; Roda-Robles, E. Detecting Lithium (Li) Mineralizations from Space: Current Research and Future Perspectives. *Appl. Sci.* **2020**, *10*, 1785. [\[CrossRef\]](#)
- Clark, R.N.; Roush, T.L. Reflectance spectroscopy: Quantitative analysis techniques for remote sensing applications. *J. Geophys. Res. Solid Earth* **1984**, *89*, 6329–6340. [\[CrossRef\]](#)
- Clark, R.N.; King, T.V.V.; Klejwa, M.; Swayze, G.A.; Vergo, N. High spectral resolution reflectance spectroscopy of minerals. *J. Geophys. Res. Solid Earth* **1990**, *95*, 12653–12680. [\[CrossRef\]](#)

21. Cardoso-Fernandes, J.; Silva, J.; Perrotta, M.M.; Lima, A.; Teodoro, A.C.; Ribeiro, M.A.; Dias, F.; Barrès, O.; Cauzid, J.; Roda-Robles, E. Interpretation of the Reflectance Spectra of Lithium (Li) Minerals and Pegmatites: A Case Study for Mineralogical and Lithological Identification in the Fregeneda—Almendra Area. *Remote Sens.* **2021**, *13*, 3688. [[CrossRef](#)]
22. Kokaly, R.F.; Clark, R.N.; Swayze, G.A.; Livo, K.E.; Hoefen, T.M.; Pearson, N.C.; Wise, R.A.; Benzel, W.M.; Lowers, H.A.; Driscoll, R.L.; et al. *USGS Spectral Library Version 7*; 1035; USGS: Reston, VA, USA, 2017; p. 68.
23. Meerdink, S.K.; Hook, S.J.; Roberts, D.A.; Abbott, E.A. The ECOSTRESS spectral library version 1.0. *Remote Sens. Environ.* **2019**, *230*, 111196. [[CrossRef](#)]
24. Cardoso-Fernandes, J.; Silva, J.; Dias, F.; Lima, A.; Teodoro, A.C.; Barrès, O.; Cauzid, J.; Perrotta, M.; Roda-Robles, E.; Ribeiro, M.A. Tools for Remote Exploration: A Lithium (Li) Dedicated Spectral Library of the Fregeneda—Almendra Aplite—Pegmatite Field. *Data* **2021**, *6*, 33. [[CrossRef](#)]
25. Adiri, Z.; Lhissou, R.; El Harti, A.; Jellouli, A.; Chakouri, M. Recent advances in the use of public domain satellite imagery for mineral exploration: A review of Landsat-8 and Sentinel-2 applications. *Ore Geol. Rev.* **2020**, *117*, 103332. [[CrossRef](#)]
26. Miller, K.A.; Thompson, K.F.; Johnston, P.; Santillo, D. An Overview of Seabed Mining Including the Current State of Development, Environmental Impacts, and Knowledge Gaps. *Front. Mar. Sci.* **2018**, *4*, 418. [[CrossRef](#)]
27. Dias, C.G.; Dias, F.L.; Lima, A.M.C. Largest spodumene lithium deposit in Western Europe. In Proceedings of the 15th Biennial SGA Meeting, Glasgow, UK, 27–30 August 2019; University of Glasgow Publicity Services: Glasgow, UK, 2019; pp. 1792–1795.
28. Duarte, L.; Teodoro, A.C.; Santos, P.; Rodrigues de Almeida, C.; Cardoso-Fernandes, J.; Flores, D. An Interactive WebGIS Integrating Environmental Susceptibility Mapping in a Self-Burning Waste Pile Using a Multi-Criteria Decision Analysis Approach. *Geosciences* **2022**, *12*, 352. [[CrossRef](#)]
29. Julivert, M. *Mapa Tectónico de la Península Ibérica y Baleares Escala 1:1,000,000*; Ministerio de Industria y Energía, Servicio de Publicaciones: Madrid, Spain, 1972; p. 1 mapa.
30. Lima, A. Estrutura, Mineralogia e Génese dos Filões Aplitepegmatíticos com Espodumena da Região do Barroso-Alvão. Ph.D. Thesis, Universidade do Porto, Porto, Portugal, 2000.
31. Vasques, J.T. Litho geochemistry and Prospection of Lithium-Bearing Pegmatites and Their Host-Rocks. Master's Thesis, Faculdade de Ciências da Universidade do Porto, Porto, Portugal, 2021.
32. Savannah Resources Plc. Annual Report and Financial Statements. Available online: <https://www.savannahresources.com/media/1n0mjo35/sav-financial-statements-31-december-2019.pdf> (accessed on 15 July 2022).
33. Martins, T. Multidisciplinary Study of Pegmatites and Associated Li and Sn-Nb-Ta Mineralisation from the Barroso-Alvão Region. Ph.D. Thesis, Faculdade de Ciências da Universidade do Porto, Porto, Portugal, 2009.
34. Dias, F. Lithium Mineralizations of Barroso-Alvão Aplite-Pegmatite Field. Master's Thesis, Faculdade de Ciências da Universidade do Porto, Porto, Portugal, 2016.
35. Černý, P.; Ercit, T.S. Classification of granitic pegmatites revisited. *Can. Mineral.* **2005**, *43*, 2005–2026. [[CrossRef](#)]
36. Wise, M.A.; Müller, A.; Simmons, W.B. A proposed new mineralogical classification system for granitic pegmatites. *Can. Mineral.* **2022**, *60*, 229–248. [[CrossRef](#)]
37. Martins, T.n.; Lima, A.; Simmons, W.B.; Falster, A.U.; Noronha, F. Geochemical fractionation of Nb–Ta oxides in Li-bearing pegmatites from the Barroso–Alvão pegmatite field, Northern Portugal. *Can. Mineral.* **2011**, *49*, 777–791. [[CrossRef](#)]
38. Bergmand, T.G. *Design for a Laser Rangefinder*; U.S. Naval Ordnance Test Station: China Lake, CA, USA, 1965; ISBN 9780852619629.
39. Langley, R.B. *RTK GPS*; GPS World: China Lake, CA, USA, 1998; Volume 9, pp. 70–76.
40. ASD Inc. *ViewSpec Pro™ User Manual*; ASD Document 600555 Rev. A; ASD Inc.: Boulder, CO, USA, 2008.
41. Menges, F. Spectragryph—Optical Spectroscopy Software, Version 1.2.14. Available online: <http://www.ffmpeg2.de/spectragryph/> (accessed on 22 July 2020).
42. U.S. Geological Survey. *Landsat—Earth Observation Satellites Fact Sheet 2015–3081*; Ver. 1.4; U.S. Geological Survey: Sioux Falls, SD, USA, 2022; p. 4. Available online: <https://pubs.usgs.gov/fs/2015/3081/fs20153081.pdf> (accessed on 1 August 2022).
43. U.S. Geological Survey. *Landsat 9*; 2019–3008; U.S. Geological Survey: Reston, VA, USA, 2019; p. 2.
44. Chavez, P.S. Image-Based Atmospheric Corrections—Revisited and Improved. *Photogramm. Eng. Remote Sens.* **1996**, *62*, 1025–1036.
45. Hunt, G.R. Spectral signatures of particulate minerals in the visible and near infrared. *Geophysics* **1977**, *42*, 501–513. [[CrossRef](#)]
46. Pontual, S.; Merry, N.J.; Gamson, P. *Spectral Interpretation Field Manual. GMEX Spectral Analysis Guides for Mineral Exploration*, 3rd ed.; AusSpec International Ltd.: Queenstown, New Zealand, 2008; Volume 1.
47. Loughlin, W.P. Component Analysis for Alteration Mapping. *Photogram. Eng. Rem. Sens.* **1991**, *57*, 1163–1169.
48. Singh, A.; Harrison, A. Standardized principal components. *Int. J. Remote Sens.* **1985**, *6*, 883–896. [[CrossRef](#)]
49. Johnson, R.A.; Wichern, D.W. *Applied Multivariate Statistical Analysis*; Pearson Prentice Hall: Upper Saddle River, NJ, USA, 2007; p. 773.
50. Santos, D.; Teodoro, A.; Lima, A.; Cardoso-Fernandes, J. Remote Sensing Techniques to Detect Areas with Potential for Lithium Exploration in Minas Gerais, Brazil. In Proceedings of the SPIE, SPIE Remote Sensing, Strasbourg, France, 9–12 September 2019; Schulz, K., Michel, U., Nikolakopoulos, K.G., Eds.; SPIE: Bellingham, WA, USA, 2019. [[CrossRef](#)]
51. Cardoso-Fernandes, J.; Teodoro, A.C.; Lima, A. Remote sensing data in lithium (Li) exploration: A new approach for the detection of Li-bearing pegmatites. *Int. J. Appl. Earth Obs. Geoinf.* **2019**, *76*, 10–25. [[CrossRef](#)]

52. Adiri, Z.; Harti, A.E.; Jellouli, A.; Maacha, L.; Bachaoui, E.M. Lithological mapping using Landsat 8 OLI and Terra ASTER multispectral data in the Bas Drâa inlier, Moroccan Anti Atlas. *J. Appl. Remote Sens.* **2016**, *10*, 016005. [[CrossRef](#)]
53. XAMPP Apache. Available online: <https://www.apachefriends.org> (accessed on 6 November 2022).
54. Isenburg, M. LAStools-Efficient Tools for LiDAR Processing. Available online: <http://www.cs.unc.edu/~isenburg/lastools/> (accessed on 16 June 2023).
55. Axelsson, P. DEM Generation from Laser Scanner Data Using Adaptive TIN Models. In Proceedings of the International Archives of Photogrammetry and Remote Sensing, Amsterdam, The Netherlands, 16–23 July 2000; Volume XXXIII, pp. 110–117.
56. Mielcarek, M.; Stereńczak, K.; Khosravipour, A. Testing and evaluating different LiDAR-derived canopy height model generation methods for tree height estimation. *Int. J. Appl. Earth Obs. Geoinf.* **2018**, *71*, 132–143. [[CrossRef](#)]
57. de Almeida, C.R.; Santos, D.; Vasques, J.T.; Cardoso-Fernandes, J.; Lima, A.; Teodoro, A.C. A LCT Pegmatite Spectral Library of the Aldeia Spodumene Deposit: Contributes to Mineral Exploration, Zenodo. Available online: <https://zenodo.org/record/7313964> (accessed on 5 June 2023).
58. McManamon, P.F. *Lidar Technologies and Systems*; SPIE Press: Washington, DC, USA, 2019; Volume PM300, p. 520.
59. Dentith, M.; Mudge, S.T. *Geophysics for the Mineral Exploration Geoscientist*; Cambridge University Press: Cambridge, UK, 2014.
60. Milsom, J.; Eriksen, A. *Field Geophysics*, 4th ed.; Wiley-Blackwell: Chichester, UK, 2011.
61. Hunt, G.R.; Salisbury, J.W. Visible and near-infrared spectra of minerals and rocks: I Silicate minerals. *Mod. Geol.* **1970**, *1*, 283–300.
62. OriginLab Corporation. *Origin(Pro), Version Number 2022*; OriginLab Corporation: Northampton, MA, USA, 2022.
63. Teodoro, A.C.; Santos, D.; Cardoso-Fernandes, J.; Lima, A.; Brönnner, M. Identification of Pegmatite Bodies, at a Province Scale, Using Machine Learning Algorithms: Preliminary Results. In Proceedings of the SPIE 11863, Earth Resources and Environmental Remote Sensing/GIS Applications XII, SPIE Remote Sensing, Online, 12 September 2021. [[CrossRef](#)]
64. Pour, A.B.; Hashim, M. Identification of hydrothermal alteration minerals for exploring of porphyry copper deposit using ASTER data, SE Iran. *J. Asian Earth Sci.* **2011**, *42*, 1309–1323. [[CrossRef](#)]
65. Chavez Jr, P.S.; Kwarteng, A.Y. Extracting spectral contrast in Landsat Thematic Mapper image data using selective principal component analysis. *Photogramm. Eng. Remote Sens.* **1989**, *55*, 339–348.
66. Santos, D.; Cardoso-Fernandes, J.; Lima, A.; Teodoro, A.C. The Potential of Spectral Unmixing Method Applied to PRISMA Hyperspectral Images in the Identification of Li Minerals: An Evaluation for Prospecting Purposes. In Proceedings of the SPIE Remote Sensing, Earth Resources and Environmental Remote Sensing/GIS Applications XIII, Berlin, Germany, 26 October 2022. [[CrossRef](#)]

Disclaimer/Publisher’s Note: The statements, opinions and data contained in all publications are solely those of the individual author(s) and contributor(s) and not of MDPI and/or the editor(s). MDPI and/or the editor(s) disclaim responsibility for any injury to people or property resulting from any ideas, methods, instructions or products referred to in the content.

Article

Conceptual Navigation and Positioning Solution for the Upcoming Lunar Mining and Settlement Missions Based on the Earth's Mining Experiences: Lunar Regional Navigation Transceiver System

Danijela Ignjatović Stupar ^{1,*}, Vukan Ogrizović ², Janez Rošer ³, Vesna Poslončec-Petrić ⁴
and Goran Vižintin ³

¹ Department of Space Application, International Space University, 1rue Dominique Cassini, 67400 Illkirch-Graffenstaden, France

² Faculty of Civil Engineering Subotica, University of Novi Sad, Kozaračka 2A, 24000 Subotica, Serbia

³ Faculty of Natural Sciences and Engineering, University of Ljubljana, Aškerčeva cesta 12, 1000 Ljubljana, Slovenia

⁴ Faculty of Geodesy, University of Zagreb, Kačićeva 26, 10000 Zagreb, Croatia

* Correspondence: danijela.stupar@isunet.edu

Abstract: Precise drilling and excavation in future Lunar mining sites as well as in building habitats areas will be supported by robotized instrumentation. To ensure accurate positioning of facilities or structures, customized surveying instruments will be used to perform measurements needed for calculating locations of surveyed objects. Precise positioning in unexplored areas is difficult, even on the Earth, with all available support. This issue becomes even more complex on the Moon's surface, considering environmental conditions and the absence of Earth logistics. This paper solves a problem of centimeter-precision positioning on the Moon's surface. The solution is called Lunar Regional Navigation Transceiver System (LRNTS). It is based on a network of transceiver facilities, holding onboard both navigation transmitters and receivers. Transmitting modules of LRNTS act in the same way as the Global Navigation Satellite Systems (GNSS) space segment, sending navigation messages to the receivers. Receiving modules are needed for self-calibration of LRNTS to calculate their coordinates. In this paper, 12 different LRNTS-simulated configuration setups within Shackleton Crater are tested against positioning accuracy and visibility along the crater. The results show that LRNTS of nine transceivers can achieve sub-centimeter horizontal and better than 2 cm vertical accuracy, with consistent visibility of six and more transceivers throughout the Shackleton Crater.

Keywords: Lunar navigation; pseudolite; transceiver; control network; Shackleton Crater; Lunar mining



Citation: Ignjatović Stupar, D.; Ogrizović, V.; Rošer, J.; Poslončec-Petrić, V.; Vižintin, G. Conceptual Navigation and Positioning Solution for the Upcoming Lunar Mining and Settlement Missions Based on the Earth's Mining Experiences: Lunar Regional Navigation Transceiver System. *Minerals* **2023**, *13*, 371. <https://doi.org/10.3390/min13030371>

Academic Editor: Paul Alexandre

Received: 24 December 2022

Revised: 27 February 2023

Accepted: 4 March 2023

Published: 7 March 2023



Copyright: © 2023 by the authors. Licensee MDPI, Basel, Switzerland. This article is an open access article distributed under the terms and conditions of the Creative Commons Attribution (CC BY) license (<https://creativecommons.org/licenses/by/4.0/>).

1. Introduction

The drastic demand for natural resources has increased drastically in the last century. The reason for this is the large increase in population and rapid progress of green and nano technologies. Population growth also causes a much greater need for energy, food, and natural resources that disappear over time and are not renewed.

By switching to sustainable sources such as solar, wind, geothermal, and hydropower, urbanization and urban expansion can provide a light economic profit. However, due to the accelerated consumption of energy sources, climate change will be significantly highlighted, and thus we automatically reach unsustainability. Not long after, the amount of non-renewable natural energy sources, such as rare-earth elements (REE), precious and platinum group metals, and phosphorus and potassium, including fossil sources, will quickly be depleted with the increase in urbanization.

The political situation is also not on the positive side of the entire issue. The existing terrestrial resources, which are not evenly distributed throughout the planet, are treated

locally, not globally, which is against the establishment of World Trade Organization (WTO) regulations [1].

Due to the possession and use of rare natural resources, the countries of the Middle and Far East such as China, Russia, India, Saudi Arabia, etc., are advancing much faster economically compared to the United States and Europe. They own these resources and run the global economic market. There is also an awareness among the countries that their “precious and globally rare” energy sources will come to an end very soon. One of the reasons why they are also in the game is to find new sources that are beyond the borders of our planet. Investing in the research and exploration of new destinations in our solar system, where new energy sources will be exploited, represents a new era of competition between economically strong countries. This time, many more of them are in the race compared to the Cold War period when the Russians and the Americans were the only rivals.

In our solar system, there are three potential destinations where space resources can be pursued. The first targeted destination will be the Moon, where excavation technologies will be tested, followed by asteroid mining, and finally the planet Mars [2–4]. This paper is focused on the Lunar exploration scenario.

Nowadays, the Moon is experiencing newfound interest four decades after the termination of the Apollo program, with an objective to become a transfer station for exploration and settling outer space soon. It is the best test bed for In Situ Resource Utilization (ISRU) and application of new technologies in the production of consumable products such as water, propellant, and construction materials for the establishment of the first human life experiences on the Moon [5]. In the exploitation of Lunar resources and the settlement race, there are many programs currently ongoing, such as ARTEMIS, with worldwide partners involved. These include the ILRS (International Lunar Research Station) as a joint program between Russian Roscosmos and the Chinese CNSA national space agencies, together with the Chinese Chang’e program, and last but not least the Chandrayaan Program from the Indian Space Research Organization (ISRO) [2,6–10]. Different from the past, there are many other private companies interested in exploring the Moon and they do not necessarily come from the space sector. One of them is Rio Tinto, who plans to expand their currently used autonomous mining technology, such as automation, digitization, and advanced data analytics, in planetary mining [11,12]. For all of them, the main objectives are to find the best solution on how to excavate and use in situ Lunar resources to sustain life and work on the Moon for a long period of time.

The experience and importance gained in mining on Earth, in terms of technique, excavation methods, treatment, etc., will be transferred to the new circles of Lunar mining, with modifications according to the Lunar environmental conditions as well. Navigation and positioning, which play important roles in mining today, will also have a special importance in the connection between external and in-mine control networks [13].

In line with that, a Lunar navigation system is one of the requirements which must be taken seriously into account when missions coming from different programs occur together and when the construction of the habitats, launching pads, and the extractions from potential Lunar mining sites start. Various needs for a high-precision positioning and navigation system will arise in mining and civil engineering fields, such as to precisely calculate the quantity of extracted ore, to build infrastructure, and to superpose objects (e.g., on top of each other or nearby).

The problem of Lunar navigation is treated mostly in projects and papers investigating landing on the Moon’s surface and the navigation of robotized Lunar vehicles in limited areas. Accuracy demands for those applications are far from the mm or even cm level, but rather close to a few hundred meters [14]. Nevertheless, the suggested methodologies can be considered as a good starting point for designing the Lunar navigation network. Most of the suggested approaches apply and improve navigating concepts already known on the Earth, namely, inertial systems or navigating by image processing. None of those technologies can be applied as-is on the Lunar surface because of special instrumentation

requirements and specific environmental conditions. The huge difference between the Earth and the Moon, in the sense of gravity, atmosphere, temperature, humidity, etc., makes replication of classical Earth-related surveying methodologies very hard to implement on the Moon. This paper elaborates on the methodology of achieving cm-level accurate positioning in real time on the Moon, which is validated by presented numerical results.

2. Materials and Methods

2.1. Overview of Previous Research

Prior to further establishment of long-time robotic and human missions on the Moon, a consistent system for precise landing, navigation, and positioning is needed to accommodate continuous and safe work. At present, the navigation of objects located on the Lunar surface is controlled by Earth-based deep space network antennas [15]. Current investigation on navigation methodologies is based on technologies and working principles related to imaging, celestial (“star sensors”), inertial, and GNSS-like systems. They are introduced in following paragraphs.

There are several propositions based on imaging concepts using a camera as a navigating tool. Vision-based navigation is a technique suggested by major space agencies, aiming to achieve 200 m accurate autonomous landing [16]. So called pin-point Lunar landing uses an optical navigation system based on tracking features on the images by measuring an angular rate and a velocity vector of the spacecraft. Another possibility is to identify those features using a geo-referenced database to determine the position of the spacecraft. Using this technique, the position and velocity estimation accuracy of a spacecraft reaches approximately 10 m at 0.05 m/s. It was noticed that illumination conditions represent main issues for this optical Lunar navigation system [16].

For path planning and rover control, the successor of Yutu-1, Chang’e-4 Yutu-2 rover, used an upgraded version of an autonomous navigation system called visual Simultaneous Localization and Mapping (SLAM), which is based on tracking rover moves detected as a part of an image by a photogrammetric computer [17].

ESA, as a collaborative member on the Luna-27 mission, is developing the PILOT system as a main navigation system for the landers. The system compares the images of terrain landmarks taken by a camera and landmarks pre-stored in a database on the spacecraft to perform optical recognition of the crater’s landmarks for soft landing [18].

In the absence of satellite navigation systems, another navigation approach is possible, using star sensors supported by inclinometers. The Strapdown Inertial Navigation System (SINS) is a method based on a combination of two operational steps, approximate and fine navigation. The coarse positioning is used for initial alignment providing a real-time solution where all navigation errors were calculated and compensated in real time by SINS. Error corrections in SINS are done by the star sensors. Results from simulation have shown that this method can achieve high precision for rovers’ autonomous navigation [19,20].

For autonomous navigation, using only inertial navigation is not efficient due to growth of imperfections of inertial sensors which can provide relatively precise autonomy only for very short time. For that reason, a combination of inertial navigation with celestial navigation was suggested in [19,20].

The simulation presented in [19,21] applied the SINS method for the autonomous navigation of the rovers. In this model, starlight imaging was used, where the star sensor determines the altitude of the vehicle. The tilt angle between the horizontal plane and a vehicle is measured by a dual-axis inclinometer. Apart from the star sensor and inclinometer, attention was also paid to the utilization of precise clocks to provide real-time data and to synchronize data between two sub-segments of the compound navigation system. Misalignment of the star sensor and inclinometer can cause a significant positioning error. To avoid this systematic influence, the QUaternion ESTimator (QUEST) calibration method is introduced. This model can provide continuous measurements for only a few minutes, providing autonomous positioning accuracy from 20 m to 70 m in distance.

To support robotic missions, a constellation of the small satellites is considered as a technology that could resolve the navigation issue. It was suggested that the satellites might be placed into halo orbits in Earth–Moon libration points or LaGrange points [22,23].

An extension of the GLONASS navigation system is proposed in [24] to modify the satellites using additional narrow-beam antennas directed to the Moon. It would be implemented in the form of a constellation of six navigation satellites located in near-circular orbits at ~100,000 km height in two perpendicular planes with an inclination of 90°. Standard Satellite Navigation Equipment (SNE), a transmitter/receiver, and modified software for Moon usage would be integrated onboard a Lunar orbiting spacecraft and objects based on the Lunar surface. Simulation of this conceptual design has shown that position and velocity of the spacecraft can reach 15 m (1σ) in position and 0.02 m/s in velocity. For the objects based on the Lunar surface, it was highlighted that instantaneous navigation solutions can be provided only if the geodetic map with high precision is memorized in the SNE. Under this condition, if the objects are in the visible Lunar disk, the navigation accuracy is 10 m (1σ). While objects move away from the center, the accuracy degrades (e.g., for 60° deviations from the disk, errors can reach 20 m to 100 m). It was concluded that the proposed method cannot be used for navigating the objects on the far side of the Moon [24].

Yet another example is a GPS-based local area positioning system developed by the Aerospace Robotics Laboratory (ARL) at Stanford University for the planet Mars. The ground-located pseudosatellites replace the space-located satellite constellation with the goal of providing similar performance to GNSS on the Earth. Enabling localization is directed by a Self-Calibrating Pseudolite Array (SCPA). A network of transceivers is a way to expand the coverage of the system. The mathematical model of positioning the transceivers, which will both transmit and receive GNSS-like signals, used SCPA [25]. Field tests were performed using a prototype of NASA Aims K-9 Mars rover achieving code- and carrier-level positioning less than 3.7 m and 8.8 cm, respectively [26,27].

In the case of open-pit mining, ARL at Stanford University developed a guidance system for transport and operational vehicles based on pseudo-assisted Carrier-Phase Differential GPS. With this system, a narrow angle of open sky above the pit and a small number of visible satellites will be mitigated by six or eight pseudolites placed around the rim. This system will augment the existing GPS constellation and ensure the availability of navigation anywhere inside the pit [27,28].

NASA envisaged the Artemis program to develop a special receiver which will be able to receive signals from the Global Positioning System (GPS). This receiver is based on the same working principles as receivers used for high-altitude navigation in Magnetospheric Multiscale mission (MMS) and Geostationary Operational Environmental Satellites (GOES) in combination with the GPS processing power of NavCube receivers [29].

To this day, there is no satellite navigation system which will help spacecraft to be navigated autonomously to the Moon. This is only supported by constant controlling from the Earth, which will be extremely complicated when multiple missions are shuttling and maneuvering backwards and forwards.

Dozens of missions to the Moon are planned and some of them already started, with initial executions such as NASA's Artemis 1 and ispace's HAKUTO-R Missions 1 [30,31].

Experiences gained via the Artemis 1 mission, where the capabilities of the Orion's systems were tested, showed that loss of communication with spacecraft can happen easily at the moment when the vehicle is located behind the Moon. Moving through space, the Earth is the only point of reference when a returning ping signal will provide the position of the spacecraft. If there is an obstacle between them, there will be plenty of blind spots and high risk of a complete loss of communication. To solve this problem, there is need for triangulation from an autonomous navigation system. NASA and ESA are working on the development of the Lunar navigation network, which will be the main system helping all upcoming Lunar missions [32].

The Moonlight Initiative ESA's program includes a series of missions which will maintain sustainable Lunar exploration. A part of the mission is the establishment of a navigation constellation of three to four Lunar Pathfinder satellites orbiting the Moon in Elliptical Lunar Frozen Orbit (ELFO), mainly covering the Lunar South Pole [18]. Launch is planned for a period between 2025 and 2026. The mission objective is to demonstrate high-bandwidth communication and navigation capabilities for the future Lunar missions. The Lunar Pathfinder will also support the Lunar Polar Sample Return mission, which aims to retrieve samples from the Moon's South Pole region. A mission developed by ESA and the satellites built by Surrey Satellite Technology LTD (SSTL) will have a NaviMoon receiver onboard [4]. The receiver's capacity will be to harness the navigation signals (strong and weak as well) from the terrestrial navigation systems (GPS and Galileo), determining the Pathfinder position with approximately 60 m accuracy. The Lunar lander Argonaut, as a part of the Moonlight Initiative mission together with the Pathfinder satellites, will help the rovers in positioning on the Lunar surface [32].

The Lunar GNSS Receiver Experiment (LuGRE) is developed in partnership between NASA and the Italian Space Agency (ASI) based on laser retroreflector technology. Mirrors on the Pathfinder's array will aim to enhance Lunar navigation and to validate operational capabilities, which will also be critical for Artemis and the future missions [33].

The review of many proposals, simulation models, and feedback from landers' and rovers' experiences can be summarized in a general conclusion that all of them are based on autonomous navigation without the possibility to connect and to collaborate under the same system. The model proposed in this paper is based on pseudolite transceiver field tests introduced by ARL from Stanford University and applied for open-pit mining and for a Mars navigation system. With a similar Moon scenario in the Shackleton Crater, our stand-alone navigation system will serve all users from the same Lunar region. In the next stage of development, when the Pathfinder constellation from the Moonlight Initiative program is operational, it will be used for referencing all local coordinates obtained by the system elaborated in this article to the Lunar reference system.

2.2. Study Area

Several environmental and technical factors influence the choice of navigation methodology: temperature, illumination, communication with Earth, and Lunar topography. The Moon's position in the solar system and its relationship with the Earth and the Sun open an important topic on the selection of regions for future settlement. Therefore, the area around the South Pole is the most attractive location for Lunar exploitation [34]. The orientation of the Moon's rotation axis, which is tilted 1.5° from the ecliptic plane, makes the Lunar poles mainly Permanently Shadowed Regions (PSRs), meaning that the floors of some craters from these regions never receive sunlight. Consequently, the temperature in these characteristic craters allows the sustainability of Lunar ice. This confirms a hypothesis based on evidence of the potential existence of water on the Moon, thus guaranteeing the possibility of living and working on the Moon [35]. However, regions which never receive direct solar illumination still receive sunlight coming to them indirectly, scattered, with the addition of starlight. This issue is elaborated in several statistics on measured quantities of solar power supply in all regions, including the polar ones [36–38].

Important conclusions on the South Pole area are drawn from results of processing topographical, geological, and environmental datasets collected by diverse Lunar missions (Apollo, Luna, Molnya, Chandrayaan, Chang'e, Lunar Reconnaissance Orbiter (LRO), Clementine [36,39], SELENE [40], etc.), making this area the best candidate for permanent Lunar settlement. Figure 1 introduces the polar-based region, where high attention is given to Shackleton Crater, located inside the rim of the South Pole Aitken (SPA) Basin [36,39,41,42].

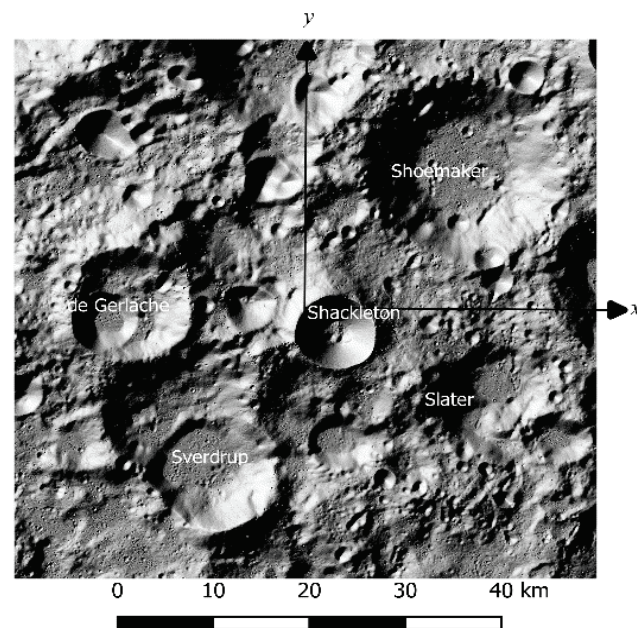


Figure 1. Lunar South Pole.

Furthermore, communication with the Earth plays an important role in site selections. That is why the potential sites in the South Pole region based near the Shackleton Crater rim and Mons Malapert crater fulfill the requested parameters. They are noted as the best areas for a relay station due to high altitude, topographic characteristics, and visibility with the Earth [43]. In the case of simultaneous establishment of the laser relay on the North Pole, communication with the Earth will be 100% covered. Two separate systems per pole with 100 km distance between them will enable robust local wireless communication coverage [36].

Concluding on the selection of the study area for this research, the analysis of the discussion on the Moon's South Pole region characteristics showed that Shackleton Crater fulfills all technical and environmental requirements. Therefore, simulation and statistical analysis of positioning accuracy will be carried out using Shackleton Crater as a case study. The presented methodology is replicable to other regions as well as other celestial bodies.

2.3. LRNTS Configuration

In Earth-based surveying, for each site, a control network is developed prior to further positioning works. The control network is designed in such a way as to spread over the whole site to avoid any extrapolation coming from a coordinate frame definition, which could jeopardize positioning accuracy. It is implemented as a set of stable, fixed points or facilities. Characteristic points of objects that are to be placed at the site are connected to the control network points with relative measurements, such as distances, angles, or coordinate differences. Consequently, both control networks and objects' points' coordinates share the same coordinate system.

The core of this research is developing a methodology that will allow real-time centimeter positioning accuracy throughout large areas of the Moon's surface. The targeted accuracy should be:

- available in real-time;
- homogeneous throughout the whole area of interest;
- independent of the size or the shape of a construction/exploration site;
- replicable elsewhere (other solar system bodies).

A solution presented in this paper suggests placing a set of transceivers along the crater rim, forming a system that would act like any GNSS cosmic segment. LRNTS distinctions from GNSS are summarized in three items:

- LRNTS is a ground-based system;
- it consists of transceivers instead of transmitters;
- it is self-adjustable.

LRNTS is implemented as a coordinate frame materialized by a set of transceivers located along a crater rim. Each transceiver acts, at the same time, as a transmitter and a receiver. As the transmitter, it broadcasts GNSS-compatible signals to other transceivers (and also inside the crater), while, as the receiver, it receives navigation messages from other transceivers. In that way, LRNTS can adjust the crater coordinate frame only by mutual measurements between LRNTS sites, unless tight fitting into the Moon reference system is needed. Self-calibration of LRNTS is performed via an iterative adjustment of measurements acquired mutually between the LRNTS nodes. One of the tested configurations analyzed in this paper, which is elaborated in detail later, is schematically represented in Figure 2. Blue dots represent LRNTS nodes, while black lines indicate established connections between the nodes. The intention is to provide as much visibility as possible between the transceivers. However, due to crater topography, not all baselines could be established.

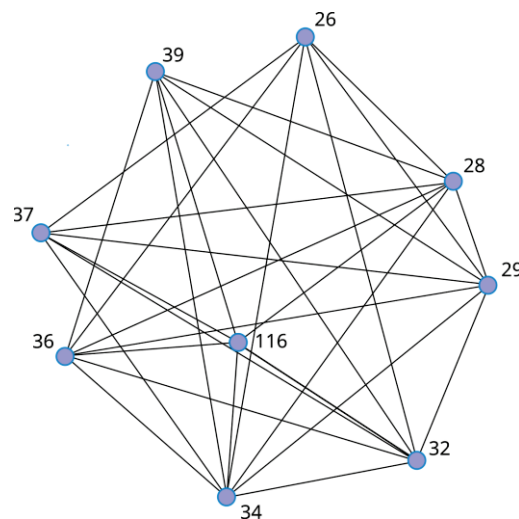


Figure 2. A scheme of interconnection between LRNTS sites.

Following the Lunar surface exploration objectives elaborated in [44], LRNTS is designed to act as a foundation positioning tool for all human and robotic missions in phases 1–3 of the Lunar surface exploration operation concept. The behavior of equipment exposed to harsh Lunar conditions can be tested against real conditions in three different environments: controlled indoor lab, virtual simulation, or outdoor analogue testing [45]. The operation of LRNTS transceivers will follow recommendations from [46], stated for robotic missions supporting the installation and maintenance of a permanent human Lunar base. Since solar power is seen as the most appropriate power source for Moon applications, microgrids can be used for powering all the facilities and vehicles in an area of interest [47].

The navigation system presented in this paper represents a solution for extra-terrestrial positioning applications where there are no satellite navigation systems available yet. Specially, because of existing data for the Moon topography, its explorations so far, and current interests for its further utilization, this paper suggests a pseudosatellite-based regional Lunar navigation system, which makes positioning activities on the Lunar surface much more precise. In addition to that, it is economic and self-sustainable, with no need for real-time monitoring.

2.4. A Coordinate System, a Map Projection, and a Timeframe

The LRNTS coordinate frame is based on 10 m Lunar Digital Elevation Model (DEM) [48]. If a more precise and detailed Moon reference frame would be introduced in the future, the LRNTS coordinate frame (and all sites within the crater tied to it) would be easily

transformed into the new system. Throughout this study case, the LRNTS frame is treated separately from any Lunar reference system. Any such connection would introduce error sources related to global reference frame definition and implementation, which would create a false result on LRNTS performance. If this methodology proves its hypotheses and if other environments like Shackleton are to be investigated, then a tie to a Lunar reference system would be implemented. A possible solution for implementing a Lunar frame would be five Lunar Laser Ranging (LLR) retroreflectors, already placed on the Lunar surface. Their positions are determined with a cm level of accuracy, which makes them a good candidate for the reference frame implementation. Their coordinates are expressed as Cartesian 3D X, Y, Z coordinates, with the coordinate system origin in the Moon's center of mass, with no projection defined. Furthermore, where appropriate, spherical latitude–longitude–height coordinates can be used [49,50].

Although very simple, Cartesian X, Y, Z coordinates with an origin at the Moon's center of mass are not convenient for practical large-scale and precise applications. Therefore, we suggest here a polar xy stereographic projection, with the origin at the Moon's South Pole, as depicted in Figure 1. All simulated measurements and calculations in this study are done in the polar xy stereographic projection.

The LRNTS timeframe is based on the transceivers' atomic clocks. Each transceiver node holds an Atomic Frequency Standard (AFS) onboard (Figure 3), thus providing the same time reference for both transmitting and receiving segments. The benefit of this approach is that clock correction terms coming from different time standards (as with GNSS, for example) are neglected in measurement equations since transmitters and receivers use the same time system. A joint LRNTS timescale is developed from all LRNTS clocks, distributing time system parameters to each transceiver. Performance of one-way GNSS timing is estimated to about 20 ns [51], where a significant share in the error budget is related to ionospheric and tropospheric delays. LRNTS timeframe stability is expected to be better for an order of quantity than GNSS, having in mind theoretical one-way transfer accuracy of 100 ps for code ranges and 1 ps for carrier phase measurements [52]. However, the stability of LRNTS clocks should be checked on regular basis by time series analysis of LRNTS daily solutions (transceivers coordinates).

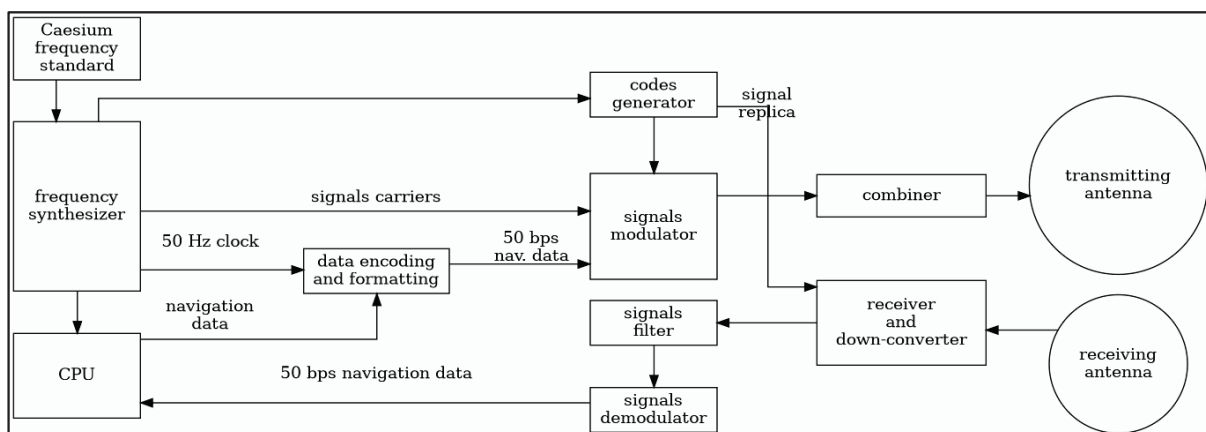


Figure 3. Conceptual diagram of a transceiver.

Furthermore, differences in gravity conditions between the Moon and Earth have an impact on the operation of atomic clocks. The differences in gravitational potential between the Moon and Earth can cause a change in the resonant frequency of the atoms, which is known as a gravitational redshift. This redshift can result in a shift in the frequency of the atomic clock, leading to inaccuracies in time measurements. Furthermore, the effects of special and general relativity also need to be considered. Special relativity affects the ticking rate of clocks, whereas general relativity causes a change in the geometry of space-time. Finally, thermal effects are important for precise definition of the Lunar timescale,

resulting from rather different temperature conditions on the Moon compared to Earth. Changes in temperature can cause changes in the resonant frequency of the atoms, leading to inaccuracies in time measurements. To mitigate these effects, atomic clocks must be designed and tested to withstand the harsh conditions on the Moon and to account for the effects of different gravity conditions. Since the Lunar timescale is developed from measurements from all transceivers, special error correction algorithms are implemented to improve the accuracy of time measurements.

When the Pathfinder constellation is completed, LRNTS transceivers would be able to collect measurements from the Pathfinder satellites and, thus, to calculate their coordinates in the Lunar reference frame. Here it is assumed that the Pathfinder satellites' coordinate frame will correspond to the Lunar reference frame. Then, transformation parameters from the local LRNTS system to the Lunar reference would be calculated using some Affine transformation models. Implementing the transformation parameters, all local coordinates could be transformed to the Lunar reference frame. LRNTS improves the concept [26] in a way that it will be used as a static transmitter constellation. After its establishment and self-calibration, when all LRNTS nodes obtain their coordinates, its role will be like any GNSS cosmic segment, providing navigation messages to the receivers performing regular surveying tasks within the crater.

3. Results

3.1. Transceiver Concept

A transceiver, in the LRNTS sense, is a system capable both of transmitting and receiving navigation messages. Basically, it would be implemented as a compound device, consisting of:

- a pseudolite generating GNSS navigation messages, which are transmitted via a transmitting antenna;
- a GNSS receiver, which receives the signals sent by other transceivers in the network.

A conceptual diagram of such a transceiver node is given in Figure 3. Some functions are shared between the transmitter and receiver: AFS, frequency synthesizer, and CPU.

The transceivers transmit and receive the signals at the same frequencies simultaneously. Therefore, interference between transmitted and received signals is likely to occur. This issue, called a near-far problem, is already recognized in terrestrial navigation applications, where augmentation of GNSS signals is needed, for example, in aircraft landing. Weak GNSS signals receive interference from strong pseudolite signals, which can completely block reception of the navigation messages by the GNSS receivers at the aircraft. Interfering signals can be processed in the transmitting and receiving phase. A latter approach is implemented, for example, in Successive Interference Calculation (SIC). This method reduces the effects of received signals with power above the ambient noise [53]. Antenna diagram shaping could help in reducing the near-far effect, which is summarized in [54]. A mitigation scheme combining two methods, Frequency Domain Excitation and Direct Reconstruction Cancellation, is used for solving for both continuous-wave and pseudolite-type interferences [55]. Narrowband interference can effectively be mitigated by temporal filtering methods, especially when the time domain and space domain methods are integrated. Such an antenna array Space Time Processing (STP) approach is elaborated in [56].

Interference between the transmitted and received signals in an LRNTS transceiver that operates in full duplex mode can be solved by using time-division multiplexing (TDM) or frequency-division multiplexing (FDM). In TDM, the transceiver alternates between transmitting and receiving at different times, effectively separating the transmitted and received signals in time. In FDM, the transceiver uses different frequencies for transmission and reception, avoiding the overlap of the signals.

Furthermore, advanced filtering techniques can be used for minimizing interference between transmitted and received signals, for example, the usage of band-pass filters or notch filters, which eventually remove the transmitted signal from the received one.

Additionally, using directional antennas can also reduce the amount of interference by limiting the amount of transmitted signal that reaches the receiver.

The decision of where exactly to land the transceiver depends on the local terrain configuration. As stated before, the approximate locations for the transceivers were determined by examination of the 10 m DEM. The landing spot, which should be horizontal and with no significant obstacles nearby, can be selected using various landing techniques, for example, a multi-model hierarchical scene matching model [57] or an indirect scheme based on a two-point boundary value problem [58]. A method for obstacle detection during landing is elaborated in [59]. The sensitivity of the transceiver node's location does not influence the stability of the LRNTS mathematical model, which is statistically proven in latter subchapters. It means that the transceiver can be landed anywhere within a few tens of meters around the preliminary location if the spot is horizontal and without significant obstacles.

The mathematical model of positioning using LRNTS, introduced in latter subchapters, assumes that both transmitting and receiving antennas of the transceiver refer to the same phase center, which is, generally, not the case. Therefore, the relative relationship between them should be determined during the calibration process, which is performed before sending the transceiver towards the Moon. The calibration of the mutual spatial relationship between the transmitting and receiving antennas is not included in further calculations. For the rest of this research, while not jeopardizing the reliability of the conclusions, it will be assumed that both antennas share the same phase center.

The multipath effect is a part of the positioning error budget. It depends on the terrain configuration and physical properties of the environment. The analysis of detailed Shackleton topography and the physical characteristics of regolith is beyond the scope of this paper. It can be assumed that multipath will not be a critical factor for accuracy degradation, since the average Bond albedo of the Moon is 0.11, but further research on this issue will give more precise conclusions. The application of Lunar surface reflectance models [60] or [61] can be used for preparing detailed multipath models of the Shackleton Crater.

All measurements from all transceiver nodes are sent in real-time to a master station, where processing is performed. Final coordinates are sent back to each transceiver. The master station is the transceiver at the location visible from all other nodes.

When the system is calibrated and fully operational, it operates as a GNSS space segment, sending navigation messages to LRNTS receivers. Then, the requirements for user LRNTS receivers can be similar to classical GNSS receivers, including the usage of crystal clocks.

3.2. Challenges of Lunar Environmental Conditions

The negative influence of the Lunar environment on hardware survival must be taken into consideration, especially for a long-duration mission. Analyzing previous mission experiences from the Luna and Apollo Programs, there are two major impacts underlined on hardware systems: Lunar regolith and sunless cold temperatures. Regolith comprises dust-sized particles between 40 μm and 130 μm and is extremely abrasive due to its chemical and physical composition [62,63]. Additionally, the Moon is permanently exposed to solar radiation and cosmic ray spallation, which makes constant contact with the regolith. Due to that phenomenon, particles are electrostatically charged, which represents a significant impact on the hardware. To mitigate Lunar dust influence on the hardware and Lunar operation, compliant mechanisms led by analytical design and topology optimization are proposed by [64,65].

Bearing in mind that solar energy will be unavailable during the lunar nights, this makes the production of heat and electricity challenging [63]. To avoid this problem, two solutions are proposed: (1) Thermal Wadis as a thermal power source to protect the systems during the cold periods and (2) Thermal Energy Storage (TES) as a system to run a heat engine producing the electricity during the periods of darkness [66].

Another problem of deploying instrumentation on the Moon's surface is related to harsh conditions on the Lunar surface, with daily temperature variations of almost 300 K. However, due to regolith's low thermal conductivity, the temperature under the surface remains almost constant, with an average of about 253 K [67]. Therefore, a possible solution for the long-term operation of a transceiver node is keeping its sensitive electronics under the surface while exposing only the necessary devices (antennas, motors, solar collectors, etc.) to the environment.

As a summary on operational consequences resulting from the specific Lunar environment, several issues are critical to keep sensitive electronic components operational. The first is related to thermal management. Electronic components must be able to withstand large temperature fluctuations and high temperatures. To mitigate this, insulation and thermal control materials, such as multilayer insulation (MLI) or thermal blankets, can be used to regulate the temperature of the electronic components.

The Lunar surface is subject to high levels of solar and cosmic radiation that can cause Single Event Upsets (SEUs) and Single Event Latchups (SELs) in electronic components. To mitigate this, various techniques such as using radiation-hardened components, shielding, and redundant systems are used.

Electronic components must also be mechanically protected from mechanical impacts and vibrations that can occur during landing and operation on the Lunar surface. This can be achieved using ruggedized packaging, shock mounts, and shock absorbers.

To ensure the longevity and reliability of electronic components, it is important to manage the power supply effectively. This can be achieved using power storage systems, such as batteries or energy harvesters, and power management systems that regulate the power supply to the electronic components.

3.3. LRNTS Observables

LRNTS observables are code pseudoranges and carrier phases, the same as with any GNSS. Regarding different Lunar conditions (geometric and environmental) compared to Earth GNSS, standard GNSS observable equations change in some terms.

A simplified form of a code pseudorange between two transceivers can be expressed as:

$$P = c(T_r - T_s) = c\Delta T \quad (1)$$

where T_r and T_s are signal reception and signal emission times, respectively, while c stands for the speed of light in a vacuum. Readings of the times T_r and T_s correspond to the receiving (r) and transmitting (s) transceiver, which yields:

$$P = c[(t_r + \delta_r) - (t_s + \delta_s)] = c\Delta t + c\Delta\delta = \rho + c\Delta\delta \quad (2)$$

With:

- t_r, t_s —readings of the received and transmitted signals, respectively;
- δ_r, δ_s —biases of the receiver and the transmitter clocks, respectively;
- ρ —the geometric distance between transceivers s and r .

The biases δ_r, δ_s are calculated per transceiver and are available via a navigation message. The complete pseudorange equation introduces other error sources:

$$P = \rho + c\Delta\delta + D_r + D_s + M_{rs} + \epsilon_{rs} \quad (3)$$

where:

- D_r, D_s —hardware delays for the receiver r and the transmitter s , respectively;
- M_{rs} —multipath term between r and s ;
- ϵ_{rs} —remaining random error of the measured pseudorange.

If a signal is transmitted at the frequency f , then the basic carrier phase equation is written as:

$$\Delta\varphi_{rs} = \varphi_r - \varphi_s = -f\frac{\rho}{c} - f\Delta\delta \tag{4}$$

where φ_s is the phase angle of the sent signal and φ_r is the received phase angle of the same signal. The carrier phase $\Delta\varphi_{rs}$ is expressed in cycles, taking values within one cycle, i.e., $[0, 2\pi]$. In order to measure the cumulative phase angle $\Delta\Phi_{rs}$, the number of whole cycles, known as the integer ambiguity N_0 , is involved. If the frequency f is expressed as a function of c and signal wavelength λ using the relation $f = \frac{c}{\lambda}$, the standard form of the carrier phase equation becomes:

$$\Delta\Phi_{rs} = -\Delta\varphi_{rs} = \frac{\rho}{\lambda} + \frac{c}{\lambda}\Delta\delta + N_0 \tag{5}$$

Elements of (5) are expressed in meters by multiplying it by λ :

$$\lambda\Delta\Phi_{rs} = -\Delta\varphi_{rs} = \rho + c\Delta\delta + \lambda N_0 \tag{6}$$

The final form of the carrier phase measurements also contains hardware delays (D_r), multipath (D_s), and a random measurement error (ϵ_{rs}), yielding:

$$\lambda\Delta\Phi_{rs} = \rho + c\Delta\delta + \lambda N_0 + D_r + D_s + M_{rs} + \epsilon_{rs} \tag{7}$$

N_0 corresponds to the number of full cycles in the first epoch. It is unknown, as in the case of GNSS. However, because LRNTS transceivers are static, the number of full cycles for a pair (transmitter, static receiver) does not change in time and can be determined after the second measuring epoch, because $N_0 = N_1 = N_2 = \dots$

3.4. LRNTS Self-Calibration Model

There are k transceivers in an LRNTS configuration setup, and they are distributed along the crater. Their approximate coordinates $T_i(X, Y, Z)_0, i = 1, 2, \dots, k$ are obtained from [48]. All transceivers are mutually connected with code ranges and carrier phase measurements:

$$P_{ij} = \sqrt{(X_i - X_j)^2 + (Y_i - Y_j)^2 + (Z_i - Z_j)^2} \tag{8}$$

$$\Delta\varphi_{ij} = \text{MOD} \left(\frac{\sqrt{(X_i - X_j)^2 + (Y_i - Y_j)^2 + (Z_i - Z_j)^2}}{\lambda}, 2\pi \right) \tag{9}$$

where $i, j = 1, 2, \dots, n$. The total number of independent measurements per epoch is, therefore,

$n = k \cdot (k - 1)$, while the number of unknown transceiver coordinates is $u = 3k$. Since all measurements are uncorrelated, the weight matrix \mathbf{P} is diagonal, with the elements $p_i = (\sigma_i^2)^{-1}$, where σ_i^2 is the measurement dispersion. The design matrix \mathbf{A} is a Jacobian with elements $a_{qm} = \frac{\partial O_{ij}}{\partial C_m}$, where O_{ij} is the observation function (8) or (9), and C_m is an unknown coordinate.

Index $q = 1, 2, \dots, n$ indicates a measurement, while $i, j, m = 1, 2, \dots, u$ are related to the unknowns.

The adjustment model used here is developed as a free 3D network. Therefore, the normal equation matrix $\mathbf{N} = \mathbf{A}^T \mathbf{P} \mathbf{A}$ is singular, so Moore–Penrose pseudoinversion is used for calculating a cofactor matrix $\mathbf{Q}_x = \mathbf{N}^+$. Coordinate increments are calculated as: $\mathbf{x} = \mathbf{Q}_x \mathbf{A}^T \mathbf{P} \mathbf{l}$, where \mathbf{l} is the vector of the measurements. After calculating the new coordinate values $\mathbf{X} = \mathbf{X}_0 + \mathbf{x}$, an iterative adjustment procedure is repeated, with coordinates

X from the previous iteration assigned as approximate ones for the next epoch. Standard deviations of the unknown parameters are calculated as:

$$\hat{\sigma}_{ii} = \hat{\sigma}_0 \sqrt{Q_{ii}} \tag{10}$$

With:

- $\hat{\sigma}_0 = \sqrt{\frac{\mathbf{v}^T \mathbf{P} \mathbf{v}}{n-u}}$ —a posteriori dispersion factor, where vector of measurement increments $\mathbf{v} = \mathbf{A}\mathbf{x} - \mathbf{l}$;
- Q_{ii} —corresponding element of the cofactor matrix \mathbf{Q}_x .

Self-calibration is a process that establishes but also regularly checks the LRNTS coordinate system. The measurements needed for self-calibration can be completed in a short time (in 1–2 min), due to the ease of solving the integer ambiguities, as stated earlier. Therefore, periodical checks of the coordinate frame may be performed on a monthly or even weekly basis. During the periodical checks, the system still broadcasts navigation messages, so the users do not need to pause their work.

3.5. Simulated Configuration Setups

Analysis and results in this research are performed on the Shackleton Crater; thus, DEM [48] is trimmed to match the area of interest. To simulate various LRNTS configuration setups, a number of points are digitized over the Shackleton DEM in order to obtain their 3D approximate positions. The points locations are not directed by any special rule, but rather spread around the crater. In Figure 4, the Shackleton Crater DEM is represented both as a false-color palette and a 300 m equidistance contour map overlapped with the possible locations of LRNTS transceiver nodes (marked as white triangles with their locally assigned IDs).

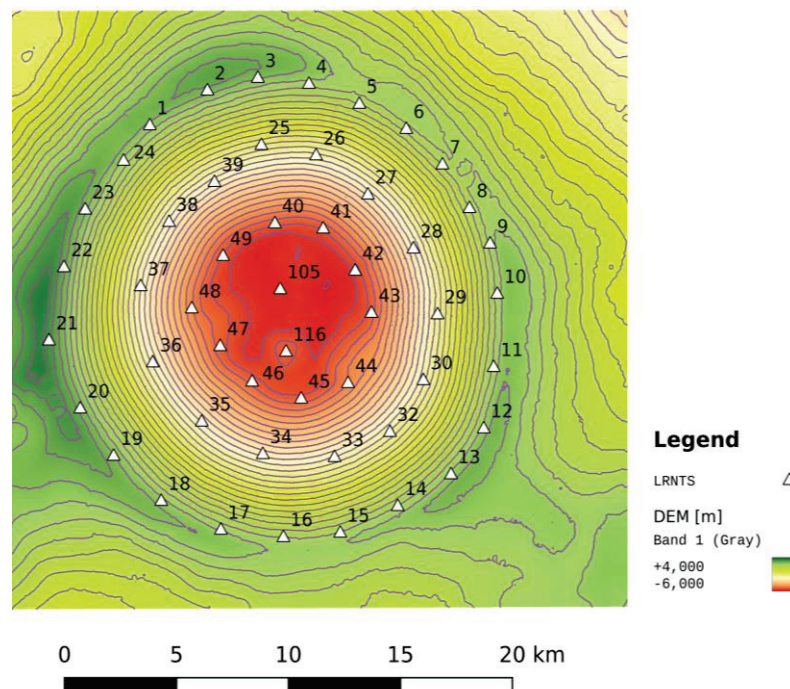


Figure 4. Candidate places for LRNTS transceivers.

The optimization of LRNTS treats locations and number of transceivers that would assure the best positioning performance within the crater. The optimal configuration of the LRNTS network should provide:

- enough measurands (i.e., number of transceiver nodes) for self-calibration of the system;
- signal coverage throughout (or, if not possible, for the majority of) the crater’s interior;

- reliable signal transmission by minimizing multipath effects.

The locations of the transceivers should allow the undisturbed mutual transmitting and receiving of navigation messages between all transceivers. The same goes for spreading the signals towards the crater bottom, where the surveying of construction sites will be done. The signals with lower elevation angles (closer to the ground) can experience multipath effects, since the transceivers are placed on the ground, not in space. Further analysis of Shackleton topography is performed by creating a slope map. The frequency histogram (Figure 5) of the Shackleton slope map shows that the majority of the crater is at cca 50° slope, which should be taken into account for future LRNTS utilization plans in order to avoid possible multipath effects during the transmission of transceivers' signals. The histogram values in Figure 5 are expressed in pixels.

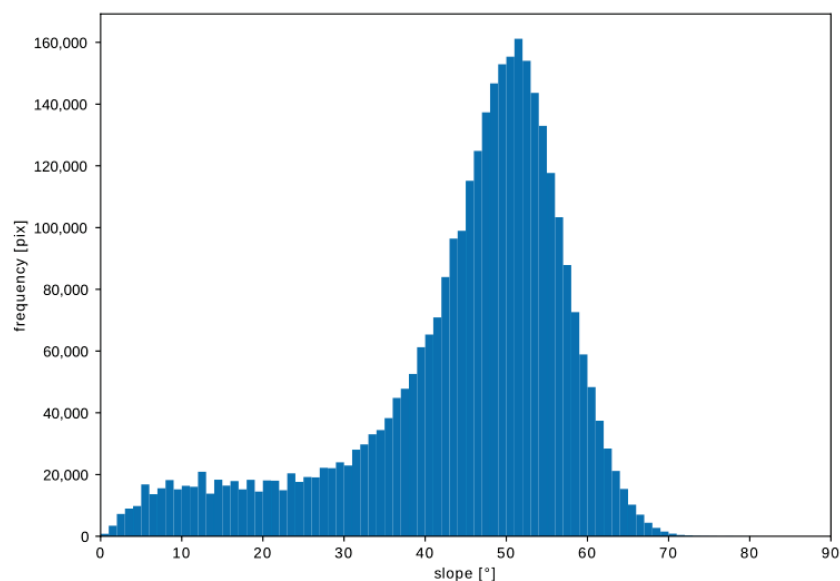


Figure 5. Histogram of frequencies for a developed slope map of the Shackleton Crater.

In addition to the careful planning of LRNTS transceivers' distribution in the sense of accuracy, the number and location of the transceivers should be optimized for the availability of the signals as well. Assuming future use of GNSS receivers for in-crater positioning, permanent visibility of at least four transceivers must be assured. Furthermore, for economic reasons, the total number of the transceiver nodes should be minimized.

Although a receiver can solve its position by collecting observations from only four satellites, experiences from terrestrial GNSS positioning show that, in realistic scenarios, it is not enough because of temporal obstacles that violate visibility of the sky. In the case of ground-based transceivers, that problem could arise as well. In addition, there is a practical maximum of the number of satellites where there is no significant increase in accuracy or reliability. Therefore, the selection of the number of transceivers per configuration and their locations is carried out by examining user experiences in terrestrial GNSS positioning.

First simulations involve 24 different configurations, from 5 to 24 transceivers. As stated before, the only criterion for choosing locations for the transceivers was their approximate uniform distribution along the crater. The positioning by four transceivers could be violated in the case of obstacles or a poor configuration. Therefore, we put 5 as a minimum for the number of LRNTS transceivers and 24 as a maximum, although the maximal number of the transceivers is theoretically not limited. However, increasing the number of LRNTS transceivers does not increase accuracy and reliability linearly. We have randomly chosen 33 different configurations. Among them, 12 are presented in this paper. Others are rejected because of their bad numerical figures.

The setups involve between 6 and 11 LRNTS transceivers. Individual setups with spatial allocation of the transceivers can be reviewed from Figure 6. Lines indicate intervisi-

bility between certain LRNTS transceivers. Only vectors between intervisible transceivers were included in the adjustment models.

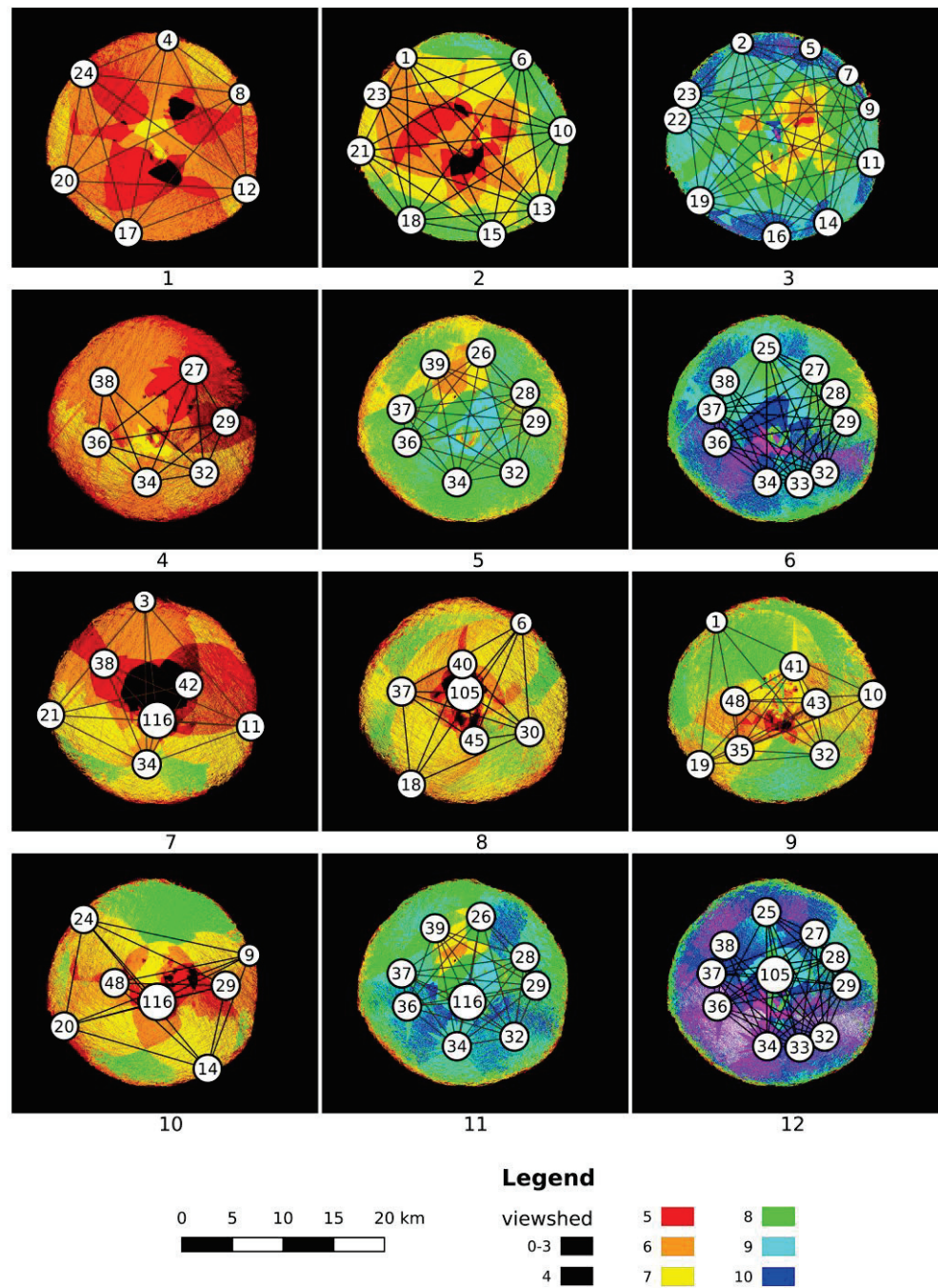


Figure 6. Viewsheds of transceiver signals.

For each configuration setup, a corresponding viewshed map is created, depicting the availability of LRNTS signals within the crater area, as shown in Table 1. In Figure 6, all maps 1–12 share the same color ramp, where each color represents a certain number of visible transceivers at the given point. All pixels with values below 4 are painted in black, suggesting that in those areas, LRNTS navigation is not possible due to the lack of the minimal number of visible transceivers. The locations of transceivers are marked as white circles, with the point ID within the circles. A quick review of the viewshed maps

indicates that the setups with more transceivers also imply better visibility on the surface of the bottom of the crater.

Table 1. LRNTS configuration setups.

Map Model No.	Number of Points	Number of Measurements	Number of Unknowns	% of Signal Availability
1	6	58	18	91.6
2	8	102	24	95.7
3	10	162	30	98.6
4	6	52	18	84.0
5	8	102	24	95.3
6	10	152	30	96.3
7	7	48	21	78.4
8	7	60	21	86.8
9	8	82	24	92.8
10	7	64	21	91.2
11	9	134	27	95.5
12	11	188	33	96.4

3.6. Self-Calibration

The self-calibration of LRNTS is performed as an iterative adjustment using the model elaborated in Section 3.3. Input parameters, in the sense of a priori quality characteristics and accuracy, are chosen by adapting standard error budget for GNSS positioning [68], adopting 300 cm for coarse-code code range accuracy and 5 mm for phase ranges. Multipath and atmospheric influences are neglected here. In addition, receiver clock bias is not treated in this study, because it refers to receiver crystal clocks, while all LRNTS transceivers hold atomic clocks aboard and use the same timescale for transmitting and receiving. The adjustment was performed adopting a 100 m spatial error of approximate LRNTS transceiver positions, resulting from DEM. The adjustment process converged after the third iteration in all tested models.

Table 2 summarizes the obtained results for all 12 tested models. Columns 2 to 7 contain minimum and maximum standard deviations of the points' spatial (3D), horizontal (2D), and vertical (1D) positions, respectively, which is further used for analyzing performance of the network geometry.

Table 2. LRNTS positioning performance depending on the model.

Map Model	(3D) σ_{xyz} (Min)	(3D) σ_{xyz} (Max)	(2D) σ_{xy} (Min)	(2D) σ_{xy} (Max)	(1D) σ_z (Min)	(1D) σ_z (Max)
(N°)	(mm)	(mm)	(mm)	(mm)	(mm)	(mm)
1	20.1	38.0	3.9	7.4	19.7	37.4
2	17.1	44.0	3.5	7.2	16.6	43.4
3	22.1	41.3	3.6	6.5	21.8	40.8
4	41.3	283.3	15.7	151.1	38.2	239.6
5	22.9	50.6	8.4	20.5	21.0	46.3
6	24.1	332.5	11.6	167	19.0	287.5
7	7.7	28.7	5.0	18.0	4.6	22.4
8	7.0	17.5	5.0	10.3	4.9	15.0
9	12.9	31.3	5.3	14.0	10.8	28.0
10	6.9	26.0	3.2	14.2	5.6	21.8
11	4.9	13.3	3.5	6.7	3.5	11.5
12	11.8	336.8	7.6	169.2	9.0	291.2

4. Discussion

Quality estimation of LRNTS is based on three criteria:

- (1) coverage of LRNTS navigation signals within the crater—viewsheds (Table 1 and Figure 6);

- (2) accuracy expressed as positional standard errors of the points (Table 2, Figures 7–9);
- (3) efficiency expressed as the number of points and measurements (Table 1).

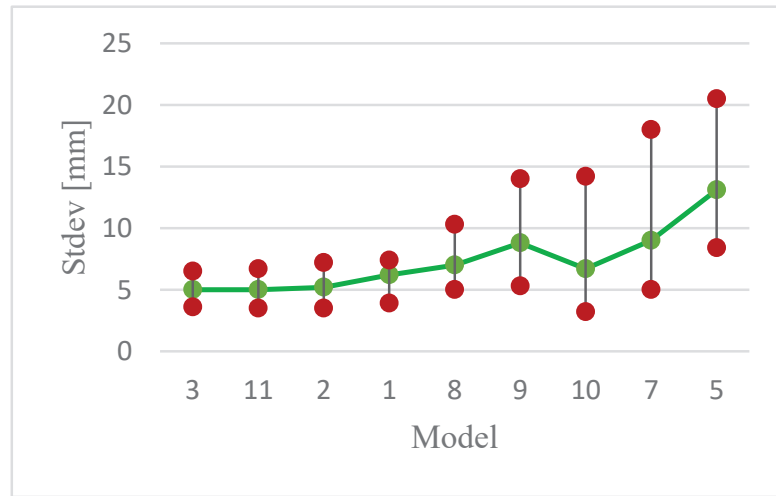


Figure 7. LRNTS horizontal standard deviations.

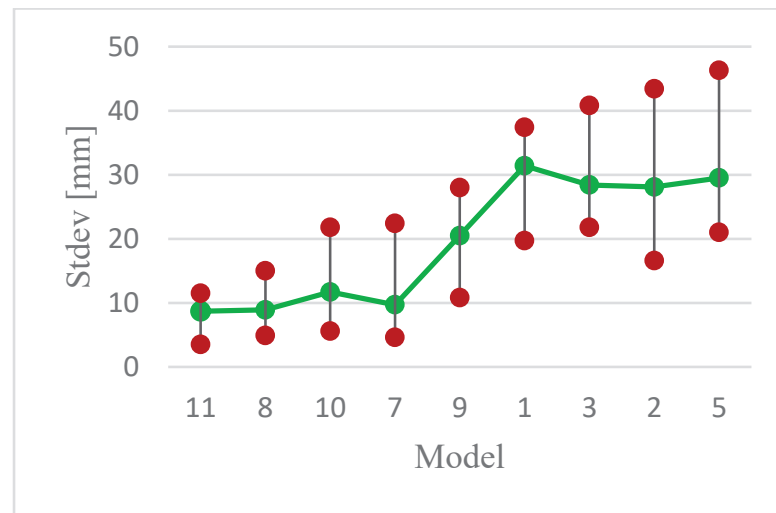


Figure 8. LRNTS vertical standard deviations.

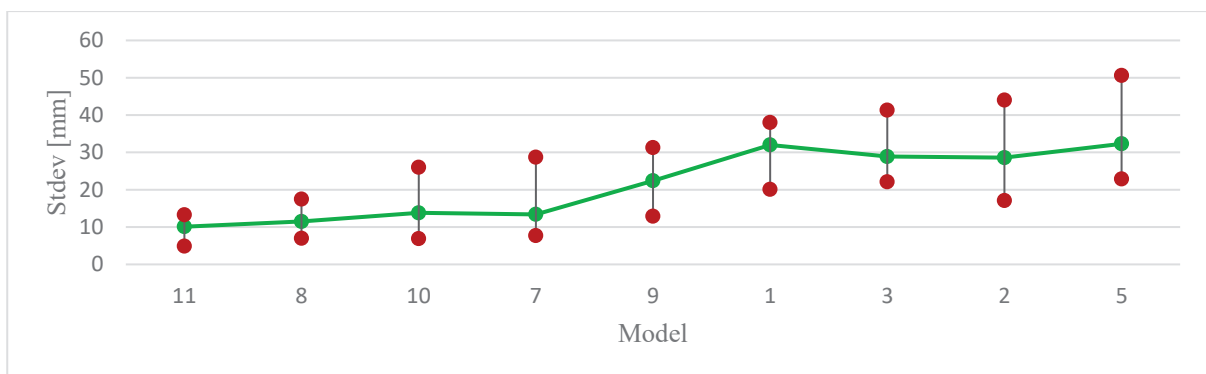


Figure 9. LRNTS spatial (3D) standard deviations.

Regarding the coverage of the crater area with transceiver signals, none of the configurations assure 100% signal availability within the crater. Table 1 displays the number of the transceivers in each configuration setup with the percentage of signal coverage within the crater. Among the 12 tested models, half of them (grey-shaded in Table 1) provide less than 95% signal availability, which limits their possible utilization.

Inspecting 3D position accuracies in Table 2, one can observe that the maximal standard deviations of the tested configuration setups are between 17.5 cm and 336.8 mm. Detailed analysis shows that the vertical component (z values) results in much larger standard deviations due to the adjustment linear model. Partial derivatives for the pseudo-distance P_{ij} (connecting transceivers i and j) over the unknown coordinate z_i of the design matrix A follow the form $\frac{\partial P_{ij}}{\partial z_i} = \frac{z_j - z_i}{D}$. Derivation over y_i and x_i gives analogue forms, replacing z with y and x , respectively. Since the transceiver height spans are smaller, in some cases, up to an order of value compared to horizontal components, the corresponding elements of A referring to the vertical component are proportionally smaller. Therefore, the cofactor matrix $Q_x = N^+ = (A^T P A)^{-1}$ produces elements related to the z coordinate much larger than for the x and y axes.

Bearing that in mind, the 3D problem is split into 2D + 1D. The calculated standard deviations of the horizontal positions and related vertical accuracies are given in columns 4–7 of Table 2. There are three models with extremely high standard deviations (shaded grey in Table 2). They are not taken into account with further processing. Graphical representations of the other nine models that fulfill the accuracy requirements, sorted with respect to their performance, are given in Figures 7–9.

The abscise holds the numbers of selected models (from Tables 1 and 2), while the results (minimum and maximum standard deviations) are given in mm and presented as short red vertical lines. The average standard deviation values for each model are connected with the green line.

Merging three criteria (viewsheds, accuracy, and the number of the transceivers), the optimal model is No. 11, with nine transceivers, a coverage of 95.5%, and maximal standard deviations of 6.7 mm for the horizontal position and 11.5 mm for the vertical component.

5. Conclusions

This paper suggests a new infrastructure for high-precision real-time positioning on the Moon, called the Lunar Regional Navigation Transceiver System. It is a ground system which transmits navigation messages similar to GNSS. The system itself is autonomous and capable of self-calibrating. It consists of a set of transceivers placed around the Lunar region where excavation or construction works are performed.

A case study presented here is implemented on the Shackleton Crater, which is a possible candidate for the first Lunar exploration works. A proof of a concept includes 12 different configuration setups for the transceivers' locations along the crater. All configurations were tested against accuracy, signal coverage (inter-visibility), and efficiency, in the sense of the number of the LRNTS nodes. Among 12 tested models, the setup consisting of nine nodes showed the best numerical figures, with horizontal accuracy of 6.7 mm and vertical accuracy of 11.5 mm and availability over 95.5% of the Shackleton area. If deployed in that way, such a reference frame allows centimeter-level real-time positioning of the user receivers throughout the crater. However, if millimeter-level accuracy is needed, local high-precision control networks can be developed around the desired construction spots in the same manner as in terrestrial applications. Then, the local control networks would be tied to the LRNTS coordinate system, including the points surveyed from the local network.

The results presented here can be replicated for other solar system bodies (preferably Mars) because the suggested methodology does not need permanent communication with the Earth, which makes the concept self-adjustable and self-sustainable. Practical implementation of this research could help all further missions aimed at Moon exploration, which will benefit from having a tested reliable system for precise positioning purposes during all construction and excavation works.

Author Contributions: Conceptualization, D.I.S.; methodology, D.I.S. and V.O.; software, V.O.; validation, J.R., V.P.-P. and G.V.; formal analysis, V.O.; investigation, D.I.S.; resources, D.I.S.; data curation, D.I.S. and V.O.; writing—original draft preparation, D.I.S. and V.O.; writing—review and editing, J.R., V.P.-P. and G.V.; visualization, D.I.S.; supervision, V.P.-P. and G.V.; project administration, V.P.-P. and G.V. All authors have read and agreed to the published version of the manuscript.

Funding: This research was funded by research program P2-0268 (ARRS Research and Infrastructure Programs) financed by the Slovenian Research Agency.

Data Availability Statement: All data used in this study are freely available on request to the authors.

Acknowledgments: This research was supported by the Slovenian Ministry of Education Science and Sport, Faculty of Natural Sciences and Engineering.

Conflicts of Interest: The authors declare no conflict of interest. The funders had no role in the design of the study; in the collection, analysis, or interpretation of data; in the writing of the manuscript; or in the decision to publish the results.

Abbreviations

The following abbreviations are used in this manuscript:

LRNTS	Lunar Regional Navigation Transceiver System
GNSS	Global Navigation Satellite System
ISRU	In Situ Resource Utilization
ISRO	Indian Space Research Organization
SLAM	Simultaneous Localization and Mapping
SINS	Strapdown Inertial Navigation System
QUEST	QUaternion ESTimator
SNE	Satellite Navigation Equipment
SCPA	Self-Calibrating Pseudolite Array
GPS	Global Navigation System
MMS	Magnetospheric Multiscale mission
GOES	Geostationary Operational Environmental Satellite
PSR	Permanently Shadowed Region
LRO	Lunar Reconnaissance Orbiter
SPA	South Pole Aitken
DEM	Digital Elevation Model
LLR	Lunar Laser Ranging
AFS	Atomic Frequency Standard
SIC	Successive Interference Calculation
STP	Space Time Processing

References

- Hurst, C. China's Rare Earth Elements Industry: What Can the West Learn? Institute for the Analysis of Global Security (IAGS). 2010. Available online: https://www.researchgate.net/publication/235080237_China_T1\textquoterights_Rare_Earth_Elements_Industry_What_Can_the_West_Learn (accessed on 13 January 2023).
- NASA. NASA's Lunar Exploration Program Overview. 2020. Available online: https://www.nasa.gov/sites/default/files/atoms/files/artemis_plan-20200921.pdf (accessed on 12 April 2022).
- Shekhtman, L.; Thompson, J.R. Asteroids—NASA Solar System Exploration, NASA. 2019. Available online: https://solarsystem.nasa.gov/asteroids-comets-and-meteors/asteroids/overview/?page=0&per_page=40&order=name+asc&search=&condition_1=101%3Aparent_id&condition_2=asteroid%3Abody_type%3Alike (accessed on 14 January 2023).
- ISECG. The Global Exploration Roadmap₂₀₂₂. 2022. Available online: https://www.globalspaceexploration.org/wp-content/isecg/GER_Supplement_Update_2022.pdf (accessed on 13 December 2022).
- Pittman, R.B.; Harper, L.D.; Newfield, M.E.; Rasky, D.J. Lunar Station: The Next Logical Step in Space Development. *New Space* **2016**, *4*, 7–14. [CrossRef]
- Goswami, N. India's space program, ambitions, and activities. *Asia Policy* **2020**, *15*, 43–49. [CrossRef]
- ESA. ESA—Gateway with Orion Docked Right. 2019. Available online: https://www.esa.int/ESA_Multimedia/Images/2019/05/Gateway_with_Orion_docked_right (accessed on 15 April 2022).
- ESA. Gateway to the Moon. 2019. Available online: https://www.esa.int/Science_Exploration/Human_and_Robotic_Exploration/Gateway_to_the_Moon (accessed on 15 April 2022).
- Li, C.; Wang, C.; Wei, Y.; Lin, Y. China's present and future lunar exploration program. *Science* **2019**, *365*, 238–239. [CrossRef]

10. Clark, S. Russia Looks to China as New Space Exploration Partner. Spaceflight Now. 2021. Available online: <https://spaceflightnow.com/2021/03/15/russia-looks-to-china-as-new-space-exploration-partner/> (accessed on 12 April 2022).
11. Rio Tinto. What in the World Do Mining and Rocket Science Have in Common? 2019. Available online: <https://www.riotinto.com/en/news/stories/mining-rocket-science-common> (accessed on 6 May 2022).
12. Woods, B. Caterpillar and NASA Developing Autonomous Vehicles to Mine the Moon. CNBC. 2019. Available online: <https://www.cnbc.com/2019/10/23/caterpillar-and-nasa-developing-autonomous-vehicles-to-mine-the-moon.html> (accessed on 6 May 2022).
13. Stupar, D.I.; Ogrizović, V.; Rošer, J.; Vižintin, G. Analytical and Numerical Solution for Better Positioning in Mines with Potential Extending Application in Space Mining. *Minerals* **2022**, *12*, 640. [CrossRef]
14. Liu, J.; Ren, X.; Yan, W.; Li, C.; Zhang, H.; Jia, Y.; Zeng, X.; Chen, W.; Gao, X.; Liu, D.; et al. Descent trajectory reconstruction and landing site positioning of Chang'E-4 on the lunar farside. *Nat. Commun.* **2019**, *10*, 4229. [CrossRef]
15. Imbriale, W.A. *Large Antennas of the Deep Space Network*; Monograph 4 Deep—Space Communications and Navigation Series; JPL: Pasadena, CA, USA; NASA: Washington, DC, USA, 2002.
16. Bilodeau, V.S.; Clerc, S.; Drai, R.; de Lafontaine, J. Optical navigation system for pin-point lunar landing. In *IFAC Proceedings Volumes (IFAC-PapersOnline)*; IFAC: New York, NY, USA, 2014; pp. 10536–10542. [CrossRef]
17. Ma, Y.Q.; Liu, S.C.; Sima, B.; Wen, B.; Peng, S.; Jia, Y. A precise visual localisation method for the Chinese Chang'e-4 Yutu-2 rover. *Photogramm. Rec.* **2020**, *35*, 10–39. [CrossRef]
18. Schönfeldt, M.; Grenier, A.; Delépaut, A.; Swinden, R.; Giordano, P.; Ventura-Traveset, J. Across the Lunar Landscape—Exploration with GNSS Technology—Inside GNSS—Global Navigation Satellite Systems Engineering. Policy, and Design, Inside GNSS. 2020. Available online: <https://insidegnss.com/across-the-lunar-landscape-exploration-with-gnss-technology/> (accessed on 6 May 2022).
19. Guan, X.; Wang, X.; Fang, J.; Feng, S. An innovative high accuracy autonomous navigation method for the Mars rovers. *Acta Astronaut.* **2014**, *104*, 266–275. [CrossRef]
20. Xu, F.; Fang, J. Velocity and position error compensation using strapdown inertial navigation system/celestial navigation system integration based on ensemble neural network. *Aerosp. Sci. Technol.* **2008**, *12*, 302–307. [CrossRef]
21. Wei, X.; Cui, C.; Wang, G.; Wan, X. Autonomous positioning utilizing star sensor and inclinometer. *Measurement* **2019**, *131*, 132–142. [CrossRef]
22. Hamera, K.E.; Mosher, T.; Gefreh, M.; Paul, R.; Slavkin, L.; Trojan, J. An evolvable lunar communication and navigation constellation architecture. In Proceedings of the 26th AIAA International Communications Satellite Systems Conference ICSSC, San Diego, CA, USA, 10–12 June 2008.
23. Delépaut, A.; Giordano, P.; Ventura-Traveset, J.; Blonski, D.; Schönfeldt, M.; Schoonejans, P.; Aziz, S.; Walker, R. Use of GNSS for lunar missions and plans for lunar in-orbit development. *Adv. Space Res.* **2020**, *66*, 2739–2756. [CrossRef]
24. Mikrin, E.A.; Mikhailov, M.V.; Orlovskii, I.V.; Rozhkov, S.N.; Krasnopol'skii, I.A. Satellite Navigation of Lunar Orbiting Spacecraft and Objects on the Lunar Surface. *Gyroscope Navig.* **2019**, *10*, 54–61. [CrossRef]
25. LeMaster, E.A. Self Calibrating Pseudolite Arrays—Theory and Experiment. Master's Thesis, Stanford University, Stanford CA, USA, 2002. Available online: <https://web.stanford.edu/group/arl/cgi-bin/drupal/sites/default/files/public/publications/LeMaster%202002.pdf> (accessed on 27 February 2023).
26. Lemaster, E.A.; Rock, S.M. A Local-Area GPS Pseudolite-Based Mars Navigation System. In Proceedings of the IEEE 10th International Conference on Advanced Robotics, Budapest, Hungary, 22–25 August 2001.
27. Stone, J.M.; LeMaster, E.A.; David Powell, J.; Rock, S. GPS Pseudolite Transceivers and their Applications. In Proceedings of the 1999 National Technical Meeting of the Institute of Navigation, San Diego, CA, USA, 25–27 January 1999.
28. Cobb, H.S. GPS Pseudolites: Theory, Design, and Applications. 1997. Available online: <https://web.stanford.edu/group/scpnt/gpslab/pubs/theses/StewartCobbThesis97.pdf> (accessed on 26 February 2023).
29. Jenner, L. NASA Eyes GPS at the Moon for Artemis Missions. NASA Space Technology. 2019. Available online: <http://www.nasa.gov/feature/goddard/2019/nasa-eyes-gps-at-the-moon-for-artemis-missions> (accessed on 1 May 2022).
30. HAKUTO-R Mission 1 | ispace. Available online: <https://ispace-inc.com/m1> (accessed on 17 January 2023).
31. NASA: Artemis, I. Available online: <https://www.nasa.gov/specials/artemis-i/> (accessed on 26 February 2023).
32. ESA—Moonlight. Available online: https://www.esa.int/Applications/Telecommunications_Integrated_Applications/Moonlight (accessed on 26 February 2023).
33. Baird, D. NASA Mirrors on ESA Pathfinder to Enhance Lunar Navigation. 2022. Available online: <http://www.nasa.gov/feature/goddard/2022/nasa-mirrors-on-esa-pathfinder-to-enhance-lunar-navigation> (accessed on 26 February 2023).
34. CSEM. *The Scientific Context for Exploration of the Moon*; National Academies Press: Washington, DC, USA, 2007. [CrossRef]
35. Mitchell, J.; Lawrence, S.; Robinson, M.; Speyerer, E.; Denevi, B. Using complementary remote sensing techniques to assess the presence of volatiles at the lunar north pole. *Planet. Space Sci.* **2018**, *162*, 133–147. [CrossRef]
36. Mazarico, E.; Neumann, G.A.; Smith, D.E.; Zuber, M.T.; Torrence, M.H. Illumination conditions of the lunar polar regions using LOLA topography. *Icarus* **2011**, *211*, 1066–1081. [CrossRef]
37. Bussey, D.B.J.; Spudis, P.D.; Robinson, M.S. Illumination conditions at the lunar South Pole. *Geophys. Res. Lett.* **1999**, *26*, 1187–1190. [CrossRef]
38. Wingo, D. Site Selection for Lunar Industrialization, Economic Development, and Settlement. *New Space* **2016**, *4*, 19–39. [CrossRef]

39. Zuber, M.T.; Head, J.W.; Smith, D.E.; Neumann, G.A.; Mazarico, E.; Torrence, M.H.; Aharonson, O.; Tye, A.R.; Fassett, C.I.; Rosenburg, M.A.; et al. Constraints on the volatile distribution within Shackleton crater at the lunar south pole. *Nature* **2012**, *486*, 378–381. [[CrossRef](#)]
40. Vanoutryve, B.; de Rosa, D.; Fisackerly, R.; Houdou, B.; Carpenter, J.; Philippe, C.; Pradier, A.; Jojaghalian, A.; Espinasse, S.; Gardini, B. *An Analasys of Illumination and Communication Conditions near Lunar South Pole Based on Kaguya Data*; ESA: Paris, France, 2010.
41. Barker, M.K.; Mazarico, E.; Neumann, G.A.; Zuber, M.T.; Haruyama, J.; Smith, D.E. A new lunar digital elevation model from the Lunar Orbiter Laser Altimeter and SELENE Terrain Camera. *Icarus* **2016**, *273*, 346–355. [[CrossRef](#)]
42. Kokhanov, A.A.; Karachevtseva, I.P.; Zubarev, A.E.; Patraty, V.; Rodionova, Z.F.; Oberst, J. Mapping of potential lunar landing areas using LRO and SELENE data. *Planet. Space Sci.* **2017**, *162*, 179–189. [[CrossRef](#)]
43. Basilevsky, A.T.; Krasilnikov, S.S.; Ivanov, M.A.; Malenkov, M.I.; Michael, G.G.; Liu, T.; Head, J.W.; Scott, D.R.; Lark, L. Potential Lunar Base on Mons Malapert: Topographic, Geologic and Trafficability Considerations. *Sol. Syst. Res.* **2019**, *53*, 383–398. [[CrossRef](#)]
44. Mahoney, E. (Ed.) *The Global Exploration Roadmap Supplement Octobar*; NASA: Washington, DC, USA, 2022. Available online: https://www.nasa.gov/sites/default/files/atoms/files/ger-supplement-update-2022-final-10-6-22_tagged.pdf (accessed on 11 December 2022).
45. Ludivig, P.; Olivares-mendez, M.; Diaz, A.C.; Ivanov, D.; Voos, H.; Lamamy, J. Testing Environments for Lunar Surface Perception Systems; Combining Indoor Facilities, Virtual Environments and Analogue Field Tests. In Proceedings of the I-SAIRAS 2020, Pasadena, CA, USA, 19–23 October 2020.
46. Sherwood, B. Principles for a practical Moon base. *Acta Astronaut.* **2019**, *160*, 116–124. [[CrossRef](#)]
47. Powering the Moon: Designing a Microgrid for Future Lunar Base. 2022. Available online: <https://phys.org/news/2022-05-powering-moon-microgrid-future-lunar-1.html> (accessed on 11 December 2022).
48. LOLA, S.T. Moon LRO LOLA DEM 118m v1 | USGS Astrogeology Science Center. 2014. Available online: https://astrogeology.usgs.gov/search/details/Moon/LRO/LOLA/Lunar_LRO_LOLA_Global_LDEM_118m_Mar2014/cub (accessed on 6 May 2021).
49. Williams, J.G.; Boggs, D.H.; Folkner, W.M. *DE430 Lunar Orbit, Physical Librations, and Surface Coordinates*; Jet Propulsion Laboratory: Pasadena, CA, USA, 2013; pp. 1–19. [[CrossRef](#)]
50. Folkner, W.M.; Williams, J.G.; Boggs, D.H.; Park, R.S.; Kuchynka, P. The Planetary and Lunar Ephemerides DE430 and DE431. *Interplanet. Netw. Prog. Rep.* **2014**, *196*, 42–196.
51. Chowdhury, D.D. *NextGen Network Synchronization*; Springer: Berlin/Heidelberg, Germany, 2021. [[CrossRef](#)]
52. Martinez, F.J.G. *Performance of New GNSS Satellite Clocks*; KIT Scientific Publishing: Karlsruhe, Germany, 2014. [[CrossRef](#)]
53. Madhani, P.H.; Axelrad, P.; Krumvieda, K.; Thomas, J. Application of successive interference cancellation to the GPS pseudolite near-far problem. *IEEE Trans. Aerosp. Electron. Syst.* **2003**, *39*, 481–488. [[CrossRef](#)]
54. Martin, S.; Kuhlen, H.; Abt, T. Interference and regulatory aspects of GNSS pseudolites. In Proceedings of the 18th International Technical Meeting of the Satellite Division of the Institute of Navigation, ION GNSS 2005, Long Beach, CA, USA, 13–16 September 2005. [[CrossRef](#)]
55. Chang, C.L.; Juang, J.C. Performance analysis of narrowband interference mitigation and near-far resistance scheme for GNSS receivers. *Signal Process.* **2010**, *90*, 2676–2685. [[CrossRef](#)]
56. Marathe, T.; Daneshmand, S.; Lachapelle, G. Pseudolite interference mitigation and signal enhancements using an antenna array. In Proceedings of the 2015 International Conference on Indoor Positioning and Indoor Navigation, IPIN 2015, Banff, AB, Canada, 13–16 October 2015. [[CrossRef](#)]
57. Zheng, Z.H.; Wang, B.; Zhou, Z.Q.; Gao, Z.F. A scene matching method for automatic and precise soft landing on the lunar surface. *Beijing Ligong Daxue Xuebao/Trans. Beijing Inst. Technol.* **2013**, *33*, 172–177.
58. Remesh, N.; Ramanan, R.V.; Lalithambika, V.R. A Novel Indirect Scheme for Optimal Lunar Soft Landing at a Target Site. *J. Inst. Eng. Ser. C* **2021**, *102*, 1379–1393. [[CrossRef](#)]
59. Hu, T.; He, L.; Cao, T.; Zhang, H.; Hu, Y.; Qian, Z. Autonomous Obstacle Detection and Avoidance of Lunar Landing Based on Active and Passive Sensors. In Proceedings of the 2021 International Symposium on Computer Science and Intelligent Controls, ISCSIC 2021, Rome, Italy, 12–14 November 2021. [[CrossRef](#)]
60. Wong, U.H.; Wu, Y.; Wong, H.C.; Liang, Y.; Tang, Z. Modeling the reflectance of the lunar regolith by a new method combining Monte Carlo ray tracing and Hapke’s model with application to chang’e-1 IIM data. *Sci. World J.* **2014**, *2014*, 457138. [[CrossRef](#)] [[PubMed](#)]
61. Petrova, E.V.; Markiewicz, W.J.; Keller, H.U. Regolith Surface Reflectance: A New Attempt to Model. *Sol. Syst. Res.* **2001**, *35*, 278–290. [[CrossRef](#)]
62. Heiken, G.H.; Vaniman, D.T.; French, B.M. *Lunar Sourcebook: A User’s Guide to the Moon*; Cambridge University Press: Cambridge, UK, 1991.
63. Gaier, J.R. The Effects of Lunar Dust on EVA Systems during the Apollo Missions. 2005. Available online: <http://www.sti.nasa.gov> (accessed on 11 December 2022).
64. Budzyń, D.; Zare-Behtash, H.; Cowley, A.; Cammarano, A. Implicit lunar dust mitigation technology: Compliant mechanisms. *Acta Astronaut.* **2023**, *203*, 146–156. [[CrossRef](#)]

65. Budzyń, D.; Tuohy, E.; Garrivier, N.; Schild, T.; Cowley, A.; Cruise, R.; Adachi, M.; Zare-Behtash, H.; Cammarano, A. Lunar Dust: Its Impact on Hardware and Mitigation Technologies. In Proceedings of the 46th Aerospace Mechanisms Symposium, Houston, TX, USA, 11–13 May 2022.
66. Climent, B.; Torroba, O.; González-Cinca, R.; Ramachandran, N.; Griffin, M.D. Heat storage and electricity generation in the Moon during the lunar night. *Acta Astronaut.* **2014**, *93*, 352–358. [[CrossRef](#)]
67. Ulamec, S.; Biele, J.; Trollope, E. How to survive a Lunar night. *Planet. Space Sci.* **2010**, *58*, 1985–1995. [[CrossRef](#)]
68. Hofmann-Wellenhof, E.; Lichtenegger, B.; Wasle, H. Observables. In *GNSS—Global Navigation Satellite Systems*; Springer Vienna: Vienna, Austria, 2007; pp. 105–160. [[CrossRef](#)]

Disclaimer/Publisher’s Note: The statements, opinions and data contained in all publications are solely those of the individual author(s) and contributor(s) and not of MDPI and/or the editor(s). MDPI and/or the editor(s) disclaim responsibility for any injury to people or property resulting from any ideas, methods, instructions or products referred to in the content.

MDPI
St. Alban-Anlage 66
4052 Basel
Switzerland
www.mdpi.com

Minerals Editorial Office
E-mail: minerals@mdpi.com
www.mdpi.com/journal/minerals



Disclaimer/Publisher's Note: The statements, opinions and data contained in all publications are solely those of the individual author(s) and contributor(s) and not of MDPI and/or the editor(s). MDPI and/or the editor(s) disclaim responsibility for any injury to people or property resulting from any ideas, methods, instructions or products referred to in the content.



Academic Open
Access Publishing

mdpi.com

ISBN 978-3-7258-0523-5